

**Model Complexes of Heme Protein NO
Adducts: Syntheses, Spectroscopy, Electronic
Structures, and Reactivity**

Dissertation

zur Erlangung des Doktorgrades
der Mathematisch-Naturwissenschaftlichen Fakultät
der Christian-Albrechts-Universität
zu Kiel

vorgelegt von

Koombil Kummaya Praneeth. V
geboren in Tellicherry, India

Kiel, 2007

Referent/in:	Prof. Dr. F. Tuzek
Korreferent/in:	Prof. Dr. N. Stock
Tag der mündlichen Prüfung:	01.02.2008
Zum Druck genehmigt:	Kiel, den 01.02.2008

Prof. Dr. J. Grotemeyer, Dekan

Kurzzusammenfassung

In dieser Arbeit wurden Eisenporphyrin-NO Komplexe mit und ohne axialen Liganden (N- oder S-Donor) als Modellsysteme für NO-gebundene Hämproteine synthetisiert, welche in biologischen Systemen wie der bakteriellen Stickstoffmonoxidreduktase (NorBC), der Stickstoffmonoxidreduktase in Pilzen (P450nor), den Nitrophorinen, der löslichen Guanylatcyclase und der Stickstoffmonoxidsynthase vorkommen. Detaillierte spektroskopische Untersuchungen der elektronischen Strukturen und Reaktivitäten dieser Modellsysteme werden hier vorgestellt. Die Unterschiede in den elektronischen Strukturen zwischen fünffach-koordiniertem (5C) $[\text{Fe}^{\text{II}}(\text{TPP})(\text{NO})]$ und sechsfach-koordiniertem (6C) $[\text{Fe}^{\text{II}}(\text{TPP})(\text{MI})(\text{NO})]$ (TPP = Tetraphenylporphyrin; MI = 1-Methylimidazol) wurden mit Hilfe des magnetischen Zirkulardichroismus (MCD), gekoppelt mit DFT-Rechnungen, untersucht. Ein reiner MCD C-Term wird im Fall des 5C Komplexes aufgrund der großen Übertragung von Spindichte vom NO auf das Eisen(II) beobachtet, was zu einer elektronischen Struktur mit merklichem $\text{Fe}(\text{I})\text{-NO}^+$ -Charakter führt. Durch das Binden des sechsten Liganden wird Elektronendichte vom Eisen auf das NO zurückgeschoben, was zu einer $\text{Fe}(\text{II})\text{-NO}(\text{Radikal})$ elektronischen Struktur führt (MCD A- und B-Terme werden beobachtet). UV-Vis- und $^1\text{H-NMR}$ -Bindungsstudien von N-Donorliganden an 5C Komplexe zeigen, dass die Koordination des axialen Liganden zu einer Schwächung der Fe-NO Bindung führt, wodurch die Abspaltung des NO's induziert wird. Die Kraftkonstanten der N-O- und Fe-NO-Bindungen sind im 5C Komplex größer als im 6C Komplex, was in Übereinstimmung mit einer Schwächung der Fe-NO Bindung im 6C Komplex ist. DFT Rechnungen zeigen, dass die Bildung von $\text{Fe}(\text{II})\text{-NO}$ Komplexen um ~ 7.5 kcal/mol im Vergleich zu entsprechenden $\text{Fe}(\text{III})\text{-NO}$ Komplexen favorisiert ist.

Verschiedene Thiolat-koordinierte $\text{Fe}(\text{II})\text{-NO}$ Komplexe wurden in Lösung synthetisiert und mit Hilfe der EPR-Spektroskopie untersucht. Die erhaltenen g-Werte und die ^{14}N -Hyperfeinaufspaltung zeigen, dass die Wechselwirkung der Thiolate mit der $\text{Fe}(\text{II})\text{-NO}$ Einheit schwach ist. Außerdem wurde die Wechselwirkung von NO mit $[\text{Fe}^{\text{III}}(\text{TPP})(\text{SPhF}_4)]$ bei tiefen Temperaturen mit Hilfe der UV-Vis Spektroskopie *in-situ* untersucht.

Die oben beschriebenen Bindungsstudien von N-Donorliganden an 5C Eisen(II)-NO Komplexe haben gezeigt, dass die Synthese eines stabilen 6C Komplexes in Lösung in Abwesenheit von überschüssiger Base schwierig ist. Dieses Ziel wurde mit Hilfe eines kovalent an das Porphyrin gebundenen N-Donorliganden realisiert. Die N-O Schwingungsfrequenz $\nu(\text{NO})$ in den so erhaltenen Eisen(II)-NO Komplexen wurde mit Hilfe der FT-IR Spektroskopie bestimmt. Für den Liganden $\text{H}_2(\text{T-}o\text{F}_2\text{PP-BzIM})$ wurde eine Frequenz von 1644 cm^{-1} bestimmt, ein Wert der jedoch immer noch höher liegt als im Fall eines freien Imidazol-Liganden. Darüber hinaus wurde ein Häm/Nicht-Häm bis-NO-Komplex synthetisiert und als ein vollständiges Strukturmodell für das aktive Zentrum der NorBC charakterisiert.

Abstract

In this thesis, iron-porphyrin NO complexes with and without axial ligand (N-donor or S-donor) have been synthesized as models for NO bound heme proteins present in biological systems such as bacterial nitric oxide reductase (NorBC), fungal nitric oxide reductase (P450nor), nitrophorins, soluble guanylate cyclase, and nitric oxide synthase. The detailed spectroscopic investigations, electronic structures, and reactivities of these model systems are presented in this work. The difference in the electronic structures between the five-coordinate (5C) $[\text{Fe}^{\text{II}}(\text{TPP})(\text{NO})]$ and the six-coordinate (6C) $[\text{Fe}^{\text{II}}(\text{TPP})(\text{MI})(\text{NO})]$ (TPP = tetraphenylporphyrin; MI = 1-methylimidazole) has been evaluated using magnetic circular dichroism (MCD) spectroscopy together with DFT calculations. The MCD **C** term is observed in the 5C case due to a large transfer of spin density from NO to Fe(II), resulting in an electronic structure with noticeable Fe(I)-NO⁺ character. Upon binding the sixth ligand, the electron density is pushed back from the iron to NO, resulting in an Fe(II)-NO(radical) type electronic structure (MCD **A** and **B** terms). UV-vis and ¹H NMR binding studies of N-donor ligands to the 5C complexes indicate that the coordination of axial ligands weakens the Fe-NO bond, thereby inducing denitrosylation. The obtained force constants of N-O and Fe-NO bonds are larger for the 5C compared to the 6C case, also in accordance with the weakening of the Fe-NO bond in the 6C complexes. DFT calculations show that the formation of nitrosyl complexes is energetically more favorable for ferrous compared to ferric systems by ~7.5 kcal/mol.

The thiolate coordinated Fe(II)-NO complexes have been synthesized and investigated in solution using EPR spectroscopy. From the obtained *g* values and ¹⁴N hyperfine splittings, it is concluded that the interaction of thiolates with the Fe(II)-NO center is weak. In addition, the interaction of NO with $[\text{Fe}^{\text{III}}(\text{TPP})(\text{SPhF}_4)]$ has been investigated at low temperature using in-situ UV-vis spectroscopy.

The synthesis of a stable six-coordinate complex in solution, in the absence of excess base, has been achieved with covalently attached axial N-donor ligands to iron(II)-porphyrins. The $\nu(\text{NO})$ value of 1644 cm⁻¹ from FT-IR shows weaker binding of benzyl linked imidazole to the Fe(II)-NO center compared to free MI. Furthermore, a heme/non-heme dinitrosyl complex has been synthesized and characterized as a complete structural model for the NorBC active site.

This thesis is dedicated to my Achan and Amma

Table of Contents

1. Introduction	08
Heme Nitrosyls.....	08
Nitric Oxide Synthase and NO Biosynthesis.....	09
Soluble Guanylate Cyclase.....	11
Denitrification.....	13
1.4.1 Bacterial and Fungal Nitric Oxide Reductases.....	15
1.5 Nitrophorins.....	21
2. Overview	25
3. Instrumentation and Background	
3.1 Fourier Transform Infrared Spectroscopy	
3.1.1 Basic Theory and Principles of Infrared Spectroscopy.....	27
3.1.2 Experimental Setup of FT-IR.....	29
3.2 Raman Spectroscopy	
3.2.1 Basic Theory and Setup of Raman Spectroscopy.....	30
3.3 Electron Paramagnetic Resonance Spectroscopy	
3.3.1 Basic Theory and Principles of EPR Spectroscopy.....	32
3.3.2 EPR Instrumentation.....	35
3.4 Experimental Section	
3.4.1 Syntheses with NO and Sample Preparation.....	36
3.4.2 Spectroscopic Instrumentation.....	36
3.4.2.1 FT-IR Spectroscopy.....	36
3.4.2.2 Nonresonance Raman and resonance Raman Spectroscopy.....	37
3.4.2.3 Magnetic Circular Dichroism Spectroscopy.....	37
3.4.2.4 UV-vis Spectroscopy.....	37
3.4.2.5 ¹ H NMR Spectroscopy.....	37
3.4.2.6 EPR Spectroscopy.....	37

3.4.2.7	Mass Spectroscopy.....	38
3.4.3.	Density Functional Calculations.....	38
4.	Ferrous and Ferric Heme Nitrosyls with <i>trans</i> N-Donor Ligands	
4.1	Scope of this Project.....	39
4.2	Spin Density Distribution in Five- and Six-Coordinate Iron(II)-Porphyrin NO Complexes Evidenced by Magnetic Circular Dichroism Spectroscopy <i>Inorg. Chem.</i> 2005 , <i>44</i> , 2570-2572.....	42
4.3	Spectroscopic Properties and Electronic Structure of Five- and Six-Coordinate Iron(II) Porphyrin NO Complexes: Effect of the Axial N-Donor Ligand. <i>Inorg. Chem.</i> 2006 , <i>45</i> , 2795-2811.....	46
4.4	Binding of NO to Ferric Hemes: Electronic Structure of Six-Coordinate Iron(III)-Porphyrin NO Complexes.....	64
5.	Thiolate Coordination to Iron-porphyrin Nitrosyls	
5.1	Scope of this Project.....	86
5.2	Thiolate Coordination to Fe(II)-Porphyrin NO Centers <i>J. Inorg. Biochem.</i> 2005 , <i>99</i> , 940-948 (special issue: Heme-Diatomic Interactions) Erratum: <i>J. Inorg. Biochem.</i> 2005 , <i>99</i> , 1744.....	88
5.3	Thiolate Coordination to Ferric Porphyrin NO Complexes: Spectroscopic Characterization.....	100
6.	Sophisticated Models for Bacterial Nitric Oxide Reductase (NorBC)	
6.1	Scope of this Project.....	110
6.2	Syntheses, Electronic and Vibrational Properties of Iron-Porphyrin NO Complexes with Covalently Attached N-Donor Ligands.....	113
6.3	A Complete Structural Model for Bacterial Nitric Oxide Reductase (NorBC): Synthesis, Characterization, and Spectroscopic Properties.....	136
7.	Collaborative Investigations	
7.1	Scope of this Project.....	155
7.2	Spectroscopic Properties and Electronic Structures of Pentammineruthenium(II) Dinitrogen Oxide and Corresponding Nitrosyl Complexes: Binding Mode of N ₂ O and Reactivity.	

	<i>Inorg. Chem.</i> 2004 , <i>43</i> , 6979-6994.....	158
7.3	Electronic structure of Iron(II)-Porphyrin Nitroxyl Complexes: Molecular Mechanism of Fungal Nitric Oxide Reductase (P450nor) J. Comp. Chem. 2006 , <i>27</i> , 1338-1351.....	175
7.4	Quantum Chemistry-Based Analysis of the Vibrational Spectra of Five- Coordinate Metalloporphyrins [M(TPP)Cl] <i>Inorg. Chem.</i> 2006 , <i>45</i> , 2835-2856.....	190
7.5	Structural and Spectroscopic Characterization of Mononuclear Copper(I) Nitrosyl Complexes: End-on versus Side-on Coordination of NO to Copper(I) <i>J. Am. Chem. Soc.</i> (2007 , Accepted).....	213
8.	Summary	223
9.	Curriculum Vitae	229
10.	Publication List	232
11.	Acknowledgement	234

Chapter 1

1 Introduction

My doctoral Thesis focuses on the syntheses, spectroscopic properties, and electronic structures of several iron-porphyrin nitric oxide (NO) complexes relevant to the heme nitrosyl (Heme-NO) structures and important functions in biology. In particular, emphasis is put on bacterial nitric oxide reductase model systems. In addition, mechanistic investigations on the reactivities of some of the model systems have been performed using various spectroscopic methods. Spectroscopic techniques employed in my doctoral research are: electronic absorption (UV-vis), vibrational (FT-IR, non-resonance Raman and resonance Raman), magnetic circular dichroism (MCD), magnetic resonance (NMR and EPR), and mass spectrometry. Density functional calculations (DFT) have been employed in order to evaluate the spectroscopic properties, electronic structures, and reactivity of the model complexes investigated. Most of my doctoral research (2003 - 2006) has been carried out at the Institut für Anorganische Chemie, Universität Kiel, Germany, and the final year (2006 - 2007) of my work has been conducted at the Department of Chemistry, University of Michigan, Ann Arbor, USA, under the guidance of Prof. Dr. Nicolai Lehnert. Instrumental facilities to carry out this research have been available in the group of Prof. Dr. Felix Tuczek (Kiel), Prof. Dr. Nicolai Lehnert (Michigan), and also at the central facility at the Department of Chemistry, University of Michigan. MCD data for the model complexes described in the Chapter 4 were obtained at the Max-Planck Institut für Bioanorganische Chemie, Mülheim, Germany, in collaboration with Prof. Dr. Frank Neese. EPR measurements described in Chapter 5 were obtained in collaboration with Dr. Erhard Haupt, Institut für Anorganische Chemie, Universität Hamburg.

1.1 Heme Nitrosyls

Nitric oxide (NO) is a ubiquitous free radical present in most living organisms. Its chemistry and biochemistry have been explored by researches for many years. However, the surprising role of NO as the endothelium derived relaxation factor in living systems has been revealed only in the late 1980's by Ignarro and Moncada.¹ It is now known that NO plays a vital role in various

physiological and pathophysiological functions, and its importance has been highlighted in the Science magazine by selecting NO as molecule of the year in 1992.² NO regulates various biological functions³ including blood flow, penile erection, platelet reactivity, neurotransmission, and acts as cytotoxic defensive agent against tumor cells and pathogens. Nitric oxide has also attracted coordination chemists due to its interesting redox active behavior.⁴ NO can be easily oxidized to the nitrosonium ion (NO^+) or can be reduced to the nitroxide ion (NO^-), which is isoelectronic with O_2 . Correspondingly, a very large volume of scientific papers has been published in the interesting field of NO complexes of transitional metals.

NO has a short half life of less than one second, when exposed to biological tissue and is highly reactive to other molecules such as dioxygen, superoxide radicals, or heme proteins. In particular, nitric oxide interaction with ferric and ferrous heme proteins attracted much attention due to its biological significance as described above.⁵ Heme-NO complexes in biology could be either five-coordinate in the absence of an axial ligand, or six-coordinate with bound axial ligands such as histidine or cysteine. The presence and absence of the sixth ligand is vital in controlling the activity of the heme-NO complexes. The heme-NO adduct is observed in nitric oxide synthase, soluble guanylate cyclase, nitric oxide reductases and nitrophorins. These NO-bound proteins carry out important biotransformations with specific functions. The following sections briefly describe the structure, properties, functions, and importance of each heme-NO adduct mentioned above.

1.2 Nitric oxide Synthase and NO Biosynthesis

Nitric oxide is synthesized *in vivo* by the nitric oxide synthase enzymes (NOS). These enzymes catalyze the five electron oxidation of L-arginine to produce L-citrulline and NO as shown in Figure 1.0.⁶ This family of enzymes is present in various cells and is classified into three subtypes depending on the cell types they occur in.⁷ Two constitutive calcium-dependent forms are known, one discovered in endothelium cells called eNOS, the other present in neuronal or brain cells, known as nNOS. The third subtype is an inducible calcium-independent enzyme, especially present in macrophages, and is represented as iNOS. All three subtypes of NOS require heme, calmodulin, flavin adenine dinucleotide (FAD), flavin mononucleotide (FMN) and

tetrahydrobiopterin (BH₄) as cofactors and NADPH and molecular oxygen as cosubstrates to oxidize L-arginine.^{6c,8}

Characterization of the heme center in NOS has been accomplished by employing electronic absorption, EPR and resonance Raman spectroscopic techniques.⁹ The heme iron is axially coordinated to the protein via a cysteine thiolate residue, as in the case of cytochrome P450s, and is five-coordinate high spin without a sixth ligand bound in the ferric state of the enzyme.

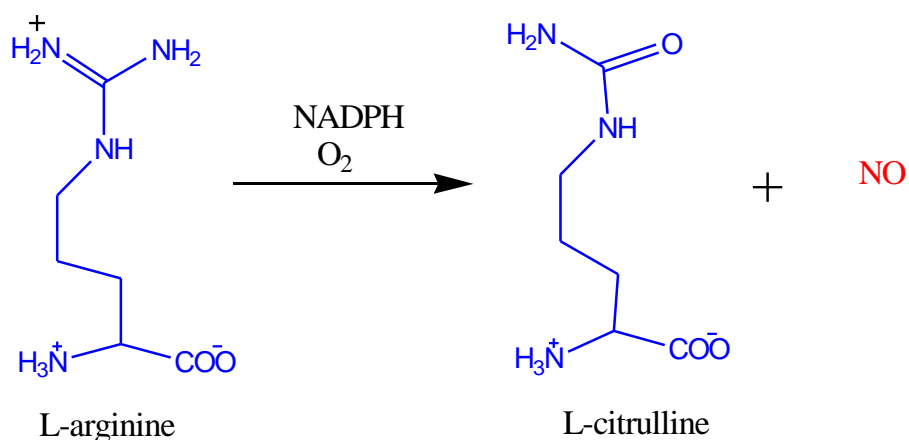


Figure 1.0. Cellular biosynthesis of NO from L-arginine by NOS.

During the NO synthesis, the substrate arginine appears to bind directly above the heme center, and then interacts with O₂ bound to the heme iron. Marletta and coworkers have shown that NOSs belong to the cytochrome P450 class of heme proteins from their CO binding studies using electronic absorption spectroscopy.¹⁰ In this study, iNOS and partially purified nNOS, which were isolated from murine macrophages and rat cerebellum, respectively, show characteristic CO binding properties (λ_{max} at 447 nm) identical to typical CO adducts of cytochrome P450s. The heme iron present at the catalytic site of NOS plays a key role by binding and activating O₂ thereby facilitating NO and citrulline synthesis. The electron transfer from NADPH to the heme iron is achieved by FAD and FMN.¹¹ The first step in this reaction involves *N*-hydroxylation of one of the guanidino nitrogen atoms utilizing NADPH and O₂ to form *N*^G-hydroxyl-L-arginine as an intermediate. This intermediate remains bound to the enzyme and is

oxidatively cleaved to L-citrulline and NO in the following steps.¹² This reaction mechanism is only a hypothesis and is not known for certain. In addition to binding O₂ to the heme iron of neuronal NOS, NO can also bind as a sixth ligand in both the ferrous and ferric states of NOS under an anaerobic atmosphere to generate stable NOS heme iron-NO adducts.¹³ Studies on nNOS purified from rat cerebellum indicate that NO inhibits by directly interacting with the enzyme-bound heme active site to form a stable five coordinated ferrous heme iron-NO adduct. This also happens after NO synthesis under oxygen-limited conditions as evidenced from UV-vis and resonance Raman spectroscopy.¹³ The inhibition of NOS activity has profound significance since excess NO production may result in neuropathology.¹⁴ Hence, the formation of a ferrous heme NO complex acts as an inhibitor for the cellular NO synthesis.

1.3 Soluble Guanylate Cyclase

Relaxation of vascular smooth muscle in arteries and veins occurs in response to various chemical and physical stresses. This blood vessel relaxation is attributed to the endothelium dependent relaxation factor; which was later discovered to be NO by Ignarro and Moncada.¹ This important physiological function of NO is mediated by the heme receptor protein, soluble guanylate cyclase (sGC).¹⁵ NO activates the enzyme by binding its ferrous heme center. The enzyme then catalyzes the cyclization of guanosine 5'-triphosphate (GTP) to guanosine 3'-5'-cyclic monophosphate (cGMP).^{6a,16} The proposed reaction mechanism is illustrated in Figure 1.1. The formed cGMP is an intracellular secondary signaling agent involved in various important cellular events. The enzyme sGC is a heterodimer of about 150 kDa mass units with α and β subunits of similar masses. The enzyme is believed to contain one heme per subunit. sGC isolated from bovine lung contains a five-coordinate ferrous heme ligated to an axial histidine with a characteristic Soret band electronic absorption maximum at 431 nm, and a single band at 555 nm. NO binding to sGC leads to the formation of the five-coordinate heme nitrosyl species as evident from the electronic Soret band shift from 431 to 398 nm and an appearance of a shoulder at 485 nm. The new band at 398 nm is directly attributed to the formation of the five-coordinate heme nitrosyl.¹⁷ This also implies the dissociation of the axial histidine ligand from the iron(II) center. From resonance Raman spectroscopy, the N-O stretch and the Fe-N(O) stretch at 1681 cm⁻¹ and 521 cm⁻¹, respectively, in the NO bound sGC have been determined. These values confirm the rupture of the Fe(II)-axial histidine bond and the formation of a 5C ferrous

heme nitrosyl adduct.¹⁸ The formation of the ferrous heme NO species is considered to trigger significant conformational changes in the enzyme structure that lead to the activation of the enzyme for cyclization of GTP.¹⁹ On the other hand, the addition of CO to sGC results in the formation of a stable 6C species with no displacement of the histidine ligand and hence, this only weakly activates the enzyme. Stone and Marletta have shown that NO activates sGC 130-fold; whereas only 4-fold activation is achieved with CO.²⁰ This result validates the fact that the interaction of NO with the heme moiety in sGC is crucial for the optimal enzymatic activity.

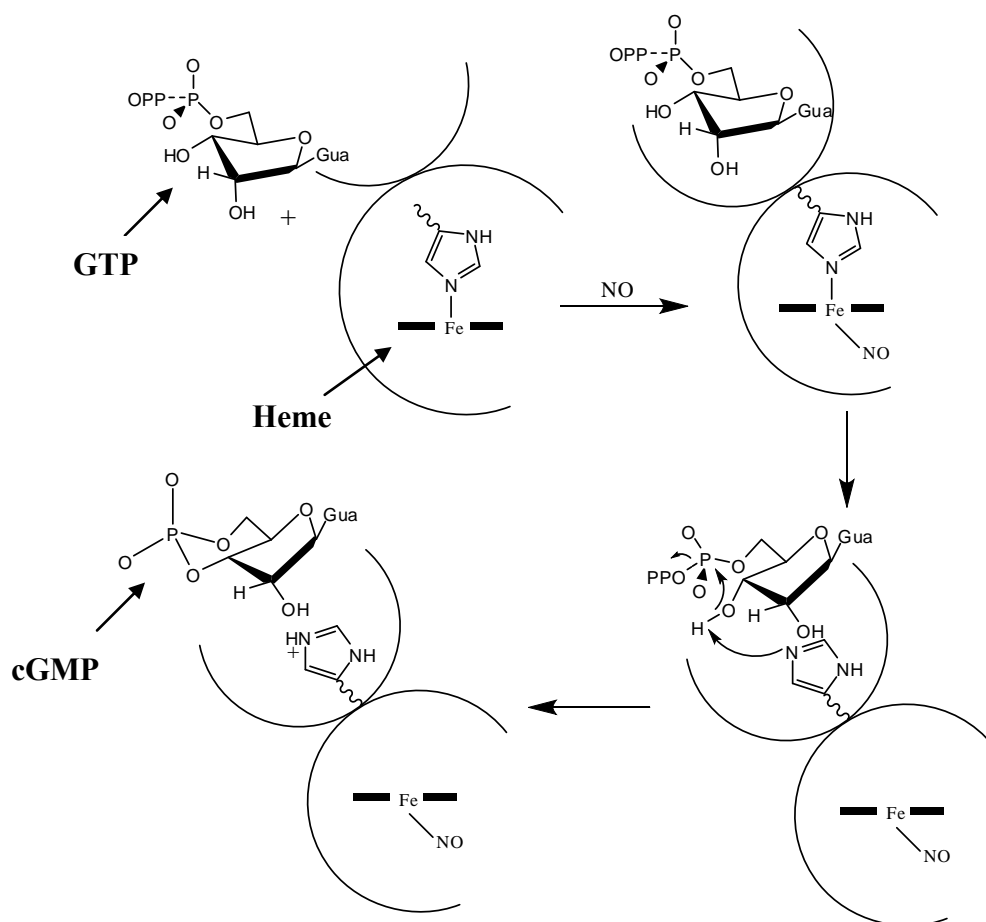


Figure 1.1. Schematic representation of the activation of soluble guanylate cyclase by NO to form cGMP.²¹

1.4 Denitrification

Denitrification is a key process in the nitrogen cycle, which transforms nitrate and releases dinitrogen gas to the biosphere.²² Denitrification has several major environmental implications as follows. First, it is a major mechanism for the loss of nitrates (fertilizer) from the soil. Second, it is an important process that liberates large quantity of N₂O, a green house gas that is also involved in the depletion of the ozone layer in the stratosphere.²³ Third, this mechanism balances and closes the global nitrogen cycle. The process of dissimilatory denitrification involves four reduction steps as shown below in equation 1.



Each step in this metabolic pathway is catalyzed by different metalloenzymes with characteristic structural and spectroscopic features.²⁴ Many high resolution X-ray structures of denitrifying enzymes have been published except the structure of nitric oxide reductase (NOR).²⁵ In the first step, NO₃⁻ is reduced to NO₂⁻ in a reaction catalyzed by several types of nitrate reductases.^{22a} The subsequent reduction of NO₂⁻ to NO, N₂O and finally to N₂ involves the action of a sequence of specific enzymes with interesting catalytic properties. Denitrification is performed mostly by bacteria for energy generation (respiration), although archaea and certain fungi can also perform these reactions. These reduction processes are functional only under anaerobic condition, since respiration of O₂ occurs in preference to the use of nitrogen oxides under aerobic condition. Oxygen respiration is found in both eukaryotes and prokaryotes, whereas denitrification is a prokaryotic pathway. Since the respiratory process results in the evolution of dinitrogen, the terms dissimilatory nitrate reduction or dissimilatory denitrification are used in the literature. Another denitrification pathway involves the formation of the ammonium ion (NH₄⁺) from the reduction of NO₃⁻. Since the released ammonia enters the nitrogen cycle and can be utilized for the assimilation of nitrogen for the synthesis of nitrogen containing organic compounds, this process is termed as assimilatory denitrification or nitrate ammonification. Figure 1.2 shows the complete biological nitrogen cycle.

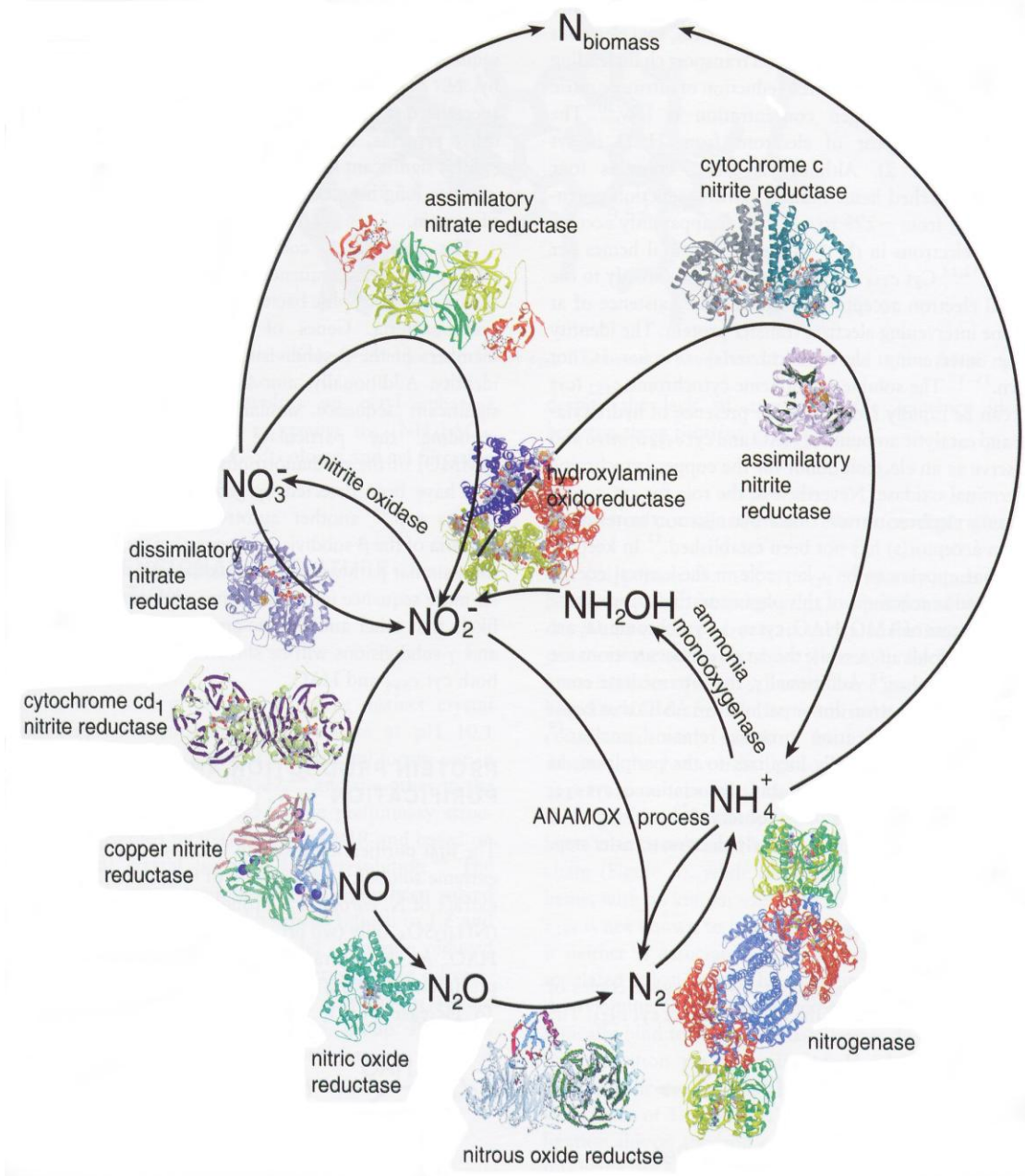
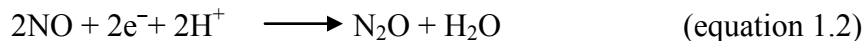


Figure 1.2. Biological nitrogen cycle. The three-dimensional structures of enzymes involved in each step are depicted.²⁶

1.4.1 Bacterial and Fungal Nitric Oxide Reductases

The reduction of two molecules of NO to N₂O is carried out by the enzyme nitric oxide reductase (NOR). The N-N bond formation in this reaction is shown below in equation 1.2.



Both bacteria and fungi perform this reaction. However, the active enzymes present in these organisms are completely different. In bacteria, the NO reduction is achieved at a di-iron heme/non-heme site. On the other hand, the fungal enzyme performs this reaction at a single heme site.

Genetic and biochemical analyses have shown that the active site of bacterial nitric oxide reductase (NorBC) closely resembles that of cytochrome *c* oxidase (CcO). Thus, it is assumed that these have evolved from a common ancestor, presumably an anaerobic NO reducing enzyme.²⁷ However, the bimetallic active site of NorBC contains two irons (a heme iron and a non-heme iron) rather than a heme iron and a copper as present in CcO.²⁸ Since the crystal structure of NorBC has not been solved so far, the active site structure of CcO is used to serve as a model for the NorBC active site. The catalytically active site of mitochondrial CcO is shown in Figure 1.3. NorBC can be classified into three types depending on the type and number of electron donors present: cNOR, qNOR and qCu_ANOR. The best studied bacterial nitric oxide reductases are the cytochrome *bc* complexes, thus the name NorBC. They belong to the category of cNOR which use a soluble cytochrome *c* types or blue copper protein (azurin or pseudoazurin) as their electron donor.²⁹ The structure of cNOR is composed of two subunits, NorB and NorC. The NorB contains the catalytic center and in total two type *b* hemes and a non-heme iron. The NorC subunit contains one type *c* heme. The second type, qNOR, consists of single subunit that accepts electrons from quinols such as ubihydroquinone (QH₂) and menahydroquinone (MQH₂).³⁰ Recently, a third type of NOR, qCu_ANOR, has been identified from the grampositive bacterium *Bacillus azotoformans*.³¹ Its structure is similar to that of cNOR, except a copper A site is present in the place of heme *c* to effect electron donation to the catalytic subunit. This type uses MQH₂ and a specific cytochrome (c₅₅) as electron donors. Interestingly, these three classes possess highly homologous active site structure that accomplish NO reduction.

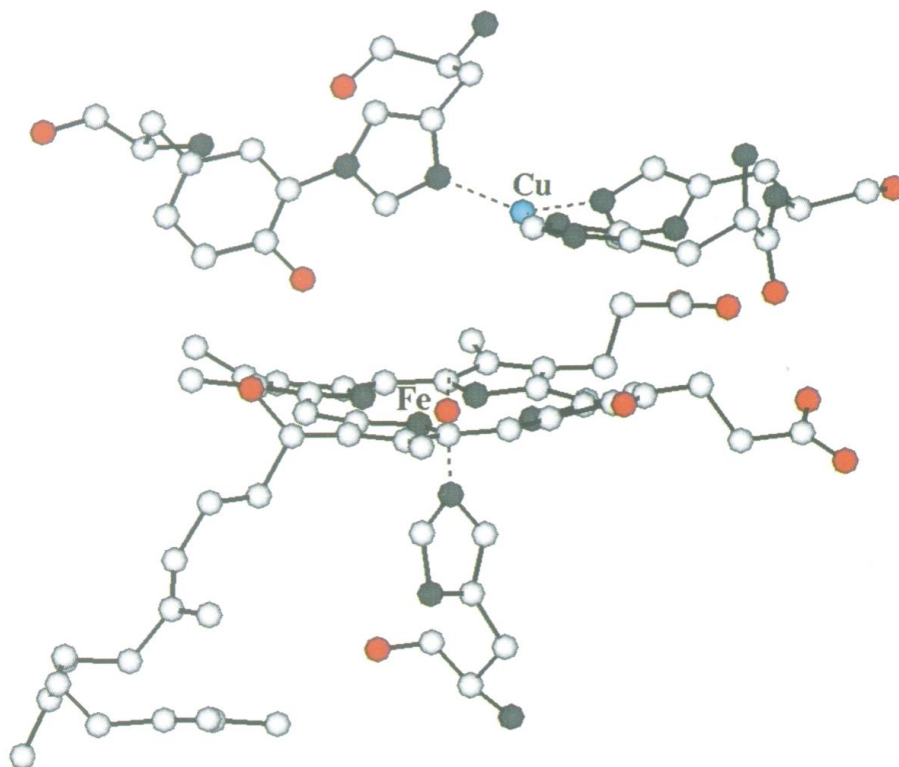


Figure 1.3. Crystal structure of the active site of mitochondrial cytochrome c oxidase.³²

The reaction mechanism of dioxygen reduction by CcO has been studied extensively.³³ In contrast, not much information is available at present regarding the NorBC catalyzed NO reduction mechanism. The resting state of the enzyme has been determined as the all ferric state with a μ -oxo bridge between the two iron centers. The nature of this complex has been characterized by resonance Raman (RR), EPR, and MCD spectroscopic methods.³⁴ The RR spectrum of oxidized NorBC in unlabelled water shows a characteristic band at 810 cm^{-1} which shifts to 780 cm^{-1} in labeled water (H_2^{18}O).³⁵ Correspondingly, this mode is assigned to a $\nu(\text{Fe-O-Fe})$ stretch. Consequently, the dinuclear site is considered bridged by the oxo group. The EPR-silent character of this species is observed and considered to arise from the antiferromagnetic coupling between the two iron centers mediated by the bridging oxo group, which further supports the aforementioned structural formulation by RR studies.

Two different mechanisms have been put forward for NorBC based on spectroscopic evidences: the *trans* and *cis* mechanism. EPR studies on the *Ps. Aeruginosa* enzyme show the formation of the intermediate ferrous non-heme NO ($S = 3/2$) species. This study along with a detail steady state kinetic measurements on NOR activity support the proposed *trans* mechanism as shown in Figure 1.4.

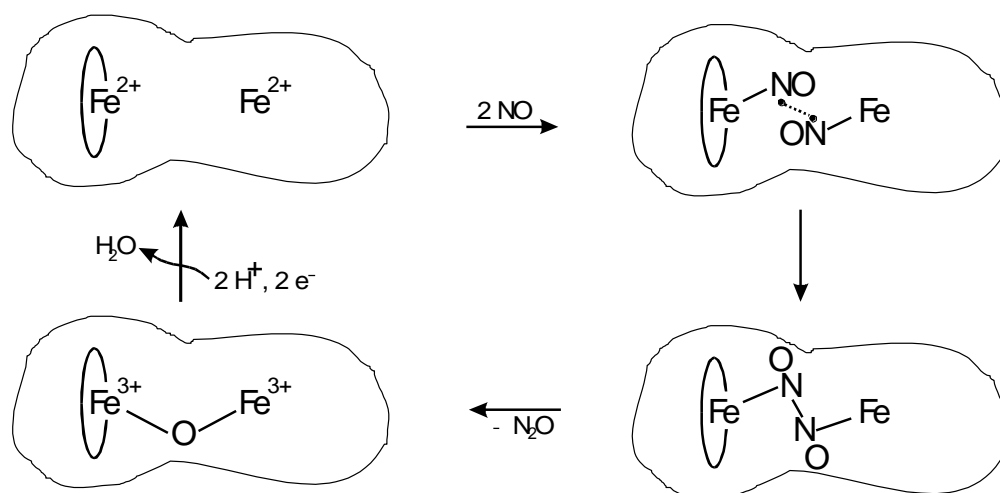


Figure 1.4: Proposed *trans* mechanism of NorBC by de Vries and coworkers.^{33b}

In this case, sequential binding of two molecules of NO to a dinuclear site leads to a diiron ferrous heme/non-heme dinitrosyl complex. Subsequent radical coupling reaction between the two coordinated NO molecules leads to the formation of an $\text{Fe-N}_2\text{O}_2\text{-Fe}$ intermediate which later decomposes to yield the product N_2O and the oxo bridged ferric centers, the enzyme's resting state. Recently, the formation of a hyponitrite intermediate species has been observed in the resonance Raman spectrum of a heme Fe-Cu binuclear center that shows NorBC activity.³⁶ The *cis* mechanism has been postulated by Gronberg et al. and is based on NO binding experiments to Cytochrome ubiquinol oxidase from *Escherichia coli*. This study reveals the binding of two *cis* NO molecules to the Cu_B site, whereas the heme moiety seems to be high spin with no NO bound to it. Therefore, an alternative mechanism for NO reduction solely at the non-heme site has been proposed (Figure 1.5a). In addition, recently, a similar *cis* mechanism has been proposed based on the NO reduction reaction mediated by the heme center alone (see Figure 1.5b). Here, studies carried out on cytochrome *cbb3* from *P. stutzeri* show a five-coordinate ferrous heme *b3* NO

complex as evidenced from RR spectroscopy. This species is thought to be attacked by the second molecule of NO to form a hyponitrite (HONNO⁻) intermediate, which decomposes to yield N₂O. However, the five-coordinate heme-NO adducts are stable toward attack of second molecule of NO. Hence, the molecular mechanism of NO reduction to N₂O appears to be complex and needs more spectroscopic investigations to elucidate the enzyme mechanism unambiguously.

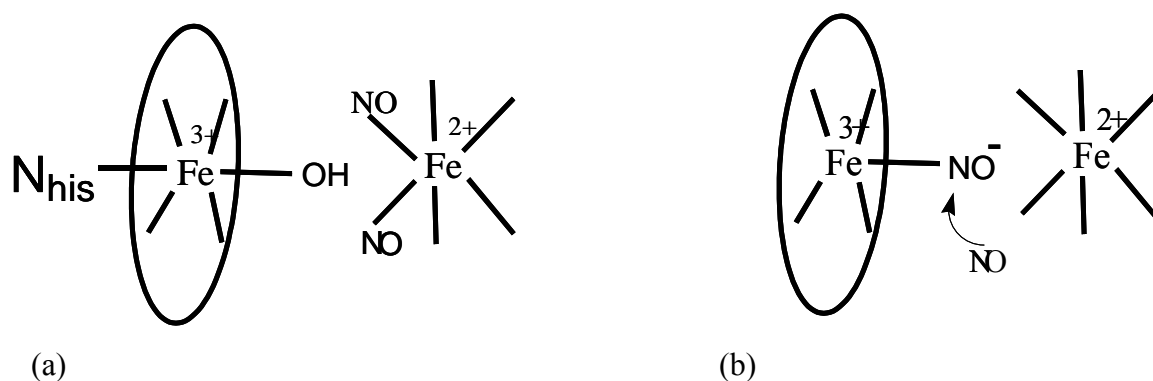
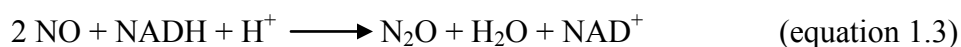


Figure 1.5: Proposed *cis* mechanism for the reduction of NO by NorBC (a) mediated exclusively by the non-heme iron; (b) mediated by the heme center

In the case of fungi, the reduction of NO to N₂O is achieved at a single heme site. Interestingly, fungal denitrification lacks the final step, the conversion of N₂O to N₂. Instead, P450nor produces N₂O as the final product.³⁷ Hence, NO reduction carried out by these fungi is not considered strictly as part of the biological denitrification process. The enzyme P450nor is structurally distinct from the NorBC in the sense that it belongs to the cytochrome P450 class of enzymes, hence the name P450nor. Cytochrome P450 enzymes normally catalyze monooxygenation or hydroxylation of a range of organic substrates. In contrast to other cytochrome P450s, P450nor is novel since it has no monooxygenase activity. The reaction catalyzed by P450nor is shown below in equation 1.3.



Crystal structures of fungal NOR have been determined from *Fusarium oxysporum* in its resting ferric state and also CO bound ferrous state.³⁷ The active site structure from wild type P450nor with NO bound to the heme in the ferric state is shown in Figure 1.6^{37b}, which shows the presence of the axial cysteinate ligand coordinated to the heme.

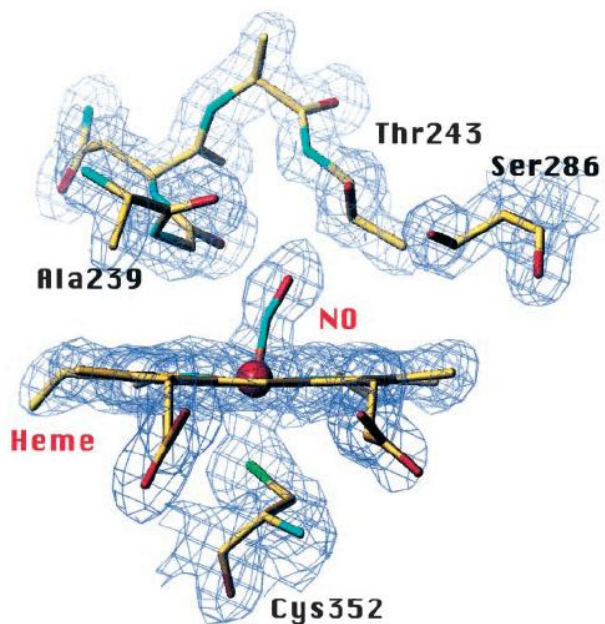


Figure 1.6: The active site structure of the NO bound wild type P450nor determined from X-ray crystallography.^{34b}

The ferric form of P450nor is considered the catalytically active form for the reaction with NO. Binding of NO to the active site gives rise to a ferric NO complex as evidenced from UV-vis, resonance Raman, and EXAFS measurements.³⁸ NO and Fe-NO stretching frequencies of 1851 cm^{-1} and 530 cm^{-1} , respectively, have been determined from resonance Raman measurements.^{38b} The further steps in this reduction process are unclear. A proposed reaction mechanism postulated by Shiro and coworkers^{37b} is shown in Figure 1.7.

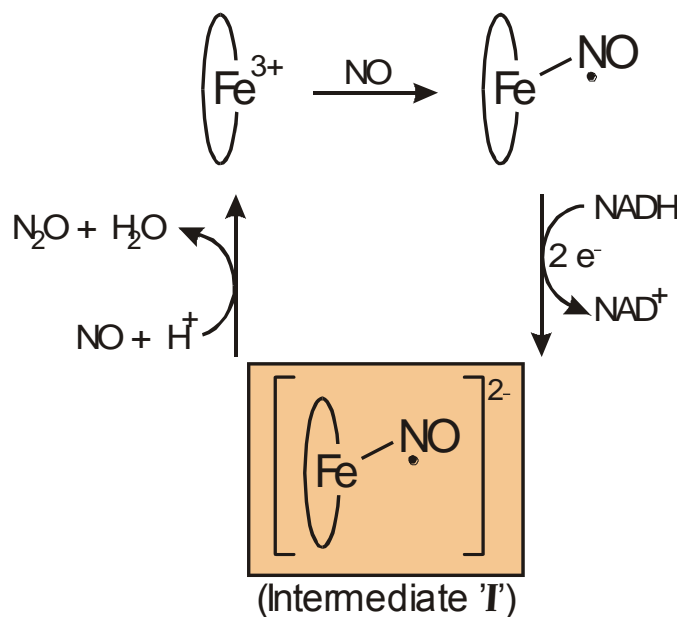


Figure 1.7: Proposed mechanism of P450nor by Shiro and coworkers.^{34b}

This mechanism is based on kinetic stopped-flow and low temperature absorption spectroscopy data on P450nor. The second step in this catalytic cycle involves the two-electron reduction of the initially formed Fe(III)-NO complex by NADH to form a transient intermediate *I*, which reacts with a second molecule of NO to yield the products N₂O and H₂O. This intermediate *I* exhibits the Soret band maximum at 444 nm, different from the Fe(III)-NO complex, which shows the Soret band at 431 nm. Intermediate *I* has been proposed as a two electron reduced species of Fe(III)-NO, and is formally represented as Fe(II)-NO⁻ or Fe(I)-NO complex. A more detailed mechanistic reaction pathway was proposed by Daiber et al. as shown in Figure 1.8.³⁹ This study employed kinetic isotope experiments and stopped-flow spectroscopy to elucidate the reaction mechanism. Here, the Soret band of intermediate *I* observed at 444 nm has been proposed as either Fe(III) with a bound NH(O)H radical (ferric hydroxylamine), or Fe(IV) with bound HNO.

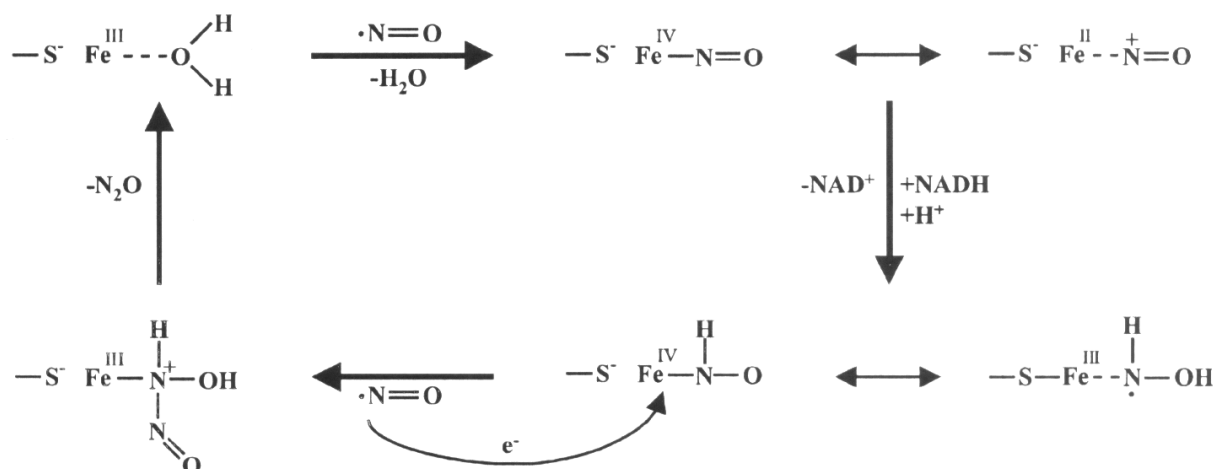


Figure 1.8. Alternative mechanism of P450nor proposed by Daiber et al.³⁹

1.5 Nitrophorins

Nitrophorins are NO carrier heme proteins present in the salivary glands of blood sucking insects. These proteins can store NO for a longer period of time under low salivary pH conditions. They are capable of binding NO reversibly and the release of NO into the host tissue is achieved at increasing pH and upon dilute protein conditions. NO release causes vasodilation and inhibits blood coagulation in the host tissue, and thereby enables insects to obtain their blood meal efficiently.⁴⁰ It has been shown that the secretion of histamine by the victim's tissue upon the insect bite is a contributing factor to the delivery of NO from the protein. Histamine could easily displace NO due to the fact that the dissociation constant of histamine bound to the protein at neutral pH is far less compared to the dissociation constant of NO from the protein.⁴¹

Four different types of nitrophorins have been isolated from the insect *Rhodnius prolixus*. They are named rNP1-rNP4 according to their relative abundance in the glands. In these proteins, the heme center is in its ferric state with axial histidine coordination.⁴² O₂ binding to nitrophorins is unlikely since dioxygen does not bind to ferric hemes. Thus, these proteins are exclusively useful for NO transport and delivery purposes. The occurrence of ferric instead of ferrous hemes in these proteins is not arbitrary, but is related to the dissociation rate constants of NO, which are approximately 4 to 8 orders of magnitude larger in ferric compared to ferrous hemes.⁴³ Hence,

the formation of ferrous heme NO adducts is considered as a dead-end for protein activity. The crystal structure of NO coordinated nitrophorin (rNP4-NO) from *Rhodnius prolixus* has been solved as shown in Figure 1.9. The Fe-N-O unit in the structure is not linear, but appears to be somewhat bent with an angle of 156° .⁴⁴ Interestingly, another type of nitrophorin has been isolated from *Cimex Lectularis*, a bed bug recently.⁴² Unlike rNPs, the ferric heme center of cNP is axially coordinated by a cysteine-cysteine ligand like in the P450 enzymes.



Figure 1.9: High resolution crystal structure of nitrophorin (rNP4-NO), shown in the ribbon presentation. The NO bound heme with axially coordinated histidine is shown in black, disulfide bonds in yellow, and protein loops are shown in other colors.

References

- ¹ (a) Palmer, R. M.; Ferrige A. G.; Moncada, S. *Nature* **1987**, *327*, 524–526. (b) Ignarro, L. J.; Byrns, R. E.; Buga, G. M.; Wood, K. S. *Circ. Res.* **1987**, *61*, 866-879.
- ² Culotta, E.; Koshland, D. E. Jr. *Science* **1992**, *258*, 1862–1865.
- ³ (a) Moncada, S.; Palmer, R. M. J.; Higgs, E. A. *Pharmacol. Rev.* **1991**, *43*, 109. (b) Butler, A. R.; Williams, D. L. *Chem. Soc. Rev.* **1993**, 233.
- ⁴ Enemark, J. H.; Feltham, R. D. *Coord. Chem. Rev.* **1974**, *13*, 339-406.
- ⁵ McCleverty, J. A. *J. Am. Chem. Soc.* **2004**, *104*, 403-418.
- ⁶ (a) Marletta, M. A. *Cell* **1994**, *78*, 927-930. (b) Moncada, S.; Palmer, R. M. J.; Higgs, E. A. *Pharmacol. Rev.*, **1991**, *43*, 109-142. (c) Nathan, C.; Xie, Q. *Cell* **1994**, *78*, 915-918.
- ⁷ Bredt, D. S.; Hwang, P. M.; Glatt, C. E.; Lowenstein, C.; Reed, R. R.; Snyder, S. H. *Nature* **1991**, *351*, 714-718.
- ⁸ (a) Hall, A. V.; Antoniou, A.; Wang, Y.; A.H. Cheung, A. H.; Arbus, A. M.; Olson, S. L.; W.C. Lu, W. C.; Kau, C. -L.; Marsden, P. A. *J. Biol. Chem.* **1994**, *269*, 33082–33090. (b) Rodríguez-Crespo, I.; Pierre Moëne-Loccoz, P.; Loehr, T. M.; Ortiz de Montellano, P. R. *Biochemistry*, **1997**, *36*, 8530-8538.
- ⁹ (a) Matsuoka, A.; Stuehr, D. J.; Olson, J. S.; Clark, P.; Ikeda-Saito, M. *J. Biol. Chem.* **1994**, *269*, 20335–20339. (b) White, K. A.; Marletta, M. A. *Biochemistry* **1992**, *31*, 6627–6631. (c) Stuehr, D. J.; Ikeda-Saito, M. *J. Biol. Chem.* **1992**, *267*, 20547–20550. McMillan, K.; Bredt, D. S.; Hirsch, D. J.; Snyder, S. H.; Clark, J. F.; Masters, B. S. S. *Proc. Natl. Acad. Sci. U. S. A.* **1992**, *89*, 11141–11145.
- ¹⁰ White, K. A.; Marletta, M. A. *Biochemistry* **1992**, *31*, 6627-6631.
- ¹¹ Abu-Soud, H. M.; Yoho, L. L.; and Stuehr, D. J. *J. Biol. Chem.* **1994**, *269*, 32047–32050.
- ¹² (a) Stuehr, D. J.; Kwon, N. S.; Nathan, C. F.; Griffith, O. W.; Feldman, P. L.; Wiseman, J. *J. Biol. Chem.* **1991**, *266*, 6259-6263. (b) Guengerich, F. P. *J. Biol. Chem.* **1991**, *266*, 10019-10022. (c) Pufahl, R. A.; Nanjappan, P. G.; Woodard, R. W.; Marletta, M. A. *Biochemistry* **1992**, *31*, 6822-6828. (d) Porter, T. D.; Coon, M. J. *J. Biol. Chem.* **1991**, *266*, 13469-13472.
- ¹³ Wang, J.; Rousseau, D. I.; Abu-Soud, H. M.; Stuehr, D. J. *Proc. Natl Acad. Sci. U. S. A.* **1991**, *91*, 10512-10516.
- ¹⁴ Huang, Z.; Huang, P. L.; Panahian, N.; Dalkara, T.; Fishman, M. C.; and Moskowitz, M. A. *Science* **1994**, *265*, 1883-1885.
- ¹⁵ (a) Garbers, D. L.; Lowe, D. G. *J. Biol. Chem.* **1996**, *269*, 30741-30744. (b) Waldman, S. A.; Murad, F. *Pharmacol. Rev.* **1987**, *39*, 163-196.
- ¹⁶ (a) Bredt, D. S.; Snyder, S. H. *Annu. Rev. Biochem.* **1994**, *63*, 175-195. (b)
- ¹⁷ (a) Rose, E. J.; Hoffman, B. M. *J. Am. Chem. Soc.* **1983**, *105*, 2866-2873. (b) Suzuki, S.; Yoshimura, T.; Nakahara, A.; Iwasaki, H.; Shidara, S.; Matsubara, T. *Arch. Biochem. Biophys.* **1984**, *229*, 126-135. (c) Maxwell, J. C.; Caughey, W. S. *Biochemistry* **1976**, *15*, 388-396. (d) Saabo, A.; Perutz, M. F. *Biochemistry* **1976**, *15*, 4427-4428.
- ¹⁸ Tomita, T.; Ogura, T.; Tsuyama, S.; Imai, Y.; Kitagawa, T. *Biochemistry* **1997**, *36*, 10155-10160.
- ¹⁹ (a) Traylor, T. G.; Sharma, V. S. *Biochemistry* **1992**, *31*, 2847–2849. (b) A.E. Yu, A. E.; Hu, S.; Spiro, T. G.; Burstyn, J. N. *J. Am. Chem. Soc.* **1994**, *116*, 4117–4118. (c) Dierks, E. A.; Hu, S.; Vogel, K. M.; Yu, A. E.; Spiro, T. G.; Burstyn, J. N. *J. Am. Chem. Soc.* **1997**, *119*, 7316–7323. (d) Y. Zhao, Y.; Hoganson, C.; Babcock, G. T.; Marletta, M. A. *Biochemistry* **1998**, *37*, 12458–12464.
- ²⁰ Stone, J. R.; Marletta, M. A. *Biochemistry* **1994**, *36*, 5636-5640.
- ²¹ Kharitonov, V. G.; Sharma, V. S.; Pilz, R. B.; Magdet, D.; Koesling, D. *Proc. Natl. Acad. Sci. USA*, **1995**, *92*, 2568-2571.
- ²² (a) Averill, B. A. *Chem. Rev.* **1996**, *96*, 2951-2964. (b) Richardson, D. J.; Watmough, N. J. *Curr. Opin. Chem. Biol.* **1999**, *3*, 207-219. (c) Zumft, W. G. *Microbiol. Mol. Biol. Rev.* **1997**, *61*, 533-616. (d) zumft, W. G. *J. Inorg. Biochem.* **2005**, *99*, 194-215. (e) Wasser, I. M.; de Vries, S.; Moëne-Loccoz, P.; Schröder, I.; Karlin, K. D. *Chem. Rev.* **2002**, *102*, 1201-1234.
- ²³ Hansen, J.; Sato, M. *Proc. Natl. Acad. Sci. USA*, **2004**, *101*, 16109-16114.
- ²⁴ Berks, B. C.; Ferguson, S. J.; Moir, J. W. B.; Richardson, D. J. *Biochim, Biophys. Acta* **1995**, *1232*, 97-173.
- ²⁵ Einsle, O.; Kroneck, P. M. *Biol. Chem.* **2004**, *385*, 875-883.
- ²⁶ *Handbook of Metalloproteins*; Wiley: Chichester, England, 2001.
- ²⁷ (a) Perira, M. M.; Santana, M.; Teixeira, M. *Biochim. Biophys. Acta* **2001**, *1505*, 185-208. (b) de Vries, S.; Schroder, I. *Biochem. Soc. Trans.* **2002**, *30*, 662-667.

- ²⁸ (a) Saraste, M.; Castresana, J. *FEBS Lett.* **1994**, *341*, 1. (b) van der Oost, J.; de Boer, A. P.; de Gier, J. W.; Zumft, W. G.; Stouthamer, A. H.; van Spanning, R. J. *FEMS Microbiol. Lett.* **1994**, *121*, 1-10.
- ²⁹ (a) Moir, J. W. B.; Ferguson, S. J. *Microbiology* **1994**, *140*, 389-397. (b) Berks, B. C.; Ferguson, S. J.; Moir, J. W.; Richardson, D. J. *Biochim. Biophys. Acta* **1995**, *1232*, 97-173. (c) Richardson, D. J.; Watmough, N. J. *Curr. Opin. Chem. Biol.* **1999**, *3*, 207-219.
- ³⁰ (a) Cram, R.; Pohlmann, B.; Friedrich, B.; *FEBS Lett.* **1999**, *460*, 6-10 (b) de Vries, S.; Stampraad, M. J. F.; Lu, S.; Moëgne-Loccoz, P. Schröder, I. *J. Biol. Chem.* **2003**, *278*, 35861-35868.
- ³¹ (a) Suharti; Stampraad, M. J. F.; Schroder, I.; de Vries, S. *Biochemistry* **2001**, *40*, 2632-2639. (b) Suharti; de vries, S. *Biochem. Soc. Trans.* **2005**, *33*, 130-133. (c) Suharti; Heering, H. A.; de Vries, S. *Biochemistry* **2004**, *43*, 13487-13495.
- ³² Yoshikawa, S.; Shinzawa-Itoh, K.; Yamashita, E.; Tsukihara, T. *Mitochondrial cytochrome c oxidase*; Wiley: Chichester, England, 2001; Vol. 1.
- ³³ (a) Collman, J. P.; Boulatov, R.; Sunderland, C. J.; Fu, L. *Chem. Rev.* **2004**, *104*, 561-588. (b) Kim, E.; Chufan, E. E.; Kamaraj, K.; Karlin, K. D. *Chem. Rev.* **2004**, *104*, 1077-1134.
- ³⁴ (a) Cheesman, M. R.; Zumft, W. G.; Thomson, A. J. *Biochemistry* **1998**, *37*, 3994-4000. (b) Moëgne-Loccoz, P.; de Vries, S. *J. Am. Chem. Soc.* **1998**, *120*, 5147-5152. (b) Girsch, P.; de Vries, S. *Biochim. Biophys. Acta* **1997**, *1318*, 202-216.
- ³⁵ (a) Moëgne-Loccoz, P.; Richter, O.-M. H.; Huang, H.; Wasser, I. A.; Ghiladi, R. A.; Karlin, K. D.; de Vries, S. *J. Am. Chem. Soc.* **2000**, *122*, 9344. (b) Pinakoulaki, E.; Gemeinhardt, S.; Saraste, M.; Varotsis, C. *J. Biol. Chem.* **2002**, *277*, 23407.
- ³⁶ Varotsis, C.; Ohta, T.; Kitagawa, T.; Soulimane, T.; Pinakoulaki, E. *Angew. Chem. Intl. Ed.* **2007**, *46*, 210-2214.
- ³⁷ (a) Park, S.-Y.; Shimizu, H.; Adachi, S.; Nagagawa, A.; Tanaka, I.; Nakahara, K.; Shoun, H.; Obayashi, E.; Nakamura, H.; Iizuka, T.; Shiro, Y. *Nat. Struct. Biol.* **1997**, *4*, 827-832. (b) Shimizu, H.; Park, S.-Y.; Gomi, Y.; Arakawa, H.; Nakamura, H.; Adachi, S.-I.; Obayashi, E.; Iizuka, T.; Shoun, H.; Shiro, Y. *J. Biol. Chem.* **2000**, *275*, 4816-4826. (c) Shimizu, H.; Park, S.-Y.; Shiro, Y.; Adachi, S.-I. *Acta Crystallogr. D* **2002**, *58*, 81.
- ³⁸ (a) Shiro, Y.; Fujii, M.; Isogai, Y.; Adachi, S.; Iizuka, T.; Obayashi, E.; Makino, R.; Nakahara, K.; Shoun, H. *Biochemistry* **1995**, *34*, 9052-9058. (b) Obayashi, E.; Tsukamoto, K.; Adachi, S.; Takahashi, S.; Nomura, M.; Iizuka, T.; Shoun, H.; Shiro, Y. *J. Am. Chem. Soc.* **1997**, *119*, 7807-7816.
- ³⁹ Daiber, A.; Nauser, T.; Takaya, N.; Kudo, P.; Weber, P.; Hultschig, C.; Shoun, H.; Ullrich, V. *J. Inorg. Biol. Chem.* **2002**, *88*, 343-352.
- ⁴⁰ (a) Ribeiro, J. M. C.; Hazzard, J. M. H.; Nussenzveig, R. H.; Champagne, D. E.; Walker, F. A. *Science* **1993**, *260*, 539-541. (b) D.E. Champagne, D. E.; Nussenzveig, R.; Ribeiro, J. M. C. *J. Biol. Chem.* **1995**, *270*, 8691-8695.
- ⁴¹ (a) Andersen, J. F.; Ding, X. D.; Balfour, C.; Champagne, D. E.; Walker, F. A.; Montfort, W. R. *Biochemistry*, **2000**, *39*, 10118-10131. (b) Weichsel, A.; Andersen, J. F.; Champagne, D. E.; Walker, F. A.; Montfort, W. R. *Nature Struct. Biol.* **1998**, *5*, 304-309.
- ⁴² Walker, F. A. *J. Inorg. Biochem.* **2005**, *99*, 216-236.
- ⁴³ (a) Ford, P. C. *Coord. Chem. Rev.* **2005**, *249*, 391-403. (b) Copper, C. E. *Biochim. Biophys. Acta.* **1999**, *1411*, 290-309.
- ⁴⁴ Roberts, S. A.; Weichsel, A.; Qiu, Y.; Shelnut, J. A.; Walker, F. A.; Montfort, W. R. *Biochemistry* **2001**, *40*, 11327-11337.

Chapter 2

Overview

In this thesis, the spectroscopic properties, electronic structures, and reactivities of iron porphyrin NO adducts in the ferric and ferrous oxidation states with axial N- and S-donor ligands are explored in-depth using various spectroscopic methods and quantum-chemical calculations. These complexes are synthesized as models for important heme nitrosyl adducts present in biology such as bacterial nitric oxide reductase, cytochrome P450_{nor}, nitric oxide synthase, and NO transport proteins (nitrophorins). In addition, various collaborative projects on other types of model compounds have been performed and are presented at the end of this thesis.

FT-IR, Raman, and electron paramagnetic resonance (EPR) spectroscopy are extensively used in this thesis to investigate the properties of the synthesized model complexes. The basic principles and instrumentation techniques of these methods are briefly described in Chapter 3.

As described in Chapter 1, ferrous porphyrin NO adducts form as an intermediates in many enzymatic reactions. This includes the dissimilatory denitrification process where NO reduction is carried out by the enzyme bacterial nitric oxide reductase (NorBC). This enzyme's active site consists of a mixed heme/non-heme di-iron(II) center, where the heme shows axial histidine coordination. Whereas the properties of ferrous non-heme iron nitrosyls have already been characterized in detail, no definitive analyses of the electronic structural descriptions of corresponding heme complexes have been published so far. Furthermore, functional NorBC models which carry out the reduction of NO have not been synthesized to this date. Hence, it is of foremost importance to investigate the properties of ferrous heme NO complexes as a function of porphyrin substitutions and *trans* ligands to NO. This will provide insight for the design of a suitable model system for NorBC to ensure that these complexes are six-coordinate in solution. In this regard, we have synthesized model complexes of type [Fe(TPP*)(L)(NO)] (TPP* = tetraphenyl porphyrin type ligand; L = N-donor), and we have investigated the compounds in detail using spectroscopic methods and quantum-chemical calculations. These studies are presented in Chapter 4. Based on these results, we were able to design and synthesize a number of new generation NorBC models,

which are presented in Chapter 6. In addition, the properties of the corresponding ferric heme nitrosyls are also evaluated applying vibrational spectroscopy and DFT calculations. These results are summarized in Section 4.4.

NO bound heme centers with axial cysteinate coordination are present in the active sites of fungal nitric oxide reductase (P450nor), nitric oxide synthase (NOS), and *Cimex* nitrophorins (cf. Chapter 1). Modelling these systems requires thiolates coordination *trans* to Fe-NO. We have synthesized and studied the effect of axial thiolate coordination on the properties of ferrous and ferric heme nitrosyl complexes, and these results are presented in Chapter 5. These studies also show that these complex with axial thiolates are very reactive and difficult to isolate as pure solids.

Chapter 6 comprises syntheses and properties of a series of ferrous porphyrin NO complexes with covalently attached N-donor ligands $[\text{Fe}^{\text{II}}(\text{P})(\text{NO})(\text{L})]$, where L = pyridine or imidazole linker. These model compounds are synthesized to obtain a stable six-coordinate ferrous heme nitrosyl complex in solution for further mechanistic reactivity studies. Attached linkers with varying chain lengths and designs were synthesized to delineate the effect of chain length and rigidity on the base binding affinity to the Fe(II)-NO center. These ligand designs were utilized further to synthesize a complete structural model for NorBC. These interesting complexes consist of a heme/non-heme mixed assembly and are presented in Section 6.3. In addition, non-heme iron complexes with (TPA) and (MPBMPA) ligands have also been studied to understand the properties of the non-heme portion of the NorBC active site.

In addition to the above mentioned studies on iron porphyrin NO complexes, I have also been involved in some interesting collaborative projects on ruthenium nitrosyls (synthesis and crystal growth), manganese porphyrins (crystal growth), P450nor mechanism (DFT calculations) and Cu(I)-NO model complexes (synthesis and spectroscopy). The Cu(I)-NO project has been carried out in collaboration with Prof. Dr. Kiyoshi Fujisawa, University of Tsukuba, Japan. All the other projects were carried out in collaboration with other members of Prof. Lehnert's research group. These results have been published recently or accepted for publication.

Finally, the research works presented in this thesis is briefly summarized in Chapter 8.

Chapter 3

Instrumentation and Background

In this chapter, the basic principles and instrumentation techniques for FT-IR, Raman, and EPR spectroscopic methods are discussed. In addition, other instruments used in this thesis are introduced in the Experimental Section of this chapter.

3.1 Fourier Transform Infrared Spectroscopy

3.1.1. Basic Theory and Principles of Infrared Spectroscopy¹

According to classical theory, a diatomic molecule with atomic masses m_1 and m_2 connected by a chemical bond vibrates as one-dimensional simple harmonic oscillator (S.H.O). The vibrational frequency in hertz is given by equation 3.1

$$\nu = \frac{1}{2\pi} \left(\frac{k}{\mu} \right)^{1/2} \quad [\text{s}^{-1}] \quad (\text{equation 3.1})$$

where k is the force constant and μ is the reduced mass. Dividing equation 3.1 by velocity of light gives the value in wavenumbers (cm^{-1})

$$\tilde{\nu} = \frac{1}{2\pi c} \left(\frac{k}{\mu} \right)^{1/2} \quad [\text{cm}^{-1}] \quad (\text{equation 3.2})$$

Vibrational energies, like all other energies are quantized. The allowed vibrational energies, ν , according to the Schrödinger equation for a simple harmonic oscillator relate to the vibrational quantum number V as is shown in equation 3.3.

$$E_\nu = \left(V + \frac{1}{2} \right) h\nu ; V = 0, 1, 2, \dots \quad (\text{equation 3.3})$$

Thus, at the lowest energy state $V = 0$, the energy is equal to $h\nu$. This is called the zero point energy.

The above equation can be converted to cm^{-1} by dividing by hc . This is shown in equation 3.4.

$$\begin{aligned} G(\nu) &= E_\nu/hc = \left(V + \frac{1}{2} \right) \nu/c \\ &= \left(V + \frac{1}{2} \right) \omega_e \end{aligned} \quad (\text{equation 3.4})$$

where ω_e is the vibrational eigen frequency of the oscillator, and $G(v)$ is called the vibrational term. The selection rule for a vibrational transition in the simple harmonic oscillator is given by equation 3.5.

$$\Delta V = \pm 1 \quad (\text{equation 3.5})$$

Thus, at room temperature, most of the molecules are in the vibrational ground state ($V = 0$) so the transition most probably to occur is from $V = 0$ to $V = 1$. This vibrational transition is designated as the fundamental vibrational frequency. In reality, molecules do not vibrate as simple harmonic oscillators, especially in highly excited vibrational states. P. M. Morse suggested an empirical expression for the anharmonic oscillator. The potential energy (V) of an anharmonic oscillator is given in equation 3.6.

$$V = D_e [1 - \exp a \{(r-r_e)\}]^2 \quad (\text{equation 3.6})$$

Here, a is a constant and D_e is the dissociation energy of the molecule. When the Schrödinger equation for the anharmonic oscillator is solved using the Morse potential energy (equation 3.6), the energy levels are given by

$$G(v) = \left(V + \frac{1}{2} \right) \omega_e - \left(V + \frac{1}{2} \right) \omega_e X_e \quad (\text{equation 3.7})$$

where $\omega_e X_e$ is the anharmonicity constant. The selection rule for vibrational transitions has now changed to $\Delta V = \pm 1, \pm 2$, etc. Thus, overtones are observed in the IR spectra following this selection rule.

In the case of polyatomic molecules, a set of Cartesian coordinates is necessary to describe the motion of each atom. Thus, there are three independent degrees of freedom in the x, y and z directions for every atom. Hence, for a molecule with N number of nuclei, there are $3N$ total degrees of motional freedom. There are three coordinates required to specify the center of gravity of a molecule. Thus, the center of gravity of a polyatomic molecule has three independent translational degrees of freedom. Apart from these, three independent rotational degrees of freedom for a non-linear molecule and two rotational degrees of freedom for a linear molecule exist. Finally, subtracting these above described translation and rotational degrees of freedom from the total number $3N$, $3N-6$ degrees of freedom for a non-linear and $3N-5$ degrees of freedom for a linear molecule remain for vibrations.

3.1.2. Experimental Setup of Fourier Transform Infrared Spectroscopy (FT-IR)

The heart of the FT-IR spectrometer is the interferometer, which was invented by Michelson in 1880. He was awarded the Nobel prize in Physics in 1907 for accurately measuring wavelengths of light using his interferometer. The interferometer consists of one fixed mirror and one movable mirror and a beam splitter. An IR source and a detector complete the spectrometer components. The optical layout of the FT-IR Bruker spectrometer (Bruker IFS 66v) used in the group of Prof. Dr. Felix Tuzek, University of Kiel, Germany, is shown in Figure 3.1 (top) along with a schematic representation of the Michelson interferometer (Figure 3.1, bottom). The beam of radiation from the source (silicon carbide heating filament) is split by the beam splitter into two components which are reflected at the fixed and movable mirrors back to the beam splitter where they recombine. This way, interference between the beams is obtained and the intensity of the output beam from the interferometer can be monitored as a function of path difference by the detector.

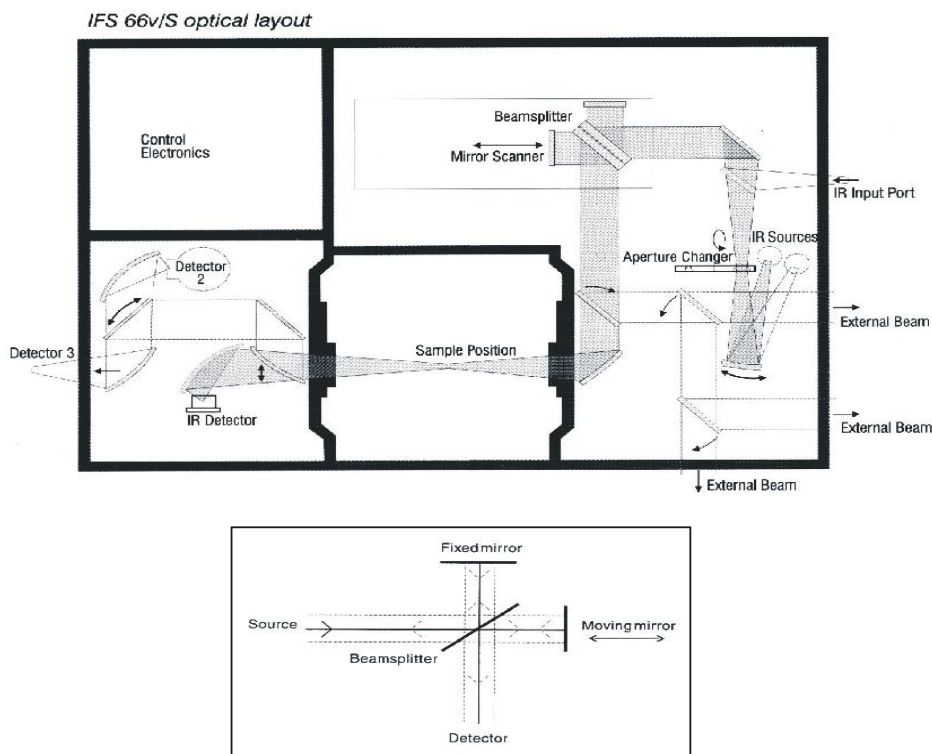


Figure 3.1. Optical layout of an FT-IR spectrometer (top), and schematic representation of the Michelson interferometer (bottom).

3.2. Raman Spectroscopy

3.2.1 Basic Theory and Setup of Raman Spectroscopy³

The Raman effect was discovered by C. V. Raman in 1928. In contrast to IR spectroscopy, Raman spectroscopy deals with the scattering of light, and not with absorption. Consider a photon of frequency ν falling on a molecule. If the collision is elastic, then the scattered photon has an energy equal to the incident photon. On the other hand, if the collision is inelastic, then the scattered photon will have a higher energy or lower energy compared to the incident photon. If we assume that the kinetic energy of the photon and the molecule remain unchanged before and after the collision then, from the law of conservation of energy,

$$h\nu + E = h\nu' + E' \quad (\text{equation 3.7})$$

where $h\nu$ corresponds to the energy of the incident photon, and $h\nu'$ corresponds to the energy of the scattered photon, respectively.

Rearranging equation 3.7 gives the following expression

$$(E-E')/h = \nu - \nu' \quad (\text{equation 3.8})$$

If the frequency or energy of the incident and the scattered photon are the same (ie. $\nu = \nu'$ or $E = E'$) then Rayleigh scattering occurs. When the photon collides with the molecule, energy from the photon can be either transferred to the molecule or taken away from the molecule, which corresponds to Raman scattering. A Pictorial representation of the Raman and Rayleigh scattering are shown in Figure 3.2. When the molecule is excited to a higher unstable electronic state then returns to the original vibrational state, then Rayleigh scattering occurs. On the other hand, if the excited molecules return back to a different vibrational state then Raman scattering occurs. If the vibrational quantum number of the final state is larger than that of the initial state before the collision, this leads to Stokes lines (cf. Figure 3.2, left). Vice versa, anti-Stokes lines are generated (cf. Figure 3.2, right).

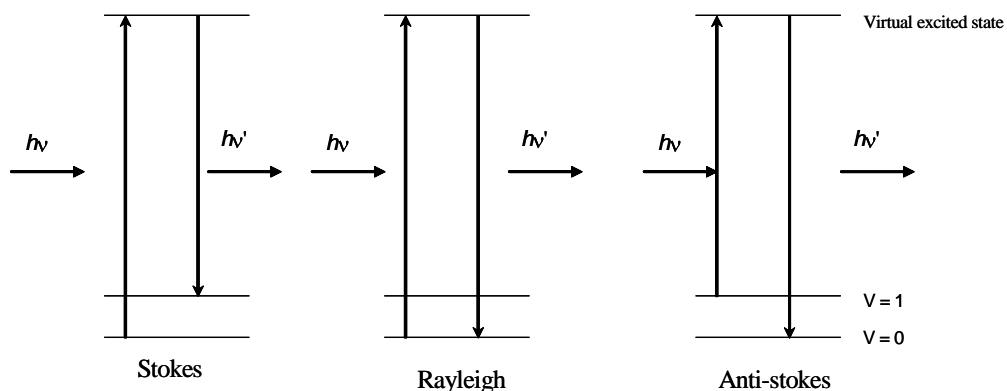


Figure 3.2. Illustration of Raman and Rayleigh scattering.

Thus, both Stokes and anti-Stokes lines are present in a Raman spectrum. Stokes lines are more intense than the anti-Stokes lines. Anti-Stokes lines are weaker since they are arising from the excitation of molecules from an excited vibrational state, and initially, there are very few molecules in the excited vibrational state at room temperature. Raman shift is represented as the shift in frequency ($\nu - \nu'$).

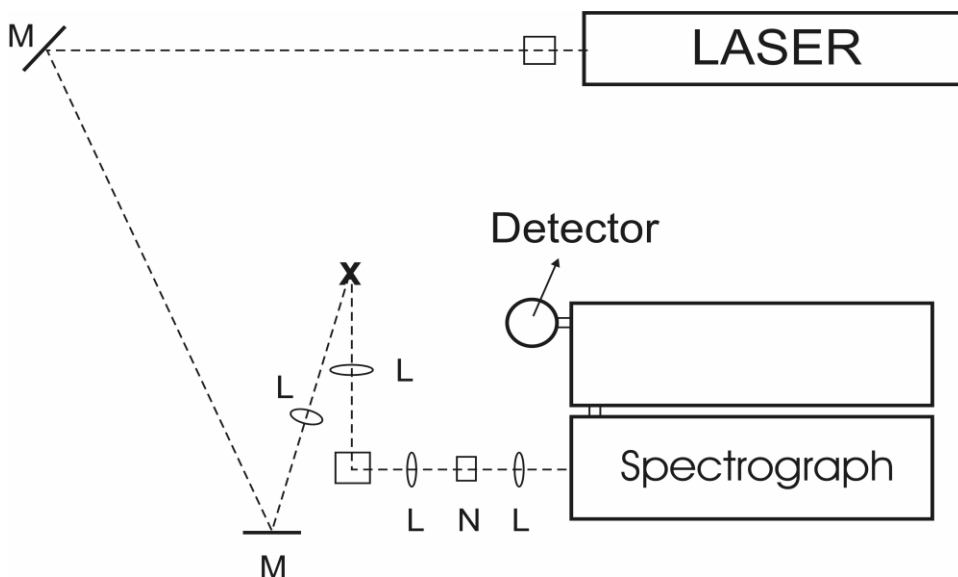


Figure 3.3. Raman spectrometer assembly built by Prof. Dr. Nicolai Lehnert and Florian Paulat in Ann Arbor, USA (M = mirror, L = lens, N = Notch filter).²

A schematic representation of the Raman spectrometer built in the group of Prof. Dr. Nicolai Lehnert is shown in Figure 3.3. The light source used for the Raman spectrometer in the Lehnert laboratory is an Argon/Krypton ion mixed gas laser. The main excitation energies

(power > 100 mW) accessible with the BeamLok 2060 are: 647.1, 568.2, (530.9), 514.5, 488.0, (476.5), 457.9, 413.1, (406.7), and 351.0 nm. The laser beam first passes through mirrors and the interference filter, etc. and is finally focussed on the sample, the position of which is indicated as 'x' in Figure 3.3. The sample is placed in a dewar (EPR cold-finger dewar), which is cooled with liquid nitrogen. The scattered light is then collected by another lens and redirected in 90° using a beam stirrer (square box in Figure 3.3). The scattered light is then collimated, the Raleigh light is blocked using a Notch filter ('N' in Figure 3.3), and finally, the remaining light is focussed on the monochromator entrance slit. The monochromator corresponds to a PI Acton TriVista DM55 double monochromator with an attached SPEC 10 400B LN CCD detector (1340x400 pixel, back-illuminated CCD, liquid nitrogen cooled) from Princeton Instruments (now PI Acton).

3.3. Electron Paramagnetic Resonance Spectroscopy

3.3.1. Basic theory and principles of EPR spectroscopy³

Electron paramagnetic resonance spectroscopy (EPR) also called electron spin resonance spectroscopy, was discovered by Zavoisky in 1945. The EPR transitions are observed in the microwave region. In EPR spectroscopy, the interaction of the spin moment of an unpaired electron ($m_s = \pm 1/2$) with an applied magnetic field results in two different energy states (Zeeman effect). A transition between these two states can be induced by the application of microwave radiation. The Zeeman Hamiltonian for the interaction of an electron with the magnetic field applied along the z direction is given by equation 3.9

$$\hat{H} = g\beta H \hat{S}_z \quad (\text{equation 3.9})$$

where g is called Lande g -factor. For a free electron, this value is 2.0023193. β is the electron Bohr magneton, \hat{S}_z is the spin operator; and H is the applied magnetic field strength. This Hamiltonian operates on the electron spin functions α and β corresponding to $m_s = +1/2$ and $m_s = -1/2$, respectively. The β spin has its magnetic moment aligned with the magnetic field direction, whereas and the α spin is aligned opposite to the field.

The energy associated with this transition is given by the equation 3.10.

$$\Delta E = g\beta H \quad (\text{equation 3.10})$$

This energy difference corresponds to frequencies in the microwave region. EPR experiments are carried out at fixed frequency for practical reasons. Normally EPR spectra are measured

in the X-band frequency range of 9.5 giga hertz (GHz), where a field strength of about 3400 gauss is employed, or in the Q-band frequency range (35 GHz, 12500 gauss).

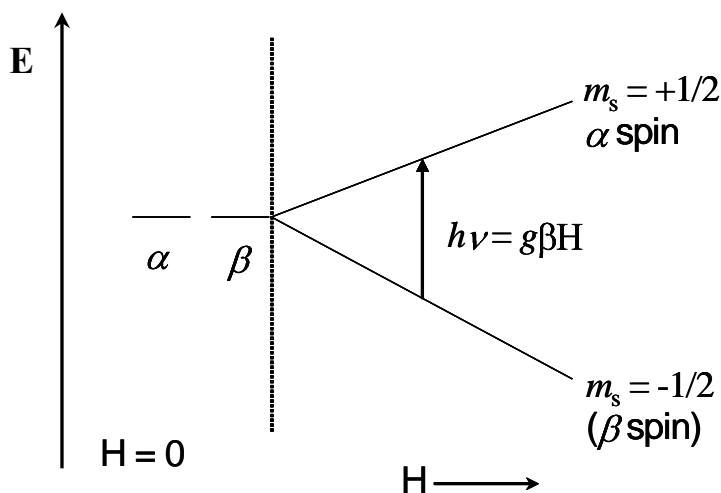


Figure 3.4 Energy level diagram associated with the electronic transition in an EPR experiment.

Hyperfine interaction is an important phenomenon which occurs as a result of the interaction of electron magnetic moment(s) with the nuclear magnetic moment(s) which, results in a splitting of the EPR signals. For example, an unpaired electron with $S = 1/2$ ($m_s = \pm 1/2$) interacts with a nucleus of nuclear spin $I = 1/2$ ($m_I = \pm 1/2$). In the absence of the magnetic field, the electron spin energy levels are degenerate. The application of a magnetic field removes the degeneracy giving rise to two sublevels as shown in Figure 3.4. These electron spin sublevels interact with the nuclear spin, thereby giving rise to further splitting. Another important feature in EPR is the g -value. For a free electron in vacuum, $g = 2.0023$. However, in a molecule, especially in the presence of a heavy nucleus, spin-orbit coupling may cause a shift in the g value from the free electron value. In this sense, the g value now reflects the nature of the orbital that is singly occupied. Correspondingly, in the case of organic free radicals, g values remain close to the free electron value. However, in the case of transitional metals with unpaired electrons, the g values often times deviate considerably due to orbital contributions.

For example, Ferrous heme nitrosyls [Fe(porphyrin)(L)(NO)], discussed mostly in this thesis, show low-spin ($S = 1/2$) ground states regardless of whether the iron is five- (5C) or six-coordinate (6C) and independent of the nature of the axial ligand L trans to NO (L = N-donor, thiolate, etc.)⁴. Since iron is in the +II oxidation state and low-spin, it has a $[d_{xz}, d_{yz}, d_{x^2-y^2}]^6 = [t_2]^6$ electron configuration. Free nitric oxide is a radical with $S = 1/2$ ground state with the unpaired electron being located in the (singly occupied) π^* orbitals. Since the t_2 orbitals of iron are fully occupied, donation from this π^* orbital of NO is only possible into the d_{z^2} orbital of iron. This leads to a partial occupation of the d_{z^2} orbital depending on the strength of this interaction. Besides this σ donor bond, π backdonation from the occupied d_{xz} and d_{yz} orbitals into the empty π^* orbitals of NO is also present.

Based on this electronic structure description, it can be expected that the EPR spectra of ferrous heme NO adducts show similar g values as low-spin d^7 complexes with the electron configuration $[d_{xz}, d_{yz}, d_{x^2-y^2}]^6 [d_{z^2}]^1$, as observed, for example, for Co(II)-porphyrin complexes. For an $S = 1/2$ system with a non-degenerate ground state, perturbation theory yields the following expression for the g values:⁵

$$g_i = g_e - 2\lambda \sum_{n \neq 0} \frac{\langle \Psi_0 | L_i | \Psi_n \rangle \langle \Psi_n | L_i | \Psi_0 \rangle}{E_n - E_0} \quad i = x, y, z$$

Here, g_e is the Landé factor of the free electron, Ψ_0 is the ground state, and the sum runs over all excited states Ψ_n ($n \neq 0$). Applying a pure ligand field model, the following states need to be considered in a first order treatment:

$$\begin{aligned} |\Psi_0\rangle &= |(\text{passiveshells})d_{yz}^2 d_{xz}^2 d_{x^2-y^2}^2 d_{z^2}^1\rangle \\ |\Psi_1\rangle &= |(\text{passiveshells})d_{yz}^2 d_{xz}^2 d_{x^2-y^2}^1 d_{z^2}^2\rangle \\ |\Psi_2\rangle &= |(\text{passiveshells})d_{yz}^2 d_{xz}^1 d_{x^2-y^2}^2 d_{z^2}^2\rangle \\ |\Psi_3\rangle &= |(\text{passiveshells})d_{yz}^1 d_{xz}^2 d_{x^2-y^2}^2 d_{z^2}^2\rangle \end{aligned}$$

Using these ligand field states, but including orbital reduction factors for covalency, the g values for the d^7 electron configuration are:

$$\begin{aligned} g_z &= g_e = 2.002 \\ g_x &= g_e - \frac{6\lambda\alpha^2\beta^2}{\Delta E_{yz \rightarrow z^2}} \\ g_y &= g_e - \frac{6\lambda\alpha^2\gamma^2}{\Delta E_{xz \rightarrow z^2}} \end{aligned} \quad (\text{equation 3.11})$$

Here, λ is the spin-orbit coupling constant for iron(II) ($\lambda_0 \approx -390 \text{ cm}^{-1}$), and α , β , γ are the coefficients of the d_{z^2} , d_{yz} and d_{xz} functions, respectively, in the corresponding molecular orbitals. The denominator ΔE corresponds to the configurational excitation energy from d_{yz} or d_{xz} to d_{z^2} , respectively. Since the unpaired electron occupies a pure d_{z^2} orbital in this model, there are no additional contributions to g_z since $L_z d_{z^2} = 0$. In addition, the excited state $|\Psi_1\rangle$ does not contribute. Based on equation 3.11 it can be expected that the EPR spectra of ferrous nitrosyls are centered around $g = 2.00$ and, since d_{yz} or d_{xz} are not degenerate due to their anisotropic interaction with NO, the EPR spectra of these species should in general be rhombic with $(g_x \neq g_y) > g_z$. The g shifts for g_x and g_y should be small and positive and hence, all g values should be larger or equal to g_e . Since the unpaired electron density on iron in ferrous heme nitrosyls resides mostly in the d_{z^2} orbital, this ligand field model also predicts that strong hyperfine lines of the coordinated NO should therefore occur mostly on g_z .

3.3.2. EPR Instrumentation

A monochromatic microwave is used as an energy source for electronic transitions in EPR spectroscopy. The usual source used for this purpose is the klystron, which emits radiation over only a very narrow frequency range. The microwave beam direction is confined with the use of waveguides (WG), which are hollow tubes of copper or silver of rectangular cross section. The sample is placed inside the cavity as shown in Figure 3.5. A simple crystal detector is normally used in the EPR spectrometer. The spectrum is then recorded by sweeping the magnetic field while irradiating the sample with (almost) monochromatic microwaves.

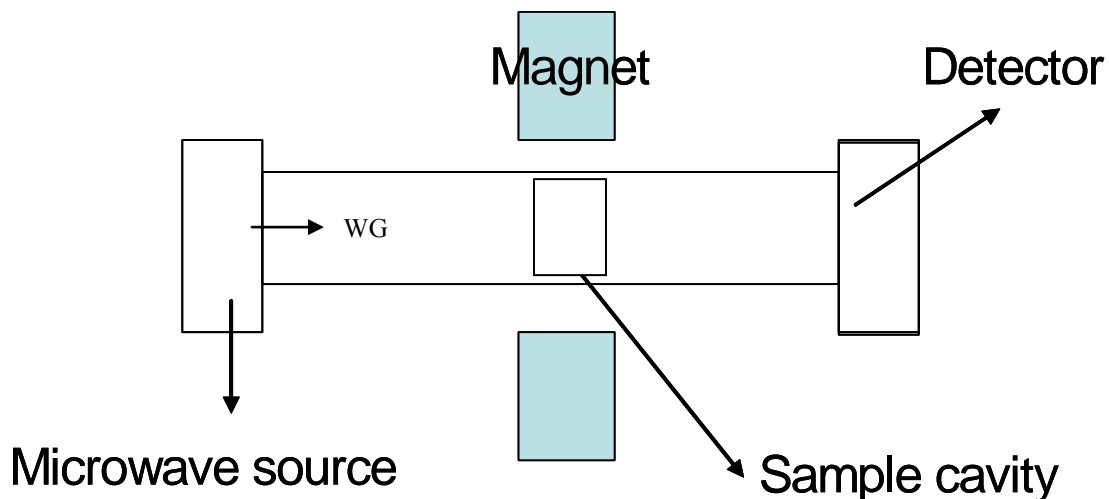


Figure 3.5. A schematic representation of the EPR spectrometer (simple block diagram).

3.4 Experimental Section

3.4.1 Syntheses with NO and Sample Preparation

For some of the syntheses (for example, the nitrosylation reactions presented in Chapters 5 and 6) performed in this work, Schlenk techniques were applied using Argon (≥ 4.6) as inert gas. The NO gas was carefully purified before usage to remove higher NO_x impurities such as N_2O_3 and NO_2 . For this purpose, the NO gas was passed through an ascarite II column (sodium hydroxide on silica gel) and then through a cold trap at -60 to -70 °C using dry ice and acetone. The $^{15}\text{N}^{18}\text{O}$ isotopically labeled gas was not further purified, and was taken directly from the lecture bottles. Sample preparation and storage of oxygen sensitive compounds was performed in an inert atmosphere using a MBraun dry box (glovebox). Oxygen sensitive samples for MCD and Raman spectroscopies were prepared in the dry box and immediately frozen in liquid nitrogen after removing from the dry box.

3.4.2 Spectroscopic Instrumentation

3.4.2.1. FT-IR Spectroscopy.

Middle- and Far Infrared spectra (MIR & FIR) were recorded on a Bruker IFS 66v vacuum instrument (University of Kiel) at room temperature. For the MIR region, KBr disks were used and the spectra were recorded at a resolution of 1 cm^{-1} . FIR spectra were obtained on

CsI pellets at a resolution of 2 cm^{-1} . At the university of Michigan, MIR spectra were recorded on a Perkin Elmer BX spectrometer and FIR spectra were recorded on a Nicolet 740 FT-IR spectrometer.

3.4.2.2. Nonresonance Raman (FT Raman) and resonance Raman Spectroscopy.

FT-Raman (nonresonance) spectra were recorded on a Bruker IFS 66 interferometer with a Bruker FRA 106 Raman attachment using a NdYAG laser for excitation ($\lambda = 1064\text{ nm}$). Measurements were performed on pure compounds. Resonance Raman spectra were measured using the instrument described in Section 3.2.1.

3.4.2.3. Magnetic Circular Dichroism Spectroscopy

The MCD spectrometer consists of a JASCO J-815 CD spectropolarimeter, a Spectromag⁴⁰⁰⁰ cryostat (OXFORD) with incorporated superconducting magnet, and the detector. Samples were measured in propionitrile and butyronitrile solvent mixtures or polystyrene films at liquid helium temperature, or as indicated as indicated in Chapter 4.

3.4.2.4 UV-Vis Spectroscopy

Absorption spectra were recorded at room temperature using a Varian CARY 5 UV/Vis-NIR spectrophotometer. The in-situ UV-Vis absorption spectroscopy was performed using an Analytik Jena Specord S600 diode array spectrophotometer and a dip probe. In this case, the operating range of the optical fibers is from 220 nm to 1100 nm.

3.4.2.5. ¹H-NMR Spectroscopy

¹H-NMR spectra at the University of Kiel were recorded on a Bruker Avance 400 pulse Fourier transform spectrometer operating at a ¹H frequency of 400 MHz. ¹H-NMR spectra at the University of Michigan were recorded on both a Varian Inova 400 spectrometer operating at 400 MHz (9.4 Tesla; Oxford Magnet) and a Varian Mercury 300 spectrometer operating at 300 MHz (7.0 Tesla; Oxford Magnet). Spectra were recorded at room temperature.

3.4.2.6. EPR Spectroscopy

EPR spectra were recorded on a X-band Bruker ESP-300E spectrometer in University of Hamburg, Germany, and Bruker EMX spectrometer at the University of Michigan, USA.

3.4.2.7. Mass Spectroscopy

Mass spectra were recorded on a Micromass Ultima spectrometer, which is a high resolution magnetic sector mass spectrometer using EI, CI, or Electrospray ionization techniques.

3.4.3. Density Functional Calculations

In general, density functional calculations were performed using the B3LYP and BP86 functionals, and the LanL2DZ and TZVP basis sets, respectively, as implemented in the program package Gaussian 03.⁶ In addition, the LanL2DZ* basis set was used, which consists of LanL2DZ plus polarization functions (from TZVP) on all heavy atoms.⁷ Details for the calculations are given in the individual chapters, when applicable. In all calculations, convergence was reached when the relative change in the density matrix between subsequent iterations was less than 1×10^{-8} . Semi-empirical calculations of absorption spectra were performed using the INDO/S-CI method as implemented in ORCA.⁸ Molecular and electronic structures as well as vibrations were visualized using the program packages GaussView⁶ and Molden.⁹

References

¹ Günzler, H.; Gremlich, H. -U. *IR Spectroscopy*, Wiley-VCH, **2002**.

² Paulat, F. *PHD Thesis*, Christian-Albrechts-Universität zu Kiel, Germany, **2007**.

³ Drago, R. S. *Physical methods in Chemistry*, W. B. Saunders company, **1977**.

⁴ Lehnert, N. 'EPR and Low-temperature MCD Spectroscopy of Ferrous Heme Nitrosyls', in: "*The Smallest Biomolecules: Diatomics and their Interaction with Heme Proteins*", Elsevier, **2007**.

⁵ Lever, A. B. P.; Solomon, E. I. 'Ligand Field Theory and the Properties of Transition Metal Complexes', in: "*Inorganic Electronic Structure and Spectroscopy*", Volume 1; Solomon, E. I.; Lever, A. B. P., eds., Wiley, New York, **1997**.

⁶ Frisch, M. J.; Trucks, G. W.; Schlegel, H. B.; Scuseria, G. E.; Robb, M. A.; Cheeseman, J. R.; Montgomery, J. A.; Vreven, Jr., T.; Kudin, K. N.; Burant, J. C.; Millam, J. M.; Iyengar, S. S.; Tomasi, J.; Barone, V.; Mennucci, B.; Cossi, M.; Scalmani, G.; Rega, N.; Petersson, G. A.; Nakatsuji, H.; Hada, M.; Ehara, M.; Toyota, K.; Fukuda, R.; Hasegawa, J.; Ishida, M.; Nakajima, T.; Honda, Y.; Kitao, O.; Nakai, H.; Klene, M.; Li, X.; Knox, J. E.; Hratchian, H. P.; Cross, J. B.; Adamo, C.; Jaramillo, J.; Gomperts, R.; Stratmann, R. E.; Yazyev, O.; Austin, A. J.; Cammi, R.; Pomelli, C.; Ochterski, J. W.; Ayala, P. Y.; Morokuma, K.; Voth, G. A.; Salvador, P.; Dannenberg, J. J.; Zakrzewski, V. G.; Dapprich, S.; Daniels, A. D.; Strain, M. C.; Farkas, O.; Malick, D. K.; Rabuck, A. D.; Raghavachari, K.; Foresman, J. B.; Ortiz, J. V.; Cui, Q.; Baboul, A. G.; Clifford, S.; Cioslowski, J.; Stefanov, B. B.; Liu, G.; Liashenko, A.; Piskorz, P.; Komaromi, I.; Martin, R. L.; Fox, D. J.; Keith, T.; Al-Laham, M. A.; Peng, C. Y.; Nanayakkara, A.; Challacombe, M.; Gill, P. M. W.; Johnson, B.; Chen, W.; Wong, M. W.; Gonzalez, C.; Pople, J. A. Gaussian, Inc., Pittsburgh PA, **2003**.

⁷ Praneeth, V. K. K.; Näther, C.; Peters, G.; Lehnert, N. *Inorg. Chem.* **2006**, *45*, 2795-2811.

⁸ Neese, F. *ORCA*, version 2.2; Max-Planck Institut fuer Bioorganische Chemie, Muelheim/Ruhr, Germany, **2004**.

⁹ Schaftenaar, G.; Noordik, J.H. *J. Comput.-Aided Mol. Design* **2000**, *14*, 123-134.

Chapter 4

Ferrous and Ferric Heme Nitrosyls with *trans* N-Donor Ligands

4.1. Scope of this project

NO adducts of ferrous heme nitrosyls occur as intermediates in many biologically important processes (cf. Chapter 1). These ferrous heme nitrosyls could either be six-coordinate (6C) with NO bound *trans* to an amino acid residue such as histidine, or five-coordinate (5C) with no *trans* ligand. The presence or absence of the *trans* ligand is vital in controlling the reactivity of the heme NO unit. NO binding to the enzyme soluble guanylate cyclase (sGC) leads to the formation of a 5C NO adduct, which activates the enzyme to catalyze the cyclization of guanosine triphosphate (GTP) to cyclic guanosine monophosphate (cGMP). It has been proposed that the formation of the five-coordinate ferrous heme NO complex induces conformational changes within sGC that lead to its activation. The 6C heme NO adduct with axially bound histidine is present in the active site of bacterial nitric oxide reductases (NorBC). It has been suggested that histidine plays a critical role in the formation of the N-N bond in the reduction of two molecules of NO.¹

Due to the importance of heme NO biochemistry, much research has been conducted toward the synthesis of either five-coordinate model complexes, or corresponding six-coordinate complexes with N-donor ligands like 1-methylimidazole (MI) in *trans* position to NO.² Despite the fact that much experimental information has been obtained on these model systems,³ their exact electronic structures are still not clearly defined. This is due to the fact that NO is a redox active ligand, which complicates the exact determination of the electronic structure and the assignment of (formal) oxidation states⁴ in these systems. We have therefore investigated five- and six-coordinate model systems of type $[\text{Fe}(\text{TPP}^*)(\text{L})(\text{NO})]^{n+}$ (TPP* = tetraphenylporphyrin type ligand; L = N-donor ligand or missing; n = 0, 1) in detail using various spectroscopic techniques coupled to DFT calculations.

We have employed low temperature magnetic circular dichroism (MCD) spectroscopy for the first time to understand the electronic structural differences between five- and six-coordinate ferrous heme-NO adducts. The MCD spectra of these complexes were evaluated with the help of DFT calculations. These results are presented in Section 4.2. The MCD

measurements on these model complexes were carried out by Prof. Dr. Frank Neese at the Max-Planck Institut für Bioanorganische Chemie, Mülheim, Germany. This work has been published as a short communication in *Inorganic Chemistry* (2005).

Section 4.3 comprises a detailed study on the five- and six-coordinate model systems with respect to the effect of the coordination of N-donor ligands (L) in trans position to NO in a much wider approach. Binding studies to five-coordinate complexes $[\text{Fe}(\text{TPP}^*)(\text{NO})]$ in solution as a function of the phenyl ring substitution in TPP and the employed nitrogen base are presented using UV-vis absorption and $^1\text{H-NMR}$ spectroscopy. This way, binding constants K_{eq} are determined, and the $^1\text{H-NMR}$ spectra of these complexes are assigned for the first time. A crystal structure of the complex $[\text{Fe}^{\text{II}}(\text{To-F}_2\text{PP})(\text{MI})(\text{NO})]$ (**2-F**, To-F₂PP = tetra(*ortho*-difluorophenyl) porphyrin) is presented. The differences in the electronic structures of five- and six-coordinate iron(II)-porphyrin NO complexes are then investigated by vibrational spectroscopy on $[\text{Fe}^{\text{II}}(\text{TPP})(\text{NO})]$ (**1**) and $[\text{Fe}^{\text{II}}(\text{TPP})(\text{MI})(\text{NO})]$ (**2**, MI = 1-methylimidazole) as examples. The vibrations of the Fe(II)-N-O subunits in **1** and **2** are completely assigned for the first time using isotope substitution. Force constants are determined using the quantum-chemistry centered normal coordinate analysis (QCC-NCA). The obtained force constants together with the $^1\text{H-NMR}$ results provide direct experimental evidence for a weakening of the Fe-NO bond in six- compared to five-coordinate Fe(II)-NO complexes. In addition, the MCD spectra of **1** and **2** presented in Section 4.2 are assigned using MCD theory and quantum chemical calculations. Based on all these spectroscopic results which are correlated to the DFT calculations, the electronic structural differences between five and six-coordinate iron(II)-porphyrin NO adducts are now defined in detail. Please note that the crystal structure of the complex $[\text{Fe}^{\text{II}}(\text{To-F}_2\text{PP})(\text{MI})(\text{NO})]$ was solved by Priv.-Doz. Dr. Christian Näther, and the NMR measurements were performed by Dr. Gerhard Peters. This work has been published in *Inorganic chemistry* (2006) as a full paper.

Section 4.4 comprises investigations on six-coordinate ferric porphyrin NO complexes. In this study, the mechanism of NO binding to ferric hemes and the possible variation in electronic structure of the formed complexes is investigated in detail using model compounds and DFT calculations. The six-coordinate model system $[\text{Fe}(\text{TPP})(\text{NO})(\text{MI})](\text{BF}_4)$ has been prepared and characterized using vibrational spectroscopy coupled to isotope substitution.

The energetics of NO binding to ferric hemes are investigated using DFT calculations. In addition, the crystal structure of the precursor, [Fe(TPP)(thf)₂](BF₄), is presented. The crystal structure was solved by Priv.-Doz. Dr. Christian Näther.

References

¹ Girsch, P.; de Vries, S. *Biochim. Biophys. Acta* **1997**, *1318*, 202-216.

² (a) Scheidt, W. R.; Elison, M. K.. *Acc. Chem. Res.* **1999**, *32*, 350-359. (b) Wyllie, G. R. A.; Scheidt, W. R. *Chem. Rev.* **2002**, *102*, 1067-1090. (c) Ford, P. C.; Fernandez, B. O.; Lim, M. D. *Chem. Rev.* **2005**, *105*, 2439-2456.

³ (a) Ford, P. C.; Lorkovic, I. M. *Chem. Rev.* **2002**, *102*, 993-1017. (b) Wyllie, G. R. A.; Scheidt, R. *Chem. Rev.* **2002**, *102*, 1067-1089. (c) Walker, F. A.; Simonis, U. 'Iron Porphyrin Chemistry', in: Encyclopedia of Inorganic Chemistry, Bruce, R. B., Ed., Wiley, in press.

⁴ Westcott, B. L.; Enemark, J. H. *Transition Metal Nitrosyls*; Solomon, E. I. and Lever, A. B. P., Ed.; Wiley: New York, 1999; Vol. Volume 2, pp 403-450.

4.2. Spin Density Distribution in Five- and Six-Coordinate Iron(II)-Porphyrin NO Complexes Evidenced by Magnetic Circular Dichroism Spectroscopy

V. K. K. Praneeth, Frank Neese, and Nicolai Lehnert*

Published in: *Inorg. Chem.* **2005**, *44*, 2570-2572.

Spin Density Distribution in Five- and Six-Coordinate Iron(II)–Porphyrin NO Complexes Evidenced by Magnetic Circular Dichroism Spectroscopy

V. K. K. Praneeth,[†] Frank Neese,[‡] and Nicolai Lehnert^{*†}*Institut für Anorganische Chemie, Christian-Albrechts-Universität Kiel, Olshausenstrasse 40, 24098 Kiel, Germany, and Max-Planck Institut für Bioanorganische Chemie, Stiftstrasse, 34-36, 45470 Mülheim an der Ruhr, Germany*

Received January 28, 2005

Using magnetic circular dichroism (MCD) spectroscopy together with DFT calculations, the spin density distributions in five-coordinate [Fe(TPP)(NO)] (**I**) and six-coordinate [Fe(TPP)(MI)(NO)] (**II**, MI = 1-methylimidazole) are defined. In the five-coordinate complex, a strong Fe–NO σ bond between π^*_h and d_z^2 is present that leads to a large transfer of spin density from the NO ligand to Fe(II) corresponding to an electronic structure with noticeable Fe(I)–NO⁺ character. Consequently, the MCD spectrum is dominated by paramagnetic C-term contributions. On coordination of the sixth ligand, the spin density is pushed back from the iron toward the NO ligand, resulting in an Fe(II)–NO(radical) type of electronic structure. This is reflected by the fact that the MCD spectrum is dominated by diamagnetic contributions.

Iron–porphyrin NO complexes play a key role in the mechanisms of many metalloproteins.^{1,2} Hence, synthetic model systems for these species have been investigated in great detail.³ Corresponding iron(II)–NO complexes are still the focus of many ongoing studies because of their interesting spectroscopic and photochemical properties⁴ and their mechanistic significance.³ In this communication, the low-temperature magnetic circular dichroism (MCD) spectra of five-coordinate [Fe^{II}(TPP)(NO)] (**I**, TPP = tetraphenylporphyrin) and six-coordinate [Fe^{II}(TPP)(MI)(NO)] (**II**, MI = 1-methylimidazole) are reported for the first time and analyzed with the help of density functional (DFT) calculations. Both complexes **I** and **II** have $S = 1/2$ ground states.⁵ From their

different EPR spectra, Wyllie et al. speculated that these systems have different electronic ground states,⁶ but no further evidence for this conjecture is provided. Judging from the MCD spectra and DFT calculations presented here, this difference in electronic structure of **I** and **II** is elucidated.

MCD intensity is generally considered to arise from three different mechanisms.⁷ The C term is temperature-dependent and originates from spin–orbit coupling of the ground and target excited states with other intermediate excited states. On the other hand, the A and B terms are temperature-independent and are also present in diamagnetic materials. Thus, the paramagnetic (C-term) contribution to the total spectrum can be extracted by subtracting MCD data taken at variable temperatures. Figure 1 shows the MCD spectra of five-coordinate (5C) [Fe^{II}(TPP)(NO)] (top) and six-coordinate (6C) [Fe^{II}(TPP)(MI)(NO)] (bottom) in comparison. As one can see, these data are very different. In the case of **I**, the C-term spectrum obtained from temperature-dependent data is identical in appearance to the total spectrum. Consequently, the MCD response is dominated by the paramagnetic C-term contribution. Because spin–orbit coupling is weak for light elements such as carbon, nitrogen, and oxygen, the C-term nature of the spectrum indicates that a significant amount of spin density of the unpaired electron in **I** must be located on the formally iron(II) center. This is dramatically different for the 6C complex **II**. From Figure 1, bottom, one can see that the deconvoluted MCD C-term spectrum is different from the total spectrum, which is, in fact, dominated by temperature-independent diamagnetic contributions (A and B terms). These are generally observed for diamagnetic metal porphyrin complexes because of the occurrence of (practically) degenerate excited states in the porphyrin dianion with approximate D_{4h}

* To whom correspondence should be addressed. E-mail: nlehnert@ac.uni-kiel.de.

[†] Christian-Albrechts-Universität Kiel.

[‡] Max-Planck Institut für Bioanorganische Chemie.

- (1) McCleverty, J. A. *Chem. Rev.* **2004**, *104*, 403.
- (2) (a) Richardson, D. J.; Watmough, N. J. *Curr. Opin. Chem. Biol.* **1999**, *3*, 207. (b) Ding, X. D.; Weichsel, A.; Andersen, J. F.; Shokhireva, T. K.; Balfour, C.; Pierik, A. J.; Averill, B. A.; Montfort, W. R.; Walker, F. A. *J. Am. Chem. Soc.* **1999**, *121*, 128. (c) Poulos, T. L.; Li, H.; Raman, C. S. *Curr. Opin. Chem. Biol.* **1999**, *3*, 131.
- (3) (a) Ford, P. C.; Lorkovic, I. M. *Chem. Rev.* **2002**, *102*, 993. (b) Wyllie, G. R. A.; Scheidt, R. *Chem. Rev.* **2002**, *102*, 1067.
- (4) Cheng, L.; Novozhilova, I.; Kim, C.; Kovalevsky, A.; Bagley, K. A.; Coppens, P.; Richter-Addo, G. B. *J. Am. Chem. Soc.* **2000**, *122*, 7142.

- (5) Westcott, B. L.; Enemark, J. H. *Transition Metal Nitrosyls*; Solomon, E. I., Lever, A. B. P., Eds.; Wiley: New York, 1999; Vol. 2, pp 403–450.

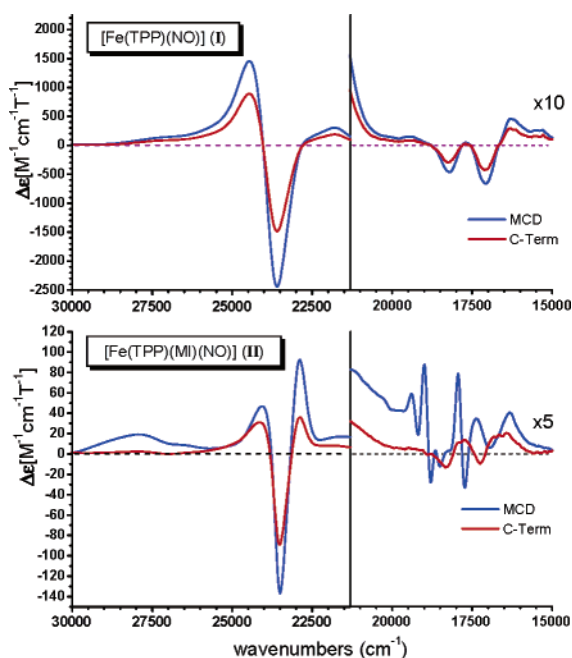
- (6) Wyllie, G. R. A.; Schulz, C. E.; Scheidt, W. R. *Inorg. Chem.* **2003**, *42*, 5722.

- (7) (a) Cheesman, M. R.; Greenwood, C.; Thomson, A. J. *Adv. Inorg. Chem.* **1991**, *36*, 201. (b) Neese, F.; Solomon, E. I. *Inorg. Chem.* **1999**, *38*, 1847. (c) Oganessian, V. S.; George, S. J.; Cheesman, M. R.; Thomson, A. J. *J. Chem. Phys.* **1999**, *110*, 762.

Table 1. Comparison between Experimental and Calculated Properties of Fe(II)–Porphyrin NO Adducts (All $S = 1/2$)^a

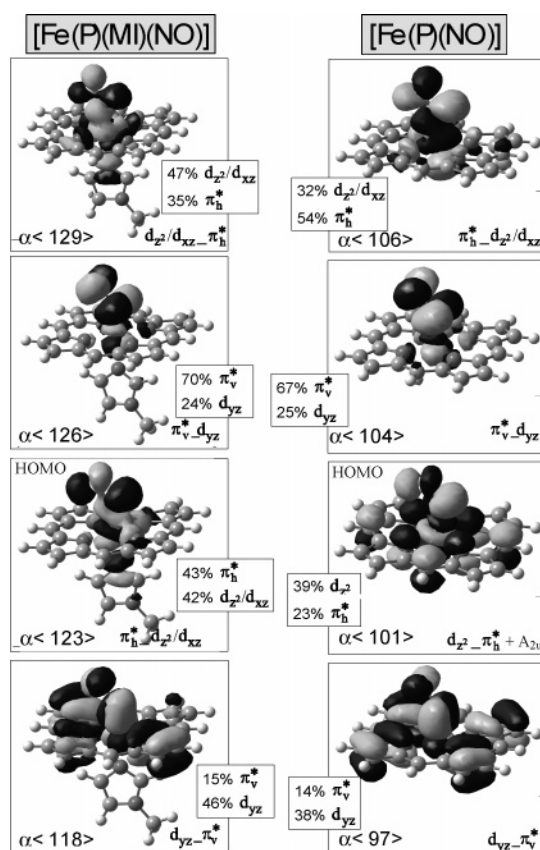
molecule	geometric parameters (Å or deg)				$\nu(\text{N–O})$ (cm^{-1})	spin density ^b		Mössbauer parameters (mm/s)		EPR parameters				ref
	Fe–N	N–O	Fe–N–O	Fe–X		Fe	NO	δ	ΔE_q	g_{max}	g_{mid}	g_{min}	orientation	
Fe(TPP)(NO) (I) ^c	1.72	1.12	149	–	1697			0.33 ^a	1.25 ^a	2.102	2.064	2.010	–	11a
Fe(OEP)(NO) ^c	1.73	1.17	143	–	1673 ^a			0.35 ^a	1.26 ^a	2.106	2.057	2.015	$g_{\text{min}}/\text{Fe–N} = 8^\circ$	11b
Fe(P)(NO) (Ia) BP86/TZVP	1.70	1.18	146	–	1703	+0.47	+0.53			2.043	2.007	1.997	$g_{\text{min}}/\text{Fe–N} = 24^\circ$	
Fe(P)(NO) ^d								0.36	0.73	2.049	2.025	2.004	$g_{\text{min}}/\text{Fe–N} = 20^\circ$	
Fe(TPP)(MI)(NO) (II) ^c	1.75	1.18	138	2.17	1630			0.34 ^a	0.73 ^a	2.079	2.004	1.972	–	11d
Fe(P)(MI)(NO) (IIa) BP86/TZVP	1.73	1.19	140	2.18	1662	+0.21	+0.78			2.031	1.998	1.972	$g_{\text{mid}}/\text{Fe–N} = 41^\circ$ $g_{\text{min}}/\text{Fe–N} = 49^\circ$	
Fe(P)(MI)(NO) ^d								0.38	[0.57]	2.024	1.991	1.955	$g_{\text{mid}}/\text{Fe–N} = 29^\circ$	

^a For abbreviations, see text. Fe–X is the Fe–N(imidazole) distance. Because there is an ambiguity about the N–O stretch in five-coordinate [Fe(TPP)(NO)] (values of 1700^{11a} and 1670^{3b} cm^{-1} have been reported), we have reinvestigated the IR spectra of **I** and **II** as shown in Figure S3. For [Fe(OEP)(NO)], $\nu(\text{N–O})$ is taken from ref 6. Experimental Mössbauer parameters are taken from ref 6. ^b Spin densities are calculated at the B3LYP/LanL2DZ* level (cf. Experimental Details in the Supporting Information). ^c Structural data: [Fe(TPP)(NO)] and [Fe(OEP)(NO)], ref 3b; [Fe(TPP)(MI)(NO)], ref 6. ^d Calculated with B3LYP and the following basis sets: Fe, CP(PPP); N, EPR–II; C and O, TZVP; H, TZV (see Supporting Information).

**Figure 1.** MCD spectra of [Fe^{II}(TPP)(NO)] (top) and [Fe^{II}(TPP)(MI)(NO)] (bottom) measured in a butyronitrile/propionitrile glass.

symmetry.⁸ This indicates that the unpaired spin density is mostly located on the NO unit in the 6C case, which leads to the temperature-independent MCD spectrum of diamagnetic low-spin Fe(II)–porphyrins. Detailed assignments of the observed electronic transitions are complicated and will therefore be presented in a forthcoming full paper.

The fact that the paramagnetic complex **II** exhibits such low C-term intensity is surprising and indicates a different ground state for **II** compared to **I**. To elucidate the electronic structural origin of this difference, DFT calculations at the BP86/TZVP level have been applied using the model systems [Fe^{II}(P)(NO)] (**Ia**) and [Fe^{II}(P)(NO)(MI)] (**IIa**, P = porphine; cf. Figure S4, Supporting Information).⁹ As shown in Table

**Figure 2.** Contour plots of important α -MOs of [Fe^{II}(P)(MI)(NO)] (left) and [Fe^{II}(P)(NO)] (right) calculated with BP86/TZVP.

1, the obtained agreement between the calculated and experimental structures is excellent. In complex **II**, the Fe–NO bond is dominated by two interactions. First, a pseudo- σ donation from the singly occupied π^*_{h} orbital of NO ($\text{h} = \text{horizontal}$, the π^* orbital in the Fe–N–O plane) into the unoccupied d_{z^2} orbital of iron(II) is present.⁹ The corresponding bonding combination, $\alpha(123)$, has an additional admixture of d_{xz} and is therefore labeled $\pi^*_{\text{h}} d_{z^2}/d_{xz}$. It is the HOMO of **II** (cf. Figure 2, left). Because d_{z^2} also interacts with the σ donor orbital of the bound 1-methylimidazole, this competition for d_{z^2} explains the strong trans effect of NO on σ -donor ligands. This can also

(8) Gouterman, M. Optical Spectra and Electronic Structure of Porphyrins and Related Rings. In *The Porphyrins*; Dolphin, D., Ed.; Academic Press: New York, 1978; Vol. III.

(9) The model systems and the applied coordinate system are shown in Figure S4. The complete MO diagram and contour plots of **II** are shown in Figures S6 and S7.

be seen from the corresponding antibonding orbital, $d_{z^2}/d_{yz}\pi^*_h$ ($\alpha(129)$). The second interaction is a medium-strength π back-bond between the π^*_v orbital of NO (v = vertical, the π^* orbital perpendicular to the Fe–N–O plane) and the d_{yz} orbital of iron.⁹ Corresponding bonding ($\alpha(118)$) and antibonding ($\alpha(126)$) orbitals are also shown in Figure 2. To calculate accurate spin densities for **IIa**, the B3LYP functional was applied, as pure density functionals tend to clearly overestimate metal–ligand covalencies. Importantly, only a small amount of spin population is obtained on iron (+0.2), which is mostly due to the Fe–NO σ bond, whereas the contribution from the back-bond is small. As shown in Table 1, most spin population is actually located on the coordinated NO ligand, in agreement with the MCD result. Altogether, a satisfactory theoretical description of the six-coordinate complex **II** is obtained. This is also reflected by the calculated N–O stretching frequency, which is in good agreement with experiment. Therefore, complex **II** must be described as the prototype of a low-spin Fe(II)–NO(radical) adduct.

The interesting question is then how this electronic structure changes when going to the five-coordinate complex **I**. The most important difference is that, because of the absence of the sixth ligand, the d_{z^2} orbital strongly decreases in energy.⁵ Hence, mixing with π^*_h becomes very strong such that the HOMO $d_{z^2}\pi^*_h$ ($\alpha(101)$) has mostly d_{z^2} character (cf. contour in Figure 2, right). Because of mixing with porphyrin orbitals, an additional 18% d_{z^2} occurs in orbital $\alpha(98)$ (π^*_h contribution = 3%). In total, this corresponds to a net transfer of about one-half of an electron to the Fe(II) center. Hence, the complex has noticeable Fe(I)–NO⁺ character. This leads to the occurrence of a large amount of positive spin density on iron (cf. Table 1) and explains the C-term MCD spectrum obtained for **I**. In agreement with this description, the N–O stretching frequency is shifted to higher energy by ~ 70 cm⁻¹ in **I** compared to **II** (cf. Table 1). On the other hand, the π back-bond is comparable for **I** and **II**, as shown in Figure 2, right.¹⁰ From single-crystal EPR spectroscopy, the spin populations in the related complex [Fe(OEP)(NO)] have been estimated to +0.9 on iron and +0.1 on NO.^{11b} Similar values have been obtained in a recent computational study using pure density functionals.¹² However, this would correspond to an almost complete electron transfer from NO to iron, leading to a low-spin

Fe(I)–NO⁺ with a d^7 configuration on iron. In contrast, the occurrence of the N–O stretching frequency below 1700 cm⁻¹ in **I** shows that this is a clear overestimate. This is also not in agreement with the calculations presented here, which show an even distribution of the unpaired electron over the Fe–N–O unit. In a previous DFT study, it was claimed that complex **I** has Fe(III)–NO⁻ character.¹³ This, however, is not in agreement with our experimental and DFT results.

The results presented above are also useful for evaluating the very different EPR spectra of five- and six-coordinate Fe(II)–porphyrin NO adducts.¹¹ For complex **I**, a characteristic spectrum is observed with hyperfine lines from the nitrogen of NO on the smallest g value g_{\min} . The six-coordinate complex **II** shows a broader spectrum, where hyperfine lines are observed for the nitrogens of NO and of the trans-N donor on g_{mid} . In addition, different g values are obtained for these complexes. It was claimed that these differences in the EPR spectra are due to different orientations of the g tensor with respect to the molecular frame.^{6,11c} In agreement with these results, our calculations show that the strong Fe–NO σ interaction in **I** mediated by the orbital $d_{z^2}\pi^*_h$ orients the g tensor along the Fe–N(O) bond as shown in Table 1. In this case, the axis of g_{\min} (the smallest g value) is almost aligned with the Fe–N(O) bond, which leads to the occurrence of the experimentally observed hyperfine lines on g_{\min} . In complex **II**, the g tensor is rotated away from the Fe–N(O) bond, with g_{mid} now being closest to the Fe–N(O) and Fe–N(imidazole) axes. Correspondingly, this g value now shows strong hyperfine splittings. We have also calculated Mössbauer parameters (cf. Table 1) and the ¹⁴N hyperfine tensor A of the coordinated NO (cf. Table S2, Supporting Information), which show acceptable agreement with experiment, further indicating that a good theoretical description of **I** and **II** is achieved.

Acknowledgment. This work was supported by the Deutsche Forschungsgemeinschaft (DFG, Grant LE 1393/1) and the Fonds der Chemischen Industrie. F.N. acknowledges financial support by the Max Planck Gesellschaft and the DFG (SPP 1137).

Supporting Information Available: Experimental details, UV–vis absorption vs MCD spectra of **I** and **II** including Gaussian fits, IR spectra of **I** and **II**, MO diagram of **II**, and contour plots. This material is available free of charge via the Internet at <http://pubs.acs.org>.

IC050144K

- (10) Small differences in π back-bonding are observed for the β -MOs. The somewhat increased β -back-bond for **I** compared to **II** leads to the transfer of a small additional amount of spin density from NO to iron in **I** relative to **II**. This will be discussed in detail in the forthcoming full paper.
- (11) (a) Wayland, B. B.; Olson, L. W. *J. Am. Chem. Soc.* **1974**, *96*, 6037. (b) Hayes, R. G.; Ellison, M. K.; Scheidt, W. R. *Inorg. Chem.* **2000**, *39*, 3665. (c) Patchkovskii, S.; Ziegler, T. *Inorg. Chem.* **2000**, *39*, 5354. (d) Hüttermann, J.; Burgard, C.; Kappl, R. *J. Chem. Soc., Faraday Trans.* **1994**, *90*, 3077. (e) Zhang, Y.; Gossman, W.; Oldfield, E. *J. Am. Chem. Soc.* **2003**, *125*, 16387.

- (12) Zhang, Y.; Mao, J.; Godbout, N.; Oldfield, E. *J. Am. Chem. Soc.* **2002**, *124*, 13921.
- (13) Rovira, C.; Kunc, K.; Hutter, J.; Ballone, P.; Parrinello, M. *J. Phys. Chem. A* **1997**, *101*, 8914.

4.3. Spectroscopic Properties and Electronic Structure of Five- and Six-Coordinate Iron(II) Porphyrin NO Complexes: Effect of the Axial N-Donor Ligand

V. K. K. Praneeth, Christian Näther, Gerhard Peters, and Nicolai Lehnert*

Published in: *Inorg. Chem.* **2006**, *45*, 2795-2811.

Spectroscopic Properties and Electronic Structure of Five- and Six-Coordinate Iron(II) Porphyrin NO Complexes: Effect of the Axial N-Donor Ligand

V. K. K. Praneeth, Christian Näther, Gerhard Peters, and Nicolai Lehnert*

Institut für Anorganische Chemie, Christian-Albrechts-Universität Kiel, Olshausenstrasse 40, D-24098 Kiel, Germany

Received May 30, 2005

In this paper, the differences in the spectroscopic properties and electronic structures of five- and six-coordinate iron(II) porphyrin NO complexes are explored using [Fe(TPP)(NO)] (**1**; TPP = tetraphenylporphyrin) and [Fe(TPP)(MI)(NO)] (**2**; MI = 1-methylimidazole) type systems. Binding of N-donor ligands in axial position trans to NO to five-coordinate complexes of type **1** is investigated using UV–vis absorption and ¹H NMR spectroscopies. This way, the corresponding binding constants K_{eq} are determined and the ¹H NMR spectra of **1** and **2** are assigned for the first time. In addition, ¹H NMR allows for the determination of the degree of denitrosylation in solutions of **1** with excess base. The influence of the axial ligand on the properties of the coordinated NO is then investigated. Vibrational spectra (IR and Raman) of **1** and **2** are presented and assigned using isotope substitution and normal-coordinate analysis. Obtained force constants are 12.53 (N–O) and 2.98 mdyn/Å (Fe–NO) for **1** compared to 11.55 (N–O) and 2.55 mdyn/Å (Fe–NO) for **2**. Together with the NMR results, this provides experimental evidence that binding of the trans ligand weakens the Fe–NO bond. The principal bonding schemes of **1** and **2** are very similar. In both cases, the Fe–N–O subunit is strongly bent. Donation from the singly occupied π^* orbital of NO into d_z^2 of iron(II) leads to the formation of an Fe–NO σ bond. In addition, a medium-strong π back-bond is present in these complexes. The most important difference in the electronic structures of **1** and **2** occurs for the Fe–NO σ bond, which is distinctively stronger for **1** in agreement with the experimental force constants. The increased σ donation from NO in **1** also leads to a significant transfer of spin density from NO to iron, as has been shown by magnetic circular dichroism (MCD) spectroscopy in a preceding Communication (Praneeth, V. K. K.; Neese, F.; Lehnert, N. *Inorg. Chem.* **2005**, *44*, 2570–2572). This is confirmed by the ¹H NMR results presented here. Hence, further experimental and computational evidence is provided that complex **1** has noticeable Fe^{II}NO⁺ character relative to **2**, which is an Fe^{II}NO(radical) complex. Finally, using MCD theory and quantum chemical calculations, the absorption and MCD C-term spectra of **1** and **2** are assigned for the first time.

Introduction

Iron porphyrin NO complexes play a key role in the mechanisms of many metalloproteins.¹ These include nitrite and nitric oxide reductases (NIRs and NORs, denitrification),² NO receptors in neural signaling,³ NO carriers in bloodsucking insects (nitrophorins),⁴ nitric oxide synthase,⁵ and guan-

ylate cyclase.⁶ Among the different hemes investigated, the NO adducts of hemoglobin and myoglobin are probably some

* To whom correspondence should be addressed. E-mail: nlehnert@ac.uni-kiel.de.

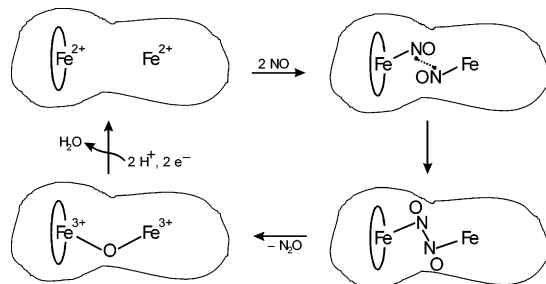
(1) McCleverty, J. A. *Chem. Rev.* **2004**, *104*, 403–418.
(2) (a) Ferguson, S. J. *Curr. Opin. Chem. Biol.* **1998**, *2*, 182–193. (b) Richardson, D. J.; Watnough, N. J. *Curr. Opin. Chem. Biol.* **1999**, *3*, 207–219. (c) Moura, I.; Moura, J. J. G. *Curr. Opin. Chem. Biol.* **2001**, *5*, 168–175.

(3) (a) Moncada, S.; Palmer, R. M. J.; Higgs, E. A. *Pharmacol. Rev.* **1991**, *43*, 109–142. (b) Bredt, D. S.; Snyder, S. H. *Annu. Rev. Biochem.* **1994**, *63*, 175–195.

(4) (a) Ribeiro, J. M. C.; Hazzard, J. M. H.; Nussenzweig, R. H.; Champagne, D. E.; Walker, F. A. *Science* **1993**, *260*, 539–541. (b) Ding, X. D.; Weichsel, A.; Andersen, J. F.; Shokhireva, T. K.; Balfour, C.; Pierik, A. J.; Averill, B. A.; Montfort, W. R.; Walker, F. A. *J. Am. Chem. Soc.* **1999**, *121*, 128–138. (c) Walker, F. A. *J. Inorg. Biochem.* **2005**, *99*, 216–236.

(5) (a) Stuehr, D. J. *Annu. Rev. Pharmacol. Toxicol.* **1997**, *37*, 339–359. (b) Poulos, T. L.; Li, H.; Raman, C. S. *Curr. Opin. Chem. Biol.* **1999**, *3*, 131–137. (c) Li, H.; Poulos, T. L. *J. Inorg. Biochem.* **2005**, *99*, 293–305.

Scheme 1



of the most-studied systems in biology.⁷ Many of these proteins that have been studied contain iron porphyrin centers with axial histidine ligation. Corresponding iron(II) porphyrin NO complexes occur as intermediates in bacterial NOR.⁸ This enzyme reduces nitric oxide to nitrous oxide at an active site that contains both an iron porphyrin and a nonheme iron center in close proximity. The proposed mechanism includes binding of two molecules of NO (one at each of the two metal centers) followed by N–N coupling of the two NO units as the central step of catalysis (cf. Scheme 1).⁹ However, evidence to prove this mechanism is still lacking and, in addition, other investigations have led to different mechanistic possibilities as well.¹⁰ It is, therefore, of central importance to define the electronic structure of the iron(II) porphyrin NO adducts in detail to obtain further insight into the catalytic mechanism of this enzyme. In the case of soluble guanylate cyclase, a five-coordinate (5C) ferrous heme with axial histidine is present in the active site, which, upon coordination of NO, forms a 5C NO adduct where histidine is no longer bound to the iron(II) center. This triggers a conformational change that activates the enzyme. Because of this general importance of iron porphyrin NO adducts, a large amount of research has been conducted toward the synthesis of corresponding model complexes. These investigations use synthetic porphyrin ligands such as tetraphenylporphyrin (TPP) or octaethylporphyrin (OEP). Most of the research is focused on either 5C species [Fe(porphyrin)-(NO)]ⁿ⁺ ($n = 0$ and 1) or corresponding six-coordinate (6C) complexes with N-donor ligands such as imidazole, pyridine (Py), piperidine, etc., in the position trans to NO.¹¹ Corresponding iron(II) model complexes are still the focus of many ongoing studies because of their interesting spectroscopic and photochemical properties¹² and their mechanistic significance.^{10c,11a,13} From crystallography, these systems are

characterized by short Fe–N(O) distances of about 1.75 Å and bent Fe–NO units with an Fe–N–O angle of about 140°. ^{14,15} Importantly, electron paramagnetic resonance (EPR) spectroscopic studies revealed interesting differences between the 5C and 6C iron(II) porphyrin NO adducts:¹⁶ 5C complexes show a characteristic spectrum with hyperfine lines from the nitrogen of NO on the smallest g value, $g(\text{min})$, whereas corresponding 6C complexes show a broader spectrum, where hyperfine lines are now observed for the nitrogens of NO and of the *trans*-N donor on $g(\text{mid})$. These differences in the EPR spectra are due to different orientations of the g tensor in these complexes.^{14,17} From vibrational spectroscopy, the 5C iron(II) porphyrin NO adduct [Fe(TPP)-(NO)] (1) has an N–O stretching frequency of about 1700 cm⁻¹, whereas the corresponding 6C complex [Fe(TPP)(MI)-(NO)] (2) with 1-methylimidazole (MI) as the axial ligand shows $\nu(\text{NO})$ at about 1630 cm⁻¹.^{11b,16a,18} Despite the large amount of experimental data available for these systems, their exact electronic structures are still not clearly defined. This is due to the fact that NO is a redox-active ligand, which complicates the exact determination of the electronic structure and the assignment of (formal) oxidation states.¹⁹ A number of density functional theory (DFT) studies have focused on these complexes, and different electronic structures have been obtained from these calculations.^{17,20} In a recent paper, we have used magnetic circular dichroism (MCD) spectroscopy²¹ coupled with DFT calculations to elucidate the differences in the electronic structures of 5C and 6C iron(II) porphyrin

- (6) (a) Garbers, D. L.; Lowe, D. G. *J. Biol. Chem.* **1994**, *269*, 30741–30744. (b) Zhao, Y.; Hoganson, C.; Babcock, G. T.; Marletta, M. A. *Biochemistry* **1998**, *37*, 12458–12464.
- (7) Møller, J. K. S.; Skibsted, L. H. *Chem. Rev.* **2002**, *102*, 1167–1178.
- (8) Wasser, I. M.; de Vries, S.; Moënné-Loccoz, P.; Schröder, I.; Karlin, K. D. *Chem. Rev.* **2002**, *102*, 1201–1234.
- (9) Girsch, P.; de Vries, S. *Biochim. Biophys. Acta* **1997**, *1318*, 202–216.
- (10) (a) Butler, C. S.; Seward, H. E.; Greenwood, C.; Thomson, A. J. *Biochemistry* **1997**, *36*, 16259–16266. (b) Watmough, N. J.; Cheesman, M. R.; Butler, C. S.; Little, R. H.; Greenwood, C.; Thomson, A. J. *J. Bioenerg. Biomembr.* **1998**, *30*, 55–62. (c) Lin, R.; Farmer, P. J. *J. Am. Chem. Soc.* **2001**, *123*, 1143–1150.
- (11) (a) Ford, P. C.; Lorkovic, I. M. *Chem. Rev.* **2002**, *102*, 993–1017. (b) Wyllie, G. R. A.; Scheidt, R. *Chem. Rev.* **2002**, *102*, 1067–1089. (c) Walker, F. A.; Simonis, U. *Iron Porphyrin Chemistry*. In *Encyclopedia of Inorganic Chemistry*; Bruce, R. B., Ed.; Wiley: New York, 2005.

- (12) (a) Zavarine, I. S.; Kini, A. D.; Morimoto, B. H.; Kubiak, C. P. *J. Phys. Chem. B* **1998**, *102*, 7287–7292. (b) Cheng, L.; Novozhilova, I.; Kim, C.; Kovalevsky, A.; Bagley, K. A.; Coppens, P.; Richter-Addo, G. B. *J. Am. Chem. Soc.* **2000**, *122*, 7142–7143. (c) Lee, J.; Kovalevsky, A. Y.; Novozhilova, I. V.; Bagley, K. A.; Coppens, P.; Richter-Addo, G. B. *J. Am. Chem. Soc.* **2004**, *126*, 7180–7181.
- (13) (a) Lorković, I. M.; Ford, P. C. *Inorg. Chem.* **1999**, *38*, 1467–1473. (b) Kurtikyan, T. S.; Martirosyan, G. G.; Lorković, I. M.; Ford, P. C. *J. Am. Chem. Soc.* **2002**, *124*, 7180–7181. (c) Lim, M. D.; Lorković, I. M.; Wedeking, K.; Zanella, A. W.; Works, C. F.; Massick, S. M.; Ford, P. C. *J. Am. Chem. Soc.* **2002**, *124*, 9737–9743. (d) Patterson, J. C.; Lorković, I. M.; Ford, P. C. *Inorg. Chem.* **2003**, *42*, 4902–4908. (e) Lim, M. D.; Lorković, I. M.; Ford, P. C. *J. Inorg. Biochem.* **2005**, *99*, 151–165.
- (14) Wyllie, G. R. A.; Schulz, C. E.; Scheidt, W. R. *Inorg. Chem.* **2003**, *42*, 5722–5734.
- (15) Scheidt, W. R.; Ellison, M. K. *Acc. Chem. Res.* **1999**, *32*, 350–359.
- (16) (a) Wayland, B. B.; Olson, L. W. *J. Am. Chem. Soc.* **1974**, *96*, 6037–6041. (b) Morse, R. H.; Chan, S. I. *J. Biol. Chem.* **1980**, *255*, 7876–7882. (c) Hüttermann, J.; Burgard, C.; Kappl, R. *J. Chem. Soc., Faraday Trans.* **1994**, *90*, 3077. (d) Hayes, R. G.; Ellison, M. K.; Scheidt, W. R. *Inorg. Chem.* **2000**, *39*, 3665–3668.
- (17) Patchkovskii, S.; Ziegler, T. *Inorg. Chem.* **2000**, *39*, 5354–5364.
- (18) Praneeth, V. K. K.; Neese, F.; Lehnert, N. *Inorg. Chem.* **2005**, *44*, 2570–2572.
- (19) Westcott, B. L.; Enemark, J. H. *Transition Metal Nitrosyls*; Solomon, E. I.; Lever, A. B. P., Eds.; Wiley: New York, 1999; Vol. 2, pp 403–450.
- (20) (a) Rovira, C.; Kunc, K.; Hutter, J.; Ballone, P.; Parrinello, M. *J. Phys. Chem. A* **1997**, *101*, 8914–8925. (b) Ghosh, A.; Wondimagegn, T. *J. Am. Chem. Soc.* **2000**, *122*, 8101–8102. (c) Zhang, Y.; Mao, J.; Godbout, N.; Oldfield, E. *J. Am. Chem. Soc.* **2002**, *124*, 13921–13930. (d) Zhang, Y.; Gossman, W.; Oldfield, E. *J. Am. Chem. Soc.* **2003**, *125*, 16387–16396.
- (21) (a) Cheesman, M. R.; Greenwood, C.; Thomson, A. J. *Adv. Chem. Phys.* **1991**, *36*, 201–255. (b) Solomon, E. I.; Pavel, E. G.; Loeb, K. E.; Campochiaro, C. *Coord. Chem. Rev.* **1995**, *144*, 369–460. (c) Neese, F.; Solomon, E. I. *Inorg. Chem.* **1999**, *38*, 1847–1865. (d) Oganessian, V. S.; George, S. J.; Cheesman, M. R.; Thomson, A. J. *J. Chem. Phys.* **1999**, *110*, 762–777. (e) Lehnert, N.; DeBeer George, S.; Solomon, E. I. *Curr. Opin. Chem. Biol.* **2001**, *5*, 176–187.

NO adducts.¹⁸ It was shown that, in the 5C complex **1**, a strong Fe–NO σ bond is present that leads to a large transfer of spin density from the NO ligand to Fe^{II} corresponding to an electronic structure with considerable Fe^INO⁺ character. In the 6C complex **2**, on the other hand, the spin density is pushed back from the iron toward the NO ligand, resulting in an Fe^{II}NO(radical)-type electronic structure. Calculated g tensors are in agreement with this description.¹⁸ In recent studies, calculated g values and ¹⁴N and ⁵⁷Fe hyperfine tensors (the latter are available from Mössbauer experiments¹⁴) have also been used to explore the structural flexibility of the NO ligand coordinated to ferrous heme.^{17,20d} These results reveal another important property of iron(II) porphyrin NO adducts, i.e., that the orientation of the NO ligand is undefined at higher temperatures in these complexes because of low barriers for a rotation of NO around the Fe–N(O) bond.²²

In this study, the spectroscopic properties and the electronic structures of 5C and 6C iron(II) porphyrin NO adducts are further elaborated in detail. Binding studies of N-donor ligands (L) to 5C complexes [Fe(TPP*)(NO)] (TPP* = tetraphenylporphyrin-type ligand) in solution as a function of the phenyl ring substitution in TPP and the employed nitrogen base are presented using UV–vis absorption and ¹H NMR spectroscopy. This way, binding constants K_{eq} are determined and the ¹H NMR spectra of these complexes are assigned for the first time. A crystal structure of the complex [Fe^{II}(To-F₂PP)(MI)(NO)] (**2-F**; To-F₂PP = tetrakis(*o*-difluorophenyl)porphyrin) is presented. The differences in the electronic structures of 5C and 6C iron(II) porphyrin NO complexes are then investigated by vibrational spectroscopy on [Fe(TPP)(NO)] (**1**) and [Fe(TPP)(MI)(NO)] (**2**) as examples. The vibrations of the Fe^{II}–N–O subunits in **1** and **2** are completely assigned for the first time using isotope substitution. Force constants are determined using quantum-chemistry-centered normal-coordinate analysis (QCC-NCA). The obtained force constants together with the ¹H NMR results provide direct experimental evidence for a weakening of the Fe–NO bond in 6C compared to 5C Fe^{II}NO complexes. In addition, the MCD spectra of **1** and **2**, which have been reported in a preceding Communication,¹⁸ are assigned using MCD theory and quantum-chemical calculations. On the basis of all these spectroscopic results, which are correlated to the DFT calculations, the electronic structural differences between 5C and 6C iron(II) porphyrin NO adducts are now defined in detail.

Experimental and Computational Procedures

Syntheses. Reactions were performed by applying Schlenk techniques using carefully purified solvents. NO gas was passed through a potassium hydroxide column and then through a cold trap at –80 °C prior to usage to remove higher nitrogen oxide impurities.

Syntheses of Ligands. Tetraphenylporphyrin (H₂TPP),²³ tetramesitylporphyrin (H₂TMP),²⁴ and tetrakis(*o*-difluorophenyl)-

porphyrin (H₂To-F₂PP)²⁵ were synthesized and purified as previously reported.

Syntheses of Precursors. [Fe(TPP)Cl] and [Fe(TMP)Cl] were prepared according to the method of Adler et al.²⁶ [Fe(To-F₂PP)Cl] was prepared by literature methods.²⁵

Syntheses of Ferrous NO Adducts. The complexes [Fe(TPP*)(NO)] and [Fe(TPP*)(MI)(NO)] (TPP* = TPP, TMP, To-F₂PP; MI = 1-methylimidazole) were synthesized using published procedures^{14,27} and isolated as microcrystalline solids.²⁸ The identities of the compounds were established using elemental analysis, vibrational spectroscopy, and EPR.

Crystals of [Fe(To-F₂PP)(MI)(NO)] suitable for X-ray analysis were prepared as follows. A sample of [Fe(To-F₂PP)Cl] (20 mg) in a glass tube was placed inside a 150-mL Schlenk tube (equipped with a rubber septum) under an argon atmosphere. A total of 5 mL of CHCl₃ and 1 mL of MI were added to [Fe(To-F₂PP)Cl], and the resulting solution was stirred for a few minutes. NO gas was passed through the Schlenk tube for 10 min, and the reaction mixture was further stirred for 30 min. *n*-Hexane (20 mL) was then introduced into the Schlenk tube outside of the glass tube for vapor diffusion. The Schlenk tube was sealed, and crystals of [Fe(To-F₂PP)(MI)(NO)] were formed after 10 days.

Crystal Structure Determination. Intensity data were collected using a STOE Image Plate Diffraction System with Mo K α radiation. The structure was solved with direct methods using *SHELXS-97*,²⁹ and refinement was done against F^2 using *SHELXS-97*.²⁹ All non-hydrogen atoms except O1A were refined with anisotropic displacement parameters. The hydrogen atoms were placed in ideal positions and were refined isotropically using the riding model. The oxygen atom is disordered in two positions and, therefore, refinement was performed using a split model. The lower occupied oxygen position (sof O1A = 0.1) was refined only isotropically (see the Supporting Information). Selected crystallographic data are presented in Table 1.

UV–Vis Spectroscopy. Absorption spectra were recorded in CH₂Cl₂ or toluene solutions as indicated at room temperature using a Varian Cary 5 UV–vis–near-infrared (NIR) spectrometer.

Vibrational Spectroscopy. Resonance Raman spectra were measured on a Dilor XY Raman spectrograph with a triple monochromator and a CCD detector. An Ar/Kr mixed-gas laser with a maximum power of 5 W was used for excitation. Spectra were recorded at excitation wavelengths of 454.5, 488.0, 514.5, 568.2, and 647.1 nm. The spectra were measured on KBr disks cooled to 10 K with a helium cryostat. The spectral band-pass was set to 2 cm^{–1}. Middle- and far-infrared spectra (MIR and FIR) were recorded on a Bruker IFS 66v vacuum instrument at room temperature. For the MIR region, KBr disks were used and the spectra were recorded at a resolution of 1 cm^{–1}. In the FIR region, CsI disks were applied and the resolution was set to 2 cm^{–1}. Low-

(22) Zemojtel, T.; Rini, M.; Heyne, K.; Dandekar, T.; Nibbering, E. T. J.; Kozłowski, P. M. *J. Am. Chem. Soc.* **2004**, *126*, 1930–1931.

(23) Adler, A. D.; Longo, F. R.; Finarelli, J. F.; Goldmacher, J.; Assour, J.; Korsakoff, L. *J. Org. Chem.* **1967**, *32*, 476.

(24) Safo, M. K.; Gupta, G. P.; Walker, F. A.; Scheidt, W. R. *J. Am. Chem. Soc.* **1991**, *113*, 5497–5510.

(25) Ghiladi, R. A.; Kretzer, R. M.; Guzei, I.; Rheingold, A. L.; Neuhold, Y. M.; Hatwell, K. R.; Zuberbühler, A. D.; Karlin, K. D. *Inorg. Chem.* **2001**, *40*, 5754–5767.

(26) Adler, A. D.; Longo, F. R.; Kampas, F.; Kim, J. J. *Inorg. Nucl. Chem.* **1970**, *32*, 2443–2445.

(27) Scheidt, W. R.; Frisse, M. E. *J. Am. Chem. Soc.* **1975**, *97*, 17–21.

(28) Under the identical reaction conditions employed for the syntheses of 6C Fe^{II}NO complexes in this study, complexes **2** and **2-F** were prepared by very slow crystallization and obtained as pure materials. However, the isolation of the pure 6C complex using TMP as the ligand was unsuccessful and always yielded mixtures of **1-Me** and [Fe(TMP)(MI)(NO)] as evidenced by IR spectroscopy.

(29) Sheldrick, W. S. *SHELXS-97 and SHELXL-97: programs for the solution and refinement of crystal structures*; University of Göttingen: Göttingen, Germany, 1997.

Table 1. Crystallographic Data for Compound **2-F**^a

chemical formula	C ₅₁ H ₃₃ F ₈ N ₇ OFe
fw	967.69
space group	P2 ₁ /c
a, Å	13.126(1)
b, Å	12.885(1)
c, Å	25.803(2)
β, deg	96.07(1)
V, Å ³	4339.6(5)
T, K	293
Z	4
D _{calcd}	1.481
μ, mm ⁻¹	0.431
λ, Å	0.71073
measured reflns	33628
independent reflns	8143
R _{int}	0.031
observed reflns	6593
R1 [I > 2σ(I)]	0.0370
wR2 (all data)	0.1009

$$^a R1 = \sum |F_o| - |F_c| / \sum |F_o|; wR2 = [\sum (w(F_o^2 - F_c^2)^2) / \sum (w(F_o^2)^2)]^{1/2}.$$

temperature MIR spectra were obtained on a Mattson Genesis type I spectrometer equipped with a cryogenic CTI cryostat. Spectra were recorded at 20 K at a resolution of 1 cm⁻¹.

NMR Spectroscopy. ¹H NMR spectra of the iron(II) porphyrin NO complexes were recorded in CD₂Cl₂ on a Bruker Avance 400 pulse Fourier transform spectrometer operating at a ¹H NMR frequency of 400.13 MHz. The spectrum of [Fe(TPP)(Pip)₂] (where Pip is piperidine-*d*₁₁) was recorded by dissolution of [Fe(TPP)] in benzene-*d*₆ and addition of Pip. For the titration experiments, commercially available Pip was used because in this case the ~2% deuterated solvent present does not show signals in the aromatic region.

MCD Spectroscopy. MCD spectra have been obtained on frozen glasses of butyronitrile/propionitrile (1:1 ratio) solutions in the 1.8–25 K temperature range. A CD spectropolarimeter (Jasco 810) with S1 and S20 photomultiplier tubes as detectors has been used in which the sample compartment was modified to accommodate an Oxford instruments SM4-10T magnetocryostat. The samples were frozen in metallic sample compartments between two Infrasil quartz disks separated by 3 mm neoprene spacers.

Normal-Coordinate Analysis (NCA). NCA calculations were performed using the QCPE computer program 576 by M. R. Peterson and D. F. McIntosh. The calculations are based on a general valence force field; force constants are refined with a nonlinear simplex algorithm. The simplex optimization was used to refine only *selected* force constants according to the quantum-chemical-assisted NCA (QCA-NCA) scheme.³⁰ Here, a force field from DFT calculations is used as a starting point to generate initial force constants, and a subset of these is fit to reproduce the known experimental frequencies. We have now fully interfaced the Gaussian output with the NCA software using a modified version of the program Redong³¹ (QCPE 628). This new version produces input files that can directly be processed by the NCA programs. Compared to the QCA-NCA procedure,^{30a} this allows for the routine treatment of very large systems because no simplifications have to be applied to the molecule or the force field. On the other hand, compared to the QCB-NCA version,^{30b} the tedious editing of the input files is no longer necessary. This new version is called quantum-chemistry-centered normal-coordinate analysis (QCC-

NCA) because it is designed for the treatment of large molecules where >99% of the force constants are purely computational.

DFT Calculations. The structures of the models [Fe(P)(NO)] (**1**; *S* = 1/2) and [Fe(P)(MI)(NO)] (**2**; *S* = 1/2) (where P is porphine) have been fully optimized using BP86/TZVP. For all of these calculations, a simplified TPP ligand has been used in which the four phenyl groups in the meso position of the porphyrin ring have been replaced by hydrogen. The resulting porphyrin model ligand P (P = porphine²⁻) is shown in Figure 4 along with the coordinate system used. Vibrational frequencies have been calculated for all structures showing no imaginary frequencies. In addition, B3LYP/LanL2DZ* calculations have been performed on these systems to obtain accurate total energies and spin densities. The LanL2DZ* basis set consists of LanL2DZ plus polarization functions (from TZVP) on all heavy atoms. These methods were used as implemented in *Gaussian 98* (G98).³² Absorption spectra of **1** and **2** were calculated using either time-dependent (TD-) DFT (G98) or the semiempirical INDO/S-CI method (active space: 160 orbitals) as implemented in *ORCA*.³³ EPR and Mössbauer parameters have also been calculated using *ORCA* and applying the B3LYP functional together with the following basis sets: Fe, CP(PPP); N, EPR-II; C and O, TZVP; H, TZV. Calculated Mössbauer isomer shifts (cf. Table S3 in the Supporting Information) were obtained after scaling the Fermi contact contribution to the ⁵⁷Fe hyperfine tensor with a factor of 1.81 as determined empirically.³⁴

Results and Analysis

A. Binding of Axial N-Donor Ligands to Five-Coordinate Iron(II) Porphyrin NO Adducts. The binding of N-donor ligands to [Fe(TPP*)(NO)] in axial position trans to NO is studied in solution using UV–vis absorption and ¹H NMR spectroscopy. Importantly, the adduct of [Fe-(To-F₂PP)(NO)] (**1-F**) with MI has by far the largest binding constant *K*_{eq} of all systems investigated. To examine whether the increased *K*_{eq} structurally influences the Fe–NO bond, the crystal structure of the product **2-F** has been determined. Vibrational spectra of [Fe(TPP)(NO)] (**1**) and [Fe(TPP)(MI)(NO)] (**2**) are then presented and analyzed using isotope substitution and NCA.

A.1. Ligand Binding to [Fe(TPP*)(NO)] Complexes in Solution Monitored by UV–Vis Absorption Spectroscopy. The coordination of the N-donor ligands 1-methylimidazole (MI) and pyridine (Py) to the five-coordinate (5C) complexes **1**, [Fe(TMP)(NO)] (**1-Me**), and **1-F** is studied in solution using UV–vis absorption spectroscopy in order to determine the equilibrium constants *K*_{eq} of the reaction



(30) (a) Lehnert, N.; Tuzcek, F. *Inorg. Chem.* **1999**, *38*, 1659–1670. (b) Studt, F.; MacKay, B. A.; Fryzuk, M. D.; Tuzcek, F. *J. Am. Chem. Soc.* **2004**, *126*, 280–290.

(31) Allouche, A.; Pourcin, J. *Spectrochim. Acta A* **1993**, *49*, 571.

(32) Frisch, M. J.; Trucks, G. W.; Schlegel, H. B.; Scuseria, G. E.; Robb, M. A.; Cheeseman, J. R.; Zakrzewski, V. G.; Montgomery, J. A., Jr.; Stratmann, R. E.; Burant, J. C.; Dapprich, S.; Millam, J. M.; Daniels, A. D.; Kudin, K. N.; Strain, M. C.; Farkas, O.; Tomasi, J.; Barone, V.; Cossi, M.; Cammi, R.; Mennucci, B.; Pomelli, C.; Adamo, C.; Clifford, S.; Ochterski, J.; Petersson, G. A.; Ayala, P. Y.; Cui, Q.; Morokuma, K.; Salvador, P.; Dannenberg, J. J.; Malick, D. K.; Rabuck, A. D.; Raghavachari, K.; Foresman, J. B.; Cioslowski, J.; Ortiz, J. V.; Baboul, A. G.; Stefanov, B. B.; Liu, G.; Liashenko, A.; Piskorz, P.; Komaromi, I.; Gomperts, R.; Martin, R. L.; Fox, D. J.; Keith, T.; Al-Laham, M. A.; Peng, C. Y.; Nanayakkara, A.; Challacombe, M.; Gill, P. M. W.; Johnson, B.; Chen, W.; Wong, M. W.; Andres, J. L.; Gonzalez, C.; Head-Gordon, M.; Replogle, E. S.; Pople, J. A. *Gaussian 98*, revision A.11; Gaussian, Inc.: Pittsburgh, PA, 2001.

(33) Neese, F. *ORCA*, version 2.2; Max-Planck Institut für Bioanorganische Chemie: Mülheim/Ruhr, Germany, 2004.

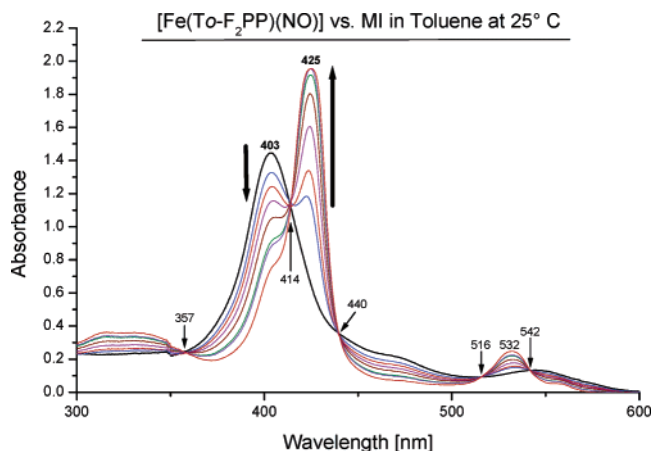


Figure 1. Titration of [Fe(*To-F*₂PP)(NO)] (**1-F**) with 1-methylimidazole (MI) in a toluene solution at room temperature monitored by UV-vis absorption spectroscopy. The Soret band of **1-F** at 403 nm disappears, while the Soret band of the product **2-F** appears at 425 nm.

Figure 1 shows a typical plot of the titration of a 5C iron(II) porphyrin NO adduct with an N-donor ligand. In this case, **1-F** was used and reacted with MI. The initial spectrum of the 5C species shows a broad peak in the Soret region centered at 403 nm. Upon the addition of the ligand, this peak decreases in intensity, whereas a band at 425 nm appears, which corresponds to the Soret band of the obtained six-coordinate (6C) complex **2-F**. Isoelectric points (cf. Figure 1) indicate that this reaction corresponds to a clean transformation of **1-F** to **2-F** without further intermediates. In the case of simple ligand binding reactions such as eq 1, the equilibrium constant K_{eq} can be determined from the equation

$$c(\text{B})^0 = c_{\text{T}}\Delta\epsilon\frac{c(\text{B})^0}{\Delta E} - K_{\text{eq}}^{-1} \quad (2)$$

which is based on a general expression that was first derived by Drago and co-workers.^{35,36} UV-vis absorption measurements are performed at different concentrations $c(\text{B})^0$ of base, and the change in absorbance ΔE is measured. A plot of $c(\text{B})^0$ vs $c(\text{B})^0/\Delta E$ then gives K_{eq}^{-1} . The advantage of this method is that the absolute concentrations of the 5C and 6C complexes do not need to be determined. Several important trends can be derived from the resulting K_{eq} values listed in Table 2. For ligand TPP (complex **1**), equilibrium constants of 26 M⁻¹ for MI and 3 M⁻¹ for Py have been determined, which correspond to a weak interaction. Correspondingly, the free binding energies ΔG° range in the region of only -1 to -5 kcal/mol. This is in agreement with the experimental finding that the isolation of 6C complexes [Fe(TPP*)(L)(NO)] is difficult.¹⁴ The obtained K_{eq} for Py is in good

Table 2. Calculated Equilibrium Constants K_{eq} [M⁻¹] and Free Reaction Energies ΔG° [kcal/mol] for the Reaction of [Fe(TPP*)(NO)] with N-Donor Ligands Following Equation 1

complex	equilib constant K_{eq}		$\Delta G^\circ = -RT \ln(K_{\text{eq}})$	
	MI	Py	MI	Py
[Fe(TPP)(NO)] (1)	26	3	-1.9	-0.7
[Fe(TMP)(NO)] (1-Me)	36		-2.1	
[Fe(<i>To-F</i> ₂ PP)(NO)] (1-F)	2055	7	-4.5	-1.2

agreement with the literature value of 0.7 M⁻¹ obtained in an ethylene chloride solution.³⁷ The lower binding constant of Py compared to MI can be rationalized with Py being a weaker base ($\text{p}K_{\text{B}} = 8.75$) than MI ($\text{p}K_{\text{B}} = 6.67$). From Table 2, K_{eq} increases in the order **1** < **1-Me** < **1-F**. Hence, ortho substitution of the phenyl rings of TPP leads to an increase in the binding constant. This is also observed for the coordination of N-donor ligands to [Fe(TPP*)]-type complexes^{11c} and can be attributed to steric shielding of the binding site.³⁸ In addition, the electron-withdrawing fluoro substituents in *To-F*₂PP lead to a further stabilization of the adducts compared to methyl groups in TMP. However, the fluoro substitution of TPP has a distinctively different effect on K_{eq} for MI and Py: compared to TPP, *usage of To-F*₂PP leads to an increase in the binding constant for MI by a factor of 80, whereas for Py, the increase is only by a factor of 2.3. This is attributed to the fact that MI has π -donor properties, whereas Py is a π acceptor. Hence, the withdrawal of electron density from the porphyrin leads to an increase in binding for MI because of electronic effects, whereas the Py adduct only experiences a small stabilization because of steric and/or electrostatic effects. To further evaluate this result, we isolated complex [Fe(*To-F*₂PP)(MI)(NO)] (**2-F**) as a solid. Importantly, a solution of solid **2-F** in toluene or benzene leads to the UV-vis absorption spectrum shown in Figure S5 in the Supporting Information, which resembles the spectrum of the corresponding 6C complex obtained from solutions of **1-F** with excess MI. In contrast, the solution spectra of solid **2** and **2-Me** resemble the data of the corresponding 5C complexes indicative of the much smaller binding constants in these cases. Hence, the combination of *To-F*₂PP and MI seems to be ideal for the preparation of 6C Fe^{II}NO complexes in solution.

A.2. Ligand Binding to [Fe(TPP*)(NO)] Complexes in Solution Monitored by NMR Spectroscopy. As shown in section A.1, UV-vis spectroscopy is a useful tool to monitor the binding of axial N-donor ligands to 5C complexes [Fe(TPP*)(NO)]. However, there is a potential problem: because of the large concentrations of base often used for the formation of the 6C complexes, a possible side reaction might occur:



leading to the diamagnetic low-spin complexes [Fe(TPP*)(L)₂]. This problem has been mostly overlooked in the

(34) Neese, F. *Inorg. Chim. Acta* **2002**, *337*, 181.

(35) (a) Rose, N. J.; Drago, R. S. *J. Am. Chem. Soc.* **1959**, *81*, 6138–6141. (b) Beugelsdijk, T. J.; Drago, R. S. *J. Am. Chem. Soc.* **1975**, *97*, 6466–6472. (c) Collman, J. P.; Brauman, J. I.; Doxsee, K. M.; Halbert, T. R.; Hayes, S. E.; Suslick, K. S. *J. Am. Chem. Soc.* **1978**, *100*, 2761–2766.

(36) $c(\text{B})^0$: initial concentration of the base (MI or Py). c_{T} : total concentration of porphyrin complexes [$c_{\text{T}} = c(6\text{C}) + c(5\text{C})$]. $\Delta\epsilon$: difference in extinction coefficients [$\Delta\epsilon = \epsilon(6\text{C}) - \epsilon(5\text{C})$]. ΔE : change in absorbance at a specific wavelength relative to the initial absorbance ($\Delta E = E - E^\circ$).

(37) (a) Choi, I.-K.; Ryan, M. D. *Inorg. Chim. Acta* **1988**, *153*, 25–30. (b) Liu, Y.; DeSilva, C.; Ryan, M. D. *Inorg. Chim. Acta* **1997**, *258*, 247–255.

(38) In this respect, it is interesting to note that NO behaves like a normal N-donor ligand in these ligand-binding experiments.

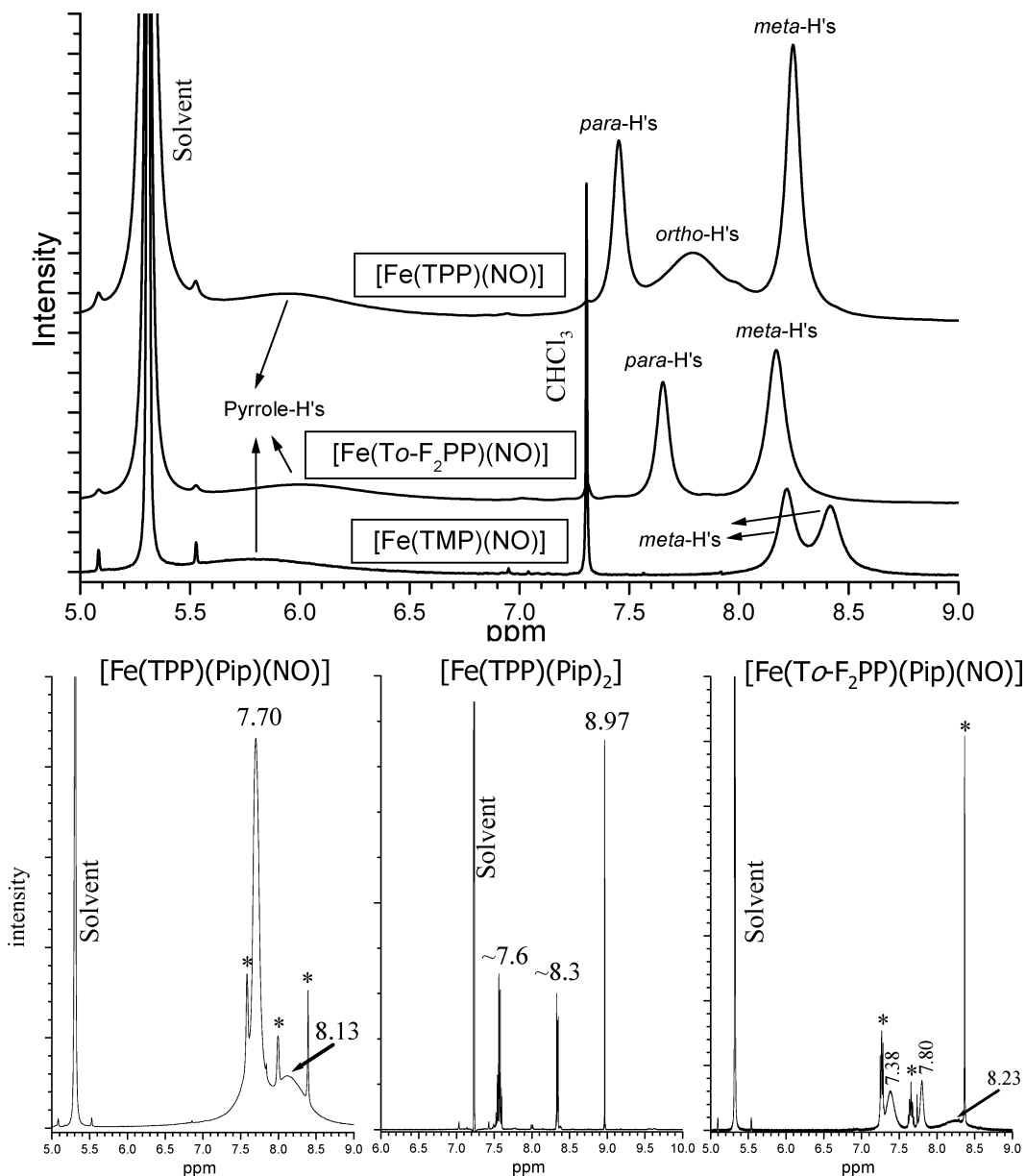


Figure 2. Top panel: ^1H NMR spectra of **1** (top), **1-F** (middle), and **1-Me** (bottom) in CD_2Cl_2 . Bottom panel: ^1H NMR spectra of $[\text{Fe}(\text{TPP})(\text{Pip})(\text{NO})]$ (left), $[\text{Fe}(\text{TPP})(\text{Pip})_2]$ (middle), and $[\text{Fe}(\text{To-F}_2\text{PP})(\text{Pip})(\text{NO})]$ (right). The spectra of the NO complexes were obtained from solutions that contain $\sim 15\%$ piperidine- d_{11} (Pip). Signals marked with asterisks in these spectra belong to the corresponding $[\text{Fe}(\text{TPP}^*)(\text{Pip})_2]$ complex.

literature for two reasons. First, the electronic absorption spectra of $[\text{Fe}(\text{TPP}^*)(\text{L})(\text{NO})]$ and $[\text{Fe}(\text{TPP}^*)(\text{L})_2]$ (cf. ref 39) are usually very similar. Solution EPR¹⁶ and IR^{42a} measurements clearly show that $[\text{Fe}(\text{TPP}^*)(\text{L})(\text{NO})]$ is

formed upon the addition of base to $[\text{Fe}(\text{TPP}^*)(\text{NO})]$, but $[\text{Fe}(\text{TPP}^*)(\text{L})_2]$ is not detected in these experiments because it is EPR-silent and does not have characteristic IR bands. Denitrosylation of **1** in the presence of Py was first observed by Lançon and Kadish.^{40a} In later studies, Bohle and Hung reported rate constants for the dissociation of NO from $[\text{Fe}(\text{TPP}^*)(\text{NO})]$ upon the addition of Py using UV-vis absorption measurements.^{40b} From these data, it was concluded that denitrosylation is highly dependent on the nature of the porphyrin ligand. We found that ^1H NMR spectroscopy is a very useful tool to monitor the formation of even small amounts of $[\text{Fe}(\text{TPP}^*)(\text{L})_2]$ in solution.

Figure 2 (top panel) shows the ^1H NMR spectra of the starting compounds **1**, **1-Me**, and **1-F**. The obtained signals are very broad because of the paramagnetic nature of these complexes. For compound **1**, four different signals are

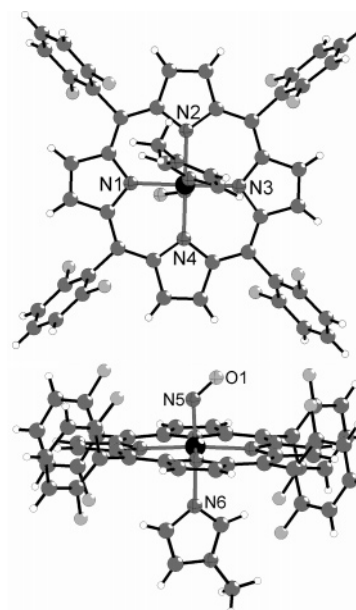
- (39) Safo, M. K.; Scheidt, W. R.; Gupta, G. P. *Inorg. Chem.* **1990**, *29*, 626–633.
 (40) (a) Lançon, D.; Kadish, K. M. *J. Am. Chem. Soc.* **1983**, *105*, 5610–5617. (b) Bohle, D. S.; Hung, C.-H. *J. Am. Chem. Soc.* **1995**, *117*, 9584–9585.
 (41) (a) Rai, B. K.; Durbin, S. M.; Prohofsky, E. W.; Sage, J. T.; Wyllie, G. R. A.; Scheidt, W. R.; Sturhahn, W.; Alp, E. E. *Biophys. J.* **2002**, *82*, 2951–2963. (b) Sage, J. T.; Paxson, C.; Wyllie, G. R. A.; Sturhahn, W.; Durbin, S. M.; Champion, P. M.; Alp, E. E.; Scheidt, W. R. *J. Phys.: Condens. Matter* **2001**, *13*, 7707–7722. (c) Leu, B. M.; Zgierski, M. Z.; Wyllie, G. R. A.; Scheidt, W. R.; Sturhahn, W.; Alp, E. E.; Durbin, S. M.; Sage, J. T. *J. Am. Chem. Soc.* **2004**, *126*, 4211–4227.
 (42) (a) Yoshimura, T. *Bull. Chem. Soc. Jpn.* **1991**, *64*, 2819–2828. (b) Vogel, K. M.; Kozłowski, P. M.; Zgierski, M. Z.; Spiro, T. G. *J. Am. Chem. Soc.* **1999**, *121*, 9915–9921.

Table 3. Experimental ^1H NMR Shifts [ppm] of $[\text{Fe}(\text{TPP}^*)(\text{NO})]$ and $[\text{Fe}(\text{TPP}^*)(\text{Pip})(\text{NO})]$ Measured against Tetramethylsilane and Assignments

complex	pyrrole	phenyl		
		ortho	meta	para
$[\text{Fe}(\text{TPP})(\text{NO})]$ (1)	5.95	7.79	8.25	7.45
$[\text{Fe}(\text{To-F}_2\text{PP})(\text{NO})]$ (1-F)	6.00		8.17	7.65
$[\text{Fe}(\text{TMP})(\text{NO})]$ (1-Me)	5.79		8.42/8.22	
$[\text{Fe}(\text{TPP})(\text{Pip})(\text{NO})]$		8.13		7.70
$[\text{Fe}(\text{To-F}_2\text{PP})(\text{Pip})(\text{NO})]$	8.23		7.38	7.80
$[\text{Fe}(\text{TMP})(\text{Pip})(\text{NO})]$? ^a		7.35	

^a The signal becomes very broad and, hence, cannot be identified from the spectra with certainty.

observed at 5.95, 7.45, 7.79, and 8.25 ppm, which belong to the pyrrole hydrogens of the porphyrin core and the hydrogens in the ortho, meta, and para positions of the phenyl rings (cf. Table 3). The two signals at 5.95 and 7.79 ppm are very broad and, hence, must belong to hydrogens that are exposed to the paramagnetic center. These signals are therefore assigned as the pyrrole and *o*-phenyl hydrogens. In compound **1-F**, the ortho positions are substituted with fluorine. Hence, the ^1H NMR spectrum of this compound should be lacking one of the four signals observed for **1**. A comparison of the spectra in Figure 2 shows that the peak around 7.79 ppm in **1** is missing in the spectrum of **1-F**. Hence, this peak can be attributed to the *o*-phenyl hydrogens, whereas the feature at 5.95 ppm must then belong to the pyrrole hydrogens. The remaining two signals at 7.45 and 8.25 ppm can be assigned by comparison with **1-Me** (cf. Table 3), where both the ortho and para positions of the phenyl rings are substituted with methyl groups. In the titration experiments, piperidine-*d*₁₁ (Pip) was then sequentially added to the $[\text{Fe}(\text{TPP}^*)(\text{NO})]$ solutions, and the formation of the 6C complexes $[\text{Fe}(\text{TPP}^*)(\text{Pip})(\text{NO})]$ was monitored by ^1H NMR. Figure S6 in the Supporting Information shows the corresponding experiment performed for **1**. As one can see, a clean conversion of the 5C complex to the 6C complex is observed. The final spectrum obtained for $[\text{Fe}(\text{TPP})(\text{Pip})(\text{NO})]$ in this experiment is also shown in the bottom panel of Figure 2. In this case, the ^1H NMR spectrum only shows two peaks at 7.70 and 8.13 ppm. These can be traced back to the corresponding signals of the 5C complex **1**, as shown in Figure S6 in the Supporting Information. From these data, the broad signal at 8.13 ppm corresponds to the peaks at 5.95 and 7.79 ppm in **1** and is therefore assigned to the pyrrole and *o*-phenyl hydrogens. On the other hand, the peak at 7.79 ppm corresponds to both the *m*- and *p*-phenyl hydrogens, which coincide in the spectrum of $[\text{Fe}(\text{TPP})(\text{Pip})(\text{NO})]$. In addition, three sharp peaks are observed in the spectra, which are marked with asterisks in Figure 2, bottom left. A comparison with the spectrum of pure $[\text{Fe}(\text{TPP})(\text{Pip})_2]$ shown in Figure 2, bottom center, shows that these signals correspond to the formation of diamagnetic $[\text{Fe}(\text{TPP})(\text{Pip})_2]$ and, hence, loss of NO upon the addition of base to the solution of **1**. Similar denitrosylation is also observed in the corresponding experiments with **1-Me** and **1-F**. The obtained spectrum of $[\text{Fe}(\text{To-F}_2\text{PP})(\text{Pip})(\text{NO})]$ is shown in Figure 2, bottom right. Importantly, the amount of diamagnetic bis-piperidine complex formed is

**Figure 3.** Top view (top) and side view (bottom) of the crystal structure of compound **2-F** with labeling. The disordered O atom is omitted for clarity.

much larger for the fluoro-substituted ligand compared to TPP. At a concentration of ~ 15 vol % Pip, the formation of the bis-piperidine complex $[\text{Fe}(\text{TPP}^*)(\text{Pip})_2]$ increases in the order TPP (8%) < TMP ($\sim 15\%$) < To-F₂PP (31%). Hence, the order for the degree of denitrosylation corresponds to the order of the N-donor binding constants described above. Whereas NO loss is only marginal for TPP, this effect is very pronounced for To-F₂PP. Therefore, although the fluoro-substituted ligand To-F₂PP is optimal for the binding of N-donor ligands to obtain 6C Fe^{II}NO complexes, it has the severe disadvantage that denitrosylation is facilitated in this system.

A.3. Crystal Structure of $[\text{Fe}(\text{To-F}_2\text{PP})(\text{MI})(\text{NO})]$ (2-F**).** To identify possible structural changes of the Fe–N–O unit induced by the stronger trans ligand binding, a crystal structure of compound **2-F** has been determined. This complex crystallizes in the monoclinic space group $P2_1/c$ with all atoms located in general positions. The iron atom is coordinated by the four porphyrin nitrogen atoms, one nitrogen atom of the MI ligand, and one nitrogen atom of nitric oxide within a slightly distorted octahedron, as shown in Figure 3. The iron atom is located in the porphyrin ring plane (deviation: 0.067 Å). The geometry of the axial N–Fe–NO unit is comparable to the general structural motif of 6C iron(II) porphyrin NO complexes with axial N-donor ligands as defined by Scheidt and co-workers.¹⁴ Important bond distances for **2-F** are presented in Table S1 in the Supporting Information and are compared to those of the structure of **2** in Table 4. The obtained Fe–NO and N–O bond lengths of 1.75 and 1.20 Å as well as the Fe–N–O angle of 138° in **2-F** are similar to the structural data of **2**. On the other hand, the Fe–N(imidazole) bond is slightly longer in **2-F** compared to **2**. The relative orientation of the MI and NO ligands in **2-F** is almost identical with that of the room-temperature structure of **2**.¹⁴ Hence, the crystal

Table 4. Geometric and Vibrational Properties of [Fe(TPP*)(L)(NO)] Complexes (L = MI or Missing; TPP* = Tetraphenylporphyrin-Type Ligand)

molecule ^a	geometric parameters [Å]					vibrational frequencies [cm ⁻¹]		
	ΔFe–N	ΔN–O	∠Fe–N–O	ΔFe–L _{tr}	ΔFe–N _p	ν(N–O)	ν(Fe–NO)	δ(Fe–N–O) ^c
[Fe(TPP)(NO)] (1) cryst. struct.: ref 27 ^b						1697	532	371 (ip)
[Fe ^{II} (TPP)(¹⁵ N ¹⁸ O)]	1.72	1.12	149		2.00	1625	515	365 (ip)
[Fe ^{II} (TMP)(NO)] (1-Me)						1676		
[Fe ^{II} (P)(NO)], calcd, BP86/TZVP (1̃)	1.705	1.179	146		2.019	1703	595	427 (ip), 313 (oop)
[Fe ^{II} (P)(NO)], calcd, B3LYP/LanL2DZ	1.742	1.212	143		2.019	1637	507	425 (ip), 308 (oop)
[Fe(TPP)(MI)(NO)] (2) cryst. struct.: ref 14						1630	440	530 (ip), 291 (oop)
[Fe ^{II} (TPP)(MI)(¹⁵ N ¹⁸ O)]	1.750	1.182	138	2.173	2.008	1556	431/423 (IR/R)	515 (ip), 287 (oop)
[Fe ^{II} (TMP)(MI)(NO)] (2-Me)						1624		
[Fe(To-F ₂ PP)(MI)(NO)] (2-F)	1.752	1.202	138	2.188	2.012	1624		
[Fe ^{II} (P)(MI)(NO)], calcd, BP86/TZVP (2̃)	1.734	1.186	140	2.179	2.022	1662	609	482 (ip), 317 (oop)
[Fe ^{II} (P)(MI)(NO)], calcd, B3LYP/LanL2DZ	1.810	1.215	142	2.063	2.030	1611	505	430 (ip), 298 (oop)

^a MI = 1-methylimidazole; P = porphine ligand used for calculations; values for ΔFe–N_p are averaged. ^b Highly disordered structure. ^c The δ(Fe–N–O) in-plane (ip) and out-of-plane (oop) vibrations. Note that the oop mode is strongly mixed with Fe–N_p stretches and other Fe–porphyrin vibrations and, hence, cannot be identified with one distinct normal mode.

structure does not provide any further evidence for the relatively large stability of **2-F** in solution compared to **2**.

A.4. Vibrational Properties and Assignments. The IR spectrum of [Fe(TPP)(NO)] (**1**) is shown in Figure S1 in the Supporting Information along with the corresponding ¹⁵N¹⁸O-labeled data. The intense band at 1697 cm⁻¹ is assigned to the N–O stretch ν(N–O) in accordance with earlier work.^{16a} It shifts to 1625 cm⁻¹ upon isotope substitution. In the FIR region, a second isotope-sensitive band is observed at 371 cm⁻¹ that shifts to 365 cm⁻¹ in the ¹⁵N¹⁸O-labeled material. This feature corresponds to the in-plane (ip) Fe–N–O bending vibration δ_{ip}(Fe–N–O). From the resonance Raman spectra of **1** shown in Figure S2 in the Supporting Information (excitation at 488 nm), another isotope-sensitive band can be identified at 532 cm⁻¹ that shifts to 515 cm⁻¹ upon isotope labeling. This band is assigned to the Fe–N stretch ν(Fe–NO) of coordinated nitric oxide. This assignment is in agreement with the results from nuclear resonance vibrational spectroscopy (NRVS),⁴¹ which show ν(Fe–NO) at 538 cm⁻¹ for powder samples of **1**. These assignments are also in agreement with resonance Raman spectra obtained on solutions of **1**, which show ν(N–O) at 1678 cm⁻¹ and ν(Fe–NO) at 524 cm⁻¹.⁴² On the other hand, the assignment of δ_{ip}(Fe–N–O) to the IR band at 371 cm⁻¹ is not in agreement with the NRVS study,^{41a} where this mode has been assigned to a band at 470 cm⁻¹. However, no strong evidence is presented for this assignment, which is only based on the experimental result that the 470 cm⁻¹ feature has an in-plane Fe displacement. Table 4 gives a compilation of the vibrational assignments presented here, which are based on actual isotope shifts coupled to a NCA. From DFT, the calculated N–O stretch for model **1̃** at 1703 cm⁻¹ is in very good agreement with experiment. The in-plane bend δ_{ip}(Fe–N–O) and especially the Fe–NO stretch, on the other hand, are predicted at 427 and 595 cm⁻¹, respectively, and, hence, are obtained too high in energy in the DFT calculations (cf. Table 4).

The IR spectrum of the 6C complex [Fe(TPP)(MI)(NO)] (**2**) is shown in Figure S3 in the Supporting Information. In this case, the N–O stretch is found at 1630 cm⁻¹, which shifts to 1556 cm⁻¹ upon isotope labeling. This is in agreement with earlier IR results.^{11b} An additional isotope-sensitive band is observed at 440 cm⁻¹ that is found at 431 cm⁻¹ in the isotope-substituted material. Figure S4 in the Supporting Information shows the resonance Raman spectra of **2** excited at 488 nm. Weak isotope-sensitive peaks are found at 530 and 440 cm⁻¹ that shift to 515 and 423 cm⁻¹, respectively, in the ¹⁵N¹⁸O compound. These two features at 530 cm⁻¹ (from Raman) and at 440 cm⁻¹ (from Raman and IR) belong to the Fe–NO stretch and the ip Fe–N–O bend. However, the detailed assignments of these vibrations are not clear because of strong mode mixing. This is evident from the fact that *both* ν(Fe–NO) and δ_{ip}(Fe–N–O) are observed in the Raman spectra of **2**, which is not the case for **1**. From DFT, the calculated ν(N–O) shows very good agreement with experiment, whereas larger deviations are observed for δ_{ip}(Fe–N–O) and ν(Fe–NO) (cf. Table 4). In agreement with experiment, the calculations predict strong mixing between these latter modes, where the feature at higher energy (609 cm⁻¹) has more Fe–NO stretching and the one at lower energy (482 cm⁻¹) has more Fe–N–O bending character in the DFT calculations.

A.5. Quantum-Chemistry-Centered Normal-Coordinate Analysis (QCC-NCA). The vibrational assignments presented above are further investigated using NCA. Because of the large sizes of the molecules **1** and **2**, the best approach for NCA is to generate an initial force field from quantum-chemical calculations. To obtain a reasonable description of the Fe–NO subunits in **1** and **2**, the TPP rings can be simplified to the porphine ligand “P” (cf. Figure 4).^{41c} The calculated force fields of models **1̃** and **2̃** are therefore used for NCA without further simplification following the QCC-NCA approach (see the Experimental Section). Masses of 77 are used for the meso hydrogen atoms to better represent

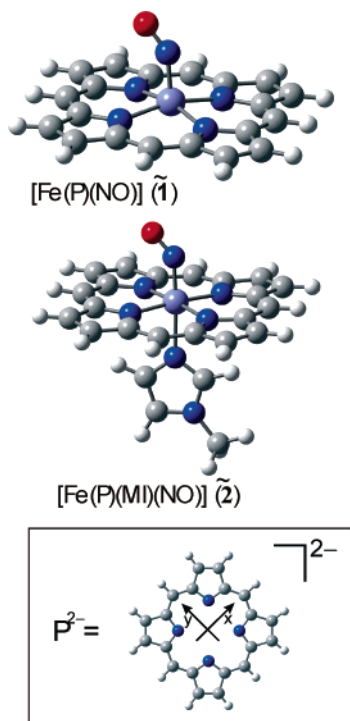


Figure 4. Figures of the fully optimized structures of **1** and **2** obtained with BP86/TZVP. Structural parameters are given in Table 4.

Table 5. Comparison of Experimental and QCC-NCA Vibrational Frequencies [cm^{-1}] and of QCC-NCA and Calculated (DFT) Force Constants [$\text{mdyn}/\text{\AA}$]

mode	exptl		QCC-NCA		force constants <i>f</i>	
	nai ^a	¹⁵ N ¹⁸ O	nai ^a	¹⁵ N ¹⁸ O	QCC-NCA	calcd ^b
[Fe(TPP)(NO)] (1)						
$\nu(\text{N}-\text{O})$	1697 ^c	1625	1698	1624	12.530	12.709
$\nu(\text{Fe}-\text{NO})$	532	515	531	517	2.975	3.619
$\delta_{\text{ip}}(\text{Fe}-\text{N}-\text{O})$	371	365	371	365	0.336	0.415
[Fe(TPP)(MI)(NO)] (2)						
$\nu(\text{N}-\text{O})$	1630	1556	1629	1557	11.550	12.224
$\delta_{\text{ip}}(\text{Fe}-\text{N}-\text{O})/$ $\nu(\text{Fe}-\text{NO})$	530	515	529	517	0.539	0.680
	440	431/(423)	440	431	2.548	3.257
$\delta_{\text{oop}}(\text{Fe}-\text{N}-\text{O})$	291	287	(332) ^d	(328) ^d		

^a nai = natural abundance isotopes. ^b Calculated with BP86/TZVP; see the Experimental Section. ^c Using a value of $\nu(\text{NO}) = 1678 \text{ cm}^{-1}$ measured in solution,⁴² force constants of 12.190 $\text{mdyn}/\text{\AA}$ for N–O and 2.985 $\text{mdyn}/\text{\AA}$ for Fe–NO are obtained. ^d Because of the fact that the oop bend shows strong mixing with porphyrin modes, a reasonable NCA fit of this mode could not be achieved within the chosen model. Hence, the energies listed are those obtained from NCA without further adjustment of force constants. Free NO: $\nu(\text{N}-\text{O}) = 1876 \text{ cm}^{-1}$; $f_{\text{N}-\text{O}} = 15.49 \text{ mdyn}/\text{\AA}$. NO^+ : $\nu(\text{N}-\text{O}) = 2387 \text{ cm}^{-1}$ in $(\text{NO}^+)(\text{BF}_4^-)$; $f_{\text{N}-\text{O}} = 25.07 \text{ mdyn}/\text{\AA}$.⁶⁷

the phenyl groups of TPP. The results of this treatment are presented in Table 5, which show excellent agreement with experiment for both **1** and **2**. This further supports the vibrational assignments presented above. For complex **1**, the observed mixing between $\nu(\text{Fe}-\text{NO})$ and $\delta_{\text{ip}}(\text{Fe}-\text{N}-\text{O})$ is quite small. The mode at 532 cm^{-1} is a pure Fe–NO stretching vibration with 88% $\nu(\text{Fe}-\text{NO})$. The mode at 371 cm^{-1} has 55% in-plane (ip) Fe–N–O bending character [39% contribution of $\delta_{\text{ip}}(\text{Fe}-\text{N}-\text{O})$ and 16% from N–Fe–N(O) bends]. The ip bend $\delta_{\text{ip}}(\text{Fe}-\text{N}-\text{O})$ is also mixed with porphyrin core modes and, hence, shows small contributions to several other vibrations. This situation changes dramati-

cally for complex **2**. Here, $\nu(\text{Fe}-\text{NO})$ and $\delta_{\text{ip}}(\text{Fe}-\text{N}-\text{O})$ are closer in energy, which leads to an almost equal mixing of these vibrations. Hence, the mode at 530 cm^{-1} has 33% $\nu(\text{Fe}-\text{NO})$ and 30% $\delta_{\text{ip}}(\text{Fe}-\text{N}-\text{O})$ character. The mode at 440 cm^{-1} , on the other hand, has 47% $\nu(\text{Fe}-\text{NO})$, 11% $\delta_{\text{ip}}(\text{Fe}-\text{N}-\text{O})$, and 9% $\delta(\text{N}-\text{Fe}-\text{N})$ bending character. Hence, the distinction between $\nu(\text{Fe}-\text{NO})$ and $\delta_{\text{ip}}(\text{Fe}-\text{N}-\text{O})$ is practically lost. Because of the fact that the 440 cm^{-1} mode has more Fe–NO stretching character, it is designated as $\nu(\text{Fe}-\text{NO})$ in Table 4.

For complex **1**, N–O and Fe–NO force constants of 12.53 and 2.98 $\text{mdyn}/\text{\AA}$ are obtained as shown in Table 5. The Fe–NO force constant of about 3 $\text{mdyn}/\text{\AA}$ corresponds to a very strong bond in agreement with the very large experimental NO binding constants for iron(II) porphyrins.⁴³ In comparison, both the N–O and Fe–NO force constants of 11.55 and 2.55 $\text{mdyn}/\text{\AA}$, respectively, are distinctively *smaller* for **2**. Because the Fe–NO interaction is mediated by π^* orbitals of NO in these complexes, these findings can only be explained if complex **1** has a stronger Fe–NO σ bond. Increased donation from a NO antibonding (π^*) orbital in the case of **1** then leads to a strengthening of both the Fe–NO and N–O bonds relative to **2**, in agreement with the trend in force constants. The weaker N–O bond in **2** could also be explained with a larger amount of back-donation from iron(II) to the π^* orbitals of NO. However, this would lead to an inverse correlation of the Fe–NO and N–O bond strengths, which is not the case experimentally. Hence, *complexes 1 and 2 differ significantly in the strength of the Fe–NO σ interaction*. The calculated force constants from DFT show, in general, good agreement with the NCA result, as presented in Table 5. The only exceptions in this respect are the Fe–NO force constants, which are calculated distinctively too large (vide infra). On the basis of their NRVS data, Rai et al. have also performed an NCA for the low-energy modes of **1** including $\nu(\text{Fe}-\text{NO})$ and $\delta_{\text{ip}}(\text{Fe}-\text{N}-\text{O})$.^{41a} The obtained force constants of 2.66 $\text{mdyn}/\text{\AA}$ for Fe–NO and 0.30 mdyn for Fe–N–O compare well with the results presented here. The lower value for the Fe–NO force constant is due to their fit of $\delta_{\text{ip}}(\text{Fe}-\text{N}-\text{O})$ to a mode at 470 cm^{-1} (vide supra), which differs from our results. However, because our analysis is supported by the experimentally determined isotope shifts and the good quality of the NCA fit of these data, we are confident that we have arrived at a more consistent assignment of the vibrational data of the Fe–N–O subunit of **1** and that the observed tendencies in the N–O and Fe–NO force constants for **1** and **2** are valid.

B. Electronic Structure of Iron(II) Porphyrin NO Adducts and Assignments of Optical Spectra. The complete bonding scheme of the six-coordinate (6C) complex [Fe(TPP)(MI)(NO)] (**2**) obtained from DFT calculations is analyzed in detail. This electronic structure is then compared to that of the corresponding five-coordinate (5C) species [Fe(TPP)(NO)] (**1**) in relation to the experimental results presented above. Calculated EPR and Mössbauer hyperfine

(43) Ford, P. C.; Laverman, L. E. *Coord. Chem. Rev.* **2005**, *249*, 391–403.

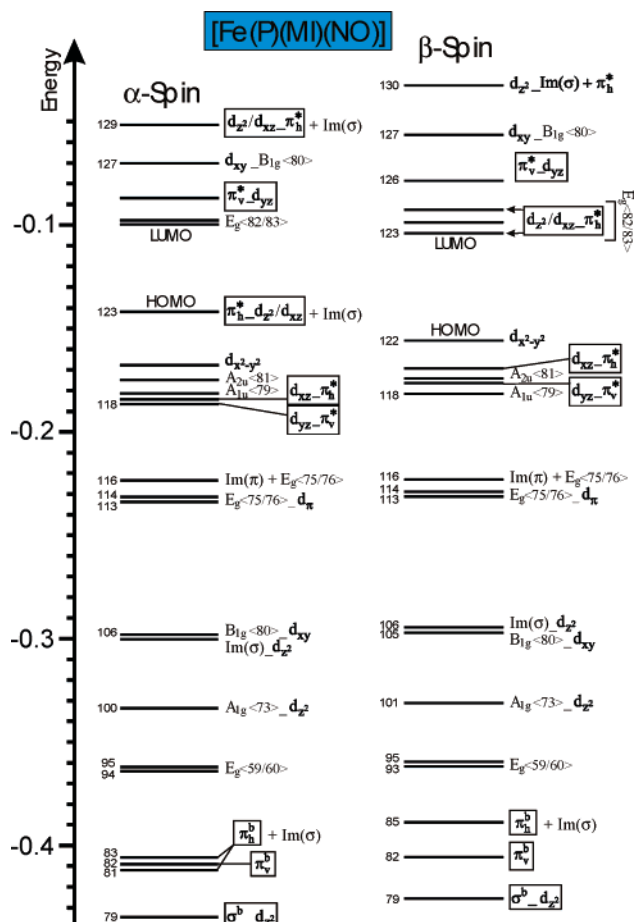


Figure 5. MO diagram of [Fe(P)(MI)(NO)] (**2**) calculated with BP86/TZVP. The applied coordinate system is shown in Figure 4. A_{1u} , A_{2u} , E_g , etc., correspond to porphyrin orbitals, as shown in Figure S7 in the Supporting Information. Ligand orbitals of NO are labeled π_v^* (v = vertical; orthogonal to the Fe–N–O plane) and π_h^* (h = horizontal; located in the Fe–N–O plane) and are shown in Figure S8 in the Supporting Information. The nomenclature a_b indicates that orbital a interacts with b and that a has a larger contribution to the resulting MO.

parameters are also discussed. Finally, the MCD spectra of complexes **1** and **2** are assigned.

B.1. Bonding Description of Complex 2 and Comparison to 1. To analyze the electronic structures of 5C and 6C iron(II) porphyrin NO complexes, the model systems [Fe(P)(NO)] (**1**) and [Fe(P)(MI)(NO)] (**2**) have been applied, as shown in Figure 4. Geometry optimization was then performed using B3LYP/LanL2DZ and BP86/TZVP. Table 4 shows that, in the case of **1**, both methods lead to very good agreement with the experimental structure. However, for the 6C complex **2**, the B3LYP geometry is clearly of a lower quality, whereas BP86 again shows excellent agreement with experiment. Hence, the analysis of the electronic structures of **1** and **2** is based on the fully optimized structures **1** and **2** from BP86/TZVP. Figure 5 presents the corresponding molecular orbital (MO) diagram for model **2**. Charge distributions are given in Table S2 in the Supporting Information. Figure 4 shows the applied coordinate system used in the following discussion. The z axis is roughly oriented along the N(imidazole)–Fe–N(O) axis. In complex **2**, iron is in the +II oxidation state and is low-spin (as is evident from EPR), which leads to a $[d_{xz}, d_{yz}, d_{x^2-y^2}] \approx [t_2]^6$

electron configuration of the metal.⁴⁴ Bonding to the porphyrin ligand is mostly mediated by the frontier orbitals of this ligand. The MO diagram of free porphine²⁻ used as a model for TPP in the calculations is shown in Figure S7 in the Supporting Information. The lowest unoccupied MO (LUMO) of the porphine ligand corresponds to a pair of degenerate π^* orbitals of E_g symmetry, labeled $E_g\langle 82/83 \rangle$ in Figure 5.⁴⁵ These undergo a very weak back-bonding interaction with the d_{xz} and d_{yz} orbitals of iron (1–3% d orbital admixture). The highest occupied π orbitals are of A_{2u} and A_{1u} symmetry and are practically nonbonding to the d orbitals. The iron–porphine σ bond is mediated by the in-plane (ip) B_{1g} orbital and the unoccupied d_{xy} orbital of iron. The MO diagram of free nitric oxide is presented in Figure S8 in the Supporting Information. This molecule is a radical ($S = 1/2$ ground state), with the unpaired electron being located in the singly occupied π^* orbitals. Because complex **2** has a total spin of $S = 1/2$, the spin-unrestricted scheme has to be applied, which distinguishes between majority (α) and minority (β) spin orbitals. The unpaired electron of NO occupies the orbital $\alpha\text{-}\pi_h^*$ (h = horizontal), which is located in the Fe–N–O plane. Because the t_2 functions of Fe^{II} are fully occupied, σ donation from $\alpha\text{-}\pi_h^*$ to the metal is only possible into the d_z^2 orbital. The corresponding bonding combination, $\pi_h^*d_z^2/d_{xz}$ ($\alpha\langle 123 \rangle$), is the highest occupied MO (HOMO) of **2** (cf. the contour plot in Figure 6). It has about 43% π_h^* and 42% mixed d_z^2/d_{xz} contribution, which corresponds to a strong interaction. Note that the interaction of π_h^* and d_{xz} does not contribute to bonding because both orbitals are occupied. The second $\alpha\text{-}\pi^*$ orbital of NO, labeled π_v^* (v = vertical), is unoccupied and oriented perpendicular to the Fe–N–O plane. It forms a medium-strong π back-bond with d_{yz} of iron. The corresponding antibonding combination, $\pi_v^*d_{yz}$ ($\alpha\langle 126 \rangle$), consists of 71% π_v^* with 24% d_{yz} admixture, as shown in Table S2 in the Supporting Information and Figure 6. An additional small contribution to the Fe–NO bond is only found for the weakly N–O σ -bonding orbital σ^b (cf. Figure S8 in the Supporting Information; 7% d_z^2 admixture). In the spin-unrestricted scheme, both $\beta\text{-}\pi_h^*$ and $\beta\text{-}\pi_v^*$ of NO are unoccupied and undergo additional π -back-bonding interactions with iron (cf. Figure 6). The corresponding bonding combinations, $d_{xz}\pi_h^*$ ($\beta\langle 121 \rangle$) and $d_{yz}\pi_v^*$ ($\beta\langle 119 \rangle$), have about 50% metal d and about 20% π^* contribution (cf. Table S2 in the Supporting Information). The antibonding combination, $\pi_v^*d_{yz}$ ($\beta\langle 126 \rangle$), consists of 67% π_v^* and 27% d_{yz} , which is comparable to α spin. In summary, NO acts as a medium-strong σ -donor and π -acceptor ligand in **2**.

The interesting question is then, how does this electronic structure change when going from 6C complex **2** to 5C complex **1**? The experimentally determined Fe–NO force

(44) In the applied coordinate system (cf. Figure 4), the $d_{x^2-y^2}$ orbital can formally be identified with one of the “ t_2 ” orbitals, whereas d_{xy} undergoes a σ bond with the porphyrin and can therefore be classified as an “ e ” orbital.

(45) For the presentation of the electronic structure of **2** (Figures 5 and 6 and Table S2 in the Supporting Information), the MOs of the porphine²⁻ ligand are labeled as shown in Figure S7 in the Supporting Information. For example, the HOMO of porphine²⁻ is $A_{2u}\langle 81 \rangle$.

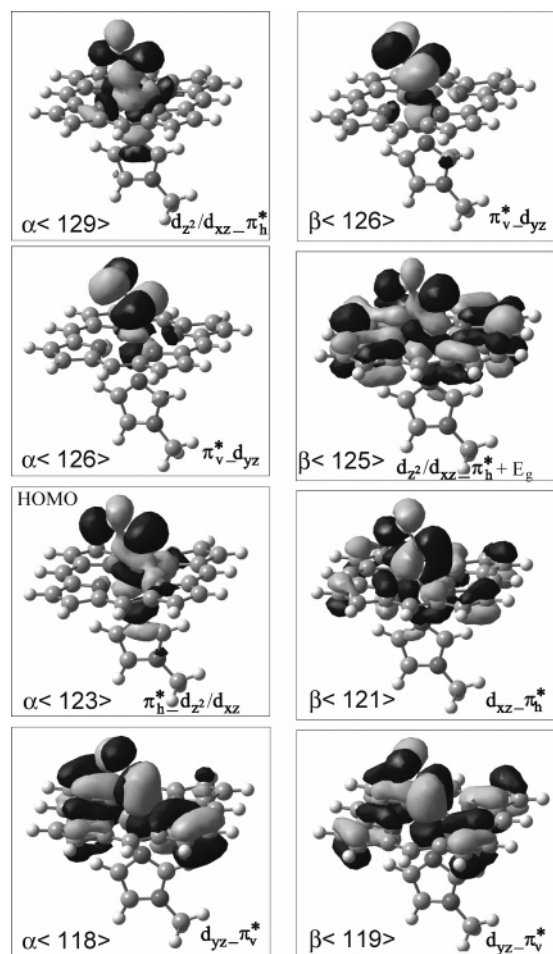


Figure 6. Contour plots of important MOs of $\tilde{2}$ calculated with BP86/TZVP. For the labels, see Figure 5 and Table S2 in the Supporting Information.

constants, which are 2.98 mdyne/Å for **1** and 2.55 mdyne/Å for **2**, show that there is a significant difference in the Fe–NO bond strengths in these complexes. As shown in section A.5, this relates to differences in the Fe–NO σ bond in agreement with DFT results published in a preceding Communication,¹⁸ which predict a stronger σ interaction in **1**.⁴⁶ This change in the Fe–NO bond strengths should be reflected by the spin densities. To calculate accurate spin densities, the B3LYP functional has to be applied because pure density functionals tend to overestimate the metal–ligand covalencies. A comparison of the calculated Fe–NO force constants from BP86 with experiment (cf. Table 5) shows that this is also the case here. Because spin polarization effects are quite small for $\tilde{1}$ and $\tilde{2}$,⁴⁷ the calculated spin densities roughly correspond to the shape of the singly occupied MOs (SOMOs) of $\tilde{1}$ and $\tilde{2}$ shown in Figure 7. The unpaired electron is mostly localized on the NO ligand (spin density: +0.8) in the 6C complex. In comparison, values

(46) The Fe–NO π back-bonds are similar for $\tilde{1}$ and $\tilde{2}$. Small differences are only observed for the β -MOs, where the π back-bond is slightly stronger for $\tilde{1}$. For example, the antibonding combination $\pi_v^*-d_{yz}$ (β -104) has 57% π_v^* and 35% d_{yz} character compared to 67% π_v^* and 27% d_{yz} (β -126) for $\tilde{2}$. This leads to the transfer of a small additional amount of spin density from NO to iron in $\tilde{1}$ relative to $\tilde{2}$.

(47) Praneeth, V. K. K.; Haupt, E.; Lehnert, N. *J. Inorg. Biochem.* **2005**, *99*, 940–948.

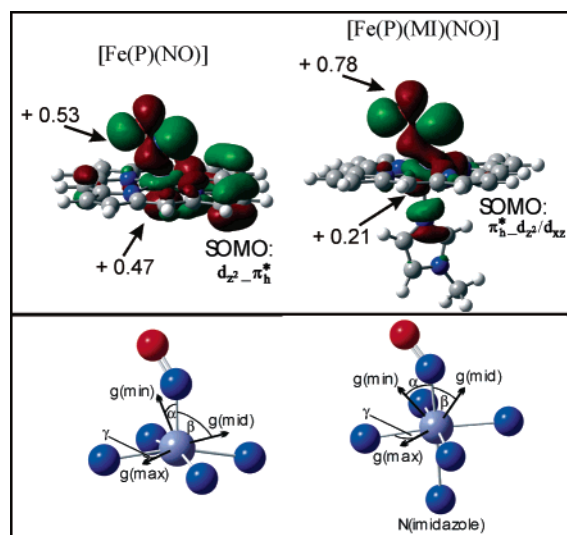


Figure 7. Top: Contour plots of the SOMOs of [Fe(P)(NO)] ($\tilde{1}$) and [Fe(P)(MI)(NO)] ($\tilde{2}$) calculated with B3LYP/LanL2DZ*. Calculated for the fully optimized structures obtained with BP86/TZVP. The calculated spin densities reflect the shape of the SOMO in both cases. Spin densities on Fe and NO are indicated. Bottom: calculated orientation of the principal axes of the g tensor relative to the molecular frame using BP86/TZVP.

of +0.5 on Fe and +0.5 on NO are obtained for $\tilde{1}$, which corresponds to an increase in the Fe–NO covalency and, hence, the metal–ligand bond strength. These spin densities are also in agreement with MCD¹⁸ and ¹H NMR results (see the Discussion section).

B.2. Calculation of Hyperfine Parameters of **1** and **2**.

The results presented above are very useful to evaluate the very different EPR spectra of 5C and 6C iron(II) porphyrin NO adducts¹⁶ (see the Introduction). In a preceding Communication, these differences were analyzed based on calculated g tensors for models $\tilde{1}$ and $\tilde{2}$.¹⁸ In agreement with earlier calculations,¹⁷ it was found that the orientation of the g tensor in the molecular frame is different in these complexes, as shown in Figure 7. However, the question of how this relates to the electronic structure descriptions of these systems as elaborated above is still open. First, the fact that complex **2** shows smaller overall g shifts than **1** reflects the decreased spin density on iron in this complex.^{17,48} Second, the rotation of the g tensor in **2** compared to **1** might relate to the change of the “magnetic orbital” of iron in these complexes. In the case of **1**, the spin density is located in an orbital of mostly d_{z^2} character, which is oriented along the z axis. On coordination of the sixth ligand, the orbital becomes stronger mixed with d_{xz} and, hence, is rotated off the z axis (cf. the SOMOs in Figure 7). Presumably, the g tensor then follows the rotation of the spin density at the iron center.

In addition to the g tensor, we have also calculated the ¹⁴N and ⁵⁷Fe hyperfine (A) tensors and Mössbauer parameters

(48) This is in agreement with the differences in spin density distribution for **1** and **2** as evidenced by MCD spectroscopy and the different ¹H NMR chemical shifts of the pyrrole hydrogens in these systems (cf. Table 3). In diamagnetic [Fe(TPP)(Pip)₂] (cf. Figure 2), these signals are observed at 8.97 ppm, which is close to the value of ~8.1 ppm for **2**. In contrast, these hydrogens show a stronger paramagnetic shift to 5.95 ppm in **1**. Correspondingly, the calculated spin densities on the pyrrole hydrogens are 2–4 times larger in **1** than they are in **2**.

Table 6. Comparison of Experimental and Calculated ^{14}N Hyperfine (A) Tensors of the Nitrosyl Nitrogen in **1** and **2** and Related Model Complexes^a

molecule	^{14}N hyperfine A [g] [MHz]			orientation
	A [g(max)]	A [g(mid)]	A [g(min)]	
[Fe(TPP)(NO)], exptl ^{16a}	37.1	49.7	48.7	?
[Fe(OEP)(NO)], exptl ^{b,16d}	40.9	49.7	42.7	g/A : 30° ^c
[Fe(P)(NO)] (1), calcd	28.3	62.0	49.9	A [g(min)]/Fe–N: 1° ^d
[Fe(TPP)(Pip)(NO)], exptl ^{16a}		60.8		?
[Fe(P)(MI)(NO)] (2), calcd	15.2	84.0	13.2	A [g(min)]/Fe–N: 30° ^e

^a The values of the A tensor [MHz] are given relative to the g tensor; i.e., a given A value is paired with the g value whose principal axis is closest to the principal axis of this A . The column “orientation” then gives the relative orientation of the A tensor. ^b Single-crystal EPR data. ^c Angle between the principal axes of the g and A tensors. ^d The angle between the principal axes of g (min)/ A [g(min)] and g (mid)/ A [g(mid)] is about 20° ; g (max) and A [g(max)] are collinear and oriented perpendicular to the Fe–N–O plane. ^e The angle between the principal axes of g (min)/ A [g(min)] and g (mid)/ A [g(mid)] is about 30° ; g (max) and A [g(max)] are collinear and oriented perpendicular to the Fe–N–O plane.

for models **1** and **2** using the B3LYP functional. For the 5C complexes, the experimental ^{14}N hyperfine tensor is quite isotropic, with A [g(mid)] \approx 50 MHz being somewhat larger than the other two values, although the experimental results for **1** and [Fe(OEP)(NO)] are somewhat different in this respect, as shown in Table 6. From the Fe^{II}NO adduct of hemoglobin, it is known that the hyperfine tensor becomes quite anisotropic in the case of a 6C complex (values of 29.6, 32.9, and 63.6 MHz (α subunit) and 26.9, 44.2, and 62.3 MHz (β subunit) have been determined).⁴⁹ In agreement with this, the A [g(mid)] value of [Fe(TPP)(Pip)(NO)] has been determined from solution EPR to be 61 MHz.^{16a} The general trend with the A tensor being more anisotropic for 6C compared to 5C Fe^{II}NO complexes is reproduced well by the calculations. The calculated values of A [g(min)] = 49.9 MHz for **1** and A [g(mid)] = 84.0 MHz for **2** can be directly compared to solution EPR data and show very good agreement. The other A values show some deviations (cf. Table 6), but the overall agreement between theory and experiment is satisfactory. In a recent publication, ^{14}N hyperfine couplings for a model similar to **2** were calculated to be 29, 31, and 74 MHz for the minimum-energy structure,^{20d} which agrees with our results. Table S3 in the Supporting Information lists the calculated Mössbauer isomer shifts δ and quadrupole splittings ΔE_q for models **1** and **2** in comparison with experiment. The isomer shifts are reproduced well, indicating that the electron densities are well described by our calculations. The quadrupole splittings and the ^{57}Fe hyperfine tensor elements show noticeable deviations (cf. Table S3 in the Supporting Information). One source of the observed errors relates to the chosen basis sets for these calculations. Previous DFT work of Oldfield and co-workers using the “locally dense” basis set approach⁵⁰ on [Fe(OEP)(NO)] and model systems comparable to **1** and **2** led to quadrupole splittings that are in excellent agreement with experiment.^{20c,d} Therefore, the calculation of the quadrupole and ^{57}Fe hyperfine tensors seems to require extensively large basis sets.

B.3. Assignment of the Optical Spectra. The absorption and MCD spectra of porphyrin complexes are dominated by intense $\pi \rightarrow \pi^*$ transitions of the porphyrin dianion.^{21a,51} These have been analyzed in detail by Gouterman. The

$A_{1u}\langle 79 \rangle$, $A_{2u}\langle 81 \rangle$ (HOMO) to $E_g\langle 82/83 \rangle$ (LUMO) (cf. Figure S7 in the Supporting Information) transitions give rise to two excited states of E_u symmetry. These show strong configuration interaction (CI) coupling, leading to the intense Soret or B band at higher energy ($\epsilon \geq 100\,000\text{ M}^{-1}\text{ cm}^{-1}$) and the Q band at lower energy, which has low to zero intensity (depending on the actual complex). The corresponding wave functions for these excited states are therefore defined as

$$|\Psi^{\text{Soret}}\rangle = \frac{1}{\sqrt{2}}|\psi_1 + \psi_2\rangle \quad \text{and} \quad |\Psi^{\text{Q}}\rangle = \frac{1}{\sqrt{2}}|\psi_1 - \psi_2\rangle$$

where ψ_1 : $A_{1u}\langle 79 \rangle \rightarrow E_g\langle 82/83 \rangle$ and ψ_2 : $A_{2u}\langle 81 \rangle \rightarrow E_g\langle 82/83 \rangle$ are the individual excited states of E_u symmetry. Because of vibronic mixing of the Q state with the Soret state, an additional quite intense band designated as Q_v is observed at about 1250 cm^{-1} to higher energy from Q.^{51,52} Because complexes **1** and **2** have a low-spin d^6 configuration, the three t_2 orbitals of iron(II) (vide supra) are fully occupied and, hence, no low-energy porphyrin (π) to metal (t_2) charge-transfer transitions are possible in these cases. Therefore, the absorption spectra of complexes **1** and **2** are dominated by only two features: the intense Soret band at around 400 nm and the Q_v band at about 540 nm.⁵¹ Figures 8 and 9 show the absorption and MCD C-term spectra of complexes **1** and **2**, respectively, which allow for the identification of 10 electronic transitions below $30\,000\text{ cm}^{-1}$. Table 7 summarizes the band positions obtained from correlated Gaussian fits of these data (included in Figures 8 and 9). Because the spectra were measured under different experimental conditions, small differences in the band positions were tolerated in the fit. To assign the electronic spectra of complexes **1** and **2**, TD-DFT calculations on the B3LYP level have been performed. Using the porphine approximation, the calculated Soret band positions of $28\,500\text{ cm}^{-1}$ for **1** and $26\,670\text{ cm}^{-1}$ for **2** only show poor agreement with experiment, as shown

(51) Gouterman, M. Optical Spectra and Electronic Structure of Porphyrins and Related Rings. In *The Porphyrins*; Dolphin, D., Ed.; Academic Press: New York, 1978; Vol. III.

(52) (a) Spiro, T. G.; Streckas, T. C. *Proc. Natl. Acad. Sci. U.S.A.* **1972**, *69*, 2622–2626. (b) Spiro, T. G. In *Iron Porphyrins*; Lever, A. B. P., Gray, H. B., Eds.; Addison-Wesley: Reading, MA, 1983; Part 2. (c) Egawa, T.; Suzuki, N.; Dokoh, T.; Higuchi, T.; Shimada, H.; Kitagawa, T.; Ishimura, Y. *J. Phys. Chem. A* **2004**, *108*, 568–577. (d) Paulat, F.; Praneeth, V. K. K.; Näther, C.; Lehnert, N. *Inorg. Chem.* **2006**, in press.

(49) Utterback, S. G.; Doetschman, D. C.; Szumowski, J.; Rizos, A. K. *J. Chem. Phys.* **1983**, *78*, 5874–5880.

(50) Chestnut, D. B.; Moore, K. D. *J. Comput. Chem.* **1989**, *10*, 648–659.

Table 7. Correlated Fit of the UV–Vis Absorption and MCD C-Term Spectra of **1** and **2**^a

no.	[Fe(TPP)(NO)] (1)				[Fe(TPP)(MI)(NO)] (2)			
	MCD C term	position	ϵ^b	assignment ^c	MCD C term	position	ϵ^b	assignment ^c
1	15268	(15200)	266	Q ⁽¹⁾				
2	16451	16298	2126	Q _v ⁽¹⁾	16551	16412	3807	Q ⁽¹⁾
3	17028	(17042)	410	Q ⁽²⁾	17239	17166	3358	Q ⁽²⁾
3a					17894	17742	6954	Q _v ⁽¹⁾
4	18252	18401	8098	Q _v ⁽²⁾	18275	18554	14180	Q _v ⁽²⁾
5	20311	20241	4893	$\pi \rightarrow \pi^*(3)$, CT ⁽¹⁾	(19935)	19955	6052	CT ⁽¹⁾ , $\pi \rightarrow \pi^*(3)$
6	21858	21499	9858	CT ⁽¹⁾ , $\pi \rightarrow \pi^*(1)$, Soret	21880	21644	9388	CT ⁽¹⁾ , $\pi \rightarrow \pi^*(1)$, Soret
6a					22867	(22331)	15185	Soret ⁽¹⁾
7	23583	23436	35030	Soret ⁽¹⁾	23507	23470	146880	Soret⁽²⁾
8	24530	24840	82184	Soret⁽²⁾	24166	24495	44087	Soret ⁽³⁾
9	25624			$\pi \rightarrow \pi^*(3)$, CT ⁽²⁾ , Soret	25127	25541	(14719)	CT ^{(1)?} , Soret
10	26869	26969	(17896)	CT ⁽²⁾				
11					28238	28180		$\pi \rightarrow \pi^*(1,3)$
12					30894	30971		$\pi \rightarrow \pi^*(1,3)$

^a The parentheses are used when a band position cannot be exactly determined from the data. For the fit, the *minimum number* of Gaussians has been used. If, for example, a band can be identified from the MCD spectrum but no corresponding band is necessary to fit the absorption spectrum, then the absorption data are not fit with this feature. Hence, in very few cases, bands appear in the correlated fit of the MCD spectra, but not in the fit of the absorption spectra (and vice versa). ^b ϵ is given in M⁻¹ cm⁻¹. ^c Electronic transitions (cf. Figures 5 and S7 in the Supporting Information): CT = charge transfer; $\pi \rightarrow \pi^*$ = porphyrin $\pi \rightarrow \pi^*$ transition; see text.

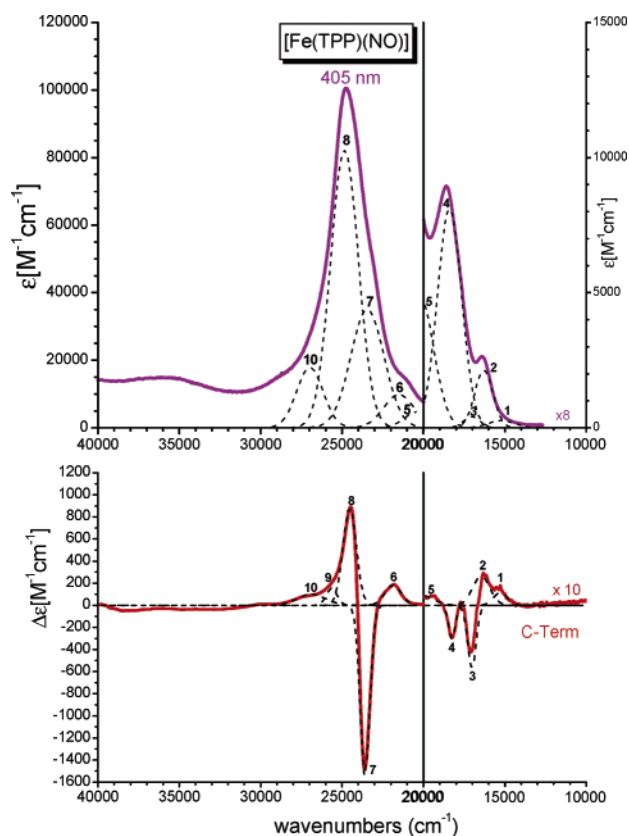


Figure 8. Electronic spectra of [Fe(TPP)(NO)] (**1**). Top: UV–vis spectrum measured in CH₂Cl₂ at room temperature. Bottom: MCD C-term spectrum measured in propionitrile/butyronitrile (1:1) at 2 K. The dashed lines represent a correlated fit of these data (cf. Table 7).

in Table 8. In addition, the shift of the Soret band from **1** to **2** is calculated to be 1830 cm⁻¹, which is too large. Using semiempirical INDO/S-CI calculations on **1** and **2** leads to some improvement of the theoretical Soret band positions, but the deviation from experiment is still unsatisfactory. This result is not surprising considering that the Soret and Q bands actually correspond to porphyrin $\pi \rightarrow \pi^*$ transitions. Hence, neglect of the phenyl substituents of TPP introduces a

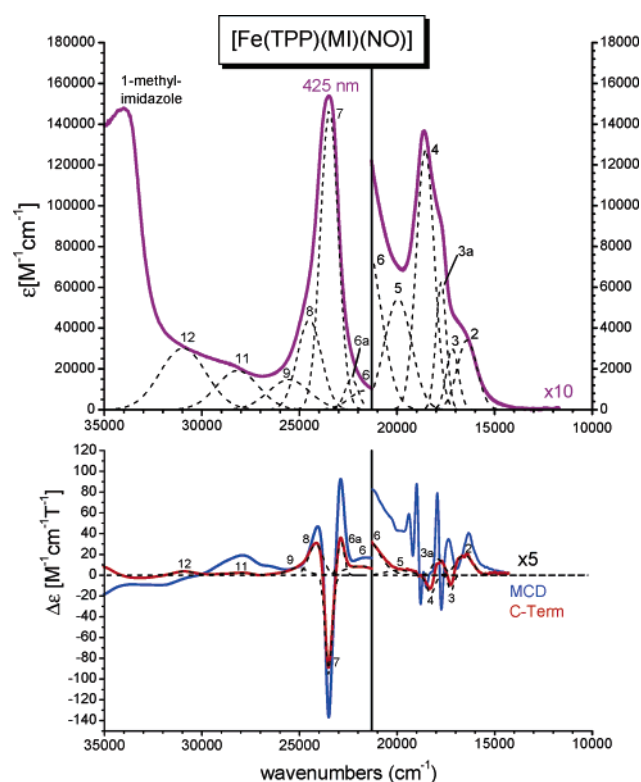


Figure 9. Electronic spectra of [Fe(TPP)(MI)(NO)] (**2**). Top: UV–vis spectrum measured in CH₂Cl₂ at room temperature. Bottom: MCD spectra measured in propionitrile/butyronitrile (1:1) at 5 K. The dashed lines represent a correlated fit of the UV–vis absorption and the MCD C-term data (cf. Table 7).

significant error to the geometric and electronic structures of the porphyrin ring. We then tried to perform TD-DFT calculations using the complete TPP ligand by applying the crystal structures of **1** and **2**,^{14,27,53} but convergence of these calculations could not be achieved. Therefore, the INDO/S-CI method was used again, and this leads to very good agreement between the experimental and calculated Soret band positions, but deviations are also observed, as shown in Table 8. Therefore, because of the fact that none of the

Table 8. Calculated Q and Soret Band Energies Compared to Experiment

model/method	transition energy		$\Delta(5C-6C)$ Soret
	Q	Soret	
[Fe(TPP)(NO)]/exp	15268/17028^a	24530^a	
[Fe(P)(NO)]/TD-DFT	19370	28500	
[Fe(P)(NO)]/INDO/S-CI	14960	26420	
[Fe(TPP)(NO)]/INDO/S-CI	15470	24740	
[Fe(TPP)(MI)(NO)]/exp	16551/17239^a	23507^a	1023
[Fe(P)(MI)(NO)]/TD-DFT	19090	26670	1830
[Fe(P)(MI)(NO)]/INDO/S-CI	14610	25730	690
[Fe(TPP)(MI)(NO)]/INDO/S-CI	14080	24260	480

^a From MCD; cf. Table 7.

excited-state calculations leads to an overall satisfactory agreement with experiment, the INDO/S-CI calculations on the entire complexes will serve as a basis for an only semiquantitative interpretation of the optical spectra of **1** and **2**.

Assignment of the Soret Region. Because of the presence of the phenyl substituents, the effective symmetry of the TPP ligand in complexes **1** and **2** is lower than D_{4h} . Hence, the 2-fold degeneracy of the LUMO $E_g(82/83)$ is lifted, which leads to a splitting of the individual excited states ψ_1 and ψ_2 into two components:

$$\begin{aligned} \psi_{1a}: A_{1u}\langle 79 \rangle \rightarrow E_g^{(1)} & \quad \psi_{2a}: A_{2u}\langle 81 \rangle \rightarrow E_g^{(1)} \\ \psi_{1b}: A_{1u}\langle 79 \rangle \rightarrow E_g^{(2)} & \quad \psi_{2b}: A_{2u}\langle 81 \rangle \rightarrow E_g^{(2)} \end{aligned}$$

In the simplest approximation used in the following, the energetically split LUMO $E_g(82/83)$ is considered but, otherwise, an effective D_{4h} symmetry is assumed. CI coupling of the individual transitions then leads via cross-coupling to the Soret and Q states:

$$|\Psi_1^{\text{Soret}}\rangle = \frac{1}{\sqrt{2}}|\psi_{1a} + \psi_{2b}\rangle$$

$$|\Psi_2^{\text{Soret}}\rangle = \frac{1}{\sqrt{2}}|\psi_{2a} + \psi_{1b}\rangle$$

$$|\Psi_1^{\text{Q}}\rangle = \frac{1}{\sqrt{2}}|\psi_{1a} - \psi_{2b}\rangle$$

$$|\Psi_2^{\text{Q}}\rangle = \frac{1}{\sqrt{2}}|\psi_{2a} - \psi_{1b}\rangle$$

As shown by Neese and Solomon, the MCD C-term intensity C_0 for an $S = 1/2$ (orbitally nondegenerate) ground state is defined by^{21c}

$$C_0 = -\frac{1}{6} \sum_{uvw} \epsilon_{uvw} g_w \sum_{K \neq A, J} \{ \Delta_{KJ}^{-1} (\vec{D}_u^{KA} \times \vec{D}_v^{AJ}) \cdot \vec{L}_w^{KJ} + \Delta_{KA}^{-1} (\vec{D}_u^{AJ} \times \vec{D}_v^{JK}) \cdot \vec{L}_w^{KA} \} \quad (4)$$

for a transition from the ground state $|A\rangle$ to the excited state $|J\rangle$, where $|K\rangle$ is an intermediate state. This expression can be used to derive an equation for the C-term intensity of the Soret band. In this case, the two Soret excited states Ψ_1^{Soret}

and Ψ_2^{Soret} represent a couple of energetically close excited states with orthogonal transition dipole moments. Excited-state spin-orbit coupling (SOC) between these states leads to the following expression for the C-term intensity as derived in the Supporting Information:

$$I^{\text{MCD}} \sim -\frac{c^2 \xi^{\text{Fe}}}{\Delta_{\text{Soret}}} (\vec{D}_u^{\text{Soret}(1)} \times \vec{D}_v^{\text{Soret}(2)}) \quad (8)$$

The corresponding SOC matrix element is proportional to $c^2 \xi^{\text{Fe}}$, where c represents the coefficient of d orbital admixture to the porphyrin E_g orbitals (<5% contribution; see the Supporting Information). Hence, the SOC matrix element is quite small because of the very small coefficients, but this is compensated for by the large transition dipole moments of the Soret band. If one alternatively considers the transition to Ψ_1^{Soret} as $|J\rangle$ and Ψ_2^{Soret} as intermediate state $|K\rangle$, the same expression for the C-term intensity in eq 8 is obtained, but because of the sign change in the denominator Δ^{-1} that occurs when $|K\rangle$ and $|J\rangle$ are exchanged, the resulting C-term signal changes its sign. Hence, this mechanism gives rise to a so-called pseudo-A term in the MCD spectrum,^{21c} where two adjacent bands are observed with opposite sign because of SOC of the corresponding excited states.

This is exactly what is observed in the MCD C-term spectrum of complex **1**, where bands 7 and 8 can therefore be assigned to the two Soret transitions (cf. Table 7), which are split by approximately 1000–1500 cm^{-1} . This is also in agreement with the INDO/S-CI calculation on the entire complex **1**, which predicts two Soret components, but their obtained splitting is too small ($\sim 100 \text{ cm}^{-1}$). From the INDO/S-CI results on **1**, mainly four different types of electronic transitions are identified in the energetical region below the Soret band (cf. Figure S7 in the Supporting Information for porphyrin MO labels):

$$\pi \rightarrow \pi^{*(1)}: A_{2u}\langle 72 \rangle, B_{2u}\langle 74 \rangle \rightarrow E_g\langle 82/83 \rangle \text{ (LUMO)}$$

$$\text{CT}^{(1)}: A_{1u}\langle 79 \rangle, A_{2u}\langle 81 \rangle \rightarrow \pi_v^* \text{-} d_{yz}, d_{z^2}/d_{xz} \text{-} \pi_h^*$$

$$\pi \rightarrow \pi^{*(2)}: \text{lower-lying } E_g(\pi) \rightarrow E_g\langle 82/83 \rangle \text{ (LUMO)}$$

$$\pi \rightarrow \pi^{*(3)}: A_{1u}\langle 79 \rangle, A_{2u}\langle 81 \rangle \rightarrow B_{1u}\langle 84 \rangle$$

Here, $\pi \rightarrow \pi^{*(1)}$ and $\text{CT}^{(1)}$ (which is a porphyrin(π) \rightarrow NO- (π^*)_iron(d_π) transition) are located closest to the Soret band followed by $\pi \rightarrow \pi^{*(3)}$, which leads to the assignments of bands 6 and 5, as given in Table 7. An additional admixture of $\pi \rightarrow \pi^{*(2)}$, which is distributed over the whole visible spectral range, is probably also present. The larger intensity of band 6 compared to 5 is due to an additional admixture of Soret character. To higher energy of the Soret transition,

(53) Because of a disorder in the crystal, the experimental structure of **1** in ref 27 has a planar TPP ring. This, however, is certainly not the case in the actual complex and, correspondingly, the INDO/S-CI calculations on this structure lead to a wrong ground state. Therefore, the conformation of the TPP ring from the crystal structure of **2** was applied in the TD-DFT calculation for **1**. This contributes to the incorrect calculation of the Soret shift.

bands 9 and 10 are observed, which have predominant charge-transfer character from $A_{1u}(79)$ and $A_{2u}(81)$ to the unoccupied d_{xy} and d_z^2 orbitals of iron (CT⁽²⁾); in the coordinate system shown in Figure 4). In the case of complex **2**, the Soret band shows a shift to lower energy,⁵⁴ which is predicted by the INDO/S-CI calculations to lead to enhanced mixing with CT⁽¹⁾ and the appearance of three Soret components in the spectrum. In fact, the MCD spectrum is able to resolve these three individual contributions as bands 6a, 7, and 8, as shown in Figure 9. Bands 6 and 5 that are observed to lower energy of the Soret band are assigned in agreement with **1**. To higher energy of the Soret feature, no contribution of CT⁽²⁾ is predicted because of the fact that both d_{xy} and d_z^2 orbitals are significantly shifted to higher energy in **2** compared to **1**. Because iron is located closer to the center of the porphyrin ring in **2**, d_{xy} is shifted to higher energy because of an increased antibonding interaction with the porphyrin orbital $B_{1g}(80)$. On the other hand, d_z^2 is strongly affected by the axial binding of the N-donor ligand (vide supra) and shifted to higher energy.¹⁸

Assignment of the Q Region. The medium-intense absorption features observed in the Q region of the spectra of both **1** and **2** actually correspond to the vibronic bands Q_v , whereas the Q bands themselves are of quite low intensity (vide supra). This is reproduced by the INDO/S-CI calculations, which do not predict any absorption features of considerable intensity in the Q region or below.⁵⁵ Theoretical analysis of the MCD C-term intensity of the Q transitions shows that both components Ψ_1^Q and Ψ_2^Q should lead to a pseudo-A-term signal in the MCD spectrum. However, because the transition dipole moments of the Q band are quite small, the product $\bar{D}_u^{Q(1)} \times \bar{D}_v^{Q(2)}$ is small and, hence, the Q transitions should also be weak in MCD. As shown in Figures 8 and 9, this is actually the case for both **1** and **2**. For complex **1**, the splitting of the two components of Q is large ($\sim 1800 \text{ cm}^{-1}$), which leads to a pattern where $Q^{(1)}$ (band 1) is followed by its vibronic band $Q_v^{(1)}$ (band 2; both with positive sign) before the second component $Q^{(2)}$ (band 3; negative sign) appears (see Table 7). In contrast, the Q splitting is smaller for **2** ($\sim 700 \text{ cm}^{-1}$) and, hence, the pseudo-A signal of Q (bands 2 and 3) is observed before the pseudo-A signal of Q_v (bands 3a and 4).

Limitations of the Model. On the basis of the simple D_{4h} model derived above, one would also predict quite similar overall C-term intensities for complexes **1** and **2**. However, this does not seem to be the case experimentally.¹⁸ As was already mentioned above, the symmetry of the porphyrin core is actually clearly lower than D_{4h} in these complexes because

of the presence of the phenyl substituents, the out-of-plane (oop) distortions of the porphyrin core, and the bent NO ligand. The deviations are especially severe for the 5C complex **1**, where the iron center shows a large displacement out of the porphyrin plane. In such cases, the porphyrin core itself usually shows a significant amount of oop distortion.⁵⁶ Importantly, a large oop distortion of the porphyrin ring will have a profound effect on the MCD intensity because it induces oop character to the Soret transitions. This opens up new channels for the MCD intensity because it allows for SOC in the x and y directions. This connects the d_z^2 orbital with d_{xz} and d_{yz} , which gives rise to additional contributions to the C term. Importantly, these contributions will be very different for **1** and **2** because of the different nature of their SOMOs (cf. Figure 7).

Discussion

In this paper, we have investigated the coordination of N-donor ligands to five-coordinate (5C) iron(II) nitrosyl complexes $[\text{Fe}(\text{TPP}^*)(\text{NO})]$ and how this influences the spectroscopic properties and electronic structures of these systems. From previous studies, it is known that this interaction is weak,^{11,14,37} but quantitative information is not available for biologically relevant imidazole-type ligands. Therefore, we have determined binding constants K_{eq} of 1-methylimidazole (MI) and pyridine (Py) to 5C complexes $[\text{Fe}(\text{TPP}^*)(\text{NO})]$ from UV-vis titrations. Corresponding free binding energies ΔG° range between -1 and -5 kcal/mol (cf. Table 2). From these data, some fundamental relationships can be established: First, the strength of the interaction strongly depends on the basicity of the applied ligand.³⁷ Hence, MI is a stronger ligand than Py. Second, the phenyl substituents in TPP*-type ligands influence the binding because of steric and electronic effects. Steric effects are introduced by *o*-methyl substitution of the phenyl rings of TPP and lead to a slight increase of the binding constants. This is due to steric shielding of the binding site. Electronic effects are observed for *o*-fluoro-substituted TPP (*To*-F₂-PP): the corresponding iron(II) porphyrin NO complex (**1-F**) exhibits an 80 times enhanced ligand affinity for MI compared to TPP, which is attributed to the fact that MI has π -donor abilities. To further investigate possible reasons for the enhanced stability of $[\text{Fe}(\text{To-F}_2\text{PP})(\text{MI})(\text{NO})]$ (**2-F**), we have determined the crystal structure of this compound. However, the obtained structure and N-O stretching frequency are similar to those of $[\text{Fe}(\text{TPP})(\text{MI})(\text{NO})]$ (**2**).¹⁴ Hence, although the free binding energy of MI is twice as large in **2-F** as it is in **2**, the properties of the Fe-N-O subunit are not noticeably affected by this change. We have further investigated the binding of N-donor ligands to complexes $[\text{Fe}(\text{TPP}^*)(\text{NO})]$ by ¹H NMR titrations. In this way, the spectra of 5C and 6C iron(II) porphyrin NO adducts are assigned for the first time. These studies provide a direct spectroscopic proof that the addition of larger amounts of N-donor ligands to 5C $[\text{Fe}(\text{TPP}^*)(\text{NO})]$ not only leads to

(54) The observed shift of the Soret band to higher energy in **1** compared to **2** is due to a larger splitting between the occupied A_{1u} and A_{2u} and unoccupied E_g orbitals in **1**. This can be traced back to two effects: (a) the different ring conformations in **1** and **2**, which leads to a stabilization of π bonding and a destabilization of π antibonding orbitals in **1** (evidenced by the energy of the A_{1u} orbital, which is nonbonding to iron) and (b) a large shift to lower energy of A_{2u} due to strong mixing with d_z^2 in **1** (induced by the out-of-plane displacement of iron).

(55) Because standard quantum-chemical methods such as HF, DFT, or CI calculations operate within the Born-Oppenheimer approximation, vibronic features such as Q_v cannot be calculated with these methods.

(56) (a) Spiro, T. G.; Strekas, T. C. *J. Am. Chem. Soc.* **1974**, *96*, 338-345. (b) Hoard, J. L. *Science* **1971**, *174*, 1295.

the formation of the 6C complex [Fe(TPP*)(L)(NO)] but also facilitates the formation of the diamagnetic complexes [Fe-(TPP*)(L)₂]. Importantly, this indicates that binding of an N-donor ligand *weakens* the Fe–NO bond, which is in agreement with kinetic studies by Kharitonov et al.⁵⁷ Our results also show that the degree of denitrosylation is strongly dependent on the employed TPP* (porphyrin) ligand: whereas TPP itself only leads to the formation of small amounts of the bis(N-donor) complex, compounds with the fluoro-substituted ligand *To*-F₂PP are very susceptible to NO loss. Therefore, the increase in the N-donor binding constant in **1-F** goes along with a decrease in the stability of the Fe–NO bond. This demonstrates the difficulty of synthesizing stable 6C iron(II) porphyrin NO complexes in solution in the absence of excess NO.

The UV–vis and NMR titration experiments show that, although the binding constants of N-donor ligands to 5C iron(II) porphyrin NO complexes are very small, their coordination has a profound effect on the electronic structure of the Fe^{II}–N–O subunit. Using vibrational spectroscopy coupled to normal-coordinate analysis (NCA), the differences in the electronic structures of 5C complex [Fe(TPP)(NO)] (**1**) and 6C complex [Fe(TPP)(MI)(NO)] (**2**) are further evaluated. Because of the size of the systems studied, force constants were obtained using quantum-chemistry-centered (QCC)-NCA. In the case of **1**, $\nu(\text{N–O})$ is observed at 1697 cm⁻¹ and $\nu(\text{Fe–NO})$ at 532 cm⁻¹, which leads to force constants of 12.53 and 2.98 mdyn/Å for these bonds, respectively. Binding of MI weakens the Fe–NO σ bond, as evidenced by the fact that *both* the N–O and Fe–NO bonds become weaker in **2**. In the case of the N–O bond, this is directly evident from the measured N–O stretching frequency of 1630 cm⁻¹, corresponding to a force constant of 11.55 mdyn/Å. The Fe–NO frequency of 440 cm⁻¹ is less diagnostic because of extensive mode mixing with the Fe–N–O bend at 530 cm⁻¹, but the NCA force constant of 2.55 mdyn/Å emphasizes this point. On the basis of these experimental findings as well as spin-density distributions evidenced by MCD spectroscopy,¹⁸ DFT calculations can be used to exactly define the electronic structures of these iron(II) porphyrin NO adducts.

The principal bonding scheme of Fe^{II}NO complexes has been described by Enemark and Feltham.⁵⁸ These complexes were classified as {FeNO},⁷ and it was predicted that they show bent Fe–NO units with radical character on the nitrosyl ligand. This description is also applicable to complexes **1** and **2** and explains their basic features. However, this description also leaves room for a large variation of the electronic structure mediated by metal–ligand covalency. In this way, the electronic structure could vary all the way from an Fe^{III}NO⁻ extreme (as has been shown for nonheme iron(II) NO adducts⁵⁹) on the one side to an Fe^INO⁺ extreme on the other side, with the Fe^{II}NO(radical) case being intermedi-

ate. These possibilities lead to very different spectroscopic properties and reactivities. Hence, a definition of the electronic structures of heme nitrosyls is very important to elucidate their function in biological signaling and catalysis. In this paper, the bonding scheme of the 6C complex **2** is analyzed in detail. Contributions to the Fe–NO bond arise from (a) a σ -donor interaction between the singly occupied π^* orbital of NO ($\alpha\text{-}\pi_{\text{h}}^*$) and the empty d_{z²} orbital of iron and (b) a medium-strong π -back-bond between the d_{xz} and d_{yz} orbitals of iron and the empty π^* orbitals of NO ($\alpha\text{-}\pi_{\text{h}}^*$, π_{v}^*). The occupied orbitals of the π back-bond are mostly metal-based and, therefore, the corresponding electrons can be assigned to the metal, leading to a low-spin iron(II) description. As evidenced from the calculated spin densities, the donation from the singly occupied π^* orbital of NO into d_{z²} of iron(II) is limited. Hence, the electronic structure of complex **2** has to be described as the prototype of an Fe^{II}-NO(radical) system. Recently, the electronic structure of the 6C low-spin Fe^{II}NO complex [Fe(cyclam–ac)(NO)]⁺ has been studied in detail.⁶⁰ In this compound, the applied cyclam–ac ligand system provides a planar N₄ donor set like porphyrin. In the axial position, acetate (ac) is bound trans to NO. Interestingly, the observed N–O stretching frequency of 1615 cm⁻¹, the EPR spectrum showing small *g* shifts and hyperfine splittings of the coordinated NO ligand on *g*(mid), and the calculated spin-density distribution in this complex closely resemble the properties of **2**. Hence, in agreement with our analysis for **2**, this complex has also been described as an Fe^{II}NO(radical) system.

As evidenced by the experimental force constants, the main difference in the electronic structures of complexes **1** and **2** relates to the Fe–NO σ bond, which is distinctively stronger for **1**. Because the π back-bond is comparable for **1** and **2**, the increased σ covalency in the case of **1** leads to an electronic structure with noticeable Fe^INO⁺ character relative to **2**.¹⁸ This does not mean that complex **1** corresponds to the Fe^INO⁺ limit where the unpaired electron has been completely transferred to the metal center but that this system is somewhat in between, with the unpaired electron being equally distributed over the Fe–NO unit. This electronic structure description is in agreement with (a) spin-density distributions elucidated from MCD spectroscopy,¹⁸ (b) the larger overall *g* shifts obtained from EPR for **1**, (c) the stronger paramagnetic shifts of the pyrrole hydrogens⁴⁸ of the porphyrin core observed for complex **1**, and (d) the weaker Fe–NO bond in **2**, as evidenced by the complex's tendency to lose NO. Hence, the obtained bonding descriptions for **1** and **2** presented here are in agreement with all available experimental data. Compared to earlier DFT studies,^{17,20} we have now arrived at a quantitative description of NO bonding to ferrous heme centers.

Because the transition from **1** to **2** corresponds to a change in the Fe–NO σ covalency and because covalency is a property that can change gradually, intermediate stages between complexes **1** and **2** should exist. This is indeed the

(57) Kharitonov, V. G.; Sharma, V. S.; Magde, D.; Koesling, D. *Biochemistry* **1997**, *36*, 6814–6818.

(58) Enemark, J. H.; Feltham, R. D. *Coord. Chem. Rev.* **1974**, *13*, 339.

(59) Brown, C. A.; Pavlosky, M. A.; Westre, T. E.; Zhang, Y.; Hedman, B.; Hodgson, K. O.; Solomon, E. I. *J. Am. Chem. Soc.* **1995**, *117*, 715–732.

(60) Serres, R. G.; Grapperhaus, C. A.; Bothe, E.; Bill, E.; Weyhermüller, T.; Neese, F.; Wieghardt, K. *J. Am. Chem. Soc.* **2004**, *126*, 5138–5153.

case. Studies of Scheidt and co-workers¹⁴ have shown that less donating ligands such as 4-methylpiperidine and 4-(dimethylamino)pyridine lead to $\nu(\text{N}-\text{O})$ of 1642 and 1653 cm^{-1} , respectively. In these cases, the weaker interaction with the iron center is documented by the longer Fe–N bond lengths of 2.29 and 2.28 Å for these ligands, respectively, compared to 2.18 Å for MI. The second important interaction between Fe^{II} and NO corresponds to a π back-bond. The strength of this interaction can also be varied, as shown by Spiro and co-workers,⁶¹ for 5C complexes where the phenyl rings of the TPP ligand carry either electron-withdrawing or electron-donating groups. Importantly, in this case, an inverse correlation of the N–O and Fe–NO bond strengths is observed.

Detailed analysis of the absorption and MCD data of complexes **1** and **2** shows that their electronic spectra are largely dominated by $\pi \rightarrow \pi^*$ transitions of the porphyrin ligand. Hence, the differences in the electronic structures of these complexes are only very indirectly reflected by the observed electronic transitions. The most obvious change is a shift of the Soret band by $\sim 1000 \text{ cm}^{-1}$ to lower energy in **2** compared to **1**. Importantly, the absorption spectra of **1** and **2** alone neither resolve many transitions nor allow for an identification and analysis of the components of the Soret and Q bands. This is solely based on the MCD C-term spectra, which again demonstrates the enormous potential of this method. Theoretical analysis shows that both the Soret and Q bands give rise to a pseudo-A term in the MCD spectra of **1** and **2** and, hence, they can easily be identified. Because the Soret band has large transition dipole moments, this feature is also intense in the MCD C-term spectrum. In contrast, the Q band is weak both in absorption and in MCD. Correlation of the spectroscopic data to TD-DFT and semiempirical INDO/S-CI calculations shows that a simplification of the TPP ligand in **1** and **2** to porphine (i.e., neglect of the phenyl substituents) leads to wrong predictions of the electronic spectra. On the basis of the INDO/S-CI results, a tentative assignment of all transitions identified in the spectra of **1** and **2** is presented. Experimentally, no charge-transfer transition between Fe^{II} and NO is observed. The INDO/S-CI calculations predict a weak $d_{xz}, d_{yz} \rightarrow \text{NO}(\pi^*)$ transition ($\epsilon \sim 500 \text{ M}^{-1} \text{ cm}^{-1}$) in the 12 000 cm^{-1} region (below the Q band) for both **1** and **2**.

The results presented in this study have important implications for the modeling of enzymatic ferrous heme nitrosyl species, which are mostly 6C. Hence, corresponding synthetic model complexes also need to be 6C in solution, which, however, is hard to achieve because of the weak binding constants of N-donor ligands trans to NO. Here we show the factors that influence the strength of this interaction, and we have identified a TPP-based ligand (To-F₂PP) that allows for the preparation of 6C iron(II) porphyrin NO adducts in

solution when MI is used as the base. However, it is also demonstrated that the systems with enhanced binding constants facilitate NO loss, which is a drawback. Considering the molecular mechanism of NorBC, a number of different proposals are currently discussed in the literature.⁶² Because of the large affinity of ferrous heme for nitric oxide,⁶³ we believe that mechanisms where NO binds exclusively to the nonheme iron center are less likely. Hence, this leaves the mechanism shown in Scheme 1 as the most probable alternative. Importantly, the enhanced radical character of NO in 6C ferrous heme complexes as identified here is advantageous for the central (radical) N–N coupling step in this mechanism, whereas 5C $\text{Fe}^{\text{II}}\text{NO}$ should be less reactive. This is in agreement with recent findings of Wasser et al., who synthesized a structural model for NorBC based on a 5C heme nitrosyl and which does not show any NO reductase activity.⁶⁴ However, it should also be noted that not much experimental information is available for the enzyme regarding the coordination number of the ferrous heme *b* NO adduct. EPR experiments under turnover conditions have identified the nonheme iron(II) NO adduct as a high-spin ($S = 3/2$) species, but the information on the heme center is limited.⁶⁵ On the basis of the properties of ferrous and ferric heme *b*, it was speculated that the heme nitrosyl intermediate is only 5C,⁶⁶ which would be in disagreement with our findings. However, no proof of this hypothesis is provided. On the basis of our results, we propose that this species is actually 6C. In this context, it should also be noted that hemoglobin and myoglobin form 6C nitrosyl adducts and, therefore, this is definitively a mechanistic possibility for NorBC.

Acknowledgment. This work was supported by the Deutsche Forschungsgemeinschaft (DFG; Grant LE 1393/1) and the Fonds der Chemischen Industrie (FCI). Dr. Frank Neese (Max-Planck Institut für Bioanorganische Chemie, Mülheim an der Ruhr, Germany) is acknowledged for recording the MCD spectra of **1** and **2**.

Supporting Information Available: Derivation of the theoretical expression for the C-term intensity; figures of the IR and Raman spectra of **1** and **2**, UV–vis absorption spectra of **1-F** and **2-F**, ¹H NMR titration of **1** with Pip, MO diagrams of free porphine²⁻ and NO, and MCD spectra of **2** and **2-F**; tables of the MO charge contributions of **2**, the calculated ⁵⁷Fe hyperfine parameters, and coordinates of all optimized structures; and crystallographic data of **2-F** (CIF). This material is available free of charge via the Internet at <http://pubs.acs.org>.

IC050865J

- (62) Zumft, W. G. *J. Inorg. Biochem.* **2005**, *99*, 194–215.
 (63) Cooper, C. E. *Biochim. Biophys. Acta* **1999**, *1411*, 290–309.
 (64) Wasser, I. M.; Huang, H.; Moënné-Loccoz, P.; Karlin, K. D. *J. Am. Chem. Soc.* **2005**, *127*, 3310–3320.
 (65) Hendriks, J.; Warne, A.; Gohlke, U.; Haltia, T.; Ludovici, C.; Lübben, M.; Saraste, M. *Biochemistry* **1998**, *37*, 13102–13109.
 (66) Moënné-Loccoz, P.; de Vries, S. *J. Am. Chem. Soc.* **1998**, *120*, 5147–5152.
 (67) Fadini, A.; Schnepel, F.-M. *Schwingungsspektroskopie*; Thieme Verlag: Stuttgart, 1985.

(61) Vogel, K. M.; Kozłowski, P. M.; Zgierski, M. Z.; Spiro, T. G. *J. Am. Chem. Soc.* **1999**, *121*, 9915–9921.

4.4. Binding of Nitric Oxide to Ferric Hemes: Electronic Structure of Six-Coordinate Iron(III)-Porphyrin NO Complexes

4.4.1. Introduction

Nitric oxide (NO) is a poisonous gas, which, however, has proven to be of great biological significance. In 1992, it was therefore voted as ‘the molecule of the year’ by the magazine Science.¹ These pioneering results triggered further research and up to this day, it is known that NO plays a key role in nerve signal transduction, vasodilation, blood clotting and immune response by white blood cells.² New biological functions of NO and the corresponding, one electron reduced nitroxyl ion are still discovered.³ Many of the biologically important reactions of nitric oxide are mediated by heme proteins. NO is produced in vivo by the nitric oxide synthase (NOS) family of enzymes,⁴ which utilize dioxygen to oxidize L-Arginine yielding L-Citrulline and NO. The cardiovascular regulation by NO (produced by endothelial (e-) NOS) is then mediated by soluble guanylate cyclase (sGC),^{3d,5} which is activated by coordination of NO to its ferrous heme active site. In addition, the role of nitric oxide in vasodilation is exploited by certain blood-sucking insects that inject NO into the bites of their victims using small NO-carrier proteins, the so-called Nitrophorins (Np).⁶ Furthermore, nitric oxide occurs as an intermediate in dissimilatory denitrification.⁷ Here, NO is produced by nitrite reductase (NIR) and further reduced to nitrous oxide by the nitric oxide reductases (NOR). In a number of these proteins, ferric heme NO adducts occur as intermediates of catalysis or as enzyme-product complexes. The observed biological Fe(III)-porphyrin NO adducts can be divided into two classes depending on the nature of the axial ligand coordinated in trans-position to NO, which is either histidine (his) or cysteine (cys). In cytochrome cd₁ NIR, a six-coordinate ferric heme NO complex with axial histidine coordination is observed as enzyme-product complex.⁸ Correspondingly, the nitrophorins from *Rhodnius prolixus* (rNp1 – rNp4) contain ferric heme centers with a histidine coordinated in the axial position.^{4a,c} The NP proteins then reversibly bind NO and release it in the victims tissue. The occurrence of ferric instead of ferrous hemes in these systems is not arbitrary, but is related to the rates of NO loss, which are approximately 4 to 8 orders of magnitude larger in ferric compared to ferrous hemes.^{2g,9} Hence, formation of ferrous heme NO adducts has often been referred to as a ‘dead-end’ of protein activity, and would certainly impose a rather dramatic limit on the dissociation of NO from the NIR enzyme-product complex or the Np’s. In a similar way, ferric heme NO adducts with axial cysteine

coordination occur at the end of the catalytic cycle of the NOS enzymes, again helping to prevent deactivation of the protein. Recently, corresponding nitrophorins containing an axial cysteine ligand have also been identified.^{4c} In the case of fungal NOR (P450nor), the ferric form of the enzyme is catalytically active and binds NO forming a Fe(III)-porphyrin NO adduct with axial cysteine coordination.¹⁰ This is followed by two-electron reduction leading to a formal Fe(I)-NO complex that reacts with a second molecule of NO forming nitrous oxide¹¹.

Table 4.4.1: Vibrational properties of ferric heme NO adducts in proteins and model complexes

Complex	$\nu(\text{N-O})$ [cm^{-1}]	$\nu(\text{Fe-NO})$ [cm^{-1}]	Reference
P450cam-NO	1806	528	10c/12a
P450cam-NO + adamantone	1818	520	10c
SR-NO ^a	1828	510	13
P450nor-NO	1851	530	10c
CPO-NO ^a	1868	538	10c
iNOS-NO		537	4d
[Fe(OEP)(NO)](ClO ₄) ^b	1868/1838	611/600	22/25a
HRP-NO ^a	1903	604	14
NorBC-NO ^a	1904	594	15
rNp1-NO	1917	591	4b/16
hHO-1-NO ^a	1918	596	17
[Fe(OEP)(MI)(NO)](ClO ₄)	1921	-	23a
Hb-NO ^a	1925	594	18
Mb-NO ^a	1927	595	19
[Fe(TPP)(HO- <i>i</i> -C ₅ H ₁₁)(NO)](ClO ₄)	1935	-	23d

^a SR = picket fence porphyrin model complex with axial thiolate ligand; CPO = chloroperoxidase; HRP = horseradish peroxidase; NorBC = bacterial NOR; hHO-1 = human heme oxygenase-1; Hb = hemoglobin; Mb = myoglobin

^b Data for the chloroform solvate and the corresponding solvent free complex, respectively.

In the so-called Enemark-Feltham scheme, the Fe(III)-porphyrin NO adducts are classified as {FeNO}⁶ complexes where the exponent “6” refers to the number of d electrons plus the unpaired electron of NO²⁰. The electronic structure of the {FeNO}⁶ heme complexes has in general been described as Fe(II)-NO⁺ (cf., for example, ref. 8) in agreement with {RuNO}⁶

systems where this electronic structure was observed before and has extensively been studied.²¹ Hence, the Fe-NO interaction in these complexes is dominated by π backbonding from two t_2 type d orbitals (' d_π ') of low-spin iron(II) into the unoccupied π^* orbitals of NO^+ . This bonding description is analogous to the isoelectronic Fe(II)-CO complexes. A number of crystal structures have been determined for Fe(III)-porphyrin NO model complexes including five-coordinate (5C) $[\text{Fe}(\text{OEP})(\text{NO})](\text{ClO}_4)$ (OEP = octaethylporphyrin)²² and six-coordinate (6C) $[\text{Fe}(\text{OEP})(\text{L})(\text{NO})](\text{ClO}_4)$ (L = neutral N-donor ligand) and related systems.²³ These complexes show linear Fe-N-O units and extremely short Fe-NO bond lengths of 1.63 - 1.65 Å in agreement with the Fe(II)- NO^+ description. In addition, the N-O stretching vibrations in these complexes are usually found in the 1900 cm^{-1} region as shown in Table 1 which also corresponds to coordinated NO^+ . Hence, it was believed for a long time that the bonding description of $\{\text{FeNO}\}^6$ is fully analogous to Fe(II)-CO. However, in recent studies it was found that the N-O and Fe-N(O) stretching vibrations in different Fe(III)-porphyrin NO adducts (mostly protein data) do *not* show an inverse correlation as in the case of Fe(II)-porphyrin CO complexes,²⁴ but a direct correlation where an increase in $\nu(\text{N-O})$ goes along with an increase in $\nu(\text{Fe-NO})$ and vice versa.²⁵ Therefore, additional contributions to the Fe-NO bond must exist in these complexes besides the strong π backbond. The fact that vibrational data obtained for proteins were mostly used for these correlations is due to the fact that Fe-NO stretching vibrations are only available for a very limited number of model complexes. The observed direct correlation was interpreted using DFT calculations.²⁵ It is related to a small admixture of a fully Fe-N-O antibonding orbital into the occupied porphyrin a_{2u} π orbital, which is very sensitive to porphyrin substituents and environment. Hence, this mechanism leads to the partial population of an Fe-N-O antibonding orbital, which explains the experimental trend: a stronger population of this orbital leads to a lowering of both $\nu(\text{N-O})$ and $\nu(\text{Fe-NO})$ and vice versa. Interestingly, it has been postulated that the nature of this Fe-N-O antibonding orbital is different for five- and six-coordinate complexes: in the 5C case, it corresponds to the antibonding combination of the d_{z^2} orbital of iron(II) and σ^* of NO ,^{25a} whereas for 6C it is the antibonding combination of d_π and π^* .^{25b} In addition to these slight variations in the 'classic' π backbonding electronic structure model for heme $\{\text{FeNO}\}^6$ systems, it has been pointed out by Walker in a recent review^{4c} that the $\{\text{FeNO}\}^6$ formalism leaves room for an even wider variation in electronic structure, as has been discussed recently for analogous $\{\text{FeNO}\}^7$ complexes.²⁶ Here, the Fe(III)-porphyrin NO adducts could also exhibit an Fe(III)-NO(radical) electronic structure, where the unpaired electrons of low-spin iron(III) and NO are antiferromagnetically coupled leading to the experimentally observed

diamagnetic ground state. This would be advantageous for the nitrophorins because it would prevent the autoxidation reaction of Fe(II)-NO⁺ complexes²⁷, which ultimately leads to ferrous NO adducts and hence, deactivation of the proteins as NO carriers. In order to understand the functioning of the nitrophorins and the nature of ferric heme NO interactions in general, it is necessary to elucidate the electronic structures of the formed Fe(III)-porphyrin NO complexes in detail. The established Fe(II)-NO⁺ and the elusive Fe(III)-NO(radical) electronic structures, for example, will lead to very different reactivities of the resulting complexes. In addition, the formation of an Fe(II)-NO⁺ complex from a ferric heme and NO requires the occurrence of an NO to Fe(III) electron transfer. However, not much is known about the mechanism of complex formation in these systems.

In this study, the mechanism and energetics of NO binding to ferric hemes and the possible variation in electronic structure of the formed complexes is investigated in detail using model complexes and density functional (DFT) calculations. The six-coordinate model system [Fe^{III}(TPP)(MI)(NO)](BF₄) (**1**; TPP = tetraphenylporphyrin, MI = 1-methylimidazole) has been prepared and characterized using vibrational spectroscopy coupled to isotope substitution. This way, $\nu(\text{N-O})$ and $\delta(\text{Fe-N-O})$ are assigned. In addition, the crystal structure of the precursor, [Fe(TPP)(thf)₂](BF₄), is presented. The energetics of NO binding to ferric hemes are then investigated using DFT calculations. Complex formation energies are calculated and compared to the values obtained for corresponding ferrous systems to elucidate the difference in complex stabilities of these systems.

4.4.2. Experimental and Computational Procedures

4.4.2.1. Syntheses

Reactions were performed applying Schlenk techniques using carefully purified solvents. NO gas was purified by first passing through an ascarite II column (NaOH on silica gel) and then through a cold trap at -80°C to exclude higher nitrogen oxide impurities.

Syntheses of ligand. Tetraphenylporphyrin (H₂TPP) was synthesized and purified as previously reported.²⁸

Syntheses of precursors. [Fe(TPP)Cl] was prepared according to the method of Adler et al.²⁹ [Fe(TPP)ClO₄] was prepared by literature methods.³⁰

Synthesis of the ferric NO adduct [Fe^{III}(TPP)(MI)(NO)](BF₄) (1).

A sample of [Fe(TPP)ClO₄] (100 mg, 0.13 mmol) and KBF₄ (160mg, 1.3mmol) is placed in a 100ml Schlenk flask. The flask is purged three times with argon and 20ml of CHCl₃ are added. This heterogeneous reaction mixture is then stirred at room temperature for about 2 hrs and filtered. The obtained filtrate, [Fe^{III}(TPP)(BF₄)] (precursor complex), is collected in a 100ml schlenk flask and 1-methylimidazole (10μL, 0.13mM) is added. NO gas is then passed through the stirred solution for 10 minutes. *n*-Hexane (15ml) is slowly added to the reaction mixture which is then stored in a freezer (-20°C) for 2 days. The resulting precipitate is filtered and obtained as microcrystalline solid. The IR spectrum shows the NO stretching band at 1 cm⁻¹, indicative of the formation of **1**. Yield: 95 mg (84 %).

Synthesis of the ferric NO adduct [Fe^{III}(TPP)(NO)(NO₂)] (1A).

0.1 g of [FeTPP]₂O were dissolved in 20 mL of CHCl₃ in a 100 mL Schlenk flask under an argon atmosphere. The solution was stirred for few minutes and then nitric oxide was added. Then 0.2 mL of air was injected into the reaction. The resulting solution was allowed to stir under NO atmosphere for 1 hour. Finally, *n*-hexane (20 mL) was added and the obtained precipitate was stored under an argon atmosphere. Yield: 75 mg (72 %).

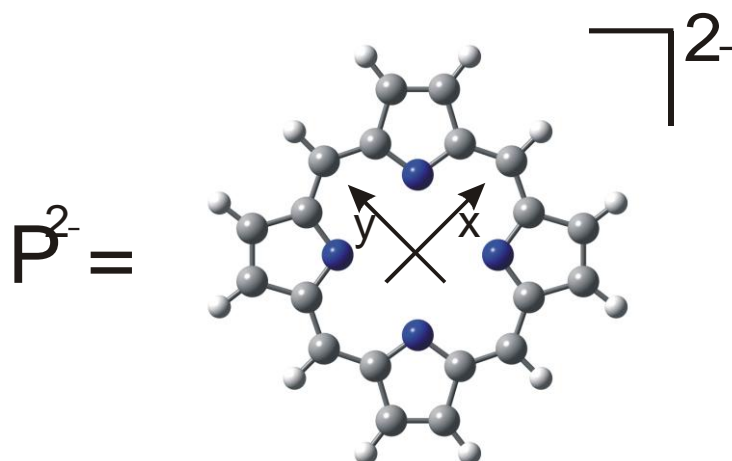
4.4.2.2. Crystal Structure Determination.

Single crystals of the bis-(thf) coordinated precursor complex, [Fe^{III}(TPP)(thf)₂](BF₄), suitable for x-ray structural analysis were obtained after two weeks from a saturated solution of the precursor in thf layered with *n*-hexane. Intensity data were collected using a STOE Image Plate Diffraction System with Mo-Kα radiation. The structure was solved with direct methods using SHELXS-97³¹ and refinement was done against F² using SHELXL-97. All non-hydrogen atoms were refined with anisotropic displacement parameters. The hydrogen atoms were placed in ideal position and were refined isotropically using the riding model. There are three crystallographically independent thf molecules in the asymmetric unit. In two cases, three carbon atoms are disordered and were refined using a split model. There is one additional thf molecule in the asymmetric unit which is disordered and for which no appropriate split model can be found. Therefore, the data were corrected for disordered solvent using the "Squeeze" option in Platon. Selected crystallographic data are presented in Table 4.4.6. Selected bond lengths and angles are presented in Table 4.4.7. [Fe(TPP)(thf)₂](BF₄) crystallizes in the triclinic space group P-1 with all atoms located in general positions. The iron atom is coordinated by the four porphyrin nitrogen atoms and two

oxygen atoms of the tetrahydrofuran ligands within a slightly distorted octahedron (Figure 4.4.6). The iron atom is located in the porphyrin ring plane (deviation from the mean plane: 0.0044 Å).

4.4.2.3. Density Functional Calculations.

The structures of the models $[\text{Fe}(\text{P})(\text{MI})(\text{NO})]^+$ ($\tilde{\mathbf{I}}$, $S = 0$), $[\text{Fe}(\text{P})(\text{MI})]^+$ ($S = 1/2, 5/2$) and $[\text{Fe}(\text{P})(\text{MI})]$ ($S = 0, 2$) were fully optimized using BP86/TZVP. For these calculations, a simplified TPP ligand has been used where the four phenyl groups in meso position of the porphyrin ring have been replaced by hydrogen. The resulting porphyrin model ligand P (P = porphine) is shown in Scheme 4.4.1 along with the coordinate system used. Vibrational frequencies have been calculated for $\tilde{\mathbf{I}}$ showing no imaginary frequencies. In addition, B3LYP/LanL2DZ and B3LYP/LanL2DZ* geometry optimizations have been performed on these models and the corresponding ferrous NO adduct $[\text{Fe}(\text{P})(\text{MI})(\text{NO})]$ ($S = 1/2$) to investigate the method dependence of the complex formation energies. B3LYP/TZVP single points on the fully optimized B3LYP/LanL2DZ* structures were also employed. The LanL2DZ* basis set^{26a} consists of LanL2DZ³² plus polarization functions (from TZVP³³) on all heavy atoms. All these methods were used as implemented in the Gaussian 98 package³⁴. Orbitals were plotted using GaussView.



Scheme 4.4.1 Porphine ligand

4.4.3 Results and Analysis

4.4.3.1. Vibrational Spectroscopy and Electronic Structure of Fe(III)-Porphyrin NO Adducts.

4.4.3.1.1. Vibrational Properties and Assignments

The MIR spectrum of $[\text{Fe}(\text{TPP})(\text{MI})(\text{NO})](\text{BF}_4)$ (**1**) is shown in Figure 4.4.2 together with the corresponding $^{15}\text{N}^{18}\text{O}$ isotope labeled data. The N-O stretching vibration $\nu(\text{N-O})$ is identified as the band at 1896 cm^{-1} that shifts to 1816 cm^{-1} upon isotope substitution. One other isotope sensitive band is found at 588 cm^{-1} . This feature appears at 572 cm^{-1} in the $^{15}\text{N}^{18}\text{O}$ compound. In the case of a linear Fe-N-O unit, it can be expected that the Fe-N-O bend is IR active, whereas the Fe-NO stretch should be Raman active. This is, for example, observed for $[\text{Ru}(\text{NH}_3)_5(\text{NO})]\text{X}_2$ ($\text{X} = \text{Hal}^-$, etc.), a linear Ru(II)- NO^+ complex. Hence, the band at 588 cm^{-1} is assigned to $\delta(\text{Fe-N-O})$. From solution studies on $[\text{Fe}(\text{OEP})(\text{Py})(\text{NO})]\text{Cl}$ and $[\text{Fe}(\text{SP-14})(\text{Py})(\text{NO})]\text{Cl}$ (SP-14 = strapped porphyrin ligand), $\nu(\text{Fe-NO})$ has been assigned to bands at 602 cm^{-1} and 603 cm^{-1} , respectively, using resonance Raman measurements with 407 nm excitation.³⁵ The bending modes have not been identified in this study.

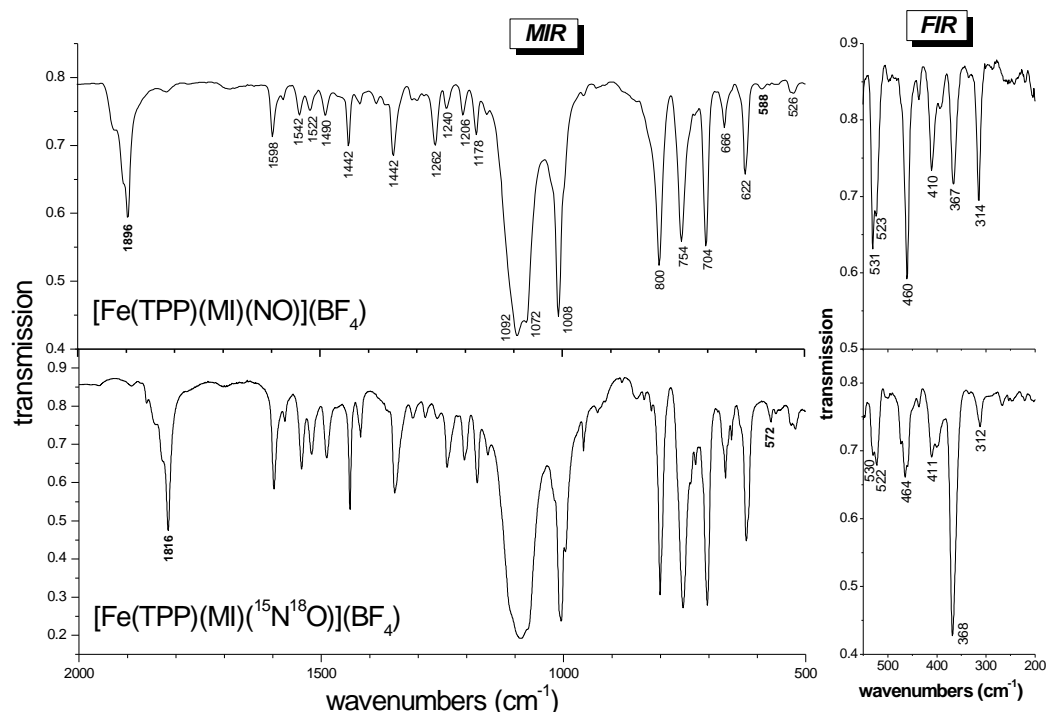


Figure 4.4.1. IR spectra of $[\text{Fe}(\text{TPP})(\text{MI})(\text{NO})](\text{BF}_4)$ (**1**, top) and of the corresponding isotope labeled complex (bottom).

The observed $\nu(\text{N-O})$ frequency of 1896 cm^{-1} for **1** is in good agreement with the literature value of 1921 cm^{-1} obtained for $[\text{Fe}^{\text{III}}(\text{OEP})(\text{MI})(\text{NO})](\text{ClO}_4)$ as shown in Table 4.4.2. Six-coordinate ferric heme NO adducts in proteins with *trans* histidine ligation also show N-O frequencies in the 1900 cm^{-1} region as listed in Table 4.4.1. The calculated $\nu(\text{N-O})$ and $\delta(\text{Fe-N-O})$ frequencies for model **1** are in very good agreement with experiment (cf. Table 4.4.2).

As mentioned in the Introduction, detailed vibrational studies on ferric heme NO model complexes are rare. This is most likely due to the fact that these complexes are unstable, and tend to decompose by either loss of NO, or reaction with O_2 to form the nitro-nitrosyl adduct $[\text{Fe}(\text{porphyrin})(\text{NO})(\text{NO}_2)]$. In order to make certain that compound **1** does not correspond to $[\text{Fe}(\text{TPP})(\text{NO})(\text{NO}_2)]$ (**1A**), we prepared this complex and investigated its vibrational properties. Figure S1 shows a comparison of the IR spectra of **1** and **1A**, which are clearly different. In the case of **1A**, $\nu(\text{N-O})$ is located at 1876 cm^{-1} . The N-O stretching frequencies of the coordinated nitrite ligand are observed as characteristic bands at 1460 cm^{-1} for $\nu_{\text{as}}(\text{NO}_2)$ and 1298 cm^{-1} for $\nu_{\text{s}}(\text{NO}_2)$ (assignments from ref. ³⁶). These shift to 1400 and 1238 cm^{-1} upon $^{15}\text{N}^{18}\text{O}$ isotope labeling as shown in Figure 4.4.2, which is in agreement with the assignment of these features to $\nu(\text{NO}_2)$. Importantly, both bands are missing in the spectrum of **1**, which confirms that this complex is in fact the ferric heme NO adduct with axial MI coordination.

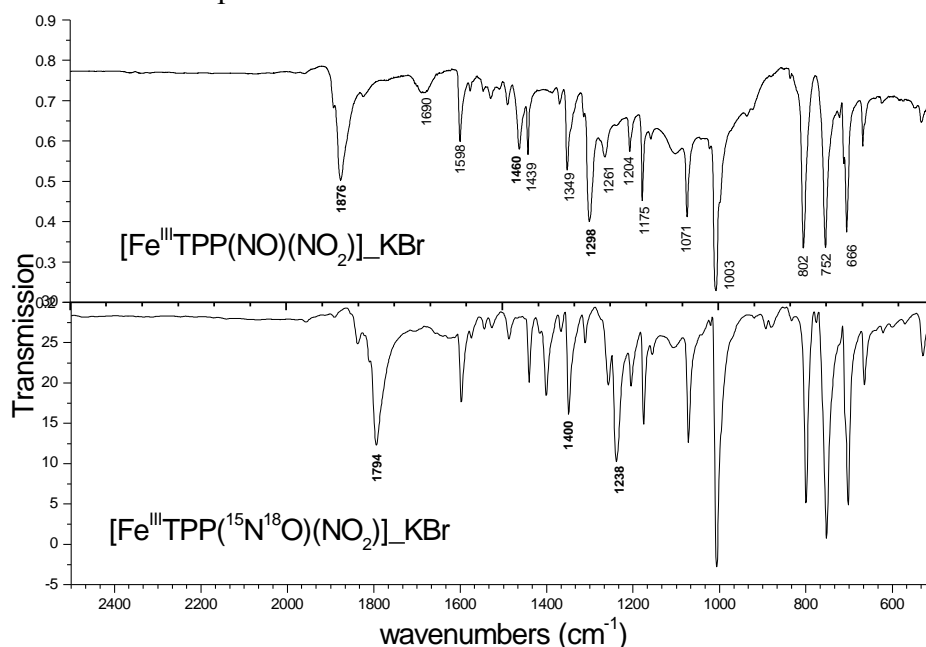


Figure 4.4.2. IR spectra of $[\text{Fe}(\text{TPP})(\text{NO})(\text{NO}_2)]$ (**1A**, top) and of the corresponding isotope labeled complex (bottom).

Table 4.4.2: Geometric and vibrational properties of [Fe(P*)(L)(NO)] complexes (L = MI, Py, etc., or missing; P* = tetraphenylporphyrin or octaethylporphyrin type ligand)

Molecule ^a	Geometric Parameters [Å]					Vibrational Frequencies [cm ⁻¹]		
	ΔFe-N(NO)	ΔN-O	∠Fe-N-O	ΔFe-L _{tr}	ΔFe-N _p	v(N-O)	v(Fe-NO)	δ(Fe-N-O)
Fe ^{III} Complexes								
[Fe ^{III} (OEP)(NO)](ClO ₄) ^{b,c}	1.644	1.112	177		1.994	1868	611	
[Fe ^{III} (OEP)(MI)(NO)](ClO ₄) ^b	1.646	1.135	177	1.988	2.003	1921		
[Fe ^{III} (OEP)(Py)(NO)]Cl ^d							602	
[Fe ^{III} (SP-14)(Py)(NO)]Cl ^d							603	
[Fe ^{III} (TPP)(NO)](BF ₄)						1853		
[Fe ^{III} (TPP)(MI)(NO)](BF ₄)						1896		588
[Fe ^{III} (TPP)(MI)(¹⁵ N ¹⁸ O)](BF ₄)						1816		572
[Fe ^{III} (P)(1-MI)(NO)] ⁺ – calc BP86/TZVP	1.644	1.147	180	2.018	2.022	1933	639	606/598
[Fe ^{III} (P)(1-MI)(NO)] ⁺ – calc B3LYP/LanL2DZ	1.639	1.169	180	1.976	2.023	1908	657	613/601
Fe ^{II} Complexes								
[Fe ^{II} (TPP)(MI)(NO)]	1.750	1.182	138	2.173	2.008	1630	440	530(ip) 291(oop)
[Fe ^{II} (P)(MI)(NO)] – calc BP86/TZVP	1.734	1.186	140	2.179	2.022	1662	609	482(ip) 317(oop)

^a MI = 1-methylimidazole; P = Porphine ligand used for calculations; values for ΔFe-N_p are averaged

^b Taken from refs. 23a,b

^c Chloroform solvate

^d Taken from ref. 35

^e DFT predicts a small splitting of the δ modes.

Table 4.4.3. Comparison of experimental vibrational frequencies [cm⁻¹] and calculated (DFT) force constants [mdyn/Å]

Mode	exp.		Force constants f
	n.a.i. ^a	¹⁵ N ¹⁸ O	Calculated ^b
v(N-O) ^c	1896	1816	15.62
v(Fe-NO)			4.82
δ _{1b} (Fe-N-O)	588	572	0.46/0.47

^a n.a.i. = natural abundance isotopes

^b Calculated with BP86/TZVP; see Experimental Section

^c Free NO: v(N-O) = 1876 cm⁻¹; f_{N-O} = 15.49 mdyn/Å

NO⁺: v(N-O) = 2387 cm⁻¹ in (NO⁺)(BF₄⁻); f_{N-O} = 25.07 mdyn/Å ³⁷

4.4.3.1.2. Electronic Structure of [Fe(P)(MI)(NO)]⁺ (**1**)

The electronic structure of the six-coordinate complex [Fe^{III}(TPP)(MI)(NO)]⁺ (**1**) is analyzed in this study using the model [Fe(P)(MI)(NO)]⁺ (P = porphine ligand). Geometry optimization has been performed on this system using BP86/TZVP and B3LYP/LanL2DZ. As shown in Table 4.2.2, both methods give very good agreement with the crystal structure of the six-coordinate complex [Fe^{III}(OEP)(MI)(NO)](ClO₄).^{23a} In particular, the very short Fe-NO bond < 1.65 Å and the linear Fe-N-O unit are reproduced by the DFT treatment. For the further

analysis of the electronic structure of **1**, the BP86/TZVP optimized model $[\text{Fe}(\text{P})(\text{MI})(\text{NO})]^+$ ($\tilde{\mathbf{1}}$) is used for consistency with earlier work on ferrous heme NO adducts.²⁶ The obtained structure of $\tilde{\mathbf{1}}$ is shown in Figure 4.4.3. For the following evaluation of the MO diagram of $\tilde{\mathbf{1}}$, the applied coordinate system given in Scheme 4.4.1 is used.

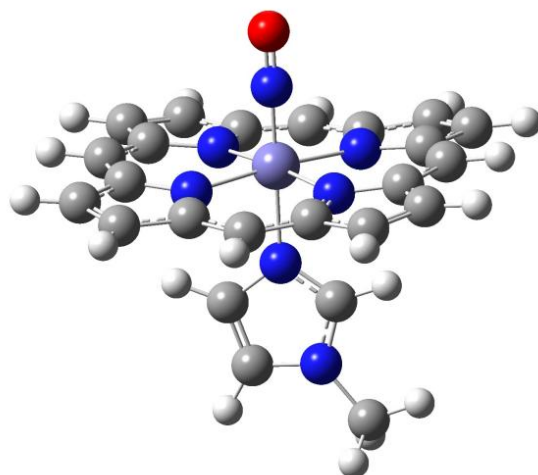


Figure 4.4.3. Fully optimized structure of $[\text{Fe}(\text{P})(\text{MI})(\text{NO})]^+$ ($\tilde{\mathbf{1}}$; P = porphine; MI = 1-methylimidazole) obtained with BP86/TZVP. Important structural parameters are given in Table 4.4.2.

Figure 4.4.4 shows the obtained MO diagram of complex $\tilde{\mathbf{1}}$. Contour plots of important molecular orbitals are presented in Figure 4.4.5. As evidenced by the N-O stretching frequency of $> 1900 \text{ cm}^{-1}$ (vide supra), the linear Fe-N-O unit, and in agreement with the literature^{8a,20} and recent DFT results,²⁵ the electronic structure of complex **1** can in general be classified as $\text{Fe}(\text{II})\text{-NO}^+$. Since iron is in the +II oxidation state and low-spin (as evident from magnetic Mössbauer measurements), it has a $[\text{d}_{xz}, \text{d}_{yz}, \text{d}_{x^2-y^2}]^6 \approx [\text{t}_2]^6$ electron configuration. Both π^* orbitals of the NO^+ ligand (isoelectronic to N_2) are empty and hence, undergo π backbonding interactions with the d_{xz} and d_{yz} orbitals of the metal in the applied coordinate system. The corresponding bonding combinations, $\text{d}_{xz}\text{-}\pi_x^*$ and $\text{d}_{yz}\text{-}\pi_y^*$, are delocalized over several molecular orbitals. Major contributions are found in MO $\langle 111 \rangle$, which has 55% d_{xz} and 19% π_x^* character, and $\langle 110 \rangle$ that corresponds to a mixture of 36% d_{yz} and 18% π_y^* (cf. Table 4). Hence, the strength of this backbond is better estimated from the corresponding antibonding combinations, $\pi_x^*\text{-}\text{d}_{xz} \langle 123 \rangle$ and $\pi_y^*\text{-}\text{d}_{yz} \langle 124 \rangle$, which are the LUMOs of complex $\tilde{\mathbf{1}}$. Both have about 68% π^* and 27% d orbital character, which corresponds to a very strong π backbonding interaction. Contour plots of these orbitals are shown in Figure 5.

The third t_2 type d orbital of iron, $d_{x^2-y^2}$ <118>, is practically non-bonding (cf. Table 4.4.4). Hence, the calculated orbital coefficients are also in agreement with the Fe(II)-NO⁺ description. However, the obtained N-O force constant of 15.2 mdyn/Å is markedly lower than that of free NO⁺ (25.1 mdyn/Å) and is actually very close to that of free NO³⁷. This is in agreement with the two very strong Fe-NO π backbonds, which lead to a transfer of a significant amount of electron density from the d_{xz} and d_{yz} orbitals of Fe to the π^* orbitals of NO. The total donation corresponds to about one electron. In addition, there is a weak σ interaction between σ_{nb} of NO⁺ and d_{z^2} of Fe. The corresponding bonding combination, $\sigma_{nb_d_{z^2}}$ <66>, has 51% σ_{nb} and 4% d contribution, which corresponds to a very weak interaction. Note that the HOMO of complex **1** is an almost pure porphyrin A_{2u} <81> orbital (see ref. 26b) with a small admixture of a Fe-NO σ antibonding orbital (cf contour plot in Figure 5). This has been previously described from B3LYP calculations²⁵. The charge contributions obtained here are 1% d_{z^2} and 0.3% σ^* , which is negligible for the total Fe-NO bond strength (cf. Table 4.4.4).

Having elaborated a detailed electronic structure description of complex **1**, it is now interesting to make a comparison with the corresponding, one-electron reduced complex [Fe(P)(MI)(NO)] (**2**)^{26b}. This compound has been described as Fe(II)-NO(radical),^{26a} which shows that the reduction in going from **1** to **2** is mostly ligand (NO) based. A closer comparison of the electronic structures of these complexes reveals further differences. In the case of **2**, the Fe-N-O unit is bent, which leads to a strong Fe-NO σ bond between d_{z^2} of iron and the singly occupied in-plane π^* orbital of NO. This explains the large stability of the Fe-NO bond in this case and the observed trans-effect of the NO ligand on axially coordinated N-donor ligands, which induces long Fe(II)-N_L bond lengths compared to the corresponding bis(imidazole) ligated Fe(II)-porphyrins³⁸. In contrast, the Fe-NO σ bond in **1** is very weak, because it is mediated by the σ_{nb} orbital of NO, which is located at very low energy and exhibits poor donor abilities. The negligible σ bond in **1** leads to the observed very short Fe-NO bond and the lack of a trans-effect of NO on the bound MI ligand. In fact, all Fe(II)-NO⁺ complexes with trans N-donor ligands exhibit Fe-N_L bond lengths comparable to the corresponding [Fe^{III}(porphyrin)(imidazole)₂]⁺ complexes^{23a}. On the other hand, the Fe-NO π backbond is distinctively stronger for **1** compared to **2**. However, this does actually not relate to the observed π^*_d mixing, but to the fact that the number of backbonds is reduced from two in **1** to 1.5 in **2**. This is evident from the orbital decompositions of the corresponding

antibonding orbitals: for **1**, d contributions of 27% are observed, which is comparable to the (average) 25% d character of the $\pi_v^*_{d_{yz}}$ (α/β <126> in ref. 26b) orbital in **2**. This indicates that the linear Fe-N-O unit and the shorter Fe-NO bond by itself do *not* facilitate the π backbond in **1** compared to **2**.

Table 4.4.4: Charge contributions of important molecular orbitals of $[\text{Fe}(\text{P})(\text{MI})(\text{NO})]^+$ (**1**) calculated with BP86/TZVP.

Nr.	label	Energy [Hartree]	Fe	N		O		N_{MI}	ΣMI
			d	s	p	s	p	s+p	
<125>	$d_{z^2} \sigma_{\text{nb}} + \text{Im}(\sigma)$	-0.23526	56	4	3	1	2	9	11
<124>	$\pi_v^*_{d_{yz}}$	-0.25401	27	0	42	0	26	0	1
<123>	$\pi_x^*_{d_{xz}}$ (LUMO)	-0.25465	27	0	42	0	26	0	0
<122>	A_{2u} <81> + $d_{z^2} \sigma^*$ (HOMO)	-0.29701	1	0.2	0.1	0	0	2	2
<121>	A_{1u} <79>	-0.30203	0	0	0	0	0	0	0
<120>	E_g <75/76> + $d_{yz} \pi_v^*$	-0.32744	10	0	2	0	2	0.5	1
<119>	E_g <75/76> + $d_{xz} \pi_x^*$	-0.32773	10	0	3	0	2	0	0
<118>	$d_{x^2-y^2}$	-0.33166	86	0	0	0	0	0	0
<117>	B_{2u} <74> + $\text{Im}(\pi)$	-0.33288	0	0.3	0.2	0	0	1	41
<116>	A_{2u} <72> + $d_{x^2-y^2}$	-0.34318	6	0.3	0.2	0	0	2	2
<114>	$\text{Im}(\pi) + d_{yz} \pi_v^*$	-0.36820	14	0	2	0	4	18	52
<112>	E_g <70/71>	-0.37193	2	0	0	0	0	5	13
<111>	$d_{xz} \pi_x^*$	-0.39427	55	0	6	0	13	1	1
<110>	$d_{yz} \pi_v^* + \text{Im}(\pi)$	-0.40249	36	0	5	0	13	5	14
<109>	E_u <77/78> + π_x^*	-0.40746	1	0	1	0	4	0	0
<108>	B_{1u}	-0.41055	0	0	0	0	0	0	0
<107>	E_u <77/78> + $\text{Im}(\pi) d_{yz}$	-0.41102	4	0	0	0	0	5	21
<106>	B_{1g} <80> d_{xy}	-0.43033	19	0	0	0	0	0	0
<102>	$\text{Im}(\sigma) d_{z^2} + \sigma_{\text{nb}}$	-0.44589	13	1	1	0	1	36	67
<73>	π_x^b	-0.61229	2	0	41	0	47	0	0
<72>	π_y^b	-0.61271	3	0	43	0	48	0	0
<66>	$\sigma_{\text{nb}} d_{z^2} + \text{Im}(\sigma)$	-0.63694	4	2	14	9	26	2	7

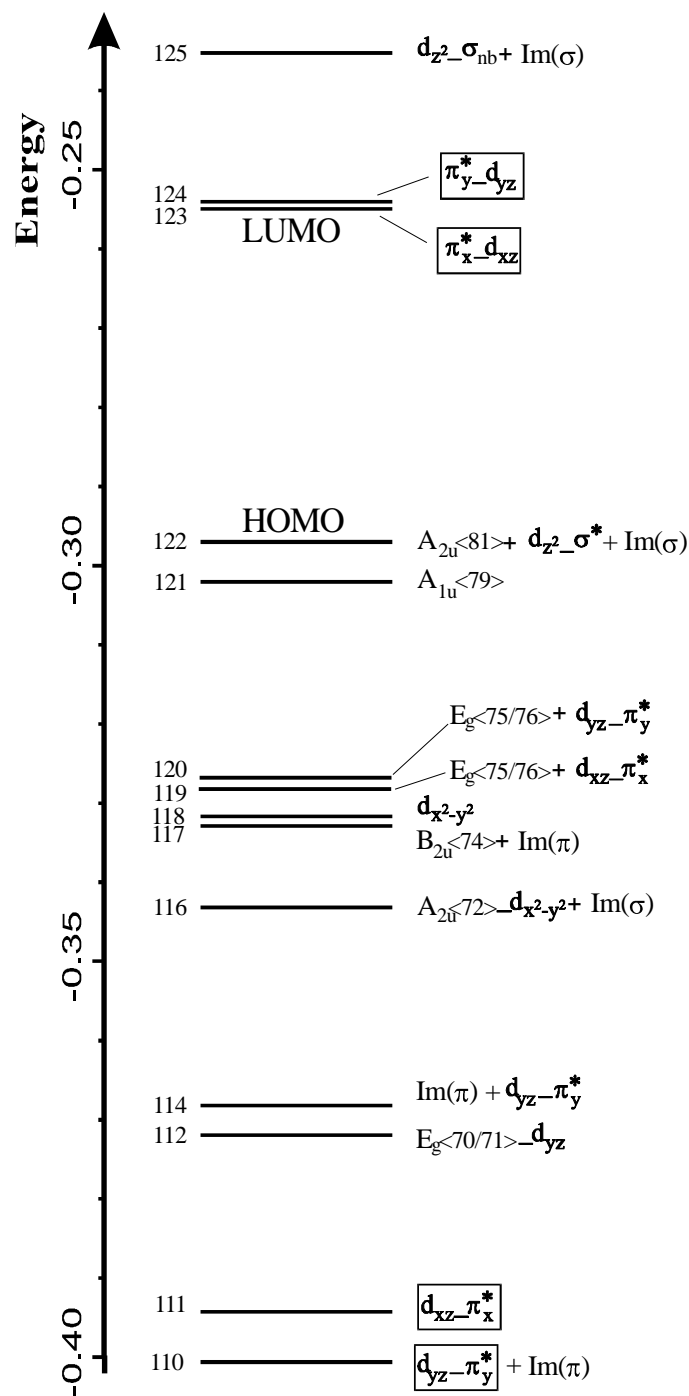


Figure 4.4.4. MO diagram of $[\text{Fe}(\text{P})(\text{MI})(\text{NO})]^+$ ($\tilde{\mathbf{I}}$) calculated with BP86/TZVP. The applied coordinate system is shown in Scheme 1. A_{1u} , A_{2u} and E_g , etc. correspond to porphine orbitals.^{26b} The nomenclature ‘ a_b ’ indicates that orbital a interacts with b and that a has a larger contribution to the resulting MO.

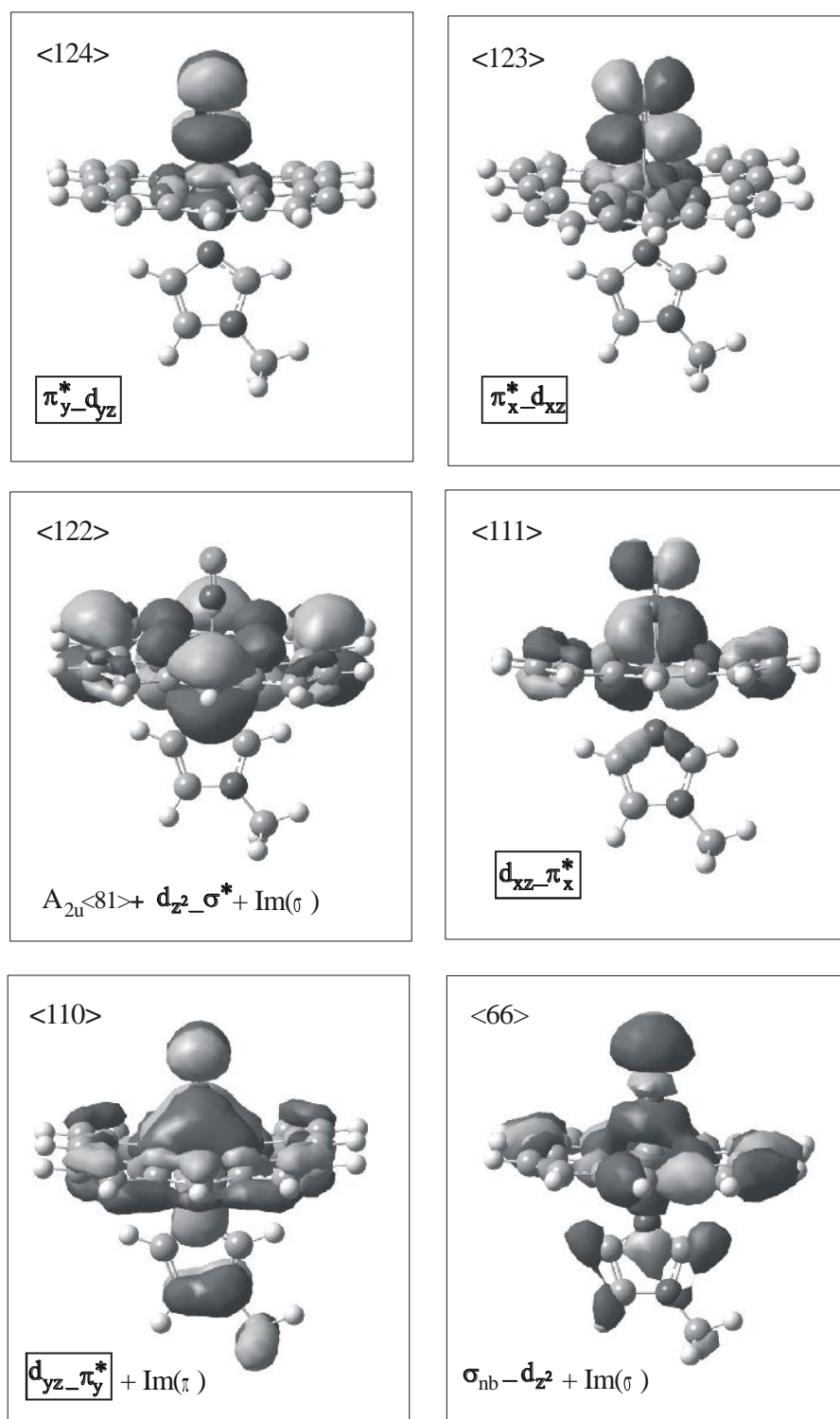


Figure 4.4.5. Contour plots of important molecular orbitals of $[\text{Fe}(\text{P})(\text{MI})(\text{NO})]^+$ ($\tilde{\mathbf{1}}$) calculated with BP86/TZVP. For labels see Figure 4.4.4 and Table 4.4.4.

4.4.3.2. Nitric Oxide Binding to Ferrous and Ferric Porphyrin Complexes: Energetic Considerations

The stability of the ferrous and the ferric NO complexes is determined from the following complex formation reactions using DFT calculations:



The calculated complex formation energies considering both low-spin (ls) and high-spin (hs) reactants $[\text{Fe(P)(MI)}]^{n+}$ are listed in Table 4.4.5. From experiment, it is known that both ferrous and ferric five-coordinate hemes with axial imidazoles are high-spin^{39,40,41}. As will be shown in the following analysis, the prediction of the correct ground state for the reactant turned out to be a major challenge for DFT; especially for the ferric complex. Importantly, the calculated reaction energies show a large degree of method dependency as shown in Table 4.4.5. Using BP86/TZVP, unrealistically large energies > -30 kcal/mol are obtained. In addition, for both the ferrous and the ferric case, the five-coordinate reactants are predicted to be low-spin. Hence, as has been discussed in the literature before, total energy calculations with gradient-corrected functionals are problematic (see, for example, ref.⁴²). Therefore, we have then focused on the B3LYP functional. Using B3LYP/LanL2DZ* calculations on the fully optimized structures from BP86/TZVP leads to much more realistic reaction energies. For the ferrous case, eqn.1 is exothermic with -16.7 kcal/mol. In this case as well as in all other B3LYP calculations, the correct high-spin ground state for the ferrous reactant is predicted. In the ferric case, this approach leads to degenerate hs- and ls-states for $[\text{Fe(P)(MI)}]^+$ and a reaction energy of about -12.5 kcal/mol. In order to further improve on these numbers, we then applied full geometry optimizations using B3LYP/LanL2DZ*. This way, reaction energies of -16 kcal/mol (ferrous) and about -13 kcal/mol (ferric) are obtained; in the latter (ferric) case, the wrong ground state for the reactant is still predicted. Finally, we used B3LYP/TZVP single points on the B3LYP/LanL2DZ* structures. In this case, a complex formation energy of -11.4 kcal/mol is obtained in the ferrous case. Importantly, this method finally predicts the correct hs ground state for ferric $[\text{Fe(P)(MI)}]^+$ with a calculated energy difference $\Delta E(\text{hs/ls})$ of 5.6 kcal/mol. Because of this stabilization of the hs state of the reactant, the reaction energy for eqn.1 dramatically drops to only -4 kcal/mol. In summary, these calculations show that the formation of nitrosyl complexes is energetically more favorable for ferrous compared to ferric systems by ~ 7.5 kcal/mol. This number is equivalent to a difference in binding constant by a factor of 3×10^5 . This is in excellent agreement with the experimentally determined trend in dissociation rate constants: for ferric heme systems, dissociation rate constants range from 0.65 to 40 s^{-1} , leading to a relatively small binding

constant for NO ($K_{\text{eq}} = 10^3$ to 10^5 M^{-1}). In contrast, for Fe(II) systems, the dissociation rate constants are in the order of 10^{-4} s^{-1} , leading to very large binding constants for NO ($K_{\text{eq}} = 10^{11}$ to 10^{12} M^{-1})⁴³.

Table 4.4.5. Reaction energies for $[\text{Fe}(\text{P})(\text{MI})]^{n+} + \text{NO} \rightarrow [\text{Fe}(\text{P})(\text{MI})(\text{NO})]^{n+}$ ($T = 298.15\text{K}$)

Complex/Method	$\Delta\varepsilon$ (BP86)[kcal/mol]		$\Delta\varepsilon$ (B3LYP)[kcal/mol]	
	Educt: hs	Educt: ls	Educt: hs	Educt: ls
$[\text{Fe}^{\text{II}}(\text{P})(\text{MI})] + \text{NO}$ BP86/TZVP full OPT	-44.1	-37.9	-16.7	-22.3
$[\text{Fe}^{\text{III}}(\text{P})(\text{MI})]^+ + \text{NO}$ BP86/TZVP full OPT	-53.4	-41.2	-12.6	-12.3
$[\text{Fe}^{\text{II}}(\text{P})(\text{MI})] + \text{NO}$ B3LYP/LANL2DZ full OPT	Structure of NO adduct incorrectly described			
$[\text{Fe}^{\text{III}}(\text{P})(\text{MI})]^+ + \text{NO}$ B3LYP/LANL2DZ full OPT			-8.9	-9.2
$[\text{Fe}^{\text{II}}(\text{P})(\text{MI})] + \text{NO}$ B3LYP/LANL2DZ* full OPT			-16.1	-21.7
$[\text{Fe}^{\text{III}}(\text{P})(\text{MI})]^+ + \text{NO}$ B3LYP/LANL2DZ* full OPT			-13.3	-12.8
$[\text{Fe}^{\text{II}}(\text{P})(\text{MI})] + \text{NO}$ B3LYP/LANL2DZ*//B3LYP/TZVP			-11.4	-18.8
$[\text{Fe}^{\text{III}}(\text{P})(\text{MI})]^+ + \text{NO}$ B3LYP/LANL2DZ*// B3LYP/TZVP			-3.9	-9.5

4.4.4. Discussion

In this paper, the new six-coordinate Fe(III)-porphyrin NO complex $[\text{Fe}^{\text{III}}(\text{TPP})(\text{MI})(\text{NO})](\text{BF}_4)$ (**1**) has been prepared from $[\text{Fe}^{\text{III}}(\text{TPP})(\text{thf})_2](\text{BF}_4)$ by careful reaction with purified NO. The structure of the precursor has been determined. Using complex **1**, the spectroscopic properties and electronic structures of ferric heme nitrosyl model complexes are then explored. This is achieved using IR spectroscopy coupled to DFT

calculations. For complex **1**, $\nu(\text{N-O})$ and $\delta(\text{Fe-N-O})$ frequencies of 1896 and 588 cm^{-1} are assigned using isotope labeling. The electronic structure of this complex is in agreement with the widely accepted Fe(II)-NO^+ description for ferric nitrosyls as reflected by the N-O stretching frequency $>1890 \text{ cm}^{-1}$ and the linear Fe-N-O unit^{8a,20}. The Fe-NO interaction is dominated by π backbonding between two d_π orbitals of the metal and two empty π^* orbitals of NO^+ . This is manifested in the corresponding antibonding orbitals, which have 68% π^* and 27% d_π character, which corresponds to a strong interaction. This leads to a net transfer of half an electron from the metal to the ligand and explains the lowering of the N-O stretching frequency from 2390 cm^{-1} in free NO^+ to 1896 cm^{-1} in complex **1**. In contrast, the Fe-NO σ interaction is negligible, due to the generally poor donor abilities of the σ_{nb} orbital in diatomics with multiple bonds. Corresponding to this strong π and weak σ bonding description, the Fe-N-O unit is linear and short to maximize the π interaction. Recently, it was proposed that the ferric heme NO adducts in nitrophorins might have an electronic structure that corresponds to $\text{Fe(III)-NO}(\text{radical})$ in order to prevent autoxidation.^{4c} However, the N-O stretching frequency of ferric rNp1-NO of 1917 cm^{-1} is very close to the values obtained for model complexes like **1** or $[\text{Fe}^{\text{III}}(\text{OEP})(\text{MI})(\text{NO})]^+$, or corresponding enzymatic species (cf. Table 4.4.1). Hence, the good agreement between the calculated and experimentally observed $\nu(\text{N-O})$ mode for model **1** with the Fe(II)-NO^+ ground state indicates that the nitrophorins do not differ in this respect from the other ferric nitrosyl species. The electronic structure of **1** also shows a very small admixture of an Fe-NO antibonding $d_{z^2}\text{-}\sigma^*$ orbital into the $A_{2u} \langle 81 \rangle$ HOMO of the complex. This is in agreement with DFT calculations for corresponding five-coordinate ferric heme NO complexes^{25a}. Interestingly, it has been proposed recently that the nature of this N-O antibonding orbital admixed into $A_{2u} \langle 81 \rangle$ changes to a π^* type orbital in the six-coordinate case^{25b}. We do not find any evidence for this in six-coordinate **1**.

The calculated formation energy for the ferric heme NO adduct **1** is about -4 kcal/mol. This value is relatively low, but in agreement with the experimentally determined complex formation constants in the 10^3 to 10^5 M^{-1} range and the observed tendency of these complexes to lose NO. However, this is in contrast to the Fe-NO force constant of 4.9 $\text{mdyn}/\text{\AA}$, which indicates a strong Fe-NO bond. This contradiction is explained based on the calculated complex formation energies. Since the ferric nitrosyl complex is low-spin, the force constant is a measure for the steepness of the *low-spin* potential energy surface, where the formation energy of the NO complex is -9.5 kcal/mol corresponding to a strong bond. However, the actual binding of the NO ligand to the iron center is accompanied by a spin transition, since

the initial five-coordinate reactant complex is actually high-spin. From the calculations, the stabilization of the high-spin over the low-spin state of the NO-free complex is 5.6 kcal/mol, which reduces the ‘low-spin’ formation energy of -9.5 kcal/mol by more than half. Hence, this shows how careful one has to be when correlating force constants with actual (thermodynamic) bond strengths in transition metal complexes, where spin state changes are a common phenomenon.

The quantitative description of the Fe-NO bond in the ferric heme system **1** provided above allows for a detailed comparison with the corresponding ferrous complex [Fe(TPP)(MI)(NO)] (**2**) studied before ^{26a,b}. Interestingly, the one-electron reduction of the Fe(II)-NO⁺ complex **1** is mostly ligand centered resulting in an Fe(II)-NO(radical) electronic structure description of **2**. This is evident from the N-O stretching frequency, which is reduced from 1896 cm⁻¹ in **1** to 1630 cm⁻¹ in **2**. The Fe-NO bond in the ferrous complex corresponds to a σ bond mediated by the singly occupied π^* orbital of NO and d_{z^2} of iron, and a π backbond between the unoccupied π^* orbitals of NO and the d_{π} orbitals of the metal ^{26b}. In comparison, the σ bond is clearly much stronger in **2** compared to **1**. On the other hand, the π backbond is stronger in **1**, but only due to the fact that two π bonds are formed in **1** compared to 1.5 in **2**. The actual $d_{\pi}\text{-}\pi^*$ orbital mixing is similar in these cases, which is surprising considering the distinctively shorter Fe-NO bond observed for **1**. Due to the quite strong σ bond present in **2**, the overall Fe-NO bond strength is larger in the ferrous complex. This is reflected by the four to five orders of magnitude larger (experimental) complex formation constants of ferrous compared to ferric nitrosyls. This in turn relates to larger NO dissociation rates in the ferric case. For example, for the water soluble iron porphyrins [Fe^{II}(TPPS)(NO)] and [Fe^{III}(TPPS)(NO)], dissociation rate constants of $6.4 \times 10^{-4} \text{ s}^{-1}$ and $0.5 \times 10^3 \text{ s}^{-1}$ respectively, have been determined ⁹. In addition, the calculated complex formation energy of -11.4 kcal/mol for **2** is -7.5 kcal/mol larger than obtained for **1**. However, the thermodynamically stronger Fe-NO bond in complex **2** is not in agreement with the observed trend in force constants, where **1** has a much larger Fe-NO force constant (4.82 mdyn/Å, obtained from DFT) compared to **2** (2.55 mdyn/Å, obtained from QCC-NCA, see Section 4.3). Even if it is taken into account that the coordination of NO is accompanied by a spin state change of the metal (vide supra), this still does not offer any explanation for the observed trend. We believe that the difference in force constants relates to the different nature of the Fe-NO bond in these compounds: since complex **1** exhibits a pure π bond, the potential energy is automatically steeper than in a case where a σ bond of significant strength is present. This, in turn, is due to the fact that π overlap

decreases much faster with distance than σ overlap. Hence, the force constants are not a good measure to determine relative bond strengths in this case due to the fact that the nature of the Fe-NO bond is very different in **1** and **2**.

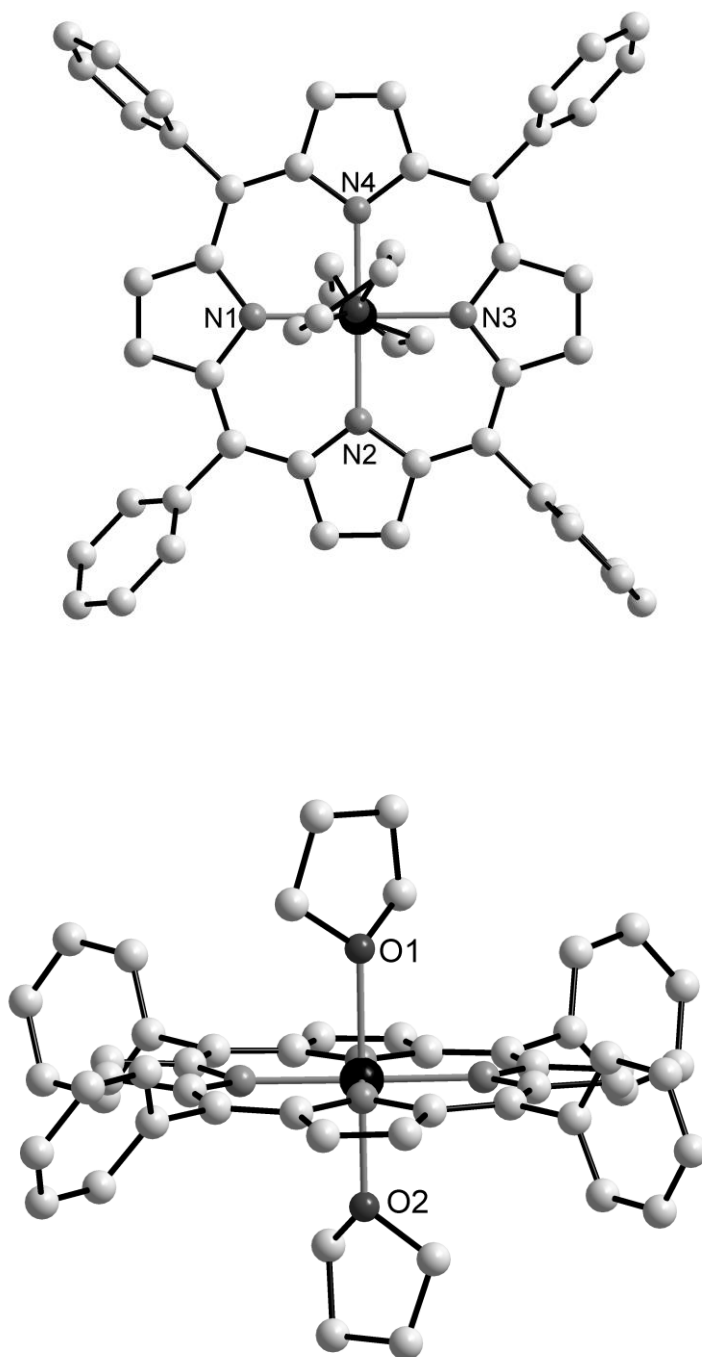


Figure 4.4.6. Top view (top) and side view (bottom) of the crystal structure of [Fe^{III}(TPP)(thf)₂](BF₄) with labelling. The hydrogen atoms, the disordered solvent molecules, and the counter anion are not shown for clarity.

Table 4.4.6. Crystallographic data for [Fe^{III}(TPP)(thf)₂](BF₄).

Chemical formula	C ₅₆ H ₅₂ BF ₄ FeN ₄ O ₃
Formula weight	971.68
Space group	P-1
a	10.6964(9) Å
b	13.4320(10) Å
c	18.7082(15) Å
α	78.173(9)°
β	86.379(10)°
γ	82.788(9)°
V	2608.1(4) Å ³
T	170 K
Z	2
D _{calcd}	1.237 Mg/m ³
μ	0.349 mm ⁻¹
λ	0.71073 Å
Measured reflections	21052
Independent reflections	11889
R _{int}	0.0367
Observed reflections	8221
R ₁ [I > 2σ(I)]	0.0475
wR ₂ (all data)	0.1310

$$R1 = \frac{\sum ||F_o| - |F_c||}{\sum |F_o|}; wR2 = \frac{[\sum [w(F_o^2 - F_c^2)^2]}{\sum [w(F_o^2)^2]}]^{1/2}$$

Table 4.4.7. Selected bond lengths and angles for [Fe^{III}(TPP)(thf)₂](BF₄).

Fe(1)-N(1)	2.026(2)	Fe(1)-N(2)	2.031(2)
Fe(1)-N(3)	2.028(2)	Fe(1)-N(4)	2.031(2)
Fe(1)-O(1)	2.190(2)	Fe(1)-O(2)	2.137(2)
N(1)-Fe(1)-N(3)	179.44(7)	N(2)-Fe(1)-O(2)	89.70(6)
N(1)-Fe(1)-N(2)	89.78(6)	N(4)-Fe(1)-O(2)	90.81(6)
N(3)-Fe(1)-N(2)	90.09(6)	N(1)-Fe(1)-O(1)	89.78(6)
N(1)-Fe(1)-N(4)	90.04(6)	N(3)-Fe(1)-O(1)	89.68(6)
N(3)-Fe(1)-N(4)	90.08(6)	N(2)-Fe(1)-O(1)	91.70(6)
N(2)-Fe(1)-N(4)	179.45(7)	N(4)-Fe(1)-O(1)	87.78(6)
N(1)-Fe(1)-O(2)	90.55(6)	O(2)-Fe(1)-O(1)	178.56(5)
N(3)-Fe(1)-O(2)	89.99(6)		

References

- ¹ Culotta, E.; Koshland, D. E. *Science* **1992**, *258*, 1862-1865.
- ² (a) Moncada, S.; Palmer, R. M.; Higgs, E. A. *Pharmacol. Rev.* **1991**, *43*, 109-142. (b) Snyder, S. H. *Science* **1992**, *257*, 494-496. (c) Butler, A. R.; Williams, D. L. H. *Chem. Soc. Revs.* **1993**, 233-241. (d) Bredt, D. S.; Snyder, S. H. *Annu. Rev. Biochem.* **1994**, *63*, 175-195. (e) Lancaster, J. R., Jr.; in: *Encyclopedia of Inorganic Chemistry*, Bruce, R. B., Ed., Wiley: Chichester, 1994. (f) *Methods in Nitric Oxide Research*; Feelisch, M.; Stamler, J. S., Eds.; Wiley: Chichester, 1996. (g) Cooper, C. E. *Biochim. Biophys. Acta* **1999**, *1411*, 290-309.
- ³ (a) Stamler, J. S.; Singel, D. J.; Loscalzo, J. *Science* **1992**, *258*, 1898-1902. (b) Hughes, M. N. *Biochim. Biophys. Acta* **1999**, *1411*, 263-272. (c) *Nitric Oxide: Biology and Pathobiology*; Ignarro, L., Ed.; Academic Press: San Diego, 2000. (d) Ballou, D. P.; Zhao, Y.; Brandish, P. E.; Marletta, M. A. *Proc. Natl. Acad. Sci. USA* **2002**, *99*, 12097-12101. (e) Feelisch, M.; Rassaf, T.; Mnaimneh, S.; Singh, N.; Bryan, N. S.; Jourdain, D.; Kelm, M. *FASEB J.* **2002**, *16*, 1775-1785. (f) McCleverty, J. A. *Chem. Rev.* **2004**, *104*, 403-418. (g) Farmer, P. J.; Sulc, F. *J. Inorg. Biochem.* **2005**, *99*, 166-184. (h) Boon, E. M.; Marletta, M. A. *J. Inorg. Biochem.* **2005**, *99*, 892-902. (i) Luchsinger, B. P.; Rich, E. N.; Yan, Y.; Williams, E. M.; Stamler, J. S.; Singel, D. J. *J. Inorg. Biochem.* **2005**, *99*, 912-921.
- ⁴ (a) Stuehr, D. J. *Annu. Rev. Pharmacol. Toxicol.* **1997**, *37*, 339-359. (b) Poulos, T. L.; Li, H.; Raman, C. S. *Curr. Opin. Chem. Biol.* **1999**, *3*, 131-137. (c) Li, H.; Poulos, T. L. *J. Inorg. Biochem.* **2005**, *99*, 293-305. (d) Rousseau, D. L.; Li, D.; Couture, M.; Yeh, S.-R. *J. Inorg. Biochem.* **2005**, *99*, 306-323.
- ⁵ (a) Garbers, D. L.; Lowe, D. G. *J. Biol. Chem.* **1994**, *269*, 30741-30744. (b) Zhao, Y.; Hoganson, C.; Babcock, G. T.; Marletta, M. A. *Biochemistry* **1998**, *37*, 12458-12464. (c) Karow, D. S.; Pan, D.; Tran, R.; Pellicena, P.; Presley, A.; Mathies, R. A.; Marletta, M. A. *Biochemistry* **2004**, *43*, 10203-10211. (d) Gilles-Gonzalez, M.-A.; Gonzales, G. *J. Inorg. Biochem.* **2005**, *99*, 1-22.
- ⁶ (a) Ribeiro, J. M. C.; Hazzard, J. M. H.; Nussenzweig, R. H.; Champagne, D. E.; Walker, F. A. *Science* **1993**, *260*, 539-541; (b) Ding, X. D.; Weichsel, A.; Andersen, J. F.; Shokhireva, T. K.; Balfour, C.; Pierik, A. J.; Averill, B. A.; Montfort, W. R.; Walker, F. A. *J. Am. Chem. Soc.* **1999**, *121*, 128-138; (c) Walker, F. A. *J. Inorg. Biochem.* **2005**, *99*, 216-236.
- ⁷ (a) Ferguson, S. J. *Curr. Opin. Chem. Biol.* **1998**, *2*, 182-193; (b) Richardson, D. J.; Watmough, N. J. *Curr. Opin. Chem. Biol.* **1999**, *3*, 207-219; (c) Moura, I.; Moura, J. J. G. *Curr. Opin. Chem. Biol.* **2001**, *5*, 168-175
- ⁸ (a) Averill, B. A. *Chem. Rev.* **1996**, *96*, 2951-2964. (b) Wasser, I. M.; de Vries, S.; Moënné-Loccoz, P.; Schröder, I.; Karlin, K. D. *Chem. Rev.* **2002**, *102*, 1201-1234.
- ⁹ Ford, P. C.; Laverman, L. E. *Coord. Chem. Rev.* **2005**, *249*, 391-403.
- ¹⁰ (a) Park, S.-Y.; Shimizu, H.; Adachi, S.-I.; Nakagawa, A.; Tanaka, I.; Nakahara, K.; Shoun, H.; Obayashi, E.; Nakamura, H.; Iizuka, T.; Shiro, Y. *Nature Struct. Biol.* **1997**, *4*, 827-832. (b) Shimizu, H.; Park, S.-Y.; Gomi, Y.; Arakawa, H.; Nakamura, H.; Adachi, S.-I.; Obayashi, E.; Iizuka, T.; Shoun, H.; Shiro, Y. *J. Biol. Chem.* **2000**, *275*, 4816. (c) Obayashi, E.; Tsukamoto, K.; Adachi, S.-I.; Takahashi, S.; Nomura, M.; Iizuka, T.; Shoun, H.; Shiro, Y. *J. Am. Chem. Soc.* **1997**, *119*, 7807-7816. (d) Daiber, A.; Shoun, H.; Ullrich, V. *J. Inorg. Biochem.* **2005**, *99*, 185-193.
- ¹¹ (a) Shiro, Y.; Fujii, M.; Iizuka, T.; Adachi, S.-I.; Tsukamoto, K.; Nakahara, K.; Shoun, H. *J. Biol. Chem.* **1995**, *270*, 1617-1623. (b) Lehnert, N.; Paulat, F.; Praneeth, V. K. K., submitted for publication.
- ¹² (a) Hu, S.; Kincaid, J. R. *J. Am. Chem. Soc.* **1991**, *113*, 2843-2850. (b) Hu, S.; Kincaid, J. R. *J. Biol. Chem.* **1993**, *268*, 6189-6193.
- ¹³ Suzuki, N.; Higuchi, T.; Urano, Y.; Kikuchi, K.; Uchida, T.; Mukai, M.; Kitagawa, T.; Nagano, T. *J. Am. Chem. Soc.* **2000**, *122*, 12059-12060.
- ¹⁴ (a) Tomita, T.; Haruta, N.; Aki, M.; Kitagawa, T.; Ikeda-Saito, M. *J. Am. Chem. Soc.* **2001**, *123*, 2666-2667. (b) Benko, B.; Yu, N. T. *Proc. Natl. Acad. Sci. USA* **1983**, *80*, 7042-7046.
- ¹⁵ Pinakoulaki, E.; Gemeinhardt, S.; Saraste, M.; Varotsis, C. *J. Biol. Chem.* **2002**, *277*, 23407-23413.
- ¹⁶ Maes, E. M.; Walker, F. A.; Montfort, W. R.; Czernuszewicz, R. S. *J. Am. Chem. Soc.* **2001**, *123*, 11664-11672.
- ¹⁷ Wang, J.; Lu, S.; Moënné-Loccoz, P.; Ortiz de Montellano, P. R. *J. Biol. Chem.* **2003**, *278*, 2341-2347.
- ¹⁸ (a) Sampath, V.; Zhao, X.; Caughey, W. S. *Biochem. Biophys. Res. Commun.* **1994**, *198*, 281-287. (b) Wang, Y.; Averill, B. A. *J. Am. Chem. Soc.* **1996**, *118*, 3972-3973.
- ¹⁹ Miller, L. M.; Pedraza, A. J.; Chance, M. R. *Biochemistry* **1997**, *36*, 12199-12207.
- ²⁰ Enemark, J. H.; Feltham, R. D. *Coord. Chem. Rev.* **1974**, *13*, 339-406.
- ²¹ (a) Bottomley, F. *Coord. Chem. Rev.* **1978**, *26*, 7-32 and ref. herein. (b) Paulat, F.; Kuschel, T.; Näther, C.; Praneeth, V. K. K.; Sander, O.; Lehnert, N. *Inorg. Chem.* **2004**, *43*, 6979-6994.
- ²² Ellison, M. K.; Schulz, C. E.; Scheidt, W. R. *Inorg. Chem.* **2000**, *39*, 5102-5110.

- ²³ (a) Ellison, M. K.; Scheidt, W. R. *J. Am. Chem. Soc.* **1999**, *121*, 5210-5219. (b) Ellison, M. K.; Schulz, C. E.; Scheidt, W. R. *J. Am. Chem. Soc.* **2002**, *124*, 13833-13841. (c) Scheidt, W. R.; Lee, Y. J.; Hatano, K. *J. Am. Chem. Soc.* **1984**, *106*, 3191-3198. (d) Yi, G.-B.; Chen, L.; Khan, M. A.; Richter-Addo, G. B. *Inorg. Chem.* **1997**, *36*, 3876-3885.
- ²⁴ (a) Li, X.-Y.; Spiro, T. G. *J. Am. Chem. Soc.* **1988**, *110*, 6024. (b) Ray, G. B.; Li, X.-Y.; Ibers, J. A.; Sessler, J. L.; Spiro, T. G. *J. Am. Chem. Soc.* **1994**, *116*, 162 and ref. herein.
- ²⁵ (a) Linder, D. P.; Rodgers, K. R.; Banister, J.; Wyllie, G. R. A.; Ellison, M. K.; Scheidt, W. R. *J. Am. Chem. Soc.* **2004**, *126*, 14136-14148. (b) Linder, D. P.; Rodgers, K. R. *Inorg. Chem.* **2005**, *44*, 1367-1380.
- ²⁶ (a) Praneeth, V. K. K.; Neese, F.; Lehnert, N. *Inorg. Chem.* **2005**, *44*, 2570-2572. (b) Praneeth, V. K. K.; Näther, C.; Peters, G.; Lehnert, N. *submitted for publication*. (c) Praneeth, V. K. K.; Haupt, E.; Lehnert, N. *J. Inorg. Biochem.* **2005**, *99*, 940-948.
- ²⁷ (a) Ehrenberg, A.; Szczepkowski, T. W. *Acta Chem. Scand.* **1960**, *14*, 1684-1692. (b) Hoshino, M.; Maeda, M.; Konishi, R.; Seki, H.; Ford, P. C. *J. Am. Chem. Soc.* **1996**, *118*, 5702-5707. (c) Fernandez, B. O.; Lorkovic, I. M.; Ford, P. C. *Inorg. Chem.* **2004**, *43*, 5393-5402. (d) Møller, J. K. S.; Skibsted, L. H. *Chem. Eur. J.* **2004**, *10*, 2291-2300. (e) Lim, M. D.; Lorkovic, I. M.; Ford, P. C. *J. Inorg. Biochem.* **2005**, *99*, 151-165.
- ²⁸ Adler, A. D.; Longo, F. R.; Finarrelli, J. F.; Goldmacher, J.; Assour, J.; Korsakoff, L. *J. Org. Chem.* **1967**, *32*, 476.
- ²⁹ Adler, A. D.; Longo, F. R.; Kampas, F.; Kim, J. *J. Inorg. Nucl. Chem.* **1970**, *32*, 2443-2445
- ³⁰ Reed, C. A.; Mashiko, T.; Bently, P.; Kastner, M. E.; Scheidt, W. E.; Spartalian, K.; Lang, G. *J. Am. Chem. Soc.* **1979**, *101*, 2948-2958.
- ³¹ Sheldrick, W. S. SHELXS-97 and SHELXL-97. Programs for the solution and refinement of crystal structures. **1997**. University of Göttingen.
- ³² (a) Hay, P. J.; Wadt, W. R. *J. Chem. Phys.* **1985**, *82*, 270 and 299. (b) Wadt, W. R.; Hay, P. J. *J. Chem. Phys.* **1985**, *82*, 284.
- ³³ Schaefer, A.; Horn, H.; Ahlrichs, R. *J. Chem. Phys.* **1992**, *97*, 2571.
- ³⁴ Frisch, M. J.; Trucks, G. W.; Schlegel, H. B.; Scuseria, G. E.; Robb, M. A.; Cheeseman, J. R.; Zakrzewski, V. G.; Montgomery, J. A., Jr.; Stratmann, R. E.; Burant, J. C.; Dapprich, S.; Millam, J. M.; Daniels, A. D.; Kudin, K. N.; Strain, M. C.; Farkas, O.; Tomasi, J.; Barone, V.; Cossi, M.; Cammi, R.; Mennucci, B.; Pomelli, C.; Adamo, C.; Clifford, S.; Ochterski, J.; Petersson, G. A.; Ayala, P. Y.; Cui, Q.; Morokuma, K.; Salvador, P.; Dannenberg, J. J.; Malick, D. K.; Rabuck, A. D.; Raghavachari, K.; Foresman, J. B.; Cioslowski, J.; Ortiz, J. V.; Baboul, A. G.; Stefanov, B. B.; Liu, G.; Liashenko, A.; Piskorz, P.; Komaromi, I.; Gomperts, R.; Martin, R. L.; Fox, D. J.; Keith, T.; Al-Laham, M. A.; Peng, C. Y.; Nanayakkara, A.; Challacombe, M.; Gill, P. M. W.; Johnson, B.; Chen, W.; Wong, M. W.; Andres, J. L.; Gonzalez, C.; Head-Gordon, M.; Replogle, E. S.; Pople, J. A. *Gaussian 98 Rev. A.11*; Gaussian, Inc.: Pittsburgh, 2001.
- ³⁵ Lipscomb, L. A.; Lee B-A, Yu, N-T. *Inorg. Chem.* **1993**, *32*, 281-286.
- ³⁶ Novozhilova, I. V.; Coppens, P.; Lee, J.; Richter-Addo, G. B.; Bagley, K. A. *J. Am. Chem. Soc.* **2006**, *128*, 2093-2104.
- ³⁷ Fadini, A.; Schnepel, F.-M.; *Schwingungsspektroskopie*, Thieme Verlag, Stuttgart, 1985.
- ³⁸ Wyllie, G. R. A.; Schulz, C. A.; Scheidt, W. R. *Inorg. Chem.* **2003**, *42*, 5722-5734.
- ³⁹ Walker, F. A.; Simonis, U. 'Iron Porphyrin Chemistry', in: Encyclopedia of Inorganic Chemistry, Bruce, R. B., Ed., Wiley, in press.
- ⁴⁰ Scheidt, W. R.; Geiger, D. K.; Lee, Y. L.; Reed, C. A.; Lang, G. *J. Am. Chem. Soc.* **1985**, *107*, 5693.
- ⁴¹ Momenteau, B.; Loock, B.; Tetreau, D.; Lavalette, D.; Croisy, A.; Schaeffer, C.; Huel, C.; Lhoste, J. M.; *J. Chem. Soc., Perkin Trans. 2*, **1987**, 249.
- ⁴² (a) Ghosh, A.; Pesson, B. J.; Taylor, P. R. *J. Biol. Inorg. Chem.* **2003**, *8*, 507. (b) Ghosh, A.; Vangberg, T.; Gonzalez, E.; Taylor, P. *J. Porphyrins Phthalocyanines* **2001**, *5*, 345. (c) Swart, M.; Groenhof, A. R.; Ehlers, A. W.; Lammertsma, K. *J. Phys. Chem. A* **2004**, *108*, 5479. (d) Chang, C. H.; Boone, A. J.; Bartlett, R. J.; Richards, N. G. *J. Inorg. Chem.* **2004**, *43*, 458.
- ⁴³ (a) Antonini, E.; Brunori, M.; Wyman, J.; Noble, R. W. *J. Biol. Chem* **1966**, *241*, 3236-3238. (b) Traylor, T. G.; Sharma, V. S. *Biochemistry*. **1992**, *31*, 2847-2849. (c) Sharma, V. S.; Traylor, T. G.; Gardiner, R.; Mizukami, H. *Biochemistry*. **1987**, *26*, 3837-3843. (d) Hoshino, M.; Ozawa, K.; Seki, H.; Ford, P. C. *J. Am. Chem. Soc.* **1993**, *115*, 9568-9575.

Chapter 5

Thiolate Coordination to Iron Porphyrin Nitrosyls

5.1. Scope of this Project

In recent years, there has been a tremendous interest in understanding the chemistry of nitric oxide bound heme proteins owing to their important functions in various biological processes (cf. Chapter 1). Accordingly, much research has been carried out with iron porphyrin NO model complexes to gain in-depth knowledge about their various properties including their structural, optical, and electronic characteristics. In many biochemical processes, axial ligand coordination *trans* to NO is vital to fine-tune heme-NO reactivity. In this respect, several six-coordinate iron porphyrin NO complexes with N-donor ligands have been prepared and the effect of the *trans* ligand on the Fe-NO unit has been explored in detail (cf. Chapter 4). However, much less research has been directed toward the corresponding six-coordinate complexes with *trans* S-donor ligands. Nonetheless, these systems are of great biological importance. NO bound heme centers with axial cysteinate coordination are present in the active sites of fungal nitric oxide reductase (P450_{nor}), nitric oxide synthase (NOS), and *Cimex* nitrophorins (cf. Chapter 1). Only two iron porphyrin model complexes with axial thiolate coordination are available in the literature. The first complex is based on a picket fence iron porphyrin covalently linked to a benzylthiolate group, prepared by Suzuki et al.¹ UV-vis studies on this complex show reversible binding of NO to its ferric state. Reduction of this ferric NO complex using NaBH₄ leads to the characteristic EPR spectrum of a thiolate coordinated Fe(II)-porphyrin NO complex. However, these thiolated ligated ferrous and ferric NO adducts have not been isolated as solids. The second complex, was prepared by Xu et al.², is based on non-covalently attached thiolate bound to octaethylporphyrin iron(III). The crystal structure of this complex is shown in Figure 5.1.1. This complex is the only structurally characterized thiolate bound heme NO adduct available to this date.

In order to obtain more insight into the vibrational properties and electronic structures of these enzymatic species, we have synthesized a series of six-coordinate Fe(II)-NO adducts [Fe^{II}(TPP)(SR)(NO)]⁻ (TPP = tetraphenylporphyrin) with substituted thiophenolates (SR) and tetrahydrothiophene, and we have investigated solutions of these compounds using

electron paramagnetic resonance (EPR) spectroscopy. The interaction of the Fe(II)-NO center with different thiolate ligands has also been explored computationally. The six-coordinate model complex $[\text{Fe}(\text{P})(\text{SR})(\text{NO})]^-$ (P = porphine ligand) has an interesting electronic structure where NO acts as a medium strong σ donor and π acceptor ligand. The vibrational properties, bond distances and force constants have been determined for this model system from DFT calculations and vibrational analysis. This studies are summarized in Section 5.2.

In addition, the coordination behavior of thiolates to Fe(III)-NO centers has been explored using UV-vis, vibrational, and NMR spectroscopy. The initially formed $[\text{Fe}^{\text{III}}(\text{TPP})(\text{SPhF}_4)(\text{NO})]$ adduct, shows decomposition, and the corresponding products have been analyzed using spectroscopic techniques. A detailed mechanistic investigations has been carried out on this species, and its reaction with excess NO and N_2O_3 . These results are elaborated in Section 5.3.

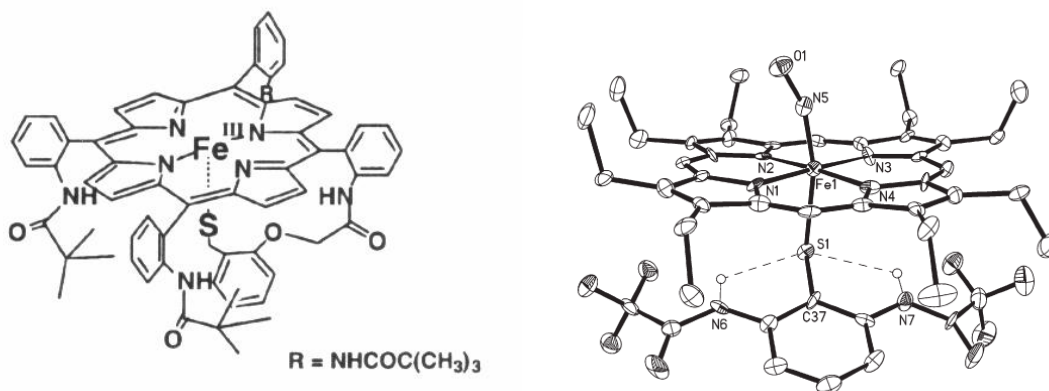


Figure 5.1.1. Model compounds synthesized by Suzuki et al.¹ (left) and Xu et al. (right)

References

¹ Suzuki, N.; Higuchi, T.; Urano, Y.; Kikuchi, K.; Uchida, T.; Mukai, M.; Kitagawa, T.; Nagano, T. *J. Am. Chem. Soc.* **2000**, *122*, 12059-12060.

² Xu, N.; Powell, D. R.; Cheng, L.; Richter-Addo, G. B. *Chem. Commun.* **2006**, 2030.

5.2 Thiolate Coordination to Fe(II)-Porphyrin NO Centers

V. K. K. Praneeth, Erhard Haupt, and Nicolai Lehnert*

J. Inorg. Biochem. **2005**, *99*, 940-948

(special issue: Heme-Diatomic Interactions)

Erratum: *J. Inorg. Biochem.* **2005**, *99*, 1744

Thiolate coordination to Fe(II)–porphyrin NO centers

V.K.K. Praneeth ^a, Erhard Haupt ^b, Nicolai Lehnert ^{a,*}

^a *Institut für Anorganische Chemie, Christian-Albrechts-Universität Kiel, Olshausenstrasse 40, D-24098 Kiel, Germany*

^b *Institut für Anorganische Chemie, Universität Hamburg, Martin-Luther-King-Platz 6, D-20146 Hamburg, Germany*

Received 12 November 2004; received in revised form 7 February 2005; accepted 10 February 2005

Available online 5 March 2005

Abstract

The interaction of the Fe(II)–porphyrin NO model complex [Fe(TPP)(NO)] (**1**, TPP = tetraphenylporphyrin) with thiophenolate ligands and tetrahydrothiophene is explored both computationally and experimentally. Complex **1** is reacted with substituted thiophenolates and the obtained six-coordinate adducts of type [Fe(TPP)(SR)(NO)][−] are investigated in solution using electron paramagnetic resonance (EPR) spectroscopy. From the obtained *g* values and ¹⁴N hyperfine pattern of the NO ligand it is concluded that the interaction of the thiophenolates with the Fe(II) center is weak in comparison to the corresponding 1-methylimidazole adduct. The strength of the Fe–S bond is increased when alkylthiolates are used as evidenced by comparison with the published EPR spectra of ferrous NO adducts in cytochromes P450 and P450nor, which have an axial cysteinate ligand. These results are further evaluated by density functional (DFT) calculations. The six-coordinate model complex [Fe(P)(SMe)(NO)][−] (**1-SMe**; P = porphine ligand used for the calculations) has an interesting electronic structure where NO acts as a medium strong σ donor and π acceptor ligand. Compared to the N-donor adducts with 1-methylimidazole (1-MeIm), etc., donation from the π_{h} orbital of NO to Fe(II) is reduced due to the stronger *trans* effect of the alkylthiolate ligand. This is reflected by the predicted longer Fe–NO bond length and smaller Fe–NO force constant for **1-SMe** compared to the 1-MeIm adduct. Therefore, the Fe(II)–porphyrin NO adducts with *trans* alkylthiolate coordination have to be described as Fe(II)–NO(radical) systems. The N–O stretching frequency of these complexes is predicted below 1600 cm^{−1} in agreement with the available experimental data. In addition, **1-SMe** has a unique spin density distribution where Fe has a negative spin density of −0.26 from the calculations. The implications of this unusual electronic structure for the reactivity of the Fe(II)–NO alkylthiolate adducts as they occur in cytochrome P450nor are discussed.

© 2005 Elsevier Inc. All rights reserved.

Keywords: Nitric oxide; Porphyrin; P450nor; Density functional calculations

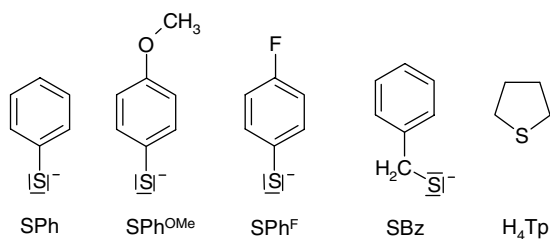
1. Introduction

Iron–porphyrin NO adducts occur as intermediates in many biologically important processes [1–5]. Correspondingly, much research has been conducted toward the synthesis of either five-coordinate model complexes [Fe(porphyrin)(NO)]²⁺ or corresponding six-coordinate complexes with N-donor ligands like 1-methylimidazole

(1-MeIm) in *trans* position to NO [6–9]. Much less research has been directed toward the corresponding six-coordinate complexes with *trans* S-donor ligands. Nevertheless, these systems are of great biological importance. NO bound heme centers with axial cysteinate coordination are present in fungal nitric oxide reductase (P450nor) [10–16] and nitric oxide synthase (NOS) [5]. Yoshimura studied the interaction of iron(II)–NO adducts with thiols and thioethers by EPR using protoporphyrin IX dimethylester as the porphyrin ligand [17]. From these data, it was concluded that the Fe(II)–sulfur interaction is weak. The only synthetic iron–porphyrin NO model complex with *trans*

* Corresponding author. Tel.: +49 04318801739; fax: +49 04318801520.

E-mail address: nlehnert@ac.uni-kiel.de (N. Lehnert).



Scheme 1.

thiolate coordination was prepared by Suzuki et al. [18–20]. This compound is based on a picket fence porphyrin with a covalently attached linker containing a benzyl thiolate group for coordination to the iron center. The corresponding Fe(III)–NO adduct has been studied using vibrational and absorption spectroscopies. Reduction of this compound led to the corresponding Fe(II)–NO complex which has been studied with electron paramagnetic resonance (EPR) spectroscopy. In order to further investigate the binding of sulfur ligands to Fe(II)–porphyrin NO adducts in solution, EPR spectra of the model complex [Fe(TPP)(NO)] (**1**, TPP = tetraphenylporphyrin) with added thiophenolates (cf. Scheme 1) and tetrahydrothiophene (a thioether) are presented in this study. The obtained data are correlated to the EPR spectra of **1** itself and of the corresponding adduct with 1-methylimidazole (**1-MI**) [21–26] as well as EPR data of NO adducts of ferrous P450 and P450nor [15,16]. Density functional (DFT) calculations on the simplified model [Fe(P)(SMe)(NO)][−] (P = simplified Porphyrin ligand) are then used to explore the general properties of Fe(II)–NO complexes with *trans* S-donor ligands as they occur in the P450 enzymes (bacterial P450cam, liver microsomal P450_{LM} and P450nor) in detail. This way, the electronic structure of these systems is defined and calculated spectroscopic properties are discussed.

2. Experimental and computational procedures

2.1. Syntheses

Reactions were performed using Schlenk techniques. The starting material [Fe(TPP)(NO)] (TPP = tetraphenylporphyrin) was synthesized using published procedures [27]. The different tetrabutylammonium (TBA) phenyl and benzyl thiolates (TBA)(SR) were synthesized using the corresponding thiols HSR purchased from Aldrich by reacting them with (TBA)(OMe) in methanol. Recrystallization from tetrahydrofuran/diethylether (1:2) yielded the TBA salts in high yields (>90%). The identity of the compounds was established using NMR spectroscopy and elemental analysis.

2.2. EPR spectroscopy

EPR spectra were recorded on a conventional X-band spectrometer (Bruker ESP-300E) equipped with a liquid nitrogen flow cryostat. Spectra were taken at 120 K and a microwave power of 20 mW, a modulation frequency of 100 kHz, and a modulation amplitude of 1 G. Samples were prepared by dissolving **1** in purified toluene (concentration: ~1 mM) and adding the corresponding (TBA)(SR) salt in large excess in a glove box.

2.3. Density functional calculations

Spin-unrestricted DFT calculations using the BP86 functional [28,29] and the TZVP basis set [30,31] were performed with the program package Gaussian 98 [32]. The structure of the anion [Fe(P)(SR)(NO)][−] (‘P’ = Porphyrin) was fully optimized for R = methyl, phenyl leading to the models **1a-SMe** and **1a-SPh**, respectively. For these calculations, the TPP ligand has been simplified by replacing the four phenyl substituents with hydrogen leading to the ligand P (cf. Figure S1) which also serves as a model for the enzymatic porphyrin ligands. The obtained structures for **1a-SMe** and **1a-SPh** correspond to true minima as evident from frequency calculations. In addition, geometry optimization of the tetrahydrothiophene complex **1a-h4tp** was attempted. However, due to the weak Fe(II)–S interaction in this case, the fully optimized structure could not be obtained. The Fe–S bond length in the optimization varies between 2.85 and 2.9 Å indicative of the weak interaction. In all these calculations, convergence was reached when the relative change in the density matrix between subsequent iterations was less than 1×10^{-8} . Force constants in internal coordinates were extracted from the Gaussian output using the program Redong (QCPE 628) [33]. Orbitals were plotted with the program GaussView. Since pure density functional theory tends to overestimate metal-ligand covalencies, the B3LYP functional was used for the calculation of accurate spin densities. EPR parameters were calculated using BP86/TZVP and the program ORCA [34].

3. Results and analysis

Different synthetic approaches are possible for the preparation of Fe(II)–porphyrin NO adducts with *trans* thiolates. In this study, [Fe(TPP)(NO)] (**1**) was used as starting material and reacted with a large excess of the corresponding TBA thiolate salt leading to compounds **1-SPh**, **1-SPh^{OMe}** and **1-SPh^F** with coordinated thiophenolate, *para*-methoxy thiophenolate and *para*-fluoro thiophenolate ligands (cf. Scheme 1), respectively, in solution. A corresponding thioether complex (**1-h4tp**) was also prepared. In comparison, reaction of an

Fe(III)–porphyrin precursor $[\text{Fe}(\text{TPP})\text{X}]$ ($\text{X} = \text{Cl}^-$, etc.), with excess NO in the presence of thiolate seems unfavorable, since the intermediate Fe(III)–NO species is reactive towards bases [35]. Corresponding Fe(II)–NO complexes are more stable and less reactive. Using **1** as starting material also avoids the presence of free NO, which might react with (coordinated) thiolates [36,37]. In addition, benzylthiolate was also used. However, the obtained product in this case was EPR silent indicating that the stronger reductant benzylthiolate reacts with the Fe(II)–NO moiety in contrast to the thiophenolates. The nature of the reaction product is still under investigation. Fig. 1 presents the EPR spectra obtained for **1-SPh** and **1-h₄tp** in comparison with **1** and **1-MI** measured under the same conditions. EPR spectra were recorded over the whole spectral range and no further signals were observed indicating that no iron(III) impurities are present (iron(II) impurities are EPR silent). As shown in Table 1, the g values determined for **1** and **1-MI** are similar to the literature results. In addition, the obtained resolution of the ^{14}N hyperfine is comparable to that previously reported [21,22]. As shown in Fig. 1, the coordination of the 1-MeIm ligand to **1** leads to a distinct decrease of the g values. This is accompanied by a shift of the strong ^{14}N hyperfine of the coordinated NO ligand from the smallest g value $g(\text{min})$ (min = minimum) in **1** to $g(\text{mid})$ (mid = middle) in the case of **1-MI** due to a rotation of the g tensor [24–26]. Addition of thiophenolate or tetrahydrothiophene to solutions of **1** leads to EPR spectra that show distinct changes in their overall appearance as compared to the spectrum of **1** (cf. Fig. 1). However, analysis of the data shows that the observed g values for both **1-SPh** and **1-h₄tp** are very similar to **1** (cf. Table 1) and, in addition, that the ^{14}N hyperfine of the coordinated NO is observed on $g(\text{min})$ as in the case of **1**. These findings indicate that the interaction of the thiophenolates and thioethers (cf. also Ref. [17]) with the Fe(II)–NO center is much weaker compared to N-donor ligands like 1-MeIm. This is further evidenced by comparison with the Fe(II)–NO adducts of P450_{nor}, P450_{cam} and P450_{LM} from Refs. [15,16]. The obtained g values as well as the observed ^{14}N hyperfine on $g(\text{mid})$ both resemble the properties of **1-MI** as given in Table 1. Therefore, the enzymatic species with cysteinyl as axial ligand show a stronger Fe–S interaction (similar to N-donor ligands) than the thiophenolates and thioethers. This result follows the simple trend in basicity with cysteinyl being a stronger base than the thiophenolates or thioethers.

In order to evaluate the electronic structure of the Fe(II)–NO thiolate adducts in comparison to the corresponding thioether and N-donor complexes, density functional calculations have been performed on models $[\text{Fe}(\text{P})(\text{SMe})(\text{NO})]^-$ (**1a-SMe**), $[\text{Fe}(\text{P})(\text{SPh})(\text{NO})]^-$ (**1a-SPh**) and $[\text{Fe}(\text{P})(\text{H}_4\text{Tp})(\text{NO})]$ (**1a-h₄tp**; P = Porphine;

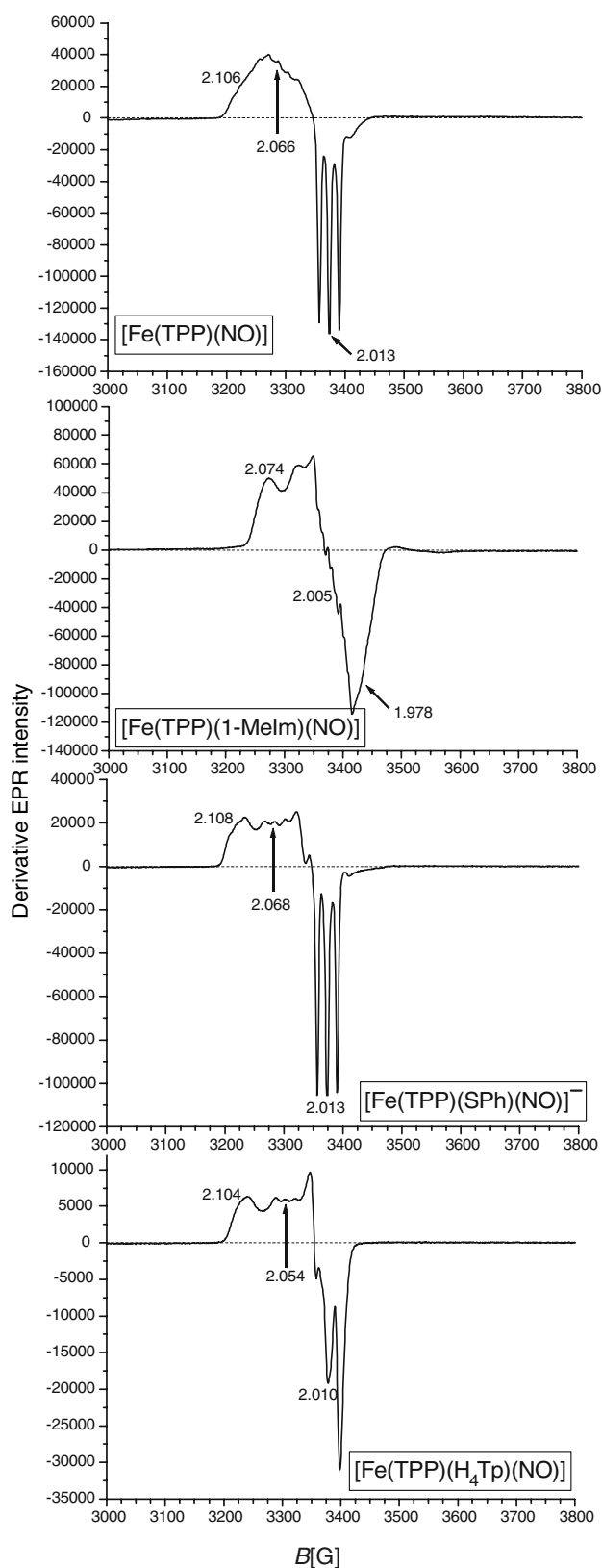


Fig. 1. EPR spectra of frozen toluene solutions of $[\text{Fe}(\text{TPP})(\text{NO})]$ (**1**, top) and of adducts of **1** with 1-methylimidazole (1-MeIm, Concentration ~ 1 M), thiophenolate (SPh, Concentration ~ 1 M) and tetrahydrothiophene (H_4Tp , Concentration ~ 1 M) as indicated.

Table 1
Comparison of experimental g values of $[\text{Fe}(\text{porphyrin})(\text{L})(\text{NO})]^{n-}$ ($n = 0, 1$) centers in model complexes and enzymes

Molecule/enzyme ^a	$g(\text{max})$	$g(\text{mid})$	$g(\text{min})$	Solvent	Reference
[Fe(TPP)(NO)]	2.102	2.064*	2.010	Toluene	[21]
	2.106	2.066*	2.013	Toluene	^b
[Fe(TPP)(1-MeIm)(NO)]	2.079	2.004*	1.972	CHCl ₃	[22]
	2.074	2.005*	1.978	Toluene	^b
[Fe(TPP)(SPh)(NO)] ⁻	2.108	2.068	2.013*	CHCl ₃	^b
[Fe(TPP)(SPh ^{OMe})(NO)] ^{-c}	2.108	2.067	2.012*	Toluene	^b
[Fe(TPP)(SPh ^F)(NO)] ^{-c}	2.109	2.067	2.013*	Toluene	^b
[Fe(TPP)(H ₄ Tp)(NO)]	2.104	2.054	2.010*	Toluene	^b
P450nor: Fe(II)–NO	2.082	2.007*	1.97	Buffer	[15]
P450cam: Fe(II)–NO	2.073	2.009*	1.976	Buffer	[16]
[Fe(SR)(NO)] ^{-d}	2.07	(2.04)	2.00*	Toluene	[18]

^a P = Porphine²⁻; * = shows ¹⁴N hyperfine lines of the coordinated NO ligand.

^b This work.

^c The spectra also show the presence of other species (impurities ?) in the $g = 2$ region.

^d Model complex of Suzuki et al. (see Section 1). In this case, the g values have been assigned in a different way compared to P450nor and P450cam and hence, $g(\text{min})$ shows the ¹⁴N hyperfine here in contrast to the enzymes.

cf. Experimental Section) in comparison to the 1-MeIm adduct (**1a-MI**). Table 2 shows a compilation of the obtained bond distances and vibrational properties. Since no crystal structure is known for the Fe(II)–NO thiolate adducts, comparison of the obtained structure with experiment is only possible for **1a-MI**. In this case, the calculations show excellent agreement with experiment as shown in Table 2. Therefore, it is reasonable to assume that a good theoretical description is also obtained for the S-donor adducts from the DFT calculations. Hence, the calculations can serve as a basis to analyze general trends in the electronic structures along this series of complexes. The calculated Fe–S bond length for **1a-SMe** (2.42 Å) as a model for the P450 NO adducts is distinctively shorter than that obtained for **1a-SPh** (2.51 Å). This indicates that methyl thiolate undergoes a stronger interaction with Fe(II) than thiophenolate in agreement with the EPR results. This is also evident from the calculated Fe–S force constants. For **1a-SPh**, a value of 0.57 mdyne/Å is obtained for Fe–S compared to 0.81 mdyne/Å in **1a-SMe**. The Fe–S bond distance of the tetrahydrothiophene adduct **1a-h4tp** is very long (calculated: >2.80 Å) which is borderline between compound formation and solvation. Altogether, the

trend in the calculated Fe–S bond strengths follows the trend in the basicity of the different sulfur donors and is in agreement with the EPR results. In comparison, for the 1-MeIm adduct **1a-MI**, the calculated Fe–N(imidazole) force constant is 0.61 mdyne/Å and hence, comparable to the Fe–S force constant in **1a-SPh**. However, the EPR data show that for **1a-MI** the interaction of the Fe(II) center with the *trans* ligand is strong, whereas it is weak for **1a-SPh**. Since the calculated Fe–N(imidazole) distance in **1a-MI** is in good agreement with experiment, this indicates that the Fe–S interaction is somewhat overestimated in **1a-SPh**. Table 2 also lists the calculated Fe–NO bond lengths, which reflect the σ donor ability of the *trans* ligand to NO. This is further evaluated based on the electronic structure of **1a-SMe**.

Fig. 2 shows the obtained MO diagram for model **1a-SMe** using BP86/TZVP. Charge distributions are given in Table 3. In this complex, iron is in the +II oxidation state and low-spin (as evident from EPR) which leads to a $[d_{xz}, d_{yz}, d_{xy}]^6 = [t_2]^6$ electron configuration on the metal. Free nitric oxide is a radical with $S = 1/2$ ground state with the unpaired electron being located in the singly occupied π^* orbitals. Since complex **1a-SMe** has a total spin of $S = 1/2$, the spin-unrestricted scheme has

Table 2
Comparison of calculated geometries, vibrational frequencies and force constants for $[\text{Fe}(\text{P})(\text{L})(\text{NO})]^{n-}$ ($n = 0, 1$) centers using BP86/TZVP

Molecule ^a	Geometric parameters (Å)				$\nu(\text{N-O})$ (cm ⁻¹)	Force constants (mdyne/Å)		
	$\Delta\text{Fe-N}$	$\Delta\text{N-O}$	$\angle\text{Fe-N-O}$	$\Delta\text{Fe-X}_{\text{tr}}$		$f(\text{Fe-N})$	$f(\text{N-O})$	$f(\text{Fe-X}_{\text{tr}})$
[Fe(TPP)(1-MeIm)(NO)] experimental ^b	1.750	1.182	138	2.173	1630 ^c			
[Fe(P)(1-MeIm)(NO)] ^c	1.734	1.186	140	2.179	1662	3.25	12.22	0.61
[Fe(P)(SCH ₃)(NO)] ⁻	1.788	1.198	138	2.416	1599	2.38	11.26	0.81
[Fe(P)(SPh)(NO)] ⁻	1.766	1.194	139	2.513	1617	2.81	11.51	0.57

^a P = Porphine²⁻ ligand used for the calculations (cf. Figure S1); X_{tr} is the ligand *trans* to NO.

^b Crystallographic data: see Ref. [25].

^c Taken from Ref. [26].

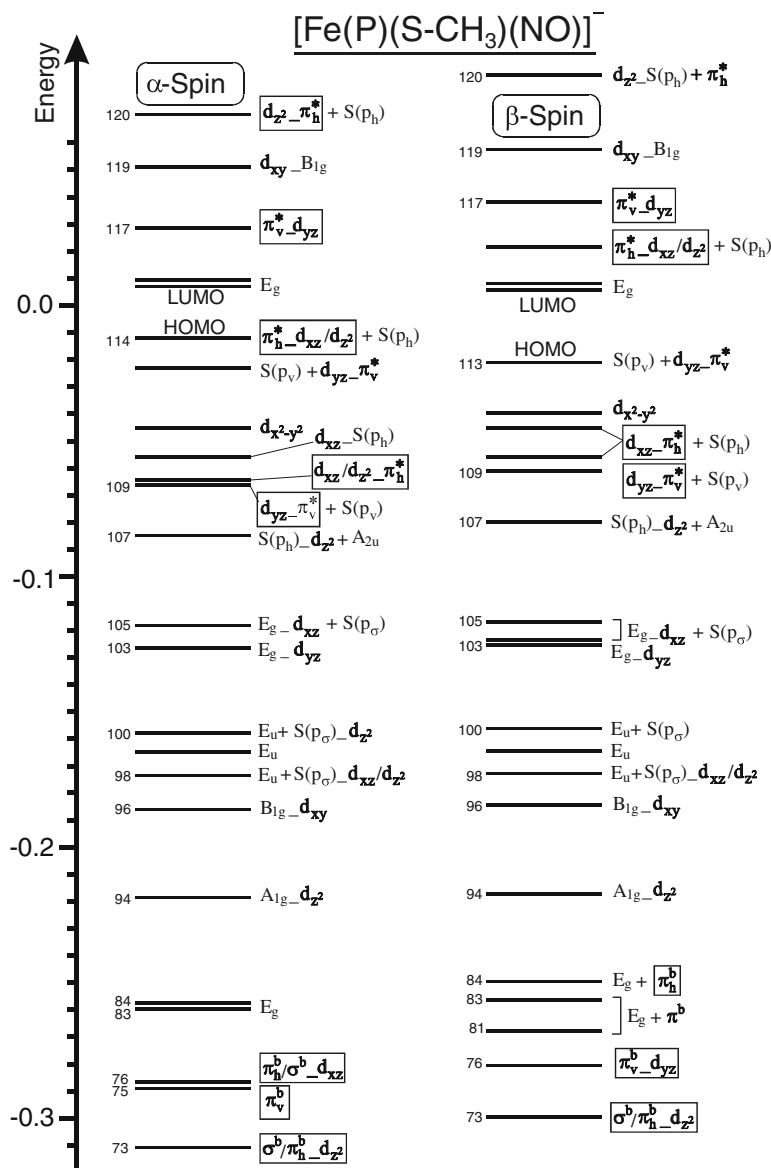


Fig. 2. MO diagram of $[\text{Fe}(\text{P})(\text{SCH}_3)(\text{NO})]^-$ (**1a-SMe**) calculated with BP86/TZVP. The applied coordinate system is shown in Figure S1. A_{1u} , A_{2u} and E_g correspond to porphyrin π orbitals. A_{1u} , A_{2u} are the highest occupied orbitals of the free ligand P^{2-} . Correspondingly, E_g is the LUMO of free porphine(2-). B_{1g} is the in-plane donor orbital of the porphyrin nitrogens that interacts with the d_{xy} orbital of iron. Ligand orbitals of NO are labeled π_v^* (v = vertical; orthogonal to the Fe–N–O plane) and π_h^* (h = horizontal; located in the Fe–N–O plane). $S(p_h)$ and $S(p_v)$ are the sulfur p donor orbitals within (p_h) and orthogonal to (p_v) the Fe–N–O plane. The nomenclature ‘ a_b ’ indicates that orbital a interacts with b and that a has a larger contribution to the resulting MO.

to be applied which distinguishes between majority (α) and minority (β) spin orbitals. Hence, the unpaired electron of NO occupies the orbital $\alpha-\pi_h^*$ (h = horizontal) which is the $\alpha-\pi^*$ function located in the Fe–N–O plane. The corresponding $\beta-\pi_h^*$ orbital is unoccupied. Since the t_2 functions of Fe(II) are fully occupied in **1a-SMe**, σ donation from $\alpha-\pi_h^*$ to the metal is only possible into the d_{z^2} orbital (the applied coordinate system with the S–Fe–N(O) unit roughly along the z axis is given in Figure S1). The corresponding bonding combination, $\pi_h^*-d_{xz}/d_{z^2}$ ($\alpha(114)$), is the highest occupied molecular orbital (HOMO) of **1a-SMe** (cf. Fig. 2). It has about

41% π_h^* and 24% d contribution. Since the metal contribution corresponds to a mixture of d_{xz} and d_{z^2} , the strength of this interaction is better estimated from the corresponding antibonding combination, $d_{z^2}-\pi_h^*$ ($\alpha(120)$), which has 25% π_h^* and 50% d_{z^2} contribution (cf. Fig. 3). Hence, this corresponds to a medium strong Fe–N σ bond. In addition, this orbital has a 10% admixture of the *trans* thiolate p donor orbital oriented along the Fe–S axis, labeled $S(p_h)$, as shown in Fig. 3. This competition of π_h^* and $S(p_h)$ for d_{z^2} explains the sensitivity of the calculated Fe–N(O) bond lengths for the nature of the *trans* ligand as shown in Table 2.

Table 3

Charge contributions of important molecular orbitals of [Fe(P)(SMe)(NO)]⁻ (**1a-SMe**) calculated with BP86/TZVP

Nr.	Label	Energy [HARTREE]	Fe d	N		O		S s + p	Σ SR
				s	p	s	p		
α(120)	d _{z²} -π _h [*] + S(p _h)	0.0706	50	1	17	0	7	10	11
α(119)	d _{xy} -B _{1g}	0.0513	69	0	0	0	0	0	0
α(117)	π _v [*] -d _{yz}	0.0286	27	0	42	0	25	2	2
α(116)	E _g	0.0078	3	0	1	0	0	1	1
α(115)	E _g (LUMO)	0.0077	6	0	0	0	0	0	0
α(114)	π _h [*] -d _{xz} /d _{z²} + S(p _h) (HOMO)	-0.0119	24	1	23	0	17	21	22
α(113)	S(p _v) + d _{yz} -π _v [*]	-0.0231	3	0	4	0	4	78	85
α(112)	d _{x²-y²} -d _{yz}	-0.0452	92	0	0	0	0	0	0
α(111)	d _{xz} -S(p _h)	-0.0560	31	1	1	0	1	13	14
α(110)	d _{xz} /d _{z²} -π _h [*]	-0.0643	33	1	10	0	15	2	2
α(109)	d _{yz} -π _v [*] + S(p _v)	-0.0649	49	0	6	0	9	4	5
α(107)	S(p _h)-d _{z²} + A _{2u}	-0.0848	13	1	2	0	3	38	42
α(96)	B _{1g} -d _{xy}	-0.1859	28	0	0	0	0	0	0
α(94)	A _{1g} -d _{z²}	-0.2185	10	0	1	0	0	1	11
α(76)	π _h ^b /σ ^b -d _{xz}	-0.2859	3	4	33	2	39	0	1
α(75)	π _v ^b	-0.2867	3	1	34	1	41	0	0
α(73)	σ ^b /π _h ^b -d _{z²}	-0.3106	5	3	30	6	38	0	0
β(120)	d _{z²} -S(p _h) + π _h [*]	0.0851	43	1	23	0	11	8	10
β(117)	π _v [*] -d _{yz}	0.0380	25	0	44	0	25	2	2
β(116)	π _h [*] -d _{xz} /d _{z²} + S(p _h)	0.0214	37	2	20	0	15	12	13
β(111)	d _{xz} -π _h [*] + S(p _h)	-0.0452	46	0	2	0	4	15	17
β(110)	d _{yz} -π _v [*]	-0.0558	24	1	4	0	8	15	16
β(109)	d _{yz} -π _v [*] + S(p _v)	-0.0612	51	0	5	0	8	6	6

Note that the interaction of π_h^{*} and d_{xz} does not contribute to bonding since both orbitals are occupied. The second α-π^{*} orbital of NO, labeled π_v^{*} (v = vertical), is unoccupied and oriented perpendicular to the Fe–N–O plane. It forms a π backbond with the d_{yz} orbital of iron. The bonding combination, d_{yz}-π_v^{*} (α(109)), has 49% d_{yz} and 15% π_v^{*} contribution. Correspondingly, the antibonding combination π_v^{*}-d_{yz} (α(117)) has mostly π_v^{*} character as shown in Table 3. The metal d_{yz} function also interacts with the thiolate S(p_v) orbital which is the p donor function of sulfur oriented perpendicular to the Fe–N–O plane. Since both d_{yz} and S(p_v) are occupied, this interaction is repulsive and leads to a weakening of the Fe–S bond. In the spin-unrestricted scheme, both β-π^{*} orbitals of NO are unoccupied. Hence, both β-π_h^{*} and β-π_v^{*} undergo additional π backbonding interactions with iron(II) (cf. Fig. 2, right). The corresponding bonding combinations, d_{xz}-π_h^{*} (split into β(111) and β(110); cf. Table 3) and d_{yz}-π_v^{*} (β(109)), are shown in Fig. 3. In summary, this electronic structure is qualitatively comparable to that obtained for **1a-MI** [26]. In both cases, NO acts as a medium strong σ donor and π acceptor ligand. However, the strengths of the individual interactions are different in the different complexes.

Based on this electronic structure description, the observed trends in the Fe–N(O) bond lengths and N–O stretching frequencies shown in Table 2 can be analyzed. Importantly, the Fe–NO σ bond mediated by the interaction of π_h^{*} and d_{z²} is weakened in the case of **1a-SMe**. This is evident from a comparison of the corresponding

antibonding orbitals, d_{z²}-π_h^{*} (cf. Figure S2); in the case of **1a-MI** (α(129)), this MO has a 35% π_h^{*} contribution which is decreased to 25% in **1a-SMe** (α(120)). This weakening of the Fe–NO σ bond in **1a-SMe** is due to the fact that alkylthiolate is a stronger σ donor than 1-MeIm. This is again evident from the charge contributions of the orbital d_{z²}-π_h^{*} (cf. Figure S2): it has a 10% contribution of the sulfur donor orbital S(p_h) in **1a-SMe** (α(120)), whereas the admixture of the σ donor function of 1-MeIm is only 3% in the corresponding orbital of **1a-MI** (α(129)). Therefore, since alkylthiolate donates stronger into the d_{z²} orbital than 1-MeIm, this reduces the donation of π_h^{*} and leads to an elongation of the Fe–NO bond by ~0.05 Å. Correspondingly, the Fe–NO force constant decreases from 3.25 mdyn/Å in **1a-MI** to 2.38 mdyn/Å in **1a-SMe** as shown in Table 2. Based on magnetic circular dichroism (MCD) spectroscopic data and density functional calculations, it was shown that **1a-MI** has an electronic structure that is best described as Fe(II)–NO(radical) [26]. Due to the reduced donation from π_h^{*}, the unpaired electron of nitric oxide is even stronger localized on the NO ligand in **1a-SMe**. Hence, the Fe(II)–NO(radical) description is even more pronounced for **1a-SMe** than for **1a-MI**. Table 4 gives the calculated spin densities for the different model complexes which show that the NO ligand carries a larger amount of spin density in **1a-SMe** than in **1a-MI** in agreement with this analysis. The increased population of π_h^{*} in **1a-SMe** is also evident from the calculated NO stretching frequencies. From Table 2, the predicted

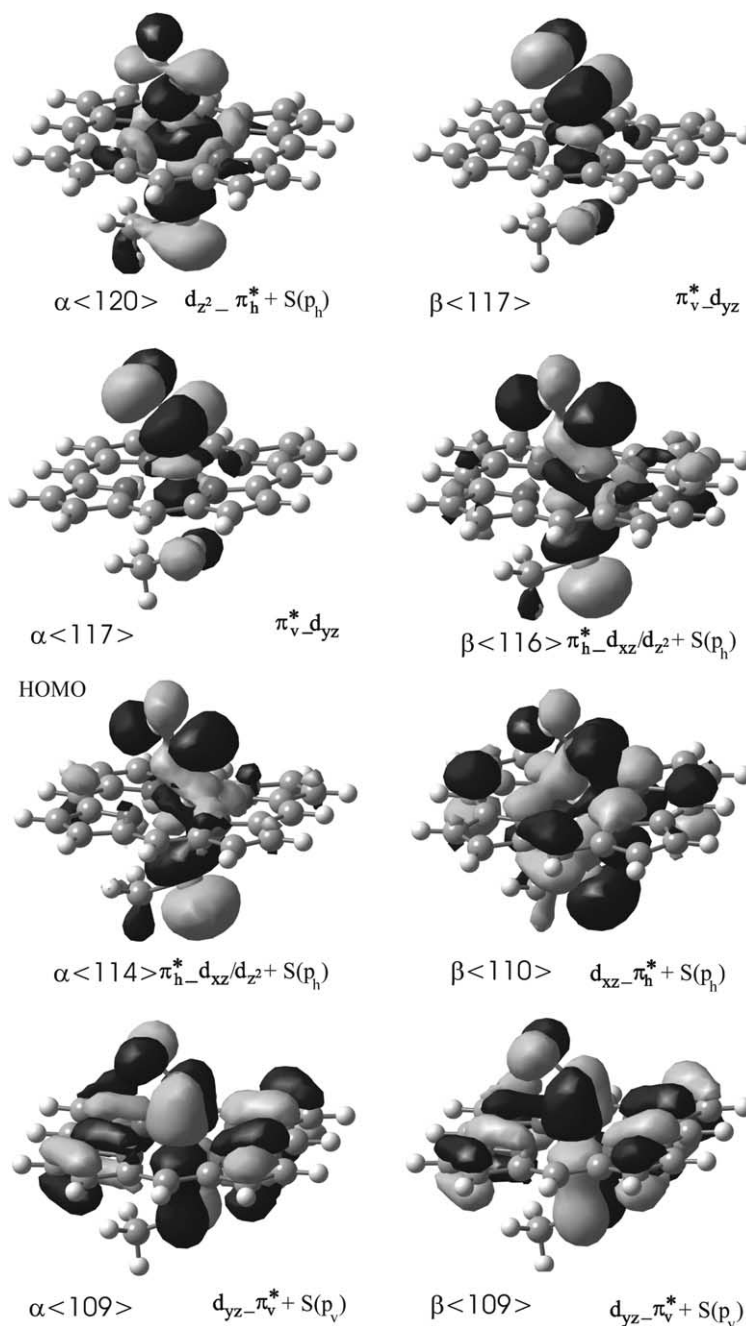


Fig. 3. Contour plots of important molecular orbitals of $[\text{Fe}(\text{P})(\text{SCH}_3)(\text{NO})]^-$ (**1a-SMe**) calculated with BP86/TZVP. For the labels see Fig. 2 and Table 3.

value for $\nu(\text{NO})$ is 1662 cm^{-1} for **1a-MI** compared to 1599 cm^{-1} for **1a-SMe**. This latter value compares well with the measured N–O stretching frequency of the ferrous P450cam NO adduct, which has been determined to 1591 cm^{-1} from resonance Raman spectroscopy [38]. This further indicates that **1a-SMe** is a good model for the enzymatic Fe(II)–NO complexes with axial cysteinate.

Another important difference in the electronic structures of **1a-SMe** and **1a-MI** is evidenced from the differ-

ent spin density distribution in these complexes. As shown in Table 4, the Fe center carries an unusual negative (β) spin density in the case of **1a-SMe** which is exclusively observed for the alkylthiolate adduct. This is due to the fact that the Fe–NO π backbonding interaction is much stronger for the α than for the β spin in the B3LYP wavefunction of **1a-SMe**. This leads to a transfer of a significant amount of α spin density to the π_v^* orbital of NO and hence, creates β spin density on the metal. This also explains the fact that the

Table 4

Comparison of calculated g values and spin densities for $[\text{Fe}(\text{P})(\text{L})(\text{NO})]^{n-}$ ($n = 0, 1$) centers calculated with BP86/TZVP

Molecule ^a	g values			Orientation	Spin density ^c		
	$g(\text{max})$	$g(\text{mid})$	$g(\text{min})$		Fe	$\Sigma(\text{NO})$	$\Sigma(\text{X}_{\text{tr}})$
$[\text{Fe}(\text{P})(\text{NO})]^{-}$ ^b	2.043	2.007	1.997	$g(\text{min})/\text{Fe}-\text{NO}: 24^\circ$	+0.47	+0.53	–
$[\text{Fe}(\text{P})(1\text{-MeIm})(\text{NO})]^{-}$ ^b	2.031	1.998	1.972	$g(\text{mid})/\text{Fe}-\text{NO}: 41^\circ$ $g(\text{min})/\text{Fe}-\text{NO}: 49^\circ$	+0.21	+0.78	+0.01
$[\text{Fe}(\text{P})(\text{SCH}_3)(\text{NO})]^{-}$	2.019	1.994	1.974	$g(\text{min})/\text{Fe}-\text{NO}: 26^\circ$	–0.27	+1.14	+0.08
$[\text{Fe}(\text{P})(\text{SPh})(\text{NO})]^{-}$	2.026	1.998	1.972	$g(\text{min})/\text{Fe}-\text{NO}: 36^\circ$	+0.01	+0.92	+0.06

^a P = Porphine²⁻ ligand used for the calculations (cf. Figure S1); X_{tr} is the ligand *trans* to NO.^b Taken from Ref. [26]; spin densities were calculated with B3LYP/LanL2DZ plus polarization functions (taken from the TZVP basis set).^c Calculated with B3LYP/TZVP; see Section 2.

calculated spin density on the NO ligand in **1a-SMe** is larger than 1 as shown in Table 4. The actual spin density distribution around the NO ligand is spherical due to the transfer of α spin density to π_v^* . In addition, the σ donor interaction between Fe(II) and the *trans* alkylthiolate ligand also shows spin polarization effects and is found to be stronger for β than for α spin. Hence, this further increases the negative (β) spin density on iron whereas at the same time, positive (α) spin density is created on the thiolate ligand as shown in Table 4. In contrast, these spin polarization effects are negligible for **1a-MI** where the spin density mostly reflects the distribution of the unpaired electron of NO and hence, has the shape of the orbital π_h^* [26].

Table 4 also presents the calculated g tensors for models **1a-SMe**, **1a-SPh** and **1a-MI**. The g values are obtained too low which is the usual finding for Fe(II)–porphyrin NO adducts [24,26]. In the case of **1a-SPh**, the principal axis of the minimal g value $g(\text{min})$ is closest to the Fe–N(O) axis in agreement with the experimentally observed ¹⁴N hyperfine splittings of $g(\text{min})$ [26]. However, the obtained g shifts (relative to the five-coordinate complex $[\text{Fe}(\text{P})(\text{NO})]^{-}$) are in the same range as those calculated for **1a-MI** which again indicates that the Fe(II)–S interaction is overestimated for **1a-SPh** in the calculations. For **1a-SMe**, the largest g shifts are obtained. The relative orientation of the g tensor in **1a-SMe** with $g(\text{min})$ being oriented approximately along the Fe–N(O) axis is in contrast to the experimental data obtained for P450 and P450nor [15,16]. Since experimental data for alkylthiolate adducts of $[\text{Fe}(\text{TPP})(\text{NO})]^{-}$ are missing (vide infra), it is not clear whether this is calculated incorrectly or if the porphyrin ligands present in the proteins have an additional influence on the EPR properties of these systems.

4. Discussion

EPR spectra of solutions of $[\text{Fe}(\text{TPP})(\text{NO})]^{-}$ (**1**) with added thiophenolate and thioether ligands are presented. The obtained g values and ¹⁴N hyperfine pattern

indicate that the resulting Fe–S bonds are very weak in agreement with an earlier binding study using thiols and thioethers [17]. Correspondingly, no solids of these complexes could be isolated so far. Comparison with EPR spectra of enzymatic NO adducts [15,16] indicates that alkylthiolates like cysteinyl form stronger bonds to Fe(II) in agreement with results from DFT calculations. However, addition of the stronger donating benzylthiolate to solutions of **1** leads to sample degradation due to the fact that it is a stronger reductant. From DFT, the Fe(II)–NO thiolate adducts have an interesting electronic structure where NO acts as a medium strong σ donor and π acceptor ligand in agreement with the results obtained for **1-MI** [26]. However, two important differences are observed for Fe(II)–porphyrin NO adducts with *trans* alkylthiolate and N-donor ligands. Firstly, σ donation from π_h^* (the singly occupied π^* orbital of NO) to d_{z^2} of Fe(II) is weakened in the alkylthiolate adducts compared to the corresponding complexes with *trans* N-donors. This is due to the fact that alkylthiolate is a stronger σ donor and hence, has a stronger *trans* effect on the coordinated NO compared to N-donor ligands. The reduced charge donation from π_h^* of NO to Fe(II) corresponds to a distinctively larger occupation of the N–O antibonding orbital π_h^* which explains the somewhat weaker N–O bond (cf. force constants in Table 2) in the case of the alkylthiolate adduct. Hence, N–O stretching frequencies below 1600 cm^{-1} are predicted for Fe(II)–NO alkylthiolate complexes in excellent agreement with published experimental data. The electronic structure of these systems has therefore to be described as Fe(II)–NO(radical), where the radical character of the NO ligand is even more pronounced than in the N-donor adducts like **1-MI** [26]. Secondly, the spin density distribution for the alkylthiolate adduct is unique for such complexes in showing a negative spin density on iron and a spherical spin density distribution around the NO ligand. This is due to strong spin polarization effects which are not observed for corresponding complexes with N-donor ligands.

Importantly, complex **1-SMe** is a model for the corresponding NO adduct of fungal nitric oxide reductase,

P450_{nor}. This enzyme is able to catalyze the reduction of two molecules of nitric oxide to nitrous oxide at a single heme center with an axial cysteinate ligand. Therefore, it is important to evaluate how the axial thiolate ligand alters the properties of the heme center to enable the catalytic NO reduction. The ferrous NO adducts studied here are not intermediates in the proposed catalytic cycle of P450_{nor} [13] and hence, this question cannot be answered from the EPR data and calculations presented here. However, our results show that the axial thiolate has a distinct effect on the coordinated NO. In the case of Fe(II), it can be expected that the increased radical character of the NO ligand will lead to an increased reactivity of this molecule compared to the corresponding systems with axial histidine. In addition, the NO should be less tightly bound to the Fe(II) center when an axial cysteinate ligand is present.

Acknowledgments

This work was supported by the Deutsche Forschungsgemeinschaft (DFG; Grant LE 1393/1) and the Fonds der Chemischen Industrie (FCI).

Appendix A. Supplementary data

Figures and cartesian coordinates of the optimized structures of **1a-SMe** and **1a-SPh**. Comparison of important molecular orbitals of **1a-MI** and **1a-SMe**. Supplementary data associated with this article can be found, in the online version, at [doi:10.1016/j.jinorgbio.2005.02.007](https://doi.org/10.1016/j.jinorgbio.2005.02.007).

References

- [1] J.A. McCleverty, *Chem. Rev.* 104 (2004) 403–418.
- [2] D.J. Richardson, N.J. Watmough, *Curr. Opin. Chem. Biol.* 3 (1999) 207–219.
- [3] D.S. Brecht, S.H. Snyder, *Annu. Rev. Biochem.* 63 (1994) 175–195.
- [4] X.D. Ding, A. Weichsel, J.F. Andersen, T.K. Shokhireva, C. Balfour, A.J. Pierik, B.A. Averill, W.R. Montfort, F.A. Walker, *J. Am. Chem. Soc.* 121 (1999) 128–138.
- [5] T.L. Poulos, H. Li, C.S. Raman, *Curr. Opin. Chem. Biol.* 3 (1999) 131–137.
- [6] P.C. Ford, I.M. Lorkovic, *Chem. Rev.* 102 (2002) 993–1017.
- [7] G.R.A. Wyllie, R. Scheidt, *Chem. Rev.* 102 (2002) 1067–1089.
- [8] I.M. Wasser, S. de Vries, P. Moënne-Loccoz, I. Schröder, K.D. Karlin, *Chem. Rev.* 102 (2002) 1201–1234.
- [9] F.A. Walker, U. Simonis, in: R.B. King (Ed.), *Encyclopedia of Inorganic Chemistry, Iron Porphyrin Chemistry*, Wiley, New York, in press.
- [10] S.-Y. Park, H. Shimizu, S.-I. Adachi, A. Nakagawa, I. Tanaka, K. Nakahara, H. Shoun, E. Obayashi, H. Nakamura, T. Iizuka, Y. Shiro, *Nat. Struct. Biol.* 4 (1997) 827–832.
- [11] H. Shimizu, S.-Y. Park, Y. Gomi, H. Arakawa, H. Nakamura, S.-I. Adachi, E. Obayashi, T. Iizuka, H. Shoun, Y. Shiro, *J. Biol. Chem.* 275 (2000) 4816.
- [12] K. Nakahara, T. Tanimoto, K. Hatano, K. Usuda, H. Shoun, *J. Biol. Chem.* 268 (1993) 8350–8355.
- [13] Y. Shiro, M. Fujii, T. Iizuka, S.-I. Adachi, K. Tsukamoto, K. Nakahara, H. Shoun, *J. Biol. Chem.* 270 (1995) 1617–1623.
- [14] E. Obayashi, K. Tsukamoto, S.-I. Adachi, S. Takahashi, M. Nomura, T. Iizuka, H. Shoun, Y. Shiro, *J. Am. Chem. Soc.* 119 (1997) 7807–7816.
- [15] Y. Shiro, M. Fujii, Y. Isogai, S.-I. Adachi, T. Iizuka, E. Obayashi, R. Makino, K. Nakahara, H. Shoun, *Biochemistry* 34 (1995) 9052–9058.
- [16] D.H. O'Keefe, R.E. Ebel, J.A. Peterson, *J. Biol. Chem.* 253 (1978) 3509–3516.
- [17] T. Yoshimura, *Inorg. Chim. Acta* 57 (1982) 99–105.
- [18] N. Suzuki, T. Higuchi, Y. Urano, K. Kikuchi, T. Uchida, M. Mukai, T. Kitagawa, T. Nagano, *J. Am. Chem. Soc.* 122 (2000) 12059–12060.
- [19] N. Suzuki, T. Higuchi, Y. Urano, K. Kikuchi, H. Uekusa, Y. Ohashi, T. Uchida, T. Kitagawa, T. Nagano, *J. Am. Chem. Soc.* 121 (1999) 11571–11572.
- [20] Y. Urano, T. Higuchi, M. Hirobe, T. Nagano, *J. Am. Chem. Soc.* 119 (1997) 12008–12009.
- [21] B.B. Wayland, L.W. Olson, *J. Am. Chem. Soc.* 96 (1974) 6037–6041.
- [22] J. Hüttermann, C. Burgard, R. Kappl, *J. Chem. Soc., Faraday Trans.* 90 (1994) 3077.
- [23] R.G. Hayes, M.K. Ellison, W.R. Scheidt, *Inorg. Chem.* 39 (2000) 3665–3668.
- [24] S. Patchkovskii, T. Ziegler, *Inorg. Chem.* 39 (2000) 5354–5364.
- [25] G.R.A. Wyllie, C.E. Schulz, W.R. Scheidt, *Inorg. Chem.* 42 (2003) 5722–5734.
- [26] V.K.K. Praneeth, F. Neese, N. Lehnert, *Inorg. Chem.*, accepted for publication.
- [27] W.R. Scheidt, M.E. Frisse, *J. Am. Chem. Soc.* 97 (1975) 17–21.
- [28] J.P. Perdew, *Phys. Rev. B* 33 (1986) 8822.
- [29] A.D. Becke, *J. Chem. Phys.* 84 (1988) 4524.
- [30] A. Schäfer, H. Horn, R. Ahlrichs, *J. Chem. Phys.* 97 (1992) 2571.
- [31] A. Schäfer, C. Huber, R. Ahlrichs, *J. Chem. Phys.* 100 (1994) 5829.
- [32] M.J. Frisch, G.W. Trucks, H.B. Schlegel, G.E. Scuseria, M.A. Robb, J.R. Cheeseman, V.G. Zakrzewski, J.A. Montgomery Jr., R.E. Stratmann, J.C. Burant, S. Dapprich, J.M. Millam, A.D. Daniels, K.N. Kudin, M.C. Strain, O. Farkas, J. Tomasi, V. Barone, M. Cossi, R. Cammi, B. Mennucci, C. Pomelli, C. Adamo, S. Clifford, J. Ochterski, G.A. Petersson, P.Y. Ayala, Q. Cui, K. Morokuma, P. Salvador, J.J. Dannenberg, D.K. Malick, A.D. Rabuck, K. Raghavachari, J.B. Foresman, J. Cioslowski, J.V. Ortiz, A.G. Baboul, B.B. Stefanov, G. Liu, A. Liashenko, P. Piskorz, I. Komaromi, R. Gomperts, R.L. Martin, D.J. Fox, T. Keith, M.A. Al-Laham, C.Y. Peng, A. Nanayakkara, M. Challacombe, P.M.W. Gill, B. Johnson, W. Chen, M.W. Wong, J.L. Andres, C. Gonzalez, M. Head-Gordon, E.S. Replogle, J.A. Pople, *Gaussian 98 Rev. A.11*, Gaussian, Inc., Pittsburgh, 2001.
- [33] A. Allouche, J. Pourcin, *Spectrochim. Acta A* 49 (1993) 571.
- [34] F. Neese, ORCA, version 2.2; Max-Planck Institut für Bioanorganische Chemie, Mülheim/Ruhr, Germany, 2004.
- [35] B.O. Fernandez, I.M. Lorkovic, P.C. Ford, *Inorg. Chem.* 43 (2004) 5393–5402.
- [36] L.V. Andreassen, I.M. Lorkovic, G.B. Richter-Addo, P.C. Ford, *Nitric Oxide* 6 (2002) 228–235.
- [37] R.K. Afshar, A.K. Patra, M.M. Olmstead, P.K. Mascharak, *Inorg. Chem.* 43 (2004) 5736–5743.
- [38] S. Hu, J.R. Kincaid, *J. Am. Chem. Soc.* 113 (1991) 9760–9766.

Erratum

Erratum to: Thiolate coordination to Fe(II)–porphyrin NO centers
[J. Inorg. Biochem. 99 (2005) 940–948]

V.K.K. Praneeth ^a, Erhard Haupt ^b, Nicolai Lehnert ^{a,*}

^a Institut für Anorganische Chemie, Christian-Albrechts-Universität Kiel, Olshausenstrasse 40, D-24098 Kiel, Germany

^b Institut für Anorganische Chemie, Universität Hamburg, Martin-Luther-King-Platz 6, D-20146 Hamburg, Germany

Available online 13 June 2005

There are two errors in Tables 1 and 3 in the original publication which need to be corrected.

1. **Table 1** (excerpt shown): [Fe(TPP)(NO)]: the stars (*) have to be moved from the g(mid) to the g(min) value, as follows:

Table 1

Comparison of experimental *g* values of [Fe(porphyrin)(L)(NO)]ⁿ⁻ (*n* = 0,1) centers in model complexes and enzymes

Molecule/enzyme ^a	<i>g</i> (max)	<i>g</i> (mid)	<i>g</i> (min)	Solvent	Reference
[Fe(TPP)(NO)]	2.102	2.064	2.010*	Toluene	[21]
	2.106	2.066	2.013*	Toluene	^b
[Fe(TPP)(1-MeIm)(NO)]	2.079	2.004*	1.972	CHCl ₃	[22]
	2.074	2.005*	1.978	Toluene	^b
[Fe(TPP)(SPh)(NO)] ⁻	2.108	2.068	2.013*	CHCl ₃	^b
[Fe(TPP)(SPh ^{OMe})(NO)] ^{-c}	2.108	2.067	2.012*	Toluene	^b

2. **Table 3** (excerpt shown): entry 8 ($\alpha(1\ 1\ 2)$): the orbital should not be labelled $d(x_2) - d(y_2)$, but $d(x_2 - y_2)$, as follows:

$\alpha(1\ 1\ 4)$	$\pi_h^* - d_{xz}/d_{z^2} + S(p_h)$ (HOMO)	-0.0119	24	1	23	0	17	21	22
$\alpha(1\ 1\ 3)$	$S(p_h) + d_{yz} - \pi_h^*$	-0.0231	3	0	4	0	4	78	85
$\alpha(1\ 1\ 2)$	$d_{x^2-y^2}$	-0.0452	92	0	0	0	0	0	0
$\alpha(1\ 1\ 1)$	$d_{xz} - S(p_h)$	-0.0560	31	1	1	0	1	13	14
$\alpha(1\ 1\ 0)$	$d_{xz}/d_{z^2} - \pi_h^*$	-0.0643	33	1	10	0	15	2	2

DOI of original article: [10.1016/j.jinorgbio.2005.02.007](https://doi.org/10.1016/j.jinorgbio.2005.02.007).

* Corresponding author. Tel.: +49 431 880 1739; fax: +49 431 880 1520.

E-mail address: nlehnert@ac.uni-kiel.de (N. Lehnert).

5.3 Thiolate Coordination to Ferric Porphyrin NO Complexes: Spectroscopic Characterization.

The major goal of this project is to synthesize a series of six-coordinate Fe(III)-porphyrin NO adducts, $[\text{Fe}^{\text{III}}(\text{TPP}^*)(\text{SR})(\text{NO})]$ (TPP* = tetraphenylporphyrin type ligand), with substituted thiophenolates (SR) in order to study the effect of different thiolates on the spectroscopic properties and the electronic structure of the Fe-NO unit. So far, most of the investigations were performed using $[\text{Fe}^{\text{III}}(\text{TPP})(\text{SPhF}_4)]$. This precursor was then exposed to one equivalent of NO and the following reactions were monitored in-situ using UV-Vis absorption and IR spectroscopies.

5.3.1 Syntheses

All reactions were carried out under an argon atmosphere using Schlenk techniques. Samples were generally handled inside an argon glove box. The iron(III)-NO complexes are susceptible to autoreduction reactions in the presence of any nucleophile yielding the corresponding (five-coordinate) iron(II)-NO complexes. Thus, all solvents employed should be free of nucleophiles such as OH^- and CH_3O^- . In addition, the ethanol present as a stabilizer in CHCl_3 has to be removed. This is achieved by washing with conc. H_2SO_4 and water. CHCl_3 and n-hexane were distilled over CaH_2 under an argon atmosphere prior to usage. NO gas was purified by first passing through an ascarite II column (NaOH on silica gel) followed by a cold trap operated at -80°C to exclude higher nitrogen oxides such as N_2O_3 and NO_2 . $[\text{Fe}^{\text{III}}(\text{TPP})(\text{SPhF}_4)]^1$ and $[\text{Fe}^{\text{III}}(\text{TPP})(\text{NO}_2)(\text{NO})]^2$ were prepared according to reported procedures and characterized using UV-Vis and NMR spectroscopic techniques.

Preparation of $[\text{Fe}^{\text{III}}(\text{TPP})(\text{SPhF}_4)(\text{NO})]$ (1) using unpurified NO (Method A): A solution of $[\text{Fe}^{\text{III}}(\text{TPP})(\text{SPhF}_4)]$ (0.1g) in 10 mL of freshly distilled CHCl_3 is prepared in a 100 mL Schlenk flask. Then, 1 equivalent of NO gas is passed into the solution at -40°C . A dramatic color change from dark brown to deep red occurs upon NO addition. The resulting solution is stirred for 15 minutes, then n-hexane (20 mL) is slowly added and the flask is stored inside a freezer (-20°C) for 1 day. The precipitate obtained is filtered and dried under vacuum. IR (KBr): $\nu(\text{N-O})$ 1872 cm^{-1} . UV-Vis in CH_2Cl_2 (λ_{max}): 431, 543, 580. UV-Vis and IR spectral data confirm the formation of $[\text{Fe}^{\text{III}}(\text{TPP})(\text{NO}_2)(\text{NO})]$ in this reaction (vide infra) as shown in

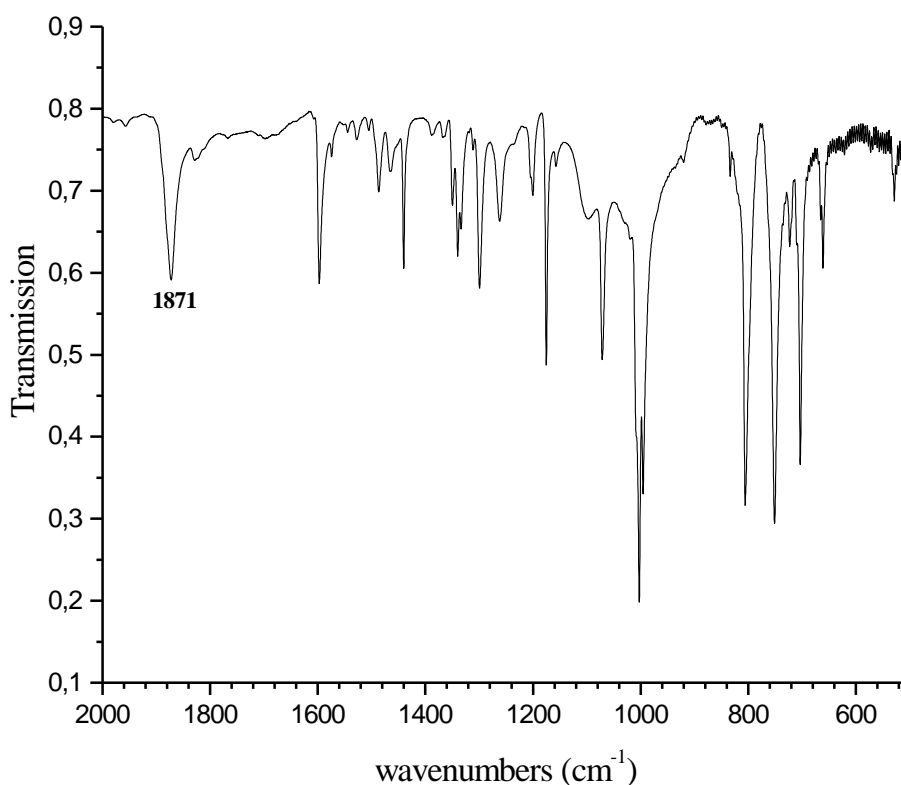


Figure 5.3.1 IR spectrum of $[\text{Fe}^{\text{III}}(\text{TPP})(\text{NO}_2)(\text{NO})]$ isolated from the reaction of $[\text{Fe}^{\text{III}}(\text{TPP})(\text{SPhF}_4)]$ with unpurified NO (Method A)

Figure 5.3.1³ Notably, several other attempts to synthesize the desired product $[\text{Fe}^{\text{III}}(\text{TPP})(\text{SPhF}_4)(\text{NO})]$ always resulted in the isolation of a mixture of $[\text{Fe}^{\text{III}}(\text{TPP})(\text{NO}_2)(\text{NO})]$ (major product) and $[\text{Fe}^{\text{II}}(\text{TPP})(\text{NO})]$ (minor product), as judged from the IR spectra. Thus, the synthesis of $[\text{Fe}^{\text{III}}(\text{TPP})(\text{SPhF}_4)(\text{NO})]$ (**1**) as a solid by this method is unsuccessful.

Preparation of $[\text{Fe}^{\text{III}}(\text{TPP})(\text{SPhF}_4)(\text{NO})]$ (1**) using purified NO (Method B):** The same procedure as described above is adopted with the exception that purified NO gas is used. Importantly, very few milligrams of solid material are isolated in this case. The IR spectrum of the obtained compound shows the $\nu(\text{N-O})$ band of five-coordinate $[\text{Fe}^{\text{II}}(\text{TPP})(\text{NO})]$ at 1698 cm^{-1} (very strong) and a small feature at 1823 cm^{-1} which corresponds to the formation of $[\text{Fe}^{\text{III}}(\text{TPP})(\text{SPhF}_4)(\text{NO})]$ as shown in Figure 5.3.2. This $\nu(\text{N-O})$ frequency of 1823 cm^{-1} is

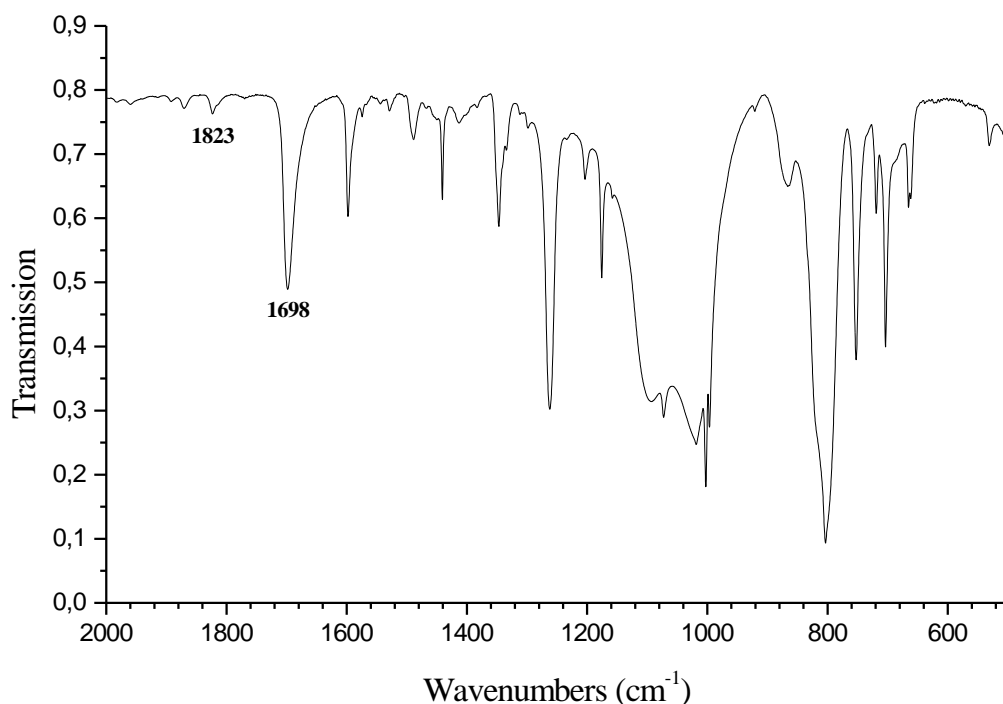


Figure 5.3.2 IR spectrum of a mixture of $[\text{Fe}^{\text{II}}(\text{TPP})(\text{NO})]$ and $[\text{Fe}^{\text{III}}(\text{TPP})(\text{SPhF}_4)(\text{NO})]$, isolated from the reaction of $[\text{Fe}^{\text{III}}(\text{TPP})(\text{SPhF}_4)]$ with purified NO (Method B).

in good agreement with the literature value of 1828 cm^{-1} for the Suzuki complex $[\text{Fe}^{\text{III}}(\text{SR})(\text{NO})]$ (cf. Section 5.1) ⁴

5.3.2 Electronic Absorption Spectroscopic Studies: Formation and Decomposition of $[\text{Fe}^{\text{III}}(\text{TPP})(\text{SPhF}_4)(\text{NO})]$ (**1**)

The formation of **1** was monitored in solution at low temperature using in-situ UV-Vis absorption spectroscopy. In a typical experiment, a solution of $[\text{Fe}^{\text{III}}(\text{TPP})(\text{SPhF}_4)]$ (approx. $1 \times 10^{-2} \text{ M}$) in 10 mL CHCl_3 is placed in a 100 mL Schlenk tube. Then about 1 equivalent of NO gas is injected via a microliter syringe into the solution at -40°C . The dark brown color of the solution changes to deep red on addition of NO. Figure 5.3.3 shows the subsequent absorption changes observed after NO addition. The Soret band of the starting material at 414 nm decreases in intensity while at the same time a new (Soret) band appears at 439 nm. In addition, bands at 380 nm and 515 nm of the starting material decrease in intensity, whereas a new band is observed at 556 nm. This corresponds to the formation of the six-coordinate NO adduct $[\text{Fe}^{\text{III}}(\text{TPP})(\text{SPhF}_4)(\text{NO})]$ as can be seen by comparison with absorption data of the Suzuki complex $[\text{Fe}^{\text{III}}(\text{SR})(\text{NO})]$.⁴ Moreover, isosbestic points at 426,

463 and 545 nm suggest a clean conversion of the starting material to the product without further intermediates. However, as can be seen from Figure 5.3.3, a complete conversion to the product is not obtained here in contrast to the Suzuki complex. In an attempt to drive the reaction to completion, an excess of NO gas was added and the resulting spectral changes were monitored.

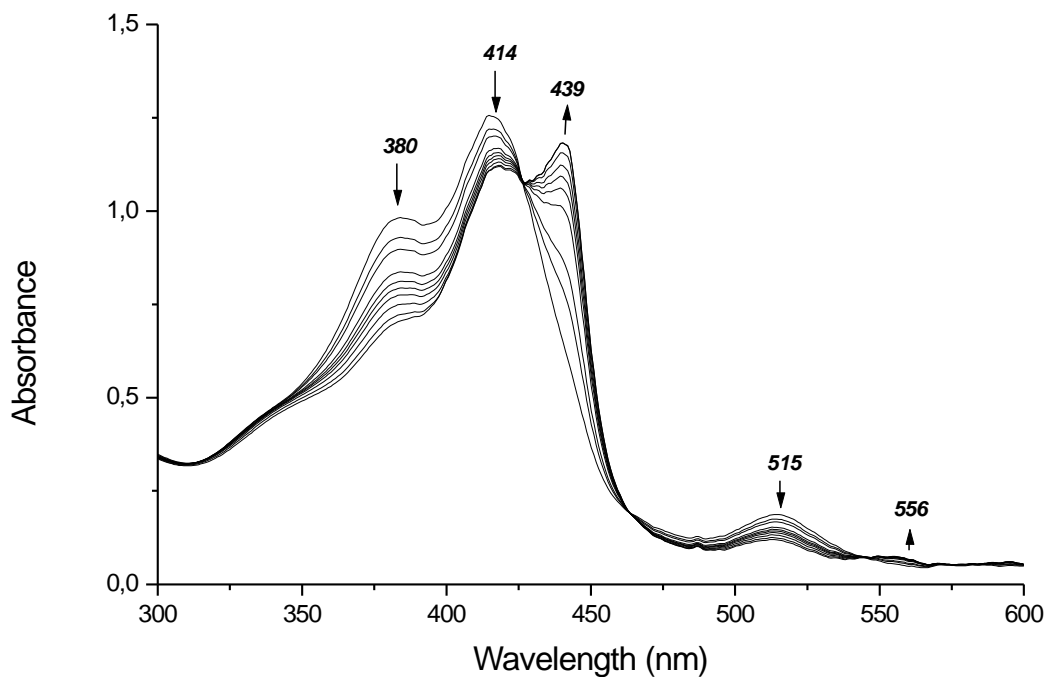


Figure 5.3.3 Electronic absorption spectral changes for the reaction of [Fe^{III}(TPP)(SPhF₄)] with purified NO gas at -40°C monitored in-situ.

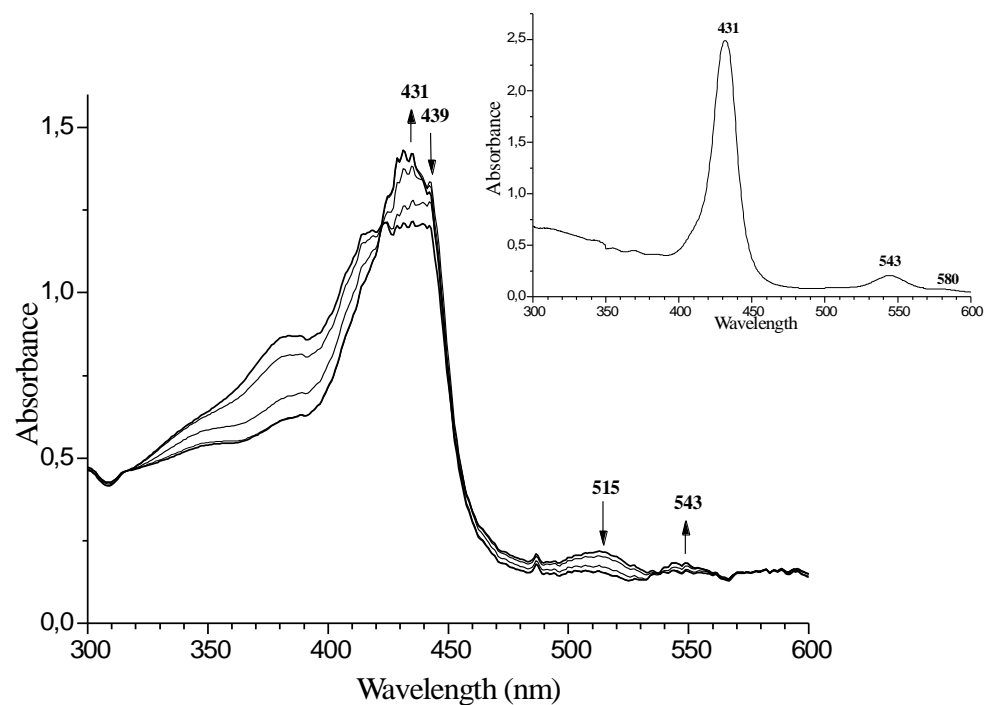


Figure 5.3.4: Spectral changes for the decomposition of $[\text{Fe}^{\text{III}}(\text{TPP})(\text{SPhF}_4)(\text{NO})]$ yielding $[\text{Fe}^{\text{III}}(\text{TPP})(\text{NO}_2)(\text{NO})]$ at -40°C . Insert: an independently prepared sample of $[\text{Fe}^{\text{III}}(\text{TPP})(\text{NO}_2)(\text{NO})]$ in CHCl_3 at room temperature.

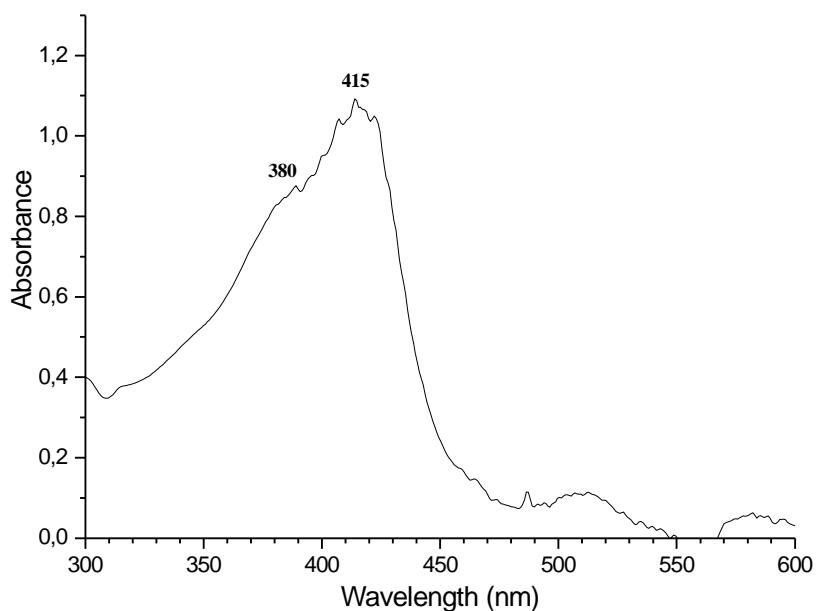
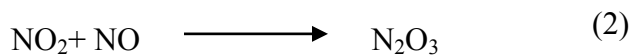
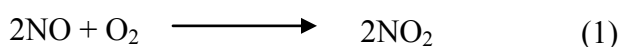


Figure 5.3.5: Electronic absorption spectrum of the final product **4** obtained from the decomposition of **2**.

Interestingly, the presence of an excess of NO leads to a slow disappearance of the 439 nm band of **1** and the appearance of a new band at 431 nm as shown in Figure 5.3.4. Similarly, in the Q region, the 556 nm band of **1** decreases in intensity while a new band at 543 nm grows in. The new complex formed exhibiting a Soret band at 431 nm (**2**) is also not very stable and decomposes after several minutes to give a new species **4**, characterized by a Soret absorption maximum at 415 nm as shown in Figure 5.3.5 There are no other spectral changes observed even after exposing this reaction mixture to air at room temperature. The electronic absorption data of complex **2** are identical with that of $[\text{Fe}^{\text{III}}(\text{TPP})(\text{NO}_2)(\text{NO})]$, which has been structurally and spectroscopically characterized in the literature.² In addition, an independently prepared sample of $[\text{Fe}^{\text{III}}(\text{TPP})(\text{NO}_2)(\text{NO})]$ shows an identical Soret position at 431 nm as presented in the insert of Figure 5.3.4. This is further confirmed by the observation of the $\nu(\text{N-O})$ vibration at 1872 cm^{-1} in the IR spectrum of **2**, which is characteristic for the nitro-nitrosyl complex. An identical IR band is found for the independently prepared $[\text{Fe}^{\text{III}}(\text{TPP})(\text{NO}_2)(\text{NO})]$ complex confirming that **2** corresponds to this species. From the literature, it is known that $[\text{Fe}^{\text{III}}(\text{TPP})(\text{NO}_2)(\text{NO})]$ can decompose to form $[\text{Fe}^{\text{III}}(\text{TPP})(\text{NO}_3)]$.⁵ Thus, the identity of **4** is presumably the five-coordinate $[\text{Fe}^{\text{III}}(\text{TPP})(\text{NO}_3)]$ complex. Importantly, the formation of complex **2** by decomposition of **1** is only possible if higher nitrogen oxides are present in the reaction mixture. Recent work of the van Eldik group and others has shown that it is practically impossible to completely remove higher NO_x impurities from NO, even after adopting rigorous purification procedures.⁶ This would explain the observed formation of $[\text{Fe}^{\text{III}}(\text{TPP})(\text{NO}_2)(\text{NO})]$. This is also in agreement with the observation that the reaction of $[\text{Fe}^{\text{III}}(\text{TPP})(\text{SPhF}_4)]$ with unpurified NO directly yields the nitro-nitrosyl compound. Under these conditions, it is assumed that the formation and successive decomposition of **1** are too fast to be spectroscopically monitored. Similarly, the reaction of $[\text{Fe}^{\text{III}}(\text{TPP})(\text{SPhF}_4)]$ with purified NO in the presence of small quantities of deliberately added air also accelerates the formation of **2**. This can be explained based on the formation of NO_x according to equations 1 and 2:

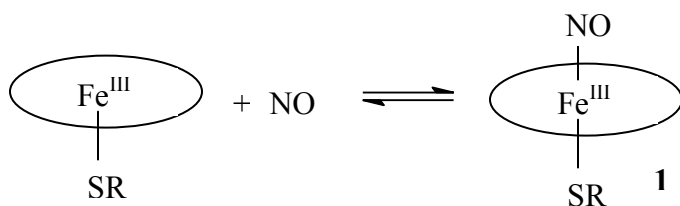


Interestingly, the decomposition pathway of **1** identified this way is identical with the results by Franke et al.⁷ on the ferric NO adduct of the Suzuki complex using stopped-flow kinetics.

The formation of $[\text{Fe}^{\text{II}}(\text{TPP})(\text{NO})]$ (**3**) in the reaction mixtures could be due to the presence of NO_2^- , which catalyzes the autoreduction of ferric porphyrin NO adducts as has been shown by Ford and coworkers.⁸ $[\text{Fe}^{\text{II}}(\text{TPP})(\text{NO})]$ has a characteristic absorption band at 408 nm (Soret) and $\nu(\text{N-O})$ at 1698 cm^{-1} in the IR spectrum.⁹ In this study, five-coordinate $[\text{Fe}^{\text{II}}(\text{TPP})(\text{NO})]$ was isolated in all reactions of $[\text{Fe}^{\text{III}}(\text{TPP})(\text{SPhF}_4)]$ with both unpurified and purified NO gas in varying quantities as described in Section 5.3.1. On the other hand, in all reactions monitored in-situ by UV-Vis spectroscopy, this species could not have been identified. However, the complex spectral changes observed after the decomposition of **1** led to poorly resolved broad bands and it is therefore likely that the band at 408 nm of **3** is masked by other absorptions.

5.3.3 Mechanism of the Formation and Decomposition of $[\text{Fe}^{\text{III}}(\text{TPP})(\text{SPhF}_4)(\text{NO})]$

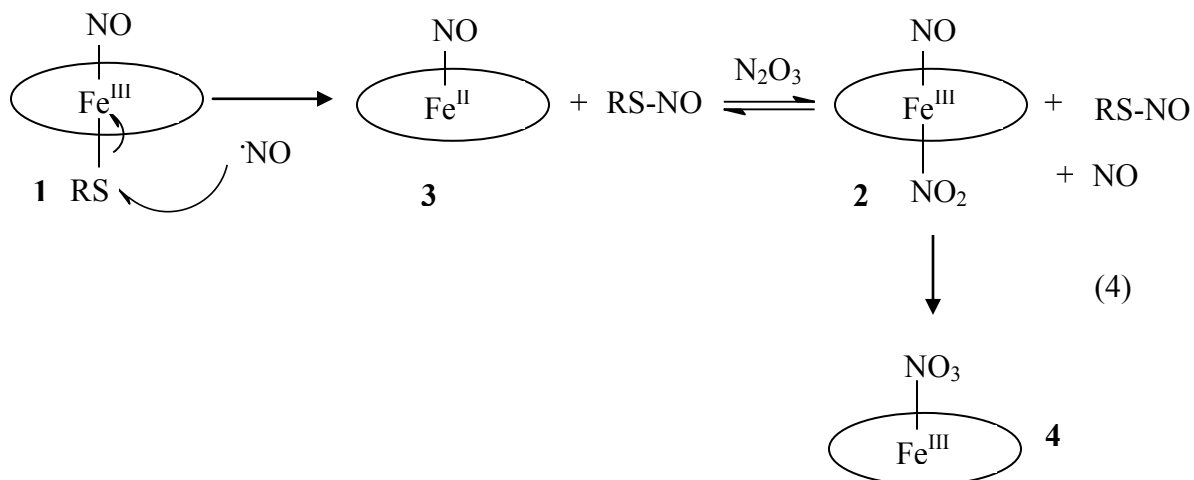
The reaction of $[\text{Fe}^{\text{III}}(\text{TPP})(\text{SPhF}_4)]$ with purified NO directly leads to the formation of the six-coordinate complex $[\text{Fe}^{\text{III}}(\text{TPP})(\text{SPhF}_4)(\text{NO})]$, which is characterized by a red shift of the Soret band from 414 nm to 439 nm and the appearance of $\nu(\text{N-O})$ at 1823 cm^{-1} . This suggests a simple binding of NO to the Fe(III) center as the first step:



R = tetrafluorophenyl

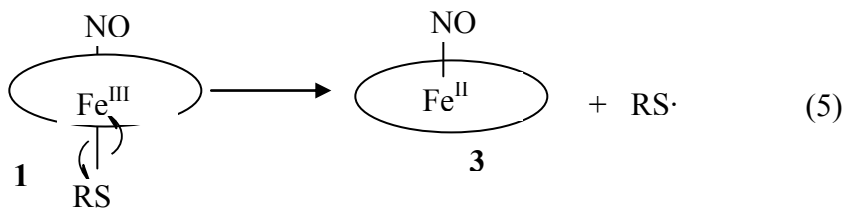
In the presence of excess NO, **1** decomposes rapidly yielding $[\text{Fe}^{\text{III}}(\text{TPP})(\text{NO}_2)(\text{NO})]$ (**2**) in the in-situ experiments. There are two possible mechanistic scenarios for the decomposition of **1**.

Mechanism A. The most likely explanation for the formation of **2** is a direct attack of a second NO molecule on the sulfur atom of the tetrafluorothiophenolate in **1**. This leads to homolytic cleavage of the Fe-S bond yielding $[\text{Fe}^{\text{II}}(\text{TPP})(\text{NO})]$ (**3**) and $\text{F}_4\text{PhS-NO}$ (S-nitrosothiol). Subsequently, the nitro-nitrosyl compound is formed by reaction of **3** with NO_2 or N_2O_3 present as an impurity in NO gas. This reaction sequence shown in equation 4 is in agreement with recent results of van Eldik and coworkers⁷:



A recent crystal structure of the NO adduct of *Cimex* nitrophorin has revealed an S-nitrosocysteine bound to a ferrous heme-NO complex (as confirmed by EPR), which indicates that the direct attack of NO on a bound thiolate as shown in eqn. 4 is a likely reaction sequence.¹⁰ Note that the formation of NO_2^- in the solution would further facilitate autoreduction of ferric NO adducts leading to the formation of **3** as discussed above.

Mechanism B. An alternative reaction mechanism involves the formation of a thiyl radical after the homolytic cleavage of the Fe-S bond in **1** independent of NO. Subsequent radical coupling of the thiyl with excess NO then also leads to the formation of **3** and the S-nitrosothiol (from $\text{RS}\cdot$ and NO):



Evidence that this mechanism could be valid is obtained from the reaction of $[\text{Fe}^{\text{III}}(\text{TPP})(\text{SPhF}_4)]$ with exactly 1 equivalent of purified NO as described here in method B (5.3.1). This led to the isolation of a mixture of five-coordinate $[\text{Fe}^{\text{II}}(\text{TPP})(\text{NO})]$ as the major product and six-coordinate $[\text{Fe}^{\text{III}}(\text{TPP})(\text{SPhF}_4)(\text{NO})]$ as the minor product. Importantly, the nitro-nitrosyl complex was not obtained. There are several possible explanations for this finding. Firstly, it is of course possible that the solubility of **2** is much larger and hence, this complex does not precipitate from the solution. On the other hand, it is also possible that the amount of NO_x impurities in the carefully purified NO gas is small enough such that **2** is not formed as shown in eqn. 4. If this is the case, then it is noteworthy that the main product from the reaction was actually **3** and not **1**. This would indicate an inherent instability of the Fe-S bond in ferric NO adducts that leads to homolytic cleavage of the Fe-S bond even in the absence of excess NO (as has been the case in this experiment) and NO_x . This would be a very important finding. If mechanism A is valid, then the synthesis of **1** should be possible by optimizing the reaction conditions and precursors. However, if mechanism B is valid, then this is not the case and **1** cannot be isolated as a pure compound.

The reactions performed with excess unpurified NO shed further light on these findings. In this case, the precursor is directly transformed into the nitro-nitrosyl complex and no ferric heme NO adduct is detected as intermediate. Considering all the experimental evidence, the most likely picture is therefore that both mechanisms A and B actually occur: A is a fast process when excess NO is present, such that **1** cannot be obtained. Complex **3** is formed initially, but quickly trapped by NO_x impurities if unpurified NO is used. If only one equivalent of carefully purified NO is added, then **1** is formed and decomposes on a much slower time scale following B. Further experiments are necessary to investigate this point.

The S-nitrosothiols formed as intermediates in mechanism A (and B in the presence of excess NO) are not easy to identify in the reaction mixtures. This is due to the inherent instability of S-nitrosoarylthiols. Kei et al¹¹ employed an aromatic dendrimer-type framework at the *ortho* positions of the phenyl rings to synthesize and isolate a stable S-nitrosoarylthiol. In this case, the NO stretching frequency is observed at 1548 cm^{-1} . Simple aromatic S-nitrosothiols as obtained from the reactions performed here only exist transiently and rapidly decompose to

the corresponding disulfides and NO¹². Thus, it is assumed that the formed F₄PhS-NO similarly yields F₄PhS-SPhF₄ and NO.

5.3.4 Summary

The formation of six coordinate [Fe^{III}(TPP)(SPhF₄)(NO)] (**1**) has been investigated in solution using UV-Vis absorption spectroscopy. The initially formed complex **1** undergoes either spontaneous or NO-assisted decomposition to **3**. Our experiments indicate that the former process is slow, while the latter occurs much faster. In the further course of the reaction, the nitro-nitrosyl complex **2** is formed by reaction with higher NO_x species either present as impurities in the NO gas or created by addition of small quantities of air. Subsequent decomposition of **2** (also a reactive species) ultimately leads to the nitrate complex **4**. Thus, the isolation of **1** as a pure solid is extremely challenging and could not have been achieved so far.

References

-
- ¹ Miller, K. M.; Strouse, C. E. *Inorg. Chem.* **1984**, *23*, 2395-2400.
 - ² Ellison, M. E.; Schulz, C. E. *Inorg. Chem.* **1999**, *38*, 100-108.
 - ³ (a) Ellison, M. E.; Schulz, C. E.; Scheidt, W. R. *Inorg. Chem.* **1999**, *38*, 100. (b) Kurtikyan, T. S.; Martirosyan, G. G.; Hakobyan, M. E.; Ford, P. C. *Chem. Commun.* **2003**, 1706.
 - ⁴ Suzuki, N.; Higuchi, T.; Urano, Y.; Kikuchi, K.; Uchida, T.; Mukai, M.; Kitagawa, T.; Nagano, T. *J. Am. Chem. Soc.* **2000**, *122*, 12059-12060.
 - ⁵ Lim, M. D.; Lorković, I. M.; Wedeking, K.; Zanella, A. W.; Works, C. F.; Massick, S. M.; Ford, P. C. *J. Am. Chem. Soc.* **2002**, *124*, 9737-9743.
 - ⁶ (a) Wolak, M.; Stochel, G.; Hamza, M.; van Eldick, R. *Inorg. Chem.* **2000**, *39*, 2018. (b) Ford, P. C.; Wink, D. A.; Stanbury, D. M. *FEBS Lett.* **1993**, *326*, 1.
 - ⁷ Franke, A.; Stochel, G.; Suzuki, N.; Higuchi, T.; Okuzono, K.; van Eldick, R. *J. Am. Chem. Soc.* **2005**, *127*, 5360-5375.
 - ⁸ Fernandez, B. O.; Lorković, I. M.; Ford, P. C. *Inorg. Chem.* **2003**, *42*, 2-4.
 - ⁹ (a) Praneeth, V. K. K.; Neese, F.; Lehnert, N. *Inorg. Chem.* **2005**, *44*, 2570-2572. (b) Praneeth, V. K. K.; Näther, C.; Peters, G.; Lehnert, N. *Inorg. Chem.* **2006**, *45*, 2795-2811.
 - ¹⁰ Walker, F. A. *J. Inorg. Biochem.* **2005**, *99*, 216-236.
 - ¹¹ Goto, K.; Takahashi, Y.; Kawashima, T.; Yamamoto, G.; Takagi, N.; Nagase, S. *Chem. Lett.* **2001**, 1204-1205.
 - ¹² (a) Oae, S.; Fukushima, D.; Kim, Y. H. *J. Chem. Soc. Chem. Com.* **1977**, 407. (b) Oae, S.; Kim, Y. H.; Fukushima, D.; Shinhma, K. *J. Chem. Soc. Perkin. Trans I.* **1978**, 913.

Chapter 6

Sophisticated Models for Bacterial Nitric Oxide Reductase (NorBC)

6.1. Scope of this Project

As mentioned previously, NO reduction by NorBC is an important step in the dissimilatory denitrification process. The active site of NorBC consists of a heme with an axially bound, histidine ligand, and a non-heme iron center in close proximity. This active site model is based on several spectroscopic investigations for NorBC, since there is no crystal structure available to this date for this enzyme. Spectroscopic evidence shows that the active site of bacterial NOR is structurally closely related to that of cytochrome *c* oxidase (CcO). Thus, the iron center in the non-heme iron site is coordinated by three histidine ligands in NorBC, similar to copper binding in CcO. In addition, it has been suggested that a glutamic acid residue binds the non-heme iron of NorBC through its carboxylate group (cf. Chapter 1). Importantly, the exact mechanism by which the enzyme works to reduce two molecules of NO to N₂O and water has not been clarified yet. Many five- (5C) and six-coordinate (6C) iron-porphyrin NO compounds of type [Fe^{II}(TPP*)(NO)(L)] (L = N-donor or missing) have been extensively investigated as model systems for the heme portion of NorBC active site (cf. Chapter 4). Nevertheless, a complete functional modeling of the NorBC's active site is cumbersome due to the following reasons:

1. The axial N-donor ligand is weakly bound to the Fe(II)-NO center. Hence, a large amount of N-donor ligand is necessary to drive the reaction to form a six-coordinate complex in solution. This fact has been investigated in detail (cf. Section 4.2) using UV-vis binding experiments on substituted iron porphyrin NO complexes with pyridine and 1-methylimidazole.
2. Addition of excess base causes denitrosylation. This base promoted loss of NO from the complex leads to the formation of [Fe^{II}(TPP*)(L)₂]. This process has been demonstrated using NMR titrations in Section 4.3.

Therefore, a complete NorBC model first requires optimization of the heme portion. In order to obtain a stable 6C complex in solution without excess base present, we have synthesized a series of iron-porphyrin NO compounds with covalently attached axial N-donor ligands

[Fe^{II}(TPP*)(NO)(L)] (L = pyridine or imidazole linker), and investigated their properties using several spectroscopic methods. These covalently attached N-donor linkers are supposed to increase the “local concentration” of base and this way, facilitate binding to the Fe(II)-NO center. Pyridine and imidazole tailed linkers with varying chain lengths and design have been synthesized to delineate the effect of chain length and rigidity on the base binding properties to the Fe(II)-NO center. This allows to a direct comparison to the binding affinities of different linkers with different carbon chains (number or design), and to obtain a better model for the six-coordinate species in solution. The binding affinity of these attached N-donor ligands to the iron(II)-NO center in these model complexes has been investigated using UV-vis, FT-IR, and EPR spectroscopy. These results are presented in Section 6.2. Furthermore, the obtained results shown in this section have been used to design a sophisticated model for the NorBC active site.

The synthesis and characterization of a complete model system for the NorBC active site is described in Section 6.3. This requires a sophisticated heme and a non-heme ligand assembly. Many synthetic models based on such an assembly have been used to explore the chemistry of CcO. (Figure 6.1.1).¹ However, not much insight into the fundamental chemistry of NorBC has been obtained. Recently, the Karlin group has shown that the ferrous heme/non-heme model system (using a tetradentate TPA linked porphyrin) shown in Figure 6.1.2 binds two molecules of NO, one at each metal center.² This is in agreement with the proposed mechanism for NorBC shown in Figure 1.4 (Chapter 1). Nevertheless, this complex is only considered as a structural model since it does not show any NorBC activity (NO reduction).

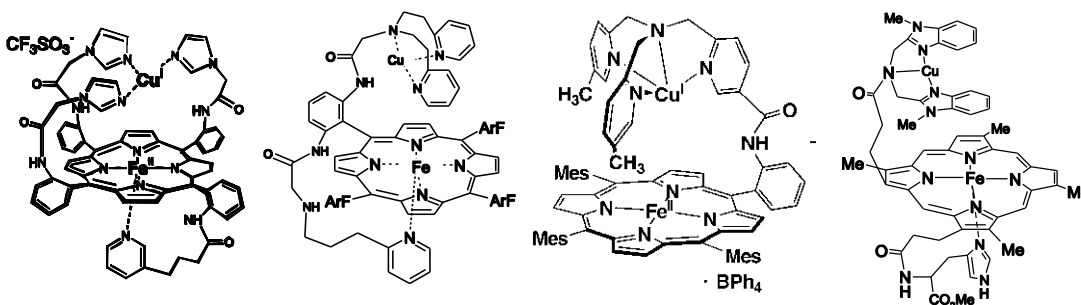


Figure 6.1.1. Model systems for cytochrome *c* oxidase (CcO) from the groups of Collman (left), Karlin (middle, left), Naruta (middle, right), and Casella (right).¹

In order to obtain a functional model system for NorBC, we have synthesized a new heme/non-heme ligand design that consists of a tridentate dipyridylamine ligand (MPBMPA) covalently attached to a fluoro-substituted porphyrin. The corresponding diiron-dinitrosyl complex has been investigated using UV-vis and FT-IR spectroscopy. To investigate the properties of the non-heme iron in NorBC, a non-heme iron(II)-NO complex using the TPA ligand has been synthesized. These studies are detailed in Section 6.3. Finally, a precursor compound of a six-coordinate iron-porphyrin NO complex with a linked non-heme iron ligand has also been synthesized.

This study is particularly useful for the comparison of the difference in reactivity between the five- and six-coordinate iron(II)-porphyrin NO complexes in solution, and how this relates to the NO reduction mechanism of NorBC.

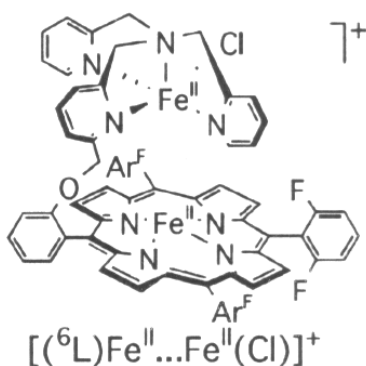


Figure 6.1.2. Model system used by Karlin and coworkers to prepare a dinitrosyl complex as a model for NorBC.²

References

- ¹ (a) Collman, J. P.; Rapta, M.; Bröring, M.; Raptova, L.; Schwenninger, R.; Boitrel, B.; Fu, L.; L'Her, M. *J. Am. Chem. Soc.* **1999**, *121*, 1387-1388. (b) Kopf, M.-A.; Karlin, K. D. *Inorg. Chem.* **1999**, *38*, 4922-4923. (c) Chishiro, T.; Shimazaki, Y.; Tani, F.; Tachi, Y.; Naruta, Y.; Karasawa, S.; Hayami, S.; Maeda, Y. *Angew. Chem.* **2003**, *115*, 2894-2897. (d) Franceschi, F.; Gullotti, M.; Monzani, E.; Casella, L.; Papaefthymiou, V. *Chem. Commun.* **1996**, 1645-1646.
- ² Wasser, I. M.; Huang, H.; Moënne-Loccoz, P.; Karlin, K. D. *J. Am. Chem. Soc.* **2005**, *127*, 3310-3320.

6.2. Synthesis, Electronic and Vibrational Properties of Iron-Porphyrin NO Complexes with Covalently Attached Axial N-Donor Ligands

6.2.1. Introduction

The interaction of Nitric oxide (NO) with ferrous heme centers in proteins results in several important biological functions such as denitrification,¹ neurotransmission, and vascular regulation.² In the bacterial denitrification process, NO is of major importance since it occurs as an intermediate in the reduction of nitrate to N₂. In this pathway, the N-N bond formation is facilitated by the reduction of NO to nitrous oxide (N₂O) at the heme/non-heme active site of the enzyme bacterial nitric oxide reductase (NorBC). In general, ferrous heme nitrosyls in biology could be either six-coordinate (6C) with NO bound *trans* to an amino acid residue such as histidine, or five-coordinate (5C) with no axial ligand. The presence or absence of the proximal ligand is vital in controlling the reactivity of the heme NO. For example, binding of NO to soluble guanylate cyclase (sGC) results in the formation of 5C ferrous heme NO due to breakage of the Fe-His bond.³ This process is associated with a major conformational change within the enzyme, and thus activates the enzyme to catalyze the cyclization of guanosine triphosphate (GTP) to cyclic guanosine monophosphate (cGMP); the latter is involved in the relaxation of vascular smooth muscle.³ The 6C heme NO with axially bound histidine is also present in the active site of NorBC. It has been suggested that histidine plays a critical role in the formation of the N-N bond in the reduction of two molecules of NO.⁴ Owing to the importance of heme NO biochemistry in living organisms, many five- and six-coordinate iron-porphyrin NO model compounds of type [Fe^{II}(TPP*)(NO)(L)] (L= N-donor or missing) have extensively been investigated as model systems for the corresponding proteins.⁵ In the 6C models, it has been shown that the proximal N-donor ligands are weakly bound to the Fe^{II}-NO center (free binding energy: -2 to -5 kcal/mole; cf. Section 4.2)⁶. Thus, a large excess of N-donor ligand has to be employed to form the 6C species in solution. However, excess base leads to facile denitrosylation to form [Fe^{II}(TPP*)(L)₂], a competitive side reaction. In order to investigate the reactivity and spectroscopic properties of the 6C complex in solution, a stable 6C species without the presence of excess base is necessary. Komatsku et al. synthesized the first stable 6C complex

in solution employing a picket fence porphyrin with a long chain alkyl imidazole linker covalently attached at the β -pyrrole position.⁷ This covalent attachment of the axial imidazole directly to the porphyrin periphery is supposed to increase the local base concentration by providing a large equilibrium constant for imidazole binding and supposedly prevents rupture of the Fe-Im bond. In order to test this strategy, we investigated the synthesis, electronic, and vibrational properties of a series of iron-porphyrin NO compounds with covalently attached proximal N-donor ligands [$\text{Fe}^{\text{II}}(\text{P})(\text{NO})(\text{L})$] (L = pyridine or imidazole linker). Linkers with varying chain lengths and designs have been synthesized to delineate the effect of chain length and rigidity on the base binding affinity to the Fe(II)-NO center. The molecular structures of the four different porphyrin ligands with covalently attached axial pyridine or imidazole linkers employed in this study are shown in Fig 6.2.1.

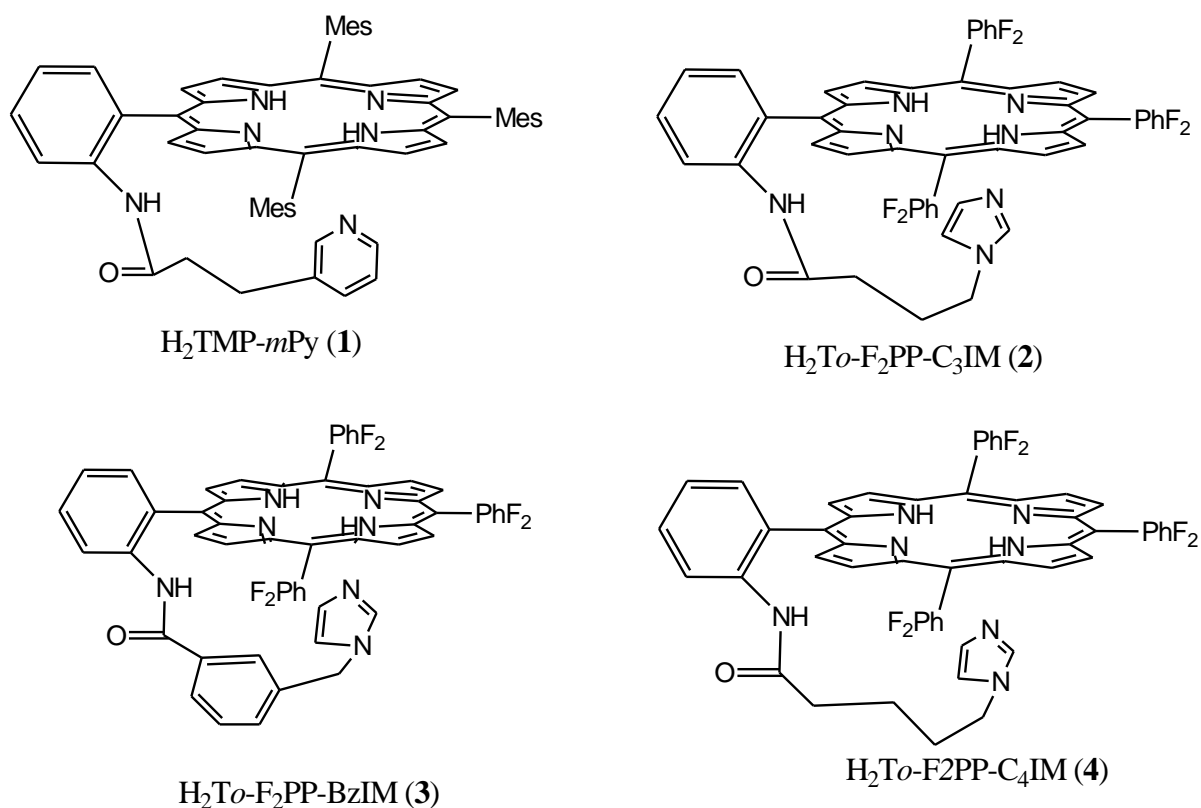


Figure 6.2.1. Molecular structures of free base porphyrins with appended linkers employed in this study.

6.2.2. Experimental Procedures

6.2.2.1 General

In general, reactions were performed applying inert Schlenk techniques. Infra red spectra were obtained on KBr disk or in chloroform solution on a Perkin-Elmer BX spectrometer. Proton magnetic resonance spectra were recorded on a Varian Inova 400 MHz and a Varian Mercury 300 MHz instrument. Electronic absorption spectra were obtained on a Analytical Jena Specord 600 instrument. Electron paramagnetic resonance spectra were recorded on a Bruker X-band EMX spectrometer.

6.2.2.2 Materials

All solvents and reagents were purchased and used as supplied except as follows. Toluene was distilled from sodium under argon. Dried and air free THF and n-hexane were obtained after passing through an MBraun solvent purification system. 1-Methylimidazole was vacuum distilled from KOH and degassed via five freeze-pump-thaw cycles. Nitric oxide (Air gas, USA) was purified by first passing through an ascarite II column (NaOH on silica gel) and then through a cold trap at -80°C to exclude higher nitrogen oxide impurities.

6.2.2.3 Syntheses

$\text{H}_2(\text{NO}_2)\text{TMPP}$, 5,10,15-Tris-(2,3,5-trimethyl-phenyl)-20-(2-nitro-phenyl)-porphyrin.

CHCl_3 (3.5 L) was added to a 4L three-necked round bottom flask, equipped with a condenser and an argon inlet port. To this, mesitaldehyde (4.8 mL, 0.04 mol), 2-nitrobenzaldehyde (4.083 g, 0.027 mol), and freshly distilled pyrrole (2.76 mL, 0.39 mol) were added. The solution was purged with argon for about 30 min and then 5 mL of BF_3 -etherate were added via a syringe. After one hour, *para*-chloranil (7.36 g) was added and the reaction mixture was gently refluxed for 90 min. The reaction was then stopped and allowed to cool to room temperature. Triethylamine (2 mL) was then added. After the reaction mixture was then cooled to room temperature, the solvent was removed using on a rotary evaporator. To this crude product, methanol (300 mL) was added to remove the impurities. A purple solid was collected via filtration. The obtained solid product was purified by column chromatography on silica using a $\text{CH}_2\text{Cl}_2/n$ -hexane solvent mixture (1:1 ratio). The second fraction was collected, yielding 1.5 g (22 %) of $\text{H}_2(\text{NO}_2)\text{TMPP}$.

^1H NMR (CD_2Cl_2 , 400 MHz): 8.78-8.58 (m, 8H, β -pyrrole), 8.50-8.45 (dd, 1H, nitrophenyl), 8.21-8.18 (dd, 1H, nitrophenyl); 7.89-7.98 (m, 2H, nitrophenyl); 7.3-7.26 (m, 6H, mesitylphenyl); 2.64 (s, 18H, *ortho*- CH_3); 1.88 (m, 9H, *para*- CH_3); -2.47 (s, 2H, NH pyrrole).

$\text{H}_2(\text{NH}_2)\text{TMPP}$, 5,10,15-Tris-(2,3,5-trimethyl-phenyl)-20-(2-amino-phenyl)-porphyrin.

$\text{H}_2(\text{NO}_2)\text{TPPH}_2$ (0.53 g, 0.67 mmol) was suspended in 30 mL of concentrated hydrochloric acid (36-38%). To this, SnCl_2 (1.278 g, 10 equivalent) was added and the resulting green colored heterogeneous reaction mixture was stirred overnight for about 14 hours. Then, the reaction mixture was poured into a 1 L beaker and cooled to 0°C using an ice bath, and then neutralized with NH_3 . The color of the suspension changed from green to brown upon neutralization. CH_2Cl_2 (170 mL) and water were added and the insoluble material was removed using filtration. The filtrate was collected and the organic layer containing the aminoporphyrin was separated and extracted several times with CH_2Cl_2 . The combined dichloromethane fractions were dried over anhydrous Na_2SO_4 , and the solvent was removed to yield the crude product. The desired product was then purified using column chromatography (silica, $\text{CH}_2\text{Cl}_2/n$ -hexane = 3:2). The obtained yield was 0.4 g (78 %). ^1H NMR (400MHz, CD_2Cl_2): 8.9-8.61 (m, 8H, β -pyrrole), 7.9-7.85 (dd, 1H, aminophenyl), 7.62-7.56 (m, 1H, aminophenyl); 7.29-7.25 (m, 6H, mesitylphenyl); 7.2-7.1 (m, 2H, aminophenyl); 3.58 (s, 2H, $-\text{NH}_2$); 2.63 (m, 18H, *ortho*- CH_3); 1.90 (m, 9H, *para*- CH_3); -2.53 (s, 2H, NH pyrrole).

$\text{H}_2\text{TMP}m\text{-Py}$ (1).

The aminoporphyrin $\text{H}_2(\text{NH}_2)\text{TMPP}$ (0.25 g, 0.33 mmol) was dissolved in 6 mL of DMF. To this, 1 mL of *N,N*-diethylaniline was added, followed by the addition of a solution of 3-(3'-pyridyl)propionic acid chloride in 3mL of DMF [prepared in situ by reacting 0.2 g of 3-(3'-pyridyl)propionic acid with 3 mL of SOCl_2], and then stirred for 4 hours at room temperature. The excess SOCl_2 and the solvent were removed under vacuum. The residue obtained was dissolved in CH_2Cl_2 and washed several times with distilled water. The solution was then dried with Na_2SO_4 and the solvent was removed using a rotary evaporator. The desired product was purified using column chromatography (silica, $\text{CH}_2\text{Cl}_2/\text{CH}_3\text{OH}$ = 99:1). Yield (0.20 g, 68 %)

^1H NMR (400MHz, CD_2Cl_2): 9.32 (s, 1H, NH-CO); 8.68 (m, 8H, β -pyrrole), 8.20 (d, 1H, pyridyl); 7.92 (m, 2H, aminophenyl); 7.8-7.4 (m, 2H, pyridylphenyl); 7.8-7.74 (m, 1H, aminophenyl); 7.5 (m, 1H, pyridyl); 7.25 (s, 6H, mesitylphenyl); 2.50 (m, 18H, *ortho* - CH_3); 2.4 (t, 2H, - CH_2 -Py); 1.90 (m, 9H, *para* - CH_3); 1.6 (t, 2H, - CH_2), 0.9 (t, 2H, - CH_2), -2.3 (s, 2H, NH pyrrole).

MS (MALDI) for $\text{C}_{61}\text{H}_{57}\text{N}_6\text{O}$: Calcd: 889, found: 889.

[Fe(TMP-*m*Py)(Cl)]

0.15 g (0.17 mmol) of $\text{H}_2\text{TMP-}m\text{Py}$ (**1**) were stirred in 10 mL of dry and air free THF. Anhydrous FeCl_2 (0.21 g, 1.7 mmol) was then added and the resulting reaction mixture was refluxed at 60 °C under an argon atmosphere for 1 hour. The reaction was then stopped and the solvent was removed under reduced pressure. The obtained residue was chromatographed on silica gel using 0.5% methanol in CH_2Cl_2 . The metallated porphyrin fraction was collected and the solvent was then removed using a rotary evaporator. The obtained product was dried; yield 0.11 g, 66 %. ^1H NMR (CDCl_3 , 400 MHz): 80 (m, 8H, β -pyrrole).

[Fe(TMP-*m*Py)(NO)]

0.05 g (0.05 mmol) of [Fe(TMP-*m*Py)(Cl)] were placed in a 100 mL Schlenk flask and freshly distilled CHCl_3 (8 mL) and CH_3OH (0.5 mL) were added. NO gas was then passed through this solution, and the resulting solution was stirred for one hour. *n*-hexane (10 mL) was slowly added to the reaction mixture, which was then stored in a freezer (-22°C) for 3 days. The resulting precipitate was filtered off using a fine pore size Schlenk filter funnel. The yield of the product obtained was very low 11 mg (22 %), and contained some impurities. FT-IR (cm^{-1}): $\nu(\text{NO}) = 1694 \text{ cm}^{-1}$.

$\text{H}_2\text{F}_6(\text{NO}_2)\text{TPP}$, 5,10,15-Tris-(2,6-difluoro-phenyl)-20-(2-nitro-phenyl)-porphyrin (**5**).⁸

To a 2 L Schlenk flask equipped with a magnetic stir bar, 2,6-difluorobenzaldehyde (11.52 g, 0.08 moles) and 2-nitrobenzaldehyde (4.083 g, 0.27 moles), 4 mL of ethanol, and 900 mL of dry CH_2Cl_2 were added. The solution was stirred and degassed with argon for several minutes, and then pyrrole (7.25 g, 0.108 moles) was added. The light yellow solution was stirred for 15 minutes under an argon atmosphere, followed by the addition of $\text{BF}_3\text{-OEt}_2$ (4 mL), which led to a change of the solution color to red. The solution was then stirred for an

additional 4 hours. Then, 8 mL of triethylamine were added, followed by 12 g of 2,5-dichloro-3,5-dicyanobenzoquinone (DDQ). The resulting reaction mixture was stirred overnight and the obtained insoluble material was filtered off using a medium porosity filter. The filtrate was collected and the solvent was removed in vacuum. The crude solid product obtained this way was washed with *n*-hexane for several times and purified by column chromatography on silica using a CH₂Cl₂/*n*-hexane solvent mixture (1:1 ratio). The second fraction (R_f = 0.3) was collected, yielding 1.52 g (5%) of H₂F₆(NO₂)TPP as purple solid. ¹H NMR (CDCl₃, 400 MHz): 8.9-8.71 (m, 8H, β-pyrrole), 8.50-8.45 (d, 1H, nitrophenyl), 8.29-8.25 (m, 1H, nitrophenyl); 8.03-7.95 (m, 2H, nitrophenyl); 7.90-7.79 (m, 3H, *para* fluorophenyl); 7.45-7.37 (m, 6H, *meta* fluorophenyl); -2.80 (s, 2H, NH pyrrole).

H₂F₆(NH₂)TPP, 5,10,15-Tris-(2,6-difluoro-phenyl)-20-(2-amino-phenyl)-porphyrin (**6**).⁸

H₂F₆(NO₂)TPP (0.5 g, 0.65 mmol) was suspended in 30 mL of concentrated hydrochloric acid (36-38 %). To this, SnCl₂ (0.62 g, 3.25 mmol) was added and the resulting green colored heterogeneous reaction mixture was stirred overnight for about 14 hours. Then, the reaction mixture was poured into a 1 L beaker and cooled to 0 °C using an ice bath, and then neutralized with Na₂CO₃. The color changed from green to brown upon neutralization. CH₂Cl₂ (200 mL) and water were added, and the insoluble material was removed using filtration. The filtrate was collected, and the organic layer containing the aminoporphyrin was separated and extracted several times with CH₂Cl₂. The combined dichloromethane fractions were dried over anhydrous Na₂SO₄. The desired product was then purified using column chromatography (silica, CH₂Cl₂/*n*-hexane = 4:1, R_f = 0.6). The obtained yield was 0.38 g (79 %). ¹H NMR (400MHz, CD₂Cl₂): 8.89-8.83 (m, 8H, β-pyrrole), 7.90-7.83 (m, 4H, aminophenyl and *para* fluorophenyl), 7.63-7.57 (m, 1H, aminophenyl); 7.39-7.44 (m, 6H, *meta* fluorophenyl); 7.18-7.15 (m, 2H, aminophenyl); -2.80 (s, 2H, NH pyrrole).

Sodium imidazolate.⁹

To a 100 mL Schlenk flask, 10.8 g (0.16 moles) of imidazole and THF (40 mL) were added under an argon atmosphere. Then, 6.33 g (0.16 mol) of sodium hydride (60% suspension in mineral oil) was added slowly. The solution was allowed to stir until the evolution of the H₂ gas had ceased (4-5 hours). The reaction was then stopped and the solid was collected by

filtration, washed with THF, and dried in a vacuum desiccator for 3 days. Yield (11.4 g, 80%). ¹H NMR (400 MHz, D₂O): 7.8 (s, 2H); 7.13 (s, 1H).

4-(*N*-imidazolyl)butyronitrile.⁹

4-bromobutyronitrile (5 g, 0.03 mol) was dissolved in 30 mL of THF (dry and air free) and kept under an argon atmosphere. Sodium imidazolate (3.1 g, 0.03 mol) was added and the resulting solution was stirred for 1 day. The solution was then exposed to air and filtered. The solid obtained this way was washed with 10 mL of ACS grade CHCl₃. All solutions were then combined, and the solvent was removed using a rotary evaporator. The crude product (a thick viscous liquid) was purified by vacuum distillation. The fraction collected at 160° C under 1 mbar atmosphere was the desired product. Yield (3.3 g, 73%). ¹H NMR (400 MHz, CD₂Cl₂): 7.52 (s, 1H-CH₂Im); 7.12 (t, 1H, Im); 7.08 (t, 1H, Im); 4.18 (t, 2H, CH₂Im); 2.4 (t, 2H, CH₂CN); 2.1 (quintet, 2H, CH₂-CH₂CN).

4-(*N*-imidazolyl)butyric acid hydrobromide (7).⁹

4-(*N*-imidazolyl)butyronitrile (3 g, 0.02 mol) was dissolved in 10 mL of ethanol. To this solution, 5.5 g of KOH in 5 mL of distilled water were added. The solution was homogenized by adding more ethanol (5 mL) to the reaction mixture, and then refluxed for 5 hours. Hydrobromic acid (48%) was then added until the pH reached ~ 4, causing KBr to precipitate. The KBr was filtered off using a medium pore size filter funnel, and the obtained solution was evaporated to dryness. The solid was dried at 100° C using a P₂O₅ chamber, affording 3.8 g (76%) of the desired product. ¹H NMR (400 MHz, D₂O): 8.77 (s, 1H, Im); 7.54 (t, 1H, Im); 7.48 (t, 1H, Im); 4.31 (t, 2H, -CH₂Im); 2.46 (t, 2H, -CH₂COOH), 2.21 (quintet, 2H, -CH₂-CH₂COOH).

H₂To-F₂PP-C₃IM (2).

4-(*N*-imidazolyl)butyric acid hydrobromide (0.18 g, 0.4 mmol) was stirred in 5 mL of dry and air free dimethylformamide (DMF). The solution was cooled to 0° C using an ice bath. A solution of 35 mg (0.3 mmol) SOCl₂ in 2 mL of DMF was then added. The solution was stirred and allowed to warm up to room temperature under an argon atmosphere. After 30 minutes, a solution of F₆(NH₂)TPPH₂ (0.1 g, 0.135 mmol) in 5 mL of DMF was added and the resulting green solution was stirred overnight in the dark under argon. The reaction was

then stopped by pouring the solution into 20 mL of benzene in the dark. The resulting solution was washed with 2 X 20 mL of Na₂CO₃, and 20 mL of water, and then dried over Na₂SO₄. The solvent was removed under reduced pressure and the residue obtained was column purified on silica gel (CH₂Cl₂/CH₃OH= 95:5) to give the desired C₃ imidazole linked porphyrin ligand **2** (0.045 g, 38 %).

[Fe(T_o-F₂PP-C₃IM)(Cl)] (8).

0.03 g (0.034 mmol) of H₂T_o-F₂PP-C₃Im (**2**) was stirred in 8 mL of dry and air free THF. Anhydrous FeCl₂ (0.043g, 0.34 mmol) was then added and the resulting reaction mixture was refluxed under an argon atmosphere for 1 hour. The reaction was then stopped and the solvent was removed under reduced pressure. The obtained residue was chromatographed on silica gel using 3% methanol in CH₂Cl₂. The metallated porphyrin fraction was collected, and the solvent was then removed using a rotary evaporator. The product obtained was finally dried; yield 0.023 g (70 %). FT-IR in KBr (cm⁻¹): ν(CO) = 1700. UV-vis (nm) in CH₂Cl₂: 349, 415, 504, 572, and 649.

[Fe(T_o-F₂PP-C₃IM)(NO)] (9).

To a solution of the iron(III)-porphyrin **8** (0.02 g, 0.02 mmol) in 10 mL of freshly distilled CHCl₃ and 0.5 mL of CH₃OH, excess nitric oxide was added and the resulting solution was stirred for one hour. *n*-hexane (15ml) was slowly added to the reaction mixture, which was then stored in a freezer (-20°C) for 1 day. The resulting precipitate was filtered off and obtained compound was stored inside a glove box. The IR spectrum shows the NO stretching band at 1686 cm⁻¹, indicative of the formation of **9**. Yield: 0.010 g (52 %): FT-IR in KBr (cm⁻¹): ν(NO) = 1686.

H₂T_o-F₂PP-BzIM (3).¹⁰

α-bromotoluic acid (0.1 g, 4.64 mmol) and an excess thionyl chloride (1 mL) in methylene chloride (3 mL) were refluxed under an argon atmosphere. After 40 minutes, the evolution of gas ceased. The excess SOCl₂ and CH₂Cl₂ were removed in vacuo to yield the crude acid chloride as a yellow solid. A mixture of the porphyrin H₂F₆(NH₂)TPP (0.04 g, 0.054 mmol) and *α*-bromotoluic acid chloride in CH₂Cl₂ (10 mL) was then refluxed for 2 hours under an argon atmosphere. Subsequently, sodium imidazolite (50 mg, 1 equivalent) in CH₃CN (13

mL) was added to the reaction mixture at once. The mixture was heated to reflux for an additional 1.30 hours. After the reaction was complete, the solution was diluted with water (8 mL). The organic layer was separated and successively extracted with 5% HCl (40 mL), saturated NaHCO₃ (40 mL), and water (30 mL). Finally, the organic layer was dried over Na₂SO₄, and evaporated to dryness. The product was purified on silica gel using column chromatography with 5% MeOH in CH₂Cl₂ as eluent. Yield: 30 mg (60 %). MS (MALDI) for C₅₄H₃₄N₇F₆O; Cald: 922, found: 922.

[Fe(*To*-F₂PP-BzIM)(Cl)] (10)

0.03 g of H₂*To*-F₂PP-BzIM (**2**) were stirred in 10 mL of dry and air free THF. Anhydrous FeCl₂ (0.39g) was then added, and the resulting reaction mixture was refluxed under an argon atmosphere for 1 hour. The reaction was then stopped and the solvent was removed under reduced pressure. The obtained residue was chromatographed on silica gel using 5% methanol in CH₂Cl₂. The metallated porphyrin fraction was collected, and the solvent was removed using a rotary evaporator. The product obtained was finally dried. Yield: 27 mg (82%). FT-IR in KBr (cm⁻¹): 1684 (ν_{CO}).

[Fe(*To*-F₂PP-BzIM)(NO)] (11)

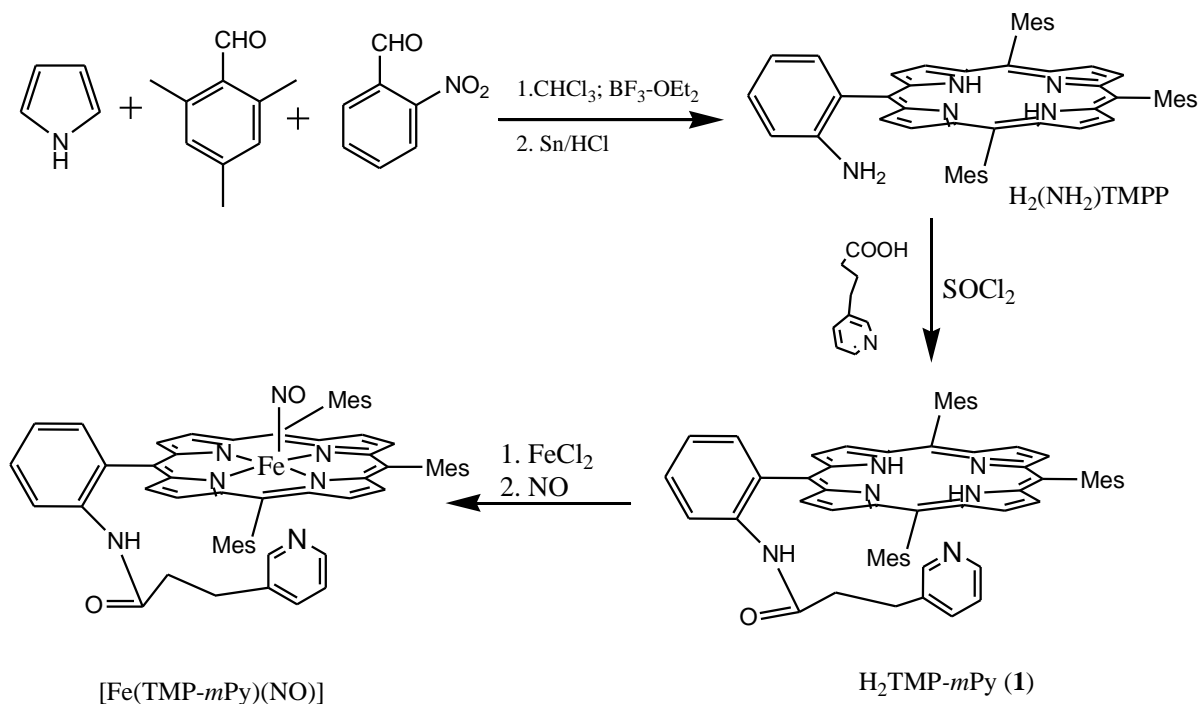
To a solution of the iron(III)-porphyrin **10** (0.02 g, 0.02 mmol) in 10 mL of freshly distilled CHCl₃ and CH₃OH (0.5 mL), excess nitric oxide was added, and the resulting solution was stirred for one hour. *n*-hexane (15ml) was slowly added to the reaction mixture, which was then stored in a freezer (-20 °C) for 1 day. The resulting precipitate was filtered off using a fine pore size schlenk filter funnel, and the obtained compound was stored inside a glove box. The IR spectrum shows the NO stretching band at 1644 cm⁻¹, indicative of the formation of **11**. Yield: 14 mg (70 %).

H₂*To*-F₂PP-C₄IM (4**), [Fe(*To*-F₂PP-C₄IM)(Cl)], and [Fe(*To*-F₂PP-C₄IM)(NO)]**

Preparation of H₂*To*-F₂PP-C₄IM was performed by the same method as described for **3**, but using 5-bromopentanoic acid in place of α-bromotoluic acid to build the alkyl chain. Iron insertion into H₂*To*-F₂PP-C₄IM and the synthesis of [Fe(*To*-F₂PP-C₄IM)(NO)] also follows the same procedures as described for **10** and **11**, respectively.

6.2.3. Results and Discussion

6.2.3.1. Porphyrin ligands with the *meta*-pyridyl linker and the C₃-alkyl imidazole linker: synthesis, characterization and base binding properties.



Scheme 6.2.1. Synthesis of the [Fe(TMP-*m*Py)(NO)] complex.

The covalent attachment of the pyridyl group to the porphyrin periphery was achieved by a simple coupling reaction of the pyridyl arm, 3-(3'-pyridyl)propionyl chloride, with tri(mesitylphenyl)mono(aminophenyl)porphyrin in the presence of SOCl₂ (Scheme 6.2.1). Iron metallation was then carried out using FeCl₂. The interaction of the resulting compound, [Fe(TMP-*m*Py)(Cl)], with NO in solution was investigated using EPR spectroscopy. EPR spectroscopy is a very powerful technique to determine the electronic structures of ferrous heme NO compounds. Five-coordinate and six-coordinate Fe-NO complexes exhibit three *g* values, *g*(min), *g*(mid) and *g*(max). The obtained *g* values and hyperfine splittings are very different for the five- and six-coordinate species (cf. Chapter 4, Section 4.2)¹¹ For example, the five-coordinate iron(II)-porphyrin NO complex [FeTPP(NO)] shows *g* values of 2.013, 2.066 and 2.106 with a well-resolved three line ¹⁴N hyperfine splitting on the smallest *g*

value $g(\text{min})$. On the contrary, a nine line hyperfine splitting (triplet of triplets) is observed on $g(\text{mid})$ for the corresponding six-coordinate complex $[\text{Fe}(\text{TPP})(\text{NO})(\text{MI})]$ (for details see Chapter 4, Section 4.2).¹² The EPR spectrum of the *m*-pyridyl linker NO complex $[\text{Fe}(\text{TMP-mPy})(\text{NO})]$ in glassy toluene at 77 K shows the characteristic 5C iron-porphyrin NO spectrum with three line ^{14}N hyperfine on $g(\text{min})$. In addition, the FT-IR spectrum of $[\text{Fe}(\text{TMP-mPy})(\text{NO})]$ presented in Figure 6.2.2 shows $\nu(\text{NO})$ at 1694 cm^{-1} which is virtually identical to the values observed for 5C species. These observations indicate that the pyridyl arm is in fact not coordinated to the Fe-NO unit. These results are also in agreement with the very weak binding affinity of pyridine to Fe-NO observed in the axial ligation titration experiments, monitored by UV-vis spectroscopy (see Chapter 4, Section 4.3).⁶ We concluded that the covalently attached pyridine linker leads to the formation of only 5C species in solution, which suggests a dominant base-off reaction upon NO binding. Hence, the concept of “increased local concentration” of base discussed in the literature is not valid in this case. Even though the pyridine linker is covalently attached to the porphyrin, it fails to bind to the Fe(II)-NO center.

In an effort to synthesis a stable 6C species in solution, a strategy involving the attachment of alkyl chained imidazole to a fluoro-substituted phenylporphyrin was developed. This strategy is based on the findings from our binding studies of different N-donors to $[\text{Fe}(\text{TPP}^*)(\text{NO})]$ type complexes as described in Section 4.3, which indicate that only the combination of the weakly electron withdrawing tetra(*ortho*-difluorophenyl)porphyrin (*To*-F₂PP) ligand and 1-methylimidazole (MI) leads to a sufficient binding constant that ensures coordination of the axial ligand in solution. As shown in Figure 6.2.3, pure $[\text{Fe}(\text{To-F}_2\text{PP})(\text{MI})(\text{NO})]$ shows in fact binding of MI in benzene solution, which is very unusual. Therefore, the ligand H₂*To*-F₂PP-C₃Im was synthesized by condensing 4-*N*-imidazolylbutyric acid hydrobromide (imidazole arm) with H₂F₆(NH₂)TPP. Iron insertion and nitric oxide reaction were then carried out to afford complex **9** as shown in Scheme 6.2.2.

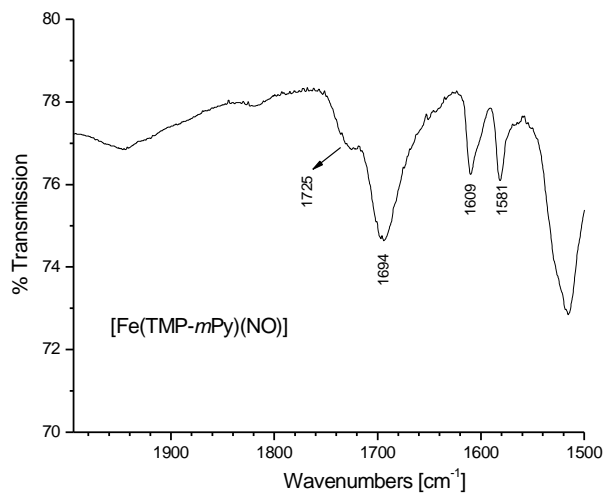


Figure 6.2.2. FT-IR spectrum of [Fe(TMP-*m*Py)(NO)].

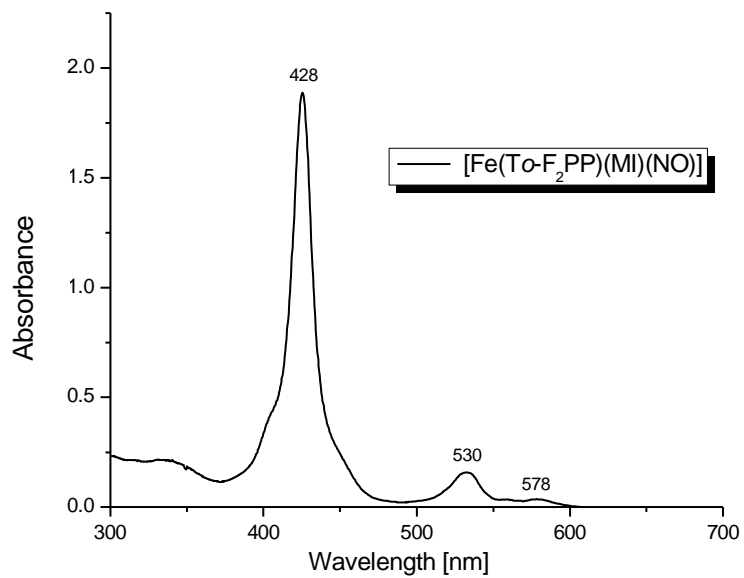
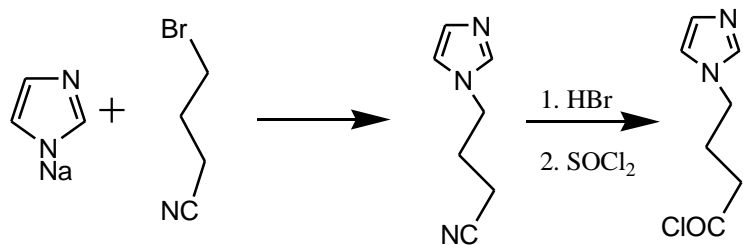
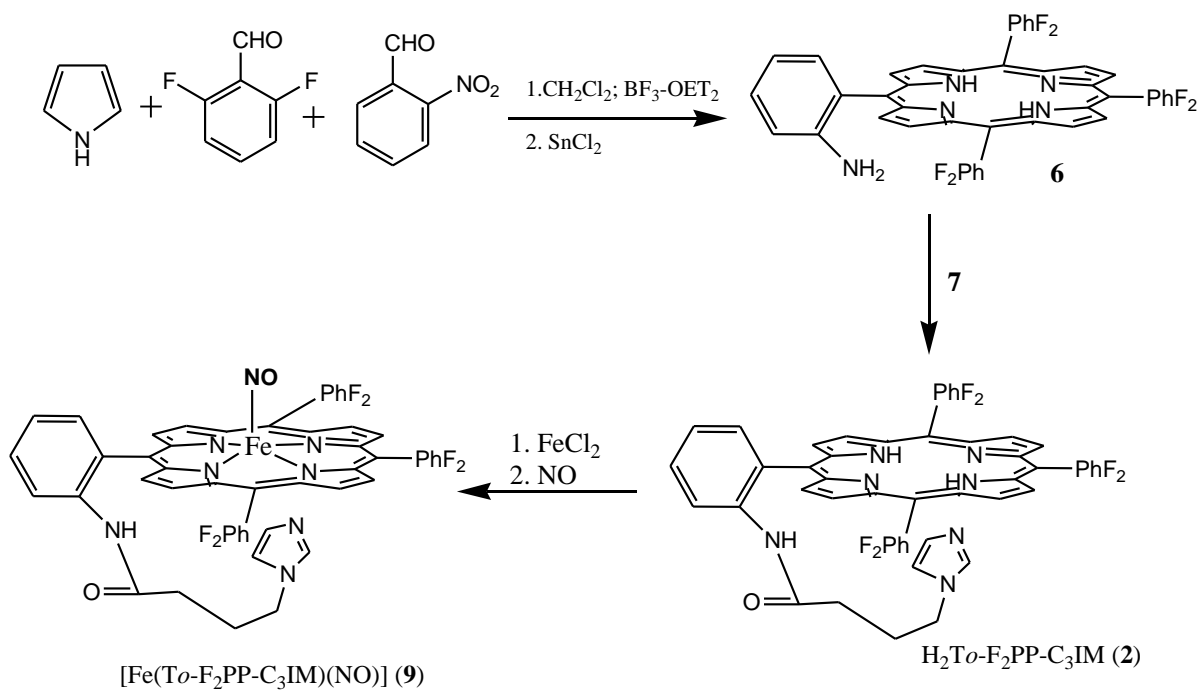


Figure 6.2.3. UV-vis spectrum of pure [Fe(To-F₂PP)(MI)(NO)] in benzene showing the characteristic 6C spectrum.

A)



(B)



Scheme 6.2.2. Synthesis of the [Fe(To-F₂PP-C₃IM)(NO)] complex (9)

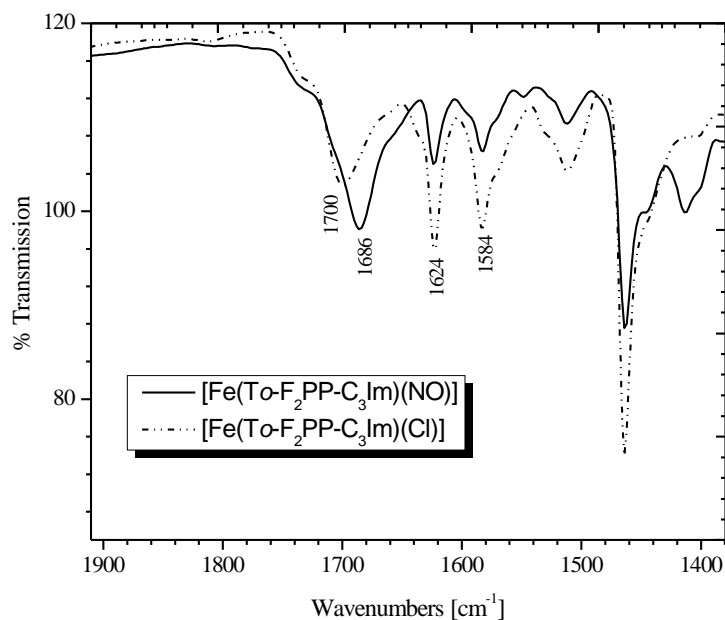


Figure 6.2.4. FT-IR spectrum of $[\text{Fe}(\text{To-F}_2\text{PP-C}_3\text{Im})(\text{Cl})]$ and the corresponding NO complex $[\text{Fe}(\text{To-F}_2\text{PP-C}_3\text{Im})(\text{NO})]$

Figure 6.2.4 shows the FT-IR spectrum of $[\text{Fe}(\text{To-F}_2\text{PP-C}_3\text{MI})(\text{Cl})]$ and $[\text{Fe}(\text{To-F}_2\text{PP-C}_3\text{MI})(\text{NO})]$ in comparison. Bands at 1624 cm^{-1} and 1584 cm^{-1} are assigned as $\nu(\text{C-C})$ stretching modes of the aminophenyl and fluorophenyl rings.¹³ This is obvious by comparison with the IR spectrum of $\text{H}_2\text{F}_6(\text{NH}_2)\text{TPP}$ (see Figure 6.2.5). A band is observed in $[\text{Fe}(\text{To-F}_2\text{PP-C}_3\text{IM})(\text{Cl})]$ at 1700 cm^{-1} which is assigned as $\nu(\text{C=O})$ of the amide group. The NO complex, $[\text{Fe}(\text{To-F}_2\text{PP-C}_3\text{IM})(\text{NO})]$ (**9**), shows a broad intense band at 1686 cm^{-1} . This mode is assigned to a superposition of $\nu(\text{C=O})$ and $\nu(\text{N-O})$. Therefore, $\nu(\text{N-O})$ is very similar in energy compared to the 5C iron-porphyrin NO complexes. This seems to indicate that this complex is also five-coordinate. More insight is available from UV-vis absorption spectroscopy. As indicated in Chapter 4, UV-vis spectroscopy is a useful technique to distinguish between 5C and 6C ferrous heme NO complexes. The absorption spectra of the five-coordinate iron porphyrin NO complexes exhibit Soret absorption maxima at 400-407 nm with a shoulder around 470 nm.

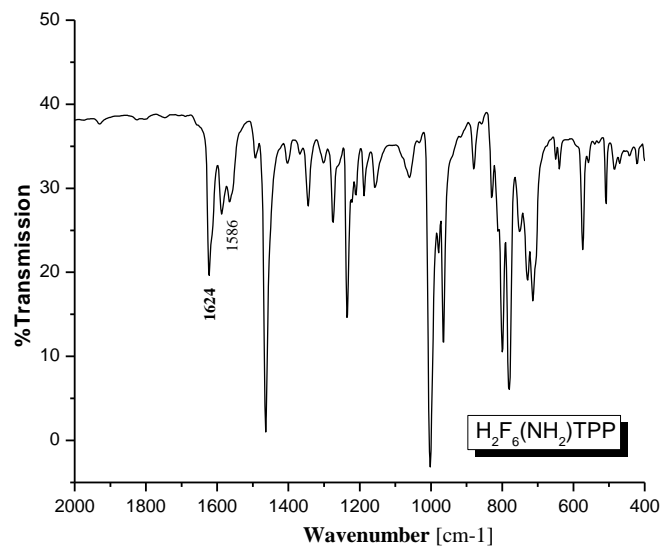


Figure 6.2.5. FT-IR spectrum of $\text{H}_2\text{F}_6(\text{NH}_2)\text{TPP}$.

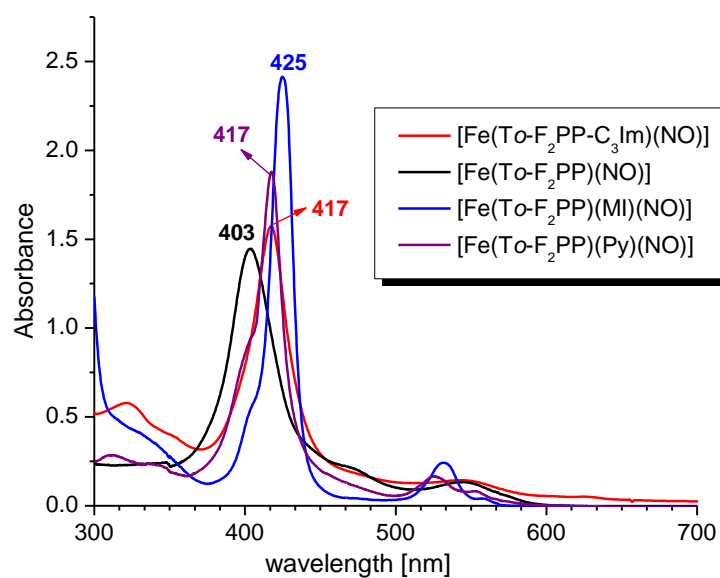


Figure 6.2.6. Electronic absorption spectra of iron(II)-porphyrin NO complexes.

On the other hand, the corresponding six-coordinate complexes with relative strongly binding axial ligand 1-methylimidazole show the Soret maximum red shifted to 425 nm. The weaker binding pyridine ligand, on the other hand, shows a smaller shift of the Soret band to about 417 nm.⁶ UV-vis absorption spectra of iron(II)-porphyrin NO complexes are shown below in

Figure 6.2.6. In comparison, the electronic absorption spectrum of $[\text{Fe}(\text{To-F}_2\text{PP-C}_3\text{Im})(\text{NO})]$ (**9**) measured in toluene at room temperature shows the Soret band maximum at 417 nm, which is similar to free pyridine coordination to $[\text{Fe}(\text{TPP})(\text{NO})]$ and $[\text{Fe}(\text{To-F}_2\text{PP})(\text{NO})]$ determined from the axial ligation studies presented in Chapter 4. The lack of a broad absorption band between 400 - 407 nm and shoulder around 470 nm confirms that there is no 5C species present in the solution. In summary, these observations (IR and UV-vis) indicate a weak binding of the C₃ imidazole linker to the Fe-NO center.

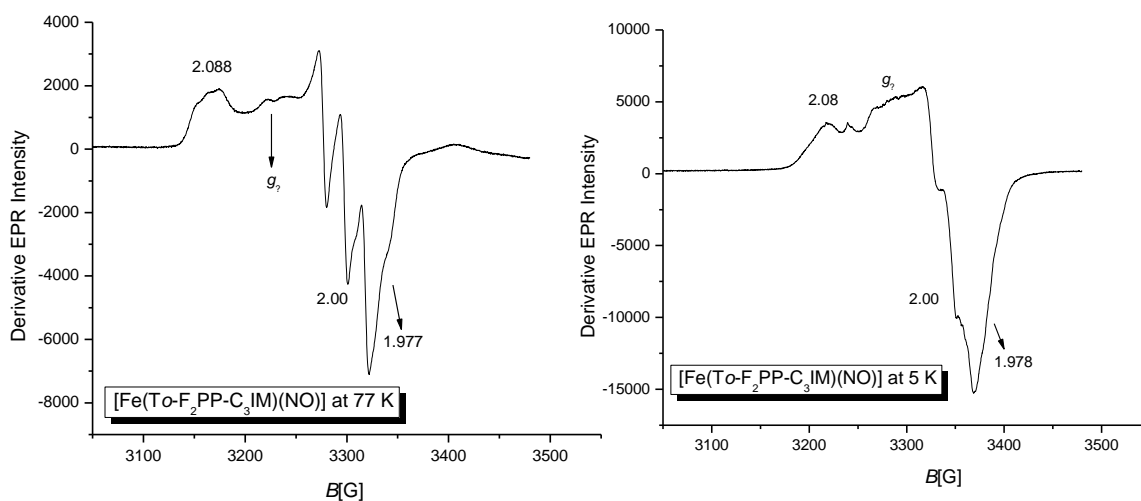


Figure 6.2.7. EPR spectra of $[\text{Fe}(\text{To-F}_2\text{PP})(\text{NO})(\text{MI})]$ (**9**) in frozen DMSO at 77 K (left) and at 5 K (right).

This result is further confirmed by EPR spectroscopy. Figure 6.2.7 depicts the EPR spectrum of **9** in glassy DMSO at 77 K (left) and at liquid helium temperature (right). The spectrum at 77 K, exhibits strong ^{14}N hyperfine lines of NO, plus unresolved hyperfine couplings of the axial IM ligand on $g(\text{mid})$. The g values are obtained at 1.977, 2.00 and 2.088. More insight is available from the low temperature (liquid helium) spectra shown in Figure 6.2.6, right. Very small hyperfine splittings of the IM ligand are detectable, indicative of a very weak binding of IM to Fe(II). Based on the FT-IR, UV-vis and EPR data obtained on complex **9**, it is concluded that the interaction of the C₃ imidazole arm with the Fe-NO center is weak. This is somewhat surprising, since compound $[\text{Fe}(\text{To-F}_2\text{PP})(\text{NO})(\text{MI})]$ shows strong binding of MI to Fe(II). There are two possible reasons for this apparent difference: (a) the alkyl chain is

too short to allow for a good interaction of IM with the iron(II) or (b) the dynamic motion of the phenyl rings (Ph-C) rotations leads to a constant alkyl chain motion in solution, which prevents effective binding of the imidazole ligand to Fe-NO. Thus, a good model for a six-coordinate heme nitrosyl has not been obtained using either the pyridyl or the C₃ imidazole linker. To rule out the effect of coordinating solvent DMSO, we have recorded EPR of the five-coordinate [Fe(TPP)(NO)] in DMSO and toluene mixture (1:1), to check whether DMSO binds to the Fe(II)-NO. The corresponding EPR spectrum is shown in Figure 6.2.8. The spectrum is identical to the five-coordinate spectrum obtained in pure toluene, which is a non-coordinating solvent. In addition, UV-vis spectrum of [Fe(TPP)(NO)] measured in DMSO shows the characteristic 5C spectrum with Soret maximum at 409 nm. Therefore, it is confirmed that the obtained EPR and UV-vis spectra of [Fe(*To*-F₂PP-C₃IM)(NO)] actually show IM binding to the Fe(II)-NO center.

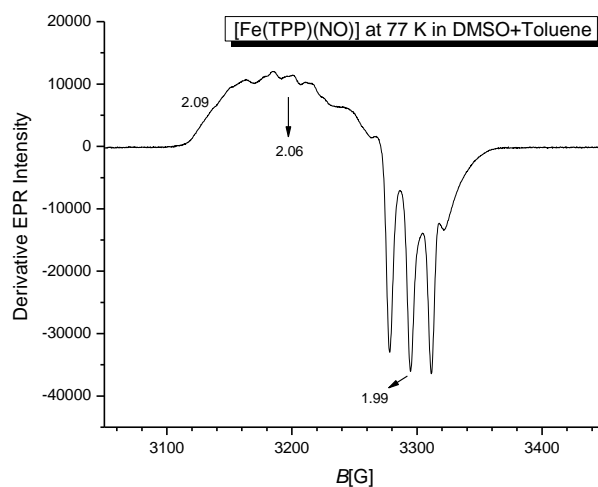
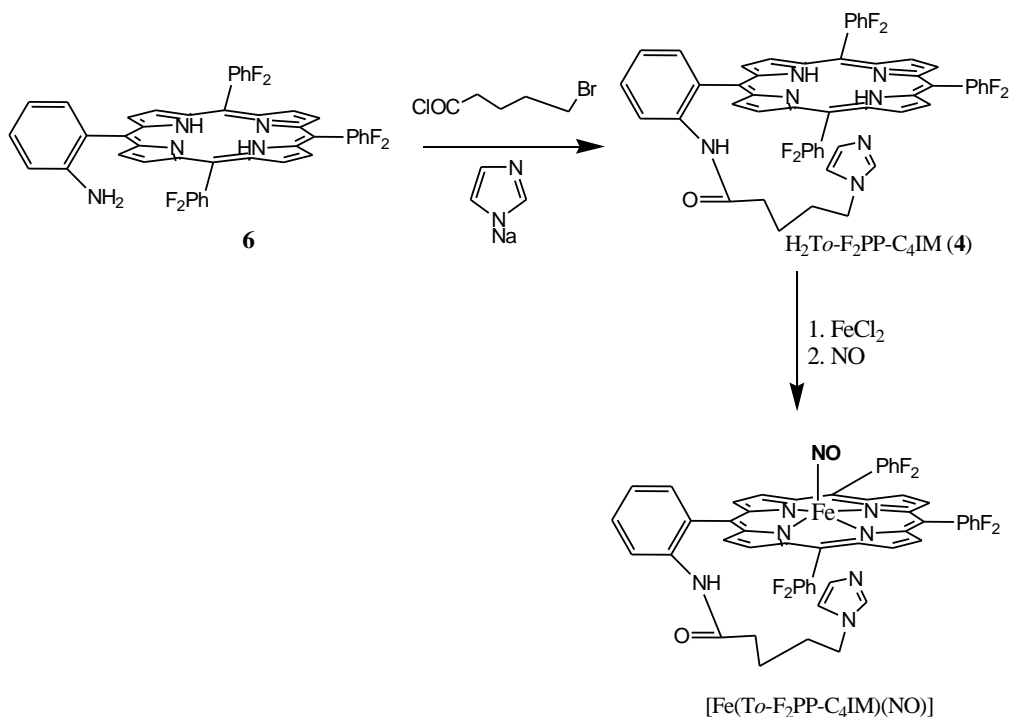


Figure 6.2.8. EPR spectrum of [Fe(TPP)(NO)] in frozen Toluene and DMSO (1:1 solvent mixture) at 77 K.

6.1.3.2. Porphyrin ligands with the C₄ chain imidazole linker and the benzyl imidazole linker: synthesis, characterization, and base binding properties.

In order to determine the influence of the carbon chain length on the base binding properties of the imidazole linked porphyrin NO complexes, we synthesized H₂*To*-F₂PP-C₄IM (**4**). This ligand contains one CH₂- group more in the alkyl chain compared to **2**. This allows to directly compare the binding affinity of different linkers varying only in carbon chain

lengths, and eventually to obtain a better model for the six-coordinate species in solution. The synthesis of $H_2To-F_2PP-C_4IM$ (**4**) was carried out by treatment of bromopentanoic acid chloride with $H_2F_6(NH_2)TPP$, and subsequent addition of sodium imidazolate. Column separation and purification using silica gel then yields pure **4**. Further reaction with $FeCl_2$ and NO gives the corresponding NO complex $[Fe(To-F_2PP-C_3Im)(NO)]$. The synthetic route is illustrated in Scheme 6.2.3.



Scheme 6.2.3. Synthesis of $[Fe(To-F_2PP-C_4IM)(NO)]$ complex.

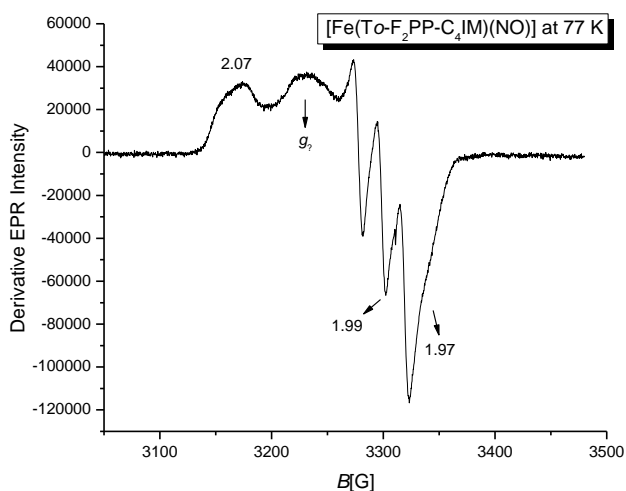
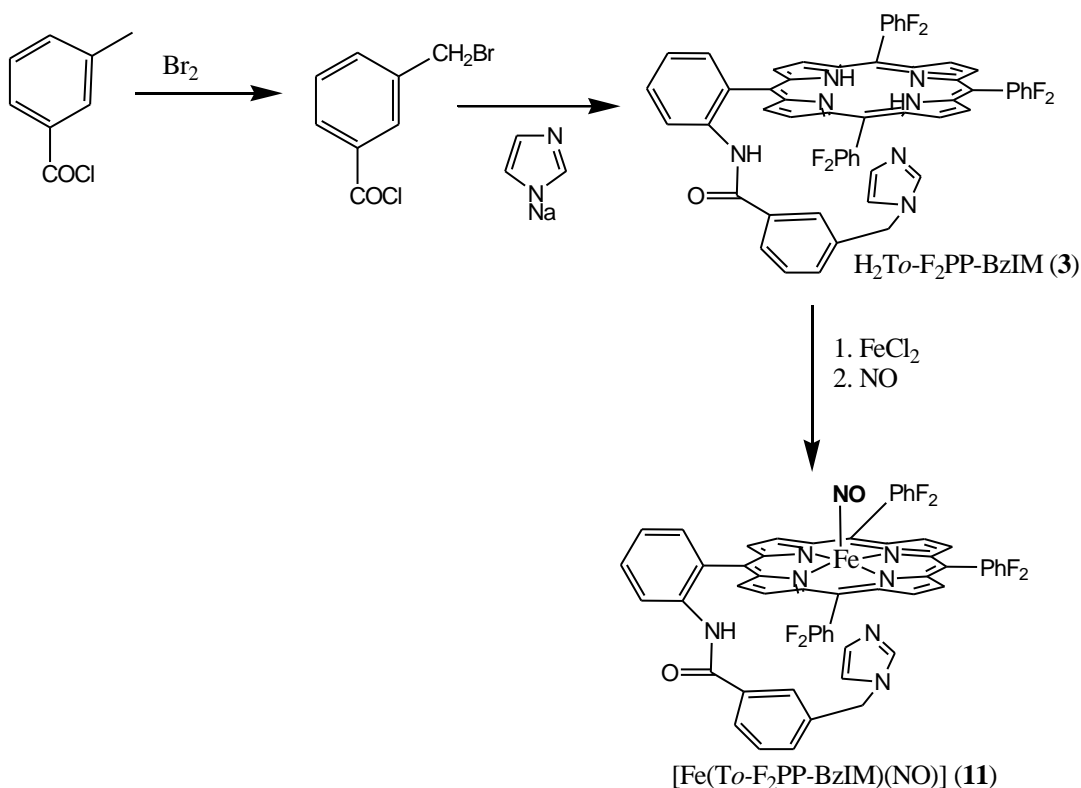


Figure 6.2.9. EPR spectrum of $[Fe(To-F_2PP-C_4IM)(NO)]$ in frozen DMSO at 77K.

The base binding affinity of the linked imidazole to Fe(II) in $[\text{Fe}(\text{To-F}_2\text{PP-C}_4\text{IM})(\text{NO})]$ was investigated using UV-vis and EPR spectroscopy. The obtained electronic and EPR spectra again show weak binding of the C_4 alkyl chained imidazole linker in $[\text{Fe}(\text{To-F}_2\text{PP-C}_4\text{IM})(\text{NO})]$. In fact, the spectra are virtually identical to those of the C_3 linker compound **9**. The EPR spectrum of $[\text{Fe}(\text{To-F}_2\text{PP-C}_4\text{Im})(\text{NO})]$ in DMSO is shown in Figure 6.2.9. Hence, this demonstrates that the length of the alkyl chain in C_3 linker **9** is not the reason for the weak binding of the linked IM ligand to Fe(II). In the next step, it is therefore probed whether a less floppy linker would improve the binding.

In an effort to construct a more rigidly linked porphyrin system to finally obtain a stable six-coordinate compound in solution, porphyrin ligand $\text{H}_2\text{To-F}_2\text{PP-BzIM}$ (**3**) was designed. This ligand is based on a fluoro-substituted porphyrin periphery with an attached benzyl imidazolyl arm. The benzyl group constitutes to a rigid spacer for the attached imidazole to bind to the Fe(II)-NO unit, and is less floppy compared to the alkyl imidazole linker applied before.



Scheme 6.2.4. Synthesis of the iron(II)-NO complex of the benzylimidazole linked porphyrin (**11**).

Moreover, the benzyl linker has one carbon atom more connecting the amide group to the imidazole donor compared to the C₃ chain alkyl linker in **2** (cf. Figure 6.2.1), and hence, corresponds directly to the C₄ linker discussed above. Reaction of H₂F₆(NH₂)TPP with α -bromotoluic acid chloride, followed by nucleophilic substitution with sodium imidazolate in acetonitrile, and subsequent column separation and purification affords ligand **3** in good yield, as shown in Scheme 6.2.4. Metallation with FeCl₂ in refluxing THF yields the corresponding iron complex, [Fe(*To*-F₂PP-BzIM)(Cl)]. The FT-IR spectrum of [Fe(*To*F₂PP-BzIM)(Cl)] is shown in Figure 6.2.12. The spectrum shows a band at 1684 cm⁻¹, which corresponds to the stretching vibration ν (C=O) of the amide group. This band is observed at 1700 cm⁻¹ in [Fe(*To*-F₂PP-C₃IM)(Cl)]. This difference may be due to the electron withdrawing nature of the benzyl group, which might somewhat weaken the C=O bond of the amide group. Bands at 1624 cm⁻¹ and 1582 cm⁻¹ are again present as in Fe(*To*-F₂PP-BzIM)(Cl)] and are assigned to C-C phenyl ring vibrations as discussed above.

The NO complex **11** was synthesized (see Scheme 6.2.4) by the reductive nitrosylation reaction of [Fe(*To*-F₂PP-BzIM)(Cl)] with NO in CHCl₃ and CH₃OH as solvent system. The complex was isolated as a solid by precipitation induced by the addition of *n*-hexane.

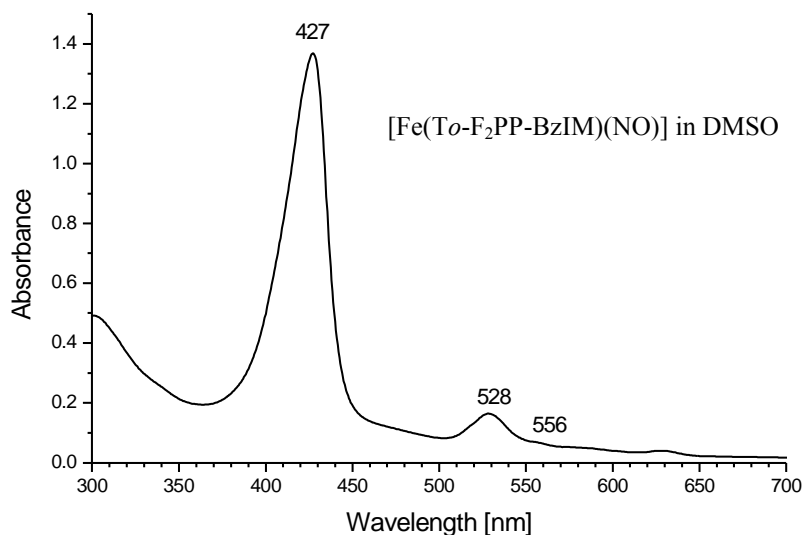


Figure 6.2.10. The UV-vis spectrum of [Fe(*To*-F₂PP-BzIM)(NO)] shows formation of a 6C complex in solution (cf. Figure 6.2.6)

We investigated the base binding properties of the benzyl imidazolyl linker to the Fe(II)-NO center using UV-vis, FT-IR and EPR spectroscopy. The UV-vis spectrum of the NO complex **11** exhibits the Soret band at 427 nm in DMSO (cf. Figure 6.2.10). This red shift of the Soret band is indicative for the formation of a stable six-coordinate adduct in solution. The spectral features compares well with the spectrum obtained by the addition of excess 1-methylimidazole to [Fe(TPP*)(NO)], as shown in Figure 6.2.6. From the obtained UV-vis absorption data of **11**, it was concluded that the appended benzyl imidazolyl linker is in fact bound to the Fe(II)-NO unit in solution.

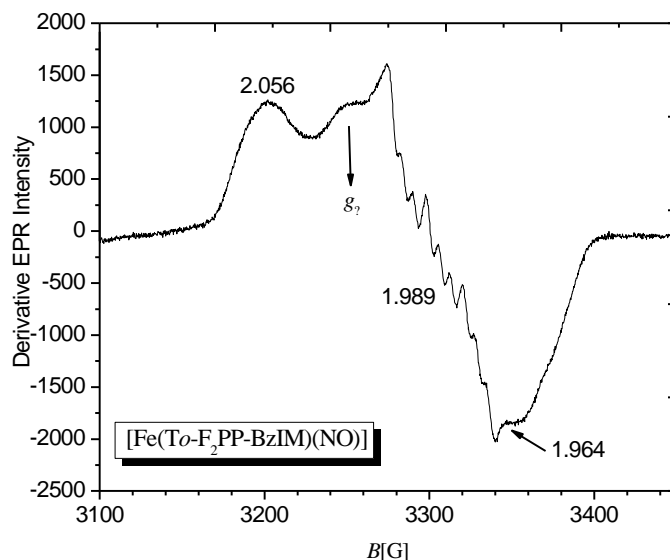


Figure 6.2.11. The EPR spectrum of [Fe(To-F₂PP-BzIM)(NO)] in frozen DMSO at 77 K.

To further investigate this, the EPR spectrum of **11** was taken in DMSO at 77 K (Figure 6.2.11). Interestingly, the observed spectral pattern characterized by a nine line hyperfine structure on $g(\text{mid})$, which originates from the interaction of the unpaired electron with both the ¹⁴N of NO and of the axial benzyl imidazolyl ligand, resembles that of the well-know 6C ferrous heme nitrosyls described in Chapter 4. The obtained g values are also in agreement with the literature values obtained for the 6C species.¹⁴ This confirms that **11** forms a stable 6C complex in solution. Notably, complex **11** also shows the g_7 absorption observed between $g(\text{min})$ and $g(\text{mid})$. This unidentified g_7 feature has been found in the in the EPR spectra of

6C complexes at low temperatures and probably arises from another conformation of the complexes in solution.¹⁵ These findings based on spectroscopic evidence (UV-vis and EPR) clearly show that the benzyl imidazolyl linker binds to the Fe-NO unit in **11** and forms a stable 6C complex in solution without the need of excess base.

To further evaluate the Fe-Im bond strength in **11**, vibrational spectroscopy (IR) was employed. The results on the simple 5C and 6C complexes [Fe(TPP*)(NO)] and [Fe(TPP*)(L)(NO)] described in Chapter 4 have shown that the N-O stretch is a sensitive probe for the strength of the Fe-Im interaction, and that $\nu(\text{NO})$ appears in the 1620 cm^{-1} to 1700 cm^{-1} range. Figure 6.2.12, right depicts the FT-IR spectrum of **11** in CHCl_3 . The spectrum of **11** shows bands at 1680 cm^{-1} and 1624 cm^{-1} , which, however, are also present in [Fe(*To*-F₂PP-BzIm)(Cl)] and have been assigned to $\nu(\text{C-O})$ and $\nu(\text{C-C})$ modes. In comparison with the precursor, a new band at 1644 cm^{-1} is observed for the NO complex **11** as shown in Figure 6.2.12. This band is therefore assigned to $\nu(\text{NO})$. Interestingly, the obtained value of $\nu(\text{NO})$ in **11** of 1644 cm^{-1} is higher in energy compared to six-coordinate compounds formed with free 1-methylimidazole, where $\nu(\text{NO})$ appears at 1625 cm^{-1} . This indirectly reflects the strength of the Fe-L bond (L= axial ligand). Therefore, IR studies show that the covalently attached benzyl imidazolyl linker still cannot bind as strongly to the Fe(II)-NO unit as free imidazole. This observation has an important consequence: the concept of increased local concentration of the attached axial ligand discussed above is not valid at all. In fact, the binding of the linked imidazole is always weaker compared to free IM.

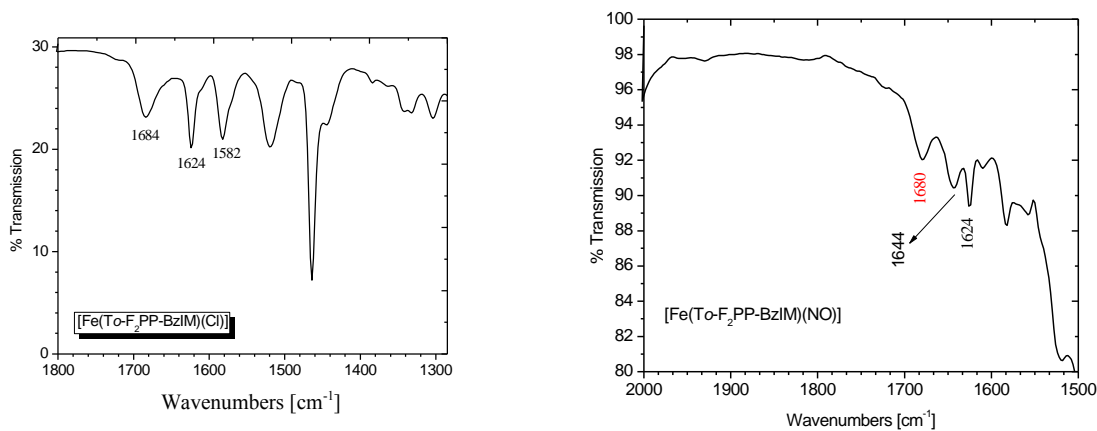


Figure 6.1.12. FT-IR spectra of [Fe(*To*-F₂PP-BzIM)(Cl)] in KBr (left) and [Fe(*To*-F₂PP-BzIM)(NO)] in CHCl_3 (right).

References

- ¹ (a) Averill, B. A. *Chem. Rev.* **1996**, *96*, 2951-2964. (b) Zumft, W. G. *Microbiol. Mol. Biol. Rev.* **1997**, *61*, 533-616. (c) Wasser, I. M.; Vries, S. D.; Moenne-Loccoz, P.; Schroder, I.; Karlin, K. D. *Chem. Rev.* **2002**, *102*, 1201.
- ² (a) Moncada, S.; Palmer, R. M. J.; Higgs, E. A. *Pharmacol. Rev.* **1991**, *43*, 109. (b) Butler, A. R.; Williams, D. L. *Chem. Soc. Rev.* **1993**, 233.
- ³ (a) Ignarro, L. J. *Angew. Chem. Intl. Ed.* **1999**, *38*, 1882-1892. (b) Stone, J. R.; Marelleta, M. A.; *Biochemistry* **1996**, *35*, 1093-1099. (c) Garbers, D. L.; Lowe, D. G. *J. Biol. Chem.* **1994**, *269*, 30741-30744. (d) Zhao, Y.; Hoganson, C.; Babcock, G. T.; Marletta, M. A. *Biochemistry* **1998**, *37*, 12458-12464. (e) Karow, D. S.; Pan, D.; Tran, R.; Pellicena, P.; Presley, A.; Mathies, R. A.; Marletta, M. A. *Biochemistry* **2004**, *43*, 10203-10211.
- ⁴ Girsch, P.; de Vries, S. *Biochim. Biophys. Acta* **1997**, *1318*, 202-216.
- ⁵ (a) Scheidt, W. R.; Elison, M. K. *Acc. Chem. Res.* **1999**, *32*, 350-359. (b) Wyllie, G. R. A.; Scheidt, W. R. *Chem. Rev.* **2002**, *102*, 1067-1090. (c) Ford, P. C.; Fernandez, B. O.; Lim, M. D. *Chem. Rev.* **2005**, *105*, 2439-2456. (d) (c) Ford, P. C.; Lorkovic, I. M. (c) Ford, P. C.; Fernandez, B. O.; Lim, M. D. *Chem. Rev.* **2005**, *105*, 2439-2456.
- ⁶ Praneeth, V. K. K.; Näther, C.; Peters, G.; Lehnert, N. *Inorg. Chem.* **2006**, *45*, 2795-2811.
- ⁷ Komatsu, T.; Matsukawa, Y.; Tsuchida, E. *Chem. Letts.* **2000**, 1060-1061.
- ⁸ Kim, E.; Shearer, J.; Lu, S.; Moenne-Loccoz, P.; Helton, M. E.; Kaderli, S.; Zuberbühler, A. D.; Karlin, K. D. *J. Am. Chem. Soc.* **2004**, *126*, 12716-12717.
- ⁹ Collman, J. P.; Brauman, J. I.; Doxee, K. M.; Halbert, T. R.; Bunnenberg, E.; Linder, R. E.; LaMar, G. N.; Gaudio, J. D.; Lang, G.; Spartalin, K. *J. Am. Chem. Soc.* **1980**, *102*, 4182-4192.
- ¹⁰ Young, R.; Chang, C. K. *J. Am. Chem. Soc.* **1985**, *107*, 898-909.
- ¹¹ (a) Yoshimura, T. *Bull. Chem. Soc. Jpn.* **1991**, *64*, 2819-2822. (b) Yoshimura, T. *Bull. Chem. Soc. Jpn.* **1978**, *51*, 1237.
- ¹² Praneeth, V. K. K.; Neese, F.; Lehnert, N. *Inorg. Chem.* **2005**, *45*, 2570-2572.
- ¹³ Paulat, F.; Praneeth, V. K. K.; Näther, C.; Lehnert, N. *Inorg. Chem.* **2006**, *45*, 2835-2856.
- ¹⁴ Praneeth, V. K. K.; Haupt, E.; Lehnert, N. *J. Inorg. Biochem.* **2005**, *99*, 940-948. Erratum; *J. Inorg. Biochem.* **2005**, *99*, 1744.
- ¹⁵ (a) Morse, R. H.; Chan, S. I. *J. Biol. Chem.* **1980**, *255*, 7876. (b) Hori, H.; SITO-Ikeda, M.; Yoneetani, T. *J. Biol. Chem.* **1981**, *256*, 7849.

6.3 A Complete Structural Model for Bacterial Nitric Oxide Reductase (NorBC): Synthesis, Characterization and Spectroscopic Properties

6.3.1. Introduction

Denitrification is an important reduction pathway in the inorganic nitrogen cycle which releases a large amount of fixed nitrogen to the biosphere. Denitrification is carried out by a variety of bacteria for energy generation by the stepwise reduction of nitrate to N_2 under anaerobic conditions.¹ A key enzyme in the dissimilatory denitrification is the bacterial nitric oxide reductase (NorBC), which is responsible for the two electron reduction of NO to N_2O . NorBCs active site consists of a high spin ferric heme and a non-heme (Fe_B) in close proximity. The proposed catalytic mechanism involves binding of two molecules of NO, each at one of the two metal centers, followed by N-N coupling to form N_2O .² Nevertheless, there is no concrete evidence to back up this mechanism. Other mechanistic possibilities have been suggested as well for the generation of N_2O at the bacterial NOR active site.³ NorBCs belong to the super family of heme-copper oxidases and are structurally closely related to the cytochrome *c* oxidases (*CcOs*). *CcOs* are believed to have evolved from the NorBCs under aerobic conditions.⁴ Owing to their biological implications, several active site model complexes have been synthesized for *CcOs* by various research groups, and their properties have been explored spectroscopically.⁵ However, only a very few reports have been published so far for a complete structural model system of NorBC. Karlin and coworkers synthesized a ferrous heme with a covalently attached ferrous tris(pyridylmethyl)amine (TPA) complex (Figure 6.3.1). This model system binds two molecules of NO as evidenced by IR spectroscopy. Nevertheless, this complex does not show any NorBC activity to form N_2O . Karlin and coworkers concluded that the sixth ligand for heme may be necessary for the NO coupling mechanism to yield N_2O .⁶ In contrast, model complex studies described in the preceding sections (cf. Chapter 4) have shown that six-coordinate ferrous heme-nitrosyls of type $[Fe(TPP^*)(MI)(NO)]$ have a large amount of radical character on the NO ligand;^{5d,5e} however, these compounds are stable in solution and do not show any N_2O formation. This seems to indicate that the simple N-N coupling mechanism is incomplete. Therefore, a

sophisticated model complex with covalently attached sixth ligand for the heme center and a non-heme ligand has to be synthesized to study the electronic structure and reactivity of the diiron (NO)₂ center. Recently, it has been indicated that the non-heme site is coordinated by three histidyl nitrogen atoms and a glutamic acid residue.⁴ The glutamic acid is considered important for the normal activity of NorBC. This carboxylic acid possibly stabilizes the Fe_B site and thus may induce the N-N coupling reaction in the enzyme.⁷ Based on this speculation, corresponding model compounds (ligands) have been prepared by the Collman group by attaching a carboxylic acid to a trisimidazole picket porphyrin porphyrins.⁸ However, metal complexation and reactivity studies on these models have not been performed so far.

In this chapter, we describe the new synthetic NorBC active site model compound [H₂T₀-F₂PP-PBMPA] (**9**) (Figure 6.3.2), which consists of a fluorosubstituted porphyrin covalently attached to the tridentate chelate dipyridylmethylamine (PBMPA, *N*-(propionic acid)-*N,N*-bis-(dipyridylmethyl)amine). We have investigated the reactivity of the diiron complex **10** with excess NO using UV-vis and IR spectroscopies. In addition, to explore the significance of the sixth ligand coordination to the ferrous heme, we are currently synthesizing a six-coordinate heme model complex with a linked non-heme ferrous site. In this section, we also discuss the synthesis and characterization of the corresponding precursor compound, dinitroporphyrin **12**. The heme portions of these model complexes (five- and six coordinate iron(II)-NO adducts) have been extensively investigated using various spectroscopic methods and DFT calculations, as previously described (see Chapter 4). However, the spectroscopic properties of the non-heme iron nitrosyl have not been explored by our group to date. In this regard, the mononuclear non-heme iron complex with the tris(2-pyridylmethyl)amine ligand (TPA) and PBMPA have been synthesized and characterized using UV-vis, IR, and EPR spectroscopic techniques. In this study, the spectroscopic properties of the non-heme iron complex have been used to characterize the non-heme part of complex **10**.

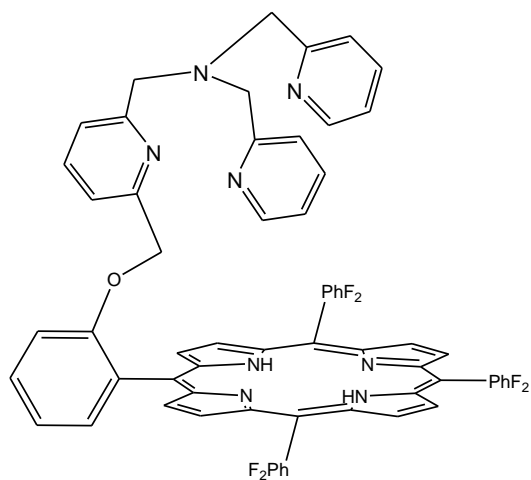


Figure 6.3.1. Molecular structure of the heme/non-heme ligand synthesized by the Karlin group.

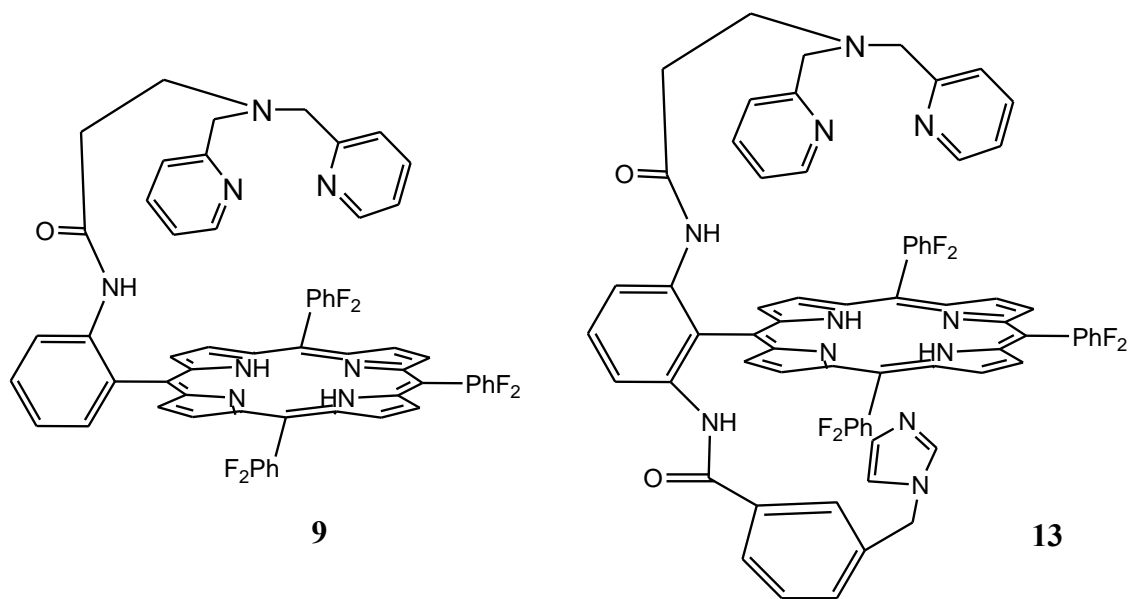


Figure 6.3.2. Heme/non-heme ligand systems: five-coordinate **9** employed in this study, and six-coordinate **13** which is currently being synthesized.

6.3.2 Experimental Procedures

6.3.2.1 General.

Most of the reactions were performed applying inert Schlenk techniques. Infrared spectra were obtained on KBr disks or chloroform solutions on a Perkin-Elmer BX spectrometer. Proton magnetic resonance spectra were obtained on a Varian Inova 400 MHz and a Varian Mercury 300 MHz instrument. Electronic absorption spectra were recorded on an Analytic Jena Specord 600 instrument.

6.3.2.2 Materials.

All solvents and reagents were purchased and used as supplied except as follows. Toluene was distilled from sodium under argon. Dried and air free THF and *n*-hexane were obtained after passing through MBraun solvent purification system. 1-Methylimidazole was vacuum distilled from KOH and degassed for five times via a freeze-pump-thraw cycle. Nitric oxide (Air gas, USA) was purified by first passing through an ascarite II column (NaOH on silica gel) and then through a cold trap at -80°C to exclude higher nitrogen oxide impurities.

6.3.2.3 Syntheses

The syntheses of 5,10,15-Tris-(2,6-difluoro-phenyl)-20-(2-nitro-phenyl)-porphyrine, $\text{H}_2\text{F}_6(\text{NO}_2)\text{TPP}$ (**1**), and 5,10,15-Tris-(2,6-difluoro-phenyl)-20-(2-amino-phenyl)-porphyrine, $\text{H}_2\text{F}_6(\text{NH}_2)\text{TPP}$ (**2**), are discussed in chapter 6. Tris(2-pyridylmethyl)amine tri-perchlorate, $\text{TPA}\cdot 3\text{HClO}_4$,⁹ *N*-(methylpropionate)-*N,N*-bis-(dipyridylmethyl)amine, MPMPBA;¹⁰ 5,10,15-Tris-(2,6-difluoro-phenyl)-20-(2,6-dinitro-phenyl)-porphyrine, $\text{H}_2\text{F}_6(\text{NO}_2)_2\text{TPP}$;¹¹ 10,15-Tris-(2,6-difluoro-phenyl)-20-(2,6-diamino-phenyl)-porphyrine, $\text{H}_2\text{F}_6(\text{NH}_2)_2\text{TPP}$ ¹¹ were synthesized according to published procedures as described in the following.

6.3.2.3.1 Synthesis of a Mononuclear Non-Heme Iron NO compound

TPA $\cdot 3\text{HClO}_4$, Tris(2-pyridylmethyl)amine tri-perchlorate, (**3**).

2 mL of 2-(aminomethyl)pyridine (0.02 mol) were added to a solution of 2-(chloromethyl)pyridine hydrochloride (6.37 g, 0.04 mol) in water (10 mL). NaOH (7.75 mL, 0.08 mol, 10 M) was added during the following 30 minutes to obtain a dark red solution. The solution was subsequently stirred and heated to 70°C for another 30 minutes. The

mixture was then cooled to a room temperature, and perchloric acid (5 mL, 6M) was added to precipitate the tan perchlorate salt. The solid was filtered off, and washed with ethanol and diethylether to obtain a white product. Yield 1.25 g (85%). ^1H NMR (200 MHz, CDCl_3) 3.8 (s, 6H); 7.1 (m, 3H); 7.5-7.7 (m, 6H); 8.5 (m, 3H).

[Fe(TPA)(CH₃CN)₂](ClO₄)₂, [Tris(2-pyridylmethyl)amine-di(actetonitrile)]iron(II) di-perchlorate (4)

TPA·3HClO₄ (1.0 g, 1.6 mol) and 0.61 g (1.6 mol) of Fe(ClO₄)₂·6H₂O were dissolved in acetonitrile (30 mL) under an argon atmosphere. The resulting solution was stirred for 3 hours. Then, 10 mL of diethyl ether were added and the resulting precipitate was filtered off under argon. The obtained compound was further purified by recrystallization using acetonitrile and slowly adding diethyl ether. The precipitate obtained by this way was filtered off. Yield: 1.3 g (85%)

[Fe(TPA)(NO)(CH₃CN)](ClO₄)₂ (5)

[Fe(TPA)(CH₃CN)₂](ClO₄)₂ (0.25 g, 0.5 mmol) was placed in a 250 mL Schlenk flask under an argon atmosphere. Then, dichloromethane (20 mL) was added to the flask to dissolve the complex to give a light orange solution. Excess nitric oxide was then added to the flask while stirring. The solution turned dark brown and a precipitate formed. The solution was stirred for another one and a half hours and cooled in a freezer at -27° C. The formed precipitate was filtered, under argon, yielding a dark brown precipitate. Yield: 0.225 g (86%). FT-IR (cm⁻¹): 1810 cm⁻¹ (ν_{NO}).

6.3.2.3.2 Synthesis of the Five-Coordinate Heme/Non-heme NorBC Model.

MPBMMA, N-(methylpropionate)-N,N-bis-(dipyridylmethyl)amine (6).

A 30 mL of a methanolic solution containing bis-(2-dipyridylmethyl)amine and methyl acrylate (5.7 mL, 0.063 mol) was stirred for one week. After this period, the solvent and the residual methylacrylate were removed under vacuum. The oily mixture obtained this way was purified using silica gel column chromatography employing methanol as eluent. The purified product was obtained as viscous brown oil (yield 5 g, 90%). ^1H NMR (CD_3OD): 2.6 (t, 2H, -CH₂CO₂CH₃); 2.9 (s, 4H, -CH₂-NCH₂Py); 3.8 (s, 3H, -COOCH₃); 7.3 (td, 2H, H_{5-Py}); 7.6(dd, 2H, H_{3-Py}); 7.3 (td, 2H, H_{4-Py}); 8.4 (dd, 2H, H_{6-Py}).

[Fe(MPBMPA)Cl₃], Trichloro[N-methylpropionate-N,N-bis(2pyridylmethyl)amine]iron(III) (7).

MPBMPA (0.3g, 1.05 mmol) was dissolved in methanol and the resulting mixture was added to a solution of FeCl₂ (0.13 g, 1.05 mmol) in 20 mL of methanol. The obtained reaction mixture was stirred at room temperature for 2 hrs. Upon allowing the solution stand overnight, single crystals suitable for X-ray analysis of the ferric form of the complex were obtained.

PBMPA, *N*-(propionic acid)-*N,N*-bis-(dipyridylmethyl)amine (8).

MPBMPA (0.525 g, 1.84 mmol) was dissolved in 5 mL of THF and an aqueous solution of 0.1M NaOH (0.21 g in 2 mL of H₂O) was added. The reaction was refluxed for 5 hrs at 70° C. During this period, the aqueous phase turned brown in color. The aqueous layer was separated and neutralized with 1 mL of 2.5 M HCl. The solvent was removed under vacuum and the product was obtained as yellow solid (yield: 0.4 g, 80%). ¹H NMR (CD₃OD): 2.43 (t, 2H, -CH₂CO₂H); 2.861(t, 2H, CH₂-CH₂-COOH); 3.8 (s, 4H, NCH₂Py); 7.244 (m, 2H, H_{5-Py}); 7.6(dd, 2H, H_{3-Py}); 7.7 (m, 2H, H_{4-Py}); 8.4 (t, 2H, H_{6-Py}).

[H₂To-F₂PP-PBMPA], 5C Heme/non-heme ligand (9).

H₂F₆(NH₂)TPP (2, 20 mg, 0.027 mmol) was stirred in 15 mL CH₂Cl₂. To this solution, 5 mL dry methanolic solution of PBMPA 8 (0.7 g, 0.26 mmol) followed by 0.1 g of dicyclohexylcarbodiimide (DCC) were added. The resulting solution was stirred at room temperature for 2 hrs. The solution was concentrated and washed with aqueous NaHCO₃. The solution was then dried with Na₂SO₄ and concentrated. The compound was purified using column chromatography on silica gel with the eluent CH₂Cl₂/CH₃OH = 4:1 to give compound 9 (yield: 18 mg, 67 %). MS (MALDI) for C₅₉H₄₀N₈F₆O [M+H]⁺: Cald. 991, found 991.

[Fe₂(To-F₂PP-PBMPA)(NO)₂], 5C Heme/non-heme diiron(NO)₂ (10).

15 mg of [H₂To-F₂PP-PBMPA] (9) were stirred in 10 mL of dry and air free THF. Anhydrous FeCl₂ (27 mg, 20 equivalents) was then added and the resulting reaction mixture was refluxed under an argon atmosphere for 2 hours. After that, the reaction was stopped and the solvent was removed under vacuum. The complex was redissolved in 10 mL dry and air

free CHCl_3 , followed by the addition of 1 mL of CH_3OH . NO gas was then added to the stirred solution for 1 hour. n-hexane (10 mL) was used to precipitate the obtained the dinitrosyl diiron complex **10**. FT-IR (cm^{-1}): 1816 (ν_{NO}), 1683 (ν_{NO}). The yield of the product is 10 mg (52 %). The quality of the IR spectrum quality is poor due to the presence of impurities.

6.3.2.3.3 Synthesis of the Precursor for a Six-Coordinate Heme/Non-Heme NorBC Model compound (**13**):

F₂DP, 2,6-(Difluorophenyl)dipyrromethane (**11**).

5 g (35.2 mmol) of 2,6-difluorobenzaldehyde were placed in a 250 mL Schlenk flask, and 100 mL of freshly distilled pyrrole were added. The resulting solution was stirred and degassed with argon for 15 minutes. Then, 0.5 mL of trifluoroacetic acid were added under an argon atmosphere, and the resulting red solution was stirred for an additional hour. The reaction was then stopped, and 100 mL of ACS grade dichloromethane were added. The organic layer was washed three times with 100 mL of 0.1 M NaOH and dried over anhydrous Na_2SO_4 . The dichloromethane was then removed and excess pyrrole was subsequently distilled off in vacuum. The obtained residue (green paste) was column chromatographed using 4:1 n-hexane/diethylether containing 1% triethylamine. The first fraction from the column was collected and purified two times by recrystallization employing n-hexane and diethyl ether mixtures (ratio of 10:1) to yield white needles (4.1g, 45%). ^1H NMR (400 MHz, CD_2Cl_2) 8.17 (s, br, 2H, N-H pyrrole); 7.16-7.26 (m, 1H, *para* phenyl); 6.87-6.93 (t, 2H, *meta* phenyl); 6.68-6.70 (m, 2H, γ -pyrrole); 6.13-6.15 (q, 2H, α -pyrrole); 6.01 (s, 2H, β -pyrrole); 5.91 (s, 1H, CH).

H₂F₆(NO₂)₂TPP, 5,10,15-Tris-(2,6-difluoro-phenyl)-20-(2,6-dinitro-phenyl)-porphyrin (**12**). 2,6-(difluorophenyl)dipyrromethane (**11**) (7.25 g, 28 mmol), 2,6-difluorobenzaldehyde (2 g, 14 mmol), and 2,6-dinitrobenzaldehyde (3.15 g, 16 mmol) were added to 1.75 L of ACS grade deaerated dichloromethane. To this, 2.0 mL of $\text{BF}_3\text{-OEt}_2$ were added, and the resulting orange solution was stirred for 30 minutes. During this time, the color changed from initially orange to red then to purple. Then, 13.6 g (60 mmol) of 2,3-dichloro5,6-

dicyanaobenzoquinone (DDQ) were added and the resulting reaction mixture was stirred at room temperature for 8 hours. Then, the reaction was stopped and the solution was evaporated to reduce the volume to around 100 mL. This solution was pre-purified by passing through an alumina column (neutral) employing CH₂Cl₂ as eluent and then further purified with silica gel column chromatography using CH₂Cl₂/n-Hexane (4:1). The second fraction was collected and dried under vacuum to afford 1.14 g (8.8 %) of H₂F₆(NO₂)₂TPP. ¹H NMR (400 MHz, CD₂Cl₂) 8.86-8.84 (m, 6H, β-pyrrole); 8.64 (d, 2H, β-pyrrole); 8.46 (d, 2H, *meta* nitrophenyl H); 8.103 (t, 1H, *para* nitrophenyl); 7.18 (m, 3H, *para* fluorophenyl); 7.37 (m, 6H, *meta* fluorophenyl); -2.72 (s, 2H, NH pyrrole).

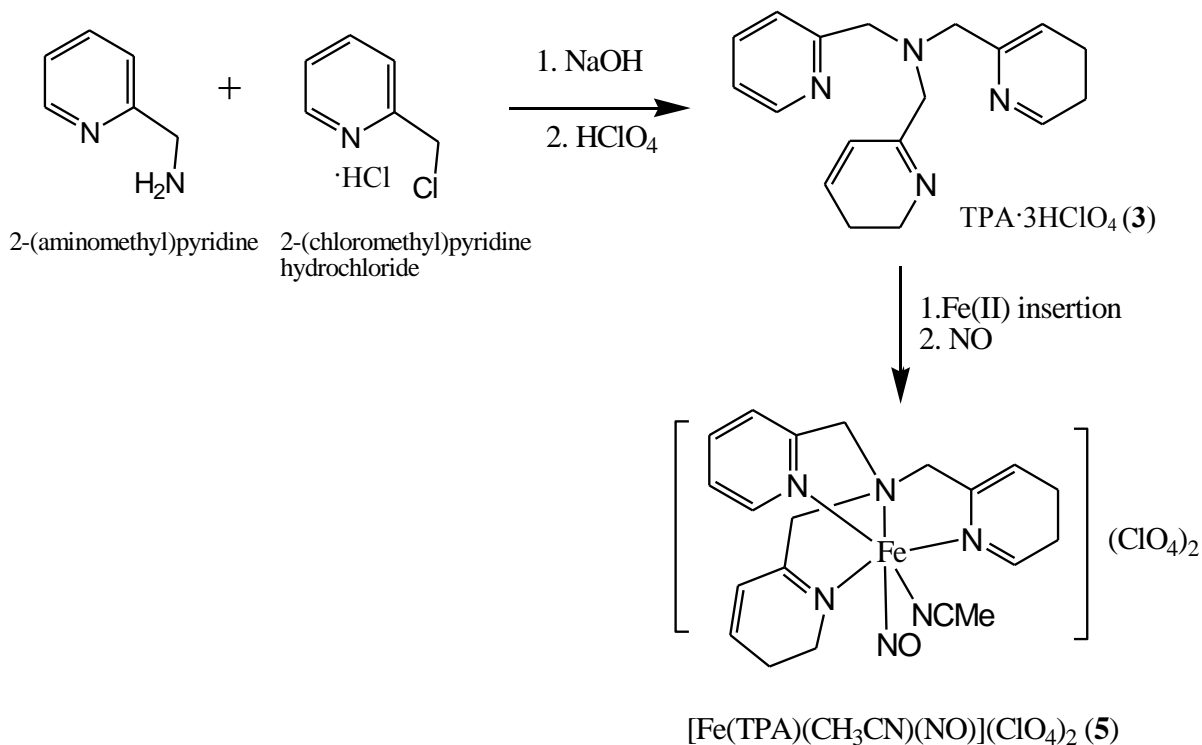
6.3.2.3.4 Crystal structure determination of [Fe(MPBMPA)Cl₃] (7)

Yellow polyhedron-shaped crystals of [Fe(MPBMPA)Cl₃] were grown from a methanol solution at 22° C. A crystal of dimensions 0.24 x 0.23 x 0.15 mm was mounted on a Bruker SMART APEX CCD-based X-ray diffractometer equipped with a low temperature device and a fine focus Mo-target X-ray tube ($\lambda = 0.71073$ Å) operated at 1500 W power (50 kV, 30 mA). The X-ray intensities were measured at 85(1) K; the detector was placed at a distance 5.055 cm from the crystal. A total of 3730 frames were collected with a scan width of 0.5° in ω and ϕ with an exposure time of 10 s/frame. The integration of the data yielded a total of 58849 reflections to a maximum 2θ value of 56.80° of which 4672 were independent and 4502 were greater than $2\sigma(I)$. The final cell constants were based on the xyz centroids of 9959 reflections above $10\sigma(I)$. Analysis of the data showed negligible decay during data collection; the data were processed with SADABS and corrected for absorption. The structure was solved and refined with the Bruker SHELXTL (version 6.12) software package, using the space group C2/c with $Z = 8$ for the formula C₁₆H₁₉N₃O₂Fe. All non-hydrogen atoms were refined anisotropically with the hydrogen atoms placed in idealized positions. Full matrix least-squares refinement based on F^2 converged at $R1 = 0.0257$ and $wR2 = 0.0665$ [based on $I > 2\sigma(I)$], $R1 = 0.0267$ and $wR2 = 0.0675$ for all data.

6.3.3. Results and Discussion

6.3.3.1 Synthesis, characterization and spectroscopic properties of the mononuclear non-heme iron NO complex

The non-heme ligand Tris(2-pyridylmethyl)amine triperchlorate, (TPA·3HClO₄, **3**) was synthesized from 2-(aminomethyl)pyridine and 2-(chloromethyl)pyridine hydrochloride. The ligand was obtained as a triperchlorate salt. The iron complex [Fe(TPA)(CH₃CN)₂](ClO₄)₂ (**4**) was prepared by mixing iron perchlorate hexahydrate and ligand **3** in acetonitrile. Then, the NO complex was synthesized by adding NO to an acetonitrile solution of **4** at room temperature in the absence of O₂. Immediate formation of a brown precipitate was observed. Allowing the reaction mixture to stand overnight at -27° C under a nitric oxide atmosphere produced 86% yield (Scheme 6.3.1). It is assumed that the sixth coordination site of iron in this complex is occupied by one acetonitrile molecule. The UV-vis absorption spectra of the NO complex were measured in methanol, acetone, and DMSO are shown in Figure 6.3.3.



Scheme 6.3.1. Synthesis of [Fe(TPA)(CH₃CN)(NO)](ClO₄)₂ (**5**).

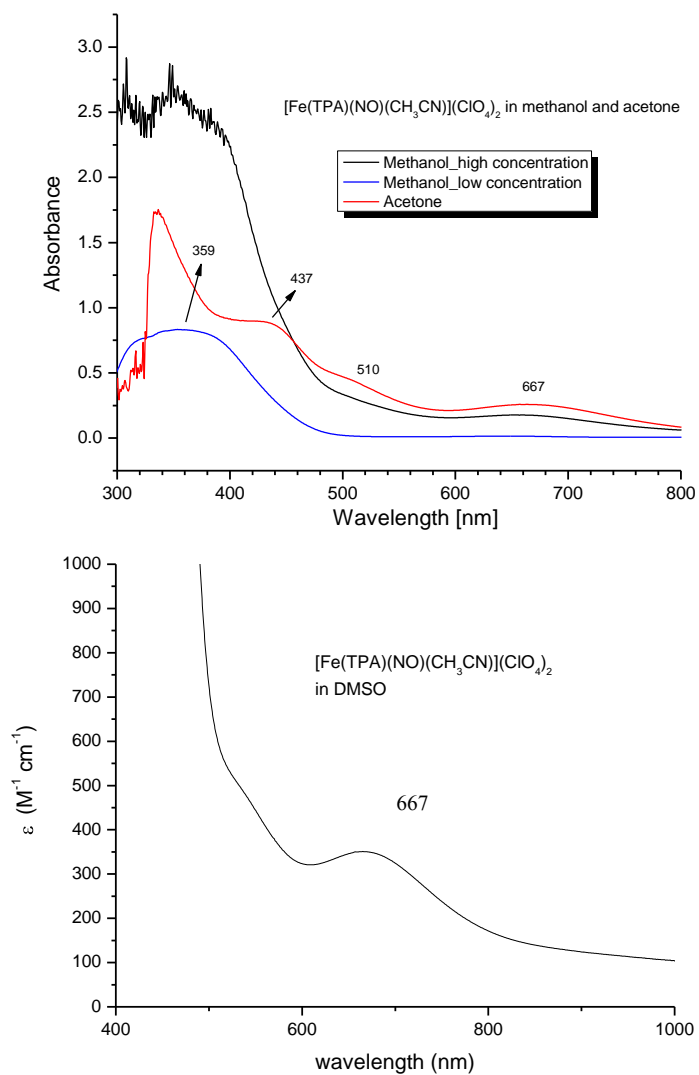


Figure 6.3.3. UV-vis spectra of $[\text{Fe}(\text{TPA})(\text{NO})(\text{CH}_3\text{CN})](\text{ClO}_4)_2$ featuring 359, 437, 520 and 654 nm bands in methanol, acetone (top), and DMSO (bottom).

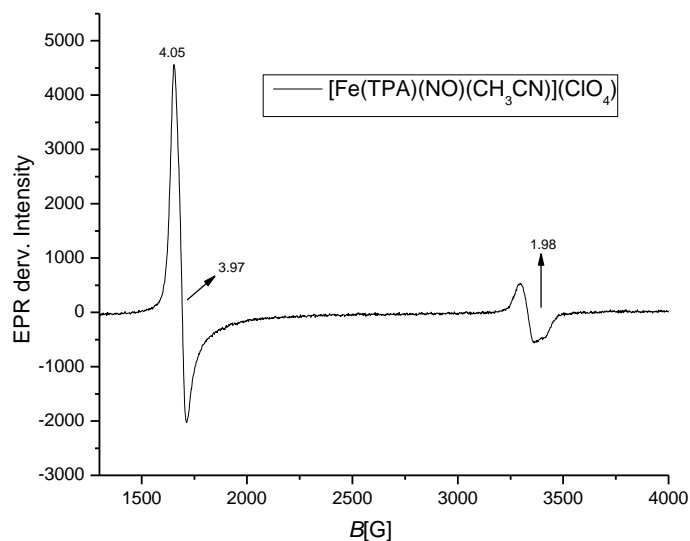


Figure 6.3.4. EPR spectrum of a frozen solution of $[\text{Fe}(\text{TPA})(\text{CH}_3\text{CN})_2](\text{ClO}_4)_2$ (**5**) in DMSO at 4.0 K.

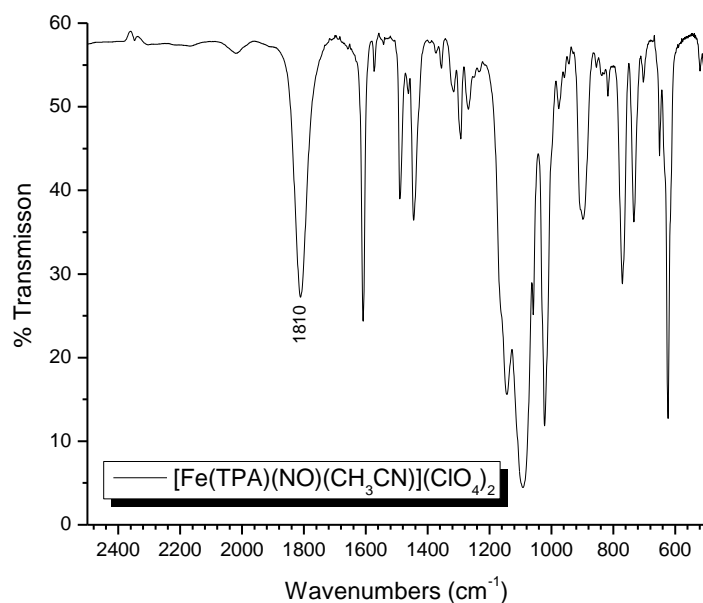


Figure 6.3.5. FT-IR spectrum of $[\text{Fe}(\text{TPA})(\text{NO})(\text{CH}_3\text{CN})](\text{ClO}_4)_2$

The UV-vis spectrum of **5** in methanol shows a weak broad band at 359 nm. In acetone, the compound shows characteristic absorption features at 437, 510 and 667 nm. The compound **5** was also recorded in DMSO. The obtained spectral features are in good

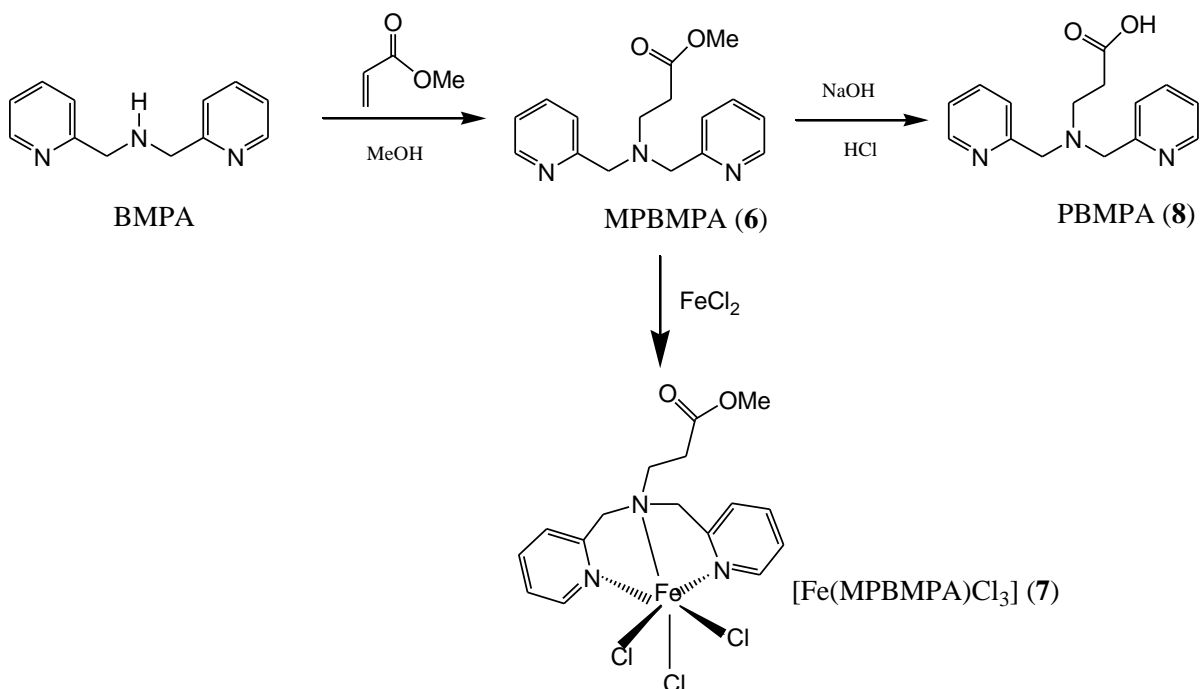
agreement with the reported absorption data for $[\text{Fe}(\text{TPA})(\text{NO})(\text{BF})](\text{ClO}_4)$, where BF = benzoyl formate.

NO coordination to $[\text{Fe}(\text{TPA})(\text{CH}_3\text{CN})_2](\text{ClO}_4)_2$ was also investigated characterized using FT-IR spectroscopy. The spectrum of **5** in a KBr pellet exhibits a strong band at 1810 cm^{-1} . This band is assigned to the stretching frequency of the coordinated NO. The obtained spectrum is shown Figure 6.3.5. Again, this result is in very good agreement with similar types of ferrous non-heme iron NO complexes prepared by Chiou and Que¹² (see Table 1). The EPR spectrum of **5** was measured in DMSO at liquid helium temperature. The obtained spectrum is shown in Figure 6.3.4. The spectrum is characterized by intense resonances at $g = 4.05, 3.93, 1.93$. This spectrum is characteristic of an axial $S = 3/2$ spin state. The obtained g values are comparable with literature values obtained for similar model systems.¹²

6.3.3.2 Synthesis and characterization of the five-coordinate heme/non-heme NorBC model:

The non-heme ligand, MPBMPA (**6**) was synthesized by the Micheal reaction of BMPA with methylacrylate according to a reported procedure.¹⁰ MPBMPA has two pyridine nitrogen donors plus one aliphatic nitrogen donor for coordination to the iron center. The ester group present is unlikely to coordinate due to its weak binding capacity. Iron insertion was carried out by mixing a methanolic solution of FeCl_2 with a solution of MPBMPA in methanol. Single crystals suitable for X-ray diffraction studies were obtained for **7** after letting the solution stand overnight. The complex crystallizes in the space group $C2/c$. An ORTEP plot of the molecule is shown in Fig. 6.3.6. The central iron(III) in the complex is coordinated by three N donors from MPBMPA, and three chloride ions. The structure is best described as a distorted octahedron.

Hydrolysis of **6** in refluxing sodium hydroxide followed by acidification with hydrochloric acid gives the corresponding acid, PBMPA **8** in 90% yield. The identity of the compound was confirmed by ^1H NMR. The synthetic scheme for the non-heme ligand and its iron(III) complex are depicted in Scheme 6.3.2.



Scheme 6.3.2. Synthesis of the non-heme ligand MPBMPA (6) and its ferric complex [Fe(MPBMPA)Cl₃] (7).

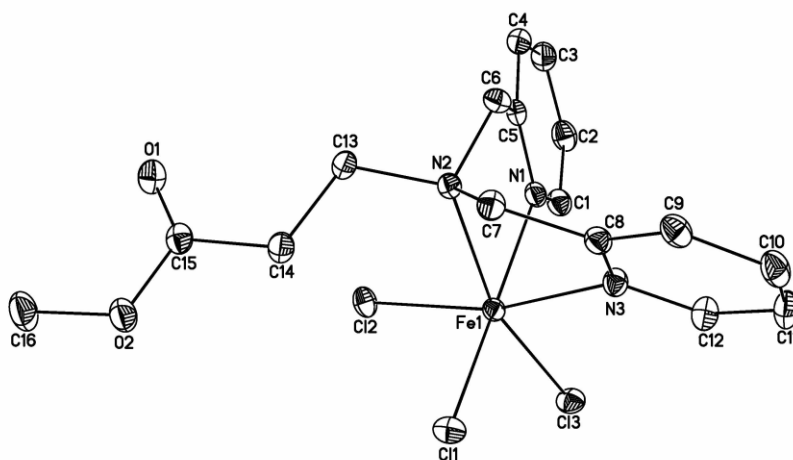
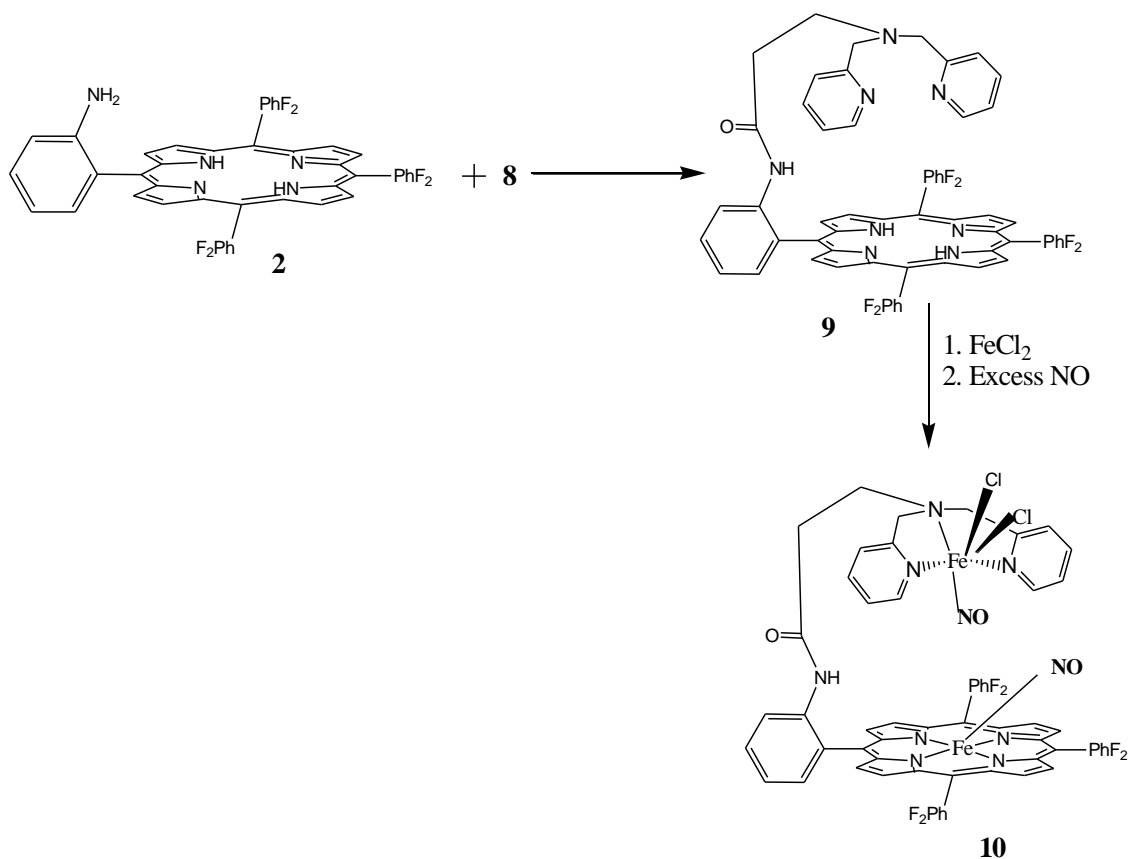


Figure 6.3.6. ORTEP diagram of [Fe(MPBMPA)Cl₃] (7). Hydrogen atoms are omitted for clarity.

Treatment of PBMFA (**8**) with monoamino porphyrin, $\text{H}_2\text{F}_6(\text{NH}_2)\text{TPP}$ (**2**) in the presence of DCC at room temperature, followed by purification using column chromatography on silica gel yields the 5C heme/non-heme ligand **9**. The identity of the compound was confirmed by MALDI mass spectrometry. The mass spectrum of **9** in methanol is dominated by the parent ion peak at $m/z = 990$ amu. Iron insertion into **9** was carried out using two equivalents of FeCl_2 as metal ion carrier in dry THF solvent mixture under very strict inert conditions. The formation of the 5C heme/non-heme diiron complex was monitored using UV-vis spectroscopy. Subsequent addition of excess nitric oxide to the reaction medium gives the dinitrosyl product **10** (Scheme 6.3.3). The UV-vis spectrum of **10** monitored during the course of the reaction exhibits the Soret band maximum (λ_{max}) at 407 nm. This is in accordance with similar Soret band positions obtained for the five-coordinate ferrous nitrosyl adducts $[\text{Fe}(\text{TPP})(\text{NO})]$ and $[\text{Fe}(\text{To-F}_2\text{PP})(\text{NO})]$. (cf. Chapter 4). These supporting data reveal that the heme part of **10** is five-coordinate.



Scheme 6.3.3. Synthesis of the 5C heme/non-heme diiron NO complex (**10**)

The absorption bands pertaining to the NO adduct of the non-heme part of **10** are not identified in the spectrum. This is due to the fact that the porphyrin signals have large extinction coefficients, and correspondingly, mask the weak signals of the non-heme iron NO adduct in the complex. In general, the non-heme iron NO complexes exhibit bands in the region around 350 nm (λ_{max}) with small extinction coefficients¹², as described above for compound **5**. For example, the non-heme complex [Fe(TPA)(NO)(CH₃CN)](ClO₄) (**5**) shows weak absorption bands, as previously described here.

FT-IR spectrum of **10** shows characteristic bands at 1682 cm⁻¹ and 1816 cm⁻¹. These bands are assigned to ν_{NO} of the ferrous heme NO and ferrous non-heme NO component, respectively. These assignments are based on our data, and are also in agreement with Wasser et al.⁶ Table 6.3.3 presents some ν_{NO} frequencies observed for iron-NO complexes in comparison to the values observed for **10**. Other possible structures such as coordination of two molecules of NO to the heme or to the non-heme center are highly unlikely due to the following reasons.

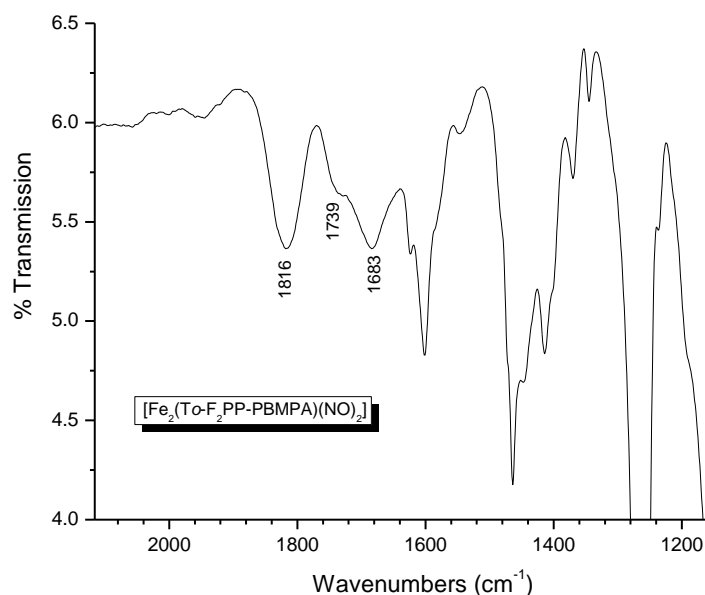


Figure 6.3.7 FT-IR spectrum of the isolated [Fe₂(To-F₂PP-PBMPA)(NO)₂] (**10**).

First, compounds of type [Fe(Porphyrin)(NO)₂] do not exist at room temperature and can only be formed at very low temperature as unstable species.¹³ In addition, complexes of the type [Fe(TPA)(X)(NO)₂] (non-heme ligand) have no vacant site for the second NO to coordinate.¹⁴ Based on these evidences it is concluded that the heme and the non-heme centers bind one molecule of NO each. The compound is stable under an inert atmosphere at room temperature. However, importantly, the N-N bond forming reaction (NorBC activity) was not observed with complex **10**. This result is similar to what has been observed by Wasser *et al* in their investigation of the reaction of NO with a heme/non-heme diiron complex. Apparently, the glutamic acid at the non-heme iron center is not present in our model and Wasser et al. The glutamic acid residue present in close proximity to the non-heme iron center could potentially drive the N-N bond formation. To investigate this point, further research is being carried out in our laboratory by analyzing the product formation from the reaction of externally supplied carboxylic acids like acetic acid and benzoic acid with **10**.

Table 6.3.1. $\nu(\text{NO})$ of heme and non-heme iron-NO complexes

Complex	$\nu(\text{NO}) \text{ cm}^{-1}$	reference
[Fe ₂ (T σ -F ₂ PP-PBMPA)(NO) ₂] (10)	1683 ^a 1816 ^b	this work
[(6L)Fe(NO) ₂ Fe(Cl)]	1689 ^a 1789 ^b	6
[Fe(TPA)(NO)(CH ₃ CN)](ClO ₄) ₂ (5)	1810	this work
[Fe(TPA)(NO)(BF)](ClO ₄)	1794	12
[Fe(T σ -F ₂ PP)(NO)]	1687	5e
[Fe(TPP)(NO)]	1697	5e
Fe(TMP)(NO)	1676	5e

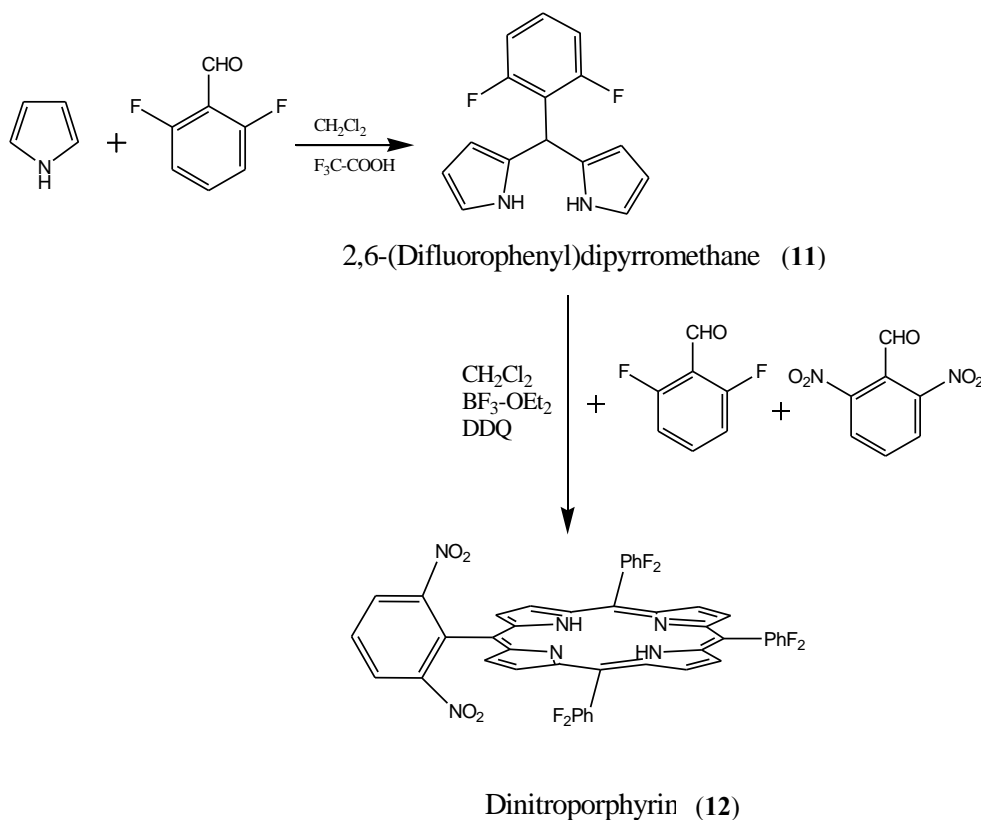
^aassigned as ν_{NO} (heme part); ^bassigned as ν_{NO} (non-heme part)

6.3.3.2 Six-coordinate heme/non-heme NorBC model: Synthesis of the precursor.

To investigate the importance of the sixth ligand to heme for the NorBC activity, we are currently synthesizing a six-coordinate heme with attached non-heme iron ligand. The precursor ligand for this complex has been synthesized according to the literature methods. First, 2,6-(difluorophenyl)dipyrromethane **11** was synthesized by the condensation of pyrrole with 2,6-difluorobenzaldehyde. Further condensation of the isolated 2,6-(difluorophenyl)dipyrromethane with difluorobenzaldehyde and dinitrobenzaldehyde results in the formation of **12** in pure form after several column chromatography steps (Scheme 6.3.4). Reduction of the dinitroporphyrin to yield the corresponding diaminoporphyrin is currently being carried out.

The sixth ligand for heme will be attached to one of the amino groups present at the porphyrin phenyl rings using the imidazole tailed benzyl linker. This rigid linker has been selected due to its ability to coordinate to the iron(II)-porphyrin NO center in solution without any base-off reaction (see Chapter 6 for further discussion). Eventually, the non-heme iron part will then be condensed with the other amino group of the porphyrin ligand. This way, a complete structural model for NorBC can be prepared and investigated in detail.

In summary, we have synthesized a new model for NorBC consisting of a five-coordinate iron(II)-porphyrin (heme) with covalently attached dichloro[N-propionate-N,N-bis-(2-pyridylmethyl)amine]iron(II) (non-heme). Interaction of this compound with excess NO leads to the formation of the corresponding dinitrosyl adduct, which does not react further to yield N₂O. Further reactions with externally supplied carboxylic acids are currently being tested. In addition, a dinitroporphyrin (precursor compound) necessary to prepare a six-coordinate heme center with attached non-heme iron ligand has been synthesized. This compound with a sixth ligand for heme replicates to the active center of NorBC most closely. The reactivity of this complex with NO will be investigated using various spectroscopic methods in future studies.



Scheme 6.3.4 Synthesis of the precursor (dinitroporphyrin)

References

- ¹ (a) Averill, B. A. *Chem. Rev.* **1996**, *96*, 2951-2964. (b) Zumft, W. G. *Microbiol. Mol. Biol. Rev.* **1997**, *61*, 533-616. (c) Wasser, I. M.; Vries, S. D.; Moenne-Loccoz, P.; Schroder, I.; Karlin, K. D. *Chem. Rev.* **2002**, *102*, 1201.
- ² Girsch, P.; de Vries, S. *Biochim. Biophys. Acta.* **1997**, *1318*, 202-216.
- ³ (a) Butler, C. S.; Sewar, H. E.; Greenwood, C.; Thomson, A. J. *Biochemistry*, **1997**, *36*, 16259-16266. (b) Watmough, N. J.; Cheeseman, M. R.; Butler, C. S.; Little, R. H.; Greenwood, C.; Thomson, A. J. *J. Bioenerg. Biomem.* **1998**, *30*, 55-62. (c) Lin, R.; Farmer, P. J. *J. Am. Chem. Soc.* **2001**, *123*, 1143-1150.
- ⁴ Butland, G.; Spiro, S.; Watmough, N. J.; Richardson, D. J. *Journal of Bacteriology.* **2001**, *183*, 189-199.
- ⁵ (a) Scheidt, W. R.; Elison, M. K. *Acc. Chem. Res.* **1999**, *32*, 350-359. (b) Wyllie, G. R. A.; Scheidt, W. R. *Chem. Rev.* **2002**, *102*, 1067-1090. (c) Ford, P. C.; Fernandez, B. O.; Lim, M. D. *Chem. Rev.* **2005**, *105*, 2439-2456. (d) Ford, P. C.; Lorkovic, I. M. (c) Ford, P. C.; Fernandez, B. O.; Lim, M. D. *Chem. Rev.* **2005**, *105*, 2439-2456. (d) Praneeth, V. K. K.; Neese, F.; Lehnert, N. *Inorg. Chem.* **2005**, *44*, 2570-2572. (e) Praneeth, V. K. K.; Näther, C.; Peters, G.; Lehnert, N. *Inorg. Chem.* **2006**, *45*, 2795-2811.
- ⁶ Wasser, I. M.; Huang, H.; Moenne-Loccoz, P.; Karlin, K. D. *J. Am. Chem. Soc.* **2005**, *127*, 3310-3320.
- ⁷ (a) Silaghi-Dumitrescu, R.; Kurtz, D. M., Jr.; Ljungdhal, L. G.; Lanzilota, W. N. *Biochemistry*, **2005**, *44*, 6492. (b) Tshuva, E. Y.; Lippard, S. J. *Chem. Rev.* **2004**, *104*, 987.
- ⁸ Collman, J. P.; Yan, Y.-L.; Lei, J.; Dinolfo, P. H. *Org. Lett.* **2006**, *8*, 923-926.
- ⁹ Mandel, J. B.; Maricondi, C.; Douglas, B. D. *Inorg. Chem.* **1988**, *27*, 2990-2996.
- ¹⁰ Carvalho, N. M. F.; Horn, A. Jr.; Faria, R. B.; Bortoluzzi, A. J.; Drago, V.; Antunes, O. A. C. *Inorg. Chim. Acta.* **2006**, *359*, 4250-4258.
- ¹¹ Kopf, M.-A.; Karlin, K. D. *Inorg. Chem.* **1999**, *38*, 4922-4923.

¹² Chiou, Y-M.; Que, J. L. *Inorg. Chem.* **1995**, *34*, 3270-3278.

¹³ Lorkovic, I.; Ford, P. C. *J. Am. Chem. Soc.* **2000**, *122*, 6516-6517.

¹⁴ Jo, D-H.; Chiou, Y-M.; Que, J. L. *Inorg. Chem.* **1995**, *34*, 3270-3278.

Chapter 7

Collaborative Investigations

7.2 Scope of this project

Apart from my doctoral research work presented in the previous Chapters, I have also been involved in some collaborative research projects carried out in my group with my supervisor Prof. Dr. Nicolai Lehnert, and outside of my group with Prof. Dr. Kiyoshi Fujisawa, University of Tsukuba, Japan. I had a great opportunity to learn and work on other interesting research topics, including ruthenium nitrosyls, manganese porphyrins and Cu-NO complexes. In this Chapter, these results are compiled together, describing their importance and my contributions to each topic. In addition, published papers and manuscripts pertaining on these works are presented in the following sections (7.2-7.5).

Nitrous oxide (N_2O) is one the biologically important molecule that forms as an intermediate in the reduction of nitric oxide (NO) in the dissimilatory denitrification process. This reaction is catalysed by the enzyme nitrous oxide reductase (N_2OR). In the terminal step of the denitrification, N_2O is then converted to N_2 and H_2O .¹ Furthermore, N_2O has been implicated as an environmentally polluting green house gas.² Despite its biological and environmental significance, not much is known about the coordination chemistry of this molecule. N_2O is an extremely inert molecule and thus a very poor ligand.³ The only well characterized N_2O complex known so far is $[\text{Ru}(\text{NH}_3)_5(\text{N}_2\text{O})]\text{X}_2$ (**1**). However, the coordination mode of N_2O to the Ru center has not yet been determined unambiguously. In Section 7.2, the spectroscopic properties and electronic structure of the complex $[\text{Ru}(\text{NH}_3)_5(\text{N}_2\text{O})]\text{X}_2$ (**1**) using bromide (**1-Br**) and tetrafluoroborate (**1-BF₄**) counterions have been investigated. Complete assignments of the IR and Raman spectra of **1** are presented using ¹⁵N isotope substitution and the quantum chemistry centered normal coordinate analysis (QCC-NCA), coupled to DFT calculations. In this study, Ru-NO⁺ precursor complex $[\text{Ru}(\text{NH}_3)_5(\text{NO})]\text{X}_3$ (**2**) using bromide (**2-Br**), tetrafluoroborate (**2-BF₄**) and triflate (**2-OTf**) counterions has been investigated in comparison to **1**. Vibrational spectra together with force constants obtained from QCC-NCA for **2** are also presented in this section. My contribution to this work corresponds to the synthesis of the Ru(II)-NO⁺ complexes with different counterions. I have synthesized natural abundance and isotope labelled NO complexes of **2** with various counterions. Furthermore, I have obtained single crystals of **2-Br** suitable for X-ray diffraction studies.

Section 7.3 comprises DFT investigations on the P450nor reaction mechanism. My supervisor Prof. Dr. Nicolai Lehnert has carried out most of this work. As mentioned earlier in the Introduction (cf. Chapter 1), the enzyme P450nor carry out the reduction of NO. The active species in this catalytic cycle is Fe(III) form, which binds NO to form a ferric NO adduct with *trans* cysteinate coordination. The next step involves two electron reduction leading to a formal Fe(I)-NO complex that reacts with a second molecule of NO forming N₂O. I have optimized the structures of the intermediates of the P450nor cycle and performed molecular orbital analysis of one of the intermediates.

Heme proteins are one the most versatile group of proteins in the living organism with various important functions such as electron transfer (eg, cytochromes), oxygen transport (eg, hemoglobin), oxygen storage (eg, myoglobin) and catalysis (eg., cytochrome P450). Vibrational spectroscopy is a valuable tool to probe the active sites of many different proteins that including heme proteins. In particular, resonance Raman spectroscopy (RR) constitutes a powerful method since it allows for the determination of the chromophore's structure due to selective resonance enhancement of the chromophore vibrations in the complex protein environment.⁴ Numerous RR studies on heme proteins have been carried out in the past to gain in-depth information about the properties of the heme cofactors. In parallel, bioinorganic synthetic metalloporphyrins have been studied to understand the catalytic reactions and functions performed by heme proteins. Metal complexes of tetraphenylporphyrin and octaethylporphyrin systems have been investigated mostly for this purpose. In Section 7.3, DFT predict the IR and Raman spectra of [M(TPP)Cl], where M = Fe (**1**), Mn (**2**) and Co (**3**), are presented. Based on these results, experimental non-resonance Raman, resonance Raman, and IR spectra of compound **1** have been assigned in detail for the first time. In this project, I have been involved in the purification of [Fe(TPP)Cl] by column chromatography with Florian Paulat, who is the first author of this paper. In addition, I have successfully carried out the crystallization of [Mn(TPP)Cl] and have obtained single crystals suitable for X-ray analysis.

Iron and copper enzymes are involved in the reduction of higher nitrogen oxides in the denitrification cycle. This cycle has a great environmental significance due to a large amount of nitrogen compounds that are consumed, and greenhouse gases (N₂O) that are released into the atmosphere in this process. Copper nitrite reductase (CuNIR) is one of the enzymes involved in the denitrification, which converts nitrite to NO.⁵ In this conversion, it has been

known that the Cu^I-NO adduct forms as an intermediate, and this species has been structurally characterized. In Section 7.4, mononuclear copper nitrosyl (Cu^I-NO) complexes with anionic [HB(3-*t*Bu-5-*i*Prpz)₃]⁻ (L3⁻) and neutral [HC(3-*t*Bu-5-*i*Prpz)₃] (L3⁰) coligands are presented. These have been crystallographically and spectroscopically (UV-Vis, IR, EPR, and MCD) characterized in correlation to DFT calculations. I have been involved in the experimental work with Prof. Dr. Kiyoshi Fujisawa synthesizing the Cu^I-NO compounds, and conducting the initial characterization of these complexes using IR spectroscopy. In addition, I have prepared samples and measured MCD and EPR spectra of these compounds.

References

-
- ¹ (a) Robertson, G. P.; Paul, E. A.; Harwood, R. R. *Science* **2000**, *289*, 1922–1925. (b) B. C. Berks, B. C.; Ferguson, S. J.; Moir, J. W. B.; Richardson, D. J. *Biochim. Biophys. Acta* **1995**, *1232*, 97–173. (c) Richardson, D. J.; Watmough, N. J. *Curr. Opin. Chem. Biol.* **1999**, *3*, 207–219. (d) Shoun, H.; Tanimoto, T. *J. Biol. Chem.* **1991**, *266*, 11078–11082. (e) Haltia, T.; Brown, K.; Tegoni, M.; Cambillau, C.; Saraste, M.; Mattila, K.; DjinoVIC-Carugo, K. *Biochem. J.* **2003**, *369*, 77–88 (f) Brown, K.; Tegoni, M.; Prudencio, M.; Pereira, A. S.; Besson, S.; Moura, J. J.; Moura, I.; Cambillau, C. *Nat. Struct. Biol.* **2000**, *7*, 191–195.
- ² Thiemens, M. H.; Trogler, W. C. *Science* **1991**, *251*, 932–934.
- ³ Bottomley, F.; Lin, I. J. B.; Mukadia, M. *J. Am. Chem. Soc.* **1980**, *102*, 5238–5242.
- ⁴ (a) Spiro, T. G.; Czernuszewicz, R. S. In *Physical Methods in Bioinorganic Chemistry*; Que, L., Jr., Ed.; University Science Books: Sausalito, CA, 2000; pp 59–120. (b) Loehr, T. M. In *Spectroscopic Methods in Bioinorganic Chemistry*; Solomon, E. I., Hodgson, K. O., Eds.; American Chemical Society: Washington, DC, **1998**; pp 136–153.
- ⁵ Averill, B. A., *Chem. Rev.* **1996**, *96*, 2951–2964. (b) Wasser, I. M.; de Vries, S.; Moënné-Loccoz, P.; Schröder, I.; Karlin, K. D., *Chem. Rev.* **2002**, *102*, 1201–1234.

7.2. Spectroscopic Properties and Electronic Structure of Pentammineruthenium(II) Dinitrogen Oxide and Corresponding Nitrosyl Complexes: Binding mode of N₂O and Reactivity

Florian Paulat, Torben Kuschel, Christian Näther, V. K. K. Praneeth, Ole Sander, and Nicolai Lehnert*

Published in: *Inorg. Chem.* **2004**, *43*, 6979-6994.

Spectroscopic Properties and Electronic Structure of Pentammineruthenium(II) Dinitrogen Oxide and Corresponding Nitrosyl Complexes: Binding Mode of N₂O and Reactivity

Florian Paulat, Torben Kuschel, Christian Näther, V. K. K. Praneeth, Ole Sander, and Nicolai Lehnert*

Institut für Anorganische Chemie, Christian-Albrechts-Universität Kiel, Olshausenstrasse 40, D-24098 Kiel, Germany

Received May 28, 2004

The spectroscopic properties and the electronic structure of the only nitrous oxide complex existing in isolated form, [Ru(NH₃)₅(N₂O)]X₂ (**1**, X = Br⁻, BF₄⁻), are investigated in detail in comparison to the nitric oxide precursor, [Ru(NH₃)₅(NO)]X₃ (**2**). IR and Raman spectra of **1** and of the corresponding ¹⁵NNO labeled complex are presented and assigned with the help of normal coordinate analysis (NCA) and density functional (DFT) calculations. This allows for the identification of the Ru–N₂O stretch at ~300 cm⁻¹ and for the unambiguous definition of the binding mode of the N₂O ligand as N-terminal. Obtained force constants are 17.3, 9.6, and 1.4 mdyne/Å for N–N, N–O, and Ru–N₂O, respectively. The Ru(II)–N₂O bond is dominated by π back-donation, which, however, is weak compared to the NO complex. This bond is further weakened by Coulomb repulsion between the fully occupied t_{2g} shell of Ru(II) and the HOMO of N₂O. Hence, nitrous oxide is an extremely weak ligand to Ru(II). Calculated free energies and formation constants for [Ru(NH₃)₅(L)]²⁺ (L = NNO, N₂, OH₂) are in good agreement with experiment. The observed intense absorption at 238 nm of **1** is assigned to the t_{2g} → π* charge transfer transition. These data are compared in detail to the spectroscopic and electronic structural properties of NO complex **2**. Finally, the transition metal centered reaction of nitrous oxide to N₂ and H₂O is investigated. Nitrous oxide is activated by back-donation. Initial protonation leads to a weakening of the N–O bond and triggers electron transfer from the metal to the NN–OH ligand through the π system. The implications of this mechanism for biological nitrous oxide reduction are discussed.

Introduction

Despite the biological and environmental significance of nitrous oxide, not much is known about the coordination chemistry of this molecule. In fact, only one transition metal complex of N₂O has been prepared and isolated so far, and the coordination mode of the nitrous oxide ligand in this system is still a matter of discussion. This compound, [Ru(NH₃)₅(N₂O)] X₂ (**1**), is a Ru(II) complex with pentammine coligands. Attempts to isolate other transition metal N₂O complexes have mostly yielded metal oxide, nitride, or nitrosyl products so far.¹ Complex **1** was first reported as an unstable species in solution.² Later, it was also possible to isolate **1** as a solid with different counterions X (X = Cl⁻, Br⁻, BF₄⁻, etc.).^{3–5} IR data have been reported for **1**, and a simple normal coordinate analysis was performed to explore whether these vibrational data are consistent with end-on N or O coordination of the N₂O ligand. It was found

that O coordination is in better agreement with the experimental data.³ This was later challenged, and it was claimed

- (1) (a) Yamamoto, A.; Kitazume, S.; Pu, L. S.; Ikeda, S. *J. Am. Chem. Soc.* **1971**, *93*, 371–380. (b) Bottomley, F.; Lin, I. J. B.; Mukaida, M. *J. Am. Chem. Soc.* **1980**, *102*, 5238–5242. (c) Bottomley, F.; Paez, D. E.; White, P. S. *J. Am. Chem. Soc.* **1982**, *104*, 5651–5657. (d) Bottomley, F. *Polyhedron* **1992**, *11*, 1707–1731. (e) Vaughan, G. A.; Sofield, C. D.; Hillhouse, G. L.; Rheingold, A. L. *J. Am. Chem. Soc.* **1989**, *111*, 5491. (f) Matsunaga, P. T.; Hillhouse, G. L.; Rheingold, A. L. *J. Am. Chem. Soc.* **1993**, *115*, 2075. (g) Smith, M. R., III; Matsunaga, P. T.; Anderson, R. A. *J. Am. Chem. Soc.* **1993**, *115*, 7049. (h) Koo, K.; Hillhouse, G. L.; Rheingold, A. L. *Organometallics* **1995**, *14*, 456. (i) Groves, J. T.; Roman, J. S. *J. Am. Chem. Soc.* **1995**, *117*, 5594–5595. (j) Laplaza, C. E.; Odom, A. L.; Davis, W. M.; Cummins, C. C.; Protasiewicz, J. D. *J. Am. Chem. Soc.* **1995**, *117*, 4999–5000. (k) Johnson, A. R.; Davis, W. M.; Cummins, C. C.; Serron, S.; Nolan, S. P.; Musaev, D. G.; Morokuma, K. *J. Am. Chem. Soc.* **1998**, *120*, 2071–2085. (l) Khoroshun, D. V.; Musaev, D. G.; Morokuma, K. *Organometallics* **1999**, *18*, 5653–5660. (m) Cherry, J.-P. F.; Johnson, A. R.; Baraldo, L. M.; Tsai, Y.-C.; Cummins, C. C.; Kryatov, S. V.; Rybak-Akimova, E. V.; Capps, K. B.; Hoff, C. D.; Haar, C. M.; Nolan, S. P. *J. Am. Chem. Soc.* **2001**, *123*, 7271–7286. (n) Kaplan, A. W.; Bergman, R. G. *Organometallics* **1997**, *16*, 1106–1108. (o) McCarthy, M. R.; Crevier, T. J.; Bennett, B.; Dehestani, A.; Mayer, J. M. *J. Am. Chem. Soc.* **2000**, *122*, 12391–12392.

* Corresponding author. E-mail: nlehnert@ac.uni-kiel.de.

that nitrous oxide is coordinated with its terminal N atom based on mechanistic data⁴ and NMR results for a related system.⁶ Although experimental evidence is in favor of N coordination of N₂O, it is surprising that this point has never been clarified in the literature. Since there is no crystal structure available for **1**, the most promising approach to define the bonding mode of N₂O is the complete assignment of the metal–ligand stretching vibrations of **1** in connection with a normal coordinate analysis. However, the Ru(II)–N₂O stretching vibration has not been identified so far. The UV absorption spectrum of **1** shows an intense transition at 238 nm which, however, has not been assigned yet. It was noted that N₂O is a weak ligand, but the nature of the Ru(II)–N₂O bond has not been defined. Hence, although complex **1** has been known for quite some time, neither the spectroscopic properties nor the electronic structure of this complex nor the properties of N₂O as a ligand itself have been explored in detail so far.

Recently, the coordination chemistry of nitrous oxide has gained considerable interest due to its biological significance. The enzyme nitrous oxide reductase (N2OR) catalyses the final step in denitrification, i.e., the reduction of N₂O to N₂ following the equation⁷



The catalytically active center of N2OR (called Cu_Z) is a cluster of four copper ions which are bridged by a central sulfide.^{8–10} The resting state of the enzyme has been characterized by a number of spectroscopic methods,¹¹ which ultimately lead to the assignment of one Cu(II) and three Cu(I) for resting Cu_Z.¹² Reduction of this cluster by one electron leads to the catalytically active state with four Cu(I)

which is EPR silent.¹³ The binding of nitrous oxide to the reduced Cu_Z cluster was evaluated using density functional (DFT) calculations.¹³ It was found that N₂O can bind to the cluster in various geometries; i.e., it is coordinated either end-on with its terminal N atom to Cu_I (resting Cu_Z) or side-on bridging between Cu_I and Cu_{IV} (reduced Cu_Z). In the calculations, this bridging mode leads to an increased transfer of electron density to N₂O which would be favorable for its reduction and protonation.

Besides the interest in N₂O reduction and protonation originating from bioinorganic chemistry, this process is also of great importance from an environmental point of view. Because of the increased use of nitrate containing fertilizers in agriculture, a large amount of nitrous oxide is produced by denitrifying bacteria living in soil and seawater and subsequently released to the atmosphere.¹⁴ In addition, burning of fossil fuels contributes to the N₂O emission.¹⁵ This way, nitrous oxide has become the third most important green house gas. Hence, the properties of nitrous oxide and its reactivity are not only of interest for bioinorganic chemistry, but also of global importance. Although the reduction of N₂O to dinitrogen and water (eq 1) is highly exothermic ($\Delta G^\circ \approx -80$ kcal/mol), this gas is metastable and unreactive due to a kinetic barrier to its decomposition.

In this study, the spectroscopic properties and the electronic structure of the complex [Ru(NH₃)₅(N₂O)]X₂ (**1**) using bromide (**1-Br**) and tetrafluoroborate (**1-BF₄**) counterions are investigated. Raman spectra of nitrous oxide complexes are presented for the first time. Using ¹⁵N isotope substitution, the IR and Raman spectra of **1** are fully assigned including Ru–N₂O stretching and bending vibrations using a quantum-chemistry assisted normal coordinate analysis (QCA-NCA).¹⁶ In comparison to DFT calculations on both N and O coordinated isomers of **1**, this allows for an unambiguous definition of the coordination mode of the N₂O ligand. From these calculations, the electronic structure of complex **1** is also investigated, and the properties of nitrous oxide as a ligand are evaluated. Time-dependent DFT calculations are used to assign the UV–vis spectrum of **1**. The free energy

- (2) (a) Armor, J. N.; Taube, H. *J. Am. Chem. Soc.* **1969**, *91*, 6874–6876. (b) Armor, J. N.; Taube, H. *J. Am. Chem. Soc.* **1970**, *92*, 2560–2562. (c) Armor, J. N.; Taube, H. *J. Am. Chem. Soc.* **1971**, *93*, 6476.
- (3) (a) Diamantis, A. A.; Sparrow, G. J. *Chem. Commun.* **1970**, 819–820. (b) Diamantis, A. A.; Sparrow, G. J. *J. Colloid Interface Sci.* **1974**, *47*, 455–458. (c) Diamantis, A. A.; Sparrow, G. J.; Snow, M. R.; Norman, T. R. *Aust. J. Chem.* **1975**, *28*, 1231–1244.
- (4) Bottomley, F.; Brooks, W. V. *Inorg. Chem.* **1977**, *16*, 501–502.
- (5) (a) Bottomley, F.; Crawford, J. R. *Chem. Commun.* **1971**, 200–201. (b) Bottomley, F.; Crawford, J. R. *J. Am. Chem. Soc.* **1972**, *94*, 9092–9095. (c) Bottomley, F.; Brooks, W. V. F.; Clarkson, S. G.; Tong, S.-B. *Chem. Commun.* **1973**, 919–920. (d) Bottomley, F.; Clarkson, S. G.; Tong, S.-B. *J. Chem. Soc., Dalton Trans.* **1974**, 2344–2346. (e) Bottomley, F. *Acc. Chem. Res.* **1978**, *11*, 158–163. (f) Wolfe, S. K.; Andrade, C.; Swinehart, J. H. *Inorg. Chem.* **1974**, *13*, 2567–2572.
- (6) Pamplin, C. B.; Ma, E. S. F.; Safari, N.; Rettig, S. J.; James, B. R. *J. Am. Chem. Soc.* **2001**, *123*, 8596–8597.
- (7) (a) Ferguson, S. J. *Curr. Opin. Chem. Biol.* **1998**, *2*, 182–193. (b) Richardson, D. J.; Watmough, N. J. *Curr. Opin. Chem. Biol.* **1999**, *3*, 207–219. (c) Moura, I.; Moura, J. J. G. *Curr. Opin. Chem. Biol.* **2001**, *5*, 168–175.
- (8) Brown, K.; Tegoni, M.; Prudêncio, M.; Pereira, A. S.; Besson, S.; Moura, J. J. G.; Moura, I.; Cambillau, C. *Nat. Struct. Biol.* **2000**, *7*, 191.
- (9) (a) Rasmussen, T.; Berks, B. C.; Sanders-Loehr, J.; Dooley, D. M.; Zumft, W. G.; Thomson, A. J. *Biochemistry* **2000**, *39*, 12753–12756. (b) Alvarez, M. L.; Ai, J.; Zumft, W. G.; Sanders-Loehr, J.; Dooley, D. M. *J. Am. Chem. Soc.* **2001**, *123*, 576–587.
- (10) (a) Brown, K.; Djinovic-Carugo, K.; Haltia, T.; Cabrito, I.; Saraste, M.; Moura, J. J. G.; Moura, I.; Tegoni, M.; Cambillau, C. *J. Biol. Chem.* **2000**, *275*, 41133–41136. (b) Haltia, T.; Brown, K.; Tegoni, M.; Cambillau, C.; Saraste, M.; Mattila, K.; Djinovic-Carugo, K. *Biochem. J.* **2003**, *369*, 77–88.

- (11) (a) Farrar, J. A.; Thomson, A. J.; Cheesman, M. R.; Dooley, D. M.; Zumft, W. G. *FEBS Lett.* **1991**, *294*, 11. (b) Neese, F.; Ph.D. Thesis, Universität Konstanz, Germany, 1996. (c) Farrar, J. A.; Zumft, W. G.; Thomson, A. J. *Proc. Natl. Acad. Sci. U.S.A.* **1998**, *95*, 9891. (d) Prudêncio, M.; Pereira, A. S.; Tavares, P.; Besson, S.; Cabrito, I.; Brown, K.; Samyn, B.; Devreese, B.; VanBeeumen, J.; Rusnak, F.; Fauque, G.; Moura, J. J. G.; Tegoni, M.; Cambillau, C.; Moura, I. *Biochemistry* **2000**, *39*, 3899.
- (12) (a) Chen, P.; DeBeer George, S.; Cabrito, I.; Antholine, W. E.; Moura, J. J. G.; Moura, I.; Hedman, B.; Hodgson, K. O.; Solomon, E. I. *J. Am. Chem. Soc.* **2002**, *124*, 744–745. (b) Chen, P.; Cabrito, I.; Moura, J. J. G.; Moura, I.; Solomon, E. I. *J. Am. Chem. Soc.* **2002**, *124*, 10497–10507.
- (13) Ghosh, S.; Gorelsky, S. I.; Chen, P.; Cabrito, I.; Moura, J. J. G.; Moura, I.; Solomon, E. I. *J. Am. Chem. Soc.* **2003**, *125*, 15708–15709.
- (14) (a) Intergovernmental Panel on Climate Change (IPCC). *The Science of Climate Change*; Cambridge University Press: New York, 1995. (b) Battle, M. *Nature* **1996**, *383*, 231–235. (c) Kroeze, C.; Mosier, A.; Bouwman, L. *Global Biogeochem. Cycles* **1999**, *13*, 1–8. (d) Bange, H. W. *Nature* **2000**, *408*, 301–302. (e) Robertson, G. P.; Paul, E. A.; Harwood, R. R. *Science* **2000**, *289*, 1922–1925.
- (15) (a) Berges, M. G. M.; Hofman, R. M.; Scharffe, D.; Crutzen, P. J. *J. Geophys. Res.* **1993**, *98*, 18527. (b) Becker, K. H.; Lörzer, J. C.; Kurtenbach, R.; Wiesen, P. *Environ. Sci. Technol.* **1999**, *33*, 4134–4139.
- (16) Lehnert, N.; Tuczak, F. *Inorg. Chem.* **1999**, *38*, 1659–1670.

for ligand binding is calculated for **1** in comparison to related compounds. Finally, the reduction and protonation of end-on terminally coordinated N_2O are investigated.

Ru–NO complexes with various coligands have drawn considerable interest recently due to their significance as antitumor and antiseptic agents.¹⁷ In this study, the Ru(II)–NO⁺ precursor complex $[\text{Ru}(\text{NH}_3)_5(\text{NO})]\text{X}_3$ (**2**) using bromide (**2-Br**), tetrafluoroborate (**2-BF₄**), and triflate (**2-OTf**) counterions has also been investigated in comparison with **1**. Although **2** has been the topic of numerous studies, it is quite surprising that the spectroscopic assignments for this complex are incomplete. Vibrational spectra are presented for **2** together with force constants obtained from normal coordinate analysis using QCA-NCA. The results show that complex **2** exchanges its nitrosyl oxygen during synthesis. For **2-Br**, an unusual splitting of the N–O stretching vibration is observed which is explained on the basis of the crystal structure of **2-Br** presented here. The electronic structure of **2** is briefly discussed, and the electronic spectra are assigned. The mechanistic implications of the observed oxygen exchange of NO during the synthesis are discussed. These data obtained for complex **2** serve as a reference for a quantitative interpretation of the results for **1**.

Experimental and Computational Procedures

Syntheses. Reactions were performed using Schlenk techniques. The starting material RuCl_3 was purchased from Aldrich. The precursor complexes $[\text{Ru}(\text{NH}_3)_5(\text{Cl})]\text{Cl}_2$ and $[\text{Ru}(\text{NH}_3)_6]\text{Cl}_3$ were prepared according to literature procedures.¹⁸ NO gas was passed through a potassium hydroxide column and then through a cold trap at -80°C prior to usage to remove higher nitrogen oxide impurities.

$[\text{Ru}(\text{NH}_3)_5(\text{NO})]\text{Br}_3$ (2-Br**).** This complex can be prepared by two different methods. (a) Following a procedure of Armor et al.,¹⁹ 0.3 g of $[\text{Ru}(\text{NH}_3)_6]\text{Cl}_3$ is dissolved in 35 mL of degassed 0.1 M hydrobromic acid, and then, NO is passed through the solution for about 25 min. The solution changes its color from yellow to orange. The solution is then reduced to half of its volume and stored in the refrigerator. After a few days, orange crystals of $[\text{Ru}(\text{NH}_3)_5(\text{NO})]\text{X}_3$ (X = Cl, Br) have formed. The crystals are collected by filtration and washed with 3 M HBr, ethanol, and water. Yield: 75%. To obtain pure **2-Br**, the raw product is recrystallized several times from 1 M HBr. (b) Following a method by Gleu et al.,²⁰ 0.4 g of $[\text{Ru}(\text{NH}_3)_5(\text{Cl})]\text{Cl}_2$ is dissolved in ~12 mL of water and heated until boiling. The solution is removed from the oil bath, and 12 mL of concentrated NH_3 solution is added to the hot solution. Then, 1.2 g of $(\text{NH}_4)(\text{S}_2\text{O}_8)$ is added slowly, and the solution is swirled.

- (17) (a) Chanda, N.; Mobin, S. M.; Puranik, V. G.; Datta, A.; Niemeyer, M.; Lahiri, G. K. *Inorg. Chem.* **2004**, *43*, 1056–1064. (b) Marchenko, A. V.; Vedernikov, A. N.; Dye, D. F.; Pink, M.; Zaleski, J. M.; Caulton, K. G. *Inorg. Chem.* **2004**, *43*, 351–360. (c) Patra, A. K.; Mascharak, P. K. *Inorg. Chem.* **2003**, *42*, 7363–7365. (d) Hirano, T.; Oi, T.; Nagao, H.; Morokuma, K. *Inorg. Chem.* **2003**, *42*, 6575–6583. (e) Marchenko, A. V.; Vedernikov, A. N.; Dye, D. F.; Pink, M.; Zaleski, J. M.; Caulton, K. G. *Inorg. Chem.* **2002**, *41*, 4087–4089. (f) Hadadzadeh, H.; DeRosa, M. C.; Yap, G. P. A.; Rezvani, A. R.; Crutchley, R. J. *Inorg. Chem.* **2002**, *41*, 6521–6526. (g) Nagao, H.; Hirano, T.; Tsuboya, N.; Shiota, S.; Mukaida, M.; Oi, T.; Yamasaki, M. *Inorg. Chem.* **2002**, *41*, 6267–6273.
- (18) Allen, A. D.; Bottomley, F.; Harris, R. O.; Reinsalu, V. P.; Senoff, C. V. *Inorg. Synth.* **1970**, *12*, 2–8.
- (19) Armor, J. N.; Scheidegger, H. A.; Taube, H. *J. Am. Chem. Soc.* **1968**, *90*, 5928–5929.
- (20) Gleu, K.; BÜddecke, I. Z. *Anorg. Allg. Chem.* **1952**, *268*, 202–220.

Table 1. Crystal Data and Results of the Structure Refinement for Compound **2-Br**

chemical formula	$[\text{Ru}(\text{NH}_3)_5(\text{NO})]\text{Br}_3 \cdot \text{H}_2\text{O}$
fw	474.0
<i>T</i>	room temperature
λ	0.71073
cryst syst	orthorhombic
space group	<i>Pnma</i>
<i>a</i>	12.234(1)
<i>b</i>	6.9982(4)
<i>c</i>	14.479(1)
<i>V</i>	1246.9(1)
<i>Z</i>	4
<i>D</i> _{calcd}	2.444
μ	10.85
$R1^a$ [<i>I</i> > 2 σ (<i>I</i>)]	0.0292
wR2 [all data]	0.0842

$$^a R1 = \sum |F_o| - |F_c| / \sum |F_o|; wR2 = [\sum [w(F_o^2 - F_c^2)^2] / \sum [w(F_o^2)^2]]^{1/2}.$$

A pale yellow precipitate of $[\text{Ru}(\text{NH}_3)_5(\text{NO})](\text{SO}_4)_{1/2}(\text{S}_2\text{O}_8)_{1/2}$ forms immediately which is collected by filtration after about 1 h. The product is washed with 2 M NH_3 solution and acetone and dried. Yield: 25%.

The obtained raw product is then refluxed with concentrated HCl for about 15 min to obtain $[\text{Ru}(\text{NH}_3)_5(\text{NO})]\text{Cl}_3$ (**2-Cl**) in high yield (95%). Repeated recrystallization from 1 M HBr yields **2-Br**. Structural data are available in Table 1.

$[\text{Ru}(\text{NH}_3)_5(\text{NO})](\text{BF}_4)_3$ (2-BF₄**) and $[\text{Ru}(\text{NH}_3)_5(\text{NO})](\text{OTf})_3$ (**2-OTf**).** Compound **2-BF₄** is insoluble in water or acid and can therefore be prepared by dissolving **2-Cl** in water and adding 1 M HBF_4 . The product precipitates as yellow powder. Compound **2-OTf**, on the other hand, is very soluble in water. It is obtained by repeated recrystallization of **2-Cl** from 2.5 M $\text{CF}_3\text{SO}_3\text{H}$ solution as yellow powder in relatively low yield.

$[\text{Ru}(\text{NH}_3)_5(\text{N}_2\text{O})]\text{X}_2$ (1**).** Preparation of the nitrous oxide complex **1-Br** (X = Br) follows the procedure of Bottomley et al.^{5b} Complex $[\text{Ru}(\text{NH}_3)_5(\text{NO})]\text{Br}_3$ (112 mg) and 1.12 g of $\text{NH}_2\text{OH} \cdot \text{HX}$ (X = Cl, Br; 1:1 mixture) are dissolved in 10 mL of degassed water in an ice bath. Then, 5 pellets (about 1 g) of NaOH are added, and **1-Br** starts precipitating immediately as pale yellow solid. The reaction is stopped after 3–5 min by filtration. The obtained product is washed with oxygen-free ethanol and diethyl ether and dried in vacuo. Yield: 67%. The preparation of **1-BF₄** is complicated by the fact that the precursor **2-BF₄** is insoluble in water. Complex $[\text{Ru}(\text{NH}_3)_5(\text{NO})](\text{BF}_4)_3$ (100 mg) and 560 mg of $\text{NH}_2\text{OH} \cdot \text{HBF}_4$ are suspended in ~12 mL of degassed water in an ice bath. On addition of the NaOH pellets, the precursor **2-BF₄** starts dissolving while at the same time pale yellow **1-BF₄** precipitates. In order to ensure completion of the reaction, the mixture is stirred for 5 min and then filtered. Yield: 93%. The corresponding complex with triflate could not be obtained by this method, because the triflate salts are too soluble in water.

Crystal Structure Determination. The data were collected using a 4-circle diffractometer from STOE & CIE and were corrected for absorption effects. The structure was solved with direct methods using SHELXS-97 and was refined against F^2 using SHELXL-97. All non-H atoms were refined anisotropically. The H-atoms were positioned with idealized geometry and refined using the riding model. One bromide anion is disordered in two positions and was refined using a split model. The $[\text{Ru}(\text{NH}_3)_5\text{NO}]$ unit is located on a crystallographic mirror plane, and the NO ligand is disordered in two positions due to symmetry. This disorder remains constant in the noncentrosymmetric space group *Pna*2₁.

In this space group, it is not possible to decide if the two different orientations are unequally occupied or not. However, in this case

the absolute structure cannot be refined. To check if, e.g., an ordered super structure is present, one additional data set was measured at low temperatures using an IPDS from STOE & CIE. However, from these investigations there is no hint for a super structure or any change of the symmetry.

UV–Vis Spectroscopy. Absorption spectra were recorded either in KBr disks or for pure solids (between sapphire windows) at 10 K using a Varian Cary 5 UV–vis–NIR spectrometer equipped with a CTI cryocooler.

Vibrational Spectroscopy. FT-Raman spectra were recorded on a Bruker IFS 66 interferometer with a Bruker FRA 106 Raman attachment using a Nd:YAG laser for excitation ($\lambda = 1064$ nm). Measurements were performed on pure compounds. Resolution was set to 2 cm^{-1} . Middle- and far-infrared spectra (MIR & FIR) were recorded on a Bruker IFS 66v vacuum instrument at room temperature. For the MIR region, KBr disks were used, and the spectra were recorded at a resolution of 1 cm^{-1} . In the far-IR region, PE pellets were used, and the resolution was set to 2 cm^{-1} . Low-temperature MIR spectra were obtained on a Mattson Genesis type I spectrometer equipped with a cryogenic CTI cryostat. Spectra were recorded at 20 K at a resolution of 1 cm^{-1} .

Normal Coordinate Analysis. Normal coordinate calculations were performed using the QCPE computer program 576 by M. R. Peterson and D. F. McIntosh which involves solution of the secular equation $\mathbf{GFL} = \lambda\mathbf{L}$ by the diagonalization procedure of Miyazawa.²¹ The calculations are based on a general valence force field; force constants are refined with the nonlinear optimization routine of the simplex algorithm according to Nelder and Mead.²² The simplex optimization was used to refine only selected force constants according to the quantum-chemical assisted normal coordinate analysis.¹⁶ Here, a force field from DFT calculations is used as a starting point to generate initial force constants, and a subset of these is fit to reproduce the known experimental frequencies. For the NCA, the H atoms of the NH_3 ligands have been removed since the objective is to obtain force constants for the Ru–NO and Ru– N_2O subunits. For the resulting “N” ligands, an effective mass of 18 has been used resembling NH_3 . This leads to the simplified models $[\text{Ru}(\text{N}_5)(\text{NO})]$ (**2**) and $[\text{Ru}(\text{N}_5)(\text{N}_2\text{O})]$ (**1**) which are based on the calculated structures but which have further been symmetrized (by setting all N–Ru–N angles to 90°) to have C_{4v} symmetry.

Density Functional Calculations. Spin-restricted DFT calculations using Becke’s three parameter hybrid functional with the correlation functional of Lee, Yang, and Parr (B3LYP²³) were performed using the program package Gaussian 98.²⁴ The structures of the cations $[\text{Ru}(\text{NH}_3)_5(\text{N}_2\text{O})]^{2+}$ (**1**) and $[\text{Ru}(\text{NH}_3)_5(\text{NO})]^{3+}$ (**2**) were fully optimized using the LanL2DZ basis set. Calculated

vibrational frequencies show that the obtained geometries represent true minima since no imaginary frequencies were found. IR and Raman intensities were calculated as well for vibrational assignments. The LanL2DZ basis set applies Dunning/Huzinaga full double- ζ (D95)²⁵ basis functions on first row and Los Alamos effective core potentials plus DZ functions on all other atoms.²⁶ For calculating the absorption spectrum of **1** and **2**, the time-dependent DFT formalism as implemented in G98 has been applied. To calculate the binding constants for ligands L in $[\text{Ru}(\text{NH}_3)_5(\text{L})]^{2+}$, the structures of the cations $[\text{Ru}(\text{NH}_3)_5]^{2+}$ and $[\text{Ru}(\text{NH}_3)_5(\text{L})]^{2+}$ with $\text{L} = \text{H}_2\text{O}, \text{N}_2$ have been fully optimized. In addition, $[\text{Ru}(\text{NH}_3)_5]^{3+}$ has also been fully optimized. All these structures represent true minima as evident from frequency calculations. To investigate the protonation of the coordinated N_2O ligand and the subsequent splitting of the N–O bond, the structures of $[\text{Ru}(\text{NH}_3)_5(\text{NNOH})]^{3+}$ and of $[\text{Ru}(\text{NH}_3)_5(\text{NN})]^{4+}$ have been fully optimized as well. Solvation effects were included in the calculations of the reaction energies in Scheme 1 using the Polarized Continuum Model (PCM)²⁷ with water as solvent ($\epsilon = 78$). In all calculations, convergence was reached when the relative change in the density matrix between subsequent iterations was less than 1×10^{-8} . Atomic charges were calculated using the natural population analysis (NPA). Force constants in internal coordinates were extracted from the Gaussian output using the program Redong²⁸ (QCPE 628). Orbitals were plotted with the program GaussView.

Results and Analysis

A. Crystal Structure, Spectroscopy, and Electronic Structure of $[\text{Ru}(\text{NH}_3)_5(\text{NO})]^{3+}$ (2**).** In order to explore the spectroscopic properties and the electronic structure of $[\text{Ru}(\text{NH}_3)_5(\text{N}_2\text{O})]\text{X}_2$ (**1**), the precursor complex $[\text{Ru}(\text{NH}_3)_5(\text{NO})]\text{X}_3$ (**2**) has been investigated first. In comparison, this allows for a quantitative evaluation of the results obtained for **1**, since the electronic structure and reactivity of complex **2** are known from a number of studies.^{29–31} First, the crystal structure of $[\text{Ru}(\text{NH}_3)_5(\text{NO})]\text{Br}_3$ is presented. Vibrational data for **2** with different counterions are assigned with the help of density functional (DFT) calculations and a normal coordinate analysis. Finally, low-temperature UV–vis spectra of **2** are assigned using time-dependent DFT (TD-DFT) calculations.

A.1. Crystal Structure. Compound **2-Br** crystallizes in the orthorhombic space group *Pnma* with 4 formula units in the unit cell. The asymmetric unit consists of one $[\text{Ru}(\text{NH}_3)_5(\text{NO})]^{3+}$ unit, three crystallographically independent bromide anions, and one water molecule, all of them located on crystallographic mirror planes. The ruthenium cations are coordinated by 5 ammonia molecules and one NO ligand. Due to symmetry, the NO group is disordered

(21) Miyazawa, T. *J. Chem. Phys.* **1958**, *29*, 246.

(22) Nelder, J. A.; Mead, R. *Comput. J.* **1965**, *7*, 308.

(23) (a) Becke, A. D. *Phys. Rev. A* **1988**, *38*, 3098. (b) Becke, A. D. *J. Chem. Phys.* **1993**, *98*, 1372. (c) Becke, A. D. *J. Chem. Phys.* **1993**, *98*, 5648.

(24) Frisch, M. J.; Trucks, G. W.; Schlegel, H. B.; Scuseria, G. E.; Robb, M. A.; Cheeseman, J. R.; Zakrzewski, V. G.; Montgomery, J. A., Jr.; Stratmann, R. E.; Burant, J. C.; Dapprich, S.; Millam, J. M.; Daniels, A. D.; Kudin, K. N.; Strain, M. C.; Farkas, O.; Tomasi, J.; Barone, V.; Cossi, M.; Cammi, R.; Mennucci, B.; Pomelli, C.; Adamo, C.; Clifford, S.; Ochterski, J.; Petersson, G. A.; Ayala, P. Y.; Cui, Q.; Morokuma, K.; Malick, D. K.; Rabuck, A. D.; Raghavachari, K.; Foresman, J. B.; Cioslowski, J.; Ortiz, J. V.; Stefanov, B. B.; Liu, G.; Liashenko, A.; Piskorz, P.; Komaromi, I.; Gomperts, R.; Martin, R. L.; Fox, D. J.; Keith, T.; Al-Laham, M. A.; Peng, C. Y.; Nanayakkara, A.; Gonzalez, C.; Challacombe, M.; Gill, P. M. W.; Johnson, B. G.; Chen, W.; Wong, M. W.; Andres, J. L.; Head-Gordon, M.; Replogle, E. S.; Pople, J. A. *Gaussian 98*, revision A.11; Gaussian, Inc.: Pittsburgh, PA, 1998.

(25) *Modern Theoretical Chemistry*; Dunning, T. H., Jr., Hay, P. J., Schaefer, H. F., III, Eds.; Plenum: New York, 1976.

(26) (a) Hay, P. J.; Wadt, W. R. *J. Chem. Phys.* **1985**, *82*, 270, 299. (b) Wadt, W. R.; Hay, P. J. *J. Chem. Phys.* **1985**, *82*, 284.

(27) Cramer, C. J.; Truhlar, D. G. *Chem. Rev.* **1999**, *99*, 2161–2200.

(28) Allouche, A.; Pourcin, J. *Spectrochim. Acta* **1993**, *49A*, 571.

(29) (a) Enemark, J. H.; Feltham, R. D. *Coord. Chem. Rev.* **1974**, *13*, 339.

(b) Bottomley, F. *Coord. Chem. Rev.* **1978**, *26*, 7–32. (c) Westcott, B. L.; Enemark, J. H. *Transition Metal Nitrosyls*; Solomon, E. I., Lever, A. B. P., Eds.; Wiley: New York, 1999; Vol. 2, p 403.

(30) Callahan, R. W.; Meyer, T. J. *Inorg. Chem.* **1977**, *16*, 574–581.

(31) Czap, A.; van Eldik, R. *J. Chem. Soc., Dalton Trans.* **2003**, 665–671.

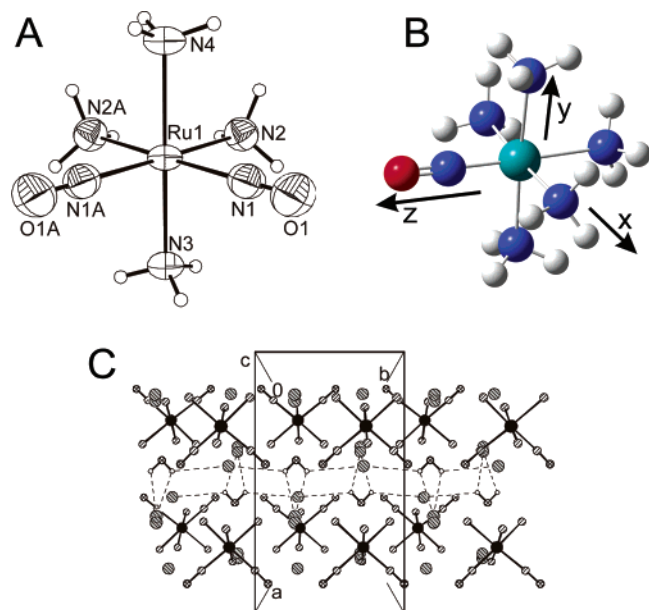


Figure 1. (A) Crystal structure of the $[\text{Ru}(\text{NH}_3)_5(\text{NO})]^{3+}$ unit in **2-Br** with labeling. Displacement ellipsoids are drawn at the 50% probability level. The two NO groups indicate the positions of disordering. (B) Optimized structure from DFT calculations. (C) Crystal structure of compound **2-Br** with view along the crystallographic c axis (N-hydrogen atoms are omitted for clarity).

in two positions and superimposed with one ammonia ligand (see Experimental Section). Figure 1A shows the $[\text{Ru}(\text{NH}_3)_5(\text{NO})]^{3+}$ cation with two NO units indicating the disordered positions. Important distances and angles are given in the Supporting Information Table 5. In the crystal structure, the $[\text{Ru}(\text{NH}_3)_5(\text{NO})]^{3+}$ units are stacked in the direction of the crystallographic a -axis. The bromide ions are connected by $\text{O}-\text{H}\cdots\text{Br}$ hydrogen bridges via the water molecules (Figure 1C).

A.2 Vibrational Spectra and Assignment. The IR spectrum of $[\text{Ru}(\text{NH}_3)_5(\text{NO})]\text{Br}_3$ is shown in Figure 2 including the corresponding ^{15}NO isotope labeled data. For the labeling experiments, $^{15}\text{N}^{18}\text{O}$ has been used. However, the observed shifts do only correspond to the presence of the ^{15}N in the complex (see NCA). This shows that complex **2** exchanges its nitrosyl oxygen during synthesis. Isotope sensitive bands are present at 1927/1912 and 602 cm^{-1} in **2-Br** which shift to 1889/1873 and 588 cm^{-1} , respectively, on isotope substitution. These bands are assigned to the N–O stretch and the Ru–N–O linear bend (doubly degenerate), respectively. In the corresponding Raman spectra in Figure 3, the N–O stretch is found at 1927/1911 cm^{-1} and the Ru–NO stretch at 594 cm^{-1} , respectively. These shift to 1888/1872 and 590 cm^{-1} , respectively, on ^{15}N isotope labeling. These assignments are confirmed by normal coordinate analysis (vide infra). The splitting of $\nu(\text{N}-\text{O})$ into two bands could be due to a correlation effect in the solid state. However, this seems unlikely since the observed intensity pattern (1911, strong; 1927, weak) is identical for IR and Raman. In addition, the splitting and intensity pattern is conserved on isotope substitution, which excludes Fermi resonance. This indicates that there are two different NO molecules in the crystal with a slightly different environment,

which is in accordance with the observed disorder (vide infra). These two species would then give rise to the two observed bands. Since no superstructure reflections could be found experimentally, the distribution of the NO ligands over the two positions must be random. Other bands in the IR and Raman spectra belong to the $[\text{Ru}(\text{NH}_3)_5]^{2+}$ subunit of **2-Br** and can be assigned with the help of a DFT calculation.

Calculated IR and Raman spectra for $[\text{Ru}(\text{NH}_3)_5(\text{NO})]^{3+}$ are shown in Figures 2 and 3 in comparison with experimental results for **2-Br**. The complete assignments are summarized in Table 6 in the Supporting Information. The N–O stretch is calculated at 1905 cm^{-1} in very good agreement with experiment. In the calculations, the two Ru–N–O linear bends are calculated at ~ 590 cm^{-1} and the Ru–NO stretch at 567 cm^{-1} , which resembles the experimental order of the vibrational energies. In agreement with the calculations, the linear bends are not observed in the Raman spectrum. Vice versa, the Ru–NO stretch is predicted by the calculations to be Raman active but only weakly IR active, and accordingly, this mode is not observed in the IR data for **2-Br**. Additional vibrations occurring in this spectral region are the Ru–NH₃ stretches. These modes are predicted to be Raman active only by the calculations and, hence, are assigned to the strong Raman bands at 508 and 487 cm^{-1} . The weak IR bands at 473 and 450 cm^{-1} are also identified with these vibrations.

In summary, with the help of DFT calculations the IR and Raman spectra of **2-Br** have been completely assigned. The most striking differences between the calculations and experiment occur (a) for the N–H stretching and H–N–H bending modes due to anharmonicity³² and (b) for the metal–ligand vibrations, the energy of which is underestimated in the calculations. The assignment of the N–H stretching and bending vibrations is in agreement with work of Mercer et al.³³ However, their assignment of $\nu(\text{Ru}-\text{NO})$ to the IR band at ~ 600 cm^{-1} and of the Ru–N–O bends to a very weak band below 400 cm^{-1} is not in agreement with the isotope data and calculations presented here. In addition, their assignment of $\nu(\text{Ru}-\text{NH}_3)$ to IR bands below 500 cm^{-1} only is incomplete. Table 6 in the Supporting Information also shows the complete vibrational assignments for **2-BF₄**, which are very similar to those of **2-Br**. Importantly, in the IR spectrum of **2-BF₄** both the Ru–N–O linear bends (at 609 cm^{-1}) and the Ru–NO stretch (weak band at 589 cm^{-1}) are observed, which further supports the above assignments. Finally, Table 6 in the Supporting Information gives the vibrational assignments for **2-OTf**. Both **2-BF₄** and **2-OTf** do not show a splitting of the N–O stretch which further indicates that this splitting in the case of **2-Br** is not an

(32) All the vibrations above 1000 cm^{-1} (with exception of the N–O stretch) correspond to modes that have dominant hydrogen displacement character. Strikingly, all these vibrations are calculated up to 10% too high in energy compared to experiment (cf. Supporting Information Table 6). This deviation is due to the anharmonicity of these modes which is not taken into account by the calculations.

(33) Mercer, E. E.; McAllister, W. A.; Durig, J. R. *Inorg. Chem.* **1966**, *5*, 1881–1886.

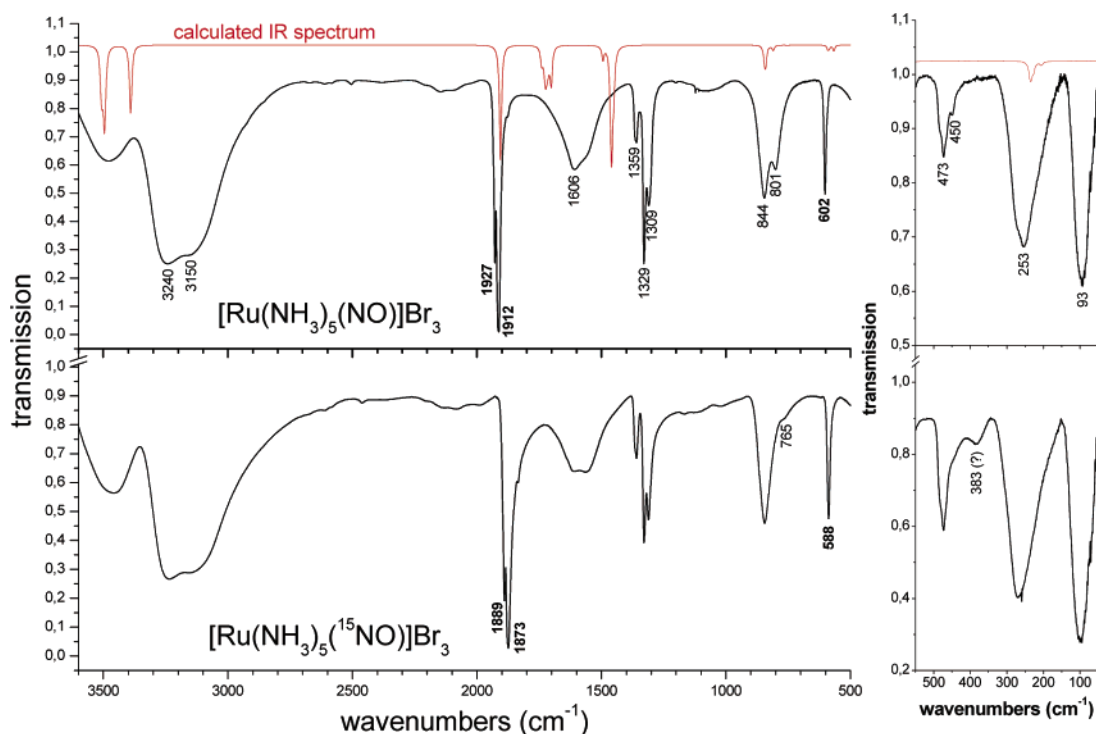


Figure 2. IR spectrum of **2-Br** (top) and of the corresponding ^{15}NO isotope labeled complex (bottom). The calculated spectrum is also included in the top panel as indicated.

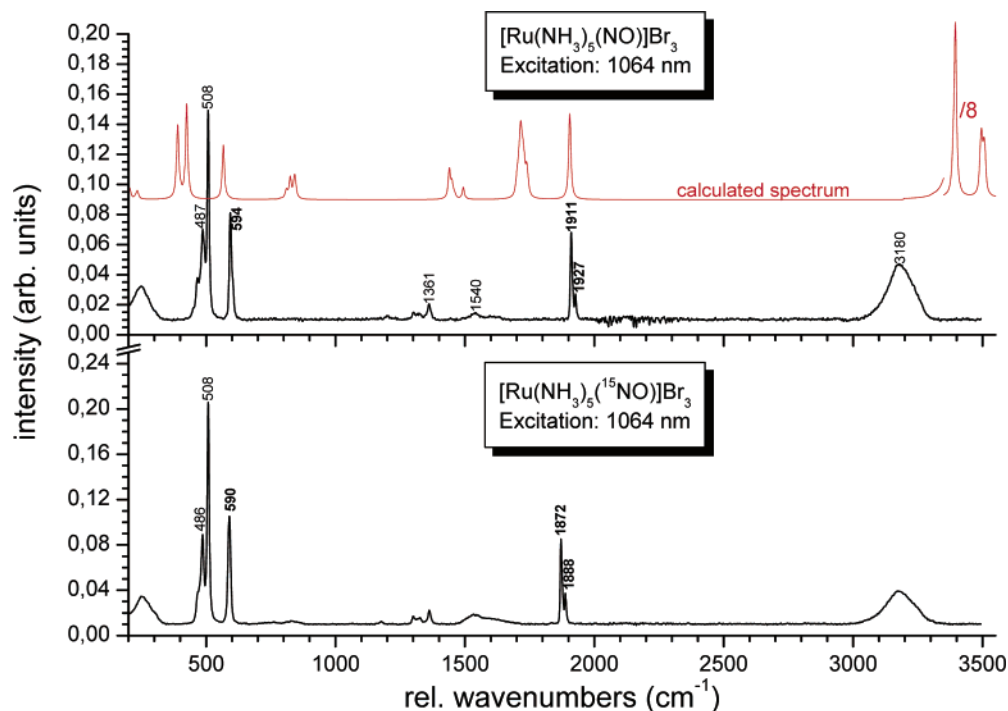


Figure 3. Raman spectrum of **2-Br** (top) and of the corresponding ^{15}N isotope labeled complex (bottom). The calculated spectrum is also included in the top panel as indicated.

intrinsic feature of the $[\text{Ru}(\text{NH}_3)_5(\text{NO})]^{3+}$ cation but is related to the crystal structure of the bromide salt.

A.3. Normal Coordinate Analysis (NCA). The assignments of the vibrations of the $[\text{Ru}(\text{NO})]^{3+}$ subunit presented above are confirmed by NCA using model $\hat{2}$. As shown in Table 2, excellent agreement is obtained between the experimental and NCA frequencies when ^{15}NO is used as the isotopically labeled ligand. The expected isotope shifts

for $^{15}\text{N}^{18}\text{O}$ are also shown. Strikingly, these are about twice as large as the shifts observed spectroscopically. This proves that the ^{18}O in the applied $^{15}\text{N}^{18}\text{O}$ gas was exchanged against an unlabeled oxygen during synthesis yielding the corresponding ^{15}NO complex (see Discussion section). In addition, the calculated ^{15}N isotope shifts clearly show that the assignment of the 594 cm^{-1} Raman band to $\nu(\text{Ru}-\text{NO})$ (isotope shift: 4 cm^{-1}) and of the 602 cm^{-1} IR band to

Table 2. Comparison of Experimental and QCA-NCA Vibrational Frequencies [cm^{-1}] and of QCA-NCA and Calculated (DFT) Force Constants [$\text{mdyn}/\text{\AA}$] for $[\text{Ru}(\text{NH}_3)_5(\text{NO})]\text{Br}_3$ (**2-Br**)

mode	exptl		QCA-NCA			force constant, f	
	nai ^a	¹⁵ NO	nai ^a	¹⁵ NO	(¹⁵ N ¹⁸ O)	QCA-NCA	calcd ^b
$\nu(\text{N}-\text{O})$	(1927)/1911	(1888)/1872	1911	1872	(1829)	15.338	15.357
$\nu(\text{Ru}-\text{NO})$	594	590	594	589	(574)	5.041	4.644
$\delta(\text{Ru}-\text{N}-\text{O})$	602	588	603	587	(583)	0.664	0.646

^a nai = natural abundance isotopes. ^b Calculated with B3LYP/LanL2DZ; see Experimental Section. Free NO: $\nu(\text{N}-\text{O}) = 1876 \text{ cm}^{-1}$; $f_{\text{N}-\text{O}} = 15.49 \text{ mdyn}/\text{\AA}$. NO^+ : $\nu(\text{N}-\text{O}) = 2387 \text{ cm}^{-1}$ in $(\text{NO}^+)(\text{BF}_4^-)$; $f_{\text{N}-\text{O}} = 25.07 \text{ mdyn}/\text{\AA}$.³⁴

Table 3. Comparison of Experimental and Calculated Bond Distances [\AA]

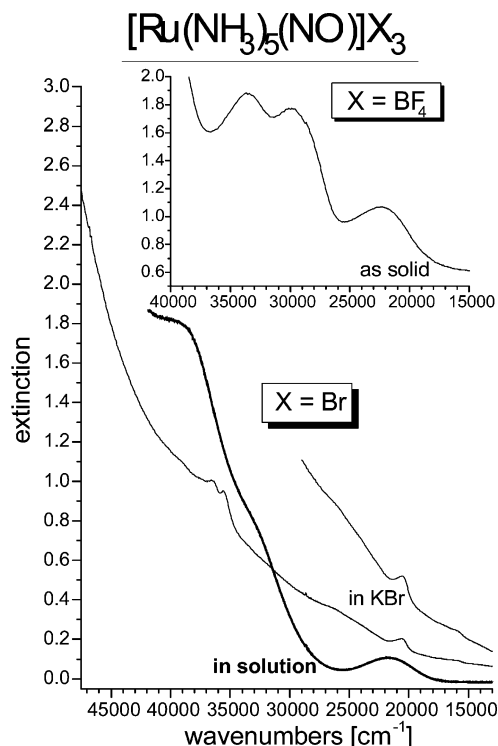
	$\Delta(\text{Ru}-\text{NO})$		$\Delta(\text{Ru}-\text{NH}_3)$	
	$\Delta(\text{Ru}-\text{NO})$	$\Delta(\text{N}-\text{O})$	trans	cis
2-Br , cryst struct	1.913 ^a	1.019	2.087 ^b	2.096 ^b
$[\text{Ru}(\text{NH}_3)_5(\text{NO})]^{3+}$	1.802	1.166	2.175	2.199 ^b

^a Overestimated since the experimental bond distance is actually an average of a Ru–NO and a Ru–NH₃ bond length due to the observed disorder in the crystal. ^b Averaged over all corresponding bond lengths.

$\delta(\text{Ru}-\text{N}-\text{O})$ (isotope shift: 14 cm^{-1}) as presented above is correct. These shifts are well reproduced by the NCA as shown in Table 2. Force constants are discussed in the next section.

A.4. Electronic Structure and Spectra. Figure 1B shows the fully optimized structure of the $[\text{Ru}(\text{NH}_3)_5(\text{NO})]^{3+}$ cation. Important bond lengths are compared to experiment in Table 3. Unfortunately, due to the disorder in the crystal (vide supra), the most interesting comparison between the experimental and the calculated Ru–NO distance is obscured. Other distances are in reasonable agreement. A more sophisticated comparison is available from the experimental and calculated force constants and vibrational frequencies given in Table 2. In the calculation, the Ru–NO and even more the Ru–NH₃ frequencies are obtained at too low an energy indicating that the metal–ligand bond strengths are generally underestimated in the calculation. This can also be seen from the Ru–NO force constant, which is calculated to $4.64 \text{ mdyn}/\text{\AA}$ compared to the experimental value of $5.04 \text{ mdyn}/\text{\AA}$. The obtained bonding description is analyzed in the following.

The MO diagram of the free NO molecule is shown in Figure 5 in the Supporting Information. Free NO is a radical with the unpaired electron occupying one of the π^* orbitals. Due to the short NO bond distance, the energy difference between the singly occupied π^* orbital and the next lower occupied orbital σ_{nb} is quite large. The orbital σ_{nb} is a combination of sp hybrids along the N–O axis but is only weakly N–O bonding. Just below σ_{nb} , the two N–O π orbitals are located. The complex $[\text{Ru}(\text{NH}_3)_5(\text{NO})]^{3+}$, formally a $\text{Ru}^{3+}-\text{NO}^+$ adduct, actually has an electronic structure corresponding to $\text{Ru}^{2+}-\text{NO}^+$. This is evident from the linear Ru–N–O unit and the observed N–O stretching frequency of $> 1900 \text{ cm}^{-1}$ as described in the literature.^{29,5e} This is also reflected by the obtained MO diagram of **2** given in Figure 6 in the Supporting Information. Figure 1b shows the coordinate system used in the following discussion with the Ru–N–O unit located on the z axis. Since NO is bound as NO^+ , its π^* orbitals are both empty and form a back-


Figure 4. Low-temperature absorption spectra of $[\text{Ru}(\text{NH}_3)_5\text{NO}]\text{Br}_3$ as KBr disk and $[\text{Ru}(\text{NH}_3)_5\text{NO}](\text{BF}_4)_3$ (insert) as a solid measured between sapphire windows. For the bromide salt, a solution spectrum is also shown.

bond with the two t_{2g} orbitals d_{xz} and d_{yz} of Ru. The corresponding antibonding combinations, $\pi^*_{-d_{xz}}$ and $\pi^*_{-d_{yz}}$, are the LUMO of complex **2**. They have about 70% π^* and 25% d character, which corresponds to strong back-bonding. The corresponding bonding combinations, $d_{xz}-\pi^*$ and $d_{yz}-\pi^*$, are occupied and have 68% d and 26% π^* contribution. The third t_{2g} orbital, d_{xy} , is also occupied and corresponds to the HOMO of **2**. This shows that Ru is in the +2 oxidation state and low-spin in agreement with the $\text{Ru}^{2+}-\text{NO}^+$ description. The strength of the π back-bond is reflected by the N–O force constant of $15.34 \text{ mdyn}/\text{\AA}$, which is distinctively lower than that of NO^+ and actually is very close to that of free NO.³⁴ Hence, a large amount of electron density is transferred from Ru^{2+} to NO^+ through the π system. Besides these two strong π back-bonds, there is also a Ru–NO σ bond mediated by the orbital σ_{nb} . The bonding combination, $\sigma_{\text{nb}}-d_z^2$, has 5% d_z^2 contribution which corresponds to a weak interaction. This bonding description is also reflected by the calculated NPA charges and d orbital populations given in Table 4. The formal +1 charge of the NO^+ ligand is reduced

(34) Fadini, A.; Schnepel, F.-M. *Schwingungsspektroskopie*; Thieme Verlag: Stuttgart, 1985.

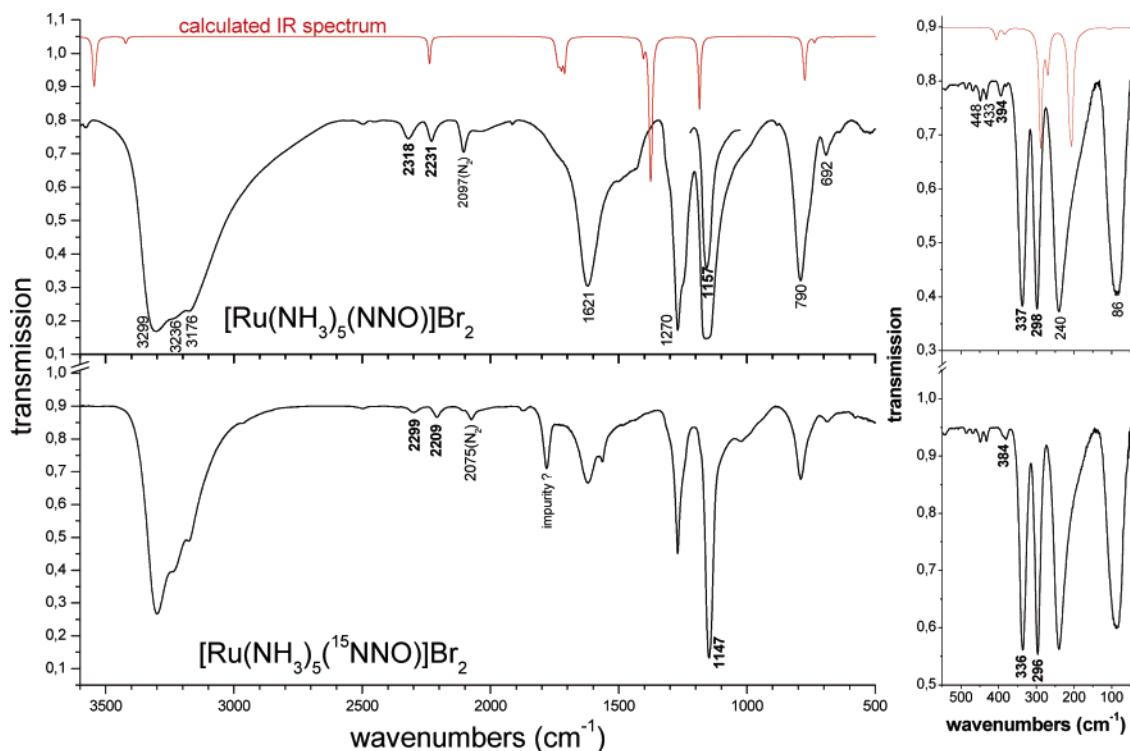


Figure 5. IR spectrum of **1-Br** (top) and of the corresponding ^{15}NNO isotope labeled complex (bottom). The calculated spectrum is also included in the top panel as indicated.

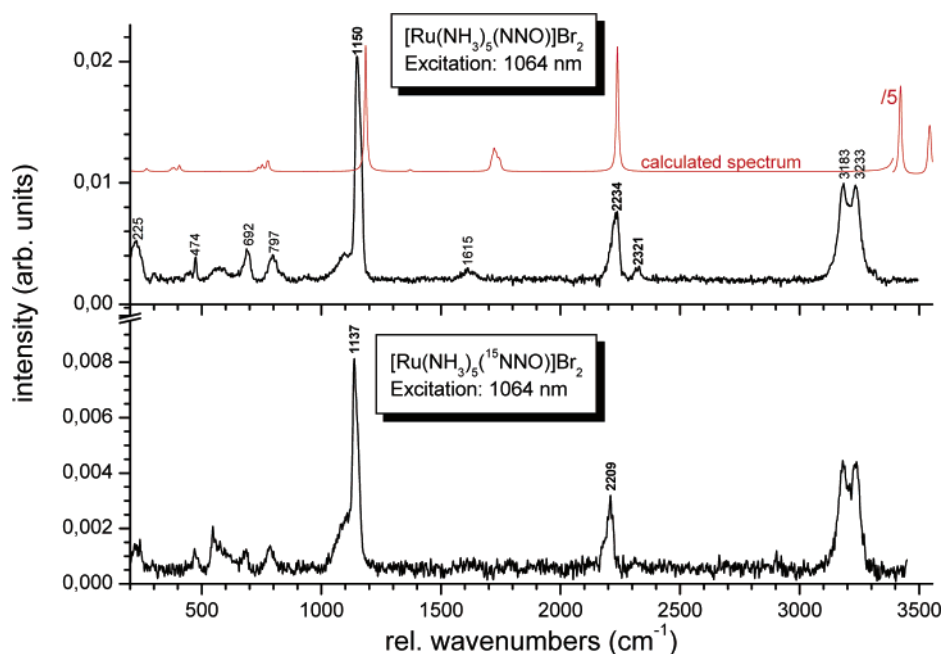


Figure 6. Raman spectrum of **1-Br** (top) and of the corresponding ^{15}NNO isotope labeled complex (bottom). The calculated spectrum is also included in the top panel as indicated.

Table 4. Calculated NPA Charges and d Orbital Populations of $[\text{Ru}(\text{NH}_3)_5(\text{NO})]^{3+}$

NPA charges			NPA d orbital populations			
Ru	N	O	d_{xy}	d_{xz}	d_{yz}	$d_z^2 + d_{x^2-y^2}$
+0.77	+0.35	+0.08	1.81	1.57	1.57	2.01

to +0.43 by back-donation from the d_{xz} and d_{yz} orbitals of Ru. Accordingly, their population is reduced to +1.57 compared to +1.81 for the nonbonding orbital d_{xy} . This roughly corresponds to a net transfer of half an electron from

d_{xz} and d_{yz} to the NO^+ ligand in accordance with its NPA charge. The large occupation number for the e_g orbitals of 2.01 is due to the strong donation of the NH_3 ligands. Contour plots of important molecular orbitals are shown in Figure 7 in the Supporting Information.

With the help of the calculated electronic structure of $\tilde{2}$ and a time-dependent (TD) DFT calculation, the electronic absorption spectra of complexes **2** can be assigned. Figure 4 shows the obtained data for **2-Br** (in a KBr disk and in

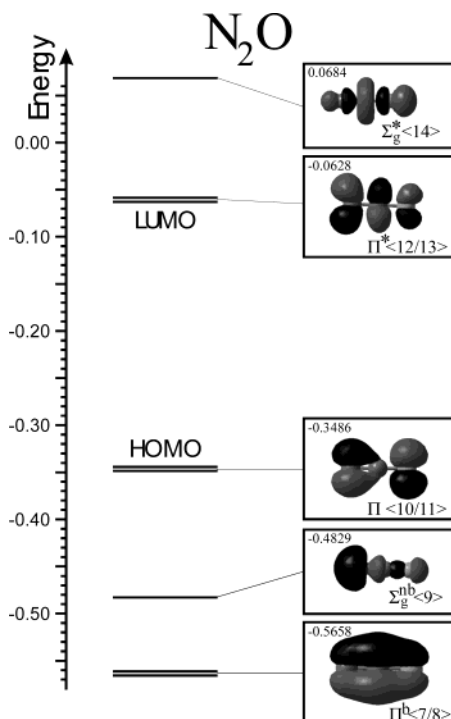


Figure 7. MO diagram of free N_2O and contour plots of important orbitals. Energies are given in Hartree.

Table 5. Experimental Absorption Band Positions [cm^{-1}] for $[\text{Ru}(\text{NH}_3)_5(\text{NO})]\text{X}_3$ (**2**) and Assignments

assignment	TD-DFT	2-Br (X = Br) ^a	2-BF₄ (X = BF ₄)	2-OTf (X = OTf) ^b
$^1\Gamma \rightarrow ^3\Gamma^c$		15990		
$d_{xy} \rightarrow \pi^*_d$	22222	20550 (21850)	22260	22940
$d_{xy} \rightarrow e_g$	28820		29450	
$d_{xy} \rightarrow e_g$	35840	(33170)	33765	33230
$d_{xz}\pi^* \rightarrow e_g$	38680	35400 (38470)		

^a Solution data in brackets. ^b Data not shown. ^c Spin forbidden transition.

solution) and **2-BF₄** (as a solid). Importantly, no intense charge transfer transition is observed above 200 nm. According to the MO diagram of **2**, the lowest energy charge transfer should correspond to a transition from the bonding ($d_{xz}\pi^*$) to the antibonding (π^*_d) MOs of the Ru–NO π bond. However, as discussed here, the splitting between these orbitals is large due to the strength of the back-bond. Hence, this transition should be at high energy below 200 nm and, accordingly, is not observed experimentally (cf. Figure 4). The observed weak absorptions are therefore assigned to d–d transitions as given in Table 5. Around 20000 cm^{-1} , the first (spin allowed) transition from d_{xy} to the antibonding orbitals π^*_d is observed. At higher energy, the transitions from d_{xy} to the e_g orbitals d_z^2 and $d_{x^2-y^2}$ occur. These can be associated with the bands at 29450 and 33765 cm^{-1} in the solid state spectrum of **2-BF₄** and the band at 33230 cm^{-1} in **2-OTf**. In addition, the solution spectrum of **2-Br** shows a corresponding transition at 33170 cm^{-1} . Interestingly, these bands appear to be missing in the spectrum of **2-Br** measured in KBr. In this case, a split band at 36490 and 35400 cm^{-1} is observed that is tentatively assigned to the transitions from the $d_{xz}\pi^*$ and $d_{yz}\pi^*$ orbitals to e_g .

B. Spectroscopy and Electronic Structure of $[\text{Ru}(\text{NH}_3)_5(\text{N}_2\text{O})]^{2+}$ (1**).** Vibrational data are presented for $[\text{Ru}(\text{NH}_3)_5(\text{N}_2\text{O})]\text{X}_2$ (**1**) and analyzed with the help of DFT calculations and a normal coordinate analysis. From the calculations, the properties of N_2O as a ligand are determined, and the electronic structure of **1** is defined. In addition, DFT is used to calculate formation constants for different $[\text{Ru}(\text{NH}_3)_5(\text{L})]^{2+}$ complexes. Finally, the potential reactivity of end-on terminally bound N_2O for N–O bond cleavage mediated by protonation and reduction is explored.

B.1. Vibrational Spectra and Assignments. The IR spectrum of $[\text{Ru}(\text{NH}_3)_5(\text{N}_2\text{O})]\text{Br}_2$ is shown in Figure 5 together with the corresponding ^{15}NNO isotope labeled complex. As will be shown in section B.4, these data are only compatible with N_2O being end-on coordinated with the nitrogen atom. Hence, for the following analysis this bonding mode of nitrous oxide is used. In Figure 5, isotope sensitive bands are present at 2231 and 1157 cm^{-1} in the MIR region that shift to 2209 and 1147 cm^{-1} in the ^{15}NNO complex. These are assigned to the N–N stretch and the N–O stretch of the nitrous oxide ligand, respectively, in agreement with the literature.³ An additional isotope sensitive band at 2318 cm^{-1} is assigned to the first overtone of the N–O stretch at 1157 cm^{-1} . The feature at 2097 cm^{-1} belongs to the corresponding $[\text{Ru}(\text{NH}_3)_5(\text{N}_2)]^{2+}$ complex that is found as an impurity in **1-Br**. It is observed at 2075 cm^{-1} in the corresponding ^{15}NN complex. Figure 6 shows the first Raman spectra recorded for an N_2O complex. The band positions of the N–N and N–O stretches at 2234 and 1150 cm^{-1} , respectively, are comparable to the IR results. Other isotope sensitive bands are found in the far-IR spectra in Figure 5. Intense bands at 338 and 298 cm^{-1} shift to 336 and 296 cm^{-1} in the ^{15}NNO complex. The band at 298 cm^{-1} is assigned to the Ru–NNO stretch, whereas the other feature corresponds to a N–Ru–N octahedral bend that is mixed with the Ru–N–N linear bend (vide infra).

Calculated IR and Raman spectra for $[\text{Ru}(\text{NH}_3)_5(\text{NNO})]^{2+}$ are shown in Figures 5 and 6 in comparison with experimental results for **1-Br**. Table 6 summarizes the complete assignments. The positions of the N–H vibrations of the $[\text{Ru}(\text{NH}_3)_5]^{2+}$ subunit are somewhat changed compared to the Ru(II)–NO⁺ complexes **2**, but the overall assignments of the $\nu_{\text{as/s}}(\text{N–H})$ stretches, the $\delta_{\text{as/s}}(\text{H–N–H})$ bends, and the $\delta(\text{Ru–N–H})$ bends are very similar and can be extracted from Table 6. Calculated energies of $\nu(\text{N–N})$ and $\nu(\text{N–O})$ for **1** are in very good agreement with experiment. At lower energy, the linear bends $\delta(\text{N–N–O})$ are calculated around 410 cm^{-1} with very low IR and Raman intensity. Correspondingly, these bands are not observed experimentally. On the other hand, the Ru–NH₃ stretching vibrations are calculated too low in energy as in the case of $[\text{Ru}(\text{NH}_3)_5(\text{NO})]^{3+}$. Bands occurring at 474 cm^{-1} in the Raman spectrum and at 448 and 433 cm^{-1} in the IR data of **2-Br** can be associated with these modes.³⁵ To lower energy, two bands are observed at 338 and 298 cm^{-1} in the far-IR spectrum. The occurrence of two quite intense bands around 300 cm^{-1} is a signature of the Ru(II)– N_2O complex, since

Table 6. Vibrational Assignments of $[\text{Ru}(\text{NH}_3)_5(\text{NNO})]\text{X}_2$ in Comparison to Results Obtained From DFT Calculations

number of modes	mode	$[\text{Ru}(\text{NH}_3)_5(\text{NNO})]^{2+}$ (calculated) ^a		$[\text{Ru}(\text{NH}_3)_5(\text{NNO})]\text{Br}_2$		$[\text{Ru}(\text{NH}_3)_5(\text{NNO})](\text{BF}_4)_2$	
		frequency [cm^{-1}]	intensity	nai ^b	¹⁵ NNO	nai ^b	¹⁵ NNO
10	$\nu_{\text{as}}(\text{N-H})$	range: 3537–3548	s, IR/s, R	3299/3236(IR) 3233(R)		3371(IR) 3374(R)	
5	$\nu_{\text{s}}(\text{N-H})$	range: 3419–3425	vs, R/w, IR	3183(R) 3176(IR)		3302/3224(R) 3301(IR)	
1	$\nu(\text{N-N})$	2238	vs, R/s, IR	2234(R) 2231(IR)	2209(IR, R)	2269(R) 2270(IR)	2243(R) 2244(IR)
10	$\delta_{\text{as}}(\text{H-N-H})$	range: 1710–1748 1741/1735 1724/1710	w, R s, IR s, IR	1621(IR)/1615(R)		1636(IR)/1640(R)	
5	$\delta_{\text{s}}(\text{H-N-H})$	range: 1361–1404 1379/1374/1371	–, R vs, IR	1270(IR)		1297(IR)	
1	$\nu(\text{N-O})$	1185	vs, IR/vs, R	1150(R) 1157(IR)	1137(R) 1147(IR)	1197(R) 1206(IR)	1182(R) 1192(IR)
10	$\delta(\text{Ru-N-H})$	range: 619–779 779/775/773 738/736	s, IR/w, R w, IR/w, R	797(R)/790(IR) 692 (IR, R)		770(IR) 755(R)	
2	$\delta(\text{N-N-O})$	408/406	–, IR/–, R	394 (IR)?	384(IR)?	454(IR)?	450(IR)?
5	$\nu(\text{Ru-NH}_3)$	range: 373–406 406(A ₁) 384	w, R/w, IR w, IR	474(R) 448/433 (IR)		452/429(R) 431/378(IR)	
1	$\nu(\text{Ru-NNO})$	289	m, IR/–, R	297.8(IR)	296.4(IR)	303.8(IR)	299.6(IR)
2	$\delta(\text{N-Ru-N})^*$	271/268	w, IR/w, R	337.5	335.7	315.1	313.1
7	$\delta(\text{N-Ru-N})$	range: 171–212 212/207/204 183	m, IR w, R	240(IR) 225(R)		245(IR) 228(R)	

^a For a given type of vibration, range gives the range of vibrational energies obtained in the calculation. Below the range value, vibrations with a certain amount of IR and/or Raman intensity are listed for comparison with experimental data (vs, very strong; s, strong; m, medium; w, weak; –, no intensity). A₁ identifies the totally symmetric vibration when applicable. ^b nai = natural abundance isotopes.

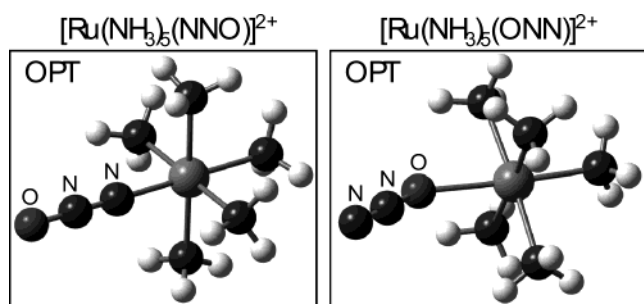


Figure 8. Fully optimized structures of the two coordination isomers of $[\text{Ru}(\text{NH}_3)_5(\text{N}_2\text{O})]^{2+}$ (**1**). Note that the complex where nitrous oxide is bound end-on terminally through its nitrogen atom (on the left) corresponds to the experimental coordination mode (see section B.4). Structural parameters are given in Table 8.

they are absent in compounds **2** and other corresponding materials. They are also found for the tetrafluoroborate salt **1-BF₄** (see Supporting Information Figure 8). In this case, the two bands are close at 315 and 304 cm^{-1} . In the

(35) Note that the $\nu(\text{Ru-NH}_3)$ vibrations of the $\text{Ru}(\text{II})-\text{NO}^+$ complexes are much more intense in the Raman spectrum compared to their $\text{Ru}(\text{II})-\text{NNO}$ counterparts (compare the strong bands at 508 and 487 cm^{-1} of **2-Br** with the weak 474 cm^{-1} feature of **1-Br** in Figures 3 and 6). This is probably due to the decreased Ru-NH_3 bond strength and, hence, covalency in **1** compared to **2**.

calculation, the Ru-NNO stretch is found at 288 cm^{-1} . Moreover, the calculation predicts two vibrations at 271 and 268 cm^{-1} that have predominant $\delta(\text{N-Ru-N})$ character (labeled $\delta(\text{N-Ru-N})^*$). These modes are shifted to higher energy compared to the remaining octahedral N-Ru-N bends by an admixture of the Ru-N-N linear bends which occur at much lower energy ($<100 \text{ cm}^{-1}$ in the calculation). Since both bands at 338 and 298 cm^{-1} in **1-Br** and the corresponding features at 315 and 304 cm^{-1} in **1-BF₄** are isotope sensitive, it is not straightforward which one of these corresponds to $\nu(\text{Ru-NNO})$ and which to $\delta(\text{N-Ru-N})^*$. However, since the $\delta(\text{N-Ru-N})^*$ modes also have some Ru-N-H bending character, they should be much more sensitive to a counterion change than the Ru-NNO stretch. Therefore, the bands at 338 cm^{-1} in **1-Br** and 315 cm^{-1} in **1-BF₄** are assigned to the octahedral bends $\delta(\text{N-Ru-N})^*$ and the features at 298 cm^{-1} in **1-Br** and 304 cm^{-1} in **1-BF₄** to $\nu(\text{Ru-NNO})$. The fact that the $\delta(\text{N-Ru-N})^*$ vibrations occur at higher energy in experiment compared to the calculation is in agreement with the observed tendency for the remaining octahedral bends, which are observed around 240 cm^{-1} in the IR spectrum and calculated around 210 cm^{-1} (cf. Table 6). Table 6 also shows the assignments for the tetrafluoroborate salt **1-BF₄**, which are essentially identical

Table 7. Comparison of Experimental and QCA-NCA Vibrational Frequencies [cm^{-1}] and of QCA-NCA and Calculated (DFT) Force Constants [$\text{mdyn}/\text{\AA}$] for $[\text{Ru}(\text{NH}_3)_5(\text{NNO})]\text{Br}_2$ (**1-Br**)

mode	exp. (cf. Table 6)		QCA-NCA		force constants	
	nai ^a	¹⁵ NNO	nai ^a	¹⁵ NNO	QCA-NCA	calcd ^b
$\nu(\text{N}-\text{N})$	2234	2209	2234	2209	17.270	17.591
$\nu(\text{N}-\text{O})$	1150	1137	1150	1136	9.603	9.732
$\nu(\text{Ru}-\text{NNO})$	297.8	296.4	297.6	296.3	1.435	1.486

^a nai = natural abundance isotopes. ^b Calculated with B3LYP/LanL2DZ; see Experimental Section. Free N_2O : $\nu(\text{N}-\text{N}) = 2224 \text{ cm}^{-1}$; $f_{\text{N}-\text{N}} = 17.88 \text{ mdyn}/\text{\AA}$; $\nu(\text{N}-\text{O}) = 1286 \text{ cm}^{-1}$; $f_{\text{N}-\text{O}} = 11.39 \text{ mdyn}/\text{\AA}$.³⁶

to **1-Br**. The corresponding IR and Raman spectra of **1-BF₄** are presented in the Supporting Information.

B.2. Normal Coordinate Analysis. The assignments of the vibrations of the $[\text{Ru}(\text{NNO})]^{2+}$ subunit as already described are confirmed by NCA using model **1**. Due to the fact that the hydrogen atoms of the ammine ligands have been omitted in **1**, no accurate description of the $\delta(\text{N}-\text{Ru}-\text{N})^*$ vibrations is possible with the chosen model. Hence, the normal coordinate fit has been limited to the stretching modes of the $[\text{Ru}(\text{NNO})]^{2+}$ subunit. As shown in Table 7, excellent agreement is obtained in these cases between the experimental and NCA frequencies. Importantly, the calculated force constants indicate a weakening of the N–O bond (free N_2O , 11.4 $\text{mdyn}/\text{\AA}$; Ru– N_2O , 9.6 $\text{mdyn}/\text{\AA}$) upon coordination of the N_2O ligand. In contrast, the N–N bond is only slightly affected (free N_2O , 17.9 $\text{mdyn}/\text{\AA}$; Ru– N_2O , 17.3 $\text{mdyn}/\text{\AA}$). The reasons for this finding are discussed in the next section. The calculated Ru–NNO force constant of only 1.4 $\text{mdyn}/\text{\AA}$ shows that nitrous oxide is a weak ligand.

B.3. Electronic Structure and Spectra. The MO diagram of free nitrous oxide is shown in Figure 7. In the following text, the bonding properties of this ligand are evaluated in comparison with N_2 , which has been shown to be a moderately π back-bonding and weakly σ donating ligand.³⁷ The LUMO of N_2O is the degenerate set of fully antibonding π^* orbitals, labeled $\Pi^*(12/13)$, as shown in the contour plot in Figure 7. Since these orbitals are somewhat lower in energy than the π^* orbitals of N_2 , nitrous oxide should be a back-bonding ligand comparable to or better than N_2 . The HOMO of nitrous oxide, $\Pi(10/11)$, corresponds to the degenerate set of π orbitals that are practically nonbonding (cf. Figure 7). They are located at low energy which indicates that the π donor ability of N_2O should be limited. Next in energy is the weakly N–N and N–O σ bonding orbital $\Sigma_g^{\text{nb}}(9)$, which mostly has lone pair character on the terminal nitrogen. This orbital could therefore act as a σ donor. However, since this orbital is located at even lower energy than the corresponding σ orbital of N_2 , the σ donor ability of N_2O should be weak. In summary, nitrous oxide can be expected to be a comparable π acceptor and a weaker σ donor than N_2 .

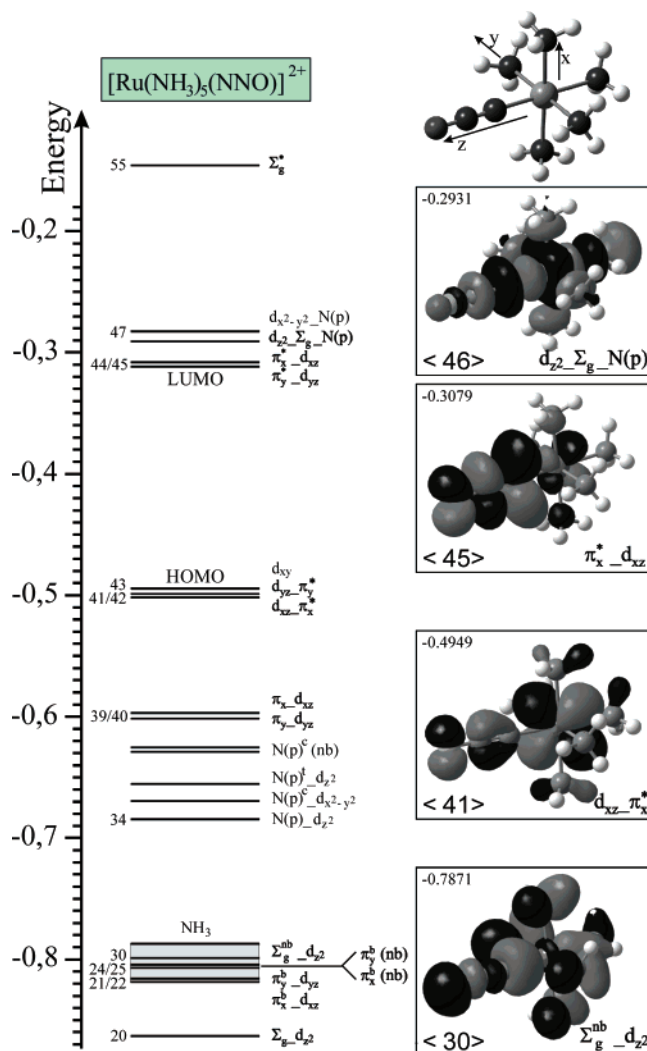


Figure 9. MO diagram of $[\text{Ru}(\text{NH}_3)_5(\text{NNO})]^{2+}$ (**1**) including contour plots of important molecular orbitals (right) and the applied coordinate system (top, right). Ligand orbitals of N_2O are labeled as given in Figure 7. The nomenclature “a_b” indicates that orbital a interacts with b and that a has a larger contribution to the resulting MO. Abbreviations: N(p) = lone-pair σ donor functions on the ammonia ligands; c = cis/trans with respect to N_2O ; nb = nonbonding.

Figure 8, left, shows the optimized structure of $[\text{Ru}(\text{NH}_3)_5(\text{NNO})]^{2+}$ (**1**) where nitrous oxide is bound end-on through its terminal nitrogen atom. This leads to a linear coordination geometry with Ru–N–N and N–N–O angles close to 180° . As will be shown in section B.4, this is the experimental bonding mode of nitrous oxide in complex **1**, and hence, this bonding mode is applied here for the discussion of the electronic structure. Calculated bond lengths of **1** are presented in Table 8. For comparison, Figure 8 and Table 8 also include the coordination isomer of **1** where nitrous oxide is bound end-on through its terminal oxygen atom. This bonding mode is discussed in section B.4.

Figure 9 shows the MO diagram of $[\text{Ru}(\text{NH}_3)_5(\text{NNO})]^{2+}$ (**1**) and contour plots of important molecular orbitals. On the top, the optimized structure from DFT is shown together with the coordinate system that is used in the following discussion. In complex **1**, Ru is in the oxidation state +II and low-spin, which leads to a $[t_{2g}]^6$ electron configuration. Hence, since the t_{2g} orbitals (d_{xy} , d_{xz} , d_{yz}) are fully occupied,

(36) (a) Richardson, W. S.; Wilson, E. B., Jr. *J. Chem. Phys.* **1950**, *18*, 694. (b) Begun, G. M.; Fletcher, W. H. *J. Chem. Phys.* **1958**, *28*, 414–418.

(37) Lehnert, N.; Tuzcek, F. *Inorg. Chem.* **1999**, *38*, 1671–1682.

Table 8. Comparison of Calculated Bond Distances [Å]

	$\Delta(\text{Ru-L})$	$\Delta(\text{N-N})$	$\Delta(\text{N-O})$	$\Delta(\text{Ru-NH}_3)$, trans	$\Delta(\text{Ru-NH}_3)$, cis
free N_2O (calcd)		1.161	1.241		
$[\text{Ru}(\text{NH}_3)_5(\text{NNO})]^{2+}$ ($\tilde{\mathbf{1}}$)	2.027	1.164	1.233	2.178	2.204 ^a
$[\text{Ru}(\text{NH}_3)_5(\text{ONN})]^{2+}$	2.294	1.153	1.262	2.151	2.206 ^a

^a Averaged over all corresponding bond lengths.

Table 9. Charge Contributions of Important Molecular Orbitals of $[\text{Ru}(\text{NH}_3)_5(\text{NNO})]^{2+}$ ($\tilde{\mathbf{1}}$)^a

no.	label	energy	Ru d	N		N		O		ΣN^b s + p
				s	p	s	p	s	p	
<45>	$\pi_{x^*}^*d_{xz}$	-0.3079	5	0	29	0	39	0	16	6
<44>	$\pi_{y^*}^*d_{yz}$	-0.3087	5	0	28	0	39	0	16	7
<43>	d_{xy}	-0.4945	91	0	0	0	1	0	3	1
<42>	$d_{yz}\pi_{y^*}^*$	-0.4947	82	0	1	0	4	0	9	1
<41>	$d_{xz}\pi_{x^*}^*$	-0.4949	85	0	1	0	3	0	7	1
<40>	$\pi_{x^*}^*d_{xz}$	-0.5984	6	0	34	0	0	0	47	12
<39>	$\pi_{y^*}^*d_{yz}$	-0.5988	6	0	34	0	0	0	48	11
<30>	$\Sigma_{g^*}^{\text{nb}}d_{z^2}$	-0.7871	2	6	14	1	11	10	11	32

^a Additional MOs are given in Table 9 in the Supporting Information.

^b Contribution of the ammonia nitrogens.

no π donation from the N_2O ligand is possible in the linear Ru-NNO bonding mode of $\mathbf{1}$. Accordingly, the observed orbital mixings between ligand orbitals Π and Π^b and t_{2g} functions of $\text{Ru}(\text{II})$ do not contribute to bonding (cf. Figure 9 and Table 9). The HOMO of complex $\tilde{\mathbf{1}}$ is the d_{xy} <43> orbital which is nonbonding. The other two t_{2g} orbitals of $\text{Ru}(\text{II})$, d_{xz} and d_{yz} , form a π back-bond with the unoccupied Π^* orbitals of N_2O (the LUMO of the ligand). The corresponding bonding combinations, $d_{xz}\pi_{x^*}^*$ <41> and $d_{yz}\pi_{y^*}^*$ <42>, are located very close in energy to the nonbonding d_{xy} orbital. This indicates that the Ru-NNO back-bond is weak. The contour plot of $d_{xz}\pi_{x^*}^*$ <41> (and correspondingly $d_{yz}\pi_{y^*}^*$ <42>) shows a very small coefficient on the coordinating nitrogen of the N_2O ligand. This is due to π/π^* mixing, i.e., mixing of these orbitals with Π <10/11> of N_2O . The antibonding combinations, $\pi_{x^*}^*d_{xz}$ <45> and $\pi_{y^*}^*d_{yz}$ <44> are the LUMO of complex $\tilde{\mathbf{1}}$. They have about 5% metal contribution which is in agreement with the weak π back-bond. Note that the occupied orbitals $d_{xz}\pi_{x^*}^*$ and $d_{yz}\pi_{y^*}^*$ are strongly N-O antibonding due to the π/π^* mixing already described, which explains the observed weakening of the N-O bond upon coordination of N_2O (vide supra). The Ru-NNO σ bond is mediated by the ligand orbital $\Sigma_{g^*}^{\text{nb}}$ which interacts with d_{z^2} . However, the corresponding bonding combination, $\Sigma_{g^*}^{\text{nb}}d_{z^2}$ <30>, only has 2% metal contribution (cf. Table 9) which corresponds to a very weak interaction. In summary, this bonding description shows that the Ru-NNO bond is extremely weak in agreement with the experimental observation that the N_2O ligand in $\mathbf{1}$ is easily replaced with water and other ligands. This electronic structure is also in agreement with the calculated d orbital populations given in Table 10. Importantly, both back-bonding orbitals d_{xz} and d_{yz} have about the same occupation number as the nonbonding orbital d_{xy} , which again indicates the weak back-bond in $\tilde{\mathbf{1}}$. The large occupation of the e_g orbitals is due to the strong donation of the amines (cf. Table 9 in the Supporting Information).

Table 10. Calculated NPA Charges and d Orbital Populations of $[\text{Ru}(\text{NH}_3)_5(\text{NNO})]^{2+}$

Ru	NPA charges			NPA d orbital populations			
	N	N	O	d_{xy}	d_{xz}	d_{yz}	$d_{z^2} + d_{x^2-y^2}$
+0.61	-0.16	+0.44	-0.22	1.95	1.90	1.90	1.42

Low-temperature absorption spectra of $\mathbf{1-Br}$ and $\mathbf{1-BF}_4$ are shown in Figure 10. In the case of $\mathbf{1-BF}_4$, it was possible to obtain a solid state spectrum which allows for the identification of weak transitions (vide supra). Two bands are observed at 28875 and 36150 cm^{-1} (346 and 277 nm, respectively). From the MO diagram, the splitting of the three t_{2g} orbitals is marginal in complex $\mathbf{1}$ due to the weak back-bonding capacity of nitrous oxide. Hence, the ligand field transitions can be assigned in first order using the Tanabe–Sugano diagram of low-spin d^6 systems. On the basis of this, the bands at 28875 and 36150 cm^{-1} are assigned to the $^1A_1 \rightarrow ^1T_1$ and $^1A_1 \rightarrow ^1T_2$ transitions, respectively. This is also in agreement with TD-DFT calculations. In addition, an intense charge transfer transition is observed in the KBr spectra of $\mathbf{1-Br}$ and $\mathbf{1-BF}_4$ (cf. Figure 10) around 42000 cm^{-1} (~ 238 nm), which has also been observed in solution.² This band is characteristic for the $\text{Ru}(\text{II})\text{-NNO}$ unit since it is absent in the $\text{Ru}(\text{II})\text{-NO}^+$ starting material (vide supra). This band is assigned to the d_{xz} <41/42> \rightarrow π^* <44/45> transition in agreement with TD-DFT calculations (predicted at 232 nm).

B.4. Binding Mode of Nitrous Oxide in $\mathbf{1}$. Two different binding modes for the nitrous oxide molecule in complex $\mathbf{1}$ have been discussed in the literature.^{3,4} As shown in Figure 8, N_2O could potentially be bound end-on terminally to $\text{Ru}(\text{II})$ with either the nitrogen or oxygen atom. From the DFT calculations, these two binding modes lead to very different structures. When coordinated with the terminal nitrogen atom, the $\text{Ru}(\text{II})\text{-NNO}$ unit is linear, whereas binding with the oxygen atom leads to a strongly bent structure (the calculated Ru-ON(N) angle is 138°). However, due to the instability of complex $\mathbf{1}$, no crystal structure could be determined. Hence, the bonding mode of nitrous oxide in $\mathbf{1}$ is uncertain. However, the mode of coordination can be determined from a correlation of the experimental data presented here for complex $\mathbf{1}$ with the results from the DFT calculations. On the basis of a normal coordinate analysis that was restricted to the four atoms of the $\text{Ru-N}_2\text{O}$ subunit, it was claimed that the observed isotope shifts of the N-N and the N-O stretch are only in agreement with O coordination of N_2O .^{3b,c} Contrary to these findings, Table 11 shows that the calculated isotope shifts for the N and O coordinated isomers of $\mathbf{1}$ (cf. Figure 8) are identical within a few wavenumbers and, hence, cannot distinguish between these isomers. Importantly, it is (a) the energy of the N-N and N-O stretches and (b) the far-IR spectral region that are actually most diagnostic for the mode of attachment of

Table 11. Comparison of Calculated Vibrational Energies and Isotope Shifts for N and O Coordinated Isomer of $[\text{Ru}(\text{NH}_3)_5(\text{N}_2\text{O})]^{2+}$

mode	1-Br (exptl)		calcd $[\text{Ru}(\text{NH}_3)_5(\text{NNO})]^{2+}$				calcd $[\text{Ru}(\text{NH}_3)_5(\text{ONN})]^{2+}$			
	nai ^a	¹⁵ N-N-O	nai ^a	¹⁵ N-N-O	N- ¹⁵ N-O	N-N- ¹⁸ O	nai ^a	O-N- ¹⁵ N	O- ¹⁵ N-N	¹⁸ O-N-N
$\nu(\text{N-N})$	2234	-25	2238	-26	-46	-3	2160	-27	-43	-2
$\nu(\text{N-O})$	1150	-13	1185	-14	-3	-39	1091	-11	-3	-38
$\nu(\text{Ru-X})$	297.8	-1.4	289	-2	-2	-3	192	-1	-1	-5

^a nai = natural abundance isotopes.

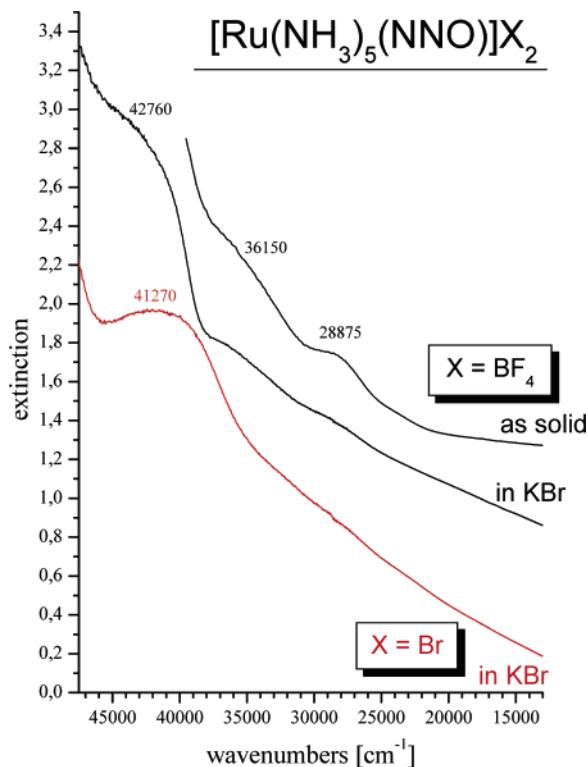


Figure 10. Low-temperature absorption spectra of $[\text{Ru}(\text{NH}_3)_5(\text{NNO})]\text{Br}_2$ as KBr disk and $[\text{Ru}(\text{NH}_3)_5(\text{NNO})](\text{BF}_4)_2$ in KBr and as a solid as indicated. Energies are given in cm^{-1} .

nitrous oxide. For $\nu(\text{N-N})$ and $\nu(\text{N-O})$, the calculated energy of the N bound isomer is close to the experimental value. In the far-IR region, the N coordinated isomer shows a pattern in the calculations with $\nu(\text{Ru-N})$ occurring at $\sim 300 \text{ cm}^{-1}$ (cf. Table 6) which is similar to experiment. In comparison, the Ru-ONN isomer has the corresponding $\nu(\text{Ru-O})$ stretch below 200 cm^{-1} and no intense band in the 300 cm^{-1} region. Therefore, this clearly shows that the nitrous oxide ligand is N coordinated in compound **1**. The lower energy of the metal-ligand stretch in the O coordinated isomer reflects a weaker bound N_2O ligand in this case (the calculated Ru-O force constant is only 0.53 mdyne/\AA). This is due to the fact that the Ru(II)-ONN isomer has a different electronic structure where no π back-bond or σ donor bond from Σ_g^{nb} is present. Instead, a pseudo- σ interaction between one of the Π orbitals (HOMO) of N_2O and d_z^2 of Ru(II) is found which is extremely weak due to the low energy of Π (vide supra).

Due to the very different electronic structures of the O and N coordinated isomers of **1**, their calculated UV-vis absorption spectra are also very different. The calculated absorption spectrum for the N bound isomer (vide supra) shows the lowest energy ligand field transition around 400

Table 12. Reaction Energies for $[\text{Ru}(\text{NH}_3)_5]^{n+} + \text{L} \rightarrow [\text{Ru}(\text{NH}_3)_5(\text{L})]^{n+}$ ($T = 298.15 \text{ K}$) [kcal/mol]

complex	$\Delta\epsilon^a$	ZPCE ^a	ΔH	ΔG	$\Delta\Delta G$	K_0^b
$[\text{Ru}(\text{NH}_3)_5(\text{NNO})]^{2+}$ (1)	-25.6	+1.4	-24.4	-14.1	0	
$[\text{Ru}(\text{NH}_3)_5(\text{ONN})]^{2+}$	-16.9	+0.6	-16.2	-6.3	+7.9	
$[\text{Ru}(\text{NH}_3)_5(\text{OH}_2)]^{2+}$	-34.0	+2.4	-32.3	-22.4	-8.2	2×10^5
$[\text{Ru}(\text{NH}_3)_5(\text{N}_2)]^{2+}$	-31.8	+2.3	-30.3	-20.1	-6.0	5×10^3
$[\text{Ru}(\text{NH}_3)_5(\text{NO})]^{3+}$ (2)	-62.4	+3.9	-59.6	-46.1		

^a $\Delta\epsilon$: difference in electronic energy. ZPCE: zero point correction energy. ^b Equilibrium constant for the reaction $[\text{Ru}(\text{NH}_3)_5(\text{NNO})]^{2+} + \text{L} \rightarrow [\text{Ru}(\text{NH}_3)_5(\text{L})]^{2+} + \text{N}_2\text{O}$.

nm and the intense charge transfer between the t_{2g} orbitals of Ru(II) and the nitrous oxide π^* orbitals around 230 nm. This is in very good agreement with experiment. On the other hand, for the O bound isomer, ligand field transitions are already predicted in the 540 nm region, and the intense $t_{2g} \rightarrow \pi^*$ transition is found around 350 nm. Hence, the experimental absorption spectrum also strongly favors N coordination of nitrous oxide in **1**.

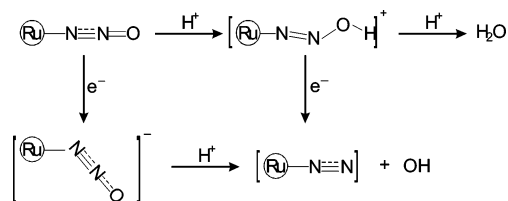
The relative stability of the N versus O coordinated isomer of **1** can also be investigated by total energy calculations of the ligand binding energy following the equation



Table 12 shows the calculated ΔH and ΔG values for this reaction for $\text{L} = \text{NNO}$, ONN , N_2 , and OH_2 . Importantly, N coordination of nitrous oxide is more favorable than O coordination by 8 kcal/mol in terms of free energy. Comparing the stability of complex **1** (the N bound isomer) with corresponding N_2 and OH_2 complexes demonstrates the weakness of nitrous oxide as a ligand (vide supra). In fact, the N_2 and the OH_2 adducts are more stable than complex **1** by 6 and 8 kcal/mol in terms of free energy, respectively. This large difference in formation energy between the Ru(II)- N_2 adduct and the Ru(II)-NNO complex is rather surprising. The reasons for this finding are further evaluated in the Discussion section.

B.5. Reactivity of End-On Terminally N-Coordinated N_2O . Using DFT calculations, the reactivity of the Ru(II)-NNO complex toward protonation and reduction is explored in order to investigate the mechanism of the biologically relevant reaction of N_2O to N_2 and H_2O mediated by nitrous oxide reductase (see Introduction). As has been shown, nitrous oxide is a very weak ligand, and hence, activation toward protonation is hard to achieve. Scheme 1 shows two different reactions that were explored in this study. Initial protonation of $[\text{Ru}(\text{NH}_3)_5(\text{NNO})]^{2+}$ (**1**) leads to the formation of $[\text{Ru}(\text{NH}_3)_5(\text{NN-OH})]^{3+}$ (**1-H**) with a bent N-O-H unit. The electronic structure of this intermediate is very

Scheme 1



interesting. It has a distinctively weakened N–O bond with a force constant of only 4.76 mdyn/Å (compared to 9.73 mdyn/Å for **1**), whereas the Ru–N bond is strengthened (force constant: 3.56 mdyn/Å compared to 1.49 mdyn/Å for **1**). The reason for this finding is that the interaction of the proton 1s function with the Π_y and Σ_g^{nb} orbitals of N₂O leads to lowering of Π_y and Π_y^* in energy and a mixing of these orbitals with σ orbitals like Σ_g^{nb} . In the case of Π_y^* , this leads to a strong increase of mixing with d_{yz} which now has a 30% contribution to the resulting antibonding orbital, $\pi_{y-d_{yz}}^*(44)$ (the LUMO of **1** – H). This corresponds to a transfer of net electron density from the metal to the nitrous oxide ligand through the π back-bond and, hence, an oxidation of the metal upon protonation of the ligand. This electron transfer occurs smoothly through the π system which indicates that in general no barrier is to be expected for this process. The corresponding bonding combinations, $d_{yz}-\pi_y^*(41)$ and $\pi_{y-d_{yz}}(35)$, are N–O antibonding, which explains the weakening of the N–O bond upon protonation. The strengthening of the Ru–N bond, on the other hand, is due to the increased back-bond mentioned above and also due to a stronger interaction of Σ_g^{nb} with d_{z^2} in **1** – H. Contour plots of these important MOs are given in the Supporting Information. As shown in Scheme 1, a subsequent electron transfer to the Ru–NNOH intermediate leads to a splitting of the N–O bond and to the release of OH.³⁸ This is due to the fact that the additional electron occupies the $\pi_{y-d_{yz}}^*(44)$ orbital (the LUMO of **1** – H), which is strongly N–O antibonding.

The alternative mechanism where electron transfer precedes protonation is less favorable for two reasons. First, the transfer of one electron to **1** leads to the occupation of one of the $\pi_{d_{xz}}^*$ antibonding orbitals. Since the Π^* orbitals of N₂O are at high energy, this does not seem likely from a thermodynamic point of view; i.e., the required reduction potential can be expected to be too high for aqueous solutions. In addition, this breaks the already weak Ru–NNO back-bond, which forces the nitrous oxide ligand to rearrange to a bent structure as indicated in Scheme 1. In this case, the occupied Π^* orbital now forms a pseudo- σ bond with the d_{z^2} function of Ru(II). This rearrangement is kinetically unfavorable and also bears the risk of losing the nitrous oxide ligand. In the reduced complex, the extra electron is mostly located on the N₂O ligand, which would therefore be highly activated for protonation. Nevertheless, because of the disadvantages described here, this mechanism can be excluded for the protonation and reduction of nitrous oxide.

(38) Note that the calculated release of the hydroxyl radical OH instead of OH⁻ after one electron reduction of **1** – H is due to the gas-phase nature of the calculations which disfavor charge separation.

The calculated free energy for the formation of **1** – H from **1** according to Scheme 1 is about +30 kcal/mol (including solvation effects in water). This shows that complex **1** is not able to perform this reaction in agreement with experiment. The reason for this is the low basicity of the coordinated nitrous oxide ligand in **1**, which is related to the weak Ru(II)–NNO back-bond (vide supra). Hence, the amount of charge transferred to the N₂O ligand upon binding to Ru(II) is too small to activate the ligand for protonation. This, in turn, relates to the oxidation potential of Ru(II), which is too high to allow for a significant amount of charge transfer. Importantly, this indicates that the application of more redox active (low valent) metal centers than Ru(II) would lead to an increase of nitrous oxide activation. In summary, although complex **1** is not activated for the protonation and reduction of nitrous oxide, the theoretical study of the corresponding reaction pathways offers a great deal of information on how transition metals can mediate the degradation of nitrous oxide and what the potential reaction mechanism is.

Discussion

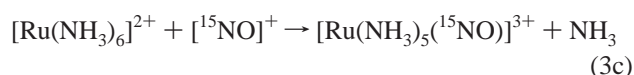
In this study, the spectroscopic properties and the electronic structure of the only nitrous oxide complex isolated so far, [Ru(NH₃)₅(NNO)]X₂ (**1**, X = Br⁻, BF₄⁻), have been defined in comparison to the [Ru(NH₃)₅(NO)]X₃ (**2**) precursor. For the bromide salt of the nitrosyl complex (**2-Br**), a new crystal structure is presented. In this structure, the NO molecule is disordered in two positions due to symmetry (space group: *Pnma*). Interestingly, **2-Br** is isostructural to the corresponding chloride salt.³⁹ Furthermore, the vibrational properties of complex **2** with different counterions are investigated using isotope substitution and density functional calculations. This way, a complete assignment of the vibrational spectra of **2** was obtained. From normal coordinate analysis, force constants have been determined to 15.34 mdyn/Å for the N–O and 5.04 mdyn/Å for the Ru–NO bond in **2-Br**. From the observed linear Ru–N–O unit in the crystal structure of **2-Br** and the occurrence of $\nu(\text{N–O})$ in the 1900 cm⁻¹ region, it is generally accepted that **2** has a Ru(II)–NO⁺ electronic structure.^{29,5e} This is also found in the DFT calculations. The strength of the Ru–NO bond is mostly due to a back-bond between two d_{π} orbitals of Ru(II) and the unoccupied set of π^* orbitals of NO⁺. The corresponding antibonding molecular orbitals, for example, have 70% π^* and 25% d_{π} character. This leads to a net transfer of approximately half an electron from the metal to the ligand and explains the lowering of the N–O stretching frequency from 2390 cm⁻¹ in free NO⁺ to ~1900 cm⁻¹ in complex **2**. In comparison to this back-bond, the Ru–NO⁺ σ interaction is weak. An important consequence of this electronic structure is the occurrence of a partial positive charge on the nitrosyl nitrogen (calculated: +0.35), which leads to an activation toward nucleophilic attack.⁵ Accordingly, it was reported that [Ru(NH₃)₅(NO)]³⁺ is in equilibrium with

(39) Bottomley, F. *J. Chem. Soc., Dalton Trans.* **1974**, 1600–1605.

$[\text{Ru}(\text{NH}_3)_5(\text{NO}_2)]^+$ in alkaline solution⁴⁰ but is unaffected by acid.³⁹ It was surprising to us that the reaction of $[\text{Ru}(\text{NH}_3)_6]^{3+}$ with $^{15}\text{N}^{18}\text{O}$ in acidic aqueous solution led to the corresponding $[\text{Ru}(\text{NH}_3)_5(^{15}\text{NO})]^{3+}$ complex where oxygen is unlabeled. On the other hand, dissolving the obtained $[\text{Ru}(\text{NH}_3)_5(^{15}\text{NO})]^{3+}$ in ^{18}O labeled water (in neutral or acidic solution) did not lead to the incorporation of the labeled oxygen into the complex. Therefore, complex **2** is inert under these conditions. This means that the exchange of the ^{18}O label in the $^{15}\text{N}^{18}\text{O}$ gas must occur during the synthesis of **2**, i.e., during the reaction of $[\text{Ru}(\text{NH}_3)_6]^{3+}$ with $^{15}\text{N}^{18}\text{O}$. A possible explanation would be that the first step of the reaction is actually an outer sphere electron transfer:

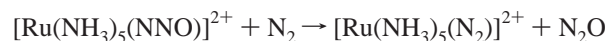


The formed NO^+ is then able to exchange its oxygen with the unlabeled water before coordination to Ru(II) occurs:



The electrophilic behavior of NO in complex **2** is used for the synthesis of the nitrous oxide complex $[\text{Ru}(\text{NH}_3)_5(\text{N}_2\text{O})]\text{-X}_2$ (**1**).^{5b} In $[\text{Ru}(\text{NH}_3)_5(\text{N}_2\text{O})]^{2+}$, possible coordination modes for the N_2O ligand are end-on terminally with either the nitrogen or oxygen atom. Since no crystal structure is available for this complex, the binding mode of N_2O to the Ru(II) center is uncertain.⁴¹ However, a detailed analysis of the vibrational properties and of the electronic spectra connected to DFT calculations enabled us to unequivocally determine the bonding mode of N_2O in complex **1**. From these analyses, nitrous oxide is coordinated end-on terminally through its N atom in complex **1**, which can therefore be formulated as $[\text{Ru}(\text{NH}_3)_5(\text{NNO})]^{2+}$. From NCA, force constants are determined to be 17.27, 9.60, and 1.44 mdyn/Å for the N–N, N–O, and Ru–NNO bonds, respectively. Compared to free nitrous oxide,³⁶ the N–N force constant is almost unchanged upon coordination whereas the N–O force constant of 11.39 mdyn/Å is distinctively lowered. Hence, the N–O bond is weakened upon coordination of the N_2O ligand. Low-temperature absorption spectra have also been recorded and completely assigned for **1**.

Experimentally, it was found that complex **1** easily loses nitrous oxide in solution, which indicates that N_2O is a weak ligand. This aspect is further investigated with the help of electronic structure calculations. Compared to dinitrogen, nitrous oxide is a comparable π acceptor (mediated by its degenerate π^* LUMO), but an even weaker σ donor, because the corresponding σ_g^{nb} orbital of N_2O is at lower energy. Altogether, one would expect that the complex stability of $[\text{Ru}(\text{NH}_3)_5(\text{NNO})]^{2+}$ is comparable to $[\text{Ru}(\text{NH}_3)_5(\text{NN})]^{2+}$. This is not the case: experimentally, it was found that the reaction



is exothermic in terms of free energy by -5.6 kcal/mol.^{2a} This value compares well with the calculated ΔG of -6.0 kcal/mol. In addition, this is also in agreement with kinetically determined complex formation constants of a Ru(II) precursor (with an amine/phosphine ligand set) with dinitrogen and nitrous oxide.⁶ The obtained data showed that the ratio of complex formation constants $K(\text{N}_2)/K(\text{N}_2\text{O})$ is approximately 10^3 , which is in good agreement with the calculated value of 5×10^3 (cf. Table 12) in favor of the N_2 complex. The reason for the reduced complex stability of the Ru(II)–NNO adduct is that nitrous oxide has an additional set of occupied π donor orbitals (the HOMO). Since Ru(II) has a low-spin $[t_{2g}]^6$ configuration, no π donation into the t_{2g} functions is possible in the linear Ru–NNO geometry. Instead, this interaction is energetically unfavorable due to Coulomb repulsion which lowers the stability of the complex. Hence, nitrous oxide is an even weaker ligand than dinitrogen. The properties of the Ru–NNO bond in **1** can further be analyzed by comparison to Ru(II)– NO^+ complex **2**. The back-bond between the π^* orbitals of N_2O and d_{π} of Ru(II) is weak. This is evident from the corresponding antibonding combinations, $\pi^*_d_{\pi}$, which only have about 5% metal contribution compared to 25% in the case of the nitrosyl complex. This accounts for the observed large difference in metal–ligand force constants between Ru–NO (5.04 mdyn/Å) and Ru–NNO (1.44 mdyn/Å). Note that the electronic structure of **1** has been investigated before; however, the calculations were of extended Hückel type which does not allow one to analyze binding energies, vibrational frequencies, or transition energies or to quantitatively evaluate the metal–ligand covalencies.⁴¹ In that study, the authors concluded that the Ru(II)–NNO bond is dominated by σ interaction. However, this is not in agreement with the calculations presented here which indicate that the π back-bond is more important than the very weak σ interaction.

From the electronic structure description of **1**, it becomes clear that it is difficult to synthesize more stable nitrous oxide complexes. Since N_2O is a weak σ and π donor, a more stable metal–NNO bond must be achieved by increasing π back-bonding. In order to strengthen this interaction, the metal should be low valent with a $[t_{2g}]^6$ electron configuration. However, there would still be the problem that the occupied t_{2g} orbitals would have the unfavorable Coulomb repulsion with the π donor orbitals of N_2O . Hence, it is unclear if this approach would lead to more stable metal– N_2O complexes. This still needs to be explored experimentally. In the enzyme nitrous oxide reductase, on the other hand, nitrous oxide is bound to the fully reduced Cu_2 cluster (see Introduction). In this case, all copper ions are in the oxidation state +1, which corresponds to a d^{10} electron configuration. Since all the d-orbitals are fully occupied, bonding of nitrous oxide to the cluster must solely be due to back-bonding. In order to explore the mechanism for N_2O degradation in the end-on terminal coordination mode, we applied DFT calculations on the model $[\text{Ru}(\text{NH}_3)_5(\text{NNO})]^{2+}$.

(40) Bottomley, F.; Crawford, J. R. *J. Chem. Soc., Dalton Trans.* **1972**, 2145.

(41) Tuan, D. F.-T.; Hoffmann, R. *Inorg. Chem.* **1985**, *24*, 871–876.

These results provide key information on how the protonation and reduction of nitrous oxide work on a molecular level. Importantly, the nitrous oxide ligand is activated for protonation by back-donation from the metal(s). Since back-donation is weak in the case of Ru(II), complex **1** is not able to undergo this reaction experimentally. However, in the case of Cu(I), the back-bond and, hence, the activation of N₂O can be expected to be much stronger. This is especially true for the side-on coordination mode of N₂O to Cu_Z favored by Ghosh et al. in their DFT study, where two metal centers simultaneously donate electron density to the ligand.¹³ Initial protonation of the coordinated nitrous oxide automatically triggers the transfer of electron density from the metal(s) to the NNOH unit. Since the electron transfer occurs through the metal–NNOH π system, this process can be expected to be barrierless. If the reduction potential of the metal(s) is strong enough to transfer a large amount of electron density, this leads to a distinct weakening of the N–O bond which nicely prepares for N–O cleavage. Hence, this process can be classified as a proton transfer with concerted electron transfer (PT/ET). The following step of the mechanism is less clear, since it depends, for example, on the coordination mode of the NNOH intermediate. Either

the second electron is transferred first leading to a splitting of the N–O bond and the formation of hydroxide, which is released and subsequently protonated in aqueous solution, or alternatively, the second proton could be transferred first which would then automatically trigger the transfer of the second electron (second PT/ET process). In any case, nitrous oxide is degraded this way yielding dinitrogen and water in a smooth and barrierless process.

Acknowledgment. This work was supported by the Deutsche Forschungsgemeinschaft (DFG; Grant LE 1393/1). Mrs. U. Cornelissen is acknowledged for recording the FT-Raman spectra of compounds **1** and **2**.

Supporting Information Available: IR and Raman spectra of **2-BF₄**, **2-OTf**, and **1-BF₄**. MO diagrams of free NO and of **2** as well as contour plots of important molecular orbitals of these species. MO contour plots for **1** – H. Details for the crystal structure determination of **2-Br** and tables of atomic coordinates, anisotropic displacement parameters, and geometric parameters. Complete vibrational assignments for **2**. Coordinates of the DFT fully optimized structures of **1** and **2**. This material is available free of charge via the Internet at <http://pubs.acs.org>.

IC049302I

7.3 Electronic Structure of Iron(II)–Porphyrin Nitroxyl Complexes: Molecular Mechanism of Fungal Nitric Oxide Reductase (P450nor)

Nicolai Lehnert, V. K. K. Praneeth, Florian Paulat

Published in: *J. Comp. Chem.* **2006**, 27, 1338-1351.

(special issue: Computational Bioinorganic Chemistry)

Electronic Structure of Iron(II)–Porphyrin Nitroxyl Complexes: Molecular Mechanism of Fungal Nitric Oxide Reductase (P450nor)

NICOLAI LEHNERT, V. K. K. PRANEETH, FLORIAN PAULAT

Institut für Anorganische Chemie, Christian-Albrechts-Universität Kiel, Olshausenstrasse 40,
D-24098 Kiel, Germany

Received 18 November 2005; Accepted 26 January 2006

DOI 10.1002/jcc.20400

Published online in Wiley InterScience (www.interscience.wiley.com).

Abstract: Density functional calculations are employed to investigate key intermediates of the catalytic cycle of fungal nitric oxide reductase (P450nor). The formal Fe(II)–nitroxyl species Fe(II)–NO/(–) can principally exist in the two spin-states $S = 0$ and $S = 1$. In the $S = 0$ case, a very covalent Fe–NO σ bond is present, which leads to an electronic structure description that is actually intermediate between Fe(I)–NO and Fe(II)–NO[–]. In contrast, the $S = 1$ case shows a ferrous Fe(II)–NO complex with the extra electron being stored in the π system of the porphyrin ligand. Importantly, the Fe(II)–NO/(–) species are very basic. The electronic structures and spectroscopic properties of the corresponding N- and O-protonated forms are very different, and unequivocally show that the Mb–HNO adduct (Mb-Myoglobin) prepared by farmer and coworkers is in fact N-protonated. The presence of an axial thiolate ligand enables a second protonation leading to the corresponding Fe(IV)–NHOH[–] species, which is identified with the catalytically active intermediate *I* of P450nor. This species reacts with a second molecule of NO by initial electron transfer from NO to Fe(IV) followed by addition of NO⁺ forming an N–N bond. This is accompanied by an energetically very favorable intramolecular proton transfer leading to the generation of a quite stable Fe(III)–N(OH)(NOH) complex. This way, the enzyme is able to produce dimerized HNO under very controlled conditions and to prevent loss of this ligand from Fe(III). The energetically disfavoured tautomer Fe(III)–N(OH₂)(NO) is the catalytically productive species that spontaneously cleaves the N–OH₂ bond forming N₂O and H₂O in a highly exergonic reaction.

© 2006 Wiley Periodicals, Inc. J Comput Chem 27: 1338–1351, 2006

Key words: electronic structure; iron(II)–porphyrin nitroxyl complex; P450nor

Introduction

Due to their tremendous significance in biology, much research has been focused on the geometric and electronic structures, spectroscopic properties, and reactivities of iron–porphyrin NO complexes.¹ Nitric oxide plays a central role in many important biological processes including nerve signal transmission, blood pressure control, and immune response with new functions of this molecule still being discovered.² Most of these tasks involve heme proteins. In addition, nitric oxide is an intermediate in assimilatory and dissimilatory denitrification.³ Assimilatory nitrite reductases are usually found in plants, and reduce nitrite to ammonia. These enzymes contain an active site that consists of a siroheme with an axially bound 4Fe–4S iron–sulfur cluster.⁴ The addition of nitrite to reduced, active enzyme leads to the immediate formation of a stable ferrous siroheme–nitrosyl complex, which is also the major species present upon enzyme turnover.^{4c,d} This species then un-

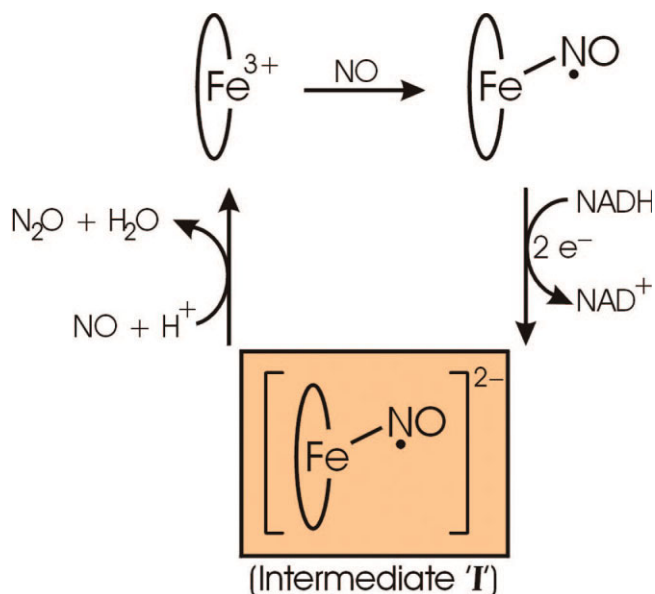
dergoes further reduction leading to a one-electron reduced Fe(II)–NO intermediate, labeled Fe(II)–NO/(–) in the following, which is readily protonated and ultimately becomes ammonia in the further course of the reaction. In contrast, the nitrite reductases in dissimilatory denitrification produce nitric oxide, which is then further reduced to nitrous oxide by a different class of enzymes, the nitric oxide reductases (NOR).⁵ In the case of fungal NOR (P450nor), the active site consists of a heme center with axially coordinated cysteinate.⁶ The proposed mechanism of this

Correspondence to: N. Lehnert; e-mail: nlehnert@ac.uni-kiel.de

Contract/grant sponsor: the Deutsche Forschungsgemeinschaft (DFG); contract/grant numbers: LE 1393/1 and 1393/1-2)

Contract/grant sponsor: the Fonds der Chemischen Industrie (FCI)

This article contains Supplementary Material available at <http://www.interscience.wiley.com/jpages/0192-8651/suppmat>



Scheme 1.

enzyme is shown in Scheme 1.⁷ Initially, nitric oxide is bound to the ferric form of the enzyme, which is then reduced by two electrons from NADH to yield intermediate *I*, which therefore corresponds to a Fe(II)—NO/(–) species. This intermediate is characterized by a Soret band position of 444 nm compared to 434 nm for the ferrous NO complex.⁷ Resonance Raman spectroscopy led to the identification of the Fe—NO stretch in *I* at 596 cm^{−1}. Importantly, this intermediate does not seem to undergo deuterium exchange, which indicates that *I* is not protonated.⁸ The further course of the reaction is less clear, but leads to reaction with another molecule of NO to create nitrous oxide. In later work, a more detailed mechanism for this enzyme was proposed by Daiber et al.⁹ based on kinetic studies, where intermediate *I* is again described as Fe(II)—NO/(–) species, but either singly or doubly protonated. The electronic structure of this intermediate has been proposed as either Fe(III) with a bound N(H)—OH radical (doubly protonated) or Fe(IV) with bound HNO and a cysteinyl radical (singly protonated), which is both counterintuitive. Hence, although Fe(II)—NO/(–) intermediates and/or corresponding protonated species are of great biological importance, not much is known about their detailed electronic structures and reactivities.

To gain more information about the properties of one-electron reduced ferrous nitrosyls, Fe(II)—NO/(–), a number of researchers have investigated corresponding model systems.¹⁰ In a series of classic studies, Ryan and coworkers¹¹ used spectroelectrochemistry to investigate synthetic model complexes of type [Fe(P)(NO)] (P = tetraphenylporphyrin, octaethylporphyrin, and related porphyrinoids). One-electron reduction of these five-coordinate species led to only small changes of the Soret band position and intensity, which shows that the reducing equivalent is not stored in the π -system of the macrocyclic ligand.^{11b} Hence, the electronic structure of the nonprotonated Fe(II)—NO/(–) species could either be of the Fe(II)—NO[−] or of Fe(I)—NO type; that is, the one-electron reduction could either be ligand (NO) or metal cen-

tered. Based on the observed strong shift of the N—O stretching frequency down to 1496 cm^{−1}, it was claimed that the complex has to be described as low-spin Fe(II)—NO[−] (*S* = 0), which is a ferrous “nitroxyl” species.^{11b} Binding studies with N-donor ligands showed that upon reduction of the Fe(II)—NO complex, the axial pyridine, or amine ligand is lost.^{11a} This indicates that nitroxyl has an even stronger *trans*-effect on coordinated axial ligands than NO.^{12,13} It was also found that the Fe(II)—NO[−] species reacts with weak acids, presumably forming corresponding Fe(II)—HNO and [Fe(II)—H₂NO]⁺ species as reactive intermediates. However, such solutions are not stable and immediately led to the formation of hydroxylamine, ammonia and ferrous bis-ammonia complexes.¹⁴ Information on corresponding protonated Fe(II)—nitroxyl complexes is available from the work of Farmer and coworkers¹⁵ using myoglobin. Reduction of ferrous Mb—NO with Cr(II) salts led to the formation of a surprisingly stable Fe(II)—HNO complex as evidenced by ¹H-NMR spectroscopy. Only a small shift of the Soret band from 421 to 423 nm is observed in this reaction. The resulting species is diamagnetic and shows resonance Raman signals at 1385 cm^{−1} for ν (N—O) and 651 cm^{−1} for the Fe—NO stretch. Bond lengths from EXAFS measurements are 1.82 Å for Fe—NO and 2.09 Å for Fe—N(imidazole) as shown in Table 1.⁸ Hence, this species corresponds to a six-coordinate complex with axial histidine coordination. An interesting question is then how an axial cysteinate as in P450_{nor} would influence the reactivity of this intermediate. This question was addressed by Farmer and coworkers¹⁶ investigating electrocatalytic nitrite reduction by myoglobin and P450 CYP119 in surfactant films. The results show a markedly reduced current and a higher product specificity for the P450 enzyme in this reaction.^{16b} The reduced activity of P450 CYP119 compared to myoglobin is somewhat surprising at the first glance, but can be explained by the known lower NO affinity of heme active sites with axial cysteinate coordination.^{2b} In addition, the P450 enzyme also seems to exhibit a reduced rate of N—N coupling.⁸

At this point it should also be underlined that there is growing evidence for an independent biological significance of free nitroxyl itself.¹⁷ This species might be created *in vivo* by nitric oxide synthase in the absence of its reduced pterin cofactor.¹⁸ Results by Barberger et al.^{17b} show that free nitroxyl is protonated under physiological conditions, and that the redox potential of the HNO/NO couple is about −0.5 V, which means that free NO should not be largely reduced to HNO in cells. The pK_A of the free ¹HNO/³NO[−] pair has been estimated to 11.4.¹⁹ Therefore, NO and HNO do not seem to interconvert *in vivo* to a significant extent, which allows them to mediate different biological functions.¹⁷ Free nitroxyl is easily trapped by ferric porphyrins (e.g., metmyoglobin and methemoglobin)²⁰ or thiols *in vivo*.^{17a} In addition, free HNO converts rapidly to N₂O through dimerization followed by dehydration ($k \sim 2 \times 10^9 \text{ M}^{-1} \text{ s}^{-1}$).^{17a}

In this study, density functional (DFT) calculations are used to define the electronic structures of the Fe(II)—nitroxyl complexes. For the calculations, six-coordinate species are chosen because the enzymatic species can be expected to be six-coordinate with either histidine or cysteinate present. These are modeled using porphine (P^{2−}; cf. Scheme 2) for the porphyrin ligand and 1-methylimidazole (MI) and methylthiolate (CH₃S[−]) as axial ligands, respectively. Spectroscopic parameters are calculated and correlated with the known experimental

Table 1. Calculated Geometric Properties and Relative Energies of $[\text{Fe}(\text{P})(\text{L})(\text{NO})]^{-/2-}$ Complexes and Corresponding Intermediates (L = MI or CH_3S^-) Compared to Experiment.

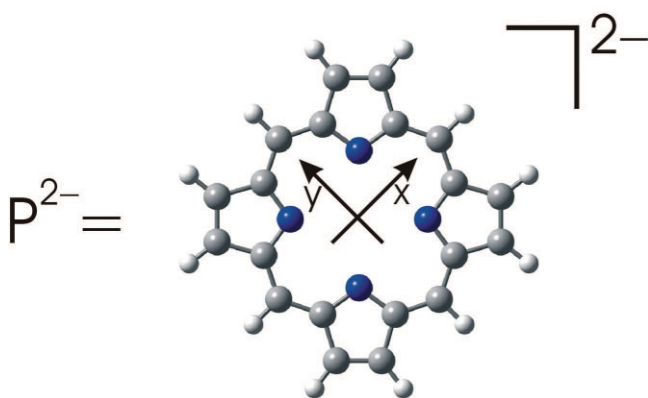
Molecule ^a	Geometric parameters [\AA]					Relative energies (kcal/mol)	
	$\Delta\text{Fe}-\text{N}$	$\Delta\text{N}-\text{O}$	$\angle\text{Fe}-\text{N}-\text{O}$	$\Delta\text{Fe}-\text{L}_{\text{tr}}$	$\Delta\text{N}-\text{N}$	BP86	B3LYP
[Mb-HNO] (ref. 8)	1.82	1.24	131	2.09	—	—	—
$[\text{Fe}(\text{P})(\text{MI})(\text{NO})]^-$ (1 , S = 0)	1.795	1.211	124	2.439	—	0	0
$[\text{Fe}(\text{P})(\text{MI})(\text{NO})]^-$ (S = 1)	1.715	1.193	141	2.256	—	+3.9	-2.7
$[\text{Fe}(\text{P})(\text{CH}_3\text{S})(\text{NO})]^{2-}$ (2 , S = 0)	1.776	1.215	131	2.587	—	0	0
$[\text{Fe}(\text{P})(\text{CH}_3\text{S})(\text{NO})]^{2-}$ (S = 1)	1.764	1.205	139	2.478	—	-0.4	-9.6
$[\text{Fe}(\text{P})(\text{CH}_3\text{S})(\text{NHO})]^-$ (3a , S = 0)	1.824	1.252	133	2.354	—	0	0
$[\text{Fe}(\text{P})(\text{CH}_3\text{S})(\text{NOH})]^-$ (3b , S = 0)	1.746	1.401	117	2.411	—	+25.4	+29.0
$[\text{Fe}(\text{P})(\text{CH}_3\text{S})(\text{NHOH})]$ (4 , S = 0)	1.810	1.397	125	2.230	—	—	—
$[\text{Fe}(\text{P})(\text{CH}_3\text{S})(\text{N}_2\text{O}_2)]^{2-}$ (5 , S = 1/2)	1.957	1.238	125	2.437	1.549	—	—
$[\text{Fe}(\text{P})(\text{CH}_3\text{S})(\text{N}_2\text{O}_2\text{H})]^-$ (6a , S = 1/2)	1.988	1.398	121	2.250	1.308	0	0
$i\text{-}[\text{Fe}(\text{P})(\text{CH}_3\text{S})(\text{N}_2\text{O}_2\text{H})]^-$ (6b , S = 1/2)	2.080	1.269	123	2.293	1.793	+27.6	+33.1
$[\text{Fe}(\text{P})(\text{CH}_3\text{S})(\text{N}_2\text{O}_2\text{H}_2)]$ (7b , S = 1/2)	2.128	1.406	115	2.177	1.250	0	0
$i\text{-}[\text{Fe}(\text{P})(\text{CH}_3\text{S})(\text{N}_2\text{O}_2\text{H}_2)]$ (7a , S = 1/2)	1.988 ^c	1.398	121	2.212	1.760	+16.5	+18.1
$[\text{Fe}^{\text{II}}(\text{P})(\text{NO})]$ -calc ¹³	1.705	1.179	146	—	—	—	—
$[\text{Fe}^{\text{II}}(\text{P})(\text{MI})(\text{NO})]$ -calc ¹³	1.734	1.186	140	2.179	—	—	—
$[\text{Fe}^{\text{II}}(\text{P})(\text{CH}_3\text{S})(\text{NO})]^-$ -calc ²⁶	1.788	1.198	138	2.416	—	—	—
$[\text{Fe}^{\text{II}}(\text{TPP})(\text{NO})]$ (ref. 29) ^b	1.72	1.12	149	—	—	—	—
$[\text{Fe}^{\text{II}}(\text{TPP})(\text{MI})(\text{NO})]$ (ref. 12)	1.750	1.182	138	2.173	—	—	—

^aMI = 1-methylimidazole; P = Porphine (2-).

^bHighly disordered structure.

^cFixed at the optimized distance obtained for **6a**. Otherwise, $\text{N}_2\text{O}_2\text{H}_2$ is lost from iron during the geometry optimization.

data described above. This allows for an identification of the key intermediate *I* in the catalytic cycle of P450nor. Comparison with the electronic structures of corresponding ferrous nitrosyls is also pro-

**Scheme 2.**

vided. Based on these results, the reaction mechanism of P450nor is investigated by optimization of key species and then application of frequency and solvent field calculations to obtain the corresponding free energies. From these results, pK_A values for the protonation of the initially formed $\text{Fe}(\text{II})-\text{NO}/(-)$ intermediate are also obtained. Finally, the biological implications of these results are discussed. Note that the mechanism of P450nor has been investigated before using DFT calculations.²¹ Structures of the model system $[\text{Fe}(\text{P})(\text{CH}_3\text{S})(\text{NO})]^{2-}$ and of corresponding protonated and nitrosylated systems have been calculated before by Silaghi-Dumitrescu,^{21a} but no correlation with experimental data is given and the mechanism of P450nor is not quantitatively evaluated in this work. In a recent publication, Vincent et al.^{21c} investigated key steps in the mechanism of P450nor using DFT. However, comparison of the calculated properties with experimental data is again limited in this article, the energies of the different protonation steps are not considered, and the entire scenario of the possible protonation equilibria of the different species involved is missing. Hence, the work presented here reaches far beyond the scope of these earlier studies.

Table 2. Calculated Vibrational Properties and Force Constants of $[\text{Fe}(\text{P})(\text{L})(\text{NO})]^{-/2-}$ Complexes and Corresponding Intermediates (L = MI or CH_3S^-) Compared to Experiment.

Molecule ^a	Vibrational frequencies (cm^{-1})		Force constants ($\text{mdyn}/\text{\AA}$)		
	$\nu(\text{N—O})$	$\nu(\text{Fe—NO})$	N—O	Fe—NO	Fe—L _{tr} ^c
$[\text{Fe}(\text{TPP})(\text{NO})]^-$	1496	—	—	—	—
$[\text{Mb-HNO}]$ (ref. 8)	1385	651	—	—	—
P450nor: intermediate I ^{7b}	—	596	—	—	—
$[\text{Fe}(\text{P})(\text{MI})(\text{NO})]^-$ (1 , S = 0)	1511	544/(435)	10.29	2.50	0.21
$[\text{Fe}(\text{P})(\text{MI})(\text{NO})]^-$ (S = 1)	1630	616	11.63	3.52	0.47
$[\text{Fe}(\text{P})(\text{CH}_3\text{S})(\text{NO})]^{2-}$ (2 , S = 0)	1500	502	9.97	2.61	0.42
$[\text{Fe}(\text{P})(\text{CH}_3\text{S})(\text{NO})]^{2-}$ (S = 1)	1567	573/453	10.77	2.73	0.61
$[\text{Fe}(\text{P})(\text{CH}_3\text{S})(\text{NHO})]^-$ (3a , S = 0)	1386	601/430	8.67	2.52	1.07
$[\text{Fe}(\text{P})(\text{CH}_3\text{S})(\text{NOH})]^-$ (3b , S = 0)	833	649	3.44	3.32	0.88
$[\text{Fe}(\text{P})(\text{CH}_3\text{S})(\text{NHOH})]$ (4 , S = 0)	952	609/544 ^b	4.50	2.63	1.56
$[\text{Fe}^{\text{II}}(\text{P})(\text{NO})]$ -calc ¹³	1703	595	12.71	3.62	—
$[\text{Fe}^{\text{II}}(\text{P})(\text{MI})(\text{NO})]$ -calc ¹³	1662	609	12.22	3.26	0.61
$[\text{Fe}^{\text{II}}(\text{P})(\text{CH}_3\text{S})(\text{NO})]^-$ -calc ²⁹	1599	531/440	11.26	2.38	0.81
$[\text{Fe}^{\text{II}}(\text{TPP})(\text{NO})]$ (ref. 13)	1697	532	12.53	2.98	—
$[\text{Fe}^{\text{II}}(\text{TPP})(\text{MI})(\text{NO})]$ (ref. 13)	1630	440/530	11.55	2.55	—

^aMI = 1-methylimidazole; P = Porphine²⁻.^bBoth modes at 609 and 544 cm^{-1} are strongly mixed with in-plane and out-of-plane Fe—N—H bends.

Computational Procedures

Density Functional Calculations

The structures of the models **1–8** listed in Tables 1–3 have been fully optimized using BP86/TZVP in the given spin states. For all these calculations, the simple porphine P^{2-} ligand as shown in Scheme 2 has been used. Axial histidine and cysteinate ligands have been modeled using 1-methylimidazole (MI) and methylthiolate (CH_3S^-), respectively. Vibrational frequencies have been calculated for all structures. Low-lying imaginary frequencies ($<25i \text{ cm}^{-1}$) have been obtained for **1** (S = 0; MI rotation), and **3a** and **3b** (rotation of the axial ligands along the z axis). The structure of $[\text{Fe}(\text{P})(\text{CH}_3\text{S})(\text{NO})]^{2-}$ (S = 1) shows one imaginary frequency at $\sim 110i \text{ cm}^{-1}$ that, however, corresponds to a rotation of the CH_3 group around the S— CH_3 axis of the thiolate ligand, and hence, is irrelevant. In addition, B3LYP/LanL2DZ* calculations have been performed on all these model systems to obtain accurate total energies for the determination of reaction energies. The LanL2DZ* basis set consists of LanL2DZ plus polarization functions (from TZVP) on all heavy atoms. Solvation effects were included in the calculations using the PCM model and water as the solvent. From these results, pK_A values can be calculated using the equation:

$$\text{pK}_\text{A} = \frac{\Delta G}{2.3026 \cdot R \cdot T}$$

Surprisingly, the calculated value for the $^1\text{HNO}/^3\text{NO}^-$ pair of 23.5 shows significant deviation from the experimental value of ~ 11.4 . Using B3LYP/TZVP instead of B3LYP/LanL2DZ* single-point calculations only leads to a small improvement of the theoretical result (calcd.: 19.1). Hence, the much more cost-efficient B3LYP/LanL2DZ* method is used for the calculations on the model complexes. All these methods were used as implemented in the Gaussian 98 package.²² Force constants in internal coordinates were calculated using a modified version of the program Redong²³ (QCPE 628). Molecular orbitals were visualized using GaussView. S^2 -expansion techniques have been applied on the ferrous nitrosyls using a program provided by Zilberberg and coworkers.²⁴

Results and Analysis

Electronic Structure of $[\text{Fe}(\text{P})(\text{MI})(\text{NO})]^-$ (**1**)

Figure 1(top) shows the optimized structure of $[\text{Fe}(\text{P})(\text{MI})(\text{NO})]^-$ (**1**) for S = 0, and Table 1 lists important structural parameters for this model complex obtained from BP86/TZVP calculations. Bond lengths of 1.795 \AA for Fe—NO and 1.211 \AA for N—O are obtained. Corresponding force constants are 2.5 $\text{mdyn}/\text{\AA}$ for Fe—NO and 10.3 $\text{mdyn}/\text{\AA}$ for N—O as listed in Table 2. The Fe—N(imidazole) bond is very long at 2.439 \AA , which is basically nonbonding. This is also reflected by the Fe—N(imidazole) force constant, which is only 0.2 $\text{mdyn}/\text{\AA}$. The calculated value of 1511

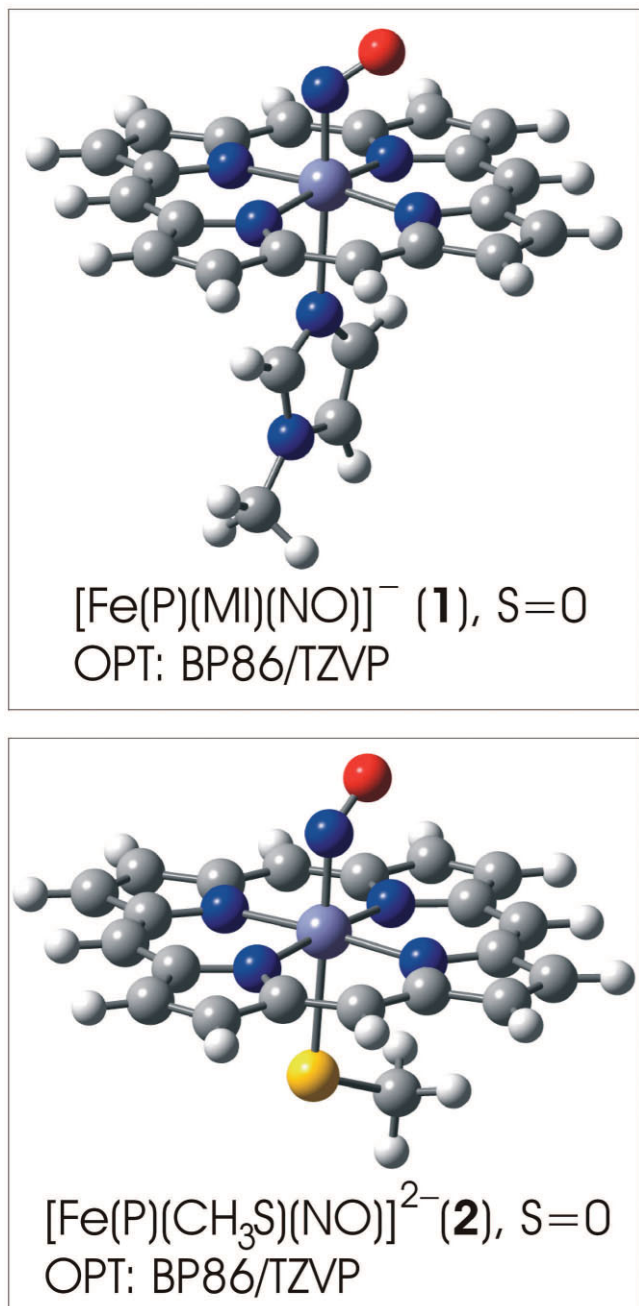


Figure 1. Figures of the fully optimized structures of $[\text{Fe}(\text{P})(\text{MI})(\text{NO})]^{-}$ (**1**, $S = 0$; P = Porphine (2-); MI = 1-methylimidazole) and $[\text{Fe}(\text{P})(\text{CH}_3\text{S})(\text{NO})]^{2-}$ (**2**, $S = 0$) obtained with BP86/TZVP. Structural parameters are given in Table 1.

cm^{-1} for the N—O stretch $\nu(\text{N—O})$ of **1** is in excellent agreement with the experimentally determined N—O stretching frequency of 1496 cm^{-1} for one-electron reduced $[\text{Fe}(\text{TPP})(\text{NO})]$ (TPP = tetraphenylporphyrine).^{11b} This is additional strong evidence that $[\text{Fe}(\text{TPP})(\text{NO})]^{-}$ has an $S = 0$ ground state as has been proposed by Ryan and coworkers (see Introduction). Therefore, the elec-

tronic structure of the corresponding six-coordinate species $[\text{Fe}(\text{P})(\text{MI})(\text{NO})]^{-}$ (**1**) in the relevant $S = 0$ state will be analyzed in the following. Note that from the calculations, the $S = 0$ and $S = 1$ states of $[\text{Fe}(\text{P})(\text{MI})(\text{NO})]^{-}$ are very close in energy (within 5 kcal/mol), that is, the ground state is $S = 0$ with BP86 and $S = 1$ for B3LYP as listed in Table 1. The MO diagram of **1** ($S = 0$) is given in Figure S1, and contour plots of important orbitals are shown in Figure S2. The coordinate system used for the following discussion is shown in Scheme 2 where the Fe—N(O) bond is roughly oriented along the z axis. The HOMO of complex **1**, labeled $\pi_{\text{h}}^* d_{z^2}/d_{xz}$ ($\langle 123 \rangle$), corresponds to an equal mixture of d_{z^2}/d_{xz} of iron and π_{h}^* of NO (h = horizontal; the π^* orbital within the Fe—NO plane). This MO is Fe—NO bonding and hence, constitutes a very strong Fe—NO σ bond. On the other hand, this orbital is σ antibonding with respect to MI, which explains the very weak Fe—N(imidazole) interaction in this complex, which has also been observed experimentally.¹¹ To lower energy, the three t_2 orbitals of iron, d_{xz} , d_{yz} , and $d_{x^2-y^2}$ (in the given coordinate system) are found, which are fully occupied. An additional contribution to the Fe—NO bond corresponds to a backbonding interaction between d_{yz} and the π_{v}^* orbital of NO (v = vertical; the π^* orbital perpendicular to the Fe—NO plane). The strength of this interaction is estimated best from the corresponding antibonding combination, $\pi_{\text{v}}^* d_{yz}$ ($\langle 127 \rangle$), which has 22% d and 67% π^* character as listed in Table S1. Based on this MO description, the Fe(II)—NO⁻ (ferrous-nitrosyl) classification of $[\text{Fe}(\text{TPP})(\text{NO})]^{-}$ as proposed by Ryan and coworkers^{11b} is not entirely correct, because the two σ electrons occupying the π_{h}^* orbital of the bound ¹NO⁻ ligand are *fully delocalized* over the Fe—N—O unit by strong mixing with d_{z^2} of iron. Because of this, the NO bond is stronger and $\nu(\text{NO})$ around 1500 cm^{-1} is higher in energy in **1** than in free NO⁻ (1290 cm^{-1} ; cf. ref. 17a). On the other hand, a one-electron reduced Fe(II)—NO/(-) species has also been characterized for a nonheme iron complex using a tethered cyclam ligand.²⁵ In this case, $\nu(\text{N—O})$ is observed at 1271 cm^{-1} , which shows that the NO ligand experiences a much stronger degree of reduction in this complex. This marks an important difference between heme vs. nonheme iron chemistry.

The electronic structure of $[\text{Fe}(\text{P})(\text{MI})(\text{NO})]^{-}$ completely changes in the $S = 1$ state. As listed in Table 1, this complex has shorter Fe—N(O), N—O, and Fe—N(imidazole) bond lengths than **1** ($S = 0$). In fact, these bond distances are actually close to the values observed for the ferrous-nitrosyl complex $[\text{Fe}(\text{P})(\text{MI})(\text{NO})]$. Correspondingly, the calculated N—O stretching frequency of 1630 cm^{-1} for the $S = 1$ complex matches the value of 1662 cm^{-1} calculated for $[\text{Fe}(\text{P})(\text{MI})(\text{NO})]$. This shows that $[\text{Fe}(\text{P})(\text{MI})(\text{NO})]^{-}$ with $S = 1$ has a ferrous-nitrosyl electronic structure, where the extra electron must then be stored in the porphyrin ligand by forming a P³⁻ radical anion. This description is confirmed by the calculated spin density of the $S = 1$ complex. As a consequence, the nature of the porphyrinoid macrocycle might play an important role in determining the ground state of $[\text{Fe}(\text{porphyrin})(\text{L})(\text{NO})]^{-}$ type complexes. Because the spectroscopic properties of the $S = 0$ and $S = 1$ states are very different, it is obvious from the experimental data on $[\text{Fe}(\text{TPP})(\text{NO})]^{-}$ that this complex has an $S = 0$ ground state as discussed above.¹¹

Electronic Structure of $[\text{Fe}(\text{P})(\text{CH}_3\text{S})(\text{NO})]^{2-}$ (**2**)

Based on the electronic structure description of $[\text{Fe}(\text{P})(\text{MI})(\text{NO})]^-$ (**1**, $S = 0$) elaborated above, it is interesting to explore how an axial thiolate ligand as observed in P450nor would alter the properties of the Fe–NO subunit. From previous work on ferrous nitrosyls it is known that this effect can be substantial (vide infra).²⁶ To this end, we have optimized the structure of the model system $[\text{Fe}(\text{TPP})(\text{CH}_3\text{S})(\text{NO})]^{2-}$ (**2**, $S = 0$) using BP86/TZVP. As shown in Table 1, the obtained Fe–NO and N–O bond distances of 1.776 and 1.215 Å are very close to those of **1**. Correspondingly, the N–O stretching frequency of **2** calculated at 1500 cm^{-1} almost matches the value of 1511 cm^{-1} for **1**. The fact that **1** and **2** have overall similar properties is not surprising, because due to the strong *trans*-effect of the coordinated nitroxyl ligand, the axial imidazole in **1** and thiolate in **2** are only very weakly bound (force constants are 0.21 mdyn/Å for Fe–N and 0.42 mdyn/Å for Fe–S, respectively). Small differences in electronic structures are evident from the calculated force constants shown in Table 2, which can be explained based on the MO diagram of **2** shown in Figure S3 (contour plots are given in Fig. S4). Analysis of the MO scheme shows that the principal bonding interactions between iron(II) and NO^- are very similar in **1** and **2**, that is, a σ bond is formed between π_{h}^* of $^1\text{NO}^-$ and a mixed d_{z^2}/d_{xz} orbital of iron and a π backbond is present due to interaction of π_{v}^* and d_{yz} . Compared to **1**, the mixing between π_{h}^* and d_{z^2} is somewhat reduced, which leads to a slight weakening of the Fe–NO σ bond and a slight increase in the occupation of π_{h}^* in **2**. This corresponds to a slight *trans*-effect of the thiolate ligand on the coordinated NO (cf. ref. 26). In the case of the π backbond, analysis of the antibonding orbital $\pi_{\text{v}}^*d_{yz}$ shows a slight increase in metal contribution in the case of **2**, which corresponds to a slight strengthening of this interaction. Taken together, both effects lead to a slight increase of the occupation of the π^* orbitals of NO in **2**, which explains the observed reduction of the N–O force constant by 0.3 mdyn/Å from 10.29 mdyn/Å in **1** to 9.97 mdyn/Å in **2**. For the Fe–NO bond, these effects cancel, leaving the corresponding force constant almost unchanged, as shown in Table 2. In the $S = 1$ state of $[\text{Fe}(\text{TPP})(\text{CH}_3\text{S})(\text{NO})]^{2-}$, a similar situation is encountered as in the case of $[\text{Fe}(\text{P})(\text{MI})(\text{NO})]^-$, where the porphyrin ring is reduced leading to a P^{3-} radical anion. However, in the case of **2**, the stabilization of the $S = 1$ state relative to the $S = 0$ state is enhanced. Calculated energies are -0.4 kcal/mol with BP86 and -9.6 kcal/mol with B3LYP in favor of $S = 1$ as shown in Table 1.

From these results, the main effect of thiolate coordination in the Fe(II)–nitroxyl complexes seems to be a stabilization of the $S = 1$ state, whereas the electronic structure of the Fe–NO subunit is hardly altered. It is, of course, tempting to conclude that this is the actual reason for axial cysteinate coordination in P450nor, which researchers have speculated about for a long time.⁸ An $S = 1$ ground state for intermediate *I* would be advantageous for the following reaction with the radical NO, which would otherwise be spin forbidden. However, as we will show below, we believe that intermediate *I* in P450nor is actually protonated, and therefore, the question of whether the Fe(II)–nitroxyl complex with thiolate coordination has an $S = 0$ or $S = 1$ ground state is not relevant for the mechanism of P450nor. At this point it should also be mentioned that electrocatalytic investigations of

Farmer and coworkers on the nitrite and NO reduction by myoglobin and P450 CYP119 did not show any enhancement of NO reductase activity for the P450 enzyme in agreement with this conclusion.¹⁶

Comparison of the Electronic Structures of Fe(II)–Nitroxyl Complexes and Ferrous NO Adducts

The electronic structure of the ferrous six-coordinate complex $[\text{Fe}(\text{P})(\text{MI})(\text{NO})]$ has been described as Fe(II)–NO(radical) adduct.^{13a} Analysis of the unrestricted single-determinantal wave function from the B3LYP calculation by expansion in the basis of Löwdin–Amos–Hall paired orbitals using the approach of Zilberberg and coworkers²⁷ again validates this description. From this analysis, the ground state of this complex has 88% Fe(II)–NO(radical) character with a 12% admixture of a ligand field excited state. The SOMO of this complex, which corresponds to a bonding combination of a mixed d_{z^2}/d_{xz} orbital of iron(II) and π_{h}^* of NO, reflects this electronic structure. Charge contributions to the SOMO of 42% Fe and 43% NO^{13b} are basically identical with the HOMO of one-electron reduced $[\text{Fe}(\text{P})(\text{MI})(\text{NO})]^-$ (**1**) in the $S = 0$ state as described above. This means that one-electron reduction of the ferrous nitrosyl simply leads to a double occupation of its SOMO, which strengthens the Fe–NO σ bond, whereas at the same time the Fe–N(imidazole) bond is further weakened in agreement with the experimental results.¹¹ Based on this large difference in σ bonding, one would expect that **1** exhibits a stronger Fe–NO bond than the ferrous nitrosyl complex. However, this is not the case, as is evident from the calculated Fe–NO force constants listed in Table 2. This is due to a reduction of π -backbonding, but also an increase of Coulomb repulsion, between d_{xz} and π_{h}^* in **1** compared to the ferrous nitrosyl complex. This is a very important result, because it indicates that the corresponding Fe–NO stretching vibration should be shifted to *lower energy* in **1** compared to $[\text{Fe}(\text{P})(\text{MI})(\text{NO})]$.

In the case of the corresponding complexes with axial thiolate coordination, a more complicated situation is encountered. This is due to the fact that the ferrous nitrosyls, $[\text{Fe}(\text{P})(\text{CH}_3\text{S})(\text{NO})]^-$ and $[\text{Fe}(\text{P})(\text{MI})(\text{NO})]$, have different electronic structures, where axial thiolate coordination leads to a distinct weakening of the Fe–NO σ bond.²⁶ In addition, spin polarization effects are observed for the π -backbond in $[\text{Fe}(\text{P})(\text{CH}_3\text{S})(\text{NO})]^-$, which leads to a large amount of positive spin density on the NO ligand (>1.0) and the occurrence of negative spin density on iron. We have now reevaluated this electronic structure using Löwdin–Amos–Hall paired orbitals, and we found that the observed spin-polarization effects are actually due to the admixture of a distinct amount of Fe(III)– NO^- character into the ground state of $[\text{Fe}(\text{P})(\text{CH}_3\text{S})(\text{NO})]^-$, which has 74% Fe(II)–NO(radical) character with 18% admixture of Fe(III)– NO^- and 6% contribution from a ligand field excited state. This is due to a stabilization of Fe(III) by the thiolate ligand. These special features of the electronic structure of the ferrous nitrosyl are lost upon one electron reduction. Because the axial thiolate has a strong effect on the Fe–NO unit in the ferrous nitrosyl, but only a weak effect in $[\text{Fe}(\text{P})(\text{CH}_3\text{S})(\text{NO})]^{2-}$ (**2**) in the $S = 0$ state (vide supra), the change of force constants and vibrational frequencies is distinctively smaller in this case compared to the complexes with axial

imidazole ligation. The Fe—NO force constant actually slightly increases from 2.38 mdyne/Å in ferrous $[\text{Fe}(\text{P})(\text{CH}_3\text{S})(\text{NO})]^-$ to 2.61 mdyne/Å in **2**. The Fe—NO stretching frequency does not follow this trend and slightly drops to 502 cm^{-1} in **2**. This is due to a change in mode mixing of $\delta(\text{Fe—N—O})$ with porphyrin vibrations, and hence, might be overestimated in the calculations. On the other hand, the N—O stretch follows the general trend and decreases by $\sim 100 \text{ cm}^{-1}$ upon one-electron reduction, reflecting the increase in the occupation of the π^* orbitals of NO in **2**. Importantly, the experimentally determined Fe—NO stretches in the ferrous P450cam and chloroperoxidase NO adducts are observed at 554 and 542 cm^{-1} , respectively,²⁸ which means that the one-electron reduced species must have a frequency at identical or lower energy. In contrast, the Fe—NO stretch in intermediate *I* has been reported at 596 cm^{-1} (cf. Table 2). Based on these results, we believe that the proposal of Daiber et al., following kinetic evidence, is correct, and that intermediate *I* is actually protonated. This aspect is further analyzed in the next section.

Protonation of $[\text{Fe}(\text{P})(\text{CH}_3\text{S})(\text{NO})]^{2-}$ (**2**) and Nature of the $[\text{Mb—HNO}]$ Adduct and Intermediate *I*

Based on the finding that intermediate *I* is most probably protonated, it is then important to investigate the resulting singly and doubly protonated ferrous-nitroxyl species. Note that the free $^1\text{HNO}/^3\text{NO}^-$ pair has a pK_A of approximately 11.4, which means that $^3\text{NO}^-$ is fully protonated in water yielding ^1HNO . Starting with the singly protonated case, the bound nitroxyl could either be protonated at the coordinating nitrogen or the terminal oxygen atom. The structures of both resulting complexes, $[\text{Fe}(\text{P})(\text{CH}_3\text{S})(\text{NHO})]^-$ (**3a**, $S = 0$, N-protonated) and $[\text{Fe}(\text{P})(\text{CH}_3\text{S})(\text{NOH})]^-$ (**3b**, $S = 0$, O-protonated), have been fully optimized using BP86/TZVP and are shown in Figure 2 [open-shell spin states ($S = 1, 2$) have not been considered in these cases, because the work of Silaghi-Dumitrescu has shown that these are at distinctively higher energies ($> +15 \text{ kcal/mol}$)]^{21a}. Importantly, the electronic structures of these intermediates are very different. This is already indicated by the obtained bond distances as shown in Table 2. In the case of **3a**, protonation leads to an increase of both the Fe—N and N—O distances to 1.824 and 1.252 Å, respectively, compared to **2**. An inspection of the MO diagram of this complex shows that the added proton binds to the π_h^* orbital of the NO ligand leading to a planar Fe—N(H)O unit. This strongly decreases π_h^* in energy, and hence, decreases its interaction with d_{z^2} of iron compared to **2**. Because the resulting bonding orbital, $\pi_\text{h}^* d_{z^2}$, is distributed over several MOs (cf. $\langle 106 \rangle$ in Fig. 2), it is useful to analyze the corresponding antibonding (unoccupied) combinations, $d_{z^2} \pi_\text{h}^*$. In the case of **3a**, this orbital has 56% d_{z^2} and only 15% π^* character (cf. Fig. 2), whereas the corresponding orbital of **2** has 43% d_{z^2} and 33% π^* contribution (cf. Table S2). Hence, upon protonation of the coordinated NO in **2**, the two electrons occupying the σ bonding orbital $\pi_\text{h}^* d_{z^2}$ are shifted toward the generated HNO ligand and the metal–ligand covalency decreases. This weakens both the Fe—N σ bond and the N—O bond in **3a** compared to **2**. The backbond between π_v^* of NO and d_{yz} of iron is somewhat stronger in the case of **3a**, where the corresponding antibonding combination, $\pi_\text{v}^* d_{yz}$ ($\langle 117 \rangle$) (cf. Fig. 2), has 60% π_v^* and 30% d_{yz} character. This somewhat compensates

the loss in Fe—N σ bonding in **3a** compared to **2**. In addition, this further weakens the N—O bond, which explains the strongly reduced N—O force constant and stretching frequency in **3a** compared to **2** (cf. Table 2). In summary, the electronic structure of the intermediate **3a** can be described as a simple Fe(II)—HNO adduct with a quite strong π backbond.

Importantly, the electronic structure of the O-protonated tautomer **3b** is very different. In this case, the Fe—N distance is decreased to 1.746 Å, whereas the N—O bond length is strongly increased to 1.401 Å compared to **2**. As in the case of **3a**, the resulting Fe—NOH unit is planar, as shown in Figure 2, which indicates that the proton interacts with the π_h^* orbital of NO. This is confirmed by inspection of key MOs of **3b** shown in Figure 2. As in the case of **3a**, the addition of a proton to π_h^* lowers this orbital in energy, which leads to a distinct increase of its occupation and a decrease of its mixing with d_{z^2} of iron compared to **2**. The corresponding antibonding combination, $d_{z^2} \pi_\text{h}^*$ ($\langle 120 \rangle$), has charge contributions of 52% d_{z^2} and 20% π_h^* , which is quite similar to **3a**. Hence, as in the case of **3a**, the two electrons occupying the $\pi_\text{h}^* d_{z^2}/d_{xz}$ HOMO in **2** are transferred to the NO ligand upon protonation. The π backbond between π_v^* and d_{yz} is further enhanced compared to **2** and **3a**. This is evident from the corresponding antibonding combination, $\pi_\text{v}^* d_{yz}$ ($\langle 117 \rangle$) (cf. Fig. 2), which has 50% π_v^* and 37% d_{yz} character in the case of **3b**. Hence, this bonding description should give rise to a somewhat stronger Fe—N bond and a somewhat weaker N—O bond in **3b** compared to **3a**. However, this is not in agreement with the observed large difference in N—O bond lengths in these complexes. The strong elongation of the N—O distance to 1.401 Å in **3b** is actually due to a *polarization* of the out-of-plane π_v^* and π_v^b orbitals of NO leaving two p orbitals behind, N(p) and O(p), that only weakly interact. Hence, the out-of plane π bond has almost disappeared in **3b**, leading to an N—O single bond. Because O(p) is occupied and N(p) is empty, the latter forms a very strong π backbond with d_{yz} , which explains the distinct shortening (strengthening) of the Fe—N bond in **3b**. In summary, the electronic structure of this complex has to be described as Fe(II)—NOH with a very weak N—O bond. The remarkably different electronic structures of the N- and O-protonated tautomers of **2** are also reflected by their vibrational properties. In the case of **3a**, the N—O force constant of 8.67 mdyne/Å corresponds to a weak N—O double bond with a predicted N—O stretch of 1386 cm^{-1} . In contrast, the N—O force constant of 3.44 mdyne/Å in **3b** confirms the single bond character with a predicted $\nu(\text{N—O})$ of only 833 cm^{-1} . Compared to the N—O stretch of **2** calculated at 1500 cm^{-1} , the position of $\nu(\text{N—O})$ therefore allows to easily distinguish between the complexes **2**, **3a**, and **3b** experimentally. Whereas the Fe—N force constant of **3a** (2.52 mdyne/Å) is almost identical to that of **2**, the Fe—NO stretch in this complex is predicted to be $\sim 600 \text{ cm}^{-1}$, and hence, about 100 cm^{-1} higher in energy than in **2**. This surprising result is due to an intrinsic admixture of the Fe—N—H bend into $\nu(\text{Fe—NO})$, which increases the energy of this mode in the case of **3a**. Complex **3b** has the strongest Fe—N bond with a force constant of 3.32 mdyne/Å and a predicted Fe—NO stretch of 649 cm^{-1} .

Farmer and coworkers reported the synthesis of an HNO adduct of Mb, which turned out to be surprisingly stable.⁸ Based on $^1\text{H-NMR}$ results it was proposed that this species is N-protonated.

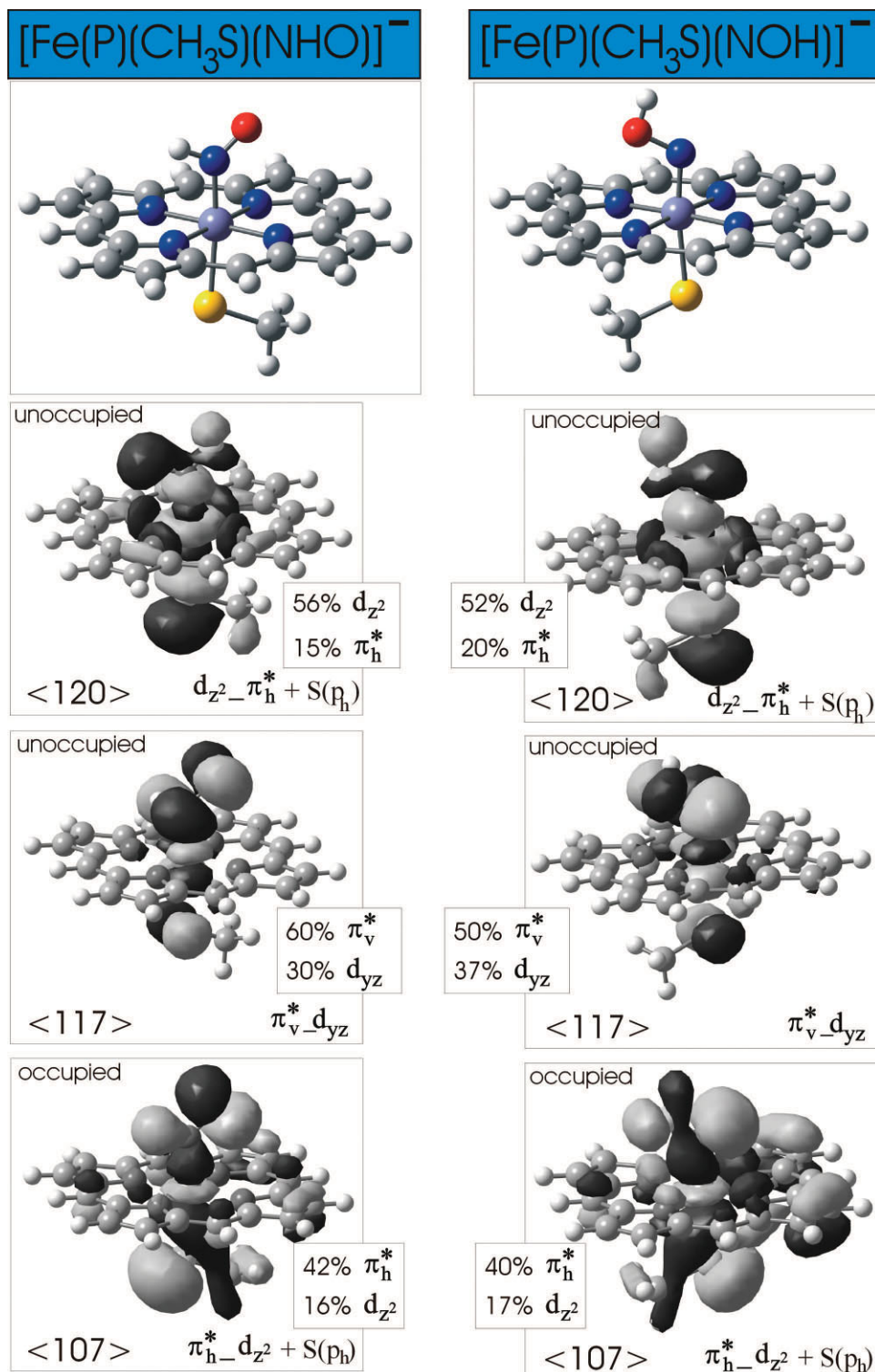


Figure 2. Optimized geometries (top) and contour plots of important molecular orbitals of [Fe(P)(CH₃S)(NHO)]⁻ (**3a**, S = 0, left) and [Fe(P)(CH₃S)(NOH)]⁻ (**3b**, S = 0, right) calculated with BP86/TZVP. Orbital decompositions are also included.

Table 3. Calculated Electronic Energies ε , and Free Energy and Solvation Corrections (G_{corr} and G_{SOLV}) for $[\text{Fe}(\text{P})(\text{CH}_3\text{S})(\text{NO})]^{-2-}$ Complexes and Corresponding Intermediates (P = Porphine(2-)) at $T = 298.15$ K. Calculated free reaction energies relative to **3a** (cf. Scheme 3) and pK_A values are also listed.

Complex	Calculated energies (Hartree)				ΔG (kcal/mol)	pK_A
	ε	G_{corr}	G_{SOLV}	G_{SUM}^a		
$[\text{Fe}(\text{P})(\text{CH}_3\text{S})(\text{NO})]^{2-}$ (2 , $S = 0$)	-1291.92578	0.24907	-0.25048	-1291.92719	+46.64	—
$[\text{Fe}(\text{P})(\text{CH}_3\text{S})(\text{NHO})]^-$ (3a , $S = 0$)	-1292.61334	0.26788	-0.07394	-1292.41940	0.0	34.2
$[\text{Fe}(\text{P})(\text{CH}_3\text{S})(\text{NOH})]^-$ (3b , $S = 0$)	-1292.56709	0.26667	-0.07726	-1292.37768	+26.2	15.0
$[\text{Fe}(\text{P})(\text{CH}_3\text{S})(\text{NHOH})]$ (4 , $S = 0$)	-1293.10301	0.28044	-0.02837	-1292.85094	-8.6	6.3 ^b
$[\text{Fe}(\text{P})(\text{CH}_3\text{S})(\text{N}_2\text{O}_2)]^{2-}$ (5 , $S = 1/2$)	-1421.89651	0.25431	-0.25295	-1421.89515	+21.2	—
$[\text{Fe}(\text{P})(\text{CH}_3\text{S})(\text{N}_2\text{O}_2\text{H})]^-$ (6a , $S = 1/2$)	-1422.58098	0.27005	-0.06977	-1422.38070	-21.3	31.1
$i-[\text{Fe}(\text{P})(\text{CH}_3\text{S})(\text{N}_2\text{O}_2\text{H})]^-$ (6b , $S = 1/2$)	-1422.52818	0.26885	-0.08156	-1422.34089	+3.7	12.8
$i-[\text{Fe}(\text{P})(\text{CH}_3\text{S})(\text{N}_2\text{O}_2\text{H}_2)]$ (7a , $S = 1/2$)	-1423.07461	0.28490 ^c	-0.00746	-1422.79717	-20.4	—
$[\text{Fe}(\text{P})(\text{CH}_3\text{S})(\text{N}_2\text{O}_2\text{H}_2)]$ (7b , $S = 1/2$)	-1423.10339	0.28505	-0.00486	-1422.82320	-36.9	—
Transition State (7c , $S = 1/2$; estim. ^d)	-1423.04991		-0.00248	-1422.76734	(-1.8)	—
$\text{hs}-[\text{Fe}(\text{P})(\text{CH}_3\text{S})]$ (8)	-1162.00805	0.24826	-0.00437	-1161.76416	-89.6 ^e	—
NO	-129.91377	-0.01574	0.00215	-129.92736	—	—
³ NO ⁻	-129.90481	-0.01751	-0.12263	-130.04495	0	—
¹ HNO	-130.49584	-0.00830	-0.00975	-130.51389	32.03	23.5 ^f
H ⁺ (see ref. 30)	0			-0.41789	—	—
N ₂ O	-184.69207	-0.01064	-0.00096	-184.70367	—	—
H ₂ O	-76.43112	0.00290	-0.01138	-76.43960	—	—

^a $G_{\text{SUM}} = \varepsilon + G_{\text{corr}} + G_{\text{SOLV}}$; ε = electronic energy, G_{corr} = thermal and entropy correction to ε , G_{SOLV} = free energy of solvation. G_{corr} is taken from the BP86/TZVP frequency calculation, the other energies are calculated with B3LYP/LanL2DZ* (see Experimental Section).

^bRelative to **3a**.

^cThe structure of **7a** has not been fully optimized (cf. Table 1). Hence, the calculated G_{corr} is only an estimate.

^dWe were not able to obtain the structure of the transition state from true transition state optimizations. The energy given here (using G_{corr} from **7b**) corresponds to a structure where the N—OH and both O—H distances have been fixed and the geometry was then optimized. This is only a crude approximation.

^eEnergy includes the formation of N₂O and H₂O.

^fExperimental pK_A value for ${}^1\text{HNO} \rightarrow {}^3\text{NO}^- + \text{H}^+$: ~ 11.4 (ref. 19a).

Vibrational energies of 1385 cm^{-1} for the N—O and 651 cm^{-1} for the Fe—NO stretch were reported for this complex. This N—O vibrational frequency is in very good agreement with the value of 1386 cm^{-1} calculated for **3a**, which nicely confirms that [Mb—HNO] is, in fact, N-protonated. The Fe—NO stretch of this species is at higher energy than the value of 601 cm^{-1} calculated for **3a**. This shift in energy could be due to the axial N- vs. S-donor ligands in [Mb—HNO] and **3a**, respectively. As shown in Table 2, bottom, the Fe—NO stretch in iron(II)–nitrosyls also shows a distinct shift to lower energy in the presence of an axial thiolate donor compared to the complex with axial imidazole ligation.²⁶

The N- and O-protonated tautomers **3a** and **3b** also strongly differ with respect to their relative energies. As shown in Table 3, N-protonation of **2** leads to a gain of 47 kcal/mol in terms of free energy (including solvation effects), which corresponds to a calculated pK_A of 34. On the other hand, O-protonation only leads to a gain of free energy of 20 kcal/mol ($\text{pK}_A \sim 15$). Hence, N-

protonation is strongly favoured over O-protonation in agreement with the experimental observation that [Mb—HNO] is also N-protonated. This result is further confirmed by calculated energies from an earlier DFT study.^{21a} At this point it should be mentioned that the absolute values of the obtained free energies are probably overestimated. This can be seen from the pK_A of free HNO, which is calculated to be 23.5 compared to an experimental value of only 11.4. Nevertheless, as observed in many cases of pK_A calculations, trends are usually reproduced very well. Hence, the calculated pK_A values of **3a** and **3b** relative to that of HNO show that (a) coordination of HNO to Fe(II) increases the pK_A value of this species, and (b) that O-protonation is clearly less favourable.

Besides the two singly protonated tautomers **3a** and **3b**, intermediate *I* could also correspond to the doubly protonated intermediate $[\text{Fe}(\text{P})(\text{CH}_3\text{S})(\text{NHOH})]$ (**4**) as proposed by Daiber et al.⁹ Total free energy calculations show that **4** is, in fact, 8.6 kcal/mol lower in energy than **3a** in agreement with this idea. The predicted

vibrational properties of **4** show a weak N—O bond with $\nu(\text{N—O})$ at 952 cm^{-1} similar to **3b** and, importantly, a predicted Fe—N stretch (mixed with Fe—N—H bends, cf. Table 2) at 609 cm^{-1} similar to **3a**. Therefore, considering the experimental Fe—N stretch in *I* observed at 596 cm^{-1} , these results are not conclusive whether this species is singly N- or doubly N,O-protonated. This could easily be decided from the N—O stretch, which, however, has not been observed experimentally. The optimized structure of **4** is shown in Figure 3. In this case, the NHOH ligand is planar, which means that both protons are bound to the former π_{h}^* orbital. This leads to a further decrease of this orbital in energy and, hence, a decrease of the strength of the Fe—N σ bond in **4**. The corresponding bonding combination, $\pi_{\text{h}}^* - d_{z^2}$ ($\langle 95 \rangle$), has 49% π_{h}^* and only 10% d_{z^2} character in agreement with this analysis (cf. Fig. 3). On the other hand, the binding of the second proton also has a profound effect on the π_{v}^* orbital, which decreases in energy and now becomes occupied. This is evident from the corresponding antibonding combination, $d_{yz} - \pi_{\text{v}}^*$ ($\langle 115 \rangle$) (cf. Fig. 3), which has 34% π_{v}^* and 40% d_{yz} character. In summary, the electronic structure of **4** is somewhat similar to **3b**, but the Fe—N σ bond is distinctively weakened in the doubly protonated species in agreement with the lower Fe—N force constant in this case (cf. Table 2). In addition, the π_{v}^* orbital now becomes occupied, which formally leads to a Fe(IV)—NHOH[−] electronic structure for complex **4**, although one has to keep in mind that the Fe—N bond is very covalent. Therefore, based on the spectroscopic and mechanistic significance, we propose that intermediate *I* is a doubly protonated Fe(IV)—NHOH[−] species.

In conclusion, the above analysis shows that the Fe(II)—NO/(−) species in myoglobin corresponds to a singly N-protonated complex, whereas the corresponding intermediate *I* in P450nor is doubly N,O-protonated. Therefore, we propose that the actual role of the axial thiolate ligand in P450nor is the stabilization of the formed Fe(IV)—NHOH[−] intermediate by strong donation of the thiolate to the iron center thus stabilizing the formal Fe(IV) oxidation state. In other words, the thiolate enables the double protonation of the Fe(II)—NO/(−) intermediate by lowering its pK_B values. As demonstrated in the next section, this intermediate leads to a clean formation of N₂O when reacted with one molecule of NO, thus avoiding the formation of potentially toxic NO_x species.

Molecular Mechanism of P450nor

From the work of Shoun and coworkers^{6,7} it is known that P450nor is catalytically active in its ferric oxidation state, which binds one molecule of NO. The next step is the reaction with NADH leading to the formation of intermediate *I* as presented in Scheme 1. As shown by our analysis presented above and kinetic studies by Daiber et al.,⁹ this step corresponds to a *direct hydride transfer* initially generating an Fe(II)—HNO species as shown in Scheme 3. This species is N-protonated, which is energetically strongly favoured over the O-protonated form. Hence, in the following mechanistic discussion all free energies will be related to this species **3a**, which is set to 0.0 kcal/mol in Scheme 3. This species is subsequently protonated leading to the fast formation of the corresponding Fe—NHOH species **4**, which therefore can be identified with intermediate *I* as observed spectroscopically in agreement with the proposal of Daiber et al.⁹ It is stabilized by approx-

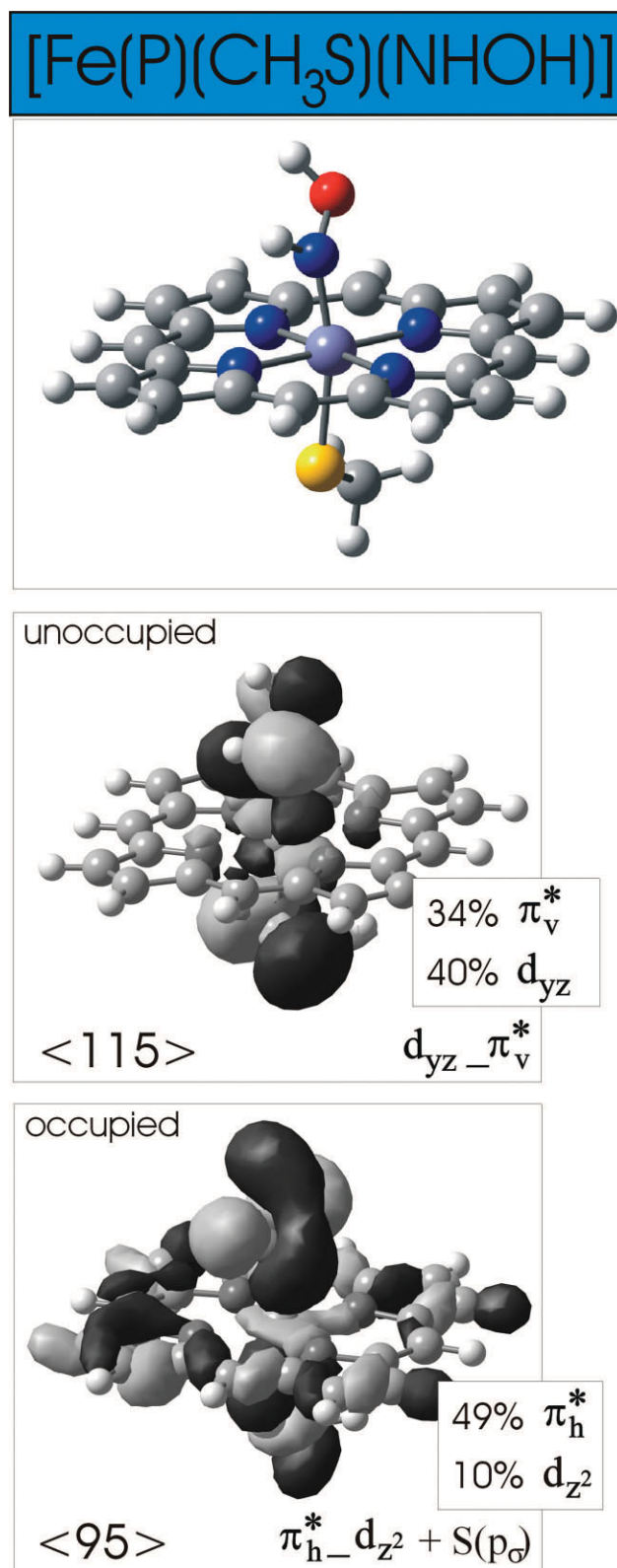
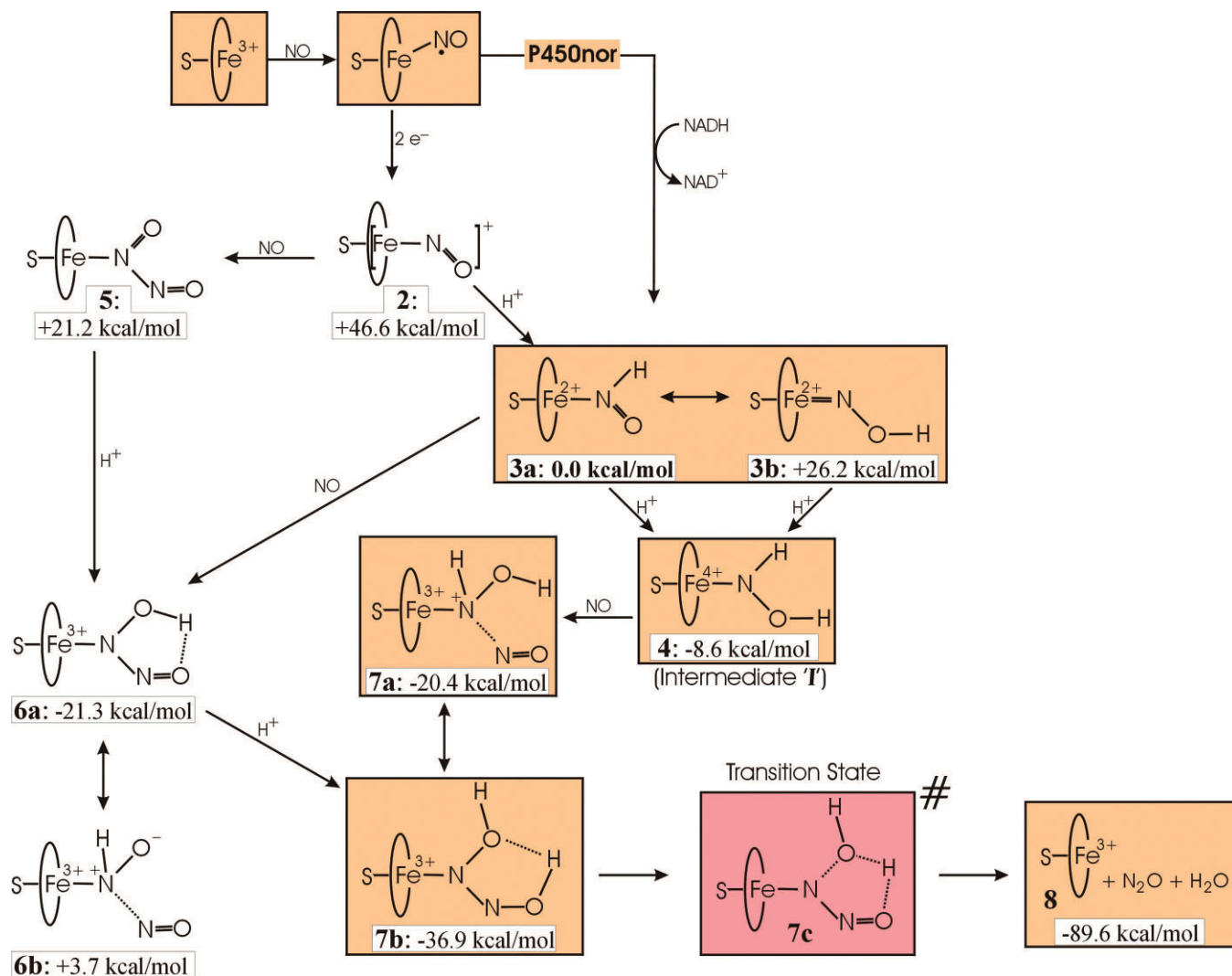


Figure 3. Optimized geometry (top) and contour plots of important molecular orbitals of [Fe(P)(CH₃S)(NHOH)] (**4**, *S* = 0) calculated with BP86/TZVP. Orbital decompositions are also included.



Scheme 3.

imately 9 kcal/mol relative to **3a**. The electronic structure of this intermediate is very interesting as described above and formally corresponds to an Fe(IV)-NHOH^- complex. Intermediate **4** could be envisioned to react with NO by an outer sphere electron transfer to the iron center creating Fe(III) and NO^+ , where the NO^+ then subsequently or concertedly attacks the lone pair on the nitrogen of the coordinated NHOH ligand. This process corresponds to a spin-allowed reaction. Importantly, the calculations show that the N-protonated $\text{Fe(III)-N}_2\text{O}_2\text{H}_2$ species formed this way is unstable and easily loses the generated $\text{N}_2\text{O}_2\text{H}_2$ ligand. However, proton transfer from the nitrogen atom of the former NHOH ligand to the oxygen of the incoming NO molecule leads to the generation of the stable O,O'-protonated $\text{Fe(III)-N}_2\text{O}_2\text{H}_2$ complex **7b** as shown in Scheme 3. The formation of **7b** from **4** and NO is highly exergonic by about 28 kcal/mol. This is a very important result, because it shows that the attack of NO on intermediate **4** is a three step process including (a) electron transfer to the formal iron(IV), (b) attachment of the resulting NO^+ forming

an N—N bond, and (c) simultaneous proton transfer from the N atom of the former NHOH ligand to the O atom of the incoming NO. This mechanism explains why the anticipated radical reaction of NO with the coordinated HNO species is efficiently catalyzed by the heme center. Based on this reaction sequence, the N-protonated $\text{Fe(III)-N}_2\text{O}_2\text{H}_2$ species is an intermediate on the reaction coordinate leading to **7b**. To estimate the energy of this species, we have optimized its structure using a fixed Fe—N distance. This leads to intermediate **7a**, where NO is loosely attached to the NHOH ligand. The energy of this species is -12 kcal/mol relative to **4** and NO. Therefore, the subsequent proton transfer generating the tautomer **7b** is highly exergonic by -16 kcal/mol, and hence, should occur extremely fast in the actual enzymatic reaction. This ensures that the formed $\text{N}_2\text{O}_2\text{H}_2$ ligand stays bound to the iron(III) center. In addition, the structure of **7b** as shown in Scheme 3 is perfectly set up for proton transfer leading to the tautomer **7c**, where the oxygen of the former NHOH ligand is doubly protonated. Upon geometry optimization, this species

relaxes back to **7b**, which therefore corresponds to the most stable tautomer of the Fe(III)—N₂O₂H₂ complex. However, fixing the two O—H bonds in **7c** at 0.97 Å and geometry optimization leads to the spontaneous cleavage of the N—OH₂ bond and the formation of a five-coordinate Fe(III) complex, nitrous oxide and water. This reaction is highly exergonic, which shows that **7c** must correspond to a transition state, because this species is higher in energy than both the reactant **7b** that it is formed from, and the products obtained after its decomposition. We therefore tried to optimize the structure of this transition state, but these calculations were not successful. To estimate the energy for proton transfer leading from **7b** to **7c**, a geometry optimization was performed where both O—H and the N—O bond distances were fixed at 0.97 and 1.41 Å, respectively. As shown in Table 3, this structure is 35 kcal/mol higher in energy than **7b**. This indicates that the transition state must have a significantly elongated N—O bond, which would lead to a substantial lowering of the barrier as evident from the strong thermodynamic driving force of the reaction. Because it is known from experiments that the five-coordinate ferric heme in P450nor is high spin, we therefore used the corresponding high-spin complex **8** to calculate the free energy for the reaction leading from **7b** to **8**, nitrous oxide and water. *This process is exergonic by about 53 kcal/mol, and therefore, thermodynamically highly favorable.* Note that the decay of **7c** initially generates an Fe(III)—N₂O complex, which loses the N₂O ligand in the calculations regardless whether the high-spin or low-spin state of the ferric heme is considered. This dissociation of nitrous oxide closes the catalytic cycle.

In model complex studies using organic solvents, Fe(II)—NO/(–) species could also potentially be generated in a proton-free environment. To investigate whether these intermediates would react with NO, we have also calculated the corresponding reaction energy. As shown in Scheme 3, this process leading from **2** to the Fe—N₂O₂ intermediate **5** is strongly exergonic by about 25 kcal/mol, and hence, this reaction should proceed smoothly. In addition, **5** is almost as basic as **2**, which indicates that this species could be doubly protonated upon addition of acid leading to **7b**, which then follows the reaction mechanism of P450nor as described above. This sequence certainly requires a protected binding site for the intermediate as present in the protein to exclude crossreactions of different species in solution or disproportionation reactions, etc.

In two very recent studies, alternative reaction mechanisms for P450nor have been also published based on DFT calculations.^{21c,d} Importantly, Vincent et al.^{21c} also concluded that intermediate *I* of P450nor corresponds to the doubly protonated species **4** as presented here, although this work does not explicitly consider the energies of the different protonation steps, which is of key importance as we have shown above. The further mechanism published in this article then differs from our results. This is due to the fact that upon reaction of **4** with NO, the initially formed, N-protonated species **7a** does lead to loss of N₂O₂H₂ from iron as discussed above. Because Vincent et al. did not consider the energetically favourable tautomer **7b**, which contains a stable Fe—N₂O₂H₂ bond, their further mechanism invokes decomposition of free N₂O₂H₂. However, we think that the tautomer **7b** is formed instantaneously from **7a** due to the strong thermodynamic driving force, and that a mechanism considering free N₂O₂H₂ is therefore

not valid. As presented above, the iron center is actually assisting in the decomposition of the coordinated N₂O₂H₂ in **7b** by fixing the structure in a conformation that is ideally set up for proton transfer leading to the transition state **7c**. In a recent DFT study by Tsukamoto et al.,^{27d} a completely different reaction mechanism is promoted where the ferric–heme NO adduct is only reduced by one electron by NADH, and the NO then dissociates from the generated ferrous heme. In the next step, a second electron transfer occurs from the NADH⁺ radical to free NO generating free NO[–], which then reacts with NAD⁺. Considering the known properties of ferric and ferrous heme nitrosyls,^{2h} this scenario is very unlikely. First, NO is bound very strongly to ferrous heme nitrosyls, and hence, a fast dissociation of NO from the heme is unlikely. Vice versa, it can be envisioned that the two-electron reduction by NADH is actually performed to *avoid* the ferrous nitrosyl complex. Second, this mechanism cannot explain the experimentally observed properties of intermediate *I*, which contains a bound NO ligand but is clearly further reduced compared to a corresponding ferrous complex (cf. Introduction). This latter mechanism is therefore highly unrealistic.

Conclusions

The main conclusions that are drawn from the calculations presented in this work are:

1. the one-electron reduced ferrous nitrosyl species Fe(II)—NO/(–) can principally exist in the two spin states $S = 0$ and $S = 1$, which are isoenergetic in the calculations for N-donor *trans* ligands, whereas thiolate leads to a slight preference for the $S = 1$ state. So far, experimental evidence is only available for the $S = 0$ case;
2. the $S = 0$ ground state of Fe(II)—NO/(–) has an electronic structure that is intermediate between Fe(II)—NO[–] and Fe(I)—NO. The effect of an axial thiolate ligand on the electronic structure is marginal. Importantly, this species is not part of the catalytic cycle of P450nor;
3. this is in contrast to the ferrous Fe(II)—NO complexes, where the axial thiolate has a profound effect on the electronic structure leading to an admixture of ~20% Fe(III)—NO[–] character into the ground state wavefunction;
4. the Mb–HNO adduct prepared by Farmer and coworkers corresponds to the N-protonated Fe(II)—NHO tautomer, which is energetically strongly preferred over the O-protonated form;
5. in contrast, intermediate *I* of P450nor is doubly protonated and formally corresponds to an Fe(IV)—NHOH[–] complex. This species is perfectly set up for reaction with a second molecule of NO;
6. the role of the thiolate is then to stabilize the Fe(IV)—NHOH[–] species and to enable the double protonation of the reduced NO ligand in P450nor;
7. the Fe(IV)—NHOH[–] intermediate reacts with nitric oxide by initial electron transfer from NO to Fe(IV) followed by addition of NO⁺ to the NHOH ligand forming an N—N bond. This process is accompanied by an intramolecular proton transfer. This reaction sequence ensures that nitrous oxide is the product of catalysis, and that no other NO_x species is formed;

8. the obtained Fe—N₂O₂H₂ intermediate is quite stable and corresponds to an Fe(III)—N(OH)(NOH) species. The doubly O-protonated tautomer Fe(III)—N(OH₂)(NO) is energetically unfavorable, but corresponds to the catalytically productive species that spontaneously decomposes to N₂O and water in a highly exergonic process;
9. this way, the enzyme produces dimerized HNO *under controlled conditions*, which, in its free form, also decomposes to N₂O and H₂O (see Introduction);
10. electrocatalytic work by Farmer et al.¹⁶ shows that Mb forms hydroxylamine and ammonia from nitrite reduction, whereas P450 CYP119 is less reactive, but more selectively produces N₂O. One possible explanation for this difference is that in Mb, the N-protonated intermediate Fe(II)—NHO is catalytically active, and that this is the route leading to NH₂OH by additional proton and electron transfer, whereas in P450nor, the corresponding doubly-protonated species is the reactive intermediate leading to N₂O formation.

Supporting Information

MO diagrams and contour plots of **1** and **2** and tables with charge decompositions of important molecular orbitals of these species; tables with cartesian coordinates of the optimized structures of 1–7 are available from the Supporting Information.

References

1. (a) McCleverty, J. A. *Chem Rev* 2004, 104, 403; (b) *J Inorg Biochem* 2005, 99, issues 1 and 4; (c) *Chem Rev* 2002, 102, issue 4.
2. (a) Moncada, S.; Palmer, R. M.; Higgs, E. A. *Pharmacol Rev* 1991, 43, 109; (b) Snyder, S. H. *Science* 1992, 257, 494; (c) Culotta, E.; Koshland, D. E. *Science* 1992, 258, 1862; (d) Butler, A. R.; Williams, D. L. H. *Chem Soc Rev* 1993, 233; (e) Bredt, D. S.; Snyder, S. H. *Annu Rev Biochem* 1994, 63, 175; (f) Lancaster, J. R., Jr. In: *Encyclopedia of Inorganic Chemistry*; Bruce, R. B., Ed.; Wiley: Chichester, 1994; (g) Feelisch, M.; Stamler, J. S., Eds.; *Methods in Nitric Oxide Research*; Wiley: Chichester, 1996; (h) Cooper, C. E. *Biochim Biophys Acta* 1999, 1411, 290.
3. (a) Ferguson, S. J. *Curr Opin Chem Biol* 1998, 2, 182; (b) Richardson, D. J.; Watmough, N. J. *Curr Opin Chem Biol* 1999, 3, 207; (c) Moura, I.; Moura, J. J. G. *Curr Opin Chem Biol* 2001, 5, 168.
4. (a) Janick, P. A.; Rueger, D. C.; Krueger, R. J.; Barber, M. J.; Siegel, L. M. *Biochemistry* 1983, 22, 396; (b) Fry, I. V.; Cammack, R.; Huckleby, D. P.; Hewitt, E. J. *FEBS Lett* 1980, 111, 377; (c) Christner, J. A.; Janick, P. A.; Siegel, L. M.; Münck, E. *J Biol Chem* 1983, 258, 11157; (d) Lancaster, J. R.; Vega, J. M.; Kamin, H.; Orme-Johnson, N. R.; Orme-Johnson, W. H.; Krueger, R. J.; Siegel, L. M. *J Biol Chem* 1979, 254, 1268; (e) *Handbook of Metalloproteins*; Wiley: Chichester, 2001, vol. 1.
5. (a) Ferguson, S. J. *Curr Opin Chem Biol* 1998, 2, 182; (b) Richardson, D. J.; Watmough, N. J. *Curr Opin Chem Biol* 1999, 3, 207; (c) Moura, I.; Moura, J. J. G. *Curr Opin Chem Biol* 2001, 5, 168.
6. (a) Nakahara, K.; Tanimoto, T.; Hatano, K.; Usuda, K. Shoun, H. *J Biol Chem* 1993, 268, 8350; (b) Obayashi, E.; Tsukamoto, K.; Adachi, S.-I.; Takahashi, S.; Nomura, M.; Iizuka, T.; Shoun, H.; Shiro, Y. *J Am Chem Soc* 1997, 119, 7807; (c) Park, S.-Y.; Shimizu, H.; Adachi, S.-I.; Nakagawa, A.; Tanaka, I.; Nakahara, K.; Shoun, H.; Obayashi, E.; Nakamura, H.; Iizuka, T.; Shiro, Y. *Nat Struct Biol* 1997, 4, 827; (d) Shimizu, H.; Park, S.-Y.; Gomi, Y.; Arakawa, H.; Nakamura, H.; Adachi, S.-I.; Obayashi, E.; Iizuka, T.; Shoun, H.; Shiro, Y. *J Biol Chem* 2000, 275, 4816.
7. (a) Shiro, Y.; Fujii, M.; Iizuka, T.; Adachi, S.-I.; Tsukamoto, K.; Nakahara, K.; Shoun, H. *J Biol Chem* 1995, 270, 1617; (b) Obayashi, E.; Takahashi, S.; Shiro, Y. *J Am Chem Soc* 1998, 120, 12964.
8. Farmer, P. J.; Sulc, F. *J Inorg Biochem* 2005, 99, 166.
9. Daiber, A.; Nauser, T.; Takaya, N.; Kudo, P.; Weber, P.; Hultschig, C.; Shoun, H.; Ullrich, V. *J Inorg Biol Chem* 2002, 88, 343.
10. (a) Olson, L. W.; Schaeper, D.; Lançon, D.; Kadish, K. M. *J Am Chem Soc* 1982, 104, 2042; (b) Lançon, D.; Kadish, K. M. *J Am Chem Soc* 1983, 105, 5610; (c) Fujita, E.; Fajer, J. *J Am Chem Soc* 1983, 105, 6743.
11. (a) Choi, I. K.; Ryan, M. D. *Inorg Chim Acta* 1988, 153, 25; (b) Choi, I. K.; Liu, Y.; Feng, D.; Paeng, K. J.; Ryan, M. D. *Inorg Chem* 1991, 30, 1832; (c) Choi, I. K.; Ryan, M. D. *New J Chem* 1992, 16, 591; (d) Liu, Y.; Ryan, M. D. *Inorg Chim Acta* 1994, 225, 57; (e) Liu, Y.; DeSilva, C.; Ryan, M. D. *Inorg Chim Acta* 1997, 258, 247.
12. Wyllie, G. R. A.; Schulz, C. E.; Scheidt, W. R. *Inorg Chem* 2003, 42, 5722.
13. (a) Praneeth, V. K. K.; Neese, F.; Lehnert, N. *Inorg Chem* 2005, 44, 2570; (b) Praneeth, V. K. K.; Näther, C.; Peters, G.; Lehnert, N. *Inorg Chem* 2006, 45, in press.
14. Liu, Y.; Ryan, M. D. *J Electroanal Chem* 1994, 368, 209.
15. (a) Lin, R.; Farmer, P. J. *J Am Chem Soc* 2000, 122, 2393; (b) Sulc, F.; Immoos, C. E.; Pervitsky, D.; Farmer, P. J. *J Am Chem Soc* 2004, 126, 1096.
16. (a) Lin, R.; Bayachou, M.; Greaves, J.; Farmer, P. J. *J Am Chem Soc* 1997, 119, 12689; (b) Immoos, C. E.; Chou, J.; Bayachou, M.; Blair, E.; Farmer, P. J. *J Am Chem Soc* 2004, 126, 4934.
17. (a) Stamler, J. S.; Singel, D. J.; Loscalzo, J. *Science* 1992, 258, 1898; (b) Bartberger, M. D.; Liu, W.; Ford, E.; Miranda, K. M.; Switzer, C.; Fukuto, J. M.; Farmer, P. J.; Wink, D. A.; Houk, K. N. *Proc Natl Acad Sci USA* 2002, 99, 10958; (c) Miranda, K. M.; Paolucci, N.; Katori, T.; Thomas, D. D.; Ford, E.; Bartberger, M. D.; Espey, M. G.; Kass, D. A.; Feelisch, M.; Fukuto, J. M.; Wink, D. A. *Proc Natl Acad Sci USA* 2003, 100, 9196.
18. Rusche, K. M.; Spiering, M. M.; Marletta, M. A. *Biochemistry* 1998, 37, 15503.
19. (a) Shafirovich, V.; Lymar, S. V. *Proc Natl Acad Sci USA* 2002, 99, 7340; (b) Lymar, S. V.; Shafirovich, V.; Poskrebyshev, G. A. *Inorg Chem* 2005, 44, 5212.
20. (a) Bazylnski, D. A.; Hollocher, T. C. *J Am Chem Soc* 1985, 107, 7982; (b) Bari, S. E.; Marti, M. A.; Amorebieta, V. T.; Estrin, D. A.; Doctorovich, F. *J Am Chem Soc* 2003, 125, 15272.
21. (a) Silaghi-Dumitrescu, R. *Eur J Inorg Chem* 2003, 1048; (b) Harris, D. L. *Int J Quantum Chem* 2002, 88, 183; (c) Vincent, M. A.; Hillier, I. H.; Ge, J. *Chem Phys Lett* 2005, 407, 333; (d) Tsukamoto, K.; Watanabe, T.; Nagashima, U.; Akiyama, Y. *J Mol Struct (Theochem)* 2005, 732, 87.
22. Frisch, M. J.; Trucks, G. W.; Schlegel, H. B.; Scuseria, G. E.; Robb, M. A.; Cheeseman, J. R.; Zakrzewski, V. G.; Montgomery, J. A., Jr.; Stratmann, R. E.; Burant, J. C.; Dapprich, S.; Millam, J. M.; Daniels, A. D.; Kudin, K. N.; Strain, M. C.; Farkas, O.; Tomasi, J.; Barone, V.; Cossi, M.; Cammi, R.; Mennucci, B.; Pomelli, C.; Adamo, C.; Clifford, S.; Ochterski, J.; Petersson, G. A.; Ayala, P. Y.; Cui, Q.; Morokuma, K.; Salvador, P.; Dannenberg, J. J.; Malick, D. K.; Rabuck, A. D.; Raghavachari, K.; Foresman, J. B.; Cioslowski, J.; Ortiz, J. V.; Baboul, A. G.; Stefanov, B. B.; Liu, G.; Liashenko, A.; Piskorz, P.; Komaromi, I.; Gomperts, R.; Martin, R. L.; Fox, D. J.; Keith, T.; Al-Laham, M. A.; Peng, C. Y.; Nanayakkara, A.; Challacombe, M.; Gill, P. M. W.; Johnson, B.; Chen, W.; Wong, M. W.; Andres, J. L.; Gonzalez, C.; Head-Gordon, M.; Replogle, E. S.; Pople, J. A. *Gaussian 98 Rev. A.11*; Gaussian, Inc.: Pittsburgh, PA, 2001.

23. Allouche, A.; Pourcin, J. *Spectrochim Acta* 1993, 49A, 571.
24. Zilberberg, I.; Ruzankin, S. Ph. Quantum Chemistry division; Boreskov Institute of Catalysis: Novosibirsk 630090, Russian Federation.
25. Serres, R. G.; Grapperhaus, C. A.; Bothe, E.; Bill, E.; Weyhermüller, T.; Neese, F.; Wieghardt, K. *J Am Chem Soc* 2004, 126, 5138.
26. Praneeth, V. K. K.; Haupt, E.; Lehnert, N. *J Inorg Biochem* 2005, 99, 940; Erratum: *J Inorg Biochem* 2005, 99, 1744.
27. (a) Zilberberg, I.; Ruzankin, S. Ph.; Malykhin, S.; Zhidomirov, G. M. *Chem Phys Lett* 2004, 394, 392; (b) Zilberberg, I.; Ruzankin, S. Ph. *Chem Phys Lett* 2004, 394, 165.
28. (a) Hu, S.; Kincaid, J. R. *J Am Chem Soc* 1991, 113, 9760; (b) Hu, S.; Kincaid, J. R. *J Biol Chem* 1993, 268, 6189.
29. Scheidt, W. R.; Frisse, M. E. *J Am Chem Soc* 1975, 97, 17.
30. Tawa, G. J.; Topol, I. A.; Burt, S. K.; Caldwell, R. A.; Rashin, A. A. *J Chem Phys* 1998, 109, 4852.

7.4 Quantum Chemistry-Based Analysis of the Vibrational Spectra of Five-Coordinate Metalloporphyrins [M(TPP)Cl]

Florian Paulat, V. K. K. Praneeth, Christian Näther, and Nicolai Lehnert*

Published in: *Inorg. Chem.* **2006**, *45*, 2835-2856.

Quantum Chemistry-Based Analysis of the Vibrational Spectra of Five-Coordinate Metalloporphyrins [M(TPP)Cl]

Florian Paulat, V. K. K. Praneeth, Christian Näther, and Nicolai Lehnert*

Institut für Anorganische Chemie, Christian-Albrechts-Universität Kiel, Olshausenstrasse 40, D-24098 Kiel, Germany

Received June 30, 2005

Vibrational properties of the five-coordinate porphyrin complexes [M(TPP)(Cl)] (M = Fe, Mn, Co) are analyzed in detail. For [Fe(TPP)(Cl)] (**1**), a complete vibrational data set is obtained, including nonresonance (NR) Raman, and resonance Raman (RR) spectra at multiple excitation wavelengths as well as IR spectra. These data are completely assigned using density functional (DFT) calculations and polarization measurements. Compared to earlier works, a number of bands are reassigned in this one. These include the important, structure-sensitive band at 390 cm⁻¹, which is reassigned here to the totally symmetric $\nu_{\text{breathing}}(\text{Fe-N})$ vibration for complex **1**. This is in agreement with the assignments for [Ni(TPP)]. In general, the assignments are on the basis of an idealized [M(TPP)]⁺ core with D_{4h} symmetry. In this Work, small deviations from D_{4h} are observed in the vibrational spectra and analyzed in detail. On the basis of the assignments of the vibrational spectra of **1**, [Mn(TPP)(Cl)] (**2**), and diamagnetic [Co(TPP)(Cl)] (**3**), eight metal-sensitive bands are identified. Two of them correspond to the $\nu(\text{M-N})$ stretching modes with B_{1g} and E_g symmetries and are assigned here for the first time. The shifts of the metal sensitive modes are interpreted on the basis of differences in the porphyrin C–C, C–N, and M–N distances. Besides the porphyrin core vibrations, the M–Cl stretching modes also show strong metal sensitivity. The strength of the M–Cl bond in **1–3** is further investigated. From normal coordinate analysis (NCA), force constants of 1.796 (Fe), 0.932 (Mn), and 1.717 (Co) mdyne/Å are obtained for **1–3**, respectively. The weakness of the Mn–Cl bond is attributed to the fact that it only corresponds to half a σ bond. Finally, RR spectroscopy is used to gain detailed insight into the nature of the electronically excited states. This relates to the mechanism of resonance enhancement and the actual nature of the enhanced vibrations. It is of importance that anomalous polarized bands (A_{2g} vibrations), which are diagnostic for vibronic mixing, are especially useful for this purpose.

Introduction

Vibrational spectroscopy is a very valuable method that is used to gain insight into the electronic structures of metalloporphyrins. Especially, heme proteins that contain iron porphyrins as prosthetic groups have been studied in detail, and information about the properties of their heme cofactors have been obtained because of the sensitivity of the vibrational frequencies to the changes in oxidation state, coordination number, and spin state.^{1,2} Hemes occur as active sites in many different proteins and have been characterized by all types of spectroscopic methods. Among these,

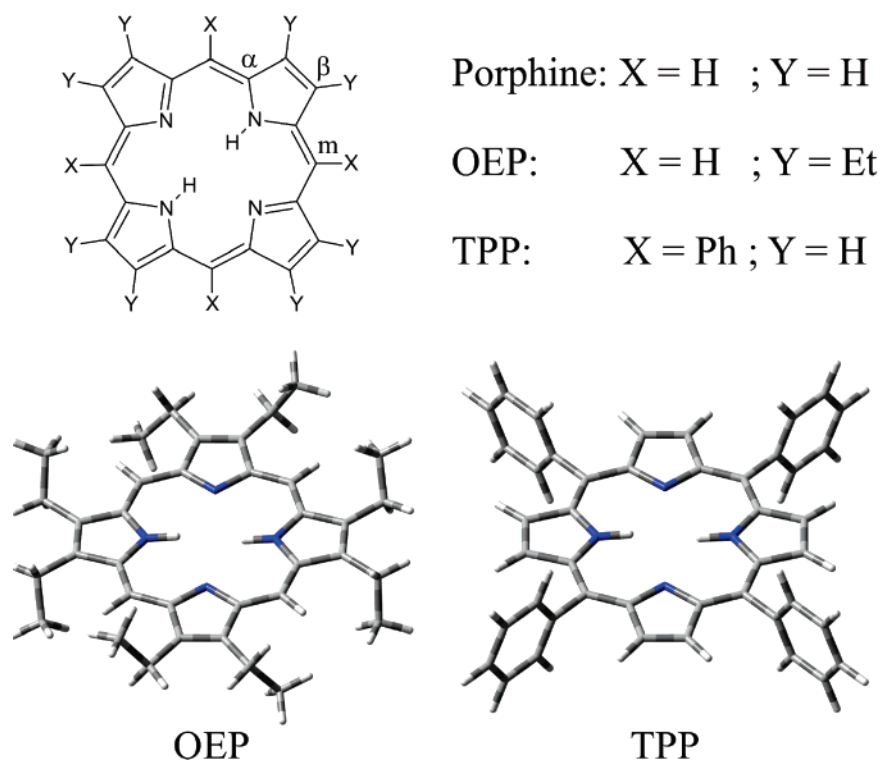
resonance Raman (RR) spectroscopy has always played a key role. RR spectroscopy selectively enhances the vibrational modes of the absorbing chromophore, whereas the remaining vibrational modes in the molecule (protein) are suppressed.^{3–5} In this way, RR spectra of a heme chromophore can be obtained selectively even in a large molecule (protein) where many other vibrations are present. From the vibrational energies as well as the nature of the enhanced modes, information about the geometric and electronic

* To whom correspondence should be addressed. E-mail: nlehnert@ac.uni-kiel.de.

- (1) Spiro, T. G. In *Iron Porphyrins*; Lever, A. B. P., Gray, H. B., Eds.; Addison-Wesley: Reading, MA, 1983; Part 2, pp 89–159.
- (2) Spiro, T. G.; Li, X.-Y. In *Resonance Raman Spectra of Heme and Metalloproteins*; Spiro, T. G., Ed.; Wiley: New York, 1988; pp 1–37.

- (3) Spiro, T. G.; Czernuszewicz, R. S. In *Physical Methods in Bioinorganic Chemistry*; Que, L., Jr., Ed.; University Science Books: Sausalito, CA, 2000; pp 59–120.
- (4) Loehr, T. M. In *Spectroscopic Methods in Bioinorganic Chemistry*; Solomon, E. I., Hodgson, K. O., Eds.; American Chemical Society: Washington, DC, 1998; pp 136–153.
- (5) Czernuszewicz, R. S.; Spiro, T. G. In *Inorganic Electronic Structure and Spectroscopy*; Solomon, E. I., Lever, A. B. P., Eds.; John Wiley & Sons: New York, 1999; Vol. 1, pp 353–441.

Scheme 1



properties of the heme as well as its environment can be obtained.^{1,5} Besides the investigation of metalloporphyrins in biological systems, synthetic porphyrin model complexes have been studied widely to gain insight into the catalytic reactions or functions performed by heme proteins.⁶ In many cases, tetraphenylporphyrin (TPP) and octaethylporphyrin (OEP) ligands have been used for such model systems. Scheme 1 shows the OEP and TPP ligands, which are based on simple porphine P, where the meso (X) and β substituents (Y) are hydrogen atoms. OEP has ethyl groups in the β position ($Y = Et$), whereas TPP has phenyl groups in the meso position ($X = Ph$). The RR spectra of such metalloporphyrin model complexes have been intensely studied, and spectral assignments have been obtained.¹ For the vibrational assignments, four-coordinate Nickel complexes have, in general, been used because they are stable and nonfluorescent. In addition, there are no complications due to axial ligands when using the four-coordinate species. Correspondingly, much effort has been spent to investigate the RR and IR spectra of the Ni(II) complexes [Ni(OEP)] and [Ni(TPP)]. On the basis of multiple isotope substitution, multiple-wavelength RR spectroscopy, and IR measurements, the spectra of [Ni(OEP)] and [Ni(TPP)] have been assigned by different groups. Kitagawa and co-workers assigned most of the infrared and RR in-plane modes of [Ni(OEP)] using variable excitation RR spectra, ¹⁵N and C_m-D isotope shifts, and a normal-coordinate analysis (NCA).^{7,8} In-plane as well

as out-of-plane modes for general metalloporphyrins [M(P)] were calculated by Warshel and Lippicirella⁹ using a semiempirical force field (QCFF/PI). This study provides the first analysis of the out-of-plane vibrations of the porphyrin core. Spiro and co-workers¹⁰ later developed a consistent empirical force field for nickel porphyrins with different substituents, including porphine, OEP, and TPP. The RR spectra of [Ni(TPP)] were completely assigned using pyrrole-¹⁵N₄, pyrrole-*d*₈, ¹³C₄-meso and phenyl-*d*₂₀ isotopomers, and NCA.¹⁰ Other simple [M(TPP)] complexes (M = Cu(II), Zn(II), and Co(II)) were studied by other groups.^{11,12} However, until now, no detailed vibrational assignments of five-coordinate complexes of type [M(P)(X)] existed.

In contrast to the RR spectra, the IR spectra of TPP complexes remained unassigned for a long time because of their complexity. The first complete assignment of an infrared spectrum of a TPP complex was performed by Rush III et al.¹³ in 2000 for [Ni(TPP)] using DFT-SQM calculations. RR intensities were also calculated using the semiempirical INDO method, which led to the reassignment of several RR bands. Hence, these new assignments are on the basis of quantum chemical calculations, which only became available

(6) Walker, F. A. In *Encyclopedia of Inorganic Chemistry*; King, R. B., Ed.; John Wiley & Sons: New York, 1994; Vol. 4, pp 1785–1846.
 (7) Kitagawa, T.; Abe, M.; Ogoshi, H. *J. Chem. Phys.* **1978**, *69*, 4516–4525.
 (8) Abe, M.; Kitagawa, T.; Kyogoku, Y. *J. Chem. Phys.* **1978**, *69*, 4526–4534.

(9) Warshel, A.; Lippicirella, A. *J. Am. Chem. Soc.* **1981**, *103*, 4664–4673.
 (10) Li, X.-Y.; Czernuszewicz, R. S.; Kincaid, J. R.; Su, Y. O.; Spiro, T. G. *J. Phys. Chem.* **1990**, *94*, 31–47. (b) Li, X.-Y.; Czernuszewicz, R. S.; Kincaid, J. R.; Stein, P.; Spiro, T. G. *J. Phys. Chem.* **1990**, *94*, 47–61. (c) Li, X.-Y.; Czernuszewicz, R. S.; Kincaid, J. R.; Spiro, T. G. *J. Am. Chem. Soc.* **1989**, *111*, 7012–7023.
 (11) Atamian, M.; Donohoe, R. J.; Lindsey, J. S.; Bocian, D. F. *J. Phys. Chem.* **1989**, *93*, 2236–2243.
 (12) Kozuka, M.; Iwaizumi, M. *Bull. Chem. Soc. Jpn.* **1983**, *56*, 3165–3166.
 (13) Rush, T. S., III; Kozlowski, P. M.; Piffat, C. A.; Kumble, R.; Zgierski, M. Z.; Spiro, T. G. *J. Phys. Chem. B* **2000**, *104*, 5020–5034.

recently for the routine treatment of large molecules such as [Ni(TPP)]. These theoretical methods provide a new tool to researchers that enables them to analyze the missing puzzle pieces of the vibrational assignments of porphyrin complexes, as will be further demonstrated in this study.

Besides the detailed assignments of nickel porphyrin complexes including [Ni(TPP)],^{10,14,15} the Spiro group has also analyzed the effects of oxidation- and spin-state changes on the RR spectra of heme proteins.^{15b,d-f,42,44} It was concluded that the oxidation-state sensitivity largely depends on the back-bonding between the metal and the porphyrin ring. In the case of iron, back-bonding is greatly reduced for Fe(III) compared to Fe(II) because of a lowering in energy of the d orbitals, which induces shifts in certain porphyrin vibrations. In agreement with this analysis, axial ligands of increasing π -acceptor strength increase the frequencies of the oxidation-state sensitive bands^{15c} by competing with the porphyrin ring for the iron d_{π} electrons. Correspondingly, using the strong π donor ligand cysteine, these oxidation-state sensitive bands shift to energies below the typical range associated with nonacceptor ligands.¹⁶ Spin-sensitivity, on the other hand, has been attributed to ring conformation.^{15b} Doming of the porphyrin ring occurs as a consequence of out-of-plane displacement of iron,^{15b} which is due to the fact that high-spin iron(II) and iron(III) are too large to fit into the center of the porphyrin ring. In this way, the high-spin state of iron causes doming that then induces band shifts. On the other hand, Spaulding et al.¹⁷ suggested that the core size is the dominant parameter for spin-state sensitivity. Because of the out-of-plane displacement of the iron atom, the pyrrole rings are expected to tilt to maintain the overlap with the metal orbitals. This leads to a lowering of certain vibrational frequencies because of the loss of π conjugation at the methine bridges of the porphyrin ring. Hence, both core expansion and pyrrole tilting are expected to contribute to the lowering of vibrational frequencies, where core expansion is dominant at moderate tilt angles.^{15f} Altogether, five structure sensitive RR signals were described in the literature and designated as bands A–E. These oxidation- and spin-state sensitive bands are also expected to be sensitive to the nature of the metal ion because of the variable occupation and energies of the d orbitals of different metals.¹⁸ Oshio et al.^{18b} observed metal-sensitivity in the IR spectra of [M(TPP)] complexes. The frequencies of

these bands I–III were found to decrease as the metal–porphyrinato nitrogen distances increased (Ni(II) > Co(II) > Cu(II) > Zn(II)).

In this study, density functional theory (DFT) is used to calculate the IR and Raman spectra of the five-coordinate complexes [M(TPP)(Cl)] with M = Fe (**1**), Mn (**2**), and Co (**3**). On the basis of these results, the experimental nonresonance Raman (NR Raman), resonance Raman, and IR spectra of compound **1** are assigned in detail for the first time. The calculated Raman spectra cannot be compared to resonance Raman measurements because of the difference in the selection rules for resonance and nonresonance Raman scattering.¹⁹ Therefore, using an excitation wavelength of 1064 nm, the nonresonance Raman spectra of **1**, including polarized measurements are presented for the first time. Resonance Raman spectra at multiple excitation wavelengths have also been obtained for **1**, which, together with polarized measurements, allow for the assignments of additional bands. Altogether, a complete assignment of all available experimental data has been achieved for compound **1**. These results are then compared to an earlier assignment²⁰ of a few RR bands of **1** in the 1000–1600 cm^{-1} range. Results of Burke et al.,¹⁴ who roughly classified the vibrations of compound **1** on the basis of RR isotope shifts and polarization measurements, are also taken into consideration. The vibrational assignments obtained for **1** are then compared to the assignments of the Raman and IR spectra of **2** and **3** to identify the metal-sensitive bands. Not surprisingly, one of the most metal-sensitive bands in these complexes is the metal–chloride stretching vibration. These are identified in the IR spectra of **1–3**, and the corresponding force constants are determined using the quantum-chemistry centered normal coordinate analysis (QCC–NCA).²¹ Finally, the correlation of our results to the detailed assignments for [Ni(TPP)] is also included.¹³ Going from [Ni(TPP)] to [M(TPP)(Cl)] type complexes adds the complexity of having (a) open shells, (b) larger distortions of the porphyrin ring, and (c) axial ligands. The influence of these electronic and structural differences on the vibrational spectra of metalloporphyrins is analyzed.

Experimental and Computational Procedures

Syntheses. The complexes [Fe(TPP)(Cl)] (**1**) and [Mn(TPP)(Cl)] (**2**) were synthesized using published procedures²² and isolated as microcrystalline solids. Complex [Co(TPP)Cl] (**3**) was synthesized using the procedure by Mahmood et al.²³ Single Crystals of **2** were obtained by slow diffusion of *n*-hexane into a solution of **2** in

- (14) Burke, J. M.; Kincaid, J. R.; Spiro, T. G. *J. Am. Chem. Soc.* **1978**, *100*, 6077–6083. (b) Burke, J. M.; Kincaid, J. R.; Peters, S.; Gagne, R. R.; Collman, J. P.; Spiro, T. G. *J. Am. Chem. Soc.* **1978**, *100*, 6083–6088.
- (15) Spiro, T. G. In *Iron Porphyrins*; Lever, A. B. P., Gray, H. B., Eds.; Addison-Wesley: Reading, MA, 1983; Part 2, pp 89–159. (b) Spiro, T. G.; Streckas, T. C. *J. Am. Chem. Soc.* **1974**, *96*, 338–345. (c) Spiro, T. G.; Streckas, T. C. *Proc. Natl. Acad. Sci. U.S.A.* **1972**, *69*, 2622–2626. (d) Burke, J. M.; Kincaid, J. R.; Peters, S.; Gagne, R. R.; Collman, J. P.; Spiro, T. G. *J. Am. Chem. Soc.* **1978**, *100*, 6083–6088. (e) Spiro, T. G.; Burke, J. M. *J. Am. Chem. Soc.* **1976**, *98*, 5482–5489. (f) Spiro, T. G.; Stong, J. D.; Stein, P. *J. Am. Chem. Soc.* **1979**, *101*, 2648–2655.
- (16) Champion, P. M.; Gunsalus, I. C. *J. Am. Chem. Soc.* **1977**, *99*, 2000–2002. (b) Champion, P. M.; Gunsalus, I. C.; Wagner, G. C. *J. Am. Chem. Soc.* **1978**, *100*, 3743–3751.
- (17) Spaulding, L. D.; Chang, C. C.; Yu, N.-T.; Felton, R. H. *J. Am. Chem. Soc.* **1975**, *97*, 2517–2525.

- (18) Kincaid, J.; Nakamoto, K. *J. Inorg. Nucl. Chem.* **1975**, *37*, 85. (b) Oshio, H.; Ama, T.; Watanabe, T.; Kincaid, J.; Nakamoto, K. *Spectrochim. Acta, Part A* **1984**, *40*, 863–870.
- (19) Tang, J.; Albrecht, A. C. In *Raman Spectroscopy*; Szymanski, H. A., Ed.; Plenum Press: New York, 1970; Vol. 2. (b) Albrecht, A. C. *J. Chem. Phys.* **1961**, *34*, 1476.
- (20) Czermszewicz, R. S.; Macor, K. A.; Li, X.-Y.; Kincaid, J. R.; Spiro, T. G. *J. Am. Chem. Soc.* **1989**, *111*, 3860–3869.
- (21) Lehnert, N.; Tuzek, F. *Inorg. Chem.* **1999**, *38*, 1659–1670. (b) Praneeth, V. K. K.; Näther, C.; Peters, G.; Lehnert, N. *Inorg. Chem.*, in press.
- (22) Adler, A. D.; Longo, F. R.; Kampas, F.; Kim, J. *J. Inorg. Nucl. Chem.* **1970**, *32*, 2443–2445.
- (23) Mahmood, A.; Liu, H.-I.; Jones, J. G.; Edwards, J. O.; Sweigart, D. A. *Inorg. Chem.* **1988**, *27*, 2149–2154.

CHCl₃. The identity of the compounds was established using ¹H NMR and UV–vis absorption spectroscopy and mass spectrometry (for compound **2**).

Crystal Structure Determination. The data were collected using an STOE imaging plate diffraction system (IPDS). The structure was solved with direct methods using SHELXS-97 and was refined against F² using SHELXL-97. All non-H atoms were refined anisotropically, except for some of the chlorine atoms of the disordered chloroform molecule. The H atoms were positioned with idealized geometry and refined using a riding model. The chloroform molecule is disordered and was refined using a split model.

Vibrational Spectroscopy. FT-Raman spectra were recorded on a Bruker IFS 66 interferometer with a Bruker FRA 106 Raman attachment using an Nd:YAG laser for excitation ($\lambda = 1064$ nm). Measurements were performed on pure compounds. The polarized FT-Raman spectra of **1** were measured in CH₂Cl₂. Resolution was set to 2 cm⁻¹. Resonance Raman spectra were measured on a Dilor XY Raman spectrograph with a triple monochromator and a CCD detector. An Ar/Kr mixed-gas laser with a maximum power of 5 W was used for excitation. The spectra were measured on KBr disks cooled to 10 K with a helium cryostat. The spectral band pass was set to 2 cm⁻¹. Middle- and far-infrared spectra (MIR and FIR) were recorded on a Bruker IFS 66v vacuum instrument at room temperature. For the MIR region, KBr disks were used, and the spectra were recorded at a resolution of 1 cm⁻¹. FIR spectra were obtained on PE pellets at a resolution of 2 cm⁻¹.

UV–Vis Spectroscopy. Absorption spectra were recorded in chloroform for **1**, in a 1/1 mixture of butyronitrile and propionitrile for **2**, and in methanol solution for **3** at room temperature using a Varian Cary 5 UV–vis NIR spectrometer. The absorption data were scaled using literature extinction coefficients as indicated in Figure 7.

Density Functional Calculations. DFT calculations using Becke's three parameter hybrid functional with the correlation functional of Lee, Yang, and Parr (B3LYP²⁴) were performed using the program package Gaussian 03.²⁵ The structures of the compounds [Fe(TPP)(Cl)] ($S = 5/2$), [Mn(TPP)(Cl)] ($S = 2$), and [Co(TPP)(Cl)] ($S = 0$) were fully optimized without simplifications using the LanL2DZ basis set. Calculated vibrational frequencies for **1** show that the obtained geometry represents a true minimum because no imaginary frequency is obtained. For compounds **2** and **3**, one imaginary frequency ($<6i$ cm⁻¹) is calculated, which corresponds to the out-of-plane deformation mode of the ruffling type²⁶ (B_{1u}) at low energy. Infrared and Raman intensities were calculated as well. In all calculations, convergence was reached

when the relative change in the density matrix between subsequent iterations was less than 1×10^{-8} . The structures of the models [Fe(P)(Cl)] (P = porphine; **1**, $S = 5/2$), [Mn(P)(Cl)] (**2**, $S = 2$), and [Co(P)(Cl)] (**3**, $S = 0$) have also been fully optimized using B3LYP/LanL2DZ. For these calculations, the TPP ligand has been simplified to porphine (Scheme 1). The illustrations of the local coordinates of bromobenzene (cf. Figure 3) were obtained using the program GaussView.

Normal Coordinate Analysis (NCA). Normal coordinate calculations were performed using the QCPE computer program 576 by M. R. Peterson and D. F. McIntosh. The calculations are on the basis of a general valence force field and the force constants are refined with a nonlinear simplex algorithm. The simplex optimization was used to refine only selected force constants according to the quantum-chemistry centered normal coordinate analysis (QCC–NCA) scheme.²¹ Here, a force field from DFT calculations is used as a starting point to generate initial force constants, and a subset of these is fitted to reproduce the known experimental frequencies. Force constants were obtained from the Gaussian output using a modified version of the program Redong²⁷ (QCPE 628). For the normal coordinate analysis, model complexes **1**–**3** were modified by using a mass of 77 corresponding to a phenyl group for the hydrogens of the meso carbon atoms. This leads to models [Fe(P*)Cl] (**1a**), [Mn(P*)Cl] (**2a**), and [Co(P*)Cl] (**3a**).

Results and Analysis

A. Crystal and DFT-optimized Structures of [Fe(TPP)(Cl)] (1**), [Mn(TPP)(Cl)] (**2**), and [Co(TPP)(Cl)] (**3**).** To calculate the vibrational spectra of **1**–**3**, their geometric structures have to be fully optimized first. In this section, the calculated structures are compared to the experimental ones, and in addition, a new crystal structure of the chloroform solvate of complex **2** is presented. Altogether, satisfactory agreement between the DFT calculations and experiment is obtained. Considering the porphyrin core bond lengths, excellent agreement with experiment is achieved in this study, as shown in Table S6.

A.1. Crystal and DFT Structures of Compound 1. The crystal structure of the tetragonal form of compound **1** has been determined by Hoard et al.²⁸ Later, Scheidt and Finnegan²⁹ obtained the structure of a monoclinic form of this complex. The monoclinic form differs significantly from the tetragonal form. It shows a small C_{4v} doming and a displacement of the iron from the N₄ plane by $\Delta\text{Fe–Ct} = 0.49$ Å. In contrast, the tetragonal form has an almost planar porphyrin core. Because of the conditions applied to the preparation of the compound (solvent used for recrystallization), it can be assumed that our compound corresponded to the tetragonal form. In this structure, the axial Fe–Cl bond is 2.192 Å, the averaged Fe–N distance is 2.049 Å, and the out-of-plane displacement of the iron atom is $\Delta\text{Fe–Ct} = 0.383$ Å. Figure 1A shows the DFT-optimized structure of **1**, which shows an overall good agreement with the crystal structure. In both cases, the porphyrin ring is almost planar

(24) Becke, A. D. *Phys. Rev. A: At., Mol., Opt. Phys.* **1988**, *38*, 3098. (b) Becke, A. D. *J. Chem. Phys.* **1993**, *98*, 1372. (c) Becke, A. D. *J. Chem. Phys.* **1993**, *98*, 5648.

(25) Frisch, M. J.; Trucks, G. W.; Schlegel, H. B.; Scuseria, G. E.; Robb, M. A.; Cheeseman, J. R.; Montgomery, J. A., Jr.; Vreven, T.; Kudin, K. N.; Burant, J. C.; Millam, J. M.; Iyengar, S. S.; Tomasi, J.; Barone, V.; Mennucci, B.; Cossi, M.; Scalmani, G.; Rega, N.; Petersson, G. A.; Nakatsuji, H.; Hada, M.; Ehara, M.; Toyota, K.; Fukuda, R.; Hasegawa, J.; Ishida, M.; Nakajima, T.; Honda, Y.; Kitao, O.; Nakai, H.; Klene, M.; Li, X.; Knox, J. E.; Hratchian, H. P.; Cross, J. B.; Bakken, V.; Adamo, C.; Jaramillo, J.; Gomperts, R.; Stratmann, R. E.; Yazyev, O.; Austin, A. J.; Cammi, R.; Pomelli, C.; Ochterski, J. W.; Ayala, P. Y.; Morokuma, K.; Voth, G. A.; Salvador, P.; Dannenberg, J. J.; Zakrzewski, V. G.; Dapprich, S.; Daniels, A. D.; Strain, M. C.; Farkas, O.; Malick, D. K.; Rabuck, A. D.; Raghavachari, K.; Foresman, J. B.; Ortiz, J. V.; Cui, Q.; Baboul, A. G.; Clifford, S.; Cioslowski, J.; Stefanov, B. B.; Liu, G.; Liashenko, A.; Piskorz, P.; Komaromi, I.; Martin, R. L.; Fox, D. J.; Keith, T.; Al-Laham, M. A.; Peng, C. Y.; Nanayakkara, A.; Challacombe, M.; Gill, P. M. W.; Johnson, B.; Chen, W.; Wong, M. W.; Gonzalez, C.; Pople, J. A. *Gaussian 03*, revision C.02; Gaussian, Inc.: Wallingford, CT, 2004.

(26) Jentzen, W.; Song, X.-Z.; Shelnut, A. *J. Phys. Chem. B* **1997**, *101*, 1684–1699.

(27) Allouche, A.; Pourcin, J. *Spectrochim. Acta, Part A* **1993**, *49*, 571.

(28) Hoard, J. L.; Cohen, G. H.; Glick, M. D. *J. Am. Chem. Soc.* **1967**, *89*, 1992–1996.

(29) Scheidt, W. R.; Finnegan, M. G. *Acta Crystallogr., Sect. C* **1989**, *45*, 1214–1216.

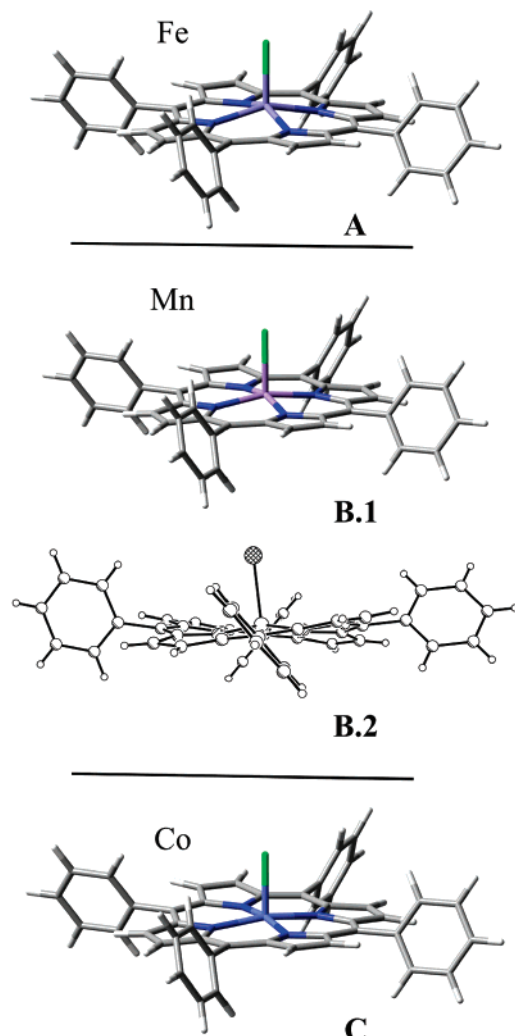


Figure 1. DFT optimized structure of **1** (A); DFT optimized structure of **2** (B.1); the crystal structure of **2** in side view (B.2); and DFT optimized structure of **3** (C).

and the phenyl rings are slightly tilted. The DFT structure also shows a very small amount of saddling of the porphyrin ring, which is not observed experimentally. The calculated Fe–N distance of 2.09 Å and the obtained Fe–Cl distance of 0.45 Å are in very good agreement with experiment. Therefore, a good theoretical description of the [Fe(TPP)]⁺ core of **1** has been obtained. The largest deviation in the calculated structure is observed for the Fe–Cl bond distance of 2.32 Å, which is too long.

A.2. Crystal and DFT Structures of Compound 2. In the new crystal structure presented here, compound **2** crystallizes in the monoclinic space group $P2_1/n$ with four formula units in the unit cell and all atoms located in general positions. The porphyrin moiety is saddled and shows a deviation of the atoms from the best least-squares plane of about 0.29 Å. The manganese atom is located 0.258 Å above the plane formed by the four nitrogen atoms. The averaged manganese nitrogen distance is 2.019 Å, and hence it is between the values for **1** and **3** (vide infra). The obtained manganese chloride distance is 2.389 Å. Note that the crystal structures of **2** as toluene³⁰ or acetone³¹ solvate are very similar. Larger deviations are observed for the solvate's free

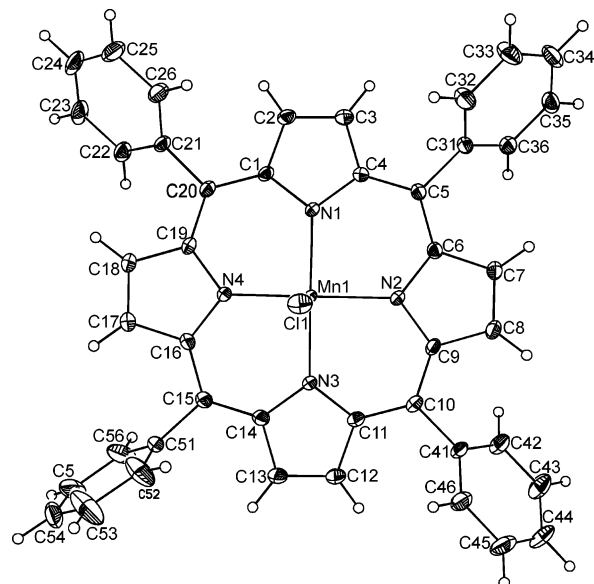


Figure 2. Crystal structure of compound **2** with labeling. Displacement ellipsoids are drawn at the 50% probability level.

crystal structure,³² which shows an almost planar porphyrin core. The DFT-optimized and the crystal structures of **2** (chloroform solvate) are shown in Figures 1B and 2. In contrast to the crystal structure, the optimized structure shows an almost planar porphyrin core with a small amount of saddling present. The averaged manganese nitrogen distance of 2.036 Å and the Mn–Cl distance of 2.420 Å, however, are both in very good agreement with experiment. In addition, the calculated displacement of the manganese atom from the nitrogen N₄ plane of the porphyrin is 0.28 Å and hence, close to the experimental value. Therefore, in this case, the largest deviation of the calculated structure is observed for the ring conformation of the TPP ligand.

A.3. Crystal and DFT Structures of Compound 3. The crystal structure of [Co(TPP)(Cl)] shows a body-centered tetragonal unit cell.³³ The coordination geometry of the Co(III) ion corresponds to a pyramid, where the cobalt atom is displaced from the porphyrin plane by only 0.05 Å. The porphyrin ring itself is almost planar. Bond distances of 1.985 Å for Co–N and 2.145 Å for Co–Cl are observed. The DFT-optimized structure of **2** is shown in Figure 1C. The optimized structure shows an almost planar porphyrin core in agreement with experiment, with a small amount of saddling present. The calculated Co–N distance of 1.99 Å is in excellent agreement with the crystal structure, whereas the out-of-plane displacement of $\Delta\text{Co–Cl} = 0.17$ Å is somewhat overestimated. As in the case of **1**, the largest deviation is observed for the Co–Cl distance, which is calculated to be 2.25 Å.

B. Vibrational Spectra and Assignment of Compound 1.

As mentioned in the Introduction, earlier vibrational

- (30) Armstrong, R. S.; Foran, G. J.; Hambley, T. W. *Acta Crystallogr., Sect. C* **1993**, *49*, 236–238.
 (31) Tulinsky, A.; Chen, B. M. L. *J. Am. Chem. Soc.* **1977**, *99*, 3647–3651.
 (32) Cheng, B.; Scheidt, W. R. *Acta Crystallogr., Sect. C* **1996**, *52*, 361–363.
 (33) Sakurai, T.; Yamamoto, K.; Naito, H.; Nakamoto, N. *Bull. Chem. Soc. Jpn.* **1976**, *49*, 3042–3046.

analyses of [Fe(TPP)(Cl)] were restricted to the RR spectrum obtained for the Soret excitation.²⁰ Additionally, three IR bands of **1** were assigned, which are considered to be structure-sensitive.^{18b} Here, we report the nonresonance Raman (NR Raman) spectrum of **1**, including polarized measurements for the first time. Complete assignments of these data are achieved using DFT calculations. In addition, RR data measured at variable wavelengths including new polarized data are presented and used to assign additional bands. Finally, the IR spectrum of **1** is assigned.

B.1. Classification of the TPP Vibrations Using Group Theory. To assign the vibrational spectra of **1**, an effective D_{4h} symmetry was applied. The analysis of the polarized data (cf. section B.5) shows that this approach is justified even for five-coordinate compounds such as **1–3**. D_{4h} symmetry is obtained for a planar porphyrin core with the metal being located in the plane with no axial ligand present. The phenyl rings are exactly perpendicular to the porphyrin plane. In this D_{4h} model system [M(TPP)] (idealized metalloporphyrin), the planar porphyrin core has 71 in-plane modes:^{10a}

$$\Gamma_{\text{in plane}} = 9A_{1g}(\text{R}) + 8A_{2g}(\text{RR}) + 9B_{1g}(\text{R}) + 9B_{2g}(\text{R}) + 18E_u(\text{IR}) \quad (1)$$

In the NR Raman spectrum, 27 in-plane vibrations are therefore expected, 9 of them polarized (A_{1g}) and 18 of them depolarized (B_{1g} and B_{2g}). The infrared spectrum shows a maximum of 18 modes with E_u symmetry. In addition, the porphyrin core of the D_{4h} model system has 34 out-of-plane vibrations:^{10a}

$$\Gamma_{\text{out of plane}} = 3A_{1u} + 6A_{2u}(\text{IR}) + 4B_{2u} + 5B_{1u} + 8E_g(\text{R}) \quad (2)$$

The eight E_g modes are Raman-active, and the six A_{2u} modes are infrared-active. Therefore, on the basis of a purely statistical consideration, many more in-plane than out-of-plane modes can be expected in the NR Raman and IR spectra of metalloporphyrins. To classify the different porphyrin core vibrations, the local coordinates defined by Li et al.¹⁰ are used (cf. Figures S6 and S7) in the following analysis of these spectra.

Besides the porphyrin core modes, a large number of phenyl vibrations are also present in TPP complexes. Different approaches can be taken in the classification of these vibrations. For example, Stein et al.³⁴ identified several phenyl modes in [(FeTPP)₂O] using biphenyl as the model system.³⁵ To give an intuitive assignment of the phenyl modes of TPP, we use bromobenzene as the model. Table 2 provides a complete list of all normal modes of bromobenzene together with calculated energies and assignments using local coordinates. Figure 3 shows the important phenyl vibrations in bromobenzene that are also observed in the spectra of **1–3**. The TPP ligand itself has four phenyl groups that are bound to the meso carbon atoms of the porphyrin

Table 1. Crystal Data and Results of Structure Refinement for Compound **2**

cmpd	2
chemical formula	C ₄₄ H ₂₈ N ₄ MnCl · CHCl ₃
fw	822.46
$T =$	150 K
$\lambda =$	0.71073
crystal system	monoclinic
space group	$P2_1/n$
$a =$	12.157 (1) Å
$b =$	21.899 (2) Å
$c =$	14.479 (1) Å
$\beta =$	102.05 (1)
$V =$	3769.7 (4) Å ³
Z	4
$D_{\text{calcd}} =$	1.449 g·cm ⁻³
$\mu =$	0.67 mm ⁻¹
$R1^a [I > 2\sigma(I)]$	0.0392
$wR2^b$ [all data]	0.1053

$$^a R1 = \sum ||F_o| - |F_c|| / \sum |F_o|. \quad ^b wR2 = [\sum [w(F_o^2 - F_c^2)^2] / \sum [w(F_o^2)^2]]^{1/2}.$$

core. Hence, for every local phenyl coordinate, there are four symmetry-adapted combinations in TPP. Because the interactions of the local vibrations of different phenyl rings are small, the obtained splittings between the resulting four combinations are also small (usually 5–10 cm⁻¹). Hence, the four resulting symmetry-adapted linear combinations are also designated as a symmetry block because they are close in energy. Because there are four different irreducible representations in C_{2v} (the point group of bromobenzene), four different symmetry blocks exist:

$$\text{out-of-plane: } B_1 \rightarrow B_{1g}(\text{R}) + A_{2g}(\text{RR}) + E_u(\text{IR}) \quad (\pi, \pi', \text{ and } \pi'') \quad (3)$$

$$\text{out-of-plane: } A_2 \rightarrow A_{1u} + B_{2u} + E_g(\text{R}) \quad (\sigma, \sigma', \text{ and } \sigma'') \quad (4)$$

$$\text{in-plane: } B_2 \rightarrow B_{1u} + A_{2u}(\text{IR}) + E_g(\text{R}) \quad (\psi, \psi', \text{ and } \psi'') \quad (5)$$

$$\text{in-plane: } A_1 \rightarrow A_{1g}(\text{R}) + B_{2g}(\text{R}) + E_u(\text{IR}) \quad (\phi, \phi', \text{ and } \phi'') \quad (6)$$

The nomenclature (π , σ , ψ , and ϕ) is taken from ref 10. To classify the different porphyrin core and phenyl modes in D_{4h} symmetry, we used the idealized model [Zn(TPP)] and calculated the vibrations of this model in D_{4h} symmetry. [Zn(TPP)] has 169 normal modes (56 of them are degenerate), where 44% are Raman- and 27% are IR-active.

B.2. NR Raman Spectrum and Assignment of **1.** The experimental and calculated NR Raman spectra of **1** are shown in the top panel of Figure 4. Corresponding polarized data are included in the lower panel. The calculated spectrum is, in general, shifted to a somewhat higher energy (the average deviation in vibrational energies is about 2 to 3%) compared to experiment, which is further evaluated in the discussion. Besides the good agreement in vibrational frequencies, very good agreement with experiment is obtained for the calculated NR Raman intensities, as shown in Figure 4 (top). This allows for a detailed assignment of the data. Importantly, additional information to support the Raman assignments is available from polarization measurements. The depolarization ratio ρ is defined as $\rho = I_{\text{perpendicular}} / I_{\text{parallel}}$. In D_{4h} symmetry, one obtains¹

(34) Stein, P.; Ulman, A.; Spiro, T. G. *J. Phys. Chem.* **1984**, *88*, 369–374.

(35) Zerbi, G.; Sandioni, S. *Spectrochim. Acta, Part A* **1968**, *24*, 511.

Table 2. Calculated Vibrational Energies (cm⁻¹) of Bromobenzene and Assignments Using Local Coordinates

frequencies				frequencies			
$\nu(\text{Ph})_i$	calcd ^a	assignment ^b	sym. ^c	$\nu(\text{Ph})_i$	calcd ^a	assignment ^b	sym. ^c
1	167	$\gamma(\text{Br})$	B ₁	16	1082	$\nu_1(\text{C}-\text{C})$	A ₁
2	242	$\delta(\text{C}-\text{C}-\text{Br})$	B ₂	17	1098	$\nu_{\text{asym}1}(\text{C}-\text{C}) + \delta(\text{C}-\text{C}-\text{H})$	B ₂
3	301	$\nu(\text{C}-\text{Br})$	A ₁	18	1206	$\delta_{\text{asym}}(\text{C}-\text{C}-\text{H})$	B ₂
4	419	$\tau(\text{ringtwist})$	A ₂	19	1216	$\delta_{\text{sym}}(\text{C}-\text{C}-\text{H})$	A ₁
5	475	$\gamma_1(\text{C})$	B ₁	20	1344	$\delta(\text{C}-\text{C}-\text{H}) + \nu_2(\text{C}-\text{C})$	B ₂
6	627	$\delta_1(\text{C}-\text{C}-\text{C})$	B ₂	21	1364	$\nu_{\text{asym}2}(\text{C}-\text{C})$	B ₂
7	669	$\delta_2(\text{C}-\text{C}-\text{C})$	A ₁	22	1468	$\nu_{\text{asym}3}(\text{C}-\text{C}) + \delta(\text{C}-\text{C}-\text{H})$	B ₂
8	712	$\gamma_2(\text{C})$	B ₁	23	1499	$\delta(\text{C}-\text{C}-\text{H}) + \nu_{\text{asym}4}(\text{C}-\text{C})$	A ₁
9	773	$\gamma_1(\text{H})$	B ₁	24	1621	$\nu_{\text{sym}}(\text{C}-\text{C})$	A ₁
10	870	$\gamma_2(\text{H})$	A ₂	25	1629	$\nu_3(\text{C}-\text{C})$	B ₂
11	952	$\gamma_3(\text{H})$	B ₁	26	3198	$\nu(\text{C}-\text{H})$	A ₁
12	1009	$\delta_{\text{sym}}(\text{C}-\text{C}-\text{C})$	A ₁	27	3209	$\nu(\text{C}-\text{H})$	B ₂
13	1014	τ_1	A ₂	28	3224	$\nu(\text{C}-\text{H})$	A ₁
14	1032	$\nu_{\text{breathing}}(\text{C}-\text{C})$	A ₁	29	3235	$\nu(\text{C}-\text{H})$	B ₂
15	1038	τ_2	B ₁	30	3242	$\nu(\text{C}-\text{H})$	A ₁

^a Calculated with B3LYP/LanL2DZ; see the Experimental section. ^b Assignments using local coordinates; see Figure 3. ^c Symmetries in the point group C_{2v}.

- (1) $0 < \rho < 0.75$ for polarized bands (A_{1g} vibrations),
- (2) $\rho = 0.75$ for depolarized bands (B_{1g} or B_{2g} vibrations), and
- (3) $\rho > 0.75$ for anomalous polarized bands (A_{2g} vibrations (only RR spectroscopy)).

Hence, the polarized measurements allow for the determination of the symmetry of a particular mode.³⁶ The complete assignments obtained in this manner are listed in Table 3. Additionally, the *d*₈ isotope shifts available for a number of bands from the RR measurements^{14b} are used for comparison with calculated isotope shifts to further confirm our assignments. For a better comparison with the literature, the notation established by Spiro and co-workers for [Ni(TPP)] is used in Table 3. Correspondingly, the porphyrin in-plane modes (both stretching and deformation modes) are labeled ν_i and the porphyrin out-of-plane modes are designated as γ_i .¹³ The phenyl mode notation is on the basis of the different symmetry blocks (eqs 3–6). For the oxidation- and spin-state sensitive modes, the common notation from the literature is included in Table 3, where bands A(p), B(dp), C(ap), D(p), and E(p)^{18b} are observed in the RR spectra and bands I, II, and III are found in the IR spectra.^{18b,42}

(36) Depolarization ratios for some of the weaker bands are difficult to determine from the polarized NR Raman spectrum in Figure 4. In these cases, the depolarization ratios from RR measurements were used. For example, the band at 1364 cm⁻¹ is strongly enhanced in Soret resonance, where the depolarized band at 1371 cm⁻¹ is not observed. Hence, from the Soret resonance spectrum, the depolarization ratio of this band can be determined.

(37) For the two weak bands at 1275 and 1467 cm⁻¹, depolarization ratios that are slightly larger than 0.75 have been obtained. However, these bands are enhanced in Q and Q_v resonance and are depolarized in these spectra. In addition, anomalous polarized bands (A_{2g}), where $\rho > 0.75$, are forbidden in NR Raman. Hence, the bands at 1275 and 1467 cm⁻¹ are classified as dp.

(38) Gouterman, M. In *The Porphyrins*; Dolphin, D., Ed.; Academic Press: New York, 1979; Vol. 3, Part A, pp 1–156.

(39) According to group theory, A_{1g} vibrations could also induce vibronic mixing. However, A_{1g} modes are ineffective because they do not induce a distortion of the molecule.

(40) Czernuszewicz, R. S.; Spiro, T. G. In *Inorganic Electronic Structure and Spectroscopy*; Solomon, E. I., Lever, A. B. P., Eds.; John Wiley & Sons: New York, 1999; Vol. 1, pp 353–441.

(41) Egawa, T.; Suzuki, N.; Dokoh, T.; Higuchi, T.; Shimada, H.; Kitagawa, T.; Ishimura, Y. *J. Phys. Chem. A* **2004**, *108*, 568–577.

(42) Spiro, T. G. *Curr. Sci.* **1998**, *74*, 304–307.

The NR Raman spectrum of **1** in Figure 4 can be divided into four regions showing different kinds of vibrations. In the low-energy region between 200 and 500 cm⁻¹, two phenyl out-of-plane vibrations, one porphyrin out-of-plane deformation, and three in-plane porphyrin vibrations are observed (cf. Table 3). The mode at 199 cm⁻¹ (calcd: 202 cm⁻¹) corresponds to the Fe–N stretching vibration of B_{1g} symmetry (ν_{18}) and is therefore depolarized. The mode at 390 cm⁻¹ (calcd: 388 cm⁻¹) is known to be oxidation-state-sensitive (band E(p)^{18b}) and was assigned previously to a porphyrin core deformation mode.^{14,18b} However, on the basis of the calculations and the fact that this mode shows strong Soret resonance enhancement, it is assigned to the totally symmetric $\nu_{\text{breathing}}(\text{Fe}-\text{N})$ vibration (ν_8). This is in agreement with the assignments for [Ni(TPP)].^{10a,13} The calculated *d*₈ isotope shift for this mode of 8 cm⁻¹ is in very good agreement with the experimental value of 10 cm⁻¹.^{14b} The weak band at 379 cm⁻¹ (calcd: 336 cm⁻¹) corresponds to the Fe–Cl stretching vibration, which is strongly IR-active (vide infra). The very weak band at 257 cm⁻¹ (calcd: 251 cm⁻¹) belongs to the Raman-forbidden $\gamma(\text{Pyr. tilting})$ vibration of B_{2u} symmetry, which gains intensity through coupling with the Raman allowed $\gamma(\text{Phenylrot.})$ phenyl vibration of B_{1g} symmetry. Hence, the fact that this mode appears in the Raman spectra is a true effect of the symmetry lowering in **1**. Correspondingly, the very weak feature at 247 cm⁻¹ (calcd: 241 cm⁻¹) is assigned to the $\gamma(\text{Phenylrot.})$ phenyl vibration with B_{1g} symmetry, which is mixed with the $\gamma(\text{Pyr. tilting})$ porphyrin core vibration with A_{2u} symmetry.

In the energy range from 800 to 1050 cm⁻¹, two weak bands are observed that are assigned to porphyrin core modes. The feature at 994 cm⁻¹ (calcd: 1008 cm⁻¹) corresponds to $\nu(\text{Pyr. breathing})$ with phenyl contribution (ν_6 ; cf. Table 3), and the band at 886 cm⁻¹ (calcd: 898 cm⁻¹) corresponds to a totally symmetric in-plane deformation mode. This latter vibration was originally assigned to a phenyl vibration,¹⁴ which, based on our calculations is described as a mixed $\delta_{\text{sym}}(\text{Pyr. deformation})$ and phenyl mode (ν_7). The calculated *d*₈ isotope shift is 5 cm⁻¹, which is in

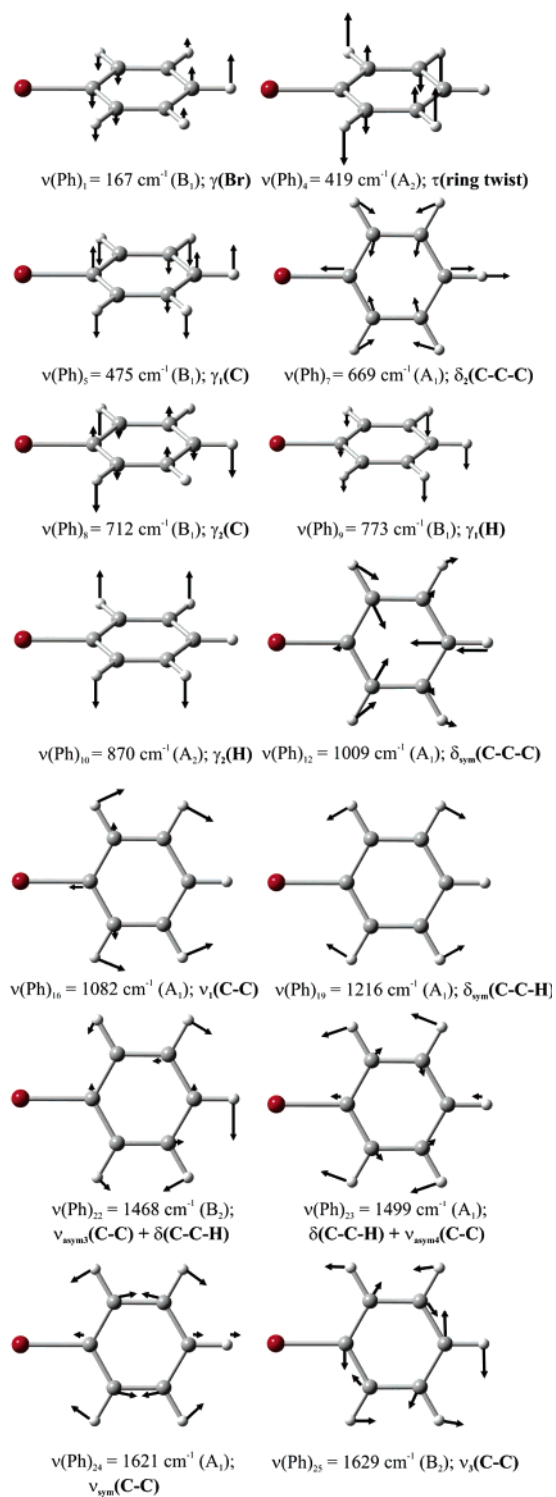


Figure 3. Illustration of the local coordinates of bromobenzene used for classification of in-plane and out-of plane phenyl modes in complexes 1–3 ($\gamma(\text{Br}) = \gamma(\text{Phenylrot.})$).

contrast to the experiment, where no shift was detected.^{14b} This indicates that the calculations overestimate the $\delta_{\text{sym}}(\text{Pyr. deformation})$ contribution to this mode (Discussion). The most intense band in this spectral region is located at 1006 cm^{-1} (calcd: 1018 cm^{-1}). This feature is assigned to a polarized (totally symmetric) phenyl in-plane vibration (ϕ_8). It was originally assigned to a $\nu(\text{C}_\alpha\text{--C}_m)$ vibration¹⁴ and later

reassigned to a $\nu(\text{Pyr. breathing})$ mode.²⁰ However, on the basis of the calculated intensities, this band has to be assigned to the mixed phenyl $\delta_{\text{sym}}(\text{C--C})$ and $\nu(\text{Pyr. breathing})$ porphyrin vibration (calcd: 1018 cm^{-1}), which is more in agreement with ref 20. The calculated d_8 isotope shift of 1 cm^{-1} is in the correct range compared to the experimental value of 6 cm^{-1} .^{14b} The observed discrepancies indicate that in this case the calculations underestimate the admixture of the porphyrin core vibration (Discussion). Finally, a weak band is found at 1030 cm^{-1} (calcd: 1054 cm^{-1}), which corresponds to an in-plane phenyl vibration (ϕ_7).

The region between 1050 and 1550 cm^{-1} contains only in-plane porphyrin core vibrations with the exception of the highly intense band at 1495 cm^{-1} , which is of the in-plane phenyl type (ϕ_5') but also has some porphyrin C–C stretching character ($\nu_{\text{sym}}(\text{C}_\alpha\text{--C}_m)$). With the exception of the totally symmetric vibration at 1072 cm^{-1} (calcd: 1124 cm^{-1}), which is a $\text{C}_\beta\text{--H}$ deformation mode (ν_9), all of the other porphyrin core vibrations are of the stretching type. The calculated frequency of ν_9 is 52 cm^{-1} , 4.9% higher in energy compared to the experimental value, which reflects the neglect of anharmonicity in the calculation (Discussion). Two totally symmetric vibrations in this region are known to be structure sensitive. The $\nu_{\text{sym}}(\text{Pyr. half-ring})$ vibration at 1363 cm^{-1} (calcd: 1379 cm^{-1}) is both oxidation- and spin-state sensitive (band A(p)^{18b}). The calculated d_8 isotope shift of 12 cm^{-1} of this mode is in excellent agreement with experiment (13 cm^{-1}).^{14b} The polarized band at 1554 cm^{-1} (calcd: 1598 cm^{-1}) is assigned to a combined $\nu(\text{C}_\beta\text{--C}_\beta) + \nu_{\text{sym}}(\text{C}_\alpha\text{--C}_m) + \delta_{\text{sym}}(\text{C}_\beta\text{--H})$ spin-state-sensitive vibration (band D(p)^{18b}). The calculated d_8 isotope shift of 21 cm^{-1} is identical to the experimental value.^{14b} These assignments are in agreement with the literature.^{14b} One additional polarized (totally symmetric) band is found at 1233 cm^{-1} (calcd: 1260 cm^{-1}), which is assigned to $\nu(\text{Pyr. breathing}) + \nu(\text{C}_m\text{--Ph})$ (ν_1) with a calculated d_8 isotope shift of 3 cm^{-1} , which is again in excellent agreement with experiment (3 cm^{-1}).^{14b} This assignment is partially in agreement with the literature, where this band was assigned to a pure $\nu(\text{C}_m\text{--Ph})$.²⁰ Finally, four depolarized bands are observed in this region. Only the $\nu_{\text{sym}}(\text{Pyr. half-ring})$ (ν_{12}) vibration at 1275 cm^{-1} (calcd: 1274 cm^{-1}) has B_{1g} symmetry,³⁷ whereas the others at 1495 , 1371 , and 1467 cm^{-1} have B_{2g} symmetry. Detailed assignments of these features are given in Table 3.

Finally, the two bands at the highest energy are both assigned to purely symmetric C–C stretching modes of the phenyl rings. From the polarized measurements, these have different symmetries: the band at 1597 cm^{-1} (calcd: 1650 cm^{-1}) is polarized (A_{1g}) and the feature at 1574 cm^{-1} (calcd 1649 cm^{-1}) is depolarized (B_{2g}). The larger deviations observed between the calculated and experimental frequencies for these modes ($\sim 4\%$) are partly due to an intrinsic inaccuracy in the calculations (Discussion). The assignment of the band at 1597 cm^{-1} is in agreement with earlier work.²⁰ No d_8 isotope shift is calculated for these features. In comparison, the experimental value for the A_{1g} mode is 5 cm^{-1} ,^{14b} indicating the presence of a small admixture of porphyrin core modes.

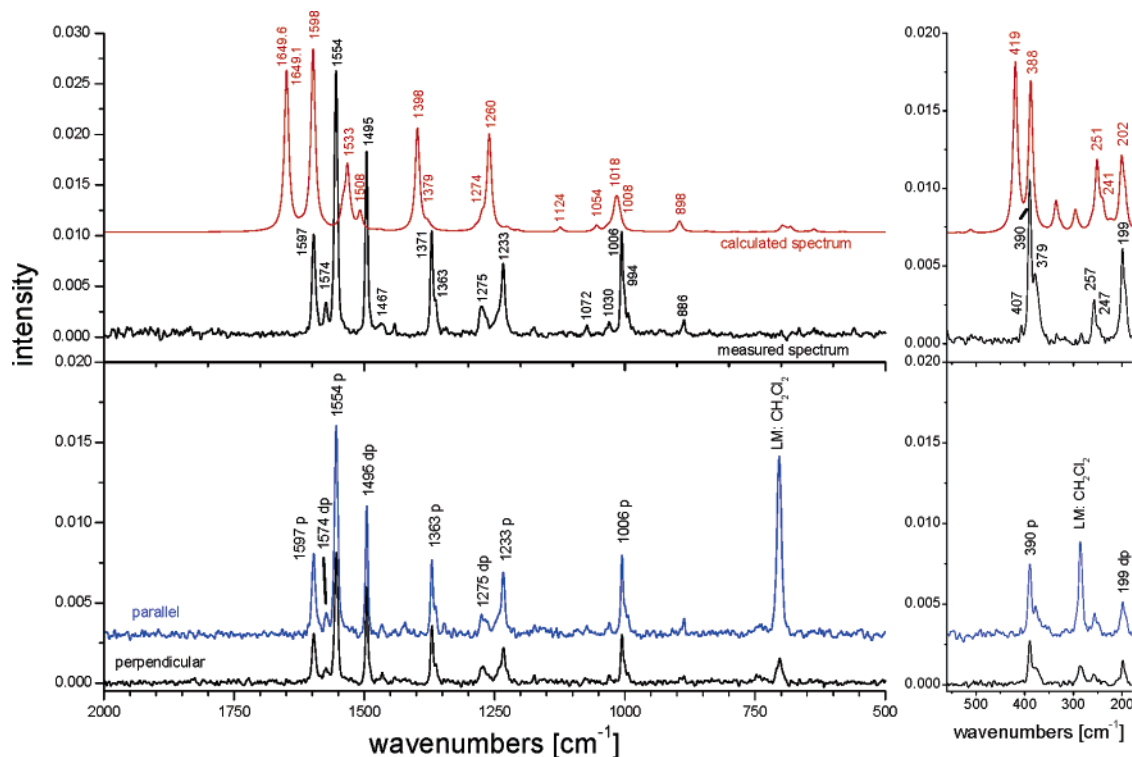


Figure 4. Comparison of the calculated and measured NR Raman spectra of **1** (top) and the polarization measurement in dichloromethane (bottom). The low energy part (560–180 cm⁻¹) of the calculated spectrum (top right) is enlarged in the Figure.

B.3. Infrared Spectrum and Assignment of 1. Figure 5 shows the experimental and calculated IR spectra of **1**. As in the NR Raman case, the calculated vibrational energies are in good agreement and the IR intensities are in very good agreement with the experimental data, reproducing the overall appearance of the experimental spectrum very well. The calculated frequencies for a number of modes are too high in energy, as analyzed below. The assignments of the infrared spectrum of **1** are on the basis of the calculated energies and intensities, and the results are summarized in Table 3. In addition, calculated d_8 isotope shifts for the structure-sensitive bands I, II, and III can be compared to the experimental data^{18b} reported for [Co(TPP)] and [{Fe(TPP)}₂O]. The IR spectrum can be divided into five regions of different types of vibrational modes.

In the far-IR region between 350 and 450 cm⁻¹, only in-plane porphyrin core vibrations are observed. The only exception is the strong band at 378 cm⁻¹ (calcd: 336 cm⁻¹), which corresponds to the $\nu(\text{Fe}-\text{Cl})$ stretching mode. More importantly, the totally symmetric Fe-N breathing vibration (ν_8) at 390 cm⁻¹ (calcd: 388 cm⁻¹; vide supra) is also observed in the IR spectrum as a weak band. This is another indication of the lowered symmetry in **1** because this band is IR forbidden in D_{4h} . Two E_u symmetric vibrations are observed in this region: the feature at 402 cm⁻¹ (calcd: 407 cm⁻¹) corresponds to a mixed $\nu(\text{Fe}-\text{N}) + \delta(\text{Pyr. translation})$ (ν_{50}) mode, whereas the band at 434 cm⁻¹ (calcd: 444 cm⁻¹) is assigned to a Pyrrol rotation $\delta(\text{Pyr. rotation})$ (ν_{49}). This latter feature corresponds to the spin-state sensitive band III, as defined by Oshio et al.^{18b} and was identified as a low-energy porphyrin core deformation mode^{18b} in agreement with our assignment. The calculated d_8 isotopic shift of 16

cm⁻¹ of this feature is in excellent agreement with the observed shifts for [Co(TPP)] and [{Fe(TPP)}₂O] of 16 and 17 cm⁻¹.^{18b}

The second region between 500 and 810 cm⁻¹ mostly comprises out-of-plane vibrations. The two features at 528 (calcd: 537) and 703 cm⁻¹ (calcd: 730 cm⁻¹) correspond to out-of-plane phenyl modes with E_u symmetry (π_5'' and π_4''), whereas the phenyl mode at 661 cm⁻¹ (calcd: 675 cm⁻¹) is of the in-plane deformation type. Besides these highly intense bands, a very weak feature is observed at 570 cm⁻¹ (calcd: 582 cm⁻¹) and assigned as shown in Table 3. The four bands between 710 and 810 cm⁻¹ are all of the out-of-plane type. The intense feature at 750 cm⁻¹ (calcd: 790 cm⁻¹) corresponds to a phenyl mode (π_3'') of E_u symmetry. Two out-of-plane porphyrin modes of A_{2u} symmetry are found at 720 (calcd: 750 cm⁻¹; γ_8) and 806 cm⁻¹ (calcd: 847 cm⁻¹; γ_5), the latter one being the oxidation-state-sensitive band II.^{18b} It was originally assigned to an in-plane deformation mode with $\delta(\text{C}_\beta-\text{H})$ character,^{18b} on the basis of an observed pyrrole- d_8 isotope shift. However, from the calculations, this band is associated with the intense band calculated at 847 cm⁻¹ that corresponds to a $\gamma(\text{H}_\beta) + \gamma_{\text{sym}}(\text{Pyr. folding})$ vibration. This mode shows a calculated- d_8 isotope shift of 40 cm⁻¹, which is in excellent agreement with the observed shift of 35 cm⁻¹ for [Co(TPP)].^{18b} On the basis of these results, band II is reassigned. Finally, the very weak band at 727 cm⁻¹ (calcd: 758 cm⁻¹) is assigned to an E_g vibration (γ_{20} ; cf. Table 3), which gains in IR intensity via coupling with a phenyl vibration with E_u symmetry. This is another indication of the lowered symmetry in **1** because these two vibrations cannot mix in D_{4h} . The deviations in energy of about 4 to 5% between calculated and experimental

Table 3. Assignment of the Infrared (IR), NR Raman ($\lambda_{\text{exc}} = 1064 \text{ nm}$), and Resonance Raman (Soret: $\lambda_{\text{exc}} = 454.5 \text{ nm}$; Q_v: $\lambda_{\text{exc}} = 514.5 \text{ nm}$; Q: $\lambda_{\text{exc}} = 568.2 \text{ nm}$) Spectra of [Fe(TPP)(Cl)] (**1**)^a

ν_1^h	mode	symmetry ^c	experimental ^d (cm ⁻¹)			calcd ^{d,f} (cm ⁻¹)
	assignment ^b		IR	NR R ^e	RR ^e	
ϕ_4	$\nu_{\text{sym}}(\text{C}-\text{C})$	A _{1g}		1597 m (p)	1597 (Soret: 1598 w,p; Q _v : 1595 vw,p; Q: shoulder)	1650 s
ϕ_4''	$\nu_{\text{sym}}(\text{C}-\text{C})$	E _u	1597 m			1649 m
ϕ_4'	$\nu_{\text{sym}}(\text{C}-\text{C})$	B _{2g}		1574 w (dp)	~1572/1577 (Soret: -; Q _v : 1571 m,dp/1576 s,dp; Q: 1573 s,dp/1578 vs,dp)	1649 m
ψ_3'	$\nu_3(\text{C}-\text{C}) + \nu_{\text{asym}}(\text{C}_\alpha-\text{C}_m)$	A _{2u} + B _{1g}	1574 vw			1618 vw
ν_2	$\frac{\nu(\text{C}_\beta-\text{C}_\beta) + \nu_{\text{sym}}(\text{C}_\alpha-\text{C}_m) + \delta_{\text{sym}}(\text{C}_\beta-\text{H})}{\nu_{\text{sym}}(\text{C}_\alpha-\text{C}_m)}$	A _{1g}		1554 vs (p)	~1556 (Soret: 1557 vs,p; Q _v : 1555 s,p; Q: 1557 s,p)	1598 vs
ν_{19}	$\frac{\nu_{\text{asym}}(\text{C}_\alpha-\text{C}_m) + \nu_{\text{asym}}(\text{C}_\alpha-\text{C}_\beta) + \delta_{\text{asym}}(\text{C}_\beta-\text{H})}{\nu_{\text{asym}}(\text{C}_\alpha-\text{C}_\beta)}$	A _{2g}			~1522/1516 (Soret: 1523/1517 vw; Q _v : 1523/1517 w,ap; Q: 1521/1515 m,ap)	1560
ϕ_5'	$\delta(\text{C}-\text{C}-\text{H}) + \nu_{\text{asym}4}(\text{C}-\text{C}) + \nu_{\text{sym}}(\text{C}_\alpha-\text{C}_m)$	B _{2g}		1495 m (dp)	~1495 (Soret: 1494 vw,-; Q _v : 1494 s,dp; Q: 1496 vs,dp)	1533 m
ϕ_5''	$\delta(\text{C}-\text{C}-\text{H}) + \nu_{\text{asym}4}(\text{C}-\text{C}) + \nu(\text{C}_\beta-\text{C}_\beta) + \nu_{\text{asym}}(\text{C}_\alpha-\text{C}_m) + \nu_{\text{sym}}(\text{C}_\alpha-\text{C}_m)$	E _u	1486 w			1521 s
ν_{28}	$\frac{\nu_{\text{sym}}(\text{C}_\alpha-\text{C}_m) + \nu_{\text{asym}}(\text{Pyr. half-ring})}{\nu_{\text{asym}}(\text{Pyr. half-ring})}$	B _{2g}		1467 vw (dp)	1467 (Soret: -; Q _v : 1467 vw,dp; Q: 1467 vw,dp)	1508 w
ν_3	$\frac{\nu_{\text{sym}}(\text{C}_\alpha-\text{C}_m) + \nu(\text{C}_\beta-\text{C}_\beta)}{\nu(\text{C}_\beta-\text{C}_\beta)}$	A _{1g}			1452 (Soret: 1452 m,p; Q _v : 1450 vw,p; Q: -)	1489
ψ_4'	$\nu_{\text{asym}3}(\text{C}-\text{C}) + \delta(\text{C}-\text{C}-\text{H})$	A _{2u}	1440 m			1470 m
ν_{29}	$\frac{\nu(\text{Pyr. quarter-ring}) + \nu(\text{C}_m-\text{Ph})}{\nu(\text{C}_m-\text{Ph})}$	B _{2g}		1371 m (dp)	~1371 (Soret: -; Q _v : 1370 s,dp; Q: 1372 m,dp)	1398 m
ν_4	$\nu_{\text{sym}}(\text{Pyr. half-ring})$	A _{1g}		1363 w	~1363 (Soret: 1364 s,p; Q _v : 1361 m,p; Q: 1365 m,p)	1379 vw
ν_{20}	$\frac{\nu(\text{Pyr. quarter-ring}) + \delta_{\text{sym}}(\text{C}_\beta-\text{H}) + \delta(\text{C}-\text{C}-\text{H}) + \nu_2(\text{C}-\text{C})}{\nu(\text{Pyr. quarter-ring})}$	A _{2g}			~1335 (Soret: -; Q _v : 1334 m,ap; Q: 1336 m,ap)	1373
ν_{41}	$\frac{\delta_{\text{asym}}(\text{C}_\beta-\text{H}) + \nu(\text{C}_m-\text{Ph}) + \nu_{\text{sym}}(\text{Pyr. half-ring})}{\nu_{\text{asym}}(\text{C}_\alpha-\text{C}_\beta)}$	E _u	1340 m 1334 m			1369 s
ν_{12}	$\nu_{\text{sym}}(\text{Pyr. half-ring})$	B _{1g}		1275 w (dp)	1278 (Soret: 1278 vw,-; Q _v : 1278 w,dp; Q: 1278 m,dp)	1274 vw
ν_{27}	$\frac{\nu(\text{Pyr. quarter-ring}) + \nu(\text{C}_m-\text{Ph}) + \nu_1(\text{C}-\text{C})}{\nu_1(\text{C}-\text{C})}$	B _{2g}			~1266 (Soret: 1266 vw,dp; Q _v : 1265 w,dp; Q: 1266 m,dp)	1286 vvw
ν_1	$\frac{\nu(\text{Pyr. breathing}) + \nu(\text{C}_m-\text{Ph})}{\nu(\text{C}_m-\text{Ph})}$	A _{1g}		1233 m (p)	~1233 (Soret: 1235 m,p; Q _v : 1230 w,p; Q: 1232 w,p)	1260 m
ν_{26}	$\frac{\delta_{\text{asym}}(\text{C}_\beta-\text{H}) + \nu_{\text{sym}}(\text{Pyr. quarter-ring})}{\nu_{\text{sym}}(\text{Pyr. quarter-ring})}$	A _{2g}			~1225 (Soret: -; Q _v : 1225 w,ap; Q: 1226 vw,ap)	1248
ν_{36}	$\frac{\nu_{\text{sym}}(\text{Pyr. half-ring}) + \nu(\text{Pyr. quarter-ring}) + \nu(\text{C}_m-\text{Ph})}{\nu(\text{C}_m-\text{Ph})}$	E _u	1200 w			1250 w
ν_{34}	$\frac{\delta_{\text{asym}}(\text{C}_\beta-\text{H}) + \nu_{\text{asym}}(\text{C}_\alpha-\text{C}_\beta)}{\nu_{\text{asym}}(\text{C}_\alpha-\text{C}_\beta)}$	B _{2g}			1182 (Soret: -; Q _v : 1181 w,dp; Q: 1182 w,dp)	1226

Table 3 (Continued)

ν_i^h	mode	symmetry ^c	experimental ^d (cm ⁻¹)			calcd ^{d,f} (cm ⁻¹)
	assignment ^b		IR	NR R ^e	RR ^e	
ν_{51}	$\nu(\text{Pyr. quarter-ring}) + \nu(\text{Pyr. breathing})$	E _u	1175 m			1236 m
ϕ_6''	$\delta_{\text{sym}}(\text{C}-\text{C}-\text{H})$	E _u	1158 w			1223 w
ν_{17}	$\delta_{\text{sym}}(\text{C}\beta-\text{H})$	B _{1g}			1080 (Soret: -; Q _v : 1081 w,dp; Q: 1080 m,dp)	1125
ν_9	$\delta_{\text{sym}}(\text{C}\beta-\text{H})$	A _{1g}		1072 vw	~1072 (Soret: 1073 m,p; Q _v : 1070 m,p; Q: 1073 m,p)	1124 vw
ψ_8'	$\nu_{\text{asym1}}(\text{C}-\text{C}) + \delta(\text{C}-\text{C}-\text{H})$	A _{2u}	1070 m			1106 m
ν_{52}	$\delta_{\text{sym}}(\text{C}\beta-\text{H})$	E _u				1117 w
ϕ_7	$\nu_1(\text{C}-\text{C})$	A _{1g}		1030 vw	~1029 (Soret: -; Q _v : 1028 vw,p; Q: 1030 vw,p)	1054 w
ν_{30}	$\nu_{\text{asym}}(\text{Pyr. half-ring})$	B _{2g}			~1017 (Soret: -; Q _v : 1015 w,dp; Q: 1018 s,dp)	1035
ν_{15}	$\nu(\text{Pyr. breathing})$	B _{1g}				1030
ϕ_8	$\delta_{\text{sym}}(\text{C}-\text{C}-\text{C}) + \nu(\text{Pyr. breathing})$	A _{1g}		1006 m (p)	1006 (Soret: 1006 w,p; Q _v : 1006 w,p; Q: 1006 m,p)	1018 w
ϕ_8''	$\delta_{\text{sym}}(\text{C}-\text{C}-\text{C}) + \nu(\text{Pyr. breathing}) + \nu_{\text{asym}}(\text{Pyr. half-ring})$	E _u	1002 vs			1017 s
ν_{47}	$\nu(\text{Pyr. breathing}) + \delta_{\text{asym}}(\text{Pyr. deformation}) + \nu_{\text{breathing}}(\text{C}-\text{C})$	E _u	995 vs			1005 s
ν_6	$\nu(\text{Pyr. breathing}) + \nu_{\text{breathing}}(\text{C}-\text{C})$	A _{1g}		994 vw (p)	994 (Soret: -; Q _v : 993 w,p; Q: 994 m,p)	1008 w
ν_7	$\delta_{\text{sym}}(\text{Pyr. deformation}) + \gamma_2(\text{H})$	A _{1g}		886 vw (p)	887 (Soret: 887 w,p; Q _v : 887 vw,p; Q: 887 vw,p)	898 w
ν_{32}	$\delta_{\text{asym}}(\text{Pyr. deformation})$	B _{2g}			851 (Soret: -; Q _v : 850 vw,dp; Q: 851 w,dp)	890
ν_{16}	$\delta_{\text{sym}}(\text{Pyr. deformation}) + \gamma_1(\text{H})$	B _{1g}				874
γ_5	$\gamma(\text{H}\beta) + \gamma_{\text{sym}}(\text{Pyr. folding})$	A _{2u}	806 s			847 s
core	overtone 390 cm ⁻¹	A _{1g}			779 (Soret: -; Q _v : 779 m,p; Q: 778 vw,p)	
π_3''	$\gamma_1(\text{H})$	E _u	750 s			790 vs
π_3	$\gamma_1(\text{H})$	B _{1g}			744 (Soret: -; Q _v : -; Q: 744 w,dp)	781
		A _{1g}			723 (Soret: 723 vw,p; Q _v : 723 vw,p; Q: -)	
γ_{20}	$\gamma_{\text{sym}}(\text{Pyr. folding}) + \gamma_{\text{asym}}(\text{Pyr. folding}) + \gamma(\text{H}\beta) + \gamma_1(\text{H})$	E _g + E _u	727 vw			758
γ_8	$\gamma_{\text{sym}}(\text{Pyr. folding}) + \gamma(\text{H}\beta) + \gamma_1(\text{H})$	A _{2u}	720 m			750
π_4''	$\gamma_2(\text{C})$	E _u	703 s			730 s
ϕ_9''	$\delta_2(\text{C}-\text{C}-\text{C}) + \delta(\text{Pyr. rotation})$	E _u	661 m			675 m
ϕ_9	$\delta_2(\text{C}-\text{C}-\text{C})$	A _{1g}			639 (Soret: 639 vw,p; Q _v : -; Q: -)	652
	combination band (184 + 391 cm ⁻¹)	A _{1g}			572 (Soret: 572 vw,p; Q _v : 570 w,p; Q: -)	
γ_7	$\gamma(\text{C}\alpha-\text{C}\beta) + \gamma_{\text{asym}}(\text{Pyr. folding}) + \gamma_{\text{sym}}(\text{Pyr. folding})$	A _{2u}	570 vw			582 vw

Table 3 (Continued)

ν_i^h	mode		experimental ^d (cm ⁻¹)			calcd ^{d,f} (cm ⁻¹)
	assignment ^b	symmetry ^c	IR	NR R ^e	RR ^e	
π_5''	$\gamma_1(\text{C}) + \delta(\text{Pyr. translation})$	E _u	528 m			537 m
ν_{49}	$\delta(\text{Pyr. rotation})$	E _u	434 s			444 m
σ_{13}''	$\tau(\text{ring twist})$	E _g		407 vw	408 (Soret: -; Q _v : -; Q: 408 vw,-)	419 w
ν_{50}	$\nu(\text{Fe-N}) + \delta(\text{Pyr. translation})$	E _u	402 m			407 m
ν_8	$\nu_{\text{breathing}}(\text{Fe-N})$	A _{1g}	390 m	390 m (p)	391 (Soret: 392 s,p; Q _v : 390 vs,p; Q: 390 w,p)	388 w
Fe-Cl	$\nu(\text{Fe-Cl})$	A _{1g}	378 s	379 w	257 (Soret: 258 vw,p; Q _v : 257 w,p; Q: 258 vw,p)	336
γ_{16}	$\gamma(\text{Pyr. tilting}) + \gamma(\text{Phenylrot.})^g$	B _{2u} + B _{1g}		257 vw	258 (Soret: -; Q _v : -; Q: -; $\lambda_{\text{exc.}} = 647.1$ nm: 258 vw,dp)	251 vw
Ph	$\gamma(\text{Phenylrot.})^g + \gamma(\text{Pyr. tilting})$	B _{1g} + A _{2u}		247 vw	247 (Soret: -; Q _v : -; Q: 247 vw, dp; 647.1 nm: 247 vw,dp)	241 vw
	porphyrin breathing				203 (Soret: 204 vw,p; Q _v : 202 w,p; Q: 202 vw,p)	200 vw
ν_{18}	$\nu(\text{Fe-N})$	B _{1g}		199 w (dp)	199 (Soret: -; Q _v : -; Q: -; 647.1 nm: 199 vw,dp)	202 vw

^a For notations of in-plane and out-of-plane core modes see Li et al.^{10a,10c} and Figures S6 and S7. ^b Assignment in local coordinates: see Table 2 and Figure 3 for the phenyl coordinates and ref 10a and c (Figures S6 and S7) for the in-plane and out-of-plane porphyrin coordinates. Porphyrin coordinates are printed in bold. Assignments for [Ni(TPP)] by Rush III et al.¹³ are underlined. ^c Effective D_{4h} symmetry: see the Results and Analysis section. ^d Calculated (DFT) and experimental intensity (vs = very strong, s = strong, m = middle, w = weak, and vw = very weak). ^e Depolarization ratio: p = polarized, dp = depolarized and ap = anomalous polarized band. ^f Calculated with B3LYP/LanL2DZ: see Experimental section. ^g $\gamma(\text{Phenylrot.})$ corresponds to $\nu(\text{Ph})_1 = \gamma(\text{Br})$ in bromobenzene. ^h Labeling used by Spiro and co-workers (cf. ref 13).

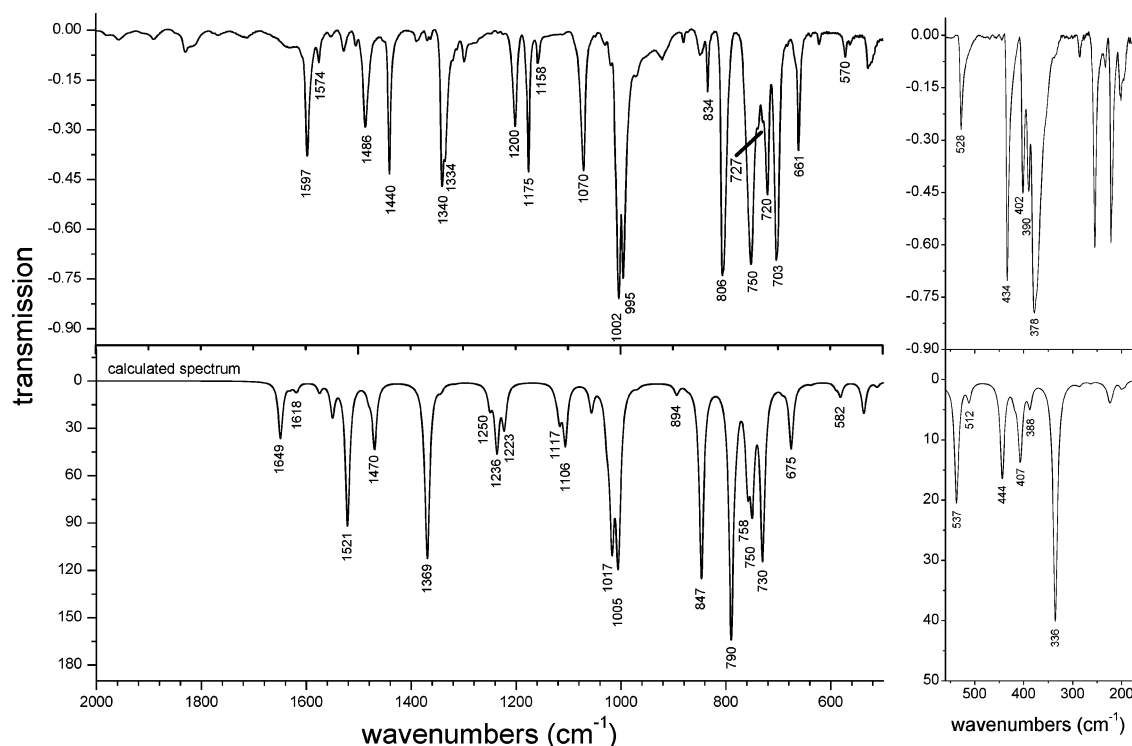


Figure 5. IR spectrum of **1**: the measured spectrum (top) and the calculated spectrum (bottom).

frequencies observed for the phenyl C–H deformation (π_4'' , π_3 and π_3'') and the $\gamma(\text{H}_\beta)$ porphyrin vibrations in this region

are due to the neglect of anharmonicity in the calculations (cf. Discussion).

The third region between 990 and 1160 cm^{-1} mostly comprises in-plane vibrations. The strong band at 995 cm^{-1} (calcd: 1005 cm^{-1}) is assigned to a $\nu(\text{Pyr. breathing}) + \delta_{\text{asym}}(\text{Pyr. deformation})$ porphyrin core vibration with $\nu_{\text{breathing}}(\text{C}-\text{C})$ phenyl contribution (ν_{47}), whereas the intense feature at 1002 cm^{-1} (calc.: 1017 cm^{-1}) corresponds to the mixed $\delta_{\text{sym}}(\text{C}-\text{C}-\text{C}) + \nu(\text{Pyr. breathing}) + \nu_{\text{asym}}(\text{Pyr. half-ring})$ mode with mostly phenyl character (ϕ_8''). Both have E_u symmetry. The assignment of the strong band at 1070 cm^{-1} is not entirely clear. One possibility is a $\delta_{\text{sym}}(\text{C}_\beta-\text{H})$ core mode with E_u symmetry, which is calculated at 1117 cm^{-1} (ν_{52}). Alternatively, this feature could be identified as the $\nu_{\text{asym}}(\text{C}-\text{C}) + \delta(\text{C}-\text{C}-\text{H})$ phenyl vibration (ψ_8') with A_{2u} symmetry, calculated at 1106 cm^{-1} . A d_8 isotope substitution would be necessary to distinguish between these possibilities. Finally, the band at 1158 cm^{-1} is assigned to a phenyl vibration as shown in Table 3.

The following region between 1160 and 1350 cm^{-1} mostly consists of E_u symmetric in-plane porphyrin vibrations. The two bands at 1175 (calcd: 1236 cm^{-1}) and 1200 cm^{-1} (calcd: 1250 cm^{-1}) are both in-plane porphyrin stretching modes, which show deviations in energy of 4 to 5% between calculation and experiment (cf. Discussion) and are assigned as shown in Table 3. The band at 1340 cm^{-1} (calcd: 1369 cm^{-1}) is assigned to a mixed $\delta_{\text{asym}}(\text{C}_\beta-\text{H}) + \nu(\text{C}_m-\text{Ph}) + \nu_{\text{sym}}(\text{Pyr. half-ring}) + \nu_{\text{asym}}(\text{C}_\alpha-\text{C}_\beta)$ vibration and is known to be spin-state-sensitive (band I^{18b}). It appears split into two components in **1**, where a shoulder at 1334 cm^{-1} is present. Previously, this band was assigned to a $\nu(\text{C}_\alpha-\text{C}_m) + \nu(\text{C}_m-\text{Ph})$ by Oshio et al.^{18b} The calculated d_8 isotope shift for this band of 19 cm^{-1} shows some deviation from the experimental value (8 cm^{-1}) obtained for [Co(TPP)].^{18b} However, this is most probably due to the highly mixed nature of this mode, where, depending on the actual complex, changes in the contributions of individual local coordinates can be expected to occur.

The region at the highest energy between 1400 and 1600 cm^{-1} consists only of phenyl-type vibrations, which are assigned as shown in Table 3. For ϕ_4'' , the frequency is obtained 52 cm^{-1} higher in energy compared to experiment. The reason for this is discussed in section B.2 for the corresponding modes ϕ_4 and ϕ_4' , which are combinations of the same local coordinate but with different symmetries (cf. Table 3). The weak band at 1574 cm^{-1} (calcd: 1618 cm^{-1}) corresponds to the $\nu_3(\text{C}-\text{C})$ phenyl vibration of A_{2u} symmetry, which is mixed with the IR forbidden $\nu_{\text{asym}}(\text{C}_\alpha-\text{C}_m)$ porphyrin vibration with B_{1g} symmetry. Hence, this is another indication of the symmetry lowering in **1**. The band at 1486 cm^{-1} (calcd: 1521 cm^{-1}) is assigned to a strongly mixed in-plane vibration (ϕ_5'') of the $\delta(\text{C}-\text{C}-\text{H}) + \nu_{\text{asym}}(\text{C}-\text{C})$ phenyl and $\nu(\text{C}_\beta-\text{C}_\beta) + \nu_{\text{asym}}(\text{C}_\alpha-\text{C}_m) + \nu_{\text{sym}}(\text{C}_\alpha-\text{C}_m)$ porphyrin type. From the calculations, we have classified this band as a phenyl type mode, but the individual contributions might vary experimentally depending on the actual complex investigated.

B.4. Resonance Raman Spectra of **1** and Assignment.

The electronic spectra of metalloporphyrins have been explained on the basis of the four-orbital model of Gouter-

man.³⁸ They are dominated by the two $\pi \rightarrow \pi^*$ transitions from the a_{1u} and a_{2u} HOMOs to the e_g LUMO of the porphyrin dianion. Both resulting excited states have E_u symmetry and show a strong configuration interaction (CI). This leads to two well-separated bands in the absorption spectra, the intense Soret band (where the individual transition moments are additive), and the weak Q band (where they nearly cancel). In addition, a third band is observed on the higher energy side of Q. This band, Q_v , is a result of vibronic mixing between the Soret and the Q band. Because both excited states are of E_u symmetry, vibronic mixing is enabled by the vibrations of A_{2g} , B_{1g} , and B_{2g} symmetries.³⁹ For the resonance Raman spectra of metalloporphyrins, A-, B-, and C-term enhancement mechanisms are important.⁴⁰ A-term enhancement is caused by a displacement of the excited state relative to the ground state and is in general only relevant for totally symmetric modes. Because A-term intensity is proportional to the square of the electric dipole transition moment of the excited electronic state, this mechanism is dominant in the region of the Soret transition. B-term enhancement is caused by the vibronic coupling between the excited state $|e\rangle$ and another excited state $|s\rangle$, which leads to the resonance enhancement of the vibrations that are effective in coupling these states. Hence, this mechanism applies to the Q band, where vibrations of A_{2g} , B_{1g} , and B_{2g} symmetries are enhanced. Additional A-term enhancement of A_{1g} modes in the Q region is also expected. Thus, resonance enhancement of nontotally symmetric modes is therefore indicative of the presence of vibronic bands in the absorption spectra. However, B_{1g} and B_{2g} enhancements could theoretically also be induced by a Jahn–Teller distortion of the excited states with E_u symmetry.⁴¹ Hence, *the enhancement of A_{2g} modes is the most diagnostic for the presence of vibronic coupling.* A_{2g} modes are easily identified in the Raman spectra because of their anomalous polarization (ap; $\rho > 3/4$), which relates to the scattering tensor being antisymmetric.^{42–44} Finally, C-term enhancement is observed upon the excitation to a vibronic sideband of a forbidden or weakly allowed 0–0 electronic transition⁴⁰ that leads to the enhancement of overtones and combination modes. This applies to the Q_v region of the absorption spectra. These different types of resonance enhancement are indeed observed for complex **1**, as shown in Figure S2. Figures 8–10 present the RR spectra of **1** including the polarized data in Q ($\lambda_{\text{exc}} = 568.2$ nm), Q_v ($\lambda_{\text{exc}} = 514.5$ nm), and Soret ($\lambda_{\text{exc}} = 454.5$ nm) resonance. Figure 7 shows the absorption spectrum of **1** indicating the different excitation wavelengths. The RR data in the Soret region are dominated by polarized (A_{1g}) bands, which can therefore easily be identified from the Soret spectrum. The Q and Q_v spectra of **1** contain depolarized, polarized, and anomalous polarized bands. The presence of A_{2g} vibrations in the Q and Q_v spectra confirms well the presence of vibronic coupling as already discussed. The Q_v RR spectra also show overtones and

(43) Placzek, G. In *Handbuch der Radiologie*; Marx, E., Ed.; Akademische Verlagsgesellschaft: Leipzig, Germany, 1934; Vol. 6, Part 2, p 205.

(44) Spiro, T. G.; Strekas, T. C. *Proc. Natl. Acad. Sci. U.S.A.* **1972**, *69*, 2622–2626.

combination bands above 1600 cm^{-1} corresponding to C-term enhancement, which confirms that Q_v is the vibronic sideband of Q.

A number of new bands are observed in the RR spectra compared to the NR Raman spectra. The assignments of the RR data included in Table 3 are on the basis of the energies of the bands in correlation to the DFT results as well as the symmetries determined from the polarized experiments. In some cases, calculated d_8 isotope shifts for **1** in comparison to experimental shifts obtained for [Ni(TPP)]¹³ are used to further confirm the assignments. The $\nu(\text{Fe-N})$ breathing mode at 390 cm^{-1} is strongly enhanced in the Q_v region of compound **1**, which is surprising because this band has A_{1g} symmetry; therefore, one would anticipate its maximum enhancement in the Soret region (Figure S3).⁴⁵ The band at 639 cm^{-1} (calcd: 652 cm^{-1}) in Soret resonance is assigned to an in-plane $\delta_2(\text{C-C-C})$ phenyl vibration (ϕ_9) with A_{1g} symmetry. This feature shows no d_8 isotope shift in the calculations and is in agreement with results for [Ni(TPP)].¹³ The depolarized band at 744 cm^{-1} (calcd: 781 cm^{-1}) observed in Q resonance corresponds to an out-of-plane $\gamma_1(\text{H})$ phenyl vibration (π_3) with B_{1g} symmetry. The calculated d_8 isotope shift of 10 cm^{-1} for this mode is in good agreement with the value of 7 cm^{-1} observed for [Ni(TPP)].¹³ Two new depolarized bands are observed at 851 and 1017 cm^{-1} in Q and Q_v resonances, respectively. In both cases, two possible features with B_{1g} and B_{2g} symmetries are present in the calculations as well as in the RR spectra of [Ni(TPP)]. Hence, no assignments of these bands are possible. The depolarized band at 1080 cm^{-1} observed in Q and Q_v resonances is assigned as shown in Table 3. The depolarized band observed at 1182 cm^{-1} in Q_v and Q resonances corresponds to either the calculated vibration at 1226 cm^{-1} (a $\delta_{\text{asym}}(\text{C}_\beta\text{-H}) + \nu_{\text{asym}}(\text{C}_\alpha\text{-C}_\beta)$ core mode) or the feature predicted at 1222 cm^{-1} (a phenyl vibration); both have B_{2g} symmetry. In [Ni(TPP)],¹³ a band at 1190 cm^{-1} with a small phenyl- d_{20} shift is observed and assigned to the $\delta(\text{C}_\beta\text{-H})$ vibration calculated at 1226 cm^{-1} . Because a larger d_{20} isotope shift is expected for the phenyl vibration, the band at 1182 cm^{-1} is tentatively assigned to this feature. The modes at 744 cm^{-1} (phenyl vibration), ν_{17} , and ν_{34} (both $\text{C}_\beta\text{-H}$ in-plane porphyrin vibrations) show larger deviations in energy between calculation and experiment compared to those of the other porphyrin modes, which are due to the neglect of anharmonicity (Discussion). The weak, anomalous polarized bands at 1225 and 1335 cm^{-1} in Q and Q_v resonances are assigned as shown in Table 3. The depolarized band at 1266 cm^{-1} (calcd: 1286 cm^{-1}) is observed in all RR spectra. It is assigned to a mixed $\nu(\text{Pyr. quarter-ring}) + \nu(\text{C}_m\text{-Ph})$ porphyrin core vibration with phenyl contribution ($\nu_1(\text{C-C})$) with B_{2g} symmetry (ν_{27}). The calculated d_8 isotope shift of 2 cm^{-1} is in very good agreement with experiment (1 cm^{-1} for [Ni(TPP)]¹³). The band at 1452 cm^{-1} in Soret and Q_v resonances is assigned to the mixed in-plane $\nu_{\text{sym}}(\text{C}_\alpha\text{-C}_m) + \nu(\text{C}_\beta\text{-C}_\beta)$ porphyrin vibration (ν_3) with A_{1g}

symmetry. The split, anomalous polarized band⁴⁶ at $1522/1516\text{ cm}^{-1}$ (calcd: 1560 cm^{-1}) is assigned to the mixed $\nu_{\text{asym}}(\text{C}_\alpha\text{-C}_m) + \nu_{\text{asym}}(\text{C}_\alpha\text{-C}_\beta) + \delta_{\text{asym}}(\text{C}_\beta\text{-H})$ in-plane porphyrin core vibration and is known to be spin-state sensitive (band C(ap)^{47,18b}). It was originally assigned to only $\nu(\text{C}_\alpha\text{-C}_m)$.^{14b} The predicted d_8 isotope shift of this feature is 6 cm^{-1} . All of these assignments are listed in Table 3.

B.5. Effects of Symmetry Lowering. There are three major effects resulting from the symmetry lowering from idealized D_{4h} to the actual symmetry of [Fe(TPP)(Cl)]. Because of the fact that the phenyl rings are no longer perpendicular to the porphyrin core, the coupling between the core and the phenyl vibrations becomes stronger. The second effect is that modes with different symmetries in D_{4h} appear mixed in **1**. Several examples are observed in the NR Raman and IR spectra as discussed above, where even (g) and odd (u) vibrations are combined. This applies, for example, to the NR Raman bands at 247 and 257 cm^{-1} and the IR bands at 390 , 727 , and 1574 cm^{-1} . Of importance though is the fact that all of these symmetry-breaking modes obtain only very small intensities because of this intensity-stealing mechanism. This together with the observation of polarized, depolarized, and anomalous polarized bands clearly shows that the [Fe(TPP)]⁺ core of **1** still behaves as if it has D_{4h} symmetry. The third effect of symmetry lowering beyond C_{4v} in **1** is that degenerate E_u vibrations appear to be split in the IR spectra. However, the observed splittings are very small (about 5 cm^{-1}). Hence, this again indicates that an effective D_{4h} symmetry is present in **1**.

C. Vibrational Spectra and Assignments of Compounds 2 and 3 in Comparison with Those of 1. The crystal as well as the DFT optimized structures of complexes **1–3** are very similar overall, as discussed in section A. Correspondingly, the averaged metal–nitrogen distances are similar and increase in the order of Co (1.985 \AA) < Mn (2.019 \AA) < Fe (2.049 \AA). The most pronounced difference among **1**, **2**, and **3** occurs for the metal–chloride bond distances, which increase in the order of Co (2.145 \AA) < Fe (2.192 \AA) \ll Mn (2.389 \AA). Another important difference is observed for the out-of-plane displacement of the metal atom from the N_4 plane of the porphyrin, which increases in the order of Co (0.05 \AA) < Mn (0.258 \AA) < Fe (0.383 \AA). On the basis of the large structural similarities of complexes **1–3**, it can be expected that the overall vibrational properties of the corresponding [M(TPP)]⁺ units are quite similar. The only exception is the metal–chloride stretching vibration, where larger differences should be observed.

Figure 6 shows the NR Raman data of **2** together with the calculated spectrum. In this case, exceptional agreement is obtained between theory and experiment. The corresponding spectra of **3** are presented in Figure S1. The agreement between the calculated and experimental data is also very good in this case. As already discussed for **1**, small shifts of certain bands to higher energy (average deviation in energy of about 2 to 3%) are also observed in the calculations for

(45) The excitation profile is a plot of the Raman intensity versus the Raman excitation energy.

(46) The origin of the splitting is not known. It might relate to the fact that the spectrum was recorded in a KBr disk.

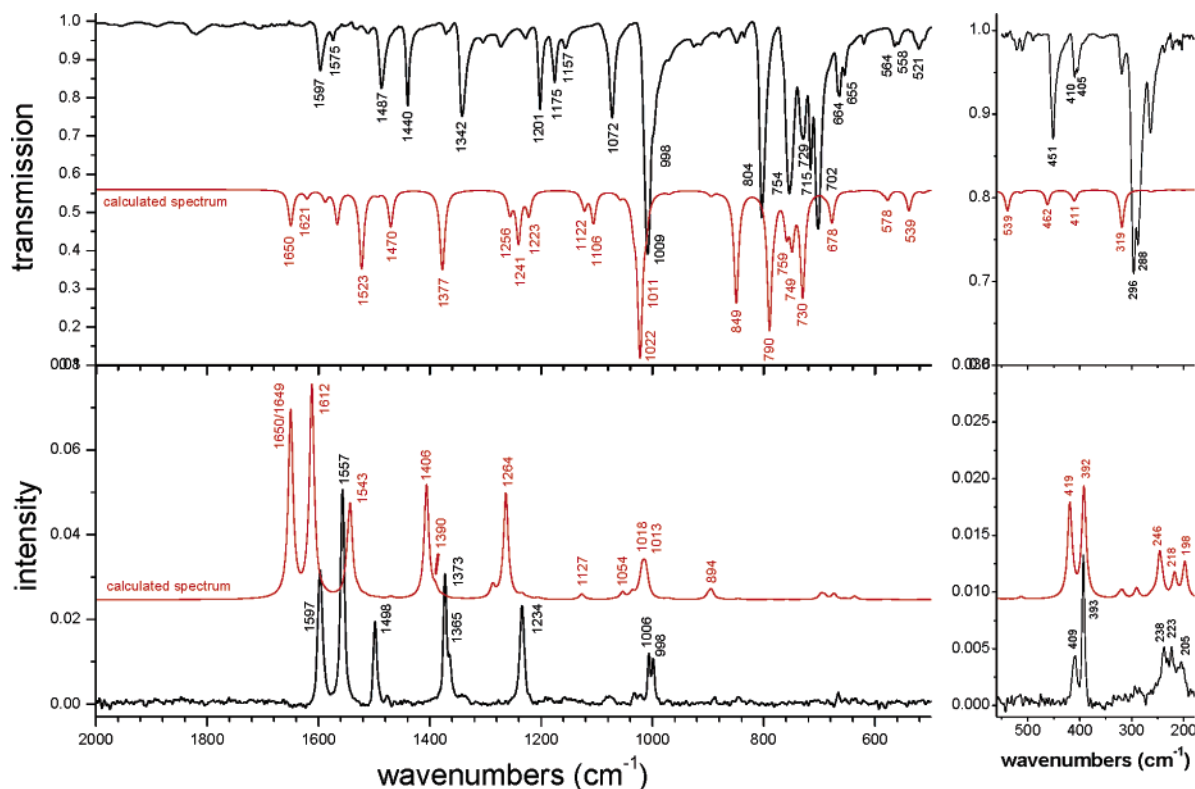


Figure 6. IR spectrum of **2** (top) and the NR Raman spectrum of **2** (bottom). The corresponding calculated spectra are included in the two panels as indicated. The low energy part (560–180 cm^{-1}) of the calculated spectra is enlarged.

Table 4. Comparison of Metal–Chloride Stretching Frequencies (cm^{-1}) and QCC-NCA as well as Calculated (DFT) Force Constants $f(\text{M}-\text{Cl})$ ($\text{mdyn}/\text{\AA}$) for [M(TPP)Cl] (**1**, **2**, and **3**) and Model Systems [M(P*)Cl] (**1a**, **2a**, and **3a**)

compound	$\nu(\text{M}-\text{Cl})$			model	$\nu(\text{M}-\text{Cl})$		$f(\text{M}-\text{Cl})$	
	calcd ^{b,f}	exptl ^c	lit.		PED ^{a,f}	calcd ^b	QCC-NCA	
1	263/336	378	360 ² 364 ⁵⁷ ^d	1a	225 (9%)/339 (86%)	1.419	1.796	
2	263/319	296	299 ⁵⁷ ^e	2a	235 (39%)/318 (74%)	1.160	0.932	
3	286/398	397		3a	262 (40%)/396 (82%)	1.704	1.717	

^a PED = potential energy distribution; the numbers in parentheses correspond to the % contribution of the M–Cl coordinate to this mode. ^b Calculated with B3LYP/LanL2DZ; see Experimental section. ^c Experimental infrared frequencies. ^d Determined from Raman data of [Fe(OEP)(Cl)]. ^e Determined from Raman data. ^f The $\nu(\text{M}-\text{Cl})$ vibration is mixed with a porphyrin mode, and hence there are two vibrations that carry $\nu(\text{M}-\text{Cl})$ contributions. As shown in the PED, the mode at higher energy has more M–Cl stretching character.

2 and **3** (Discussion). Because of the structural similarities of **1–3**, it is not surprising that the NR Raman spectra of these compounds show large similarities as evidenced by a comparison of Figures 4, 6, and S1. Hence, the assignments of the NR Raman spectra of **2** and **3** listed in Tables S1 and S2, respectively, largely parallel the assignments for **1**. Only a few differences are observed. The band at 1574 cm^{-1} in the experimental NR Raman spectrum of **1** is not observed in the spectra of compounds **2** and **3**. This band corresponds to the phenyl in-plane vibration $\nu_{\text{sym}}(\text{C}-\text{C})$ (ϕ_4') with B_{2g} symmetry. However, complex **3** shows an additional small band at 1540 cm^{-1} that could not be unambiguously assigned. The metal–chloride stretching vibration only appears in the NR Raman spectrum of **1**. Otherwise, the same vibrations are observed in the NR Raman spectra of **1–3**. Some of them show small characteristic shifts, which are discussed in section E.

Figure 6 shows the IR data of **2** together with the calculated spectrum. Again, in this case, the most exceptional agreement is obtained between theory and experiment. The

corresponding spectra of **3** are presented in Figure S1. A good agreement between theory and experiment is also achieved in this case. The IR spectra of all three compounds **1–3** basically show the same normal modes. Correspondingly, the appearances of the MIR spectra are very similar. However, the far-IR spectra look clearly different because the metal–chloride and the metal–nitrogen stretching vibrations are located in this region, which show the strongest metal sensitivity (cf. section E).

D. Metal–Chloride Bonding. For compounds **1** and **3**, the experimental frequency of the metal–chloride stretching vibration is similar with $\nu(\text{Fe}-\text{Cl}) = 378 \text{ cm}^{-1}$ and $\nu(\text{Co}-\text{Cl}) = 397 \text{ cm}^{-1}$ (cf. Table 4). In contrast, the Mn–Cl stretching vibration of 296 cm^{-1} is located at a significantly lower energy. This trend is in agreement with the metal–chloride distances with **3** (2.145 Å) < **1** (2.192 Å) << **2** (2.389 Å). As mentioned in section A, the metal–chloride bond lengths are overestimated in the calculations, especially for compound **1**. Correspondingly, the calculated frequency obtained for **1** of 336 cm^{-1} is significantly lower than the

experimental value, whereas for **2** (319 cm⁻¹) and **3** (398 cm⁻¹) a very good agreement is observed. To compare the M–Cl bond strengths in these compounds rigorously, accurate M–Cl force constants are necessary and require a normal coordinate analysis (NCA). For this purpose, simple model systems [Fe(P)(Cl)] (**1̃**), [Mn(P)(Cl)] (**2̃**), and [Co(P)(Cl)] (**3̃**; P = porphine) were fully optimized, and the force constants were calculated as listed in Table 4. In the next step, a mass of 77 was used for the meso hydrogens of these models corresponding to the phenyl groups. This leads to models **1̃a**, **2̃a**, and **3̃a**, which accurately reproduce the M–Cl frequencies of full model systems **1–3** applying TPP (cf. Table 4). This is an important result because it shows that the simple porphine ligand is a good approximation for TPP when only the properties of the central M–Cl unit are considered. Finally, using the QCC-NCA procedure,²¹ the M–Cl force constants were fitted to reproduce the experimental M–Cl stretching frequencies. In this way, experimental force constants for compounds **1**, **2**, and **3** of 1.796, 0.932, and 1.717 mdyn/Å, respectively, were obtained. The NCA force constants show that the Fe–Cl and Co–Cl bonds are twice as strong as the Mn–Cl bond. The reason for this rather surprising result is evidenced by an analysis of the MO diagrams of these complexes. For this purpose, models **1̃–3̃** were used because porphine has proven to be a good model for TPP, considering the presence of the M–Cl bond. The coordinate system is chosen such that the *z* axis is aligned with the M–Cl bond, whereas the *x* and *y* axes are oriented along the M–N bonds of the porphyrin ligand. Hence, the d_{x²–y²} orbital of the metal undergoes a strong σ bond with the pyrrole nitrogens of the porphyrin, whereas d_{xy} is partially nonbonding. However, the metal–chloride σ bond is mediated by the orbital d_{z²}, whereas d_{xz} and d_{yz} are potentially involved in π bonds with the chloride ligand. Note that the principal bonding scheme of [Fe(TPP)(Cl)] has been analyzed before; however, the main focus was the metal–porphyrin interaction.⁴⁸

[Co(TPP)(Cl)] (**3**) has the simplest electronic structure due to the low-spin d⁶ configuration of Co(III) (*S* = 0), which corresponds to a [d_{xy},d_{xz},d_{yz}]⁶ \equiv [t₂]⁶ configuration of the metal. Hence, the unoccupied d_{z²} orbital undergoes a strong σ bond with the filled p_z orbital of the chloro ligand, where the corresponding bonding combination has 29% d_{z²} and 58% chloro p_z character. Because the d_{xz} and d_{yz} orbitals of the metal are fully occupied, no π bond with the p_x and p_y orbitals of chloride is possible. In summary, the metal–Cl bond in **3** can be described as a strong (pure) σ bond. In comparison, compound **1** is a high-spin d⁵ complex with *S* = 5/2 ground state. In the spin-unrestricted scheme, this means that all α -d orbitals are fully occupied and hence, do not contribute to the bonding with σ - or π -donor ligands. Therefore, all metal–ligand bonding comprises unoccupied β -d orbitals. The Fe–Cl σ bond is mediated by the interaction of d_{z²} and p_z of the chloro ligand. The corresponding bonding combination has

26% iron d_{z²} and 60% chloro p_z orbital contributions, which corresponds to a strong σ bond. Additional π bonds between the d_{xz} and d_{yz} orbitals of iron and the p_x and p_y orbitals of the chloro ligand, respectively, are also present. The corresponding bonding combinations have about 10% metal and about 45% chloride character indicative of a medium-strength interaction. Therefore, complex **1** formally has one-half of a σ bond and one π bond. Compared to **3**, the σ bond is reduced by 50%, whereas an additional π bond is present. These effects seem to cancel, giving almost identical M–Cl force constants in these complexes.

Compound **2** is a high-spin d⁴ complex with *S* = 2 ground state and a [d_{xz},d_{yz},d_{xy},d_{z²}]⁴ electron configuration. Compared to complex **1**, the α -d_{x²–y²} orbital is unoccupied and therefore, similar M–Cl interactions would be expected in **1** and **2**. However, the force constants show that this is not the case. The Mn–Cl σ bond between d_{z²} and the p_z orbital of chloride is somewhat weaker compared to that in **1** as evidenced by the 16% metal d_{z²} and 57% chloro p_z character of the corresponding bonding combination. The largest difference occurs for the M–Cl π bond. The corresponding bonding combinations between d_{xz} and d_{yz} of Mn(III) and p_x and p_y of chloride only have about 2% metal and 75% chloro character, respectively, which corresponds to a very weak interaction. Therefore, the M–Cl bond in complex **2** corresponds only to half a σ bond. This is the reason for the much smaller M–Cl force constant of only 0.932 mdyn/Å in **2** compared to 1.796 mdyn/Å for **1**.

E. Metal-Sensitive Bands in the Raman and IR Spectra of 1–3. Boucher and Katz⁴⁹ measured the IR spectra of several divalent metal complexes of protoporphyrin IX and hematoporphyrin IX dimethyl ester and identified three metal-sensitive bands at 920–980, 500–525, and 350–365 cm⁻¹, but no definitive assignments could be made. The skeletal stretching and breathing modes were found to only have small shifts within the experimental uncertainty. Nakamoto and co-workers assigned the metal–nitrogen stretching bands of a series of OEP and TPP complexes on an empirical basis.^{50,18a} The observed shifts were attributed to the variable occupation of the σ -antibonding d_{x²–y²} orbital in these complexes. Hence, vibrations that contain a direct contribution of the M–N stretching coordinate should be the most affected. However, the oxidation- and spin-state sensitive IR bands I–III and Raman bands A, C, D, and E (band B is characteristic for penta coordination) as described in the Introduction should also be sensitive to the metal ion.¹⁸ The frequency shifts of bands I and III were correlated to the metal–porphyrinato nitrogen distances^{18b} in agreement with Nakamoto's analysis.

In the IR and NR Raman spectra of **1**, 50 and 36% of the observed modes, respectively, are of the phenyl type, which show no shifts or show only small frequency shifts.⁵¹ In contrast, frequency shifts are observed for most porphyrin

(47) Chottard, G.; Battioni, P.; Battioni, J.-P.; Lange, M.; Mansuy, D. *Inorg. Chem.* **1981**, *20*, 1718–1722.

(48) Cheng, R.-J.; Chen, P.-Y.; Lovell, T.; Liu, T.; Noodleman, L.; Case, D. A. *J. Am. Chem. Soc.* **2003**, *125*, 6774–6783.

(49) Boucher, L. J.; Katz, J. J. *J. Am. Chem. Soc.* **1967**, *89*, 1340–1345.

(50) Ogoshi, H.; Masai, N.; Yoshida, Z.; Takemoto, J.; Nakamoto, K. *Bull. Chem. Soc. Jpn.* **1971**, *44*, 49.

(51) Very small shifts of some of these bands that were observed can be traced back to small admixtures of porphyrin core vibrations.

Table 5. Metal-Sensitive Bands (Also Oxidation- and Spin-State-Sensitive) in the Infrared, NR Raman, and RR Spectra of **1–3**^a

		FeTPP(Cl) (1)		MnTPP(Cl) (2)		CoTPP(Cl) (3)	
		experimental	calcd ^b	experimental	calcd ^b	experimental	calcd ^b
	M–N (Å), averaged	2.049	2.09	2.019	1.99	1.985	1.99
IR ^{18b}	band I, spin (cm ⁻¹)	1340/1334	1369	1342	1377	1351	1387
	band II, ox. (cm ⁻¹)	806	847	804	849	795	848
	band III, spin (cm ⁻¹)	434	444	451	462	465	475
R ^{18b}	band A, ox., and spin (cm ⁻¹)	1363	1379	1365	1390	1359	1393
	band B ^c (cm ⁻¹)	1371	1398	1373	1406	1372	1408
	band C, spin (cm ⁻¹)	1522/1516	1560	1538/1532	1588	1588	1588
	band D, spin (cm ⁻¹)	1554	1598	1557	1612	1563	1626
	band E, ox. (cm ⁻¹)	390	388	393	392	403	390
IR	$\nu(\text{M–Cl})$	378	336	296	319	397	399
	ν_{50} (cm ⁻¹)	402	407	410/405	411	?	411
R	ν_{18} (cm ⁻¹)	199	202	223	218	255 ?	238

^a Frequencies are given in cm⁻¹. ^b Calculated with B3LYP/LanL2DZ. ^c Band B is a marker band for five-coordinate porphyrin complexes.^{47,18b}

Table 6. Selected Crystallographic Distances (Å) for Compound **1** (cf. Ref 28), **2** (This Article), and **3** (cf. Ref 33) that are Important for the Structure-Sensitive Bands^a

compound	$d(\text{M–N})$	$d(\text{C}_m\text{–Ph})$	$d(\text{C}_\beta\text{–C}_\beta)$	$d(\text{C}_\alpha\text{–C}_\beta)$	$d(\text{C}_\alpha\text{–N})$	$d(\text{M–Ct})$	$d(\text{C}_\alpha\text{–C}_m)$
[Fe(TPP)(Cl)] (1)	2.04(9)	1.50(8)	1.38(0)	1.44(6)	1.38(4)	0.383	1.39(9)
[Mn(TPP)(Cl)] (2)	2.019	1.496	1.357	1.440	1.385	0.258	1.399
[Co(TPP)(Cl)] (3)	1.985	1.518	1.360	1.446	1.372	0.05	1.391

^a Distances are averaged over chemically equivalent bonds.

core vibrations in the [M(TPP)(Cl)] complexes, but only a few of them are of considerable size as already correctly stated by Boucher and Katz. The bands with large shifts are mostly vibrations with a large M–N stretching contribution as proposed before.^{18,50} Hence, frequency shifts are mostly expected for bands below 500 cm⁻¹. Table 5 lists the experimental and calculated frequencies of the eight spin- and oxidation-state-sensitive bands known from the literature for complexes **1–3**. In the IR spectra, the three porphyrin vibrations I–III show metal sensitivity. In the NR Raman spectra, three modes show significant shifts for complexes **1–3** (band A, D, and E). Hence, only six of the eight structurally sensitive bands from the literature are metal-sensitive in the [M(TPP)(Cl)] series studied here. Three additional metal sensitive bands are identified here. These are ν_{18} (from NR Raman), ν_{50} (IR), and the M–Cl stretching vibration as discussed in section D (cf. Table 4). Corresponding to the relatively small frequency shifts observed for **1–3** as shown in Table 5, the underlying differences in complex geometries must be small. Therefore, to analyze the reasons for the appearance of the shifts, detailed assignments of the corresponding vibrations as obtained in this study are necessary. For the stretching vibrations, the differences in the vibrational frequencies can be correlated with the differences in bond lengths. However, the interpretation of the metal sensitivity of the deformation modes is not straightforward.

Vibrations with a considerable M–N contribution are observed in the low-energy region of the spectra. The metal–nitrogen distances decrease in the order of Fe (2.049 Å) > Mn (2.019 Å) > Co (1.985 Å), and hence the frequencies of vibrations with $\nu(\text{M–N})$ character are expected to increase in the order of Fe < Mn < Co. There are three vibrations with a pure or mostly M–N stretching contribution observed in complexes **1–3**. The most intense band corresponds to

the totally symmetric $\nu_{\text{breathing}}(\text{M–N})$ vibration (band E, ν_8), which increases in the order of 390 cm⁻¹ (Fe) < 393 cm⁻¹ (Mn) < 403 cm⁻¹ (Co) in agreement with this trend. The $\nu(\text{M–N})$ vibrations with B_{1g} symmetry (ν_{18}) observed in the NR Raman spectra of **1–3** also strongly follows this trend as shown in Table 5. Finally, the $\nu(\text{M–N})$ vibrations with E_u symmetry (ν_{50}) observed in the IR spectra of **1** and **2** are mixed with the $\delta(\text{Pyr. translation})$ porphyrin deformation mode. Nevertheless, the correlation also applies here where this feature appears at 402 cm⁻¹ in **1** and at 410/405 cm⁻¹ in **2**. The fact that this band is split in **2** reflects a small degree of symmetry lowering from ideal D_{4h} symmetry (cf. section B.5).

Bands A, C, and D in the Raman and band I in the IR spectra of **1–3** correspond to in-plane porphyrin stretching vibrations (cf. Table 3); therefore, their frequencies can be correlated with C–C, C–N, and M–N distances as observed in the crystal structures of **1–3** (cf. Table 6). Band A corresponds to the in-plane $\nu_{\text{sym}}(\text{Pyr. half-ring})$ porphyrin vibration. Hence, the frequency of this mode relates to changes in the metal–nitrogen, the C_α–C_β and the C_α–N distances. However, because the observed frequency shifts are very small, a quantitative interpretation of the observed behavior of this mode is not possible. For band C, the observed frequency is larger for the Mn than for the Fe complex. This mode has considerable $\nu_{\text{asym}}(\text{C}_\alpha\text{–C}_m)$ character; however, the C_α–C_m distance is comparable in the two complexes, as shown in Table 6. However, this mode also has some C_α–C_β contribution, and the corresponding C_α–C_β distance is slightly larger for **1** compared to that for **2**, which is consistent with the observed trend in frequencies (cf. Table 5). The totally symmetric metal-sensitive band D, which is assigned to a $\nu(\text{C}_\beta\text{–C}_\beta) + \nu_{\text{sym}}(\text{C}_\alpha\text{–C}_m)$ porphyrin vibration with a small amount of $\delta_{\text{asym}}(\text{C}_\beta\text{–H})$ contribution, is observed in both the NR Raman and RR spectra of **1–3**.

The frequency of this mode increases in the order of $1 < 2 < 3$, as shown in Table 5. This can be traced back to differences in the C–C bond lengths of the porphyrin core. First, the C_{β} – C_{β} distances are almost identical for **2** and **3**, whereas they are elongated in **1**. However, complexes **1** and **2** have almost identical C_{α} – C_m distances, whereas this bond is shorter in complex **3**. These trends are consistent, leading to the observed frequency shifts of this band. Finally, band I corresponds to the mixed $\delta_{\text{asym}}(C_{\beta}\text{--H}) + \nu(C_m\text{--Ph}) + \nu_{\text{sym}}(\text{Pyr. half-ring}) + \nu_{\text{asym}}(C_{\alpha}\text{--}C_{\beta})$ in-plane porphyrin vibration. The frequency shift of this band cannot be analyzed because of a large number of different contributions. For example, the C_m –Ph distances behave inversely to the M–N distances. Besides these stretching vibrations, two deformation modes (bands II and III; cf. Table 5) are also found to be metal-sensitive. Band II corresponds to the out-of-plane $\gamma(H_{\beta}) + \gamma_{\text{sym}}(\text{Pyr. folding})$ porphyrin deformation mode and hence, the frequency shift of this vibration is difficult to interpret. The energy increases in the order of $\text{Co} \ll \text{Mn} < \text{Fe}$. The frequency shift of band III, which is an in-plane $\delta(\text{Pyr. rotation})$ porphyrin deformation mode, seems to be correlated to the out-of-plane displacement of the metal, which increases in the order of $\text{Co} < \text{Mn} < \text{Fe}$. Correspondingly, the observed trend in the vibrational energies is $\text{Co} > \text{Mn} > \text{Fe}$.

Discussion

In this study, the vibrational properties of the five-coordinate porphyrin complexes $[\text{M}(\text{TPP})(\text{Cl})]$ ($\text{M} = \text{Fe}, \text{Mn}$, and Co) are analyzed in detail. For complex $[\text{Fe}(\text{TPP})(\text{Cl})]$ (**1**), nonresonance Raman (NR Raman) spectra including polarized data are presented for the first time. Resonance Raman (RR) spectra of this compound are also reported, including Soret, Q, and Q_v resonance data together with polarized measurements. In addition, MIR and FIR spectra of **1** are presented. Hence, a complete vibrational data set for complex **1** is obtained in this study. These data are then assigned in detail using calculated vibrational energies as well as calculated NR Raman and IR intensities, which show very good agreement with experiment overall (vide infra). Additional information that assists in assigning the spectra is available from (a) the polarized measurements that allow for the determination of the symmetries of the different vibrations and (b) d_8 isotope data reported in the literature for a number of complexes.^{13,14b,18b} The assignments are based on an idealized model system $[\text{M}(\text{TPP})]$ with D_{4h} symmetry. For the phenyl mode assignment, local internal coordinates derived from bromobenzene are used. On the basis of all this information, a complete and consistent assignment of all of the spectroscopic data obtained for **1** has been achieved. So far, no detailed vibrational assignments for five-coordinate porphyrin complexes such as $[\text{Fe}(\text{TPP})(\text{Cl})]$ are available from the literature, where most of the research has been focused on four-coordinate complexes. For compound **1**, only a small number of totally symmetric modes from the Soret RR spectrum ($\lambda_{\text{exc}} = 457.9 \text{ nm}$) have been assigned before,²⁰ on the basis of a simple comparison of the obtained spectra with those of $[\text{Ni}(\text{TPP})]$. Additional bands in the Raman and

IR spectra of **1** were identified and classified, but no further analysis was performed.^{14,18b} The assignments obtained in this study are in general consistent with recent work by Rush III et al., who assigned the RR and IR spectra of $[\text{Ni}(\text{TPP})]$ based on a DFT-SQM analysis.¹³ In some cases, large deviations in vibrational frequencies (for example, ν_2 is located at 1554 cm^{-1} in **1** and at 1572 cm^{-1} in $[\text{Ni}(\text{TPP})]$) are observed. In addition, because of very good agreement between the calculated and experimental NR Raman and IR spectra obtained here, more sophisticated assignments of the observed vibrations were possible in this study, as indicated in Table 3. The complete analysis of the vibrational spectra of **1** performed here also leads to the reassignment of a number of bands. These include features at 1233 , 1006 , and 886 cm^{-1} in the Raman spectra of **1** (cf. Table 3). The prominent band at 390 cm^{-1} , which is one of the structure-sensitive bands identified by Burke et al.,^{14b} is reassigned to the totally symmetric $\nu_{\text{breathing}}(\text{Fe}\text{--N})$ vibration on the basis of the calculated NR Raman spectra and the excellent agreement between its calculated and experimental pyrrole- d_8 isotope shift. This is in agreement with the assignments for $[\text{Ni}(\text{TPP})]$.^{10a,13} The IR spectra of complex **1** are assigned here for the first time with the exception of structure-sensitive bands I–III. However, band II at 806 cm^{-1} is reassigned in this work to the out-of-plane $\gamma(H_{\beta}) + \gamma_{\text{sym}}(\text{Pyr. folding})$ porphyrin core vibration on the basis of the calculated IR spectra and the excellent agreement between its calculated and experimental pyrrole- d_8 isotope shift. In addition, a number of new bands are assigned in this study. These include the important bands at 402 cm^{-1} in the IR (ν_{50}) and 199 cm^{-1} in the Raman spectrum (ν_{18}) of **1**, which correspond to the Fe–N stretching vibrations with E_u and B_{1g} symmetries. These modes have not been assigned yet. Similar to the corresponding A_{1g} mode at 390 cm^{-1} , these are also strongly metal-sensitive and probably oxidation- and spin-state-sensitive.

A general shift of the vibrational frequencies of **1**–**3** to somewhat higher energy (average deviation: about 2 to 3%) is observed in the calculations compared to experiment. However, in some cases, larger deviations (up to 5%) are observed. These can be traced back to different effects depending on the nature of the respective modes. First, large shifts (about 5%) are observed for the three combinations of the $\nu_{\text{sym}}(\text{C}\text{--C})$ stretching mode of the phenyl rings (ϕ_4 , ϕ_4' , ϕ_4'' in Table 3), which occur just below 1600 cm^{-1} . In this case, the deviations are partly due to an intrinsic inaccuracy of the B3LYP/LanL2DZ method. This is evident from frequency calculations on benzene. As shown in Table S7, $\nu_{\text{sym}}(\text{C}\text{--C})$ is calculated at 1641 and observed at 1594 cm^{-1} (average), which corresponds to a deviation of 2.9%. Interestingly, using the much more time consuming B3LYP/TZVP method does not lead to an improvement for this mode. The second class of vibrations in which larger deviations of the frequencies are observed correspond to in-plane and out-of-plane C–H deformation modes. This especially includes the $\delta(C_{\beta}\text{--H})$ and $\gamma(H_{\beta})$ core vibrations and the $\delta(\text{C}\text{--C}\text{--H})$ bends of the phenyl rings. (See, for example, $\delta(C_{\beta}\text{--H})$ at about 1100 cm^{-1} , $\gamma(H_{\beta})$ at about 800

cm^{-1} , and $\delta(\text{C}-\text{C}-\text{H})$ at about 1100 cm^{-1} , as listed in Table 3.) These deviations are due to the neglect of anharmonicity effects in the theoretical treatment. Calculations on benzene show that C–H vibrations usually show significant degrees of anharmonicity (cf. Table S7). These calculations indicate that $\nu_{\text{sym}}(\text{C}-\text{C})$ is also affected by deviations due to anharmonicity. Finally, differences are observed for the amount of mixing between phenyl and porphyrin core vibrations, which applies to a small number of modes (Results and Analysis). This is evident from a comparison of calculated and experimental d_8 isotope shifts, which reflect the porphyrin core mode contribution. In the case of **1**, the calculated structure shows smaller dihedral angles between the phenyl substituents and the porphyrin core compared to the crystal structure. Hence, this rotation of the phenyl rings toward the porphyrin plane introduces changes in mode mixing of phenyl and porphyrin core vibrations. This most probably explains the observed deviations.

Three major effects of symmetry lowering from the idealized D_{4h} symmetry of the $[\text{M}(\text{TPP})]^+$ core are observed for complexes **1–3**. Compared to four-coordinate $[\text{Ni}(\text{TPP})]$ and corresponding systems, the chloro complexes studied here show the additional complexity of having open shells, a larger distortion of the porphyrin core, and axial ligands. From vibrational spectra, these deviations from D_{4h} are manifested in (i) enhanced coupling between porphyrin core and phenyl vibrations, (ii) the combination of even (g) and odd (u) vibrations, and (iii) small splittings of the degenerate E_u vibrations. However, these effects are very small and therefore, together with the observation of polarized, depolarized, and anomalous polarized bands in the Raman spectra, this clearly shows that the $[\text{M}(\text{TPP})]^+$ cores of **1–3** still behave as if they have D_{4h} symmetry. As discussed above, the assignments of the vibrational spectra of complexes **1–3** are therefore carried out in an effective D_{4h} symmetry. The overall vibrational properties of the $[\text{M}(\text{TPP})]^+$ units in complexes **1–3** are quite similar, which relates to the large structural similarities of the metalloporphyrin cores of these systems. The largest differences are observed in the low-energy region of the spectra, where the M–Cl and the M–N stretching vibrations are observed. On the basis of our analysis, it is possible to give more precise assignments of the metal-sensitive modes than before, as inferred by Oshio et al.^{18b} in 1984: “In order to understand the structure-sensitivity of these bands on a quantitative basis, it is necessary to carry out theoretical calculations [...]” Not surprisingly, it is found that modes with mostly phenyl character do not show noticeable shifts. In the case of porphyrin core vibrations, frequency shifts are in general observed for most vibrations; however, only a few of them are of considerable size. Of the eight oxidation and spin-state-sensitive bands known from the literature,¹⁸ five are found to be metal-sensitive in the $[\text{M}(\text{TPP})(\text{Cl})]$ series studied here. These are bands A, D, and E (RR) and bands I–III (IR). In addition, two more metal-sensitive porphyrin core vibrations are identified here (ν_{50} and ν_{18} , vide supra). Bands with large M–N stretching contributions are sensitive because of the differences in the M–N bond lengths in **1–3**,

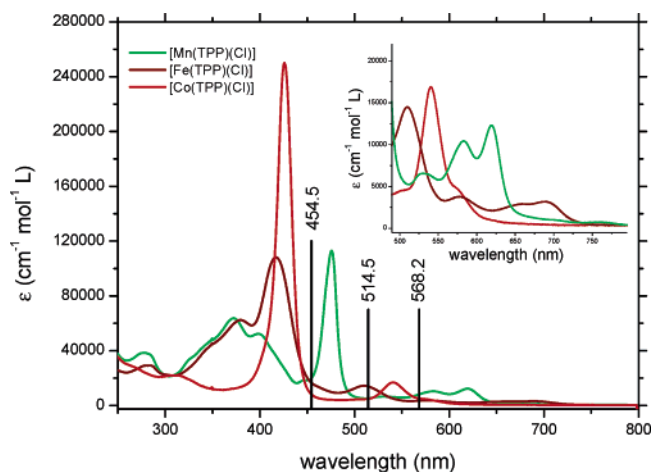
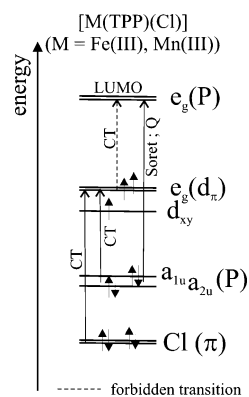


Figure 7. Solution absorption spectra of compound **1** (brown) measured in chloroform, of compound **2** (green) in a 1/1 mixture of butyronitrile and propionitrile, and of compound **3** (red) in methanol. The spectra are scaled with absorption coefficients taken from the literature.^{58,59,33}

Table 7. Absorption Bands Observed in the UV–Vis Absorption Spectra of Complexes **1–3** (in nm)

[Fe(TPP)Cl] (1)		[Mn(TPP)(Cl)] (2)		[Co(TPP)(Cl)] (3)	
position	assignment	position	assignment	position	assignment
379	Cl → M CT	390	Soret		
417	Soret	476	P → M CT	426	Soret
510	Q _v	530	?	540	Q _v
578	?	583	Q _v	574	Q
654	P → M CT	620	Q		
690	P → M CT ?				

Scheme 2



which applies to bands E, ν_{50} , and ν_{18} . These occur in the low-energy region of the spectra. Bands I, A, C, and D correspond to porphyrin core stretching modes. In this Article, we have developed a model where the shifts of these bands are interpreted on the basis of differences in the porphyrin C–C and C–N and the metal–N distances. The interpretation of the frequency shifts of remaining vibrations I and II is not straightforward because of the fact that these are deformation modes.

Besides the analysis of the metal-sensitive modes, we have investigated the strength of the metal–chloride interaction in complexes **1–3**. To this end, the M–Cl stretching vibrations have been assigned, and from normal coordinate analysis (NCA), M–Cl force constants of 1.796 (Fe–Cl), 0.932 (Mn–Cl), and 1.717 $\text{mdyn}/\text{\AA}$ (Co–Cl) have been determined. These large differences in M–Cl bond strengths

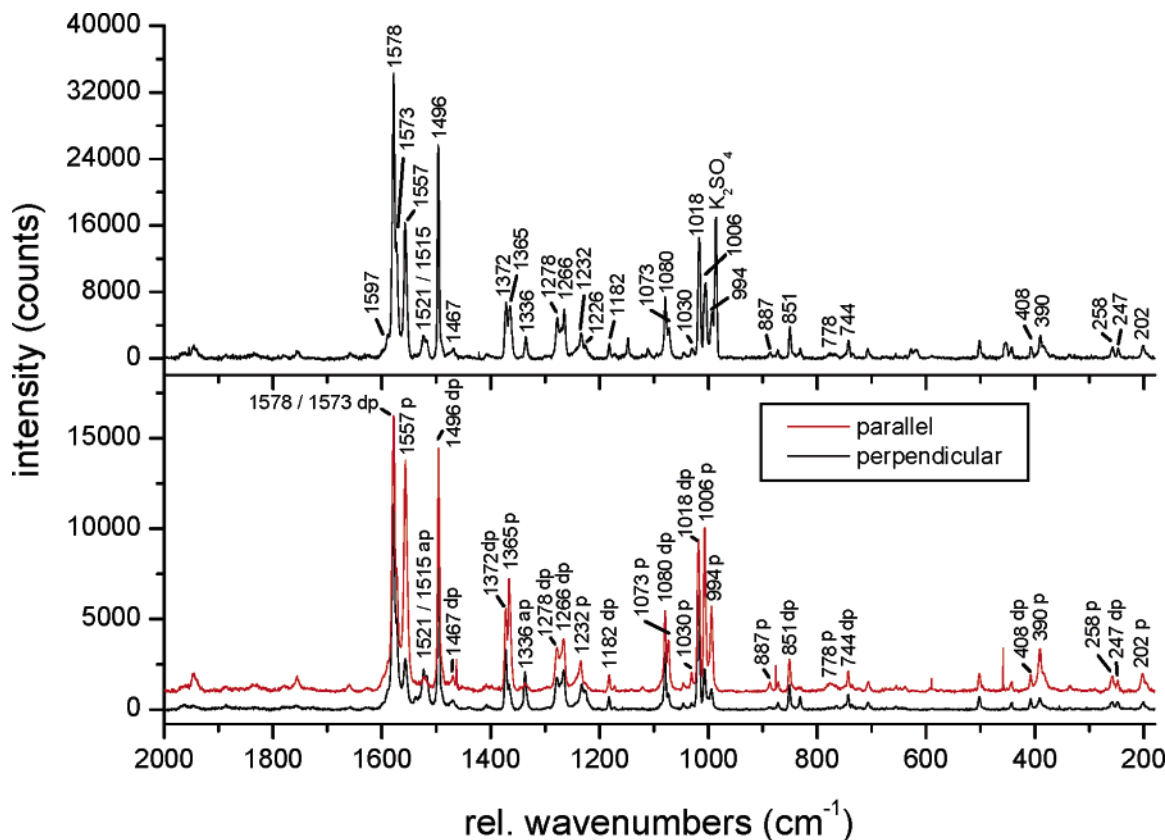


Figure 8. Resonance Raman spectra of **1**, excited at 568.2 nm (Q resonance). The RR spectra were measured with potassium sulfate as the internal standard (top). The polarized measurement is shown on the bottom.

are reflected by the M–Cl bond distances of 2.192 Å in **1**, 2.389 Å in **2** and 2.145 Å in **3**. For **2**, this value is obtained from a new crystal structure presented here. An analysis of the MO diagrams of **1–3** allows for a determination of the electronic structural reasons for these differences. In the case of compound **1**, the Fe–Cl bond can roughly be classified as one-half of a σ bond and one π bond. In comparison, the Co–Cl bond in **3** corresponds to one σ bond. The similar M–Cl force constants obtained for **1** and **3** indicate that the enhanced σ and the reduced π interaction in **3** compared to those in **1** seem to compensate and lead to comparable bond strengths. The strongly reduced M–Cl bond strength in **2** compared to that in **1** (and **3**) is mostly due to a lack of the M–Cl π bond in this complex. Correspondingly, the Mn–Cl bond only corresponds to half a σ bond in agreement with the observed reduction of the force constant by half in **2** (0.932 mdyn/Å) compared to that in **1** (1.796 mdyn/Å).

Besides its use for the determination of vibrational energies, RR spectroscopy offers detailed insight into the nature of electronically excited states. This relates to the mechanism of resonance enhancement and the actual nature of enhanced vibrations. For metalloporphyrins, A-, B- and C-term enhancements are important,⁴⁰ as described in section B.4. The A-term mechanism is dominant in the region of the intense Soret transition and leads to the enhancement of totally symmetric modes. B-term enhancement is found in the region of Q and Q_v bands and relates to vibronic coupling, which is manifested in the enhancement of anomalous polarized A_{2g} modes. Complex **3** shows the simplest absorp-

tion spectrum of compounds **1–3**, investigated here (cf. Figure 7). In this case, the Soret transition is located at 426 nm (cf. Table 7). At lower energy, the band at 540 nm is assigned to Q_v and the shoulder at 574 nm to the Q band, which is in agreement with the assignments for [Co(TPP)] from the literature.³⁸ These assignments are further confirmed using RR spectroscopy. Excitation at 514.5 and 568.2 nm leads to the enhancement of the anomalous polarized vibration ν_{20} at 1335 cm⁻¹ (cf. Table S2). This indicates that the band at 540 nm is the Q_v band and the shoulder at about 574 nm must then correspond to Q. The separation of these features of about 1100 cm⁻¹ supports this assignment.³⁸ The fact that no other bands are observed in the absorption spectrum of **3** relates to the low-spin d⁶ electron configuration of the metal, which prohibits low-energy porphyrin → metal or chloride → metal charge-transfer transitions.

The absorption spectrum of compound **1** is more complicated and shows at least six bands at 379, 417, 510, 578, 654, and 690 nm (cf. Table 7). Because of the high-spin d⁵ configuration of iron in this complex, porphyrin to metal charge-transfer (P → M CT) transitions can now occur (cf. Scheme 2). These a_{1u}(π), a_{2u}(π) → e_g(d _{π}) CT transitions have been assigned to bands near 600 nm for high-spin Fe^{III} porphyrin complexes.^{15a} Because the corresponding excited states have E_u symmetry in idealized D_{4h} symmetry, strong CI mixing with the nearby Q excited state might also occur. In addition, chloro to iron charge-transfer transitions (Cl → M CT) might also be present in the spectra. The Soret band in complex **1** appears split with its components located at

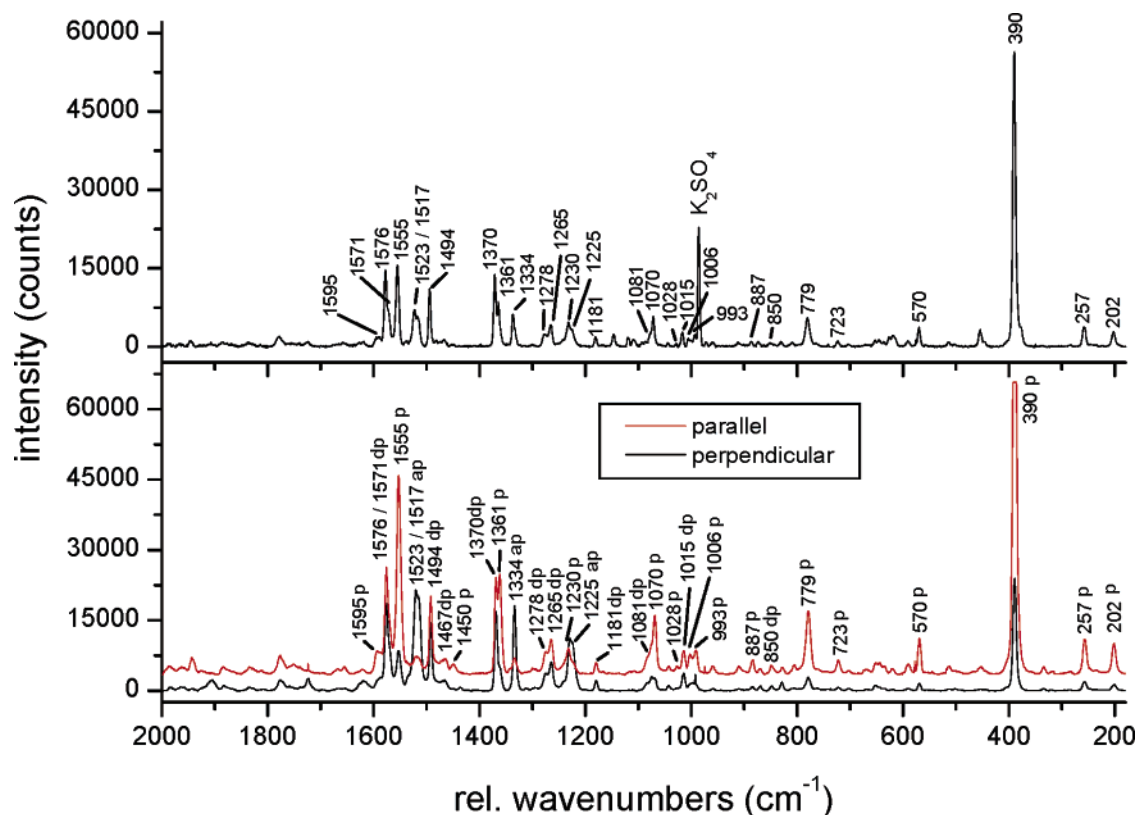


Figure 9. Resonance Raman spectra of **1**, excited at 514.5 nm (Q_v resonance). The RR spectra were measured with potassium sulfate as the internal standard (top). The polarized measurement is shown on the bottom. In the perpendicular measurement, the 390 cm^{-1} band is cut off because of its large intensity.

about 379 and 417 nm (cf. Figure 7). Further insight into these band assignments can be gained from RR measurements. The RR spectrum of **1**, excited at 454.5 nm shows mostly totally symmetric vibrations (cf. Figure 10); therefore, the absorption band at 417 nm is assigned to the Soret band. From the literature, the 379 nm band has been assigned to a chloride $\rightarrow \text{Fe}^{\text{III}}$ charge-transfer transition.^{52,53} However, the large intensity of this band indicates that the corresponding excited state might steal some intensity from the Soret band. The remaining four absorption bands are located in the Q region of **1**. The RR spectrum of **1**, excited at 568.2 nm (cf. Figure 8) shows a weak band, and the data obtained at 514.5 nm (cf. Figure 9) show medium-intensity anomalous polarized bands, indicating vibronic coupling (anomalous polarized bands that are typically observed are located at about 1520 and 1335 cm^{-1}). In addition, overtones are enhanced with excitation into the absorption band at 510 nm (cf. Figure S2), which indicates that this band is actually the Q_v band (see Section B.4). Hence, a possible assignment might be that Q and Q_v correspond to the bands at about 578 and 510 nm, respectively. However, the separation of these absorption bands of about 2350 cm^{-1} is too large. It should only be about 1250 cm^{-1} , as determined by Gouterman.³⁸ Hence, the Q band is probably weak in **1** and masked by the feature at 578 nm, the nature of which is not known. The RR spectrum,

excited at 647.1 nm (cf. Figure S5), shows not only the usually observed porphyrin A_{2g} modes at 1335 and 1522 cm^{-1} but also the low-energy anomalous polarized bands (Figure S5) that are not observed at any other excitation wavelength. These low-energy bands correspond to in-plane porphyrin deformation modes with some phenyl out-of-plane mode contribution. Hence, the band at 654 nm shows a completely different excitation behavior than the usual Q and Q_v band enhancements. This indicates that the band at 654 nm might correspond to the $P \rightarrow \text{Fe}$ CT transition in agreement with the prediction from the literature.¹ Because this transition leads to two excited states with E_u symmetries (cf. Scheme 2), the second component could correspond to the band at 690 nm, but this is only speculative.

In the case of **2**, the absorption spectrum shows two strong bands in the Soret region at 476 (band V⁵⁴) and 390 nm (band VI⁵⁵) (cf. Table 7). This has been attributed to a CI mixing of the Soret excited state with the porphyrin to metal $a_{1u}(\pi)$, $a_{2u}(\pi) \rightarrow e_g(d_\pi)$ charge-transfer states with E_u symmetry³⁸ (cf. Scheme 2). Note that this requires a shift of the $P \rightarrow \text{M}$ CT states from the visible to the UV region compared to that in **1**. Because of the stronger RR enhancement of low-energy vibrations observed, including Mn–X (X = halide) and Mn–N stretching modes in the region of band V in [Mn(ETP)(Cl)] (ETP = etioporphyrin I), this feature

(52) Spiro, T. G.; Li, X.-Y. In *Resonance Raman Spectra of Heme and Metalloproteins*; Spiro, T. G., Ed.; Wiley: New York, 1988; pp 1–37.

(53) Hendrickson, D. N.; Kinnaird, M. G.; Suslick, K. S. *J. Am. Chem. Soc.* **1987**, *109*, 1243–1244.

(54) Boucher, L. J. *Coord. Chem. Rev.* **1972**, *7*, 289–329.

(55) Parthasarathi, N.; Hansen, C.; Yamaguchi, S.; Spiro, T. G. *J. Am. Chem. Soc.* **1987**, *109*, 3865–3871. (b) Gaughan, R. R.; Shriver, D. F.; Boucher, L. J. *Proc. Natl. Acad. Sci. U.S.A.* **1975**, *72*, 433.

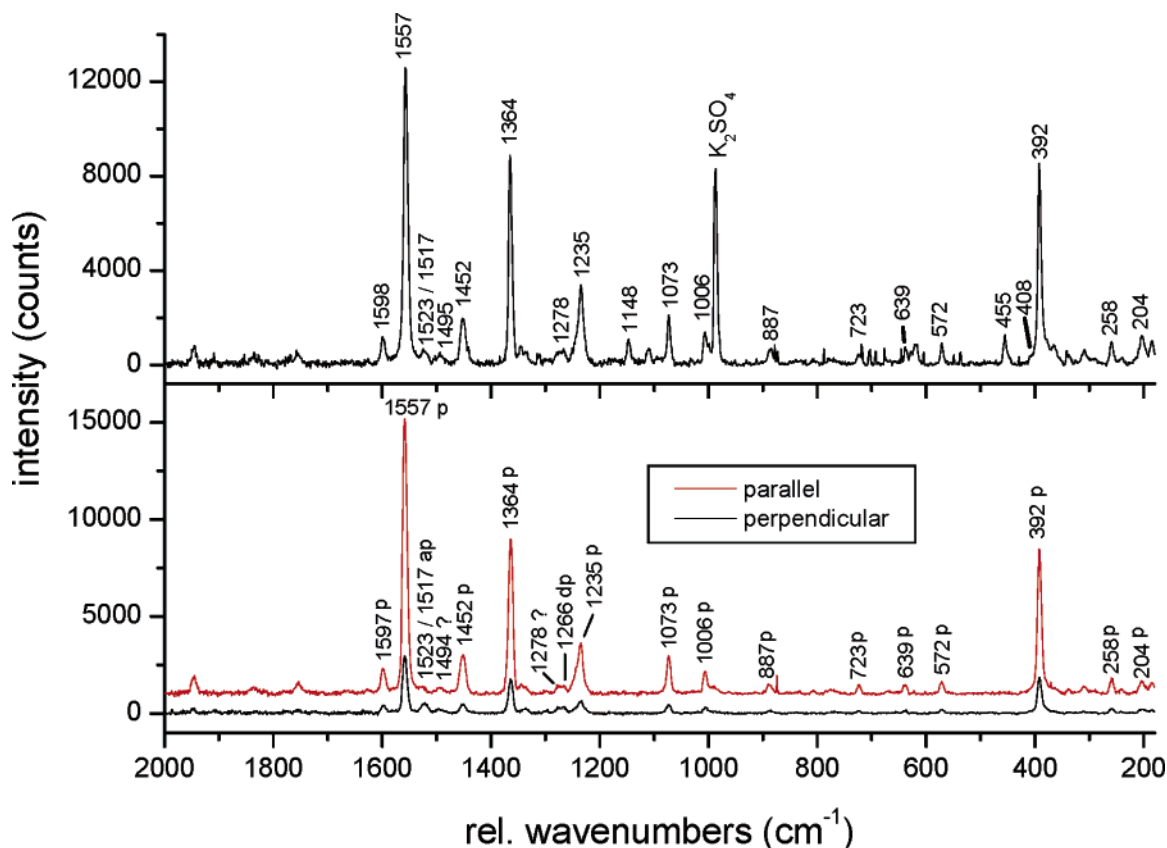


Figure 10. Resonance Raman spectra of **1**, excited at 454.5 nm (Soret resonance). The RR spectra were measured with potassium sulfate as the internal standard (top). The polarized measurement is shown on the bottom.

has been assigned to the predominant CT transition.⁵⁶ Note that Soret excitation in general leads to the enhancement of higher-energy porphyrin core vibrations. A stronger enhancement of the low-energy bands in the RR spectrum upon excitation at 488 nm is also found for compound **2** compared to that in the Soret RR spectra of **1** and **3**, indicating that this analysis is correct. It is important to note that the most intense band in this spectrum for **2** is the feature at 393 cm^{-1} , which corresponds to the totally symmetric $\nu_{\text{breathing}}(\text{Mn}-\text{N})$ vibration. The RR excitation profiles of this mode differ significantly for compounds **2** and **1**, as shown in Figures S3 and S4. For complex **1**, the maximum enhancement appears in Q_v resonance, whereas complex **2** shows the maximum upon excitation into band V. More importantly, the RR spectrum of **2**, excited at 454.5 nm shows anomalous polarized bands indicating the vibronic character of band VI, which is centered around 390 nm. This has also been observed by Parthasarathi et al.,⁵⁵ who obtained two anomalous polarized bands at 1339 and 1529 cm^{-1} upon excitation at 406.7 nm in **2**. This indicates that the simple hyperporphyrin model by Gouterman³⁸ might not be sufficient to explain the occurrence of bands V and VI in $[\text{Mn}(\text{TPP})(\text{Cl})]$. In the lower-energy region, the RR spectrum obtained at an excitation wavelength of 568 nm again shows

anomalous polarized bands that indicate vibronic coupling. Therefore, the band at about 583 nm is assigned to the vibronic band, Q_v , and the band at 620 nm to Q (cf. Table 7). The separation of these bands of about 1020 cm^{-1} is in agreement with this assignment. In addition, corresponding bands at 560 and 592 nm in $[\text{Mn}(\text{ETP})(\text{Cl})]$ have also been attributed to these features.⁵⁶ Finally, the nature of the band at about 530 nm is not clear. Anomalous polarized bands are present in the RR spectra but only with low intensity upon excitation at 514.5 nm .

Acknowledgment. We gratefully acknowledge the financial support provided by the Deutsche Forschungsgemeinschaft (DFG; grant LE 1393/1). F.P. acknowledges the Fonds der Chemischen Industrie (FCI) for a Chemiefonds-fellowship. We acknowledge Mrs. U. Cornelissen for recording the Raman spectra of compounds **1–3**.

Supporting Information Available: IR and Raman spectra of **3**, RR spectra of **1**, excitation profiles of $\nu_{\text{breathing}}(\text{M}-\text{N})$ for **1** and **2**, and illustrations of the local coordinates used for the classification of in- and out-of-plane porphyrin core modes by Li et al. Assignments of the vibrational data of complexes **2** and **3**, and details of the crystal structure determination of **2**, including atomic coordinates, anisotropic displacement parameters, and geometric parameters. Coordinates of the DFT fully optimized structures of **1–3** are also included. This material is available free of charge via the Internet at <http://pubs.acs.org>.

(56) Asher, S.; Sauer, K. *J. Chem. Phys.* **1976**, *64*, 4115–4125.

(57) Kitagawa, T.; Abe, M.; Kyogoku, Y.; Ogoshi, H.; Watanabe, E.; Yoshida, Z. *J. Phys. Chem.* **1976**, *80*, 1181–1186.

(58) Browett, W. R.; Fucaloro, A. F.; Morgan, T. V.; Stephens, P. J. *J. Am. Chem. Soc.* **1983**, *105*, 1868–1872.

(59) Mu, X. H.; Schultz, F. A. *Inorg. Chem.* **1992**, *31*, 3351–3357.

7.5 Structural and Spectroscopic Characterization of Mononuclear Copper(I) Nitrosyl Complexes: End-on versus Side-on Coordination of NO to Copper(I)

Kiyoshi Fujisawa,* Akira Tateda, Yoshitaro Miyashita, Ken-ichi Okamoto, Florian Paulat, V. K. K. Praneeth, Anna Merkle, and Nicolai Lehnert*

Accepted for Publication: *J. Am. Chem. Soc.* 2007.

Structural and Spectroscopic Characterization of Mononuclear Copper(I) Nitrosyl Complexes: End-on versus Side-on Coordination of NO to Copper(I)

Kiyoshi Fujisawa,^{*,†} Akira Tateda,[†] Yoshitaro Miyashita,[†] Ken-ichi Okamoto,[†] Florian Paulat,[‡] V. K. K. Praneeth,[‡] Anna Merkle,[‡] and Nicolai Lehnert^{*,‡}

Graduate School of Pure and Applied Sciences, University of Tsukuba, Tsukuba 305-8571, Japan, and Department of Chemistry, University of Michigan, Ann Arbor, Michigan 48109

Received July 9, 2007; E-mail: kiyoshif@chem.tsukuba.ac.jp; lehnertn@umich.edu

Abstract: Two crystal structures of the mononuclear copper(I)–nitrosyl complexes [Cu(L3)(NO)] (**1**) and [Cu(L3')(NO)](ClO₄) (**2**) with the related coligands L3[−] (hydrotris(3-*tert*-butyl-5-isopropyl-1-pyrazolyl)borate) and L3' (tris(3-*tert*-butyl-5-isopropyl-1-pyrazolyl)methane) are presented. These compounds are then investigated in detail using a variety of spectroscopic methods. Vibrational spectra show $\nu(\text{N}=\text{O})$ at 1698 cm^{−1} and $\nu(\text{Cu}=\text{NO})$ split at 365/338 cm^{−1} for **1**, which translates to force constants of 12.53 (N–O) and 1.31 mdyn/Å (Cu–NO), respectively. The weak Cu–NO force constant is in agreement with the observed instability of the Cu–NO bond. Interestingly, complex **2** with the neutral coligand L3' shows a stronger N–O bond, evident from $\nu(\text{N}=\text{O})$ at 1742 cm^{−1}. This difference is attributed to a true second coordination sphere effect, where the covalency of the Cu(I)–NO bond is not altered. The EPR spectrum of **1** is in agreement with the Cu(I)–NO(radical) electronic structure of the complexes, as obtained from density functional theory (DFT) calculations. In addition, an interesting trend between $g_{\parallel}(g_z)$ and the Cu–N–O angle is established. Finally, high-quality MCD spectra of **1** are presented and assigned using TD-DFT calculations. Based on the in-depth spectroscopic characterization of end-on bound NO to copper(I) presented in this work, it is possible to determine the binding mode of the Cu–NO intermediate of Cu nitrite reductase studied by Scholes and co-workers (Usov, O. M.; Sun, Y.; Grigoryants, V. M.; Shapleigh, J. P.; Scholes, C. P., *J. Am. Chem. Soc.* **2006**, *128*, 13102–13111) in solution as strongly bent (~135°) but likely not side-on.

1. Introduction

The copper(I)–nitrosyl {CuNO}¹¹ adduct^{1,2} is a very important intermediate in the general reactions of copper proteins with biologically available nitrogen monoxide (commonly referred to as nitric oxide, NO).^{3,4} For example, NO is believed to be a mediator of copper protein activity⁵ and might also play a role in neurodegenerative diseases.⁶ In particular, Cu nitrite reductase (CuNIR) is involved in the generation (and presumably degradation) of NO in denitrifying bacteria.^{7,8} Crystal structures of a

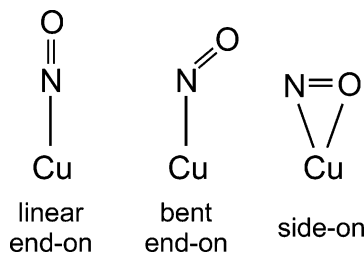
large number of CuNIR's have been determined, which show great similarities for the enzymes obtained from different organisms.⁹ CuNIR's are homotrimers where each subunit contains one copper type 1 center for electron transfer. The catalytically active type 2 centers are located at the respective interfaces of two subunits of the enzyme. In oxidized CuNIR, the type 2 centers are tetrahedrally coordinated by three histidines and a water molecule, where two histidines are provided by one subunit, whereas the third one comes from the adjacent subunit.^{10–15} The observed coordination mode of nitrite to the oxidized active site is asymmetric $\eta^2\text{-O}_2\text{O}$ corresponding to the formation of a copper(II)–nitrito intermediate.^{11,13,16,17} This binding mode is also observed in a large number of

[†] University of Tsukuba.

[‡] University of Michigan.

- (1) In the Enemark–Feltham notation,² the number of d electrons of the metal plus the unpaired electron of NO are added up and then used as a superscript (here: 11). This allows for a classification of transition metal nitrosyls, in the case of which the assignment of metal and NO oxidation states is sometimes very difficult.
- (2) Enemark, J. H.; Feltham, R. D. *Coord. Chem. Rev.* **1974**, *13*, 339–406.
- (3) Shiva, S.; Wang, X.; Ringwood, L. A.; Xu, X.; Yuditskaya, S.; Annava-jjhala, V.; Miyajima, H.; Hogg, N.; Harris, Z. L.; Gladwin, M. T. *Nat. Chem. Biol.* **2006**, *2*, 486–493.
- (4) Bryan, N. S.; Fernandez, B. O.; Bauer, S. M.; Garcia-Saura, M. F.; Milsom, A. B.; Rassaf, T.; Maloney, R. E.; Bharti, A.; Rodriguez, J.; Feelisch, M. *Nature Chem. Biol.* **2005**, *1*, 290–297.
- (5) Torres, J.; Svinstunenko, D.; Karlsson, B.; Cooper, C. E.; Wilson, M. T. *J. Am. Chem. Soc.* **2002**, *124*, 963–967.
- (6) Sorenson, J. R. *J. Inorg. Biochem.* **2001**, *87*, 125–127.
- (7) Averill, B. A. *Chem. Rev.* **1996**, *96*, 2951–2964.
- (8) Wasser, I. M.; de Vries, S.; Moënnelocoz, P.; Schröder, I.; Karlin, K. D., *Chem. Rev.* **2002**, *102*, 1201–1234.

- (9) Suzuki, S.; Kataoka, K.; Yamaguchi, K. *Acc. Chem. Res.* **2000**, *33*, 728–738.
- (10) Godden, J. W.; Turley, S.; Teller, D. C.; Adman, E. T.; Liu, M. Y.; Payne, W. J.; LeGall, J. *Science* **1991**, *253*, 438–442.
- (11) Adaman, E. T.; Godden, J. W.; Turley, S., *J. Biol. Chem.* **1995**, *270*, 27458–27474.
- (12) Murphy, M. E. P.; Turley, S.; Kukimoto, M.; Nishiyama, M.; Horinouchi, S.; Sasaki, H.; Tanokura, M.; Adman, E. T. *Biochemistry* **1995**, *34*, 12107–12117.
- (13) Murphy, M. E. P.; Turley, S.; Adman, E. T. *J. Biol. Chem.* **1997**, *272*, 28455–28460.
- (14) Dodd, F. E.; Van Beeumen, J.; Eady, R. R.; Hasnain, S. S. *J. Mol. Biol.* **1998**, *282*, 369–382.
- (15) Inoue, T.; Gotowda, M.; Deligeer; Kataoka, M.; Yamaguchi, K.; Suzuki, S.; Watanabe, H.; Gohow, M.; Kai, Y. *J. Biochem.* **1998**, *124*, 876–879.

Scheme 1. Different Binding Modes of NO to Copper

50 corresponding model complexes.^{8,18} After completion of the
 51 catalytic cycle, NO (presumably coordinated to copper(II)) and
 52 water are generated. The exact mechanism for this conversion
 53 is still under discussion.^{7,8,19} Interestingly, under anaerobic
 54 conditions with limited reductant and nitrite present, CuNIR is
 55 also able to act as an NO reductase by converting NO to
 56 N₂O,^{20,21} a reaction that has also been observed for correspond-
 57 ing model complexes.²² In this latter function, a {CuNO}¹¹
 58 complex is most likely the catalytically active species.

59 In a recent study by Murphy and co-workers, a Cu(I)–NO
 60 intermediate of CuNIR, which was generated by exposing
 61 crystals of fully reduced CuNIR to NO saturated buffer, has
 62 been structurally characterized.²³ Surprisingly, this species shows
 63 an unprecedented side-on coordination of nitric oxide to copper-
 64 (I) (cf. Scheme 1, right), which corresponds to a new interme-
 65 diate in the biological chemistry of NO. Additional crystal
 66 structures that have just appeared in the literature confirm this
 67 result.²⁴ The authors also tried to generate this species in solution
 68 by treatment of ascorbate reduced CuNIR with NO under
 69 anaerobic conditions. From electron paramagnetic resonance
 70 (EPR) measurements on these solutions, the crystallographically
 71 obtained {CuNO}¹¹ species was proposed to have a Cu(II)–
 72 NO[−] electronic structure. These spectacular results, and in
 73 particular the unusual binding mode of nitric oxide to the copper-
 74 (I) active site of CuNIR, have sparked interest in the coordina-
 75 tion chemistry of copper(I) and NO and the spectroscopic
 76 properties of corresponding species.^{25–27} Recently, Scholes
 77 and Solomon and co-workers have demonstrated spectroscopically
 78 that the solution species obtained by Murphy and co-workers
 79 is in fact a Cu(II)–NO₂[−] complex.²¹ Based on these results,
 80 these authors concluded that the crystallographically observed
 81 side-on {CuNO}¹¹ species is most likely not relevant for the
 82 catalytic cycle of the enzyme, because it is only generated in
 83 the crystal but not in solution in the presence of excess NO. In

addition, density function theory (DFT) calculations clearly
 indicate that the side-on {CuNO}¹¹ intermediate should have a
 Cu(I)–NO(radical) electronic structure.^{21,27} Independent of these
 studies, Scholes and co-workers have shown by EPR and
 electron–nuclear double resonance (ENDOR) spectroscopy that
 a {CuNO}¹¹ species can in fact be generated for CuNIR in
 solution by using fully reduced enzyme in the presence of
 limited amounts of NO.²⁶ From these studies, however, it is
 not clear whether the obtained {CuNO}¹¹ species shows end-
 on or side-on coordinated NO. Based on the crystal structure
 of a corresponding model complex (vide infra), some researchers
 favor the end-on binding mode of NO for this species.²¹ On
 the other hand, the CuNIR crystal structure by Murphy and co-
 workers points toward a side-on coordination of NO.²³ The
 question of whether a side-on bound {CuNO}¹¹ species can exist
 is therefore of high significance for the understanding of the
 NO reductase activity of CuNIR but also of fundamental interest
 for the coordination chemistry of copper(I) and NO.

In light of this biological and medicinal significance of
 copper–nitrosyls, it is surprising that the biomimetic coordina-
 tion chemistry of copper and NO and the investigation of the
 properties of these systems are not very developed. In fact, only
 one crystal structure of a mononuclear copper nitrosyl model
 complex has been reported so far by Tolman and co-workers,
 using [HB(3-*t*Bupz)₃][−] (Tp^{−Bu}) as coligand.²⁸ Key spectroscopic
 data of this complex including the N–O stretch, EPR param-
 eters, and electronic spectra were reported. Based on these data
 and unrestricted Hartree–Fock (UHF) calculations, the elec-
 tronic structure of copper(I) NO complexes was described as
 Cu(I)–NO(radical). Besides this, a dinuclear copper–nitrosyl
 has been synthesized by Karlin and co-workers.²⁹

In this work, two mononuclear copper nitrosyl complexes
 with anionic [HB(3-*t*Bu-5-*i*Prpz)₃][−] (L3[−])^{18,30,31} and neutral
 [HC(3-*t*Bu-5-*i*Prpz)₃] (L3⁰)³¹ coligands have been synthesized
 and structurally and spectroscopically characterized in detail.
 For this purpose, vibrational (IR), UV–vis absorption, EPR,
 and magnetic circular dichroism (MCD) spectroscopies have
 been applied. In correlation to DFT calculations, these data are
 analyzed in detail, and key insight about the nitrosyl binding to
 copper(I) is obtained. In addition, the effect of the total charge
 of the coligands on the properties of the Cu(I)–nitrosyls is
 discussed. Based on the detailed spectroscopic signature of end-
 on bound NO to copper(I) (cf. Scheme 1) elaborated here, the
 spectroscopic data obtained by Scholes and co-workers for the
 Cu(I)–NO complex of CuNIR in solution can be used to
 determine the binding mode of NO in this case. The conclusions
 drawn this way are further supported by DFT calculations.

2. Experimental Section

2.1. Materials. Preparation and handling of all complexes was
 performed under an argon atmosphere using standard Schlenk tube
 techniques or in an inert atmosphere glovebox. Anhydrous dichlo-
 romethane and chloroform were purchased from Aldrich Chemical Co.
 and stored in a glovebox. ¹⁵N¹⁸O gas was obtained from Shoko Co.,

- (16) Strange, R. W.; Dodd, F. E.; Abraham, Z. H. L.; Grossmann, J. G.; Brüser, T.; Eady, R. R.; Smith, B. E.; Hasnain, S. S. *Nat. Struct. Biol.* **1995**, *2*, 287–292.
 (17) Howes, B. D.; Abraham, Z. H. L.; Lowe, D. J.; Brüser, T.; Eady, R. R.; Smith, D. E. *Biochemistry* **1994**, *33*, 3171–3177.
 (18) Lehnert, N.; Cornelissen, U.; Neese, F.; Ono, T.; Noguchi, Y.; Okamoto, K.; Fujisawa, K. *Inorg. Chem.* **2007**, *46*, 3916–3933.
 (19) Kataoka, K.; Furusawa, H.; Takagi, K.; Yamaguchi, K.; Suzuki, S. *J. Biochem.* **2000**, *127*, 345–350.
 (20) Casella, S.; Shapleigh, J. P.; Toffanin, A.; Basaglia, M. *Biochem. Soc. Trans.* **2006**, *34*, 130–132.
 (21) Ghosh, S.; Dey, A.; Usov, O. M.; Sun, Y.; Grigoryants, V. M.; Scholes, C. P.; Solomon, E. I. *J. Am. Chem. Soc.* **2007**, *129*, 10310–10311.
 (22) Ruggiero, C. E.; Carrier, S. M.; Tolman, W. B. *Angew. Chem., Int. Ed. Engl.* **1994**, *33*, 895–897.
 (23) Tocheva, E. I.; Rosell, F. I.; Mauk, A. G.; Murphy, M. E. P. *Science* **2004**, *304*, 867–870.
 (24) Tocheva, E. I.; Rosell, F. I.; Mauk, A. G.; Murphy, M. E. P. *Biochemistry* **2007**, *46*, 12366–12374.
 (25) Antonyuk, S. V.; Strange, R. W.; Sawers, G.; Eady, R. R.; Hasnain, S. S. *Proc. Natl. Acad. Sci. U.S.A.* **2005**, *102*, 12041–12046.
 (26) Usov, O. M.; Sun, Y.; Grigoryants, V. M.; Shapleigh, J. P.; Scholes, C. P. *J. Am. Chem. Soc.* **2006**, *128*, 13102–13111.
 (27) Wasbotten, I. H.; Ghosh, A.; *J. Am. Chem. Soc.* **2005**, *127*, 15384–15385.

- (28) Ruggiero, C. E.; Carrier, S. M.; Antholine, W. E.; Whittaker, J. W.; Cramer, C. J.; Tolman, W. B. *J. Am. Chem. Soc.* **1993**, *115*, 11285–11298.
 (29) Paul, P. P.; Tyeklar, Z.; Farooq, A.; Karlin, K. D.; Liu, S.; Zubieta, J. J. *Am. Chem. Soc.* **1990**, *112*, 2430–2432.
 (30) Fujisawa, K.; Kobayashi, T.; Fujita, K.; Kitajima, N.; Moro-oka, Y.; Miyashita, Y.; Yamada, Y.; Okamoto, K. *Bull. Chem. Soc. Jpn.* **2000**, *73*, 1797–1804.
 (31) Fujisawa, K.; Ono, T.; Ishikawa, Y.; Amir, N.; Miyashita, Y.; Okamoto, K.; Lehnert, N. *Inorg. Chem.* **2006**, *45*, 1698–1713.

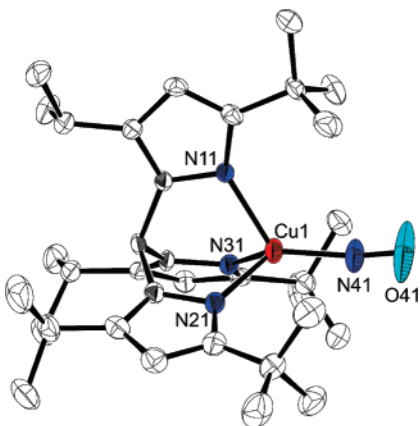


Figure 1. ORTEP view of $[\text{Cu}(\text{L3})(\text{NO})]$ (**1**) showing 50% thermal ellipsoids and the atom labeling scheme. For clarity, hydrogen atoms were omitted. Selected bond distances (Å) and angles (deg): Cu1–N41 1.779(4), Cu1–N11 2.053(2), Cu1–N21 2.064(3), Cu1–N31 2.051(3), N41–O41 1.083(7), B1–N12 1.557(5), B1–N22 1.540(5), B1–N32 1.541(4); Cu1–N41–O41 171.9(5), N41–Cu1–N11 123.66(17), N41–Cu1–N21 122.81(18), N41–Cu1–N31 122.32(17), N11–Cu1–N21 91.85(12), N11–Cu1–N31 92.28(13), N21–Cu1–N31 95.61(14), N12–B1–N22 108.9(3), N12–B1–N32 109.8(3), N22–B1–N32 110.9(2).

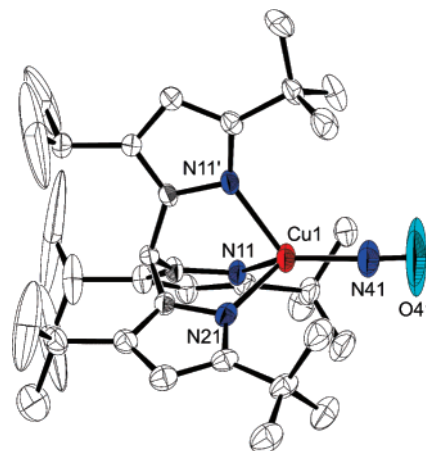


Figure 2. ORTEP view of the cation of $[\text{Cu}(\text{L3}')(\text{NO})](\text{ClO}_4)$ (**2**) showing 50% thermal ellipsoids and the atom labeling scheme. For clarity, hydrogen atoms were omitted. Selected bond distances (Å) and angles (deg): Cu1–N41 1.786(5), Cu1–N11 2.070(3), Cu1–N21 2.058(4), N41–O41 1.035(8), C1–N12 1.451(4), C1–N22 1.448(7); Cu1–N41–O41 176.4(10), N41–Cu1–N11 125.09(14), N41–Cu1–N21 125.2(2), N11–Cu1–N21 90.68(12), N11–Cu1–N11' 89.16(12), N12–C1–N22 112.2(2), N12–C1–N12' 111.3(3). Symmetry code: $x, -y + 1/2, z$.

Ltd and Aldrich Chemical Co. Other reagents are commercially available and were used without further purification. $[\text{Cu}\{\text{HB}(3\text{-}t\text{Bu}\text{-}5\text{-}i\text{Prpz})_3\}(\text{NCMe})]$ ($[\text{Cu}(\text{L3})(\text{NCMe})]$) and $[\text{Cu}\{\text{HC}(3\text{-}t\text{Bu}\text{-}5\text{-}i\text{Prpz})_3\}(\text{OCIO}_3)]$ ($[\text{Cu}(\text{L3}')(\text{OCIO}_3)]$) were prepared according to published methods.³¹ *Caution: Although we have not encountered any problems, it is noted that the perchlorate salts of metal complexes with organic ligands are potentially explosive and should be handled only in small quantities with appropriate precautions.* The elemental analyses (C, H, N) were performed by the Department of Chemistry at the University of Tsukuba.

2.2. Complex Syntheses. 2.2.1. $[\text{Cu}(\text{L3})(\text{NO})]$ (1**).** $[\text{Cu}(\text{L3})(\text{NCMe})]$ ³¹ (0.0616 g, 0.127 mmol) was dissolved in dichloromethane (2.0 mL) in a glovebox. The solution was cooled to -78 °C under an argon atmosphere, and argon was then replaced by NO. The solution was stirred for 1 h at -50 °C. The solution was kept at -30 °C for 1 day. The solution was then cooled down to -50 °C again. Crystallization from dichloromethane at -50 °C yielded red crystals (Figure 1). Elemental analysis (%) calcd for $\text{C}_{30}\text{H}_{52}\text{N}_7\text{BCuO}'\text{CH}_2\text{Cl}_2$: C, 54.27; H, 7.93; N, 14.29. Found: C, 54.87; H, 8.14; N, 14.19. IR (KBr, cm^{-1}): 2965 $\nu(\text{CH})$, 2564 $\nu(\text{BH})$, 1698 $\nu(^{14}\text{N}^{16}\text{O})$, $[\nu(^{15}\text{N}^{18}\text{O}) = 1627]$. UV–vis λ/nm ($\epsilon/\text{mol}^{-1} \text{ dm}^3 \text{ cm}^{-1}$) (dichloromethane), 506(960).

2.2.2. $[\text{Cu}(\text{L3}')(\text{NO})](\text{ClO}_4)$ (2**).** $[\text{Cu}(\text{L3}')(\text{OCIO}_3)]$ ³¹ (0.1290 g, 0.192 mmol) was dissolved in chloroform (8.0 mL) in a glovebox. The solution was cooled to -50 °C under an argon atmosphere, and argon was then replaced by NO. The solution was stirred for 1 h allowing the temperature to reach about -4 °C. The solution was further kept at -30 °C for 1 day. The solution was then cooled to -50 °C. Crystallization from chloroform at -50 °C yielded orange crystals (Figure 2). Elemental analysis (%) calcd for $\text{C}_{31}\text{H}_{52}\text{N}_7\text{CuO}_5\text{Cl}'\text{CHCl}_3$: C, 46.81; H, 6.51; N, 11.94. Found: C, 47.18; H, 6.46; N, 11.48. IR (KBr, cm^{-1}): 2970 $\nu(\text{CH})$, 1742 $\nu(^{14}\text{N}^{16}\text{O})$, $[\nu(^{15}\text{N}^{18}\text{O}) = 1710/1666]$. UV–vis λ/nm ($\epsilon/\text{mol}^{-1} \text{ dm}^3 \text{ cm}^{-1}$) (chloroform), 458(1140).

Labeled nitrosyl complexes, $[\text{Cu}(\text{L3})(^{15}\text{N}^{18}\text{O})]$ and $[\text{Cu}(\text{L3}')(^{15}\text{N}^{18}\text{O})](\text{ClO}_4)$, were synthesized by using $^{15}\text{N}^{18}\text{O}$ in the same manner as that for complexes **1** and **2**, respectively.

We did not perform detailed decomposition kinetic measurements. The $\nu(\text{N}=\text{O})$ peak of **2** had almost disappeared 15 h after MIR measurements in solid KBr disks (exposed to air for 15 h), whereas that of **1** just became somewhat weaker (Figure S5). Therefore, the stability of **1** is clearly much larger than that of **2**.

2.3. Crystal Structure Determination. The detailed crystal data, data collection, and structural refinement parameters for **1** and **2** are

given in Table S1. Complete atomic labels are shown in Figures S1 and S2. The diffraction data were measured on a Rigaku/MSC Mercury CCD system with graphite monochromated $\text{Mo K}\alpha$ ($\lambda = 0.710 69$ Å) radiation at low temperature. All crystals were mounted on glass fiber using epoxy glue. The unit cell parameters of each crystal were obtained using Rigaku Daemon software and refined using CrystalClear on all observed reflections.³² Data using 0.5° intervals in ϕ and ω for 35 s/frame (**1**) and for 30 s/frame (**2**) were collected with a maximum resolution of 0.77 Å (744 oscillation images). The highly redundant data sets were reduced using CrystalClear and corrected for Lorentz and polarization effects. An empirical absorption correction was applied for each complex.^{33,34} Structures were solved by direct methods using the program *SIR92*.³⁵ The position of the metal atoms and their first coordination sphere were located from a direct method *E*-map; other non-hydrogen atoms were found in alternating difference Fourier syntheses³⁶ and least-squares refinement cycles. These were refined anisotropically during the final cycles (CrystalStructure).^{33,34} Hydrogen atoms were placed in calculated positions. Higher *R* and GOF values are due to one disordered dichloromethane for **1** and disordered methyl carbons of the isopropyl groups of L3 as well as disordered chloroform and perchlorate molecules for **2** in the unit cell. The O atoms (O41) and N atoms (N41) of the NO molecules in both structures show somewhat large thermal ellipsoids. This phenomenon has also been observed in Tolman's structure reported before.²⁸ This is probably due to the fact that, even at low temperature, the low-energy motions of NO (rotation, etc.) are not fully frozen, giving rise to thermal motion or slight disorder. Moreover, we observed these problems in Cu(I)–CO complexes even at low temperature.³¹ Therefore, this is a common observation for Cu–X–O complexes with tris(pyrazolyl)borate and tris(pyrazolyl)methane coligands. Crystallographic data and structure refinement parameters including the final discrepancies (*R* and *R_w*) are listed in Table S1. Crystallographic data have been deposited at the

(32) Pflugrath, J. W. *CrystalClear* Ver. 1.3. *Acta Crystallogr.* **1999**, *D55*, 1718–1725.

(33) *CrystalStructure 3.70: Crystal Structure Analysis Package*, version 3.70; Rigaku and Rigaku/MSC: 2005.

(34) Watkin, D. J.; Prout, C. K.; Carruthers, J. R.; W., B. P. *Crystal Issue 10*; Chemical Crystallography Laboratory: Oxford, U.K., 1996.

(35) Altomare, A.; Cascarano, G.; Giacovazzo, C.; Guagliardi, A.; Burla, M.; Polidori, G.; Camalli, M. *SIR 92. J. Appl. Crystallogr.* **1994**, *27*, 435.

(36) Beurskens, P. T.; Admiral, G.; Beurskens, G.; Bosman, W. P.; de Gelder, R.; Israel, R.; Smits, J. M. M. *The DIRDIF-99 program system*; Technical Report of the Crystallography Laboratory, University of Nijmegen: The Netherlands, 1999.

211 CCDC, 12 Union Road, Cambridge CB2 1EZ, U.K., and copies can
 212 be obtained on request, free of charge, by quoting the publication
 213 citation and the deposition numbers: CCDC-615640 for **1** and CCDC-
 214 615641 for **2**.

215 **2.4. Spectroscopic Measurements.** UV–vis absorption data were
 216 recorded with an Ostuka Electronics MCPD-2000 system with an optical
 217 fiber attachment in the 300–1100 nm region at low temperature. The
 218 magnetic circular dichroism (MCD) setup consists of a JASCO J-810
 219 spectropolarimeter and an Oxford Instruments SPECTROMAG SM4000
 220 magnetocryostat. Samples for MCD were recorded in silicone oil (DC
 221 200) mulls. EPR spectra were recorded on a Bruker EMX EPR
 222 spectrometer in frozen solution ($\text{CH}_2\text{Cl}_2/\{\text{CH}_2\text{Cl}_2\}_2$ (1:1)) in quartz tubes
 223 (diameter 5 mm) at 5–10 K with an Oxford Instruments liquid helium
 224 cryostat in the 2000–4200 G region. The spectrum of **1** shown in Figure
 225 3 in red was measured at a frequency of 9.341 GHz and a microwave
 226 power of 20 mW. IR data were obtained with a JASCO FT/IR-550
 227 spectrometer in the 4000–400 cm^{-1} region for MIR (middle infrared)
 228 and 650–150 cm^{-1} for FIR (far-infrared) measurements.

229 **2.5. Normal Coordinate Analysis.** Normal coordinate calculations
 230 were performed using the QCPE computer program 576 by M.R.
 231 Peterson and D.F. McIntosh. The calculations are based on a general
 232 valence force field; force constants are refined with a nonlinear simplex
 233 algorithm. The simplex optimization was used to refine only *selected*
 234 force constants according to the quantum-chemical centered normal
 235 coordinate analysis (QCC-NCA) scheme.³⁷ Here, a force field from
 236 DFT calculations is used as a starting point to generate initial force
 237 constants, and a subset of these is fit to reproduce the known
 238 experimental frequencies. Force constants are extracted from the
 239 Gaussian output using a modified version of the program Redong
 240 (QCPE 628).³⁸

241 For the QCC-NCA treatment, the BP86/TZVP optimized structure
 242 of model system $[\text{Cu}(\text{L}0)(\text{NO})]$ (see DFT part) has been used, but the
 243 Cu–N–O angle has been adjusted to 180° for simplification, which is
 244 very close to the experimentally determined value of 172°. The
 245 calculated force field for $[\text{Cu}(\text{L}0)(\text{NO})]$ (BP86/TZVP) has been applied.
 246 For the QCC-NCA, the Cu–NO and N–O force constants as well as
 247 the Cu–NO/N–O nondiagonal element have been fitted to reproduce
 248 the experimentally observed vibrational energies of the Cu–N–O unit.
 249 Importantly, the QCC-NCA treatment reproduces the split appearance
 250 of the Cu–NO stretch. In order to refine the vibrational energies of
 251 the two split components, the diagonal elements of the C–C–CH₃
 252 bending coordinates of the pyrazolyl rings have been slightly adjusted
 253 (lowered by 0.04 mdyne/Å) compared to the DFT-predicted values. From
 254 these results, the Cu–NO stretch is mixed with a $[\text{Cu}(\text{L}3)]$ skeletal
 255 bending mode, which is shown in Figure S8. This mode is predicted at
 256 350 cm^{-1} in the calculations. The mixing between this core bending
 257 mode and $\nu(\text{Cu}–\text{NO})$ is reproduced accurately in the QCC-NCA, which
 258 means that the $[\text{Cu}(\text{L}3)]$ core modes are well described in the
 259 calculation. In the QCC-NCA fit, the component at lower energy has
 260 more Cu–NO character (from the potential energy distribution (PED))
 261 and, correspondingly, a larger ¹⁵N¹⁸O isotope shift. Experimentally, this
 262 trend is reversed, as apparent from the inverse trend in the isotope shifts.
 263 The Cu–N–O bends are found in the 200–250 cm^{-1} region, with small
 264 isotope shifts of 2–4 cm^{-1} . They are strongly mixed with $[\text{Cu}(\text{L}3)]$
 265 skeletal modes.

266 **2.6. Density Functional Theory (DFT) Calculations.** The structures
 267 of the model complexes $[\text{Cu}(\text{L}0)(\text{NO})]$ (L0 = hydrotris(3,5-dimethyl-
 268 1-pyrazolyl)borate) and $[\text{Cu}(\text{L}0')(\text{NO})]^+$ (L0' = tris(3,5-dimethyl-
 269 1-pyrazolyl)methane) were fully optimized with BP86/TZVP using the
 270 program package Gaussian 03.³⁹ For these calculations, the TZVP basis
 271 set⁴⁰ has been applied as implemented in G03. For method calibration,

(37) Praneeth, V. K. K.; Näther, C.; Peters, G.; Lehnert, N. *Inorg. Chem.* **2006**, *45*, 2795–2811.

(38) Allouche, A.; Pourcin, J. *Spectrochim. Acta* **1993**, *49A*, 571–580.

(39) Frisch, M. J. et al. *Gaussian 03*; Gaussian, Inc.: Pittsburgh, PA, 2003.

(40) Schäfer, A.; Horn, H.; Ahlrichs, R. *J. Chem. Phys.* **1992**, *97*, 2571–2577.

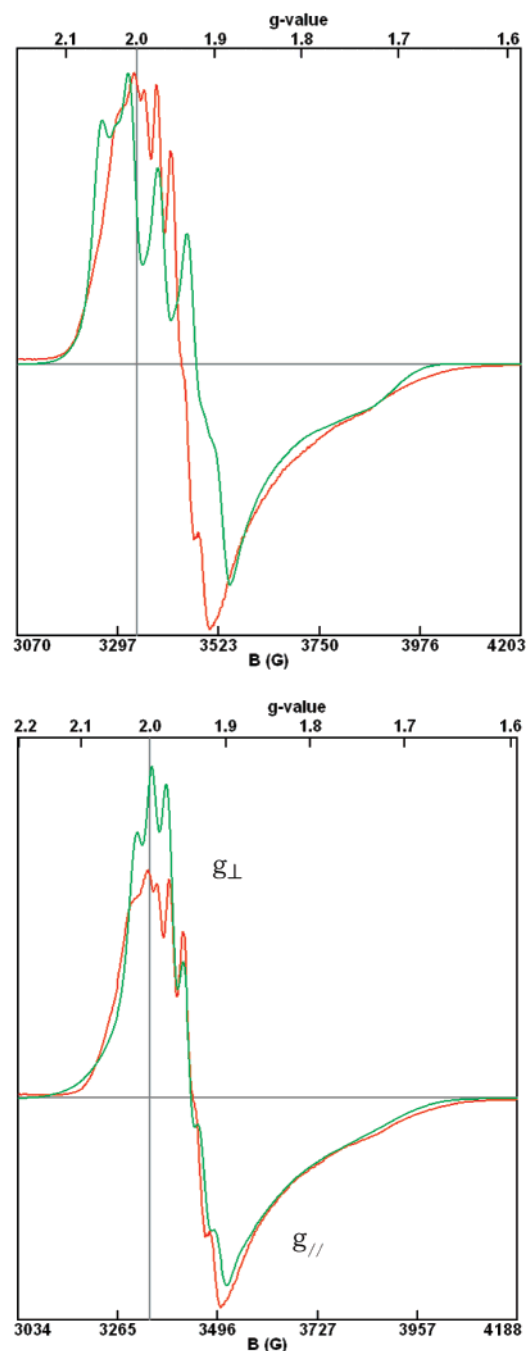


Figure 3. EPR spectrum of **1** at 5 K (red) including simulations (green). Top: for this simulation, the Cu hyperfine values determined by Tolman and co-workers (see ref 26 and 28) were used ($^{63}\text{Cu}_{\perp} = 187$ MHz; $^{63}\text{Cu}_{\parallel} = 320$ MHz). However, the central region of the spectrum could not be fit this way. Bottom: alternative simulation, where the Cu hyperfine was allowed to vary stronger. Fit: $g_x = 1.962$, $g_y = 1.972$, $g_z = 1.8$; $^{63}\text{Cu}_x = 100$ MHz, $^{63}\text{Cu}_y = 105$ MHz, $^{63}\text{Cu}_z = 270$ MHz; ^{14}N hyperfine (NO): $^{14}\text{N}_x = 98$ MHz, $^{14}\text{N}_y = 19$ MHz, $^{14}\text{N}_z = 17$ MHz. Note that g_z could not exactly be determined due to lack of spectral resolution. The value of g_z is around 1.79–1.80.

the structures of these models have also been fully optimized using 272
 B3LYP/LanL2DZ, which applies Becke's three-parameter hybrid 273
 functional with the correlation functional of Lee, Yang, and Parr 274
 (B3LYP).^{41–43} The LanL2DZ basis set consists of Dunning/Huzinaga 275
 full double- ζ (D95) basis functions⁴⁴ on first row and Los Alamos 276

(41) Becke, A. D. *Phys. Rev. A* **1988**, *38*, 3098–3100.

(42) Becke, A. D. *J. Chem. Phys.* **1993**, *98*, 1372–1377.

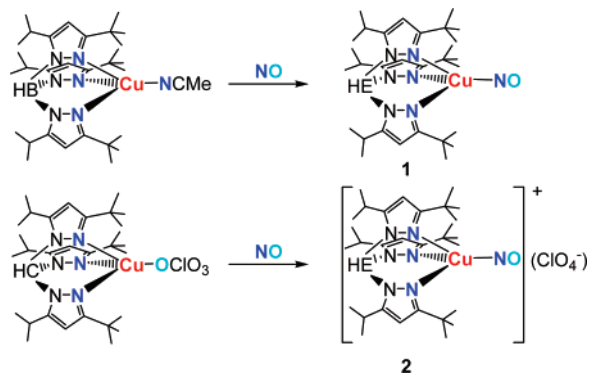
(43) Becke, A. D. *J. Chem. Phys.* **1993**, *98*, 5648–5652.

effective core potentials plus DZ functions on all other atoms.^{45,46} However, the obtained structures are in general inferior to the ones calculated with BP86/TZVP. In order to investigate whether B3LYP calculations can help improving the deviations in the Cu–N–O angle between the calculation and experiment, model [Cu(L0)(NO)] has also been fully optimized with B3LYP/TZVP and B3LYP/6-311G*. However, no improvement is observed as shown in Table S2. Calculated vibrational frequencies for all these geometry optimizations included in Table S2 show no imaginary modes, which shows that true energy minima have been obtained in all cases. Relative energies in Table 3 were either taken from BP86/TZVP calculations (“BP86”) or from B3LYP/TZVP calculations (“B3LYP”) on the BP86/TZVP optimized structures. EPR parameter (BP86/TZVP) and TD-DFT (B3LYP/TZVP) calculations were performed using the program package ORCA.⁴⁷ For Figure 4, the BP86/TZVP optimized structure of model [Cu(L0)(NO)] was used, and the Cu–N–O angle was adjusted correspondingly. For the geometry optimization of CuNIR models (cf. Figure 7), the crystal structure with bound NO (PDB:1SNR) from ref 23 was used together with the BP86/TZVP method. The histidines were fixed in space by freezing their anchor C atoms of the protein backbone, which were transformed into CH₃ groups for the calculations.

2.7. EPR Spectral Simulations. EPR spectra were simulated using the program SpinCount (version 2.2.40), written by Prof. Michael Hendrich, Carnegie Mellon University. EPR parameters are listed in the caption of Figure 3. The best fit is obtained with g_z around 1.79–1.80. The error bars for the hyperfine values are larger, around 5–10%.

3. Results and Discussion

3.1. Synthesis and Structural Characterization. The nitrosyl complexes [Cu(L3)(NO)] (**1**) and [Cu(L3′)(NO)](ClO₄) (**2**) were obtained from the reaction of [Cu(L3)(NCMe)] and [Cu(L3′)(OCIO₃)]³¹ with NO in good yield as shown in eq 1.



Detailed procedures are given in the Experimental Section. Complex **2** is very unstable toward NO loss (Figure S5). The structures of **1** and **2** determined by X-ray crystallography indicate that both complexes are mononuclear. As mentioned above, these compounds constitute only the second and third examples for mononuclear Cu(I)–NO model complex structures ever obtained in the literature. The perspective drawings of their structures are shown in Figures 1 and 2, respectively. In the copper nitrosyl complexes **1** and **2**, the copper ions have distorted tetrahedral coordination geometries. Cu–NO distances of **1** (1.779(4) Å) and **2** (1.7836(5) Å) are similar and comparable to Tolman’s compound [Cu(Tp^{t-Bu})(NO)] (**3**, 1.759–

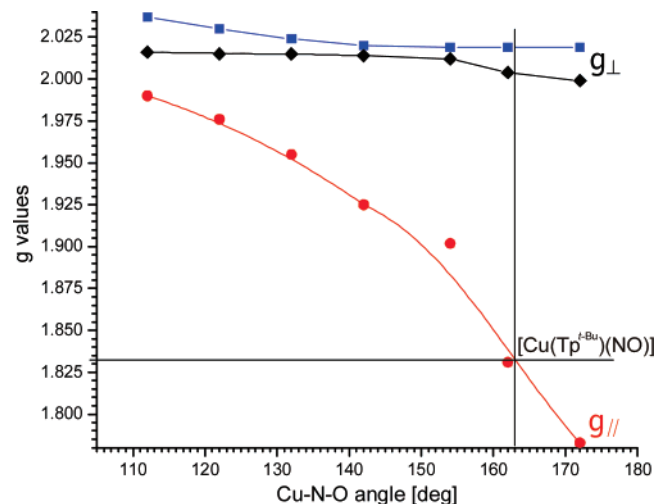


Figure 4. Calculated g values (BP86/TZVP) as a function of the Cu–N–O angle. Indicated are the predicted g values for **3**.

(6) Å; cf. Table 1). On the other hand, the N–O distance of **1** (1.083(7) Å) is distinctively longer than that of **2** (1.035(8) Å), indicating potential differences in π backbonding (vide infra). Because of the difference in the total charge of the ligands (L3[−]: anion, L3′: neutral), it is expected from previous work that π -backdonation in **1** is stronger than that in **2**,³¹ which would be in agreement with the experimental trend. The copper ions are almost linearly ligated by NO in both cases (Cu–N–O angle = 171.9(5)° for **1** and 176.4(10)° for **2**). Although electronic effects usually predominate among the factors that induce nitrosyl bending,²⁸ the possibility that there are steric influences on the Cu–N–O angle is suggested by the observed orientation of the nitrosyl oxygen atom away from one of the *tert*-butyl groups and toward the open space between two pyrazolyl substituents in **3**. In this complex, the Cu–N–O angle is 163.4–(6)°,²⁸ which is different from **1** and **2** reported here.

3.2 Vibrational Spectroscopy and Normal Coordinate Analysis. Tolman and co-workers reported the N–O stretching vibrations ν (N–O) for a number of [Cu(Tp)(NO)] type complexes (Tp[−] = substituted hydrotris(pyrazolyl)borate),^{28,48} but the critical Cu–NO stretch ν (Cu–NO) could not be identified. Clearly, the instability of the complexes renders the determination of high-quality vibrational data difficult. Figures S3 and S6 show the IR data of **1**, which show ν (N–O) at 1698 cm^{−1} and ν (Cu–NO) at 365 and 338 cm^{−1}. These bands shift to 1627, 358, and 332 cm^{−1} upon ¹⁵N¹⁸O substitution (cf. Table 1), respectively. To determine quantitative measures for the N–O and Cu–NO bond strengths and to explore the reason for the split appearance of ν (Cu–NO), a quantum-chemistry-centered normal-coordinate analysis (QCC-NCA)³⁷ was performed. As shown in Table 2, excellent agreement with experiment has been achieved, and the [Cu(L3)] skeletal mode that interacts with ν (Cu–NO) has been identified (see Figure S8). Obtained force constants are 12.53 (N–O) and 1.31 mdyn/Å (Cu–NO), where the latter value corresponds to a weak Cu–NO bond in agreement with the labile attachment of NO. In comparison, **2** exhibits ν (N–O) at 1742 cm^{−1}, and ν (Cu–NO) is tentatively assigned to the bands at 369 and 344 cm^{−1} (cf. Figures S4 and S7). Due to the poor quality of the far-infrared (FIR) data of

(44) Dunning, T. H., Jr.; Hay, P. J.; Schaefer, H. F., III. *Modern Theoretical Chemistry*; Plenum: New York, 1976.

(45) Hay, P. J.; Wadt, W. R. *J. Chem. Phys.* **1985**, *82*, 270–283 and 299–310.

(46) Wadt, W. R.; Hay, P. J. *J. Chem. Phys.* **1985**, *82*, 284–290.

(47) Neese, F. *ORCA*, version 2.2; Max-Planck Institut für Bioanorganische Chemie: Mülheim/Ruhr, Germany, 2004.

(48) Schneider, J. L.; Carrier, S. M.; Ruggiero, C. E.; Young, V. G., Jr.; Tolman, W. B. *J. Am. Chem. Soc.* **1998**, *120*, 11408–11418.

Table 1. Comparison of Experimental and Calculated Properties of Cu(I)–NO Complexes

complex	geometric parameters [Å]			vibrations [cm ⁻¹]		force constants ^b	
	Cu–NO	N–O	Cu–N–O ^a	$\nu(\text{N–O})$	$\nu(\text{Cu–NO})$	$f(\text{N–O})$	$f(\text{Cu–NO})$
[Cu(Tp ^{t-Bu})(NO)] ^c	1.759(6)	1.108(7)	163.4(6)	1712			
[Cu(L3)(NO)]	1.779(4)	1.083(7)	171.9(5)	1698	365/(338)	12.53	1.31
[Cu(L3′)(NO)](ClO ₄)	1.786(5)	1.035(8)	176.4(10)	1742	369/(344)		
$\Delta(\text{L3′–L3})$	0.007	-0.048	4.5	44	4		
			BP86/TZVP: full opt				
[Cu(L0)(NO)]	1.812	1.188	148	1707	456/(458)	12.72	2.22
[Cu(L0′)(NO)] ⁺	1.818	1.178	147	1758	453	13.56	2.14
$\Delta(\text{L0′–L0})$	0.006	-0.010	-1	51	-3	0.84	-0.07

^a In degrees. ^b In [mdyn/Å]. ^c Reference 28.

Table 2. Comparison of Experimental and QCC-NCA Vibrational Frequencies [cm⁻¹] and of QCC-NCA and Calculated (DFT) Force Constants [mdyn/Å]

mode	expt		QCC-NCA		force constants <i>f</i>	
	n.a.i. ^a	¹⁵ N ¹⁸ O	n.a.i. ^a	¹⁵ N ¹⁸ O	QCC-NCA	calculated ^b
	[Cu(L3)(NO)] (1)					
$\nu(\text{N–O})$	1698	1627	1700	1625	12.530	12.72
$\nu(\text{Cu–NO})$ ^c	365	358	366	363	1.310	2.22
	338	332	335	330		

^a n.a.i. = natural abundance isotopes. ^b Calculated with BP86/TZVP.

^c The Cu–NO stretch is mixed with a [Cu(L3)] core bending mode; see Experimental Section. Free NO: $\nu(\text{N–O}) = 1876 \text{ cm}^{-1}$; $f_{\text{N–O}} = 15.49 \text{ mdyn/Å}$.⁵²

359 this very labile complex, a QCC-NCA was not attempted. In
 360 previous studies of Cu(I)–carbonyl complexes, we determined
 361 that anionic “borate” type ligands like L3⁻ lead to more electron-
 362 rich copper centers compared to analogous neutral “methane”
 363 ligands like L3′.³¹ Hence, the borate complexes give rise to
 364 distinctively stronger π -backbonding interactions with CO,
 365 which is reflected by stronger Cu–CO and weaker C–O bonds.
 366 CO is therefore the perfect probe to measure the electronic
 367 properties of Cu(I).^{31,48} *This trend is not followed by NO:* as
 368 evident from the vibrational data on **1** and **2**, and calculations
 369 on corresponding models as shown in Table 1, there is only a
 370 slight increase in the strength of the backbond in **1** compared
 371 to **2**. Correspondingly, the difference in (calculated) Cu–NO
 372 force constants is <0.1 mdyn/Å, and $\nu(\text{Cu–NO})$ are similar.
 373 This small change in backbonding can only account for part of
 374 the observed large difference in the N–O bond strengths of **1**
 375 and **2**. The further weakening of the N–O bond in **1** is actually
 376 due to a stronger polarization of the π orbitals of NO and, hence,
 377 a true second coordination sphere effect in the case of **1**, due to
 378 the presence of the extra negative charge on the L3⁻ ligand.
 379 This is evident from an inspection of the corresponding
 380 molecular orbitals from the DFT calculations (vide infra).
 381 Importantly, the calculations reproduce the difference in vibra-
 382 tional properties very well (compare $\Delta(\text{L3′–L3})$ and $\Delta(\text{L0′–L0})$
 383 in Table 1). Interestingly, the experimental trend in $\nu(\text{N–O})$
 384 itself, $[\text{HB}(\text{3-}\text{CF}_3\text{-5-}\text{CH}_3\text{pz})_3]^- \geq \text{L3}^- > [\text{HB}(\text{3,5-}\text{Ph}_2\text{pz})_3]^-$
 385 $> [\text{HB}(\text{3-}t\text{-Bupz})_3]^- > \text{L3}^-$, is similar to the trend observed
 386 for $\nu(\text{C–O})$ in the carbonyl complexes.^{31,48}

387 **3.3. EPR Spectroscopy and Electronic Structure.** Copper–
 388 nitrosyl [CuNO]¹¹ adducts afford an $S = 1/2$ ground state with
 389 characteristic EPR spectra: complex **3** exhibits $g_{\perp} = 1.99$ and
 390 $g_{\parallel} = 1.83$ and a large ¹⁴N hyperfine coupling $^{\text{N}}A_{\perp} = 81 \text{ MHz}$
 391 as published by Tolman and co-workers.²⁸ In comparison, **1**
 392 shows $g_{\parallel} = 1.79\text{--}1.80$, and $^{\text{N}}A_{\perp} = 98 \text{ MHz}$ as shown in Figure
 393 3.⁴⁹ Comparison with the calculated *g* values in Table 3 reveals

Table 3. Calculated and Observed EPR Parameters of Cu(I)–NO Adducts

complex	EPR parameters		Cu–N–O angle	ΔE [kcal/mol]	
	g_{\perp}	g_{\parallel}		BP86	B3LYP
Cu ^I –NO in CuNIR ^a	2.046	1.926	?		
	1.998				
[Cu(Tp ^{t-Bu})(NO)] ^b	1.99	1.83	163.4(6)		
[Cu(L3)(NO)]	~1.97	~1.80	171.9(5)		
[Cu(L0)(NO)] - calcd	2.019	1.902	154	0	0
	2.012				
[Cu(L0)(NO)] - 172° ^c	2.019	1.783	172	+0.8	+2.7
	1.999				
[Cu(L0′)(NO)] ⁺ - calcd	2.015	1.907	155	0	0
	2.012				
[Cu(L0′)(NO)] ⁺ - 174° ^c	2.016	1.786	174	+0.8	+0.7
	1.998				

^a Reference 26. ^b Reference 28. ^c Obtained from the fully optimized structure (BP86/TZVP) by changing the Cu–N–O angle as indicated.

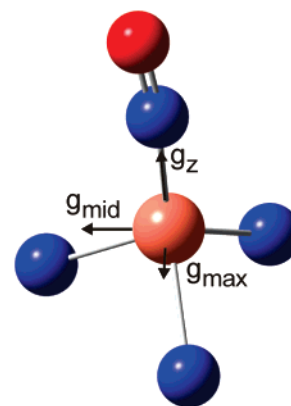
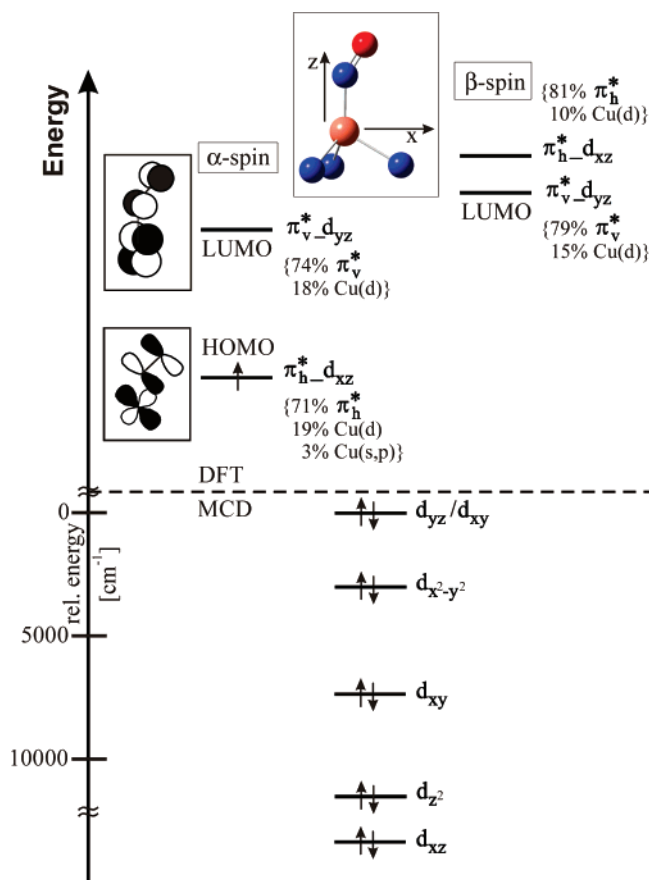


Figure 5. Calculated *g* tensor orientation for [Cu(L0)(NO)] with the Cu–N–O angle set to 172° (BP86/TZVP). In this case, g_z (g_{\parallel}) equals g_{min} exactly, whereas g_{mid} and g_{max} approximately correspond to g_x and g_y in the coordinate system shown in Scheme 2, top. Note that g_z is collinear to the Cu–N bond.

an interesting trend for the *g* values of Cu(I)–nitrosyls, where
 $g_z = g_{\parallel}$ (z points along the Cu–N(O) bond as indicated in Figure
 5) is very sensitive to the Cu–N–O angle. In order to
 investigate this further, *g* values were calculated for model [Cu–
 (L0)(NO)] varying the Cu–N–O angle, and these results are
 shown in Figure 4. Using the known Cu–N–O angle of 163°
 for **3**, $g_z = 1.833$ is predicted from Figure 4, which is in excellent
 agreement with the experimental value of 1.83 for this com-
 pound. In comparison, the Cu(I)–NO adduct of CuNIR shows
 very different *g* values as listed in Table 3,²⁶ indicative of a

(49) Unfortunately, we did not obtain good EPR data for **2**, due to decomposition.

Scheme 2^a

^a Frontier orbitals of the fully optimized model [Cu(L0)(NO)] obtained from BP86/TZVP (upper part, spin unrestricted). The relative d-orbital energies are obtained from MCD (lower part, paired electrons).

404 different coordination geometry (see Discussion). The obtained
 405 hyperfine parameters $N_{A_{\perp(x)}}$ > 80 MHz for **1** and **3** are very
 406 large and indicate *significant radical character on the bound*
 407 *NO ligand*. Scheme 2, top shows the binding scheme for **1**
 408 obtained from the DFT calculations. For the theoretical treat-
 409 ment, simplified model systems [Cu(L0)(NO)] and [Cu(L0')-
 410 (NO)](ClO₄) have been applied for **1** and **2**, respectively, as
 411 described in the Experimental Section. Different functional/basis
 412 set combinations have been used for the geometry optimizations
 413 as listed in Table S2. In general, good agreement with the
 414 experimental structures has been obtained, with exception of
 415 the Cu–N–O angle. In fact, none of the methods applied was
 416 able to reproduce the experimental value for this parameter. For
 417 further discussion, the BP86/TZVP results are used (cf. Tables
 418 1–3). As indicated in Scheme 2, the singly occupied π^* orbital
 419 of NO (α - π_h^*) is located in the Cu–N–O plane. Due to the
 420 fact that all copper(I) d orbitals are fully occupied, the overlap
 421 of this orbital with d_{xz} is actually repulsive for α -spin. This
 422 is compensated by the backbond between d_{xz} and the empty β - π_h^*
 423 orbital. The strength of this interaction is best estimated from
 424 the corresponding antibonding combination, $\pi_{h-d_{xz}}^*$, which has
 425 10% metal d character. Altogether, this leads to a spin density
 426 distribution of +0.9 on NO and +0.1 on copper, in agreement
 427 with earlier calculations.²⁷ Hence, the calculations clearly favor
 428 the Cu(I)–NO(radical) over the Cu(II)–NO[−] electronic descrip-
 429 tion in agreement with EPR and MCD (vide infra) results. The
 430 other π^* orbital, π_v^* (located perpendicular to the Cu–N–O

plane), is unoccupied and undergoes further backbonding
 interactions. The corresponding antibonding combinations show
 about 15–20% d admixture, which corresponds to a quite strong
 interaction. However, comparison of the calculated Cu–NO
 force constant of 2.215 mdyne/Å with the experimental value of
 1.310 mdyne/Å shows that the strength of this interaction is
 clearly overestimated in the calculations, which is not unusual.³⁷
 The π_v^* - d_{yz} backbond shows small spin-polarization effects
 (where the β -spin interaction is stronger), which somewhat
 lowers the total spin density on copper. This effect depends
 strongly on the applied DFT functional, which makes the
 prediction of very accurate total spin densities difficult. This
 bonding scheme is in agreement with the observed, large $N_{A_{\perp(x)}}$
 value and also explains the observed strong dependence of g_z
 on the Cu–N–O angle (cf. Figure 4). This relates to the spin-
 orbit coupling matrix element $2\lambda\langle\pi_{h-d_{xz}}^*|L_z|\pi_{v-d_{yz}}^*\rangle/\Delta E$ in the
 theoretical equation for the g shifts from perturbation theory,⁵⁰

$$g_i = g_e - 2\lambda \sum_{n \neq 0} \frac{\langle\Psi_0|L_i|\Psi_n\rangle\langle\Psi_n|L_i|\Psi_0\rangle}{E_n - E_0}$$

which maximizes at 180° when $\pi_{h-d_{xz}}^*$ and $\pi_{v-d_{yz}}^*$ become
 almost degenerate ($\Delta E \approx 0$).

3.3. Electronic Spectra. In previous work,²⁸ UV–vis absorp-
 tion and MCD data above 300 nm have been presented for **3**,
 but no detailed analysis of the data has been provided. The
 characteristic absorption band at 494 nm for **3** has been loosely
 assigned to a Cu(I)-d to NO- π^* transition, but no further details
 are provided. As shown in Figure S9, this feature is observed
 at 506 nm ($\epsilon = 960 \text{ M}^{-1} \text{ cm}^{-1}$) for **1** and at 458 nm ($\epsilon = 1140$
 $\text{M}^{-1} \text{ cm}^{-1}$) for **2**. We have reinvestigated complex **1** using low-
 temperature MCD spectroscopy in silicone mulls, which allows
 for the measurement of high-quality data. Based on the spectrum
 obtained shown in Figure 6, five electronic transitions can
 actually be identified in the electronic spectra of the Cu(I)–
 NO complex (bands 2–6), and an additional weak feature is
 identified at 810 nm. These transitions can be assigned for the
 first time with the help of TD-DFT calculations. Application
 of B3LYP/TZVP and the experimental Cu–N–O angle of 172°
 reproduces the general shape of the electronic spectra well, but
 all transitions appear shifted to lower energy by $\sim 4000 \text{ cm}^{-1}$
 (cf. Figure 6). This is due to the fact that all bands observed in
 the visible region correspond to CT transitions of type $d \rightarrow \pi^*$,
 which are usually obtained too low in energy by TD-DFT. The
 tentative assignments as shown in Figure 6 are further supported
 by the appearance of pseudo-A term signals in the spectra (pairs
 of bands 2–3 and 4–5/6; see Table S3), which are in agreement
 with the calculated polarizations of these transitions. In order
 for a pseudo-A term to arise, two electronic transitions with
 orthogonal electric transition dipole moments are needed, which
 are coupled by spin–orbit coupling. These requirements are
 fulfilled by the given assignment (see Table S3). Based on these
 results, the medium strong absorption band of the Cu(I)–NO
 complexes in the visible region around 500 nm is due to $d \rightarrow$
 π_v^* type CT transitions into the unoccupied π_v^* orbital of NO
 (bands 2–5, cf. Figure 6). The observed transition energies allow
 for the determination of the relative energies of the correspond-

(50) Lever, A. B. P.; Solomon, E. I. *Ligand Field Theory and the Properties of Transition Metal Complexes*. In *Inorganic Electronic Structure and Spectroscopy*; Solomon, E. I., Lever, A. B. P., Eds.; Wiley: New York, 1999; Vol. 1.

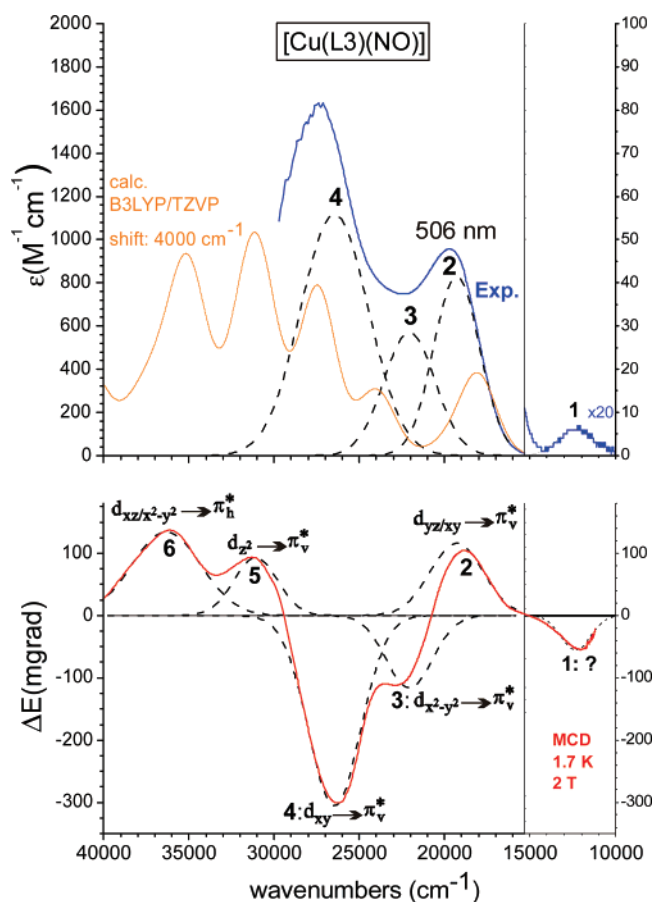


Figure 6. UV-vis (top) and MCD spectrum (bottom) of **1** including Gaussians obtained from a correlated fit and TD-DFT based assignments. The TD-DFT calculated spectrum is shown in orange (shifted by 4000 cm^{-1} to higher energy).

484 ing four d orbitals of highest energy, as included in Scheme 2,
 485 bottom. The fifth d orbital, d_{xz} , is probably located at lowest
 486 energy in these complexes, due to a strong interaction with the
 487 singly occupied π_h^* orbital of NO. Since the corresponding CT
 488 transition is of $d \rightarrow \pi_h^*$ type (band 6, cf. Figure 6), the relative
 489 energy of this orbital cannot exactly be scaled to the other four
 490 d-orbitals as indicated in Scheme 2. Importantly, the lack of
 491 intense (low-energy) $d-d$ bands in the MCD spectra of **1** is a
 492 further indication that copper has a d^{10} electron configuration,
 493 in agreement with the Cu(I)–NO(radical) description of the end-
 494 on coordinated $\{\text{CuNO}\}^{11}$ complexes elaborated above. This is
 495 further supported by the TD-DFT results. Note that band 1 in
 496 Figure 6 corresponds to an impurity of $[\text{Cu}^{\text{II}}(\text{L3})(\text{ONO})]$, which
 497 shows a very intense MCD transition in this area.¹⁸ The obser-
 498 vation of a very small amount of Cu(II) impurity is in agreement
 499 with corresponding, very weak features in the EPR spectra that
 500 account for about 5% of the total copper concentration.

501 Discussion

502 In this paper, two new crystal structures of mononuclear end-
 503 on Cu(I)–NO complexes are presented, and the first detailed
 504 spectroscopic analyses (vibrational and electronic) of this type
 505 of complexes are provided. Experimental force constants for
 506 $[\text{Cu}(\text{L3})(\text{NO})]$ are 12.53 $\text{mdyn}/\text{\AA}$ (N–O) and 1.31 $\text{mdyn}/\text{\AA}$
 507 (Cu–NO); the latter value is in agreement with the very labile
 508 Cu–NO bond in these systems. In comparison, the correspond-
 509 ing complex with a tris(pyrazolyl)methane ligand has a stronger

N–O bond due to a second coordination sphere effect. The EPR
 510 spectrum of $[\text{Cu}(\text{L3})(\text{NO})]$ is indicative of the Cu(I)–NO-
 511 (radical) electronic structure of the complexes in agreement with
 512 the DFT results. Interestingly, the g_z value correlates very well
 513 with the geometric structure of the Cu–N–O unit and decreases
 514 upon increase of the Cu–N–O angle. Finally, high-quality
 515 MCD spectra of $[\text{Cu}(\text{L3})(\text{NO})]$ are presented and assigned using
 516 TD-DFT calculations. These results provide the first in-depth
 517 assignment of the electronic spectra of the end-on $\{\text{CuNO}\}^{11}$
 518 species. In particular, the observed CT absorption band in the
 519 visible region is due to $d \rightarrow \pi_v^*$ type transitions. Based on the
 520 MCD results, an approximate determination of the d-orbital
 521 energy scheme for $[\text{Cu}(\text{L3})(\text{NO})]$ is possible. Importantly, the
 522 lack of intense low-energy $d-d$ bands in the MCD spectra is a
 523 further indication that copper has a d^{10} electron configuration,
 524 in agreement with the Cu(I)–NO(radical) description of the
 525 complexes.

In summary, based on the experimentally calibrated electronic
 527 structure description of end-on Cu(I)–NO complexes elaborated
 528 here, and in agreement with results published previously,^{27,28} it
 529 is therefore now demonstrated that the Cu(I)–NO unit has to
 530 be described as Cu(I)–NO(radical).
 531

The detailed spectroscopic characterization of end-on bound
 532 Cu(I)–NO complexes provided in this work allows us to draw
 533 further conclusions about the Cu(I)–NO intermediate observed
 534 by Scholes and co-workers for CuNIR in solution.²⁶ From their
 535 EPR and ENDOR results, it is not clear whether this species
 536 has end-on or side-on coordinated NO. Although the crystal
 537 structure of Murphy and co-workers shows side-on bound NO,²³
 538 others have speculated that this structure is an “artifact” observed
 539 in the crystal but that this binding mode does not exist in
 540 solution. This opinion is supported by recent DFT calculations
 541 on the CuNIR active site, which predict that the end-on geometry
 542 is more stable by about 7 kcal/mol compared to the side-on
 543 bound species.²¹ These contradictory findings pose the important
 544 question whether the side-on coordination mode of NO to Cu-
 545 (I) is feasible or not. As we have demonstrated in this paper,
 546 the EPR g_z value of the Cu(I)–NO species shows a strong
 547 correlation with the Cu–N–O angle. Hence, our EPR results
 548 in comparison with the data obtained by Scholes and co-workers
 549 for the Cu(I)–NO complex of CuNIR (cf. Figure 4) do in fact
 550 support a strongly bent or even side-on coordination of NO in
 551 the enzyme. As shown in Table 3, the end-on bound Cu(I)–
 552 NO model complexes show g_z around 1.83, whereas, in the case
 553 of CuNIR, g_z is found at 1.93. Based on this, we believe that
 554 the Cu(I)–NO intermediate of CuNIR generated in the presence
 555 of low concentrations of NO does in fact show a strongly bent
 556 to side-on binding mode of NO. How is it possible, though,
 557 that the enzyme behaves so differently than the model complexes
 558 studied so far? A first indication as to why this is in fact possible
 559 comes from recent DFT results of Wasbotten et al.,²⁷ which
 560 show that the type of coligand bound to copper actually has a
 561 large influence on the relative energies of the end-on and side-
 562 on coordinated species. In order to further investigate this point,
 563 we have performed DFT geometry optimizations on the CuNIR
 564 active site with bound NO, where the three histidines are held
 565 in position by fixing their anchor C atoms (of the CH_3 groups)
 566 in space. For these calculations, the BP86/TZVP method has
 567 been applied again, which produces reasonable structures for
 568 the model complexes. As shown in Figure 7, the obtained Cu-
 569

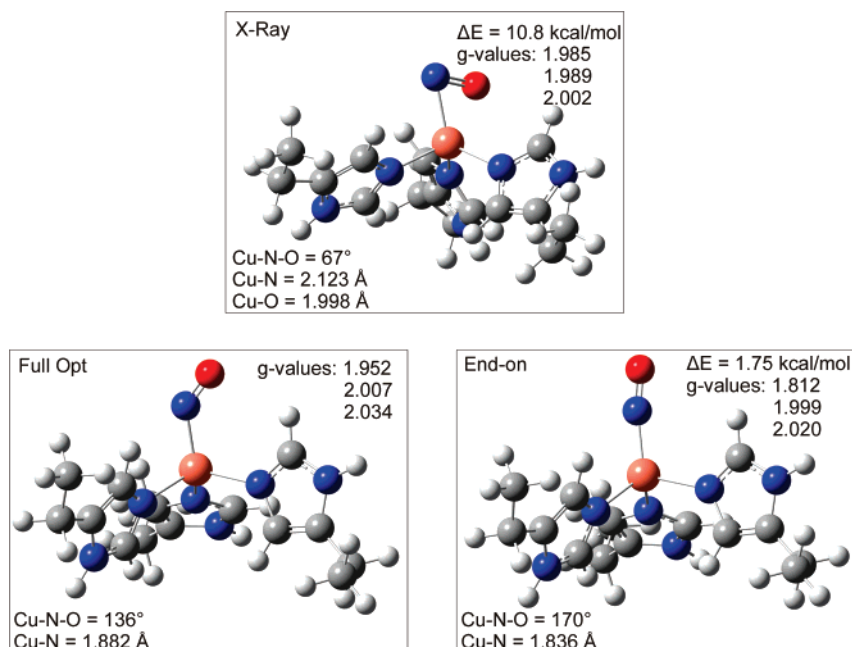


Figure 7. Geometry optimized (BP86/TZVP) structures of Cu(I)–NO species in CuNIR. For these calculations, the anchor atoms (C atoms of the artificial CH₃ groups) of the three histidines were frozen at their crystallographic positions. Top: optimized structure with frozen Cu–N–O angle at the crystallographically determined value.²³ Bottom, left: fully optimized structure. Bottom, right: optimized structure with frozen Cu–N–O angle at a value typical for the model complexes. Listed are relative energies with respect to the fully optimized structure and calculated *g* values for the three structures (BP86/TZVP).

570 (I)–NO geometry from this calculation shows a Cu–N–O angle
 571 of 136° (cf. Figure 7, bottom left), which is intermediate between
 572 end-on (>160°; from the model complexes) and side-on (71°;
 573 from Murphy’s structure). We have further generated end-on
 574 and side-on bound structures for CuNIR by fixing the Cu–
 575 N–O angle at 170° and 67°, respectively, and reoptimization
 576 of the structures. The resulting geometries are shown in Figure
 577 7 top and bottom right. To test whether these three structures
 578 also follow the trend in *g_z* values as described above, we have
 579 then calculated the *g* tensors for the three binding modes.
 580 Importantly, as shown in Figure 7, the general trend in *g* values
 581 is in fact followed by the CuNIR models. Based on these results,
 582 two important conclusions can be drawn:

583 (a) the side-on coordination of NO to copper(I) is reasonable
 584 and depends on the coligand(s) bound to copper;

585 (b) the EPR parameters of the Cu(I)–NO species of CuNIR
 586 as determined by Scholes and co-workers²⁶ do in fact reflect a
 587 strongly bent or side-on coordination of NO to copper(I).

588 Comparison of the calculated *g* tensors with the *g* values
 589 obtained by Scholes and co-workers shows in fact the best
 590 agreement between the fully optimized structure (Cu–N–O
 591 angle = 136°; cf. Figure 7, bottom left) and the experimental
 592 data. However, the calculated difference in *g* values between
 593 this structure and the side-on bound species is relatively small,
 594 so it would be unjustified to claim that the fully optimized
 595 structure exactly reflects the Cu(I)–NO geometry present in
 596 the enzymatic species detected in solution. Nevertheless, the
 597 results clearly indicate that the Cu(I)–N–O unit is strongly bent
 598 in the enzyme in solution and not linear like in the model
 599 complexes.

600 In summary, the geometry of the Cu(I)–NO subunit in
 601 proteins and model complexes has a much larger flexibility in
 602 terms of the coordination mode of NO and the Cu–N–O angle
 603 than previously anticipated from model complex studies. These
 604 results are also in agreement with the crystal structure of NO
 605 bound amine oxidase, which shows a Cu(I)–N–O angle of 117°
 606 (assuming that this species corresponds to a Cu(I)–NO complex,
 607 which, however, is somewhat unclear in this case).⁵¹

608 **Acknowledgment.** In memory of Swiatoslaw (Jerry) Trofi-
 609 menko, the pioneer of scorpionate ligands. This work was
 610 supported by the Grant-in-Aid for Scientific Research (B) (No.
 611 17350043) from the Japan Society of the Promotion of Science
 612 (to K.F.) and the Fonds der Chemischen Industrie (FCI) (to F.P.
 613 and N.L.).

614 **Supporting Information Available:** Complete ref 39, crystal-
 615 lographic data (Table S1), complete atomic labels (Figures S1
 616 and S2), vibrational (IR) and electronic absorption spectra for
 617 **1** and **2** (Figures S3–S7, S9), table of DFT geometry optimized
 618 structures and vibrational frequencies for models of **1** and **2**
 619 using different combinations of functionals and basis sets (see
 620 Experimental Section) (Table S2), table of the results of TD-
 621 DFT calculations for **1** (Table S3). This material is available
 622 free of charge via the Internet at <http://pubs.acs.org>.

JA075071D

623

- (51) Wilmot, C. M.; Hajdu, J.; McPherson, M. J.; Knowles, P. F.; Phillips, S. E. V. *Science* **1999**, *286*, 1724–1728.
 (52) Fadini, A.; Schnepel, F.-M. *Schwingungsspektroskopie*; Thieme Verlag: Stuttgart, 1985.

Chapter 8

Summary

In this thesis, the syntheses of iron-porphyrin NO complexes as models for NO bound heme proteins are presented. Their spectroscopic properties, electronic structures, and reactivities are investigated in detail using spectroscopic methods correlated to quantum-chemical calculations. The overall work done in this thesis gives further insight into the active site structures, properties and mechanisms of heme proteins present in biological systems such as bacterial NOR, P450nor, soluble guanylate cyclase, nitric oxide synthase, and nitrophorins. The results obtained in these studies are summarized in the following.

The electronic structures of five-coordinate (5C) $[\text{Fe}^{\text{II}}(\text{TPP})(\text{NO})]$ and six-coordinate (6C) $[\text{Fe}^{\text{II}}(\text{TPP})(\text{MI})(\text{NO})]$ ferrous heme nitrosyl complexes are explored using MCD spectroscopy coupled to DFT calculations. In the 5C case, the MCD spectrum is dominated by the paramagnetic **C**-term contributions. This indicates that a significant amount of spin density of the unpaired electron is located on the formally low spin iron(II) center. On the other hand, in the 6C case, the spectrum is dominated by the temperature independent **A** and **B** terms. This shows that the unpaired electron spin density is mostly located on the NO unit in the 6C case, which leads to the temperature-independent MCD spectrum of diamagnetic low-spin Fe(II)-porphyrins. DFT calculations show a strong Fe-NO σ bond mediated by the singly occupied π^* orbital of NO and the empty d_{z^2} orbital of low-spin Fe(II) in the 5C. This leads to a large transfer of spin density from the NO ligand to Fe(II) corresponding to an electronic structure with noticeable Fe(I)-NO⁺ character. In the six-coordinate complex, on the other hand, the spin density is pushed back from the iron toward the NO ligand resulting in an Fe(II)-NO(radical) type electronic structure. The MCD and DFT results are also useful for evaluating the EPR spectra of five- and six-coordinate Fe(II)-porphyrin NO adducts, which are characteristically different.

Axial ligation experiments show very weak binding of N-donor ligands to five-coordinate $[\text{Fe}(\text{TPP}^*)(\text{NO})]$ complexes. Corresponding free binding energies ΔG° range between -1 and -5 kcal/mol. We have further investigated the binding of N-donor ligands to $[\text{Fe}(\text{TPP}^*)(\text{NO})]$ complexes by ¹H NMR titrations. In this way, the ¹H NMR spectra of 5C

and 6C iron(II) porphyrin NO adducts are assigned for the first time. These results provide a direct evidence that the addition of larger amounts of N-donor ligands to the 5C complexes [Fe(TPP*)(NO)] not only leads to the formation of the 6C complex [Fe(TPP*)(L)(NO)], but also facilitates the formation of the diamagnetic complexes [Fe(TPP*)(L)₂]. Importantly, this indicates that binding of an N-donor ligand *weakens* the Fe-NO bond. This is further confirmed by vibrational spectroscopy coupled to normal coordinate analysis (QCC-NCA), which allows for the determination of force constants of the Fe-NO subunit. The obtained force constants for the Fe-NO subunit are 12.53 (N-O) and 2.98 mdyn/Å (Fe-NO) for the five-coordinate compared to 11.55 (N-O) and 2.55 mdyn/Å (Fe-NO) for the six-coordinate complex. This is in agreement with the MCD result that indicates a distinct decrease of the spin density on iron in the six-coordinate case, which corresponds to a decrease of the Fe-NO covalency and hence, bond strength. The increased spin density on NO in the six-coordinate complex is advantageous for the proposed N-N bi-radical coupling mechanism of NorBC.

We have also experimentally and computationally investigated the properties of the ferric heme nitrosyls. In this study, the mechanism and energetics of NO binding to ferric hemes and the possible variation in electronic structure of the formed complexes is investigated in detail using model systems and DFT calculations. The six-coordinate model system [Fe^{III}(TPP)(MI)(NO)](BF₄) (**1**; TPP = tetraphenylporphyrin, MI = 1-methylimidazole) has been synthesized and characterized using vibrational spectroscopy coupled to isotope substitution. The electronic structure of the ferric six-coordinate complex **1** is analyzed in this study using the model [Fe(P)(MI)(NO)]⁺ (P = porphine ligand). The Fe-NO interaction is dominated by π backbonding between two d_{π} orbitals of the metal and two empty π^* orbitals of NO⁺. The calculated formation energy of the ferric heme NO adduct is about -4 kcal/mol. This value is relatively low, but in agreement with the experimentally determined complex formation constants in the 10³ to 10⁵ M⁻¹ range, and the observed tendency of these complexes to lose NO. In comparison, a complex formation energy of -11.4 kcal/mol is obtained in the ferrous case. These calculations show that the formation of nitrosyl complexes is energetically more favorable for ferrous compared to ferric hemes by ~7.5 kcal/mol. This number is equivalent to a difference in binding constant by a factor of 3 x 10⁵. This is in excellent agreement with the experimentally determined trend in dissociation rate constants: for ferric heme systems, dissociation rate constants range from 0.65 to 40 s⁻¹,

leading to a relatively small binding constant for NO ($K_{\text{eq}} = 10^3$ to 10^5 M^{-1}). In contrast, Fe(II) systems display dissociation rate constants that are in the order of 10^{-4} s^{-1} , leading to very large binding constants for NO ($K_{\text{eq}} = 10^{11}$ to 10^{12} M^{-1}). However, this result contradicts the Fe-NO bond force constant, which is larger for the Fe(III)-NO complex compared to Fe(II)-NO, indicating a stronger Fe-NO bond in the ferric systems. This contradiction is explained based on the calculated complex formation energies. Since the ferric nitrosyl complex is low-spin, the force constant is a measure for the steepness of the *low-spin* potential energy surface, where the formation energy of the NO complex is -9.5 kcal/mol, corresponding to a strong bond. However, the actual binding of the NO ligand to the iron center is accompanied by a spin transition, since the initial five-coordinate reactant complex is actually high-spin. Thus the binding constant is related to the energy of the high-spin state.

NO bound ferrous and ferric heme centers with axial thiolate coordination are of extraordinary biological importance since they are present in the active sites of fungal nitric oxide reductase (P450nor), nitric oxide synthase (NOS) and *Cimex* nitrophorins. Despite their importance, only two bioinorganic synthetic model complexes are available in the literature for these enzymes to date. The reason is attributed to the high reactivity of the thiolates towards the Fe-NO center, and also to the general unstability of the thiolate ligated Fe-NO complexes. In order to obtain more insight into the vibrational properties and electronic structures of these enzyme active sites, we have synthesized a series of six-coordinate Fe(II)-NO adducts $[\text{Fe}^{\text{II}}(\text{TPP})(\text{SR})(\text{NO})]^-$ (TPP = tetraphenylporphyrin) with substituted thiophenolates and tetrahydrothiophene as models. These were investigated in solution using electron paramagnetic resonance (EPR) spectroscopy. From the obtained g values and ^{14}N hyperfine pattern of the NO ligand, it is concluded that the coordination of thiophenolates to the Fe(II) center is weak in comparison to the corresponding 1-methylimidazole adduct and ferrous NO adducts of P450nor and P450cam. The interaction of the Fe(II)-NO center with different thiolate ligands, SR, has also been explored computationally. The six-coordinate model complex $[\text{Fe}(\text{P})(\text{SR})(\text{NO})]^-$ (P = porphine ligand) has an interesting electronic structure where NO acts as a medium strong σ donor and π acceptor ligand. DFT calculations show the axial alkyl thiolates have an even stronger effect on the Fe-NO bond than N-donors, leading to a further weakening of the Fe-NO bond, and thus a further increase in spin density on the coordinated NO. The observed spin density of larger

than 1 on NO can be interpreted as an admixture of Fe(III)-NO⁻ character into the Fe(III)-NO(radical) ground state of these complexes.

Correspondingly, the coordination behavior of thiolates with Fe(III)-NO centers has been explored using UV-vis, vibrational, and NMR spectroscopy. For this study, we have synthesized the precursor complex [Fe(TPP)(SPhF₄)], and allowed it to react at low temperature with one equivalent of NO. The progress of the reaction was monitored by in-situ UV-vis absorption spectroscopy. The Soret band of the precursor complex [Fe(TPP)(SPhF₄)] at 414 nm decreases in intensity with the concomitant appearance of a new Soret band at 439 nm. In addition, bands at 380 nm and 515 nm of the starting material decrease in intensity, whereas a new band is observed at 556 nm. This corresponds to the formation of the six-coordinate NO adduct [Fe^{III}(TPP)(SPhF₄)(NO)], as can be seen by comparison with absorption data of the Suzuki complex [Fe^{III}(SR)(NO)]. Moreover, isosbestic points at 426, 463 and 545 nm suggest a clean conversion of the starting material to the product without further intermediates. However, a complete conversion to the product is not achieved here in contrast to the Suzuki complex. The initially formed NO complex [Fe^{III}(TPP)(SPhF₄)(NO)] undergoes either spontaneous or NO-assisted decomposition to the iron(III) nitro-nitrosyl complex, [Fe^{III}(TPP)(NO)(NO₂)]. Our experiments indicate that the former process is slow, while the latter occurs much faster. In the course of the reaction, the nitro-nitrosyl complex is formed by reaction of the intermediate [Fe(TPP)(NO)] with higher NO_x species either present as impurities in the NO gas or generated by addition of small quantities of air. Subsequent decomposition of [Fe^{III}(TPP)(NO)(NO₂)] ultimately leads to the nitrate complex [Fe^{III}(TPP)(NO₃)]. Using carefully purified NO gas and very inert reaction conditions, we were able to isolate a thiolate coordinated ferric porphyrin NO complex. However, the yield of the product is small, and it is only obtained as an impure solid. The NO stretching frequency of this complex is observed at 1823 cm⁻¹. Thus, the isolation of the six-coordinate complex [Fe^{III}(TPP)(SPhF₄)(NO)] as a pure solid is extremely challenging and could not be achieved under these conditions.

In addition, we have started to design and synthesize a complete model for the NorBC active site by employing an iron(II)-porphyrin covalently attached to a non-heme iron(II) complex. However, a complete functional modeling of the NorBC active site is challenging due to the following reasons: Firstly, the axial N-donor ligand is weakly bound to the heme-NO center. Hence, a large amount of N-donor ligand is necessary to drive the reaction to

form the corresponding six-coordinate complex in solution. Secondly, addition of excess base causes denitrosylation. The base promoted loss of NO from the complex, leads to the formation of $[\text{Fe}^{\text{II}}(\text{TPP}^*)(\text{L})_2]$. These issues have been investigated in detail using UV-vis and NMR binding experiments on substituted iron porphyrin NO complexes with pyridine and 1-methylimidazole as N-donor ligands. Therefore, a complete NorBC model first requires optimization of the heme portion. In order to obtain a stable 6C complex in solution without excess base present, we have synthesized a series of iron-porphyrin NO compounds with covalently attached axial N-donor ligands $[\text{Fe}^{\text{II}}(\text{TPP}^*)(\text{NO})(\text{L})]$ (L = pyridine or imidazole linker), and investigated the properties of these compounds using several spectroscopic methods. These covalently attached N-donor linkers are supposed to “increase the local base concentration” and this way, facilitate binding to the Fe(II)-NO center. Pyridine and imidazole tailed linkers with varying chain lengths and design have been synthesized to delineate the effect of chain length and rigidity on the base binding properties to the Fe(II)-NO center. This allows to compare directly the binding affinity of different linkers with different carbon chains (number or design), and to obtain a better model for the six-coordinate species in solution. The EPR and FT-IR spectrum of $[\text{Fe}(\text{TMP-}m\text{Py})(\text{NO})]$ (TMP-*m*Py = *meta*-pyridyl ligand attached to mesityl porphyrin) show features identical to those observed for the 5C $[\text{Fe}(\text{TPP})(\text{NO})]$ complex. These observations indicate that the pyridyl arm is in fact not coordinated to the Fe-NO unit. These results are also in agreement with the very weak binding affinity of pyridine to Fe-NO observed in the axial ligation titration experiments, as monitored by UV-vis spectroscopy. We concluded that the covalently attached pyridine linker leads to the formation of only 5C species in solution, which suggests a dominant base-off reaction upon NO binding. On the other hand, the C₃ chain imidazole linker, $[\text{Fe}(\text{To-F}_2\text{PP-C}_3\text{IM})(\text{NO})]$, shows weak binding of the linker to the Fe-NO center. In order to determine the influence of the carbon chain length on the base binding properties of the imidazole linked porphyrins NO complexes, we have synthesized the H₂To-F₂PP-C₄IM ligand. This ligand contains one more alkyl carbon (CH₂) group compared to the C₃ linker. However, the NO complex $[\text{Fe}(\text{To-F}_2\text{PP-C}_4\text{IM})(\text{NO})]$ shows similar spectroscopic behavior as the C₃ linker complex, demonstrating that the length of the alkyl chain in the C₃ linker $[\text{Fe}(\text{To-F}_2\text{PP-C}_3\text{IM})(\text{NO})]$ is not the reason for the weak binding of the IM ligand. Finally, in an effort to construct a more rigidly linked porphyrin system, we have synthesized the porphyrin H₂To-F₂PP-BzIM. This ligand design is based on a

fluorosubstituted porphyrin with an attached benzyl imidazolyl arm. The UV-vis spectrum of the corresponding metallated NO complex $[\text{Fe}(\text{To-F}_2\text{PP-BzIM})(\text{NO})]$ shows the Soret maximum band at 427 nm in DMSO. The EPR spectrum shows the characteristic nine line hyperfine splitting, corresponding to the coordination of the axial benzyl imidazole linker to the Fe(II)-NO center. In addition, the $\nu(\text{NO})$ band is observed at 1644 cm^{-1} in the FT-IR spectrum. Interestingly, this value is higher in energy compared to six-coordinate compounds formed with free 1-methylimidazole, where $\nu(\text{NO})$ appears at 1625 cm^{-1} . This indirectly reflects the strength of the Fe-L bond (L = axial ligand) showing that the covalently attached benzyl imidazolyl linker still cannot bind as strongly to the Fe(II)-NO unit as free imidazole. Thus, the concept of the “increased local concentration” of the attached axial ligand is not valid at all in this case. In fact, the binding of the linked imidazole is always weaker compared to free MI.

Lastly, we have synthesized a sophisticated model (heme/non-heme) for NorBC by the coupling of a fluorosubstituted porphyrin to the tridentate chelate dipyridylmethylamine (PBMPA, *N*-(propionic acid)-*N,N*-bis-(dipyridylmethyl)amine). The synthesized ligand $[\text{H}_2\text{To-F}_2\text{PP-PBMPA}]$ was characterized using UV-vis and mass spectrometry. The corresponding diiron-dinitrosyl complex $[\text{Fe}_2(\text{To-F}_2\text{PP-PBMPA})(\text{NO})_2]$ has been synthesized and characterized using UV-vis and FT-IR spectroscopy. The UV-vis spectrum shows the Soret band maximum at 407 nm. The stretching frequencies of NO are observed at 1683 cm^{-1} and 1816 cm^{-1} . These bands are assigned to $\nu(\text{NO})$ of the ferrous heme NO and ferrous non-heme NO component, respectively. Based on FT-IR spectroscopy, it is concluded that the heme and the non-heme centers bind one molecule of NO each. This compound is stable under an inert atmosphere at room temperature. Importantly, the NO reduction was not observed with $[\text{Fe}_2(\text{To-F}_2\text{PP-PBMPA})(\text{NO})_2]$. Further reactions of carboxylic acids with $[\text{Fe}_2(\text{To-F}_2\text{PP-PBMPA})(\text{NO})_2]$ are being carried out in order to drive the N-N bond formation. In addition, the coordination chemistry of non-heme iron complexes with NO is also investigated using TPA and MPBMPA ligands. Furthermore, to investigate the importance of the sixth ligand of the heme NO unit for the NorBC activity, we are currently synthesizing a six-coordinate heme with attached non-heme iron ligand. The precursor ligand, dinitroporphyrin, has been synthesized and characterized in this work using several spectroscopic methods.

9. Curriculum Vitae

PERSONAL INFORMATION:

Date of Birth 04.11.1976
Place of Birth Tellicherry, Kerala, India
Nationality Indian

EDUCATION:

Ph.D., Inorganic Chemistry (Aug 2003- Jan 2008)

Institut für Anorganische Chemie	Department of Chemistry
Universität Kiel	University of Michigan
Kiel, Germany.	Ann Arbor, MI, USA.

Thesis: Model Complexes of Heme Protein NO Adducts: Syntheses, Spectroscopy, Electronic Structures and Reactivity.

Advisor: Prof. Dr. Nicolai Lehnert.

Doctor Father: Prof. Dr. Felix Tuzcek

Master of Science, General Chemistry (1998-2000)

Department of Chemistry
Post Graduate Center
Pondicherry University
India.

Bachelor of Science, General Chemistry (1994-1997)

Department of Chemistry
Tagore Arts College Pondicherry
India.

RESEARCH EXPERIENCE:

Doctoral Research, Universität Kiel, Germany and University of Michigan, USA, Aug **2003**-Jan **2008**.

Junior Research Fellow (Bioinorganic/Supramolecular Chemistry), Department of Chemistry, Indian Institute of Technology Madras, India, **July 2000-2002**.

- Synthesized various substituted electron deficient metalloporphyrins and studied their axial ligation behavior (UV-Vis titration) with bases of varying pK_a to elucidate the effect of substituents on the electron deficiency of the porphyrin macrocycle. Electrochemical redox properties of these porphyrins were measured using cyclic voltammetry.
- Supramolecular hydrogen bonded porphyrinic networks were prepared using carboxy, pyridyl and ester substituted porphyrins and characterized by several spectroscopic technique and single crystal XRD.

Masters Studies, PG center, Pondicherry University, India, **1998-2000**.

- Studied the reaction kinetics for the oxidation of secondary alcohols to ketones using pyridinium chlorochromate as oxidizing agent.
- Determination of CFSE of Ni(II) complexes containing ligands , such as NH_3 , ethylenediamine, DMG, etc. and calculation of the Nephelauxetic parameters.

HONORS:

- Recipient of Pondicherry University chemfab medal for academic excellence in Masters (Chemistry) – 2001.
- Qualified in national graduate aptitude test in engineering – GATE 2000.
- Qualified in council of scientific and industrial research fellowship (CSIR) and Lectureship (LH)- 2000.
- Qualified in graduate record exam (GRE) and TOEFL- 2003.

SKILLS:

- Six years of experience in porphyrin synthesis.
- Bioinorganic model complex design and Synthesis (heme and non-heme)
- Profound efficiency in handling of hygroscopic, air sensitive reagents and reactions (Schlenk technique, glove box, etc.)
- Well versed with various organic synthetic and purification techniques (Preparative TLC, distillation, column chromatography, recrystallization, etc.) backed up with a sound theoretical knowledge.
- Spectroscopic techniques for analyses- good knowledge and experience in the analysis of UV-Vis, IR, Raman, ^1H NMR, ^{13}C NMR, Paramagnetic NMR, Mass (EI, ESI, MALDI), EPR and MCD spectra.
- Good knowledge in retrosynthetic analysis.
- Well acquainted in growing single crystals.
- Computational chemistry (DFT calculations) - energy optimization, evaluation of electronic structure and vibrational properties using Gaussian and Gauss view.
- Capable of collaborative and independent work.
- Proficiency in the handling of computers and various software packages like MS Office, Chem Office, Origin, etc.

ADVANCE COURSES ATTENDED:

- Bioinorganic Chemistry, Coordination Chemistry, Spectroscopy, Quantum Chemical Methods in Inorganic Chemistry, Organometallics, Synthetic Organic Chemistry, Natural Product Synthesis.

CONFERENCE PRESENTATION:

- V. K. K. Praneeth, E. Haupt, N. Lehnert (July-Aug **2005**) SPECTROSCOPIC PROPERTIES AND ELECTRONIC STRUCTURES OF THIOLATE COORDINATE IRON PORPHYRIN NO ADDUCTS. Poster presented at ICBIC 12, July-Aug, University of Michigan, Ann Arbor, MI, USA.
- V. K. K. Praneeth, E. Haupt, N. Lehnert (Nov **2005**) SPECTROSCOPIC PROPERTIES AND ELECTRONIC STRUCTURES OF THIOLATE COORDINATE IRON PORPHYRIN NO ADDUCTS. Poster presented at Doctoral students colloquium, Warnemünde, Germany.

10. Publication List

1. F. Paulat, T. Kuschel, C. Näther, **V. K. K. Praneeth**, O. Sander, N. Lehnert
“Spectroscopic Properties and Electronic Structure of Pentammineruthenium(II) Dinitrogen Oxide and Corresponding Nitrosyl Complexes: Binding Model of N₂O and Reactivity”
Inorg. Chem. **2004**, *43*, 6979-944.
2. **V. K. K. Praneeth**, F. Neese and N. Lehnert
“Spin Density Distribution in Five- and Six-Coordinate Iron(II)-Porphyrin NO Complexes Evidenced by Magnetic Circular Dichroism Spectroscopy”
Inorg. Chem. **2005**, *44*, 2570-2572.
3. **V. K. K. Praneeth**, E. Haupt, N. Lehnert
“Thiolate Coordination to Fe(II)-Porphyrin NO Centers”
J. Inorg. Biochem. **2005**, *99*, 940-948 (Special issue: Heme-Diatomic Interactions, Vol.2). Erratum: *J. Inorg. Biochem.* **2005**, *99*, 1744.
4. F. Paulat, **V. K. K. Praneeth**, C. Näther, N. Lehnert
“Quantum Chemistry Based Analysis of the Vibrational Spectra of Five-Coordinate Metalloporphyrins [M(TPP)(Cl)]”
Inorg. Chem. **2006**, *45*, 2835-2856.
5. **V. K. K. Praneeth**, C. Näther, G. Peters, N. Lehnert
“Spectroscopic Properties and Electronic Properties of Five- and Six-Coordinate Iron(II)-Porphyrin NO Complexes: Effect of Axial N-Donor Ligand”
Inorg. Chem. **2006**, *45*, 2795-2811
6. N. Lehnert, **V. K. K. Praneeth**, F. Paulat
“Electronic Structure of Fe(II)-Porphyrin Nitroxyl Complexes: Molecular Mechanism of fungal Nitric Oxide Reductase (P450nor)”

J. Comput. Chem. **2006**, *27*, 1338-1351 (special issue: Computational Bioinorganic Chemistry).

7. K. Fujisawa, A. Tateda, Y. Miyashita, K. Okamoto, F. Paulat, **V. K. K. Praneeth**, A. Merkle, N. Lehnert
“Structural and Spectroscopic Characterization of Mononuclear Copper(I) Nitrosyl Complexes: End-on versus Side-on Coordination of NO to Copper(I)”
Accepted for publication (*J. Am. Chem. Soc.* **2007**).

8. **V. K. K. Praneeth**, F. Paulat, C. Näther, N. Lehnert
Electronic Structure of Six-Coordinate Iron(III)-Porphyrin NO Adducts: the Elusive Iron(III)-NO(radical) State and its Influence on the Properties of these Complexes”
Manuscript in preparation.

11. Acknowledgements

I would like to express my deep and sincere gratitude to Prof. Dr. Nicolai Lehnert for his valuable guidance. I am greatly indebted to him for the constant encouragement and unfailing support during the tenure of my Ph.D. His unique approach of allowing full rein is a great boon to the ambitious researchers and I consider myself the luckiest of them. His emphasis is always on loving the work rather than working hard, since, loving the work one hardly feels that one works hard. I could bring the best of my efforts inspired by his optimistic way of treating problems and outcomes. Above all he is more than a guide; he is friendly, affectionate and caring. It has been my great privilege to have worked under his support.

I wish to acknowledge my thanks to Prof. Dr. Felix Tuzcek for his valuable suggestions and encouragement in our group seminars.

I thank my beloved parents for their immense affection and care.

My gratitude extends to Dr. Gehard Peters (NMR), Ushi (Raman). I am thankful to Priv-Doz Dr. Christian Näther for his help in solving crystal structures.

I also would like to thank Shannon and Sophia for their care and support during all my studentship in Germany and USA.

I am obliged to my friends Maha, Arun, Vinith, Seenu, Raj, Venkat, Florian, Khoi, Anna, Corinne, Huayang, Klaus, Gerald, Deepa, Harun, Saumen, Tim, and Yuki, for their help, care and support. I wish to thank all my friends of both departments (Kiel and Michigan) who created a pleasant atmosphere and made my stay here a memorable one.

Finally, I would like to thanks the funding agencies, Deutsche Forschungsgemeinschaft (DFG), Germany, and the University of Michigan, USA.

Praneeth

Eidesstattliche Erklärung

Hiermit erkläre ich an Eides statt, dass die vorliegende Abhandlung—abgesehen von der Beratung durch meine Betreuer Herrn Prof. Dr. Nicolai Lehnert und Herrn Prof. Dr. Felix Tuzek- nach Inhalt und Form meine eigene Arbeit ist.

Diese Arbeit hat weder in Auszügen noch in ganzer Form in anderen Prüfungsverfahren vorgelegen.

Koombil Kummaya Praneeth. V